The University Of Sheffield.

DNA BINDING OF METAL COMPLEXES WITH MIXED RECOGNITION MOTIFS. PHOTOPHYSICAL AND BIOPHYSICAL STUDIES.

By Verónica González González

A thesis submitted for degree of doctoral philosophy

Supervisor: Dr Jim A. Thomas
Department of Chemistry
University of Sheffield
May 2006

THESIS CONTAINS

CD

A mi madre, la mejor persona que he conocido, quien me ha inculcado el valor del trabajo y que espero que esté orgullosa de mi.

A mis hermanas

Abstract

New rhodium complexes containing tripodal ligands have been synthesised and their physical properties have been investigated. [Rh(tpm*)Cl_3] has been synthesised and its reaction with pyridyl-based ligands has been studied. These complexes may be convenient building blocks for construction of dinuclear complexes, as they are achiral and coordinative saturated they offer facile routes of synthesis.

Several ruthenium (II)-dppz complexes have been synthesised which have been designed to show mixed motif binding to DNA (e.g. hydrogen-bond and intercalation). The binding of these complexes with different DNA sequences has been studied using a variety of techniques, including melting points, viscometry, UV-Vis, luminescence, CD, ITC and SPR. In most of the cases, the metal complexes stabilised DNA, bind via intercalation and their affinity with CT-DNA are in the micromolar range. We have observed a remarkable modulation of the binding of our complexes to DNA by changing the R-subsistent of the pyridine ring.

DNA binding properties of some monomeric and bimetallic Ru(II)-azo(bpy)s complexes synthesised in the Otsuki's group were explored. These metal complexes stabilise DNA and viscosity measurements shows no intercalation between base pairs. It has been observed that the shape of the bridging ligand is an important factor for the interaction of the complexes with DNA.

Acknowledgments

At the end of my PhD I would like to thank all the people who have helped me in so many different ways during these years.

First of all I would like to thank Jim A. Thomas (Jim T.) for giving me the opportunity to do a PhD, and therefore to be a student a bit longer and learn a bit more about chemistry. Thanks to him, these years have been great; the optimism and love for Chemistry that he passes on provide a constant encouragement to keep going.

I would further like to thank all the members of Jim Thomas' group for their friendship and help in and outside the lab: Chatna Rajput (Chatnita), and "my boys": Tim Phillips (Timmy Timmy), Simon Foxon (Foxy), James Ingram (Fingers) and Phillip Waywell (Filipo), as well as Clive, Naz, Baldy, the project and Erasmus students and other members of the group. I further thank them for being very patient with me and even tolerating me as "the boss".

I would like to thank Michelle Webb, Alice Sturdy and Faiza Touil for their help with the SPR; Sham Haq for his help with the ITC and Sharon Jennings for helping me with the CD.

During these years I have shared offices and labs with several different groups.

In chronological order, I would like to thank Chris Hunter and all the members of his group for allowing us to be in their lab (and leave the "footprints" of our metal complexes) and for their friendship and help... Especially I would like to thank Niek Buurma (Nicolasín) for his help with the ITC, computers and ... most of my problems!

It has been very nice to share the office with everyone in E74; there has been a really nice atmosphere, including a lot of joint activities (not only going to the pub...). Together, we have enjoyed the summer furrrboll tournament and Friday's basketball games ...

Me gustaría dar las gracias a mis hermanas Mónica y Marta por su apoyo en la distancia y mantener ese especial lazo que nos une. Han tenido que escuchar muchas quejas sobre la química y alguna que otra alegría, pero siempre me han

brindado su apoyo y buen humor. Y por supuesto, todos los amigos que han mantenido contacto conmigo a pesar de los km: Mauro, Viyorín, Xurdín, Mar, Paloma, Cristina, Sergio...

Me gustaría agradecer el apoyo que me han ofrecido Juan padre y Carmen madre ya que su ayuda me ha hecho llegar hasta aquí.

I also thank all the technicians in the department for their help in the lab. In particular, I thank Harry Adams for all his help with my crystals, for patiently teaching me a little bit of crystallography and for his friendship during all these years.

Finally, I thank all the friends that Sheffield has brought me. I spent a great time together with la mia famiglia italiana Beppe, Marina, Melchiorre and Rox, and I thank them for their help and especially for their friendship. And life in Sheffield would definitely not have been as nice without Anu, Julieta, Luca, Ian, Ana, Mentxu, Salva, Andreotido, Damien, Suyji, Olivier, the "No Balls" team...

Declaration

Except where specific references have been made to other sources, the work in this thesis is the original work of the author. It has not been submitted, in whole or in part, for any other degree. Certain results have already been published in peer review journals.

Verónica González González

May 2006

Table of contents

Table of contents

Abbreviations

A	Adenine
bpy	2,2′-bipyridine
Bp	Base pairs
C	Cytosine
CD	Circular dichroism
Chrysi	5,6-chrysinequinone diimine
CT-DNA	Calf thymus DNA
Cp	Cyclopentadiene ligand
CV	Cyclic Voltametry
DCM	Dichloromethane
DMSO	Dimethyl sulfoxide
DNA	Deoxynucleic acid
Dmb	4,4′-dimethyl-2,2′-bpy
Dmp	Dimethylphenanthroline
dpb	2,3-bis(2-pyridyl)benzo[g]quinoxaline
dppn	Benzodipyridophenazine
dppz	Dipyrido[3,2-a:2′,3′-c]phenazine
dpq	1,10-phenanthroline-5,6-dione
en	Ethylene diamine
FAB-MS	Fast atom bombardment mass spectrometry
G	Guanine
HMG	High mobility group proteins
Hp	3-hydroxypyrrole
HOMO	Highest occupied molecular orbital
Im	Imidazole
ITC	Isothermal titration calorimetry
LC	Ligand centered
LD	Linear dichroism

LUMO	Lowest unoccupied molecular orbital
MC	Metal centered
Me_2bipy	4,4′-dimethyl-2,2′-bipyridine
MLCT	Metal to ligand charge transfer
mRNA	Messenger RNA
MS	Mass spectrometry
MWCO	Molecular weight cut off
NMR	Nuclear magnetic resonance
Ph	Phenyl
PHEHAT	1,10-phenanthroline-[5,6-b]-1,4,5,8,9,12-hexaazatriphenylene
Phen	1,10-phenantrhroline
Phi	9,10-phenanthrinequinone diimine
Phzi	Benzo[*a*]phenazine-5,6-quinone diimine
pqp	6-phenylquino[8,7-*k*][1,8]phenanthroline
Py	Pyridine
Pztp	3-(pyrazin-2-yl)-as-triazino[5,6-f]1,10-phenanthroline
rac	Racemic
RNA	Ribose nucleic acid
rRNA	Ribosomal RNA
Sat	Saturated
SPR	Surface plasmon resonance
T	Thymine
Tactp	4,5,9,18-tetraazachryseno[9,10-*b*]-triphenylene
TLC	Thin layer chromatography
***T*m**	Melting point
Tp	Hydridotris(pyrazolyl)borate anion
Tpm	Tris-(1-pyrazolyl)methane
Tpm*	Tris (3,5-dimethyl-1-pyrazol) methane
Tpqp	7,8,13,14-tetrhydro-6-phenylquino[8,7-*k*][1,8]phenanthroline
tRNA	Transfer RNA
UV-Vis	Ultra violet-visible

Chapter One

Introduction

1 DNA function and structure

1.1 Biological importance of DNA

In all forms of life, there are only two forms of nucleic acid, deoxynucleic acid (DNA) and ribonucleic acid (RNA). The store of genetic information in cells resides in the sequence of base pairs of DNA. Although DNA molecules contain sequences of nucleotides whose purpose is not completely understood, the genetic code is expressed through specific sequences known as genes that determine which proteins will be produced in a cell.

Over the last half-century, scientists have begun to study the mechanisms of the process surrounding the function of DNA, such as replication, transcription, function in the cell cycle and damage repair. The processes of replication, transcription and translation are known as "the central dogma of molecular biology" and are represented in figure 1.1.

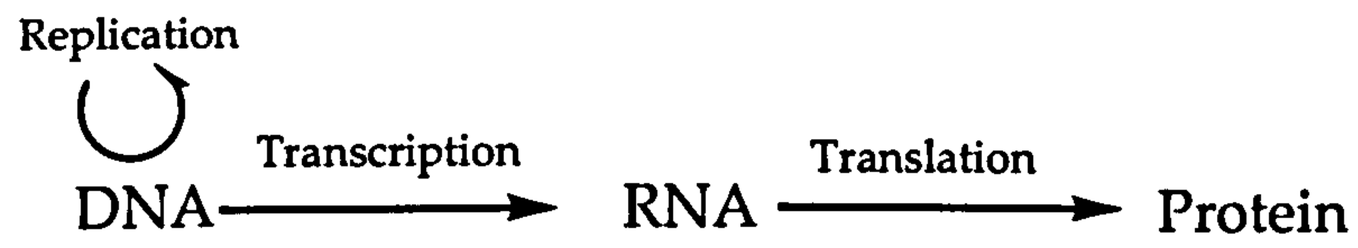

Figure 1.1: Representation of replication, transcription and translation

When the cell divides, DNA duplicates itself in a process called replication. Transcription is the process that transfers information from the DNA to messenger RNA (mRNA) so that it can be carried to the ribosome in the cytoplasm where the proteins are synthesised during translation.

1.2 Structure of DNA

Nucleic acids are very long polymers composed of nucleotides units. In the case of DNA these nucleotides are deoxyribonucleotide units. Such nucleotides are constructed from three components: a pentose sugar, a nitrogen heterocyclic base and a phosphate ester. The sugar in a deoxyribonucleic is deoxyribose and the nitrogenous bases are adenine (A) and guanine (G) (purines) and thymine (T) and cytosine (C) (pyrimidines). A nucleoside consists of a purine or pyrimidine base bonded to a sugar, the N-9 of a purine or the N-1 of a pyrimidine is attached to the C-1 of the sugar. The chains of nucleosides are joined together by phosphodiester bonds spanning from the 5′ position of one nucleoside to the 3′ position of the adjacent nucleoside (figure 1.2).

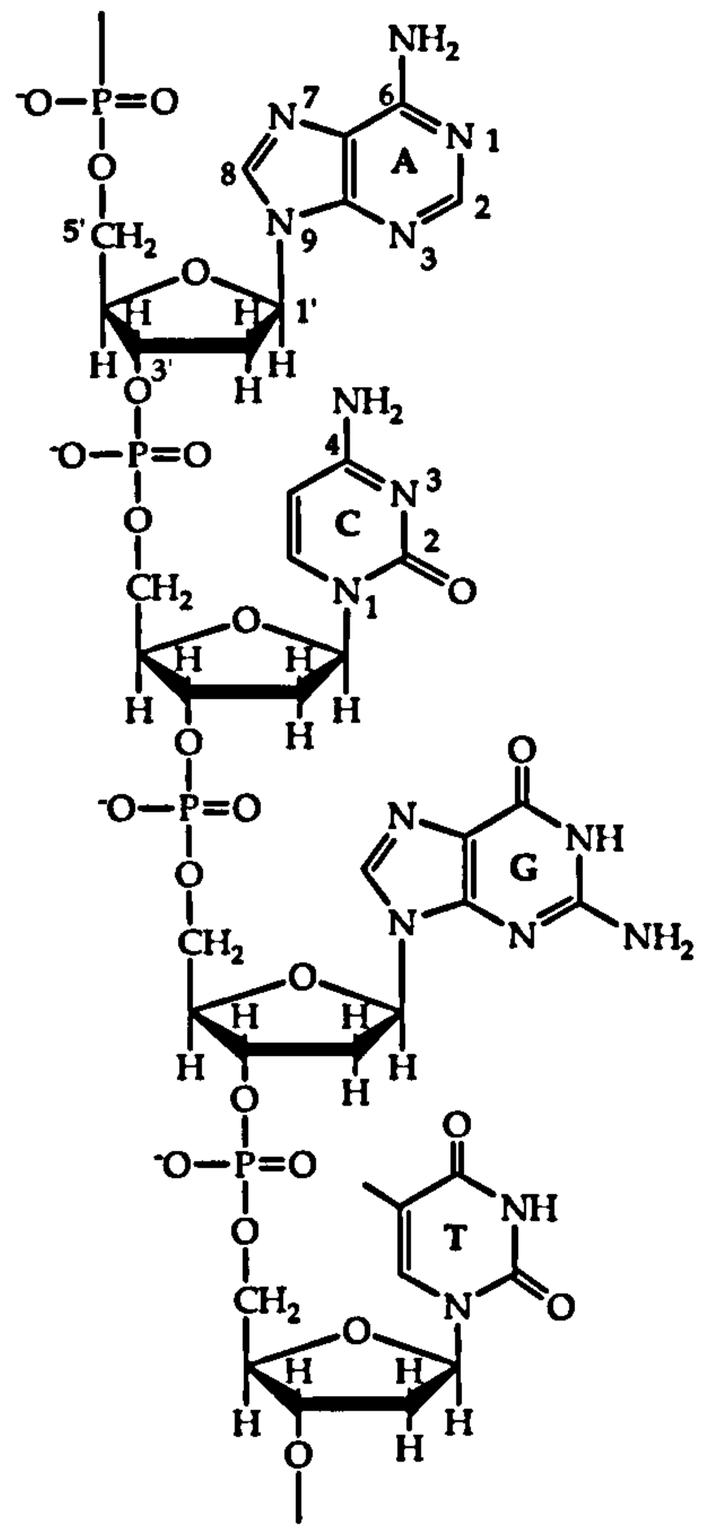

Figure 1.2: Structure of part of DNA chain: nucleosides joined by phosphodiester to grow the nucleotides

In 1953, James Watson and Francis Crick deduced that the three dimensional structure of DNA contains the following major features[1]: DNA consist of two helical chains running opposite to each other that are coiled around a common axis. Adjacent base pair are separated by 3.4 Å and the diameter of the helix is 20 Å. Purines and pyrimidines are in the inside of the helix whereas the phosphate and sugar units are in the outside. The purines and pyrimidines hold the two chains together through hydrogen bonds (adenine pairs with thymine and cytosine pairs with guanine) and the genetic information is carried by the precise sequence of base pair (figure 1.3).

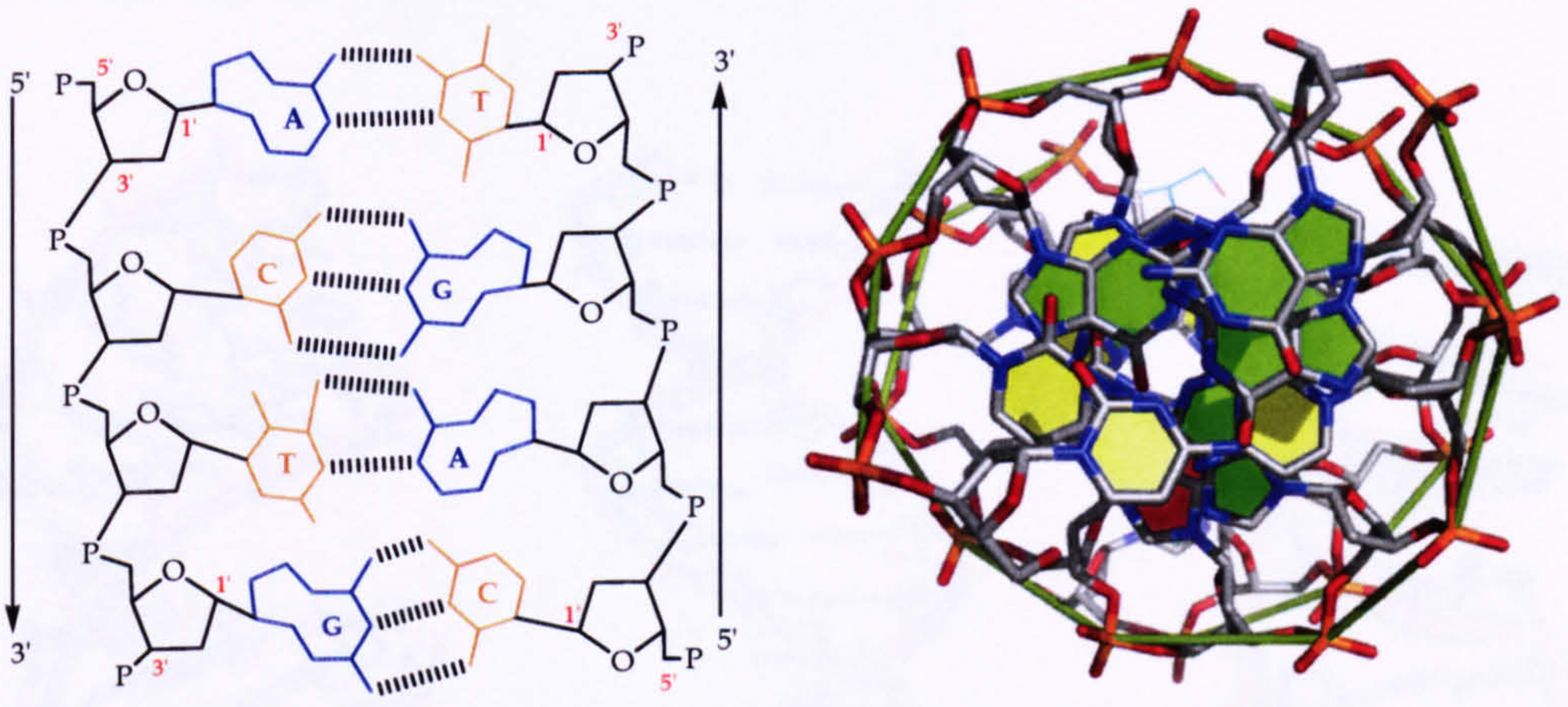

Figure 1.3: Watson and Crick DNA structure. Schematic showing base pairing and directions of strands (left) and phosphate and base pairs radial view (right)

The conformation of the sugar unit (figure 1.4) and the *syn* or *anti* conformation of the nucleic acid base relative to the sugar (figure 1.5) are important for the final structure of the nucleic acid.

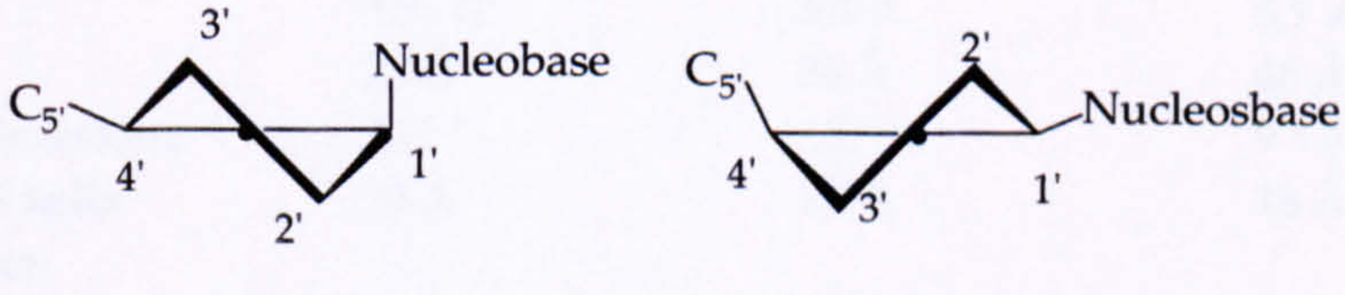

Figure 1.4: Conformation of the sugar unit

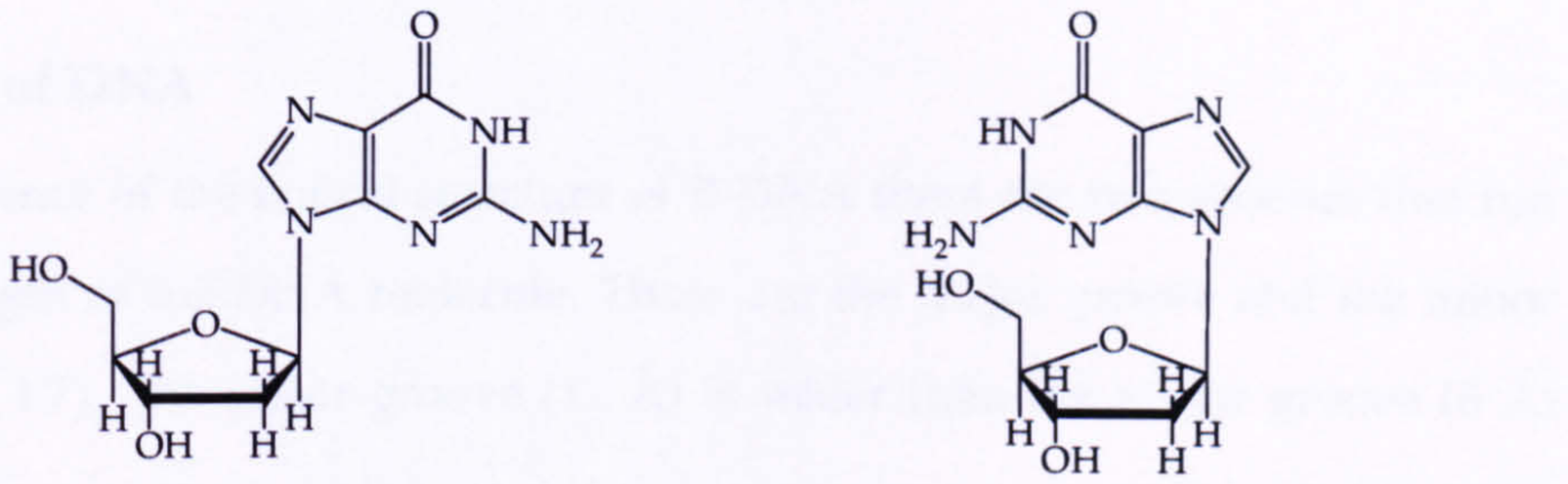

Figure 1.5: *Anti* (left) and *syn* (right) conformation of deoxyguanosine relative to the sugar

DNA can be found in three major conformations, A-DNA, B-DNA and Z-DNA (left handed) (figure 1.6) (table 1.1)[2]. In physiological conditions, most of the DNA is in the Watson and Crick B-form.

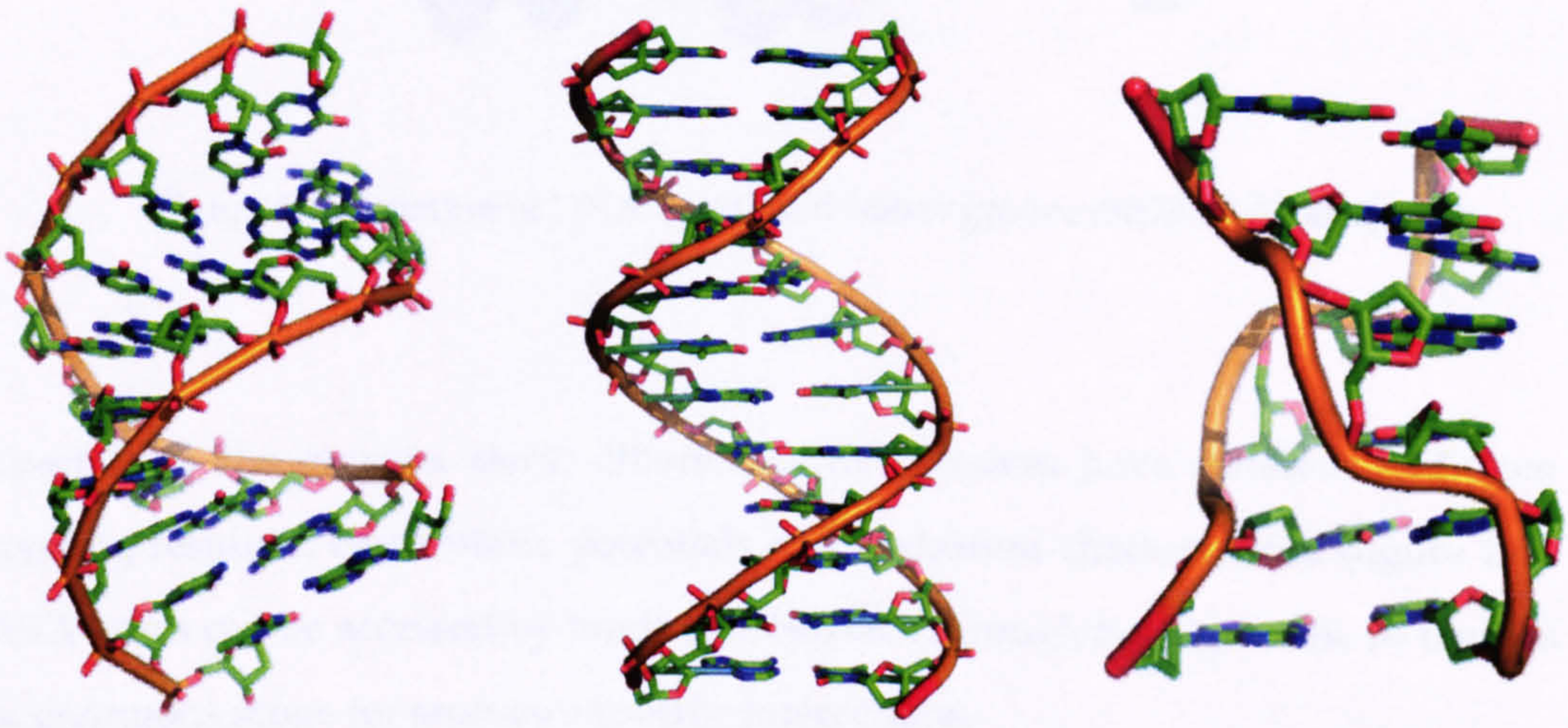

Figure 1.6: Major nucleic acid duplex conformations from left to right:

A-DNA, B-DNA and Z-DNA

Table 1.1: Major helix parameters

Parameter	A-DNA	B-DNA	Z-DNA
Helix sense	Right	Right	Left
Residue per turn	11	10.5	11.6
Axial rise	2.55 Å	3.4 Å	3.7 Å
Helix pitch	28 Å	36 Å	45 Å
Rotation per residue	32.7 °	36 °	9 ° 51
Diameter of helix	23 Å	20 Å	18 Å
Sugar pucker:			
dA, dT, dC	C3'endo, anti	C2'endo, anti	C2'endo, anti
dG	C3'endo, anti	C2'endo, anti	C3'endo, syn
Major groove	Narrow, deep	Wide, open	Flattened
Minor groove	Wide, shallow	Narrow, deep	Narrow, deep

1.3 Grooves of DNA

As a consequence of the helical structure of B-DNA there are two grooves that run the entire length of the DNA molecule. These are the major groove and the minor grove (figure 1.7). The major groove (12 Å) is wider than the minor groove (6 Å) (table 1.1).

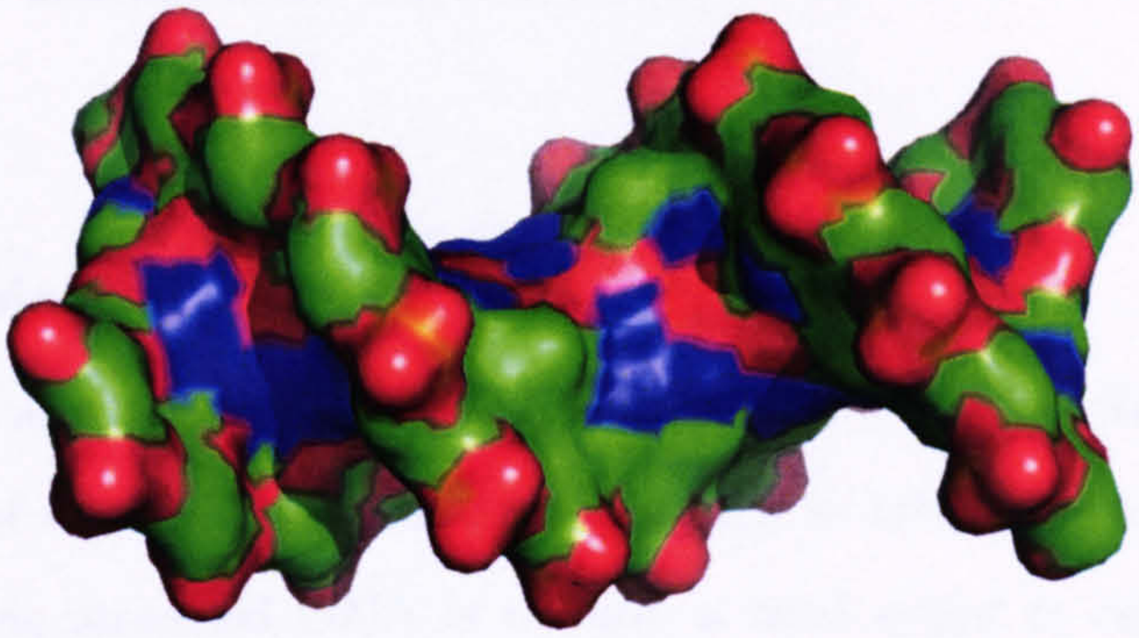

Figure 1.7: Structure of DNA: major and minor groove (NDB ID: BD003)

Apart from the obvious steric differences, the grooves have different hydrogen bonding residues, electrostatic potentials and hydration characteristics (figure 1.8). DNA bases can be accessed by binding substrates through both grooves, so there is an enormous scope for sequence specific interactions.

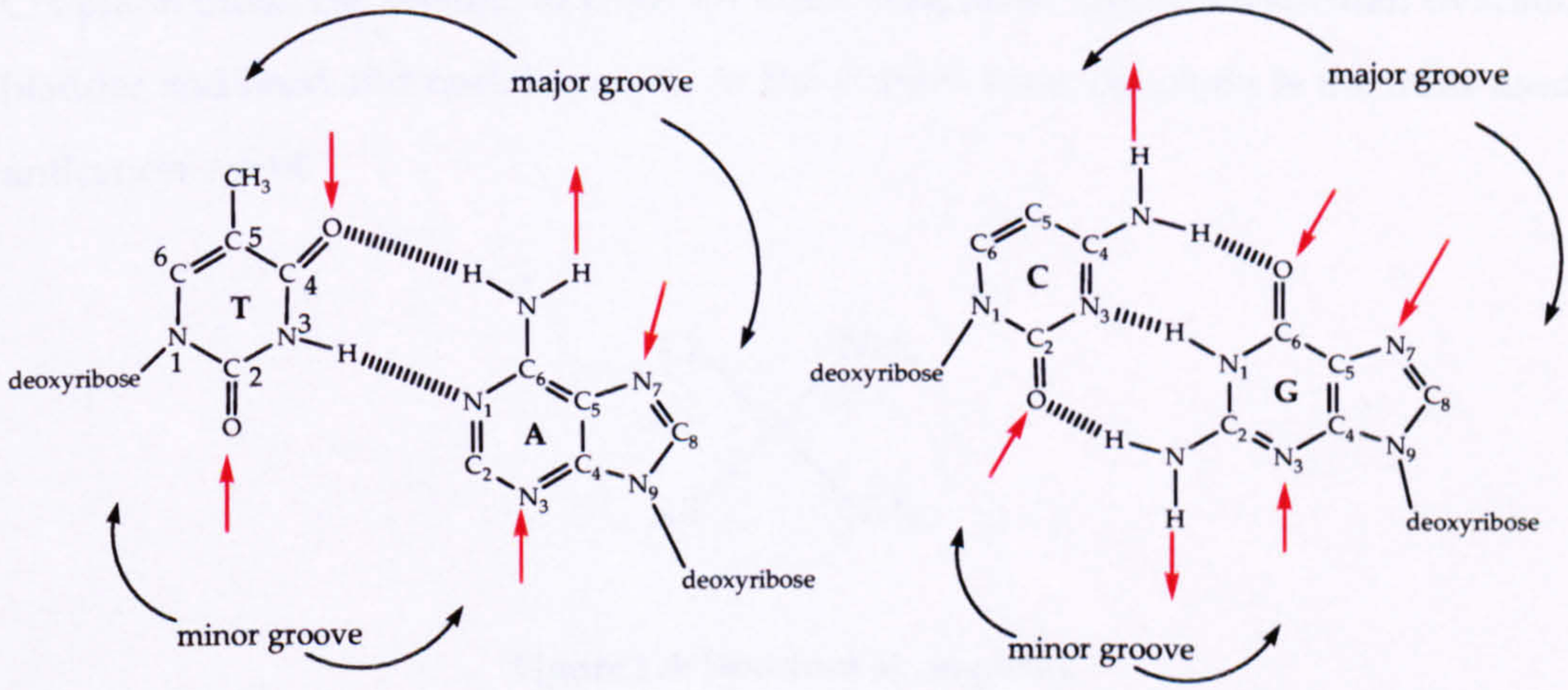

Figure 1.8: DNA grooves and base composition. The arrows indicate the direction of the hydrogen bonds to and from the base pair

In the major groove, a G-C base pair has a pattern of hydrogen bonding that is different from C-G base pairs. The A-T and T-A base pair have identical major groove donor/acceptor patterns but the presence of methyl group on thymine introduces asymmetry that in principle can allow distinctions between the two base pair. Hydrogen bonding patterns in the minor groove of each base pair sequences are symmetric so discrimination is not so direct.

2 Irreversible binding to DNA

Non-specific covalent binding can take place to the phophosdiester backbone or sugar residues of the DNA. This is usually a step in DNA strand scission and the rupture of double stranded DNA is usually a fatal event to cells since they are difficult to repair. Also, particular sites on DNA-bases can be under nucleophilic attacks. Drugs can bind to the double stranded DNA either to the same strand (intrastrand) or crosslink from a base on one strand to a base on the complementary strand (interstrand).

One of the most studied complex used in medicine is cis-diamminedichloroplatinum(I) or cis-platin known to exhibit antitumor activity (figure 1.9). In the mid-1960's Rosenberg studying the growth of bacterial cell in presence of electric field observed a filamentous growth rather than cell division. Cis-platin binds irreversible to DNA and this drug main target is testicular, ovarian, bladder and head and neck tumours. At the current time, cis-platin is the most used anticancer agent.

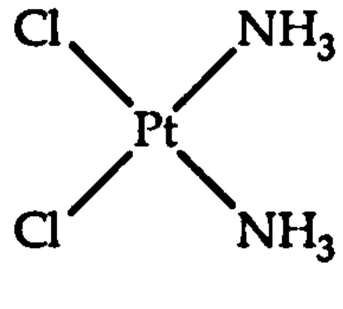

Figure 1.9: Structure of cis-platin

The mechanism of action of the cis-platin has been under much study and it is believed than cis-platin enters the cell through passive or active diffusion, although the process is not well understood. Inside the cell the chloride concentration is low and the hydrolysis of the complex takes place. The chloride ligand is a better leaving group than the ammonia ligand, hence the ammine ligands remain while the chloride ions are displaced by water. The water ligands are replaced by nucleobase DNA strands, forming a thermodynamic stable complex. The preferred point of attachment has been found to be at the N7 of guanine (scheme 1.1)[3]. The probable sequence of events is first hydrolysis of one chloride ligand followed by the reaction with one guanine ligand, then hydrolysis of the second chloride ligand followed by attachment of the second guanine.

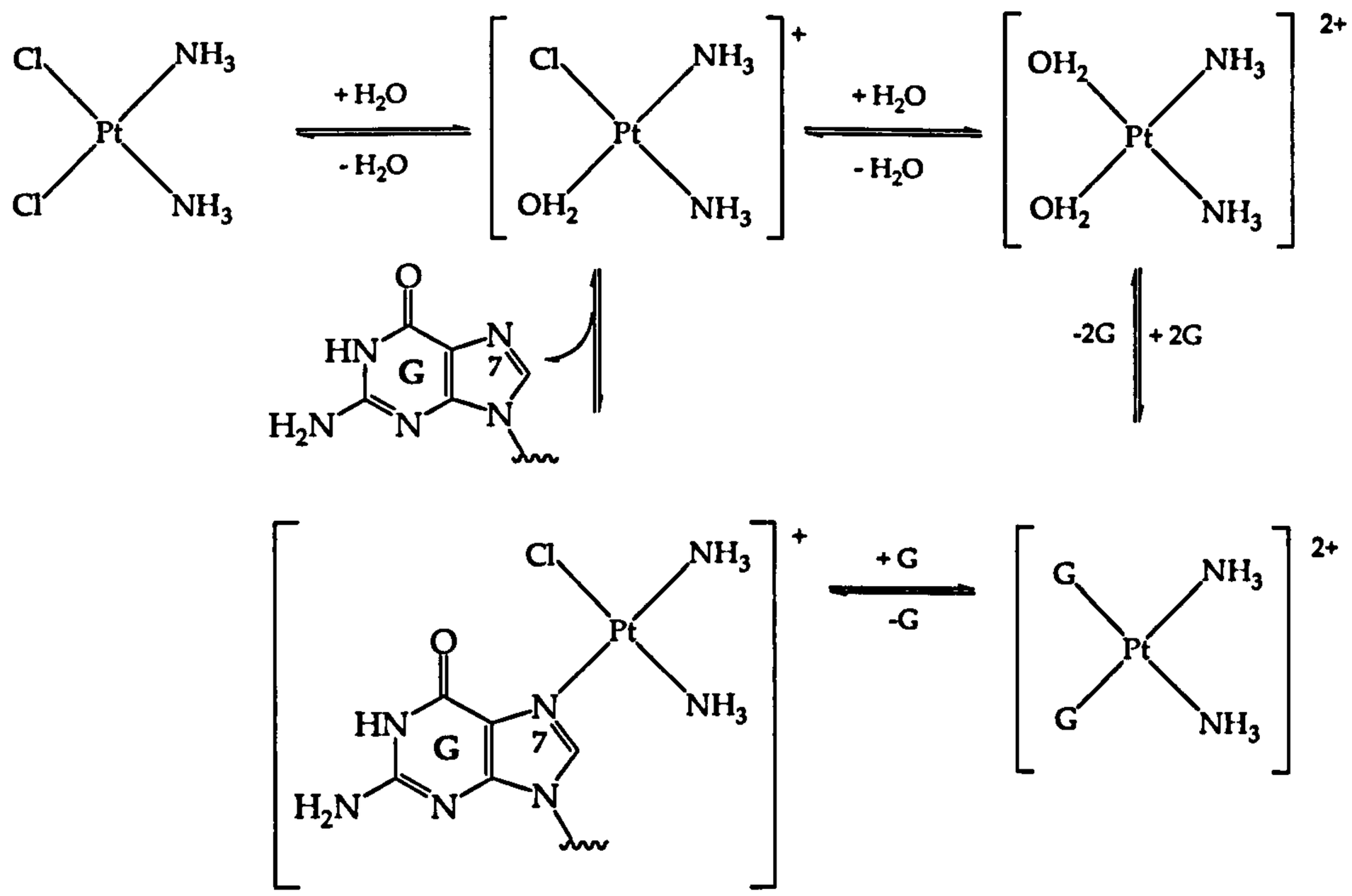

Scheme 1.1: Aqueous chemistry of cis-platin

In 1995 Lippard and co-workers published the X-ray crystal structure of a double stranded dodecamer–platinum(II) unit, showing the point of platination and the bending of the helix (figure 1.10)[4].

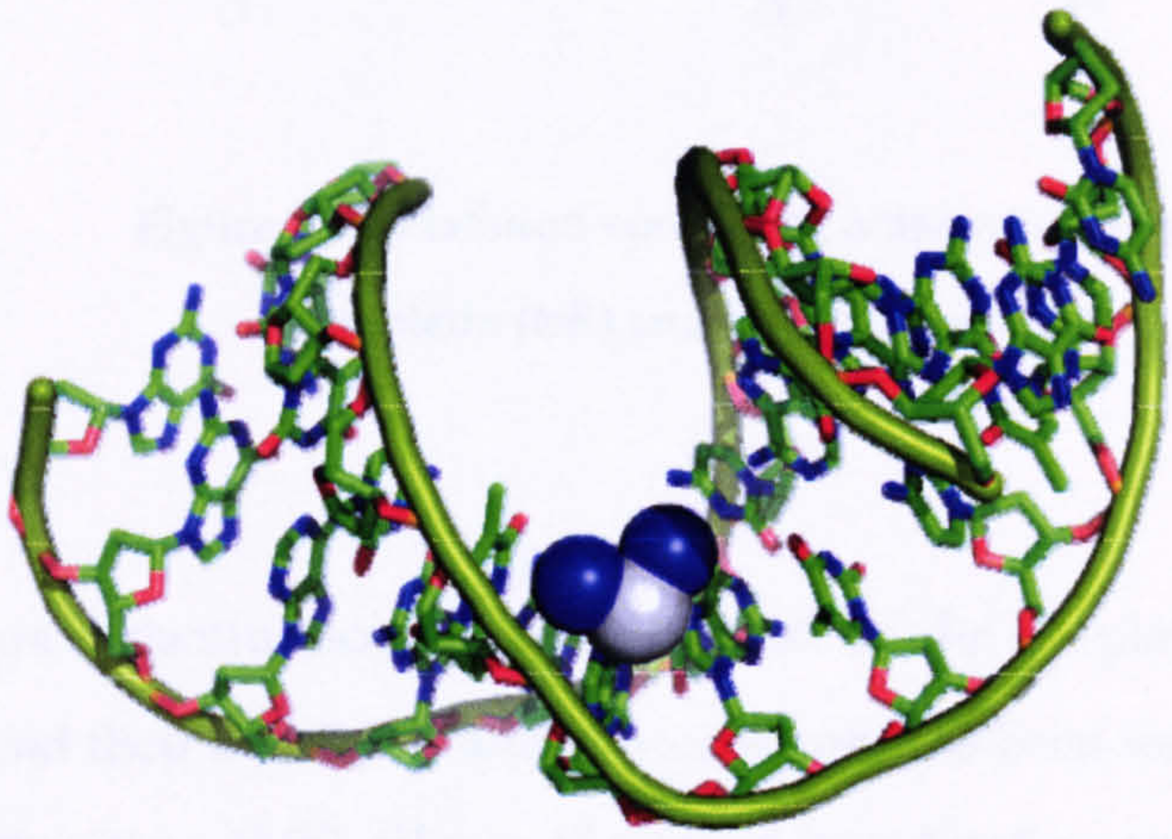

Figure 1.10: X-ray crystal structure of cis-platin binding covalently to (CCTCTG*G*TCTCC) (NBD ID DDLB73)

It has been suggested that the DNA-cisplatin complex is recognised by the high mobility group proteins (HMG) which recognise kinked or bent DNA. Possibly, the HMG-Pt-DNA lesion prevents binding of DNA repair proteins, stopping replication and causing cell death.

Because cis-platin is toxic, it is active against a limited range of tumours, and tumours can acquire cis-platin resistance the use of this compound is restricted. New derivatives of cis-platin with anticancer activity have been developed, for example carboplatin has a similar spectrum of treatment but is less toxic and oxaliplatin is used for the treatment of metastatic colorenal cancer (figure 1.11)[5].

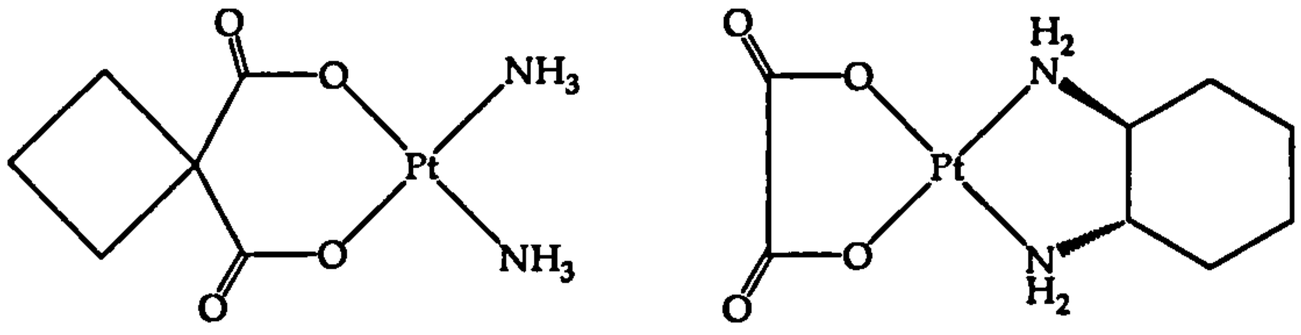

Figure 1.11: Platinum-containing anticancer agents: carboplatin (left) and oxaliplatin (right)

In recent years ruthenium-complexes designed on the cis-platin model have been synthesised and their activity as anti-cancer agents has been tested. Using transition metal ions other than Pt(II) allows additional coordination sites and alterations of the shape of the complexes. Several ruthenium compounds with nitrogen ligands show good anti-tumour activity[6]. For example cis-$[Ru(NH_3)_4Cl_2]Cl$ or trans-$[Ru(Im)_2Cl_4]^-$ (Im=imidazole, figure 1.12) exhibit activity against primary tumours. Dimethyl sulfoxide complexes of both Ru(II) and Ru(III) also exhibit anti-tumour activity and are relatively non toxic, but high doses are necessary to obtain therapeutic effect. Since a number of redox proteins are able to reduce Ru(III) complexes *in vivo*, it was suggested that Ru(III) complexes serve as prodrugs. The low O_2 content and lower pH in tumour cells favour the Ru(II) oxidation state which is kinetically more reactive than Ru(III). Since Ru(III) compounds are active by reduction, Ru(II) complexes were also investigated as chemotherapeutic agents.

Arene ligands stabilise Ru(II) and provide a hydrophobic face which might enhance molecular recognition and transport though the cell membranes. Morris, *et al.* studied the inhibition of cancer grown cell by different complexes of the type $[(\eta^6\text{-arene})Ru^{II}(en)X]^+$ (en = ethylenediamine and X = halide) showing that $[(\eta^6\text{-p-cymene})Ru^{II}(en)Cl]^+$ and $[(\eta^6\text{-}C_6H_5C_6H_5)Ru^{II}(Y)Cl]^+$ (where Y= ethylenediamine or N-ehtylethylenediamine) (figure 1.12) inhibit growth of ovarian cancer cells with similar potency to carboplatin[7,8].

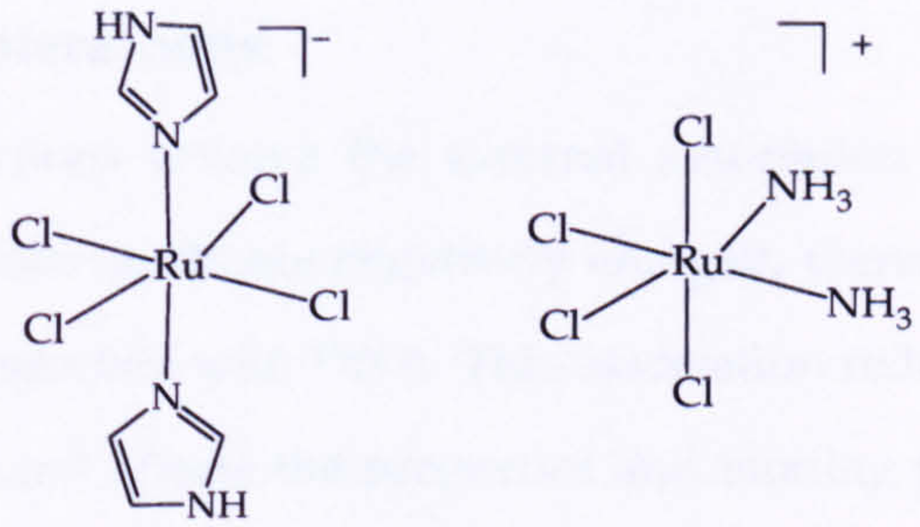

trans-$[Ru(Im)_2Cl_4]^-$ cis-$[Ru(NH_3)_2Cl_4]^+$

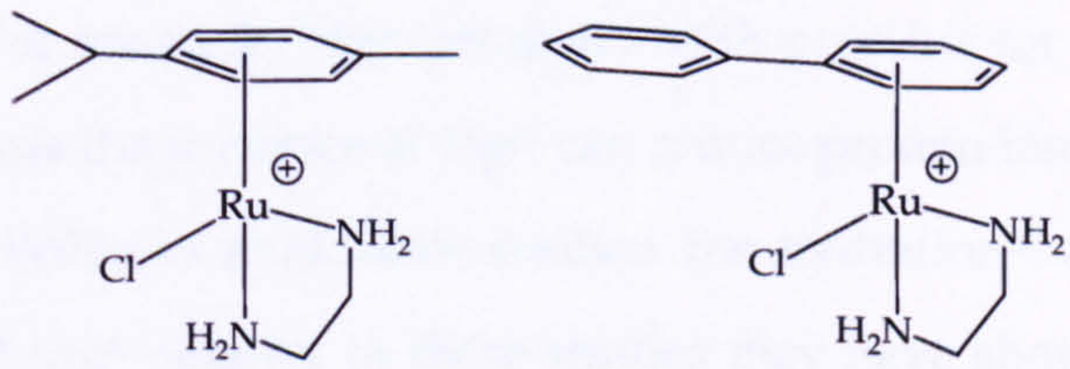

$[(\eta^6\text{-p-cymene})Ru(en)Cl]^+$ $[(\eta^6\text{-}C_6H_5C_6H_5)Ru(en)Cl]^+$

Figure 1.12: Some Ru-complexes with anti-tumour activity

3 Reversible interactions of small molecules with DNA

There are three main ways that a molecule can reversibly bind to DNA (figure1.13):

- Electrostatic binding
- Groove binding
- Intercalation

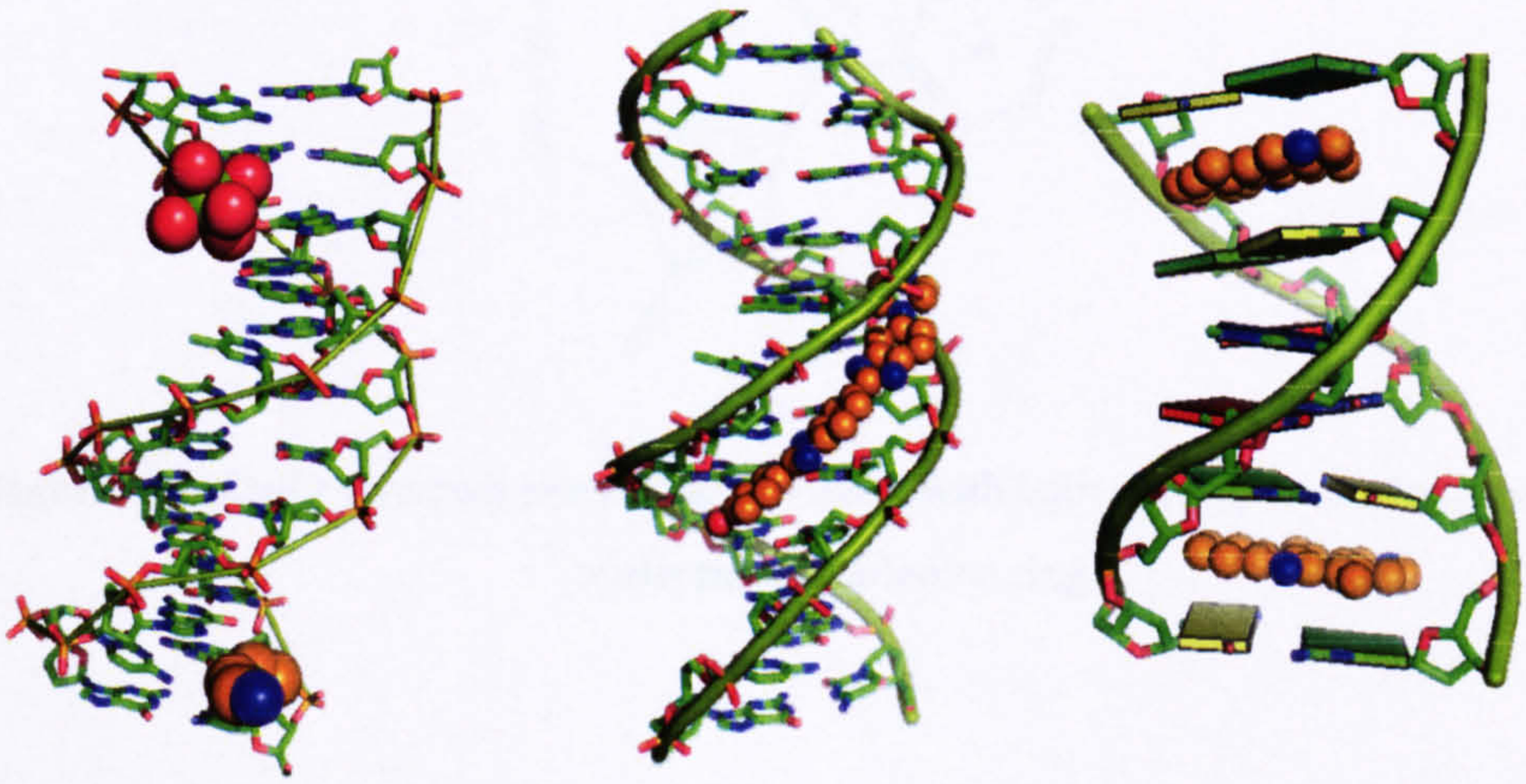

Figure 1.13: Cartoon representation of reversible interaction of molecules to DNA

3.1 Electrostatic interactions

Electrostatic interactions involve the external association of ions with the DNA polyelectrolyte. Nucleic acids are negatively charged, therefore simple cations such as Na^+ or Ca^{2+} can associate with DNA. This association reduces the effective charge on the nucleic acid and affects the properties and binding properties of the nucleic acids.

In 1976, Haseth and co-workers described the effects of ions on ligand nucleic acid interactions[9]. The association of molecules to DNA is dependent on ion concentrations. For example, Mg^{2+} competes with proteins for binding sites on the DNA, and therefore the presence of Mg^{2+} can reduce protein binding affinity.

In recent years, Williams *et al.* have studied the hydration[10] and stabilisation[11] of DNA by Na^+ and Mg^{2+} cations. In these studies they have shown that the so called spine of hydration is not only composed of water molecules, but also contains sodium ions. They also showed that divalent cations interact with DNA by binding to electron lone pairs of phosphate oxygen and binding to the π system of bases (figure 1.14), suggesting that these interactions have unforeseen roles in the structure, recognition and base flipping of DNA.

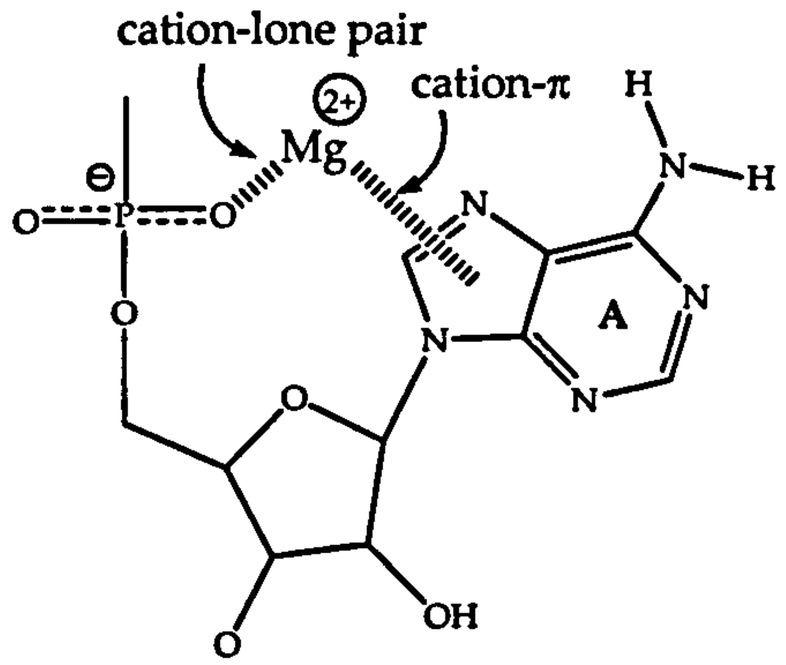

Figure 1.14: Cyclic structure where Mg^{2+} interacts with both a lone pair of electrons and the π–electrons of adenine ring.

Positively charged polyamines also stabilise and modify the conformation of the DNA in living cells. Studies on the interaction of the polyamines spermine and spermidine with DNA showed that they cause aggregation of DNA, increasing melting point and can induce B-Z transition under near physiological conditions[12-14].

3.2 Groove binding

In this interaction molecules come within van der Waals contacts of DNA and locate in the groove through hydrophobic and/or hydrogen bonding interactions.

Basic oligopeptides such us netropsin or distamycin-A (figure 1.15) bind in the minor groove of DNA. Interaction of both compounds with DNA was studied using several techniques which revealed high specificity to duplexes that contain A-T sites[15]. X-ray diffraction[16] and NMR spectroscopy[17] data showed that both complexes fit well in the narrowed minor groove and interact with DNA through hydrogen bonding between amide NH groups of the N-methylpyrrolecarboxamides and adjacent adenine N-3 and thymine O-2 on opposite helix strands. The binding of netropsin covers four A-T base pairs whereas the distamycin covers five A-T base pairs, the difference is associated with the additional pyrrole amide group in the distamysin molecule and also the different terminal residues[18]. Marky *et al.* reported the complete thermodynamic parameters for the interaction of netropsin with several DNA duplexes explaining the nature of the binding[19]. These studies demonstrated that netropsin binds by deep penetration into the minor groove with the high binding affinity for A-T sequences ($K \approx 10^9\ M^{-1}$ at 25 °C). The binding to alternating poly(dA-dT)·poly(dA-dT) is enthalpically driven, this is in contrast to binding to the homopolymer poly(dA)·poly(dT) which is entropically driven.

Hoechst 33258 (H33258) is a bisbenzimidazole that also binds to A-T rich DNA sequences in the minor groove (figure 1.16). H33258 has shape similarities with netropsin and dystamicin although it possesses a different chemical structure (figure 1.16). H33258 also has two NH recognition motifs able to bind to adenine-N3 or thymine-O2 atoms on opposite helix strands in the minor groove. A comparison

of these three groove binders suggests that flat aromatic rings twisted in a screw sense fit well in between the walls of the DNA helix[20].

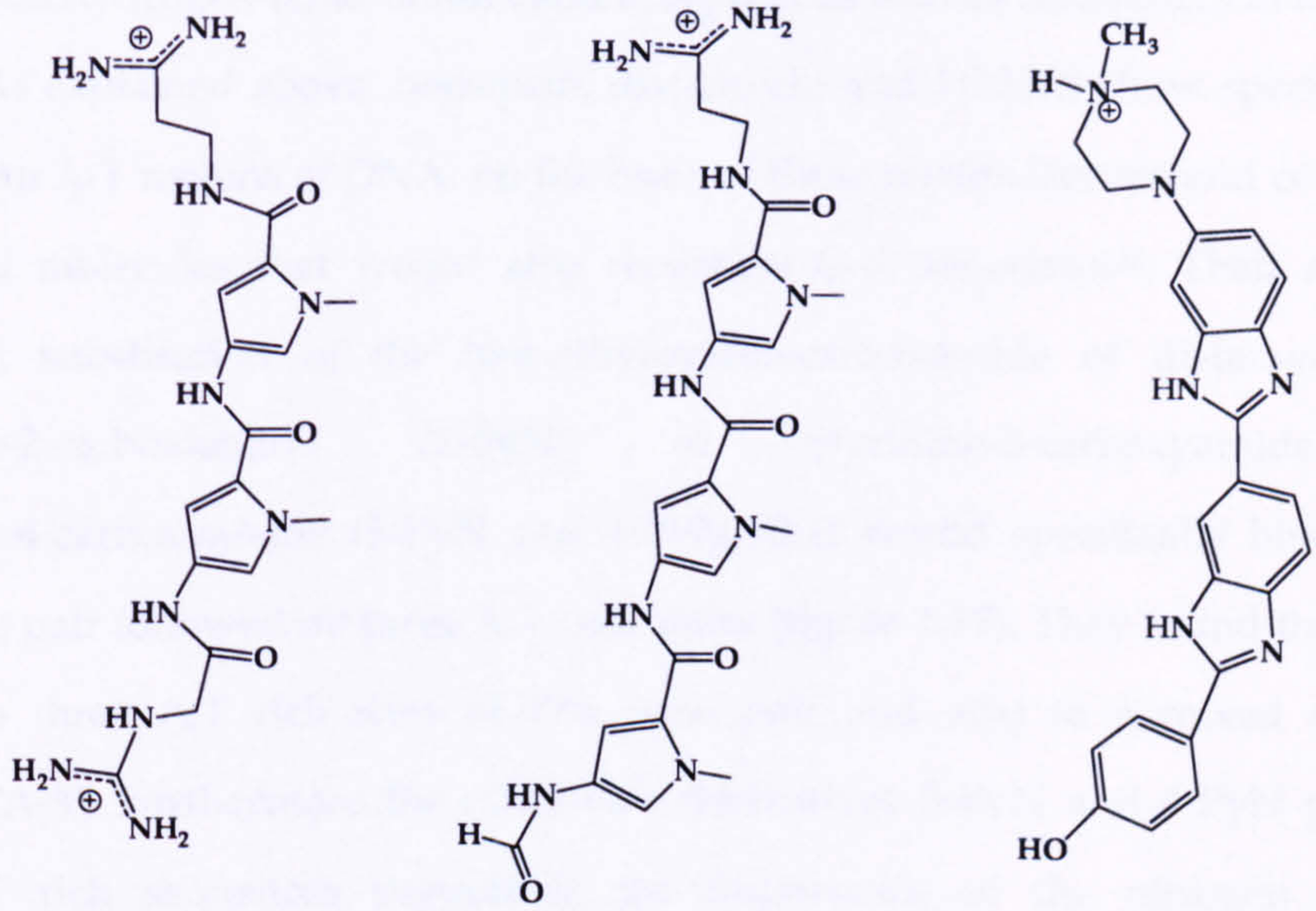

Figure 1.15: Structures of (left to right) netropsin, distamycin and H33258

Fox and co-workers have studied the A-T selectivity of these three groove binders and demonstrated that the affinities are also dependent on different arrangements of the A-T base pairs, for example H33258 discriminates with high affinity for AATT sequences[21].

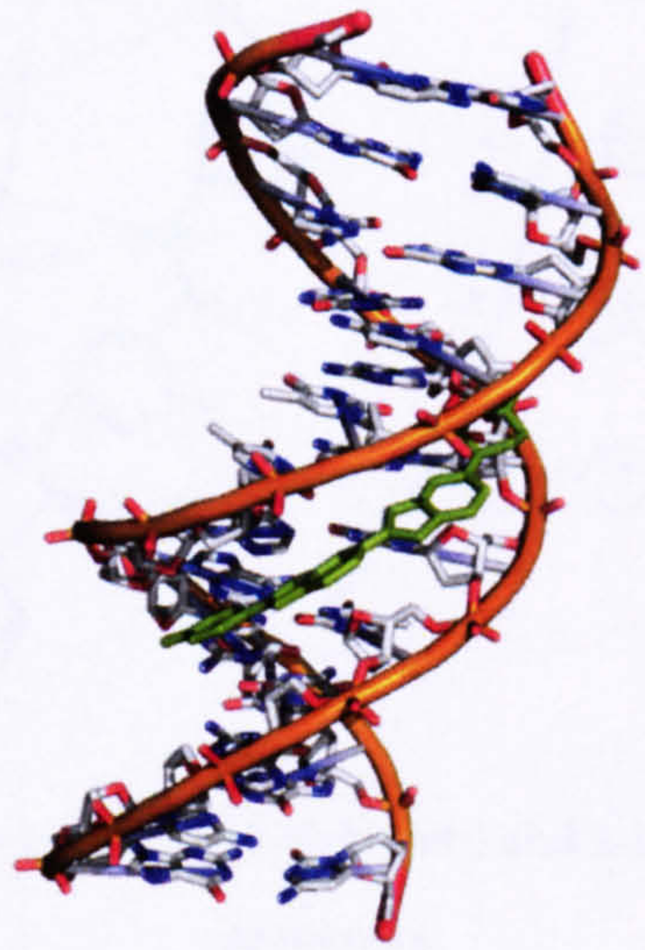

Figure 1.16: X-ray crystal structure of H33258 binding to DNA (NDB ID GDL002)

Peter Dervan, *et al.* have studied the specific interactions of pyrrole-imidazole polyamides in the minor groove of the DNA. Again the specificity of these systems is based on hydrogen-bond donors and acceptors as well as differences in molecular shape. As explained above, netropsin, distamycin and H33258 show specificity for binding to A-T regions of DNA, on the basis of these results Dervan and co-workers designed molecules that would also recognise G-C sequences[22]. Their approach involved substitution of the N-methylpyrrolecarboxamide of distamycin with pyridine-2-carboxiamide (2-PyN) or pyridine-3-carboxyamide and pyridine-4-carboxyamide (3-PyN and 4-PyN) that would specifically bind to one G,C base pair followed by three A,T base pairs (figure 1.17). They found that 2-PyN binds to three A,T rich sites of five base pair and also to a mixed sequence 5′-TGTCA-3′. Furthermore the other two derivatives 3-PyN and 4-PyN preferred just A,T rich sequences suggesting the importance of the nitrogen ring for recognition. In order to study the structural limitations of binding to 5′-TGTCA-3′, Devan and co-workers synthesised a new compound where the pyridine ring was replaced with N-methylimidazole (2-ImN), and this showed higher affinity for the 5′-TGTCA-3′ sequence than 2-PyN derivatives (figure 1.17).

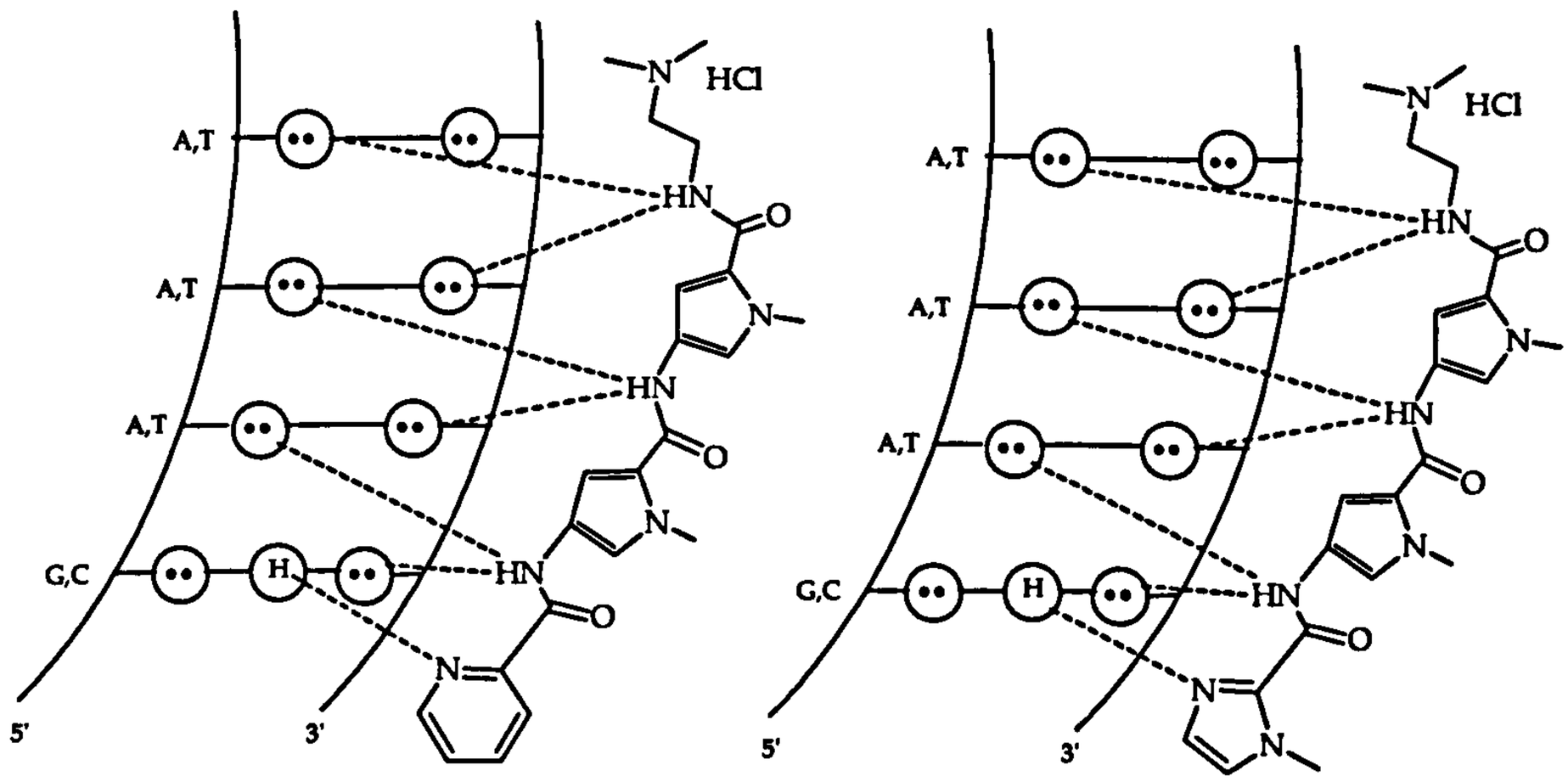

Figure 1.17: 1:1 models for the binding of 2-PyN (left) and 2-ImN (right) to 5′-(G,C)(A,T)$_3$-3′ sequences

Models of a 1:1 ligand-DNA complex did not explain the recognition of G,C base pairs in the second and fourth positions of the 5′-TGACT-3′ sequence. NMR studies and cleavage experiments for the interaction of 5-(A,T)G(A,T)$_3$-3′ with 2-ImN showed that the interaction actually involved an antiparallel 2:1 ligand-DNA stoichiometry [22,23] (figure 1.18).

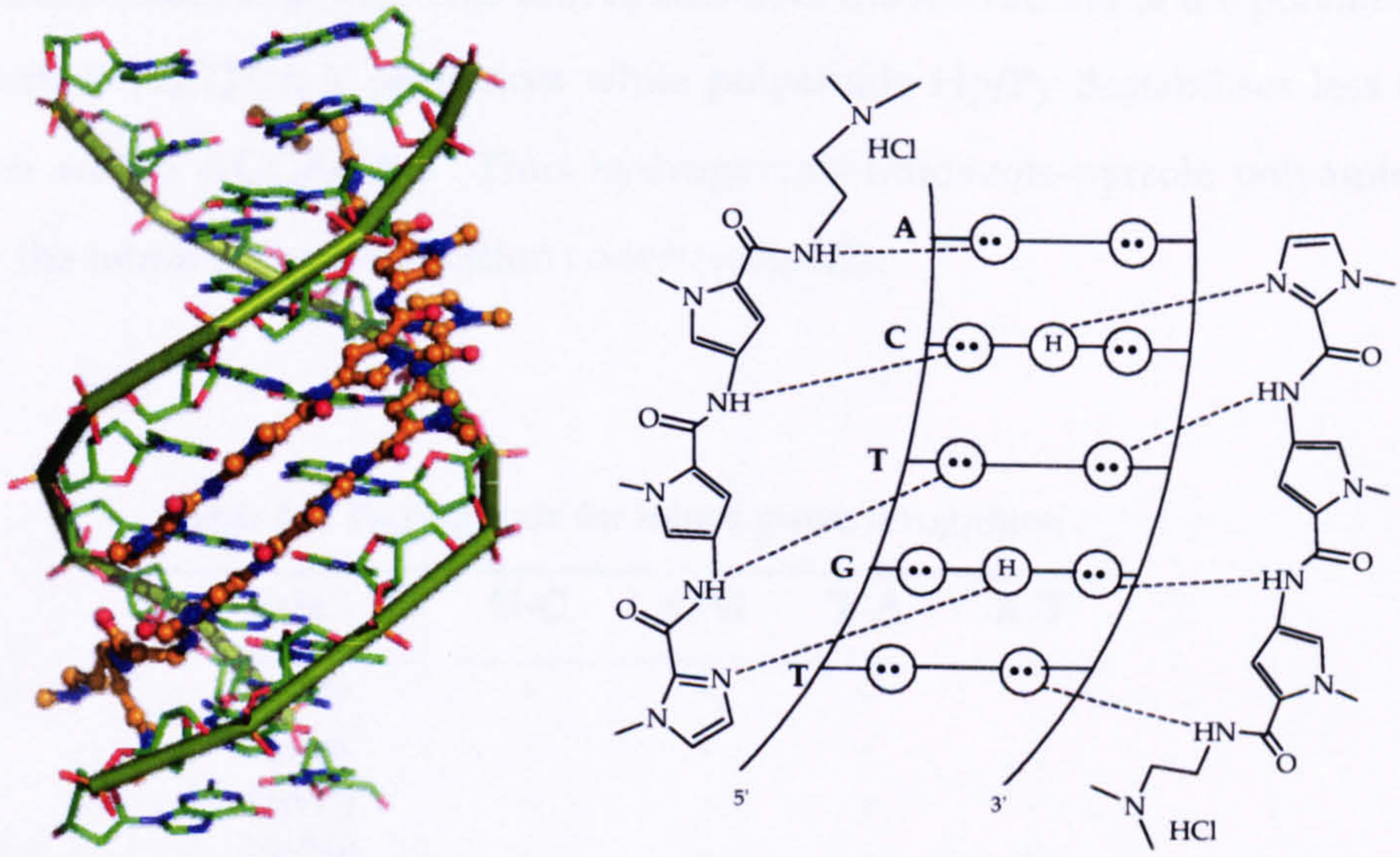

Figure 1.18: 2:1 binding model for the interaction 2-ImN to 5′-TGTCA-3′ sequence (right) and x-ray structure (NDB ID BDD003)

Following this discovery, pairing rules were developed: polyamides containing pyrrole (Py) and imidazole (Im) distinguished G-C from C-G and A-T/T-A base pairs.

Covalent linking two antiparallel polyamide strands increases affinity and specificity[24]. Hairpins displayed 100-fold higher affinity than the homodimers. The polyamide ImPyPy-γ-PyPyPy-Dp (Dp = 3-(dimethylamino)propylamine) containing γ-aminobutyric acid (γ–turn) was found to specifically bind to 5′-TGTTA-3′. The γ-turn showed selectivity for A,T over G,C base pairs, probably due to increased steric clashes with GC residues. The similarity of binding affinities to 5′-TG(A,T)$_3$-3′

sequences was a limit to the specificity of these hairpin polyamides[25]. In order to increase the specificity of pyrrole-imidazole polyamides, Dervan and collagues added a new aromatic amino acid, 3-hydroxypyrrole (Hp). DNase I footprint titrations for three different polyamides containing pairings of Im/Py, Py/Im (opposite G-C /C-G) and either Py/Py, Hp/Py or Py/Hp with different DNA fragments show that is possible to discriminate between A-T and T-A bases with the new aromatic amino acid, Hp. This unit destabilises the interaction of the polyamide Py/Hp with 5′-TGGTCA-3′ sequences while polyamide Hp/Py destabilises less the interaction with 5′-TGGACA-3′. Thus hydropyrrole-imidazole-pyrrole polyamides complete the minor grove recognition code[26] (table1.2).

Table 1.2: Pairing code for minor grove recognition

Pair	G-C	C-G	T-A	A-T
Im/Py	+	-	-	-
Py/Im	-	+	-	-
Hp/Py	-	-	+	-
Py/Hp	-	-	-	+

3.3 Intercalation

This binding mode involves the insertion of a planar aromatic ring between the base pair of DNA, leading to significant π overlap, as well as van der Waals and electrostatic interactions. Lerman introduced the concept of intercalation when he studied the interaction of acridines with DNA[27]. Since then many different compounds have been proven to be intercalators, for example proflavine, ethidium bromide and daunomycin (figure 1.19).

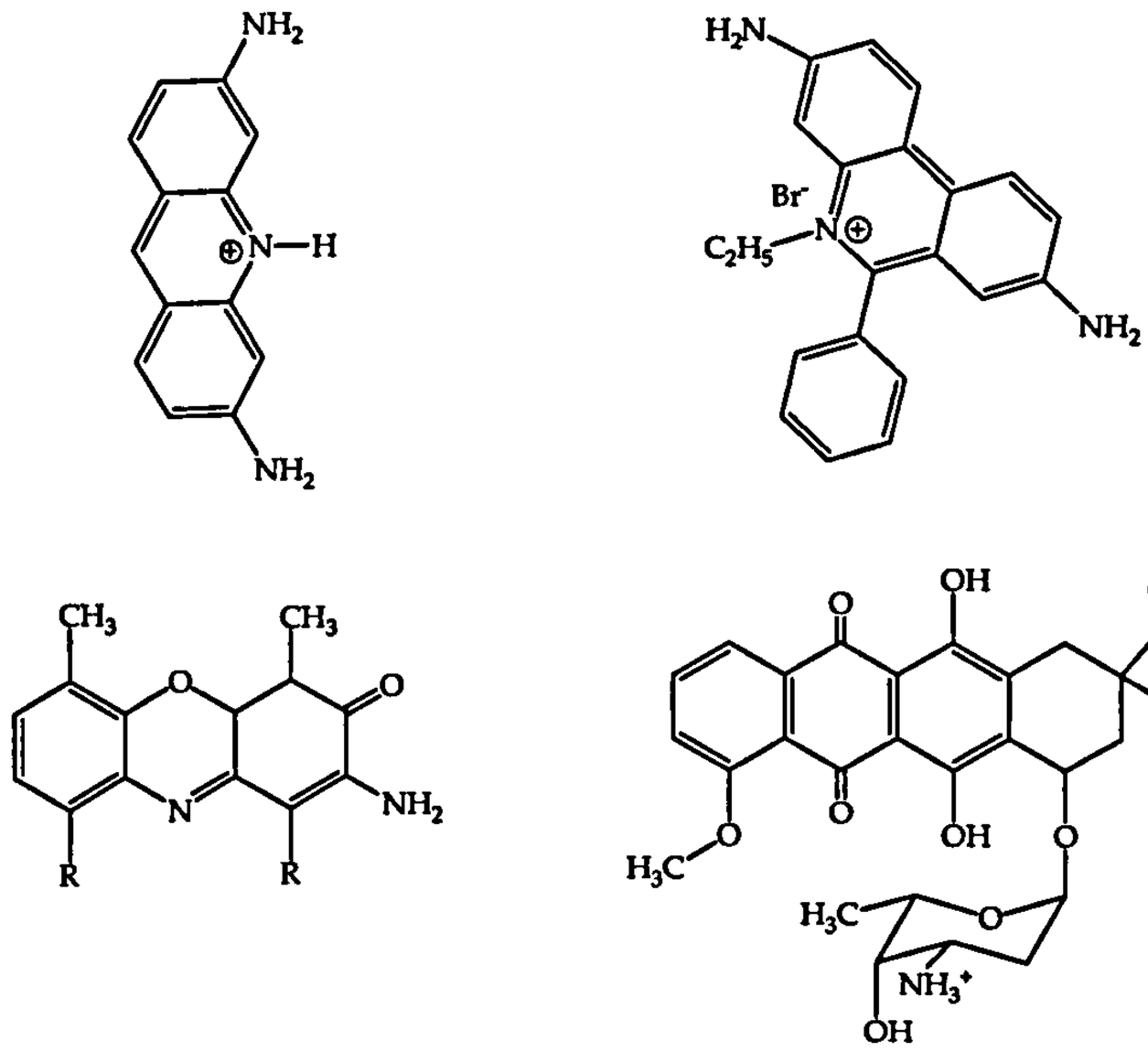

Figure 1.19: Structure of (left to right) proflavine, ethidium bromide (first row) and actinomycin D and daunomycin (second row)

3.3.1. Examples of organic intercalators

A typical example of an organic intercalator is daunomycin. This compound is an antibiotic in cancer chemotherapy and is one of the best characterised intercalators. The Chaires' group studied the binding of daunomycin with different deoxypolynucleotides. Daunomycin stabilises CT-DNA and binds preferentially to alternating purine-pyrimidine tracks[28], with the following selectivity: poly[d(A-T)]poly[d(A-T)] > poly[d(G-C)]poly[d(G-C)] > poly(dG)poly(dC)> poly(dA)·poly(dT)[29]. Binding to poly[d(A-T)]poly[d(A-T)] and poly[d(G-C)]poly[d(G-C)] is enthalpy driven whereas binding to poly(dG)·poly(dC) and poly(dA)poly(dT) is entropy driven. Further studies showed that daunomycin interacts preferentially with G-C rich DNA that also contains A-T base pairs. X-ray crystal structure of daunomycin bound to d(CGTACG) showed intercalation of the chromophore between the C-G base pair with the non-planar substituent interacting with DNA through H-bonds and van der Waals contacts that help to stabilise the complex[30] (figure 1.20).

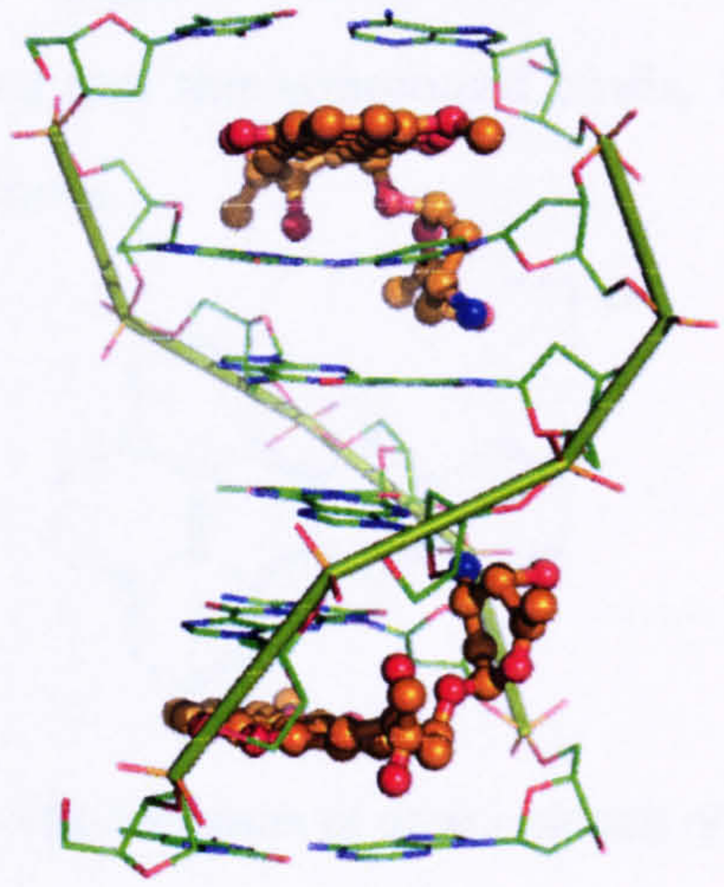

Figure 1.20: X-ray structure of daunomycin bound to d(CGTACG) (NDB DDF018)

Actinomycin D (figure 1.19) is used as an anti-tumour agent in treatment of a limited number of cancers. It also binds to DNA by intercalation with a strong binding preference for 5′-GC sites. NMR[31] studies and X-ray diffraction[32] supported the rationalised specificity of this compound for that sequence, revealing hydrogen bonding of the 2-amino group and N3 of guanine bases at the intercalation point. The unsymmetrical intercalator has been showed to bind to DNA in both possible orientations with the phenoxazone ring over the G base in the central base pair of the GCGC sequences. At ratios up to one:one only free duplex and a 1:1 adduct is observed, increasing the ratio of Actinomycin D leads to stoichiometric formation of the 2:1 complex. This anti-cooperativity describes the number of base pairs in the binding site, for example three consecutive G-C binding sites permit only two actinomycin molecules to be bound[33,34].

In the Thomas' group, the interaction with DNA of the dicationic dibromide salt of dppz (figure 1.21) has also been studied[35]. This organic derivative of the dppz ligand binds to DNA with moderate affinity showing intercalation between the base pairs of the DNA. Thermodynamics of binding to CT-DNA showed negative enthalpy and positive entropy similar to other organic intercalators, such as ethidium bromide[36,37]. The structural similarities of this dibromide salt of dppz to the intercalative segment of actinomycin D, a minor groove binder, and the slightly

higher affinity of this organic compound for poly(dG)·poly(dC) over poly(dA)·poly(dT) suggested that this compound binds, like actinomycin D, to the DNA through the minor groove.

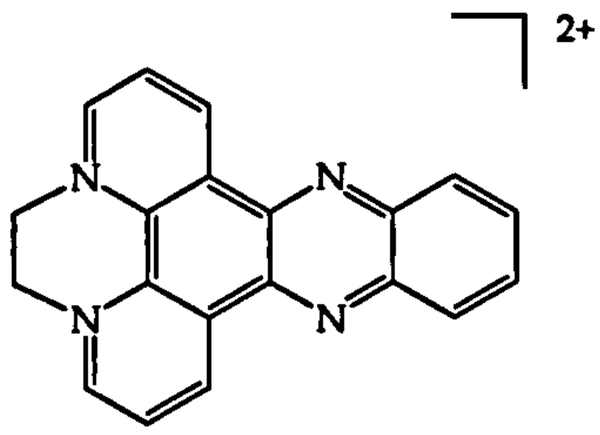

Figure 1.21: Structure of dicationic salt of dppz

3.3.2 Monometallic intercalators

Metal complexes are often positively charged and this can enhance DNA binding due to electrostatic interactions. Their distinctive coordination geometries and stability in aqueous solution, as well as their rich photophysical properties, offer useful characteristics for the construction of metal-based DNA binding agents.

During the 1970's, Lippard and co workers, established that square planar metal complexes containing an aromatic heterocyclic ligand could bind to DNA through intercalation[38]. Since then, a variety of new systems based on metal centres have been reported.

In the early 1980s, Barton and co-workers started to investigate octahedral metal complexes as DNA binding agents. These studies initially focused on the binding of tris-(phenanthroline) complexes of zinc, cobalt and ruthenium to DNA[39-41]. The binding of Δ- and Λ-$[Ru(phen)_3]^{2+}$ to DNA led to a decrease and small shift in the visible absorption of the ruthenium complexes and an increase and shift in luminescence, suggesting affinity in the millimolar range[42]. ^1H NMR studies on Δ- and Λ-$[Ni(phen)_3]^{2+}$ and Δ- and Λ-$[Cr(phen)_3]^{3+}$ bound to oligonucleotides suggested different behaviours depending on the isomer, with Λ–isomers preferring surface binding and the Δ-isomers intercalation[43]. In 1992, Chaires *et al.* studied the interaction of Δ- and Λ-$[Ru(phen)_3]^{2+}$ with DNA using several techniques and

showed that both isomer stabilised DNA but neither bind to DNA by classical intercalation[44].

Barton, *et al.* realised that to make true octahedral metallo-intercalating binding agents, the surface of the intercalative ligand needed to be significantly increased, so the interaction of $[Ru(phen)_2(dppz)]^{2+}$ and $[Ru[(bpy)_2(dppz)]^{2+}$ with DNA was studied (figure 1.22)[45,46]. Both complexes showed what has become known as a "light switch effect": in aqueous solution the MLCT luminescence is quenched but when these complexes are bound to DNA they emit[47-51]. This effect has been used extensively to study the interaction of different complexes with DNA.

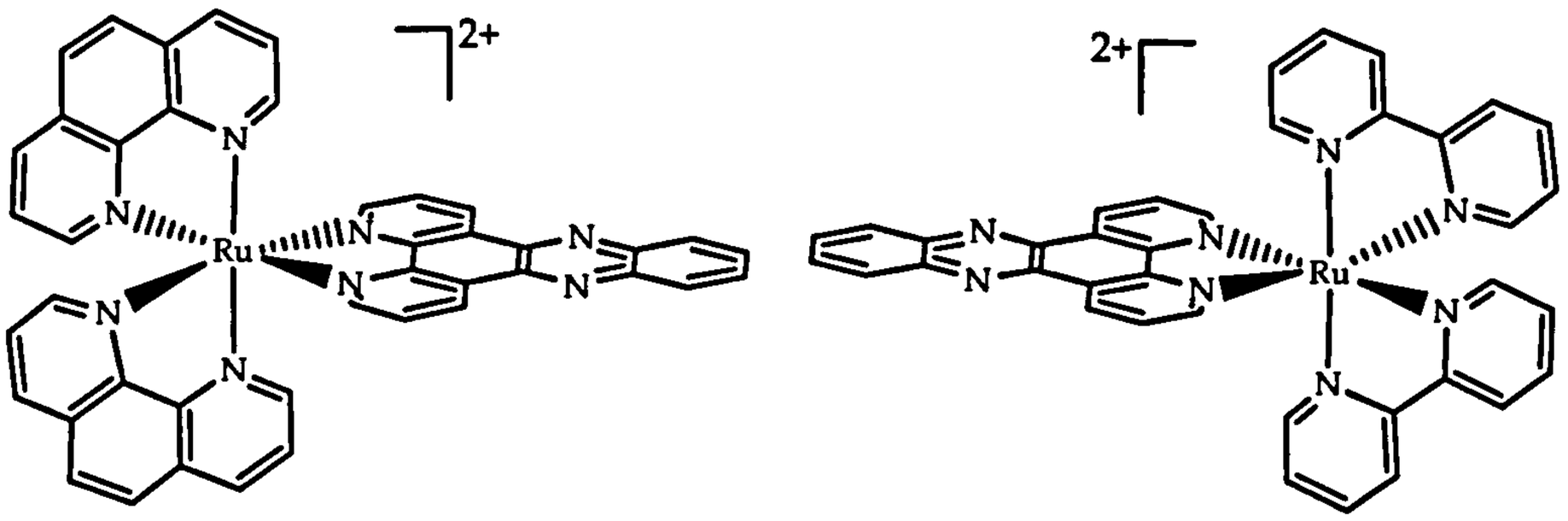

Figure 1.22: Structure of Λ -$[Ru(phen)_2(dppz)]^{2+}$ (left) and Δ -$[Ru(bpy)_2(dppz)]^{2+}$ (right)

In 1988, while Barton and colleagues were studying the spectroscopic properties of the interaction of polypyridyl-ruthenium complexes with anionic polyelectrolytes (such as NaPA (sodium poly(acrylate)) and NaPSS (sodium poly(styrenesulfonate)) they realised that the emission of the complexes was influenced by the hydrophobicity of the environment[52]. Further studies on the emission of the complexes showed that the excited-state energy is localised on the ligands in the lowest metal to ligand charge transfer (MLCT) state and is funnelled into the energetically favoured ligand after initial excitation[53]. In the case of $[Ru(phen)_2(dppz)]^{2+}$ and $[Ru[(bpy)_2(dppz)]^{2+}$ the MLCT is preferentially on the electron-accepting dppz ligand[54] and the excited state may be written as $^*Ru^{III}\text{-}(L)_2(dppz^{\bullet-})^{2+}$. The emission of Ru(II)-dppz complexes is quenched by H_2O and

less effectively by D_2O, which is indicative of proton complexation and/or transfer to the nitrogens of the reduced dppz ligand[50].

Studies on the emission properties of $[Ru(phen)_2(dppz)]^{2+}$ in different solvents showed that upon excitation of the $[Ru(phen)_2(dppz)]^{2+}$ complex, the MLCT state is formed with the electron localised in a π^* orbital of either one of the three bidentate ligands (state A, figure 1.23). This state converts into another MLCT state where the electron is localised on the dppz ligand (state B). After that, there is a reorganisation of the solvent that includes H-bonding (blue circle) to both phenazine nitrogens (state C), the conversion from state C to state B also occurs at higher temperatures[48,51].

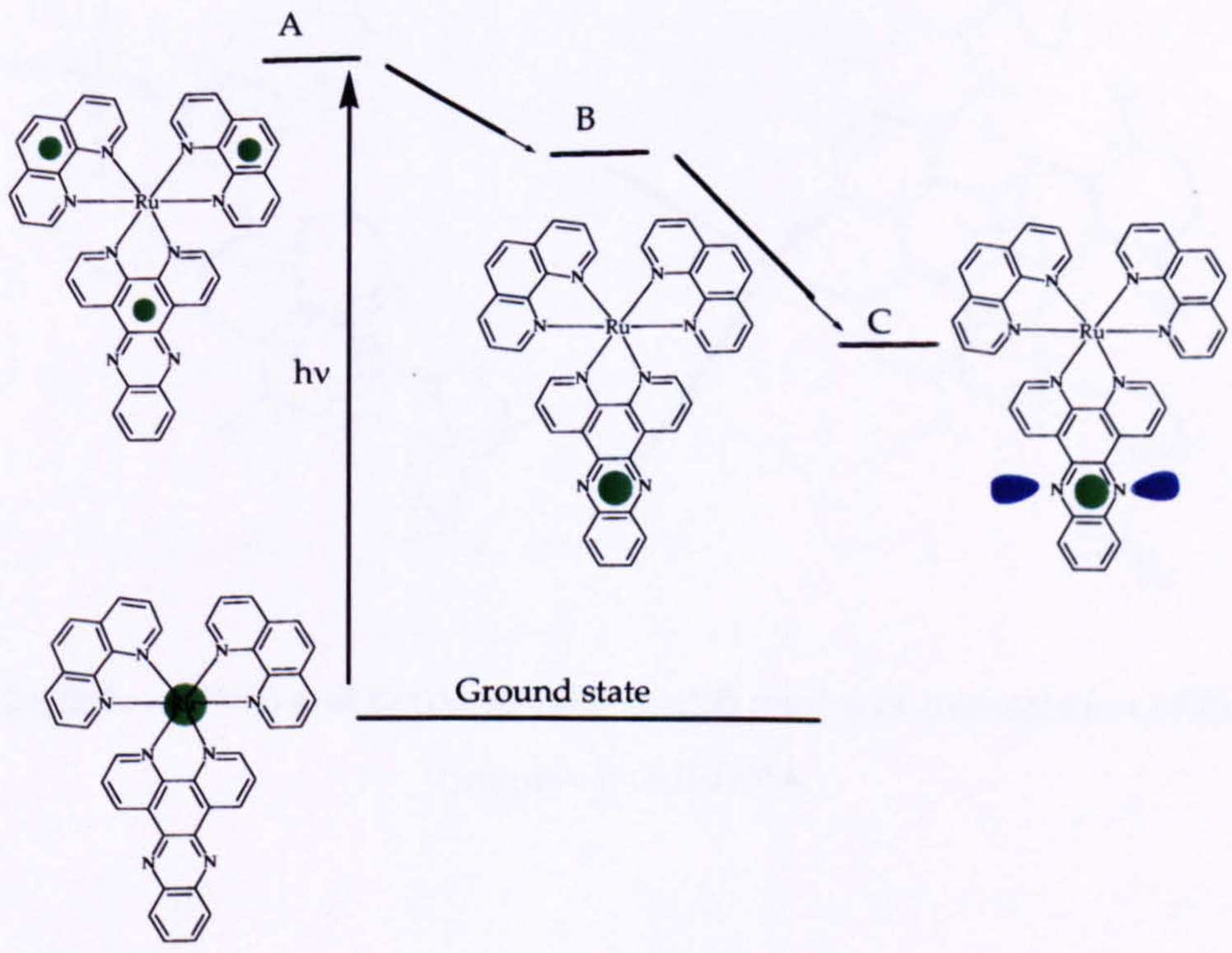

Figure 1.23: Model describing the photophysics of $[Ru(phen)_2(dppz)]^{2+}$ in water

In aqueous solutions, water binds by hydrogen bonding to the phenazine nitrogen atoms and quenches the charge-transfer excited state. When the $[Ru(phen)_2(dppz)]^{2+}$ complex binds to DNA, the dppz ligand is protected from water and therefore these complexes luminescence. This is usually accompanied by the UV-Vis spectrum of the complex showing a is slight shift to longer wavelength (bathochromic shift) and the absorption decreasing (hypochromic effect)[52,55].

Although the mode of interaction of $[Ru(phen)_2(dppz)]^{2+}$ with DNA has been recognised as intercalation of the phenazine ligand into the base pair, luminescence lifetime studies on the interaction of $[Ru(phen)_2(dppz)]^{2+}$ with all nucleic acids showed bi-exponential decay indicating the presence of two emitting species, one with a longer lifetime than the other. These two emitting species were explained by two different orientations of the dppz ligand to the helix in the major groove: one in which the metal-phenazine is parallel to the DNA dyad axis and another perpendicular (figure 1.24)[46].

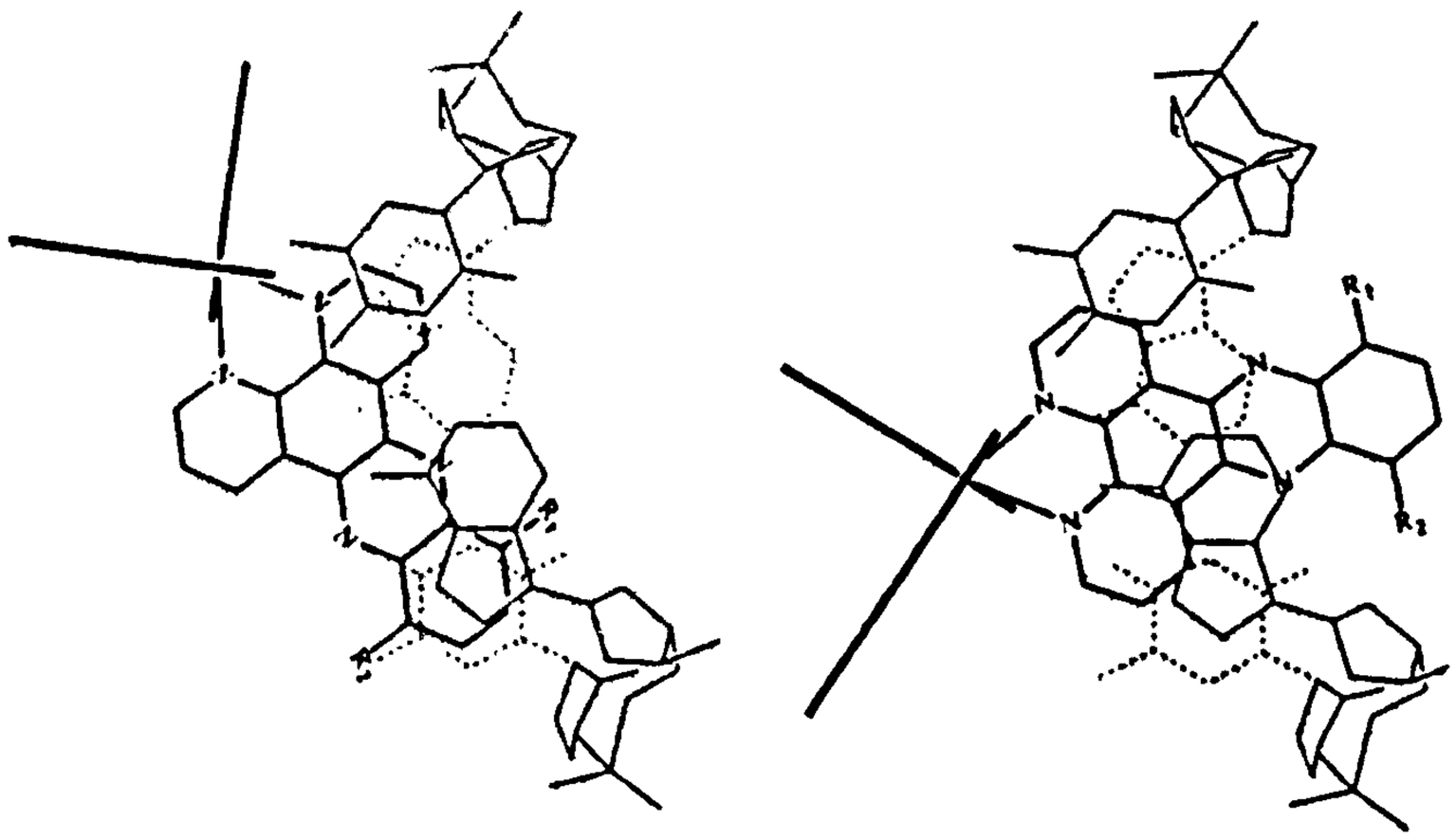

Figure 1.24: Side on (left) and perpendicular (right) modes of intercalation of Ru(II)-dppz complex into B-DNA

Nordén and co-workers also studied the interaction of Δ- and Λ- $[Ru(phen)_2(dppz)]^{2+}$ with CT-DNA using several techniques[56]. Binding constant obtained by luminescence titrations for both complexes was found to be similar (in the 10^7 M^{-1} range) showing little enantiomeric selectivity, but the relative quantum yield of the Δ-enantioner bound to DNA is 6-10 times higher than that of the bound Λ-isomer, meaning that the 85% of the emission observed for the racemic $[Ru(phen)_2(dppz)]^{2+}$ bound to DNA, comes from the Δ-enantiomer. Linear dichroism confirmed that both complexes bind to DNA with the dppz motif parallel to the plane of the bases. In 1997, Nordén *et al.* studied the interaction of both $[Ru(phen)_2(dppz)]^{2+}$ enantiomers

with T-4 DNA (100 % glycosylated at the cytosine 5-CH_2-OH position in the major groove, having a significant impediment to any binding in this groove). Both enantiomers emit strongly when bound to T-4 DNA with lifetimes and stoichiometries that are similar to CT-DNA. Therefore they concluded that the metal complex was confined in the minor groove[57].

A later luminescence study by Barton *et al.* investigated the interaction of Δ–$[Ru(phen)_2(dppz)]^{2+}$ with 1:1 mixture of poly d(AT) and poly d(GC)[58]. The analysis of the data indicated that 85 % of the complex is bound preferentially to poly d(AT) and therefore a similar emission is expected for the binding of Δ–$[Ru(phen)_2(dppz)]^{2+}$ with CT-DNA (42% of AT base pairs) and T-4 DNA. Competition experiment with known groove orientation DNA-binding molecules were also reported providing information for binding of these complexes via the major groove.

In contrast, NMR studies of the interaction of Δ–$[Ru(phen)_2(dppz)]^{2+}$ with $d(GTCGAC)_2$ indicate that this complex binds via the minor groove[59].

Despite the large number of reported studies for the interaction of $[Ru(phen)_2(dppz)]^{2+}$ with different DNA using several techniques, the exact model for the binding of this complex to DNA is still under debate.

Since $[Ru(phen)_2(dppz)]^{2+}$ and $[Ru[(bpy)_2(dppz)]^{2+}$ complexes were first reported as probes for nucleic acids a variety of other related metal complexes with different intercalating and ancillary ligands have been synthesised and their binding properties to DNA have been reported[60].

Palaniandavar *et al,* studied the interaction of $[Ru(5,6\text{-dmp})_2(dppz)]^{2+}$ (dmp = dimethylphenanthroline) (figure 1.25) with DNA and showed that 5,6-dimethyl groups increased DNA-binding affinity though favourable hydrophobic interactions of the methyl groups with the surface of DNA major groove[61].

On the other hand, Ji and co-workers synthesised a series of derivatives of $[Ru(L)_2(dppz)]^{2+}$ where L was dmp (2,9-dimethyl-1,10-phenanthroline) or dmb (4,4′-dimethyl-2,2′-bpy) (figure 1.26) and examined their different DNA-binding properties[62]. Both complexes showed perturbation of the $\pi \rightarrow \pi^*$ UV-Vis transition on the dppz when bound to DNA. From equilibrium dialysis experiments, they

concluded that neither compound binds with enantioselectivity to CT-DNA. However kinetic studies show that substitution on the 4 and 4′ position of the ancillary bpy ligand increased the discrimination of Δ and Λ isomers binding to DNA, with the isomer Λ binding more rapidly than the Δ enantiomer. Substitution on the position 2 and 9 of the phen ligand prevents deep intercalation into the base pairs of DNA and subsequently decreases the affinity.

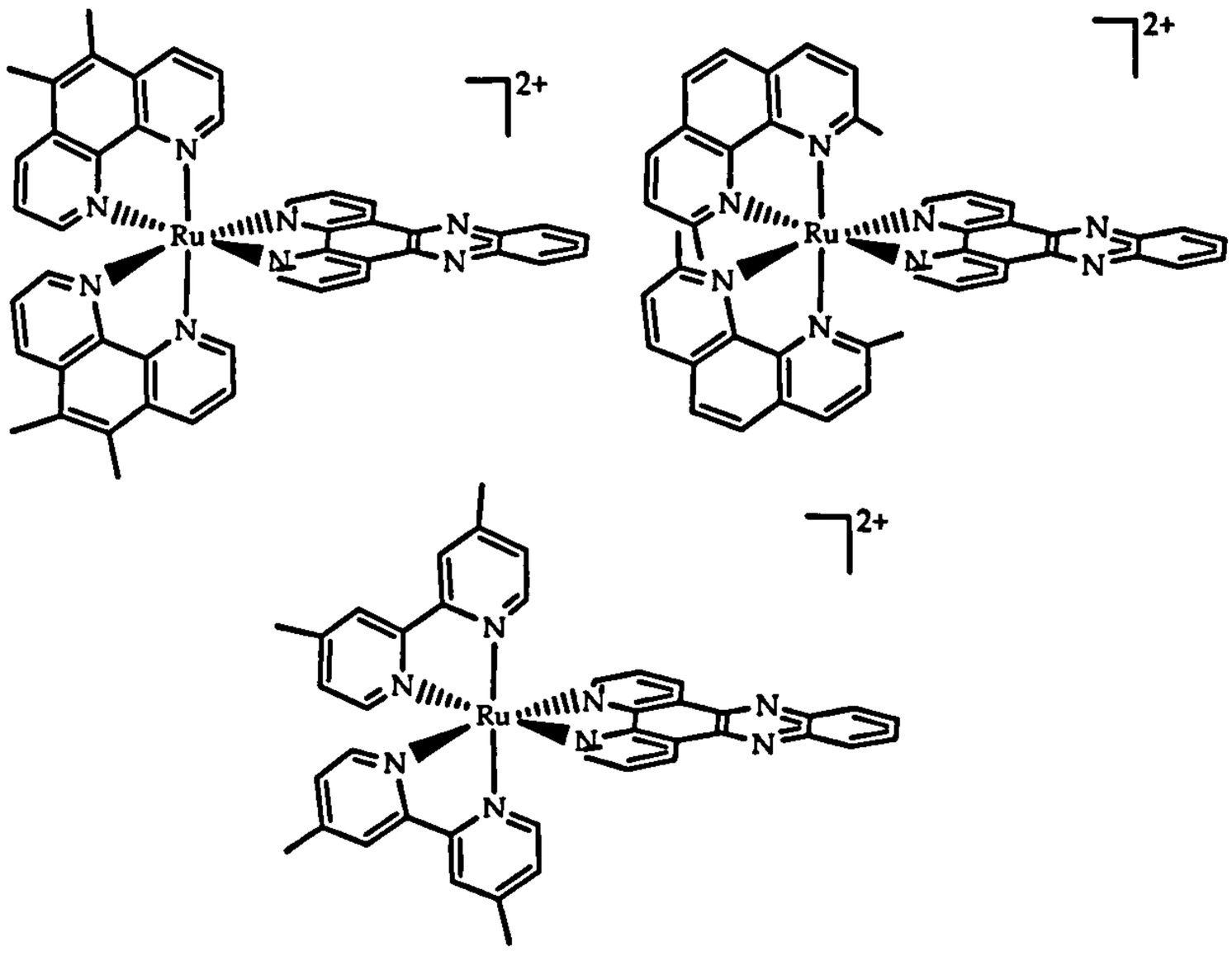

Figure 1.25: Structure of a series of $[Ru(L)_2(dppz)]^{2+}$ derivatives: $[Ru(5,6\text{-dmp})_2(dppz)]^{2+}$ (upper left), $[Ru(2,9\text{-dmp})_2(dppz)]^{2+}$ (upper right) and $[Ru(4,4'\text{-dmb})_2(dppz)]^{2+}$ (lower centre)

Modifications can also be made in the intercalative ligand. Jing *et al.* studied the interaction of $[(bpy)_2RuL]^{2+}$, where L are imidazo[f]-1,10-phenanthrolines, with DNA[63] (figure 1.26). The complexes were shown to have different affinities for DNA, and they suggested that this can not be explained by factors such as size or shape because all complexes are similar, so they attributed the higher affinity of **3** to the effect of hydrogen bonding between intercalative ligand and DNA. An

alternative explanation is that the difference may be due to hydrophobicity and steric effects.

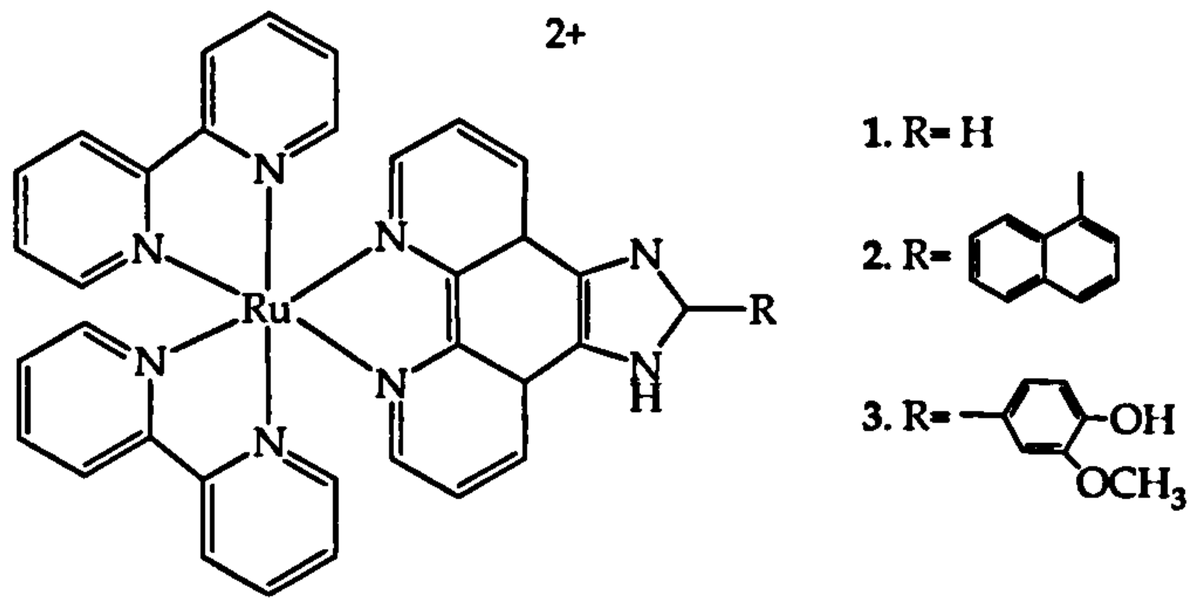

Figure 1.26: Structures of $[(bpy)_2RuL]^{2+}$ complexes synthesised by Jing et al.

Interaction of $[Ru(phen)_2(PHEHAT)]^{2+}$ (where PHEHAT is 1,10-phenanthrolino[5,6-b]1,4,5,8,9,12-hexaazatriphenylene, figure 1.27) with DNA was also studied[64]. This complex intercalates in between the base pairs of DNA showing a light switch effect, and photoinduced electron transfer from GMP (guanosine-5′-monophosphate) to the excited complex occurs although with poor efficiency[64].

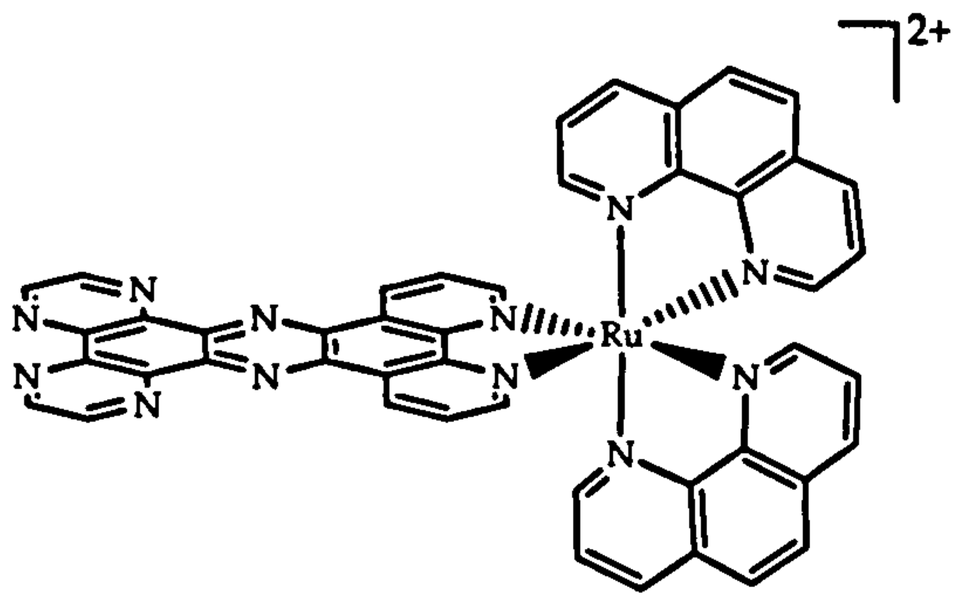

Figure 1.27: Structure of $[Ru(phen)_2(PHEHAT)]^{2+}$

3.3.3 Phi complexes

In contrast to the dppz ligand, complexes containing the 9,10-phenanthrenequinone (phi) ligand intercalate with the long axis of the phi ligand parallel to the axis of the DNA. Another characteristic of the phi ligand is its photochemistry, phi complexes of Rh(III) are known to have rich electrochemistry and photoredox chemistry. Barton and co-workers have used the Rh(III)-phi complexes for cleavage of DNA[65]. They found that $[Rh(phen)_2(phi)]^{3+}$ and $[Rh(bpy)(phi)_2]^{3+}$ are similarly efficient at nucleic acid strand scission in the presence of low wavelength UV, but possess different DNA recognition properties. $[Rh(phen)_2(phi)]^{3+}$ cleaves double stranded DNA selectively at 5′-pyrimidine-purine-3′ sites and in particular 5′-CCAG-3′, while $[Rh(bpy)(phi)_2]^{3+}$ cleaves DNA in a neutral sequence way. While both complexes contain a phi ligand that intercalates in between the base pair of the DNA, in the case of $[Rh(bpy)(phi)_2]^{3+}$ there is also an ancillary phi ligand that can potentially bind through H-bonding to guanine sites at the O6. However this interaction was not detected, suggesting that the sequence selectivities found are not due to H-bonding. In fact, differences in recognition can be understood by considering the different shapes of the complexes (figure 1.28)[66,67]. In the interaction of $[Rh(phen)_2(phi)]^{3+}$ with DNA, the phi ligand is inserted deeply between the base pairs requiring sites with more opened major groove, otherwise steric clashes between bases above and the intercalation site below may happen. In contrast in the $[Rh(bpy)(phi)_2]^{3+}$ the ancillary ligands do not project over the metal centre and only the imine protons are close to the helical groove.

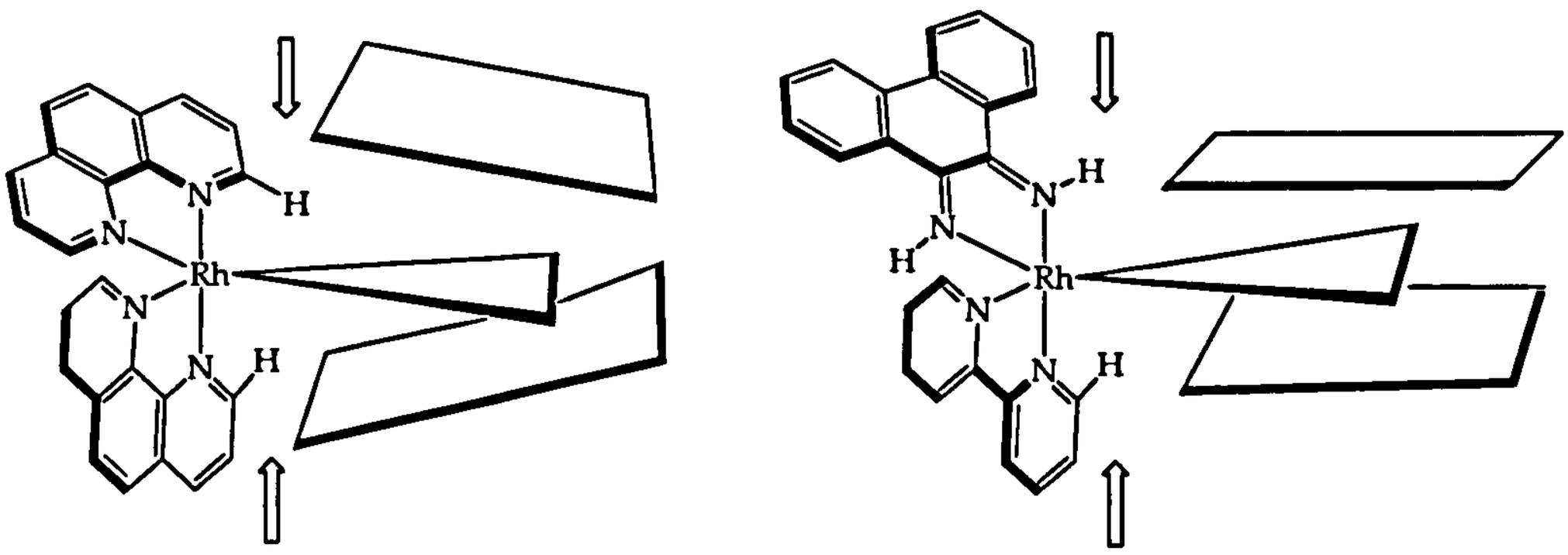

Figure 1.28: Matching Rh(III)-phi complexes to DNA sites

It is known that $[Rh(phen)_2(phi)]^{3+}$ cleaves DNA from the major groove, this fact is in contrast to many synthetic compounds that bind duplex DNA in the minor groove and is similar to sequence-specific DNA-binding proteins[68].

A variety of phi complexes of rhodium have been synthesised and the intercalation in the DNA major groove have been studied. A family of amine-Rh(III)-phi complexes ($[Rh(NH_3)_2(phi)]^{3+}$, $[Rh(en)_2(phi)]^{3+}$, etc) showed strong cleavage of 5′-GC-3′ sites due to H-bonding of the axial amines of the metal complex and the O6 of guanine. Using this specificity, a new complex Δ-α–$[Rh[(R,R)Me_2trien](phi)]^{3+}$ was designed to bind to 5′-TGCA-3′ through H-bonds between the amine group as well as van der Waal interactions between the methyl groups of the complex and thymine methyl groups. ^1H NMR studies[69] and a crystal structure[70] of this intercalator bound to DNA confirmed that the complex binds specifically to 5′-TGCA-3′ from the major groove (figure 1.29).

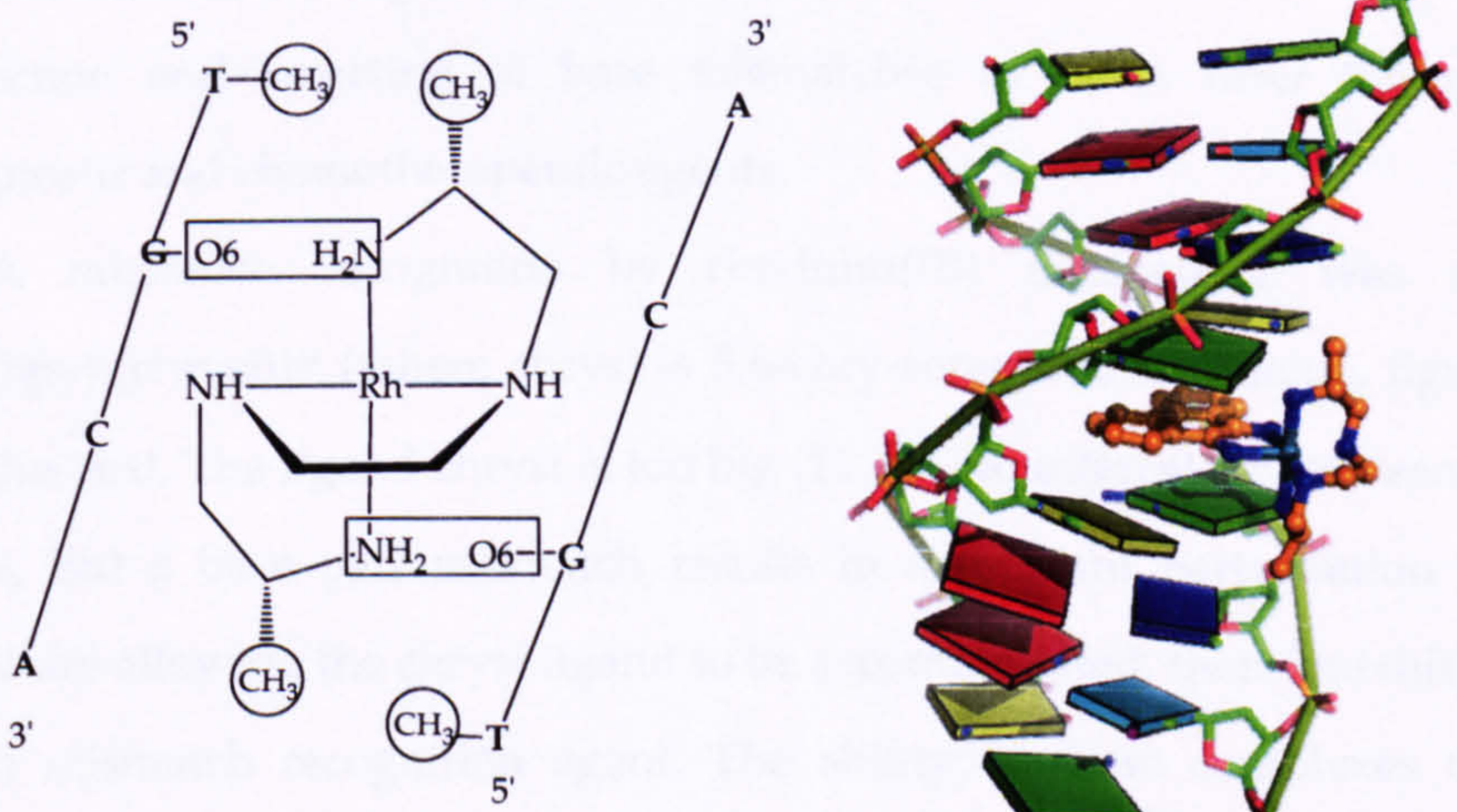

Figure 1.29: Schematic interaction of Δ-α–$[Rh[(R,R)Me_2trien](phi)]^{3+}$ to 5′-TGCA-3′ (left) and x-ray crystal structure (right) (NDB ID: UD005)

The influence of ancillary ligands with hydrogen bonding sites on DNA binding specificities of Rh(III)-phi was also studied. Barton *et al.* synthesised new derivatives of $[Rh(phen)_2(phi)]^{3+}$ and $[Rh(bpy)(phi)_2]^{3+}$ attaching different functionalities in a defined stereochemistry. It was found that complexes that incorporate hydrogen donor groups showed specific binding preference for 5'-GC-3' sites, whereas the complexes containing hydrogen bond acceptor sites showed no such preference[71,72].

Inhibition of transcription leads to incomplete coding of RNA and proteins and ultimately to cell death. Complexes $[Rh(phen)_2(phi)]^{3+}$ and $[Rh(bpy)(phi)_2]^{3+}$ are able to stabilise DNA, such stabilisation results in suppression of transcription through inhibition of the DNA elongation step in vitro[73,74]. In competition experiment with yeast activator protein 1, the metal complex $[Rh(phen)_2(phi)]^{3+}$ was able to compete with the protein for a binding domain, showing their potential as therapeutic agents for gene regulation[65].

3.3.4 Mismatches recognition

Detection and targeting of base mismatches in DNA offer the possibility of diagnostic and chemotherapeutic agents.

DNA mismatch recognition by rhodium(III) intercalator was studied and $[Rh(bpy)_2(chrysi)]^{3+}$ (where chrysi is 5,6-chry-serequinone diimine, figure 1.31) was synthesised. The ligand chrysi is too big (11.3 Å) to intercalate between normal base pairs, but a base pair mismatch results in significant perturbation of the DNA structure allowing the chrysi ligand to be accommodated, therefore this complex is a good mismatch recognition agent. The ability of these complexes to selectively target these mismatch sites show their enormous potential as future diagnostic or site specific chemotherapeutic agents[75,76]. A second generation heterocyclic mismatch recognition agent, $[Rh(bpy)_2(phzi)]^{3+}$ (figure 1.30) was synthesised[77], showing higher affinity than the chrysi analogous complex without losing site selectivity.

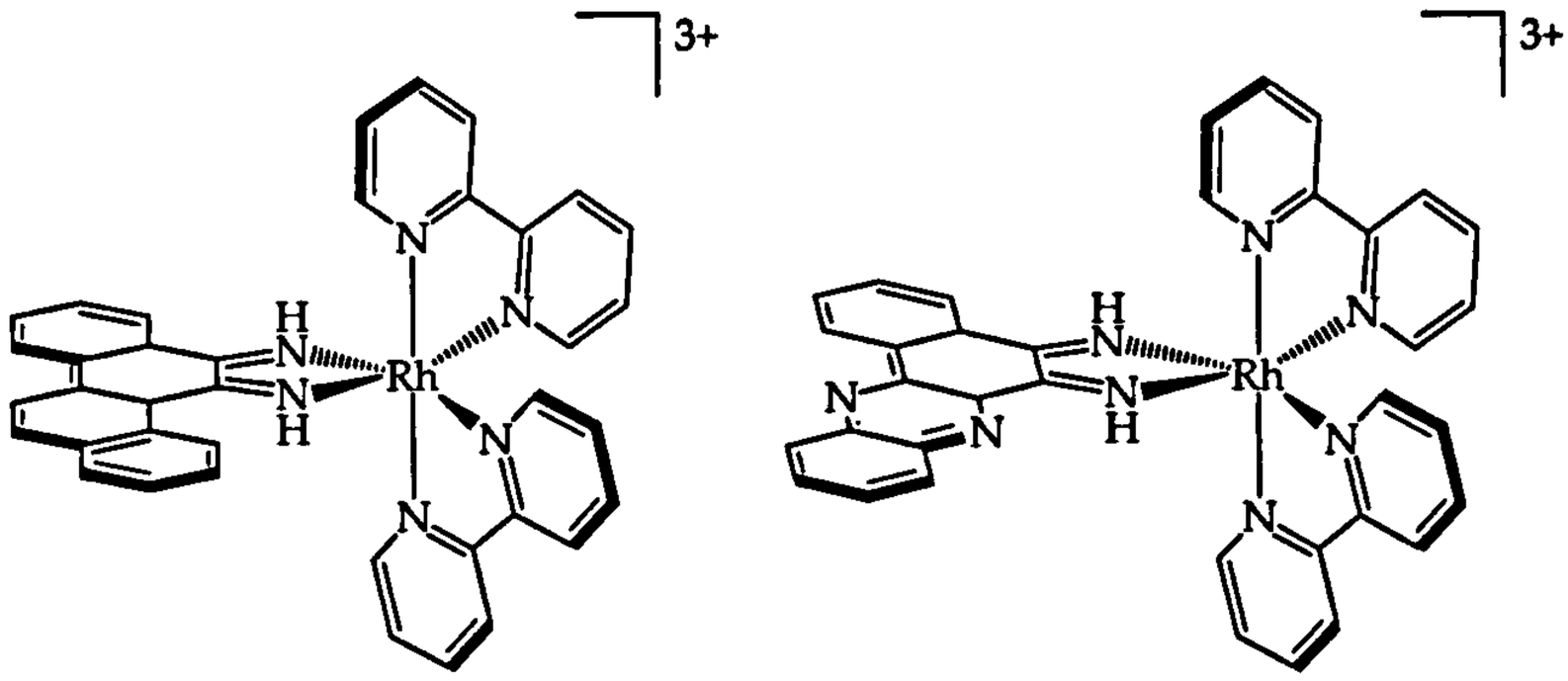

Figure 1.30: Structure of the complexes $[Rh(bpy)_2(chrysi)]^{3+}$ (left) and $[Rh(bpy)_2(phzi)]^{3+}$ (right)

In 2004, Barton and co-workers explored the possible design of luminescence metal complexes that specifically target mismatches in DNA[78]. Their approach was to synthesise octahedral Ru(II) complexes containing a bulky intercalating ligand as a fluorescence probe for mismatches (figure 1.31). Using a variety of techniques such as luminescence titration and footprinting they showed that although both complexes bind to regular duplex DNA, they bind more tightly to CC mismatches.

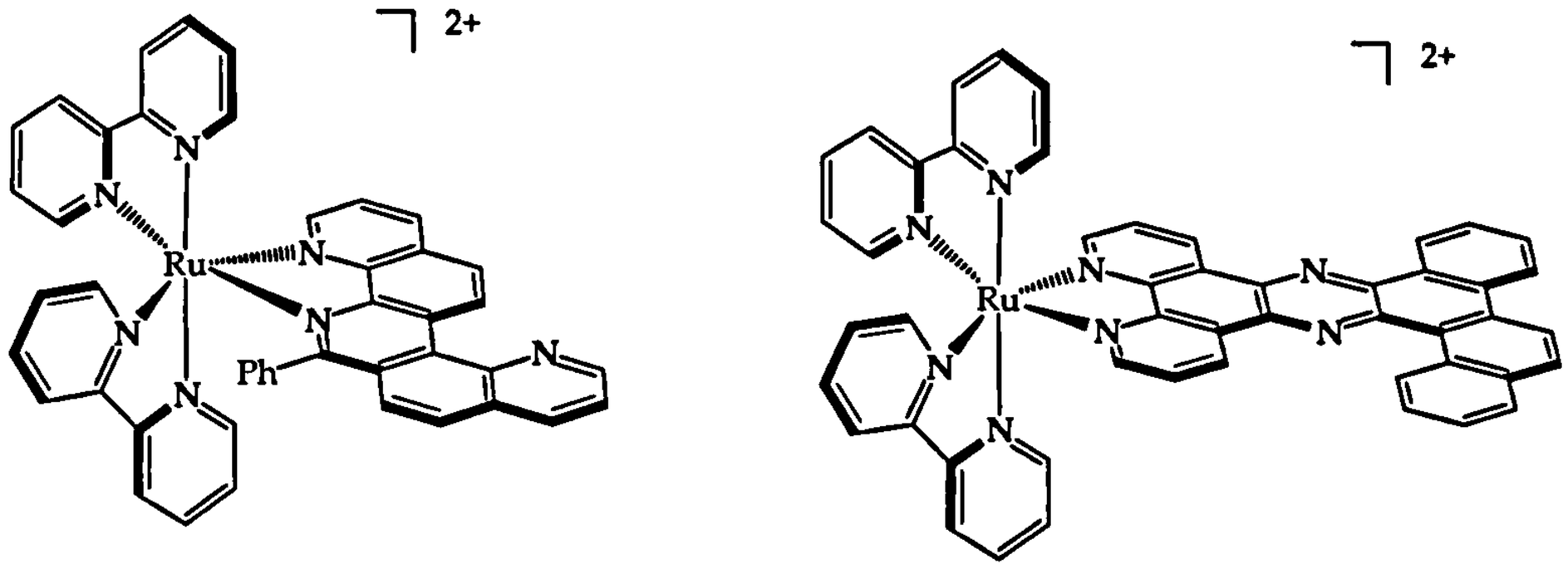

Figure 1.31: Structure of Ru(II) luminescence complexes for targeting mismatches $[Ru(bpy)_2(tpqp)]^{2+}$ (left) and $[Ru(bpy)_2(tactp)]^{2+}$ (right)

3.3.5 Oligometallic complexes

Several natural antibiotics are bis-intercalators. For example quinoxaline antibiotics contain a cyclic octapeptide with linked chromophores capable of simultaneous intercalation[79,80]. A related bis-intercalator triosin, inhibits DNA replication and has a slight specificity towards A-T sites. Synthetic bis-intercalators were later constructed by linking two herterocycles such as acridines and methidium with chains of varying length to allow both of the systems to interact between base pairs. In general these molecules bind to DNA with high affinity but show a lack in sequence selectivity.

In 1992, Murphy *et al.* studied the interaction of a new class of DNA metallointercaltors: ligand-bridged bimetallic complexes[81]. The interaction of $[Ru(NH_3)_4]_2(dpb)^{4+}$ (where dpb is 2,3-bis(2-pyridyl)benzo[g]quinoxaline, figure 1.32) with DNA showed large binding constant, however the analogous $[Ru(bpy)_4]_2(dpb)^{4+}$ bound weakly, if at all, to DNA, showing that incorporation of different spectator ligands can modulate the binding and enhance specific interactions of this bimetallic complexes.

Ji *et al.* studied the interaction of mono- and bi- nuclear ruthenium complexes containing an asymmetric ligand. $[Ru(bpy)_2(pztp)]^{2+}$ and $[(bpy)_2Ru(pztp)Ru(bpy)_2]^{4+}$ (where pztp is 3-(pyrazin-2-yl)-as-triazino[5,6-f]1,10-phenanthroline, figure 1.32) were synthesised and the binding properties to DNA were studied[82]. Both complexes showed distinctive UV-Vis changes when bound to DNA. The monomer increased DNA viscosity, binding via intercalation, while the bimetallic complex decreased viscosity, binding by electrostatic interaction to DNA.

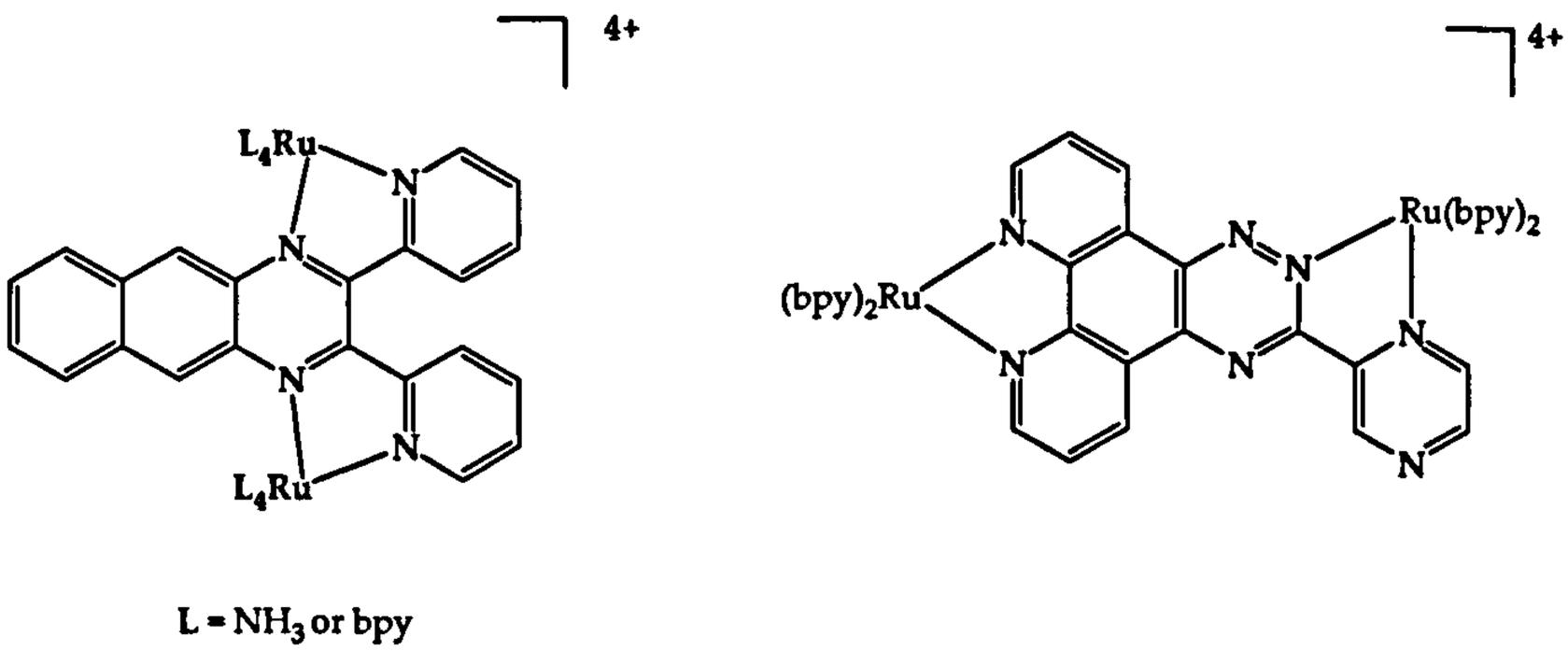

Figure 1.32: Structures of $[Ru(L)_4]_2(dpb)^{4+}$ (left) and $[(bpy)_2Ru(pztp)Ru(bpy)_2]^{4+}$ (right)

In 1998, Kelly and co-workers studied the interaction of $[(phen)_2(Me\text{-}bpy)\text{-}(CH_2)_n\text{-}(bpyMe)Ru(bpy)_2]^{2+}$ (n = 5, 7 or 10, figure 1.33) with DNA, which shows higher DNA binding affinity than the monomer $[Ru(phen)_2(Me_2bpy)]^{2+}$ (Me_2bpy= 4,4′-dimehtyl-2,2′-biyridyl)[83,84]. They also reported that the linker chain length, n, is a crucial factor in the determination of DNA binding affinities, showing that only the bimetallic heptanelinked complex allows full interaction of both centres.

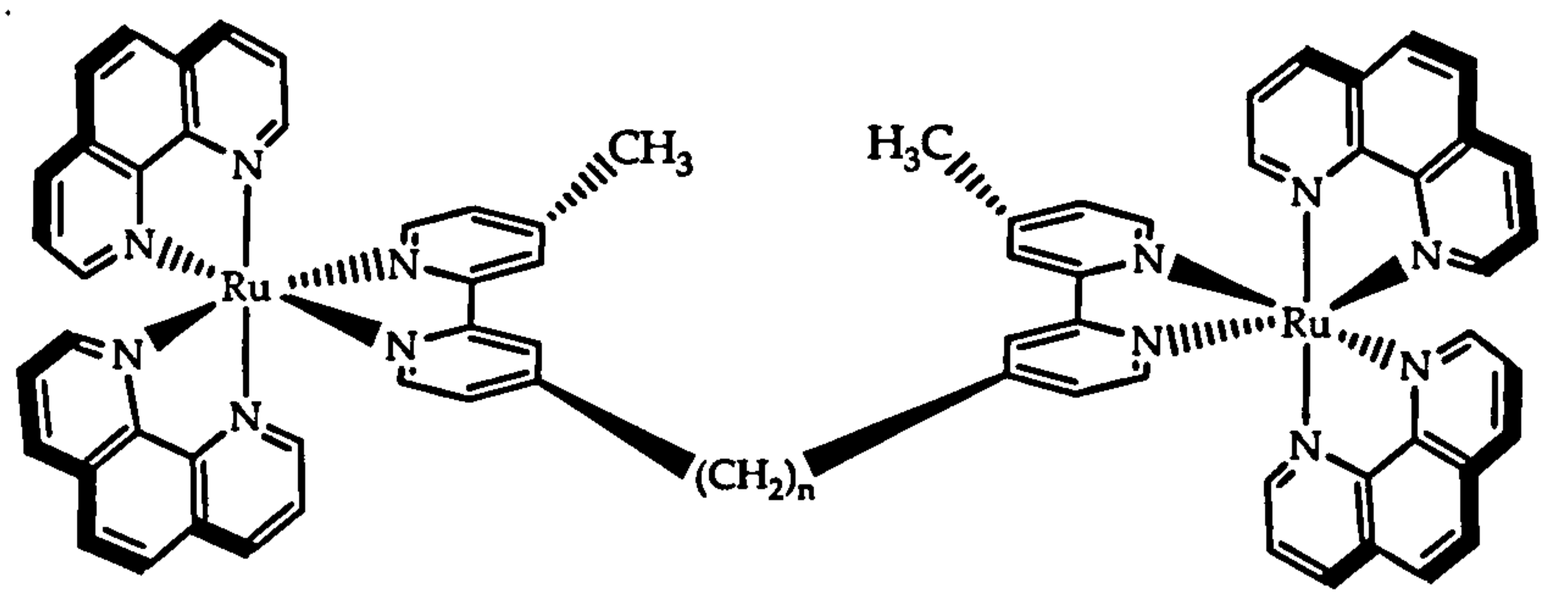

Figure 1.33: Structure of $[(phen)_2(Me\text{-}bpy)\text{-}(CH_2)_n\text{-}(bpyMe)Ru(bpy)_2]^{2+}$ (with n = 5, 7 or 10)

Nordén *et al.* reported the interaction of a dimeric complex with two linked dppz units (figure 1.34)[85]. The four compounds (ΔΔ-bpy/ΛΛ-bpy and ΔΔ–phen/ΛΛ-phen) were found to bind to DNA with high affinities ($K \approx 10^{12}$ M^{-1}), but in different modes, none of them via intercalation. Both ΔΔ and ΛΛ-bpy isomers, as well as ΛΛ-phen, showed a binding geometry in which the (dppz-11,11′-dppz) ligand straddles the sugar-phosphate backbone placing the RuL_2 moiety in each groove, however the ΔΔ-phen showed markedly different behaviour. Further studies on the interaction of the ΔΔ-phen isomer with CT-DNA showed that this complex switches from groove binding to intercalation by threading one of the $[Ru(phen)_2]^{2+}$ moieties through the DNA duplex, intercalating the bridged dppz units and leaving one metal centre in each groove[86].

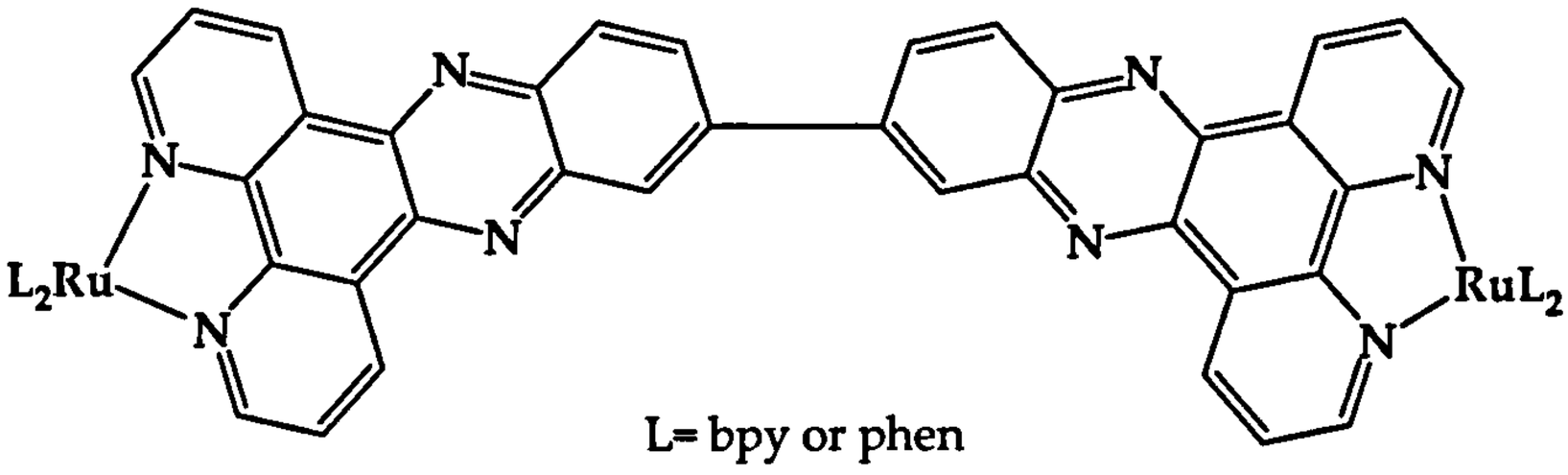

Figure 1.34: Structures of $[L_2Ru\{dppz(11\text{-}11')dppz\}RuL_2]^{4+}$

The phenomenon of DNA threading was studied in related systems, using dppz tethered units with a longer and more flexible linker. Nordén and co-workers synthesised the three enantiomers of $[\mu\text{-}c4(cpdppz)_2\text{-}(phen)_4Ru_2]^{4+}$ and characterised their binding to DNA (figure 1.35)[87,88]. Luminescence, LD and other studies showed intercalation of all the complexes between base pair of DNA, with the intercalating ligands separated by two base pairs (figure 1.36).

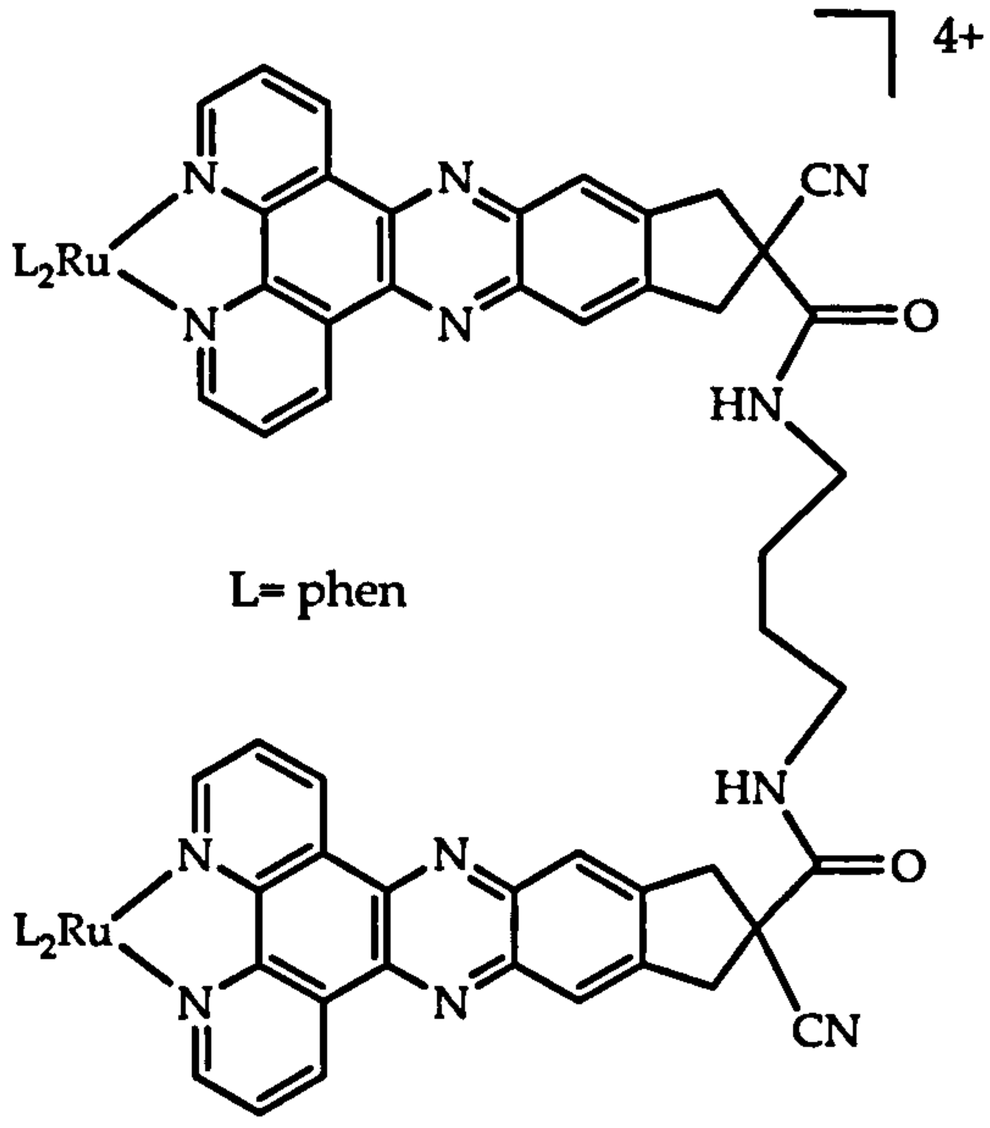

Figure 1.35: Structure of the threading $[\mu\text{-}c4(cpdppz)_2\text{-}(phen)_4Ru_2]^{4+}$ dimer

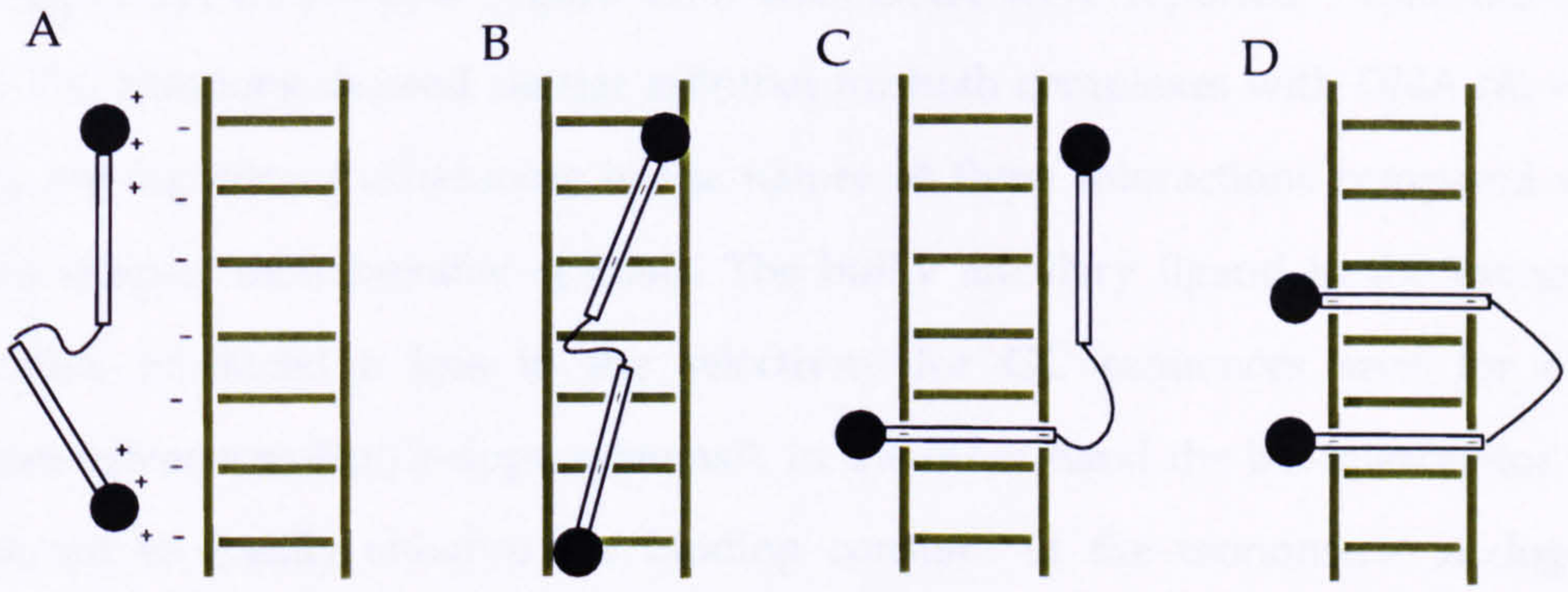

Figure 1.36: Schematic DNA-interaction modes of Nordén's dimers: A) External binding B) groove binding C) Mono-intercalation D) Bis-intercalation

Metcalfe, *et al*. developed a facile route to the synthesis of new bimetallic Re(I) complexes containing two dppz intercalating ligands[89]. DNA bindings of $[(CO)_3Ru(dppz)]_2(dpe)^{2+}$ and $[(CO)_3Ru(dppz)]_2(dpp)^{2+}$ (figure 1.37) showed that the propane tether is insufficient long to allow both centres to intercalate into the same duplex, however the binding curves constructed from changes in the absorption on CT-DNA suggested a second interaction. This second binding can only occurred if the second Re(I) centre interacts with another duplex, through interstrand binding.

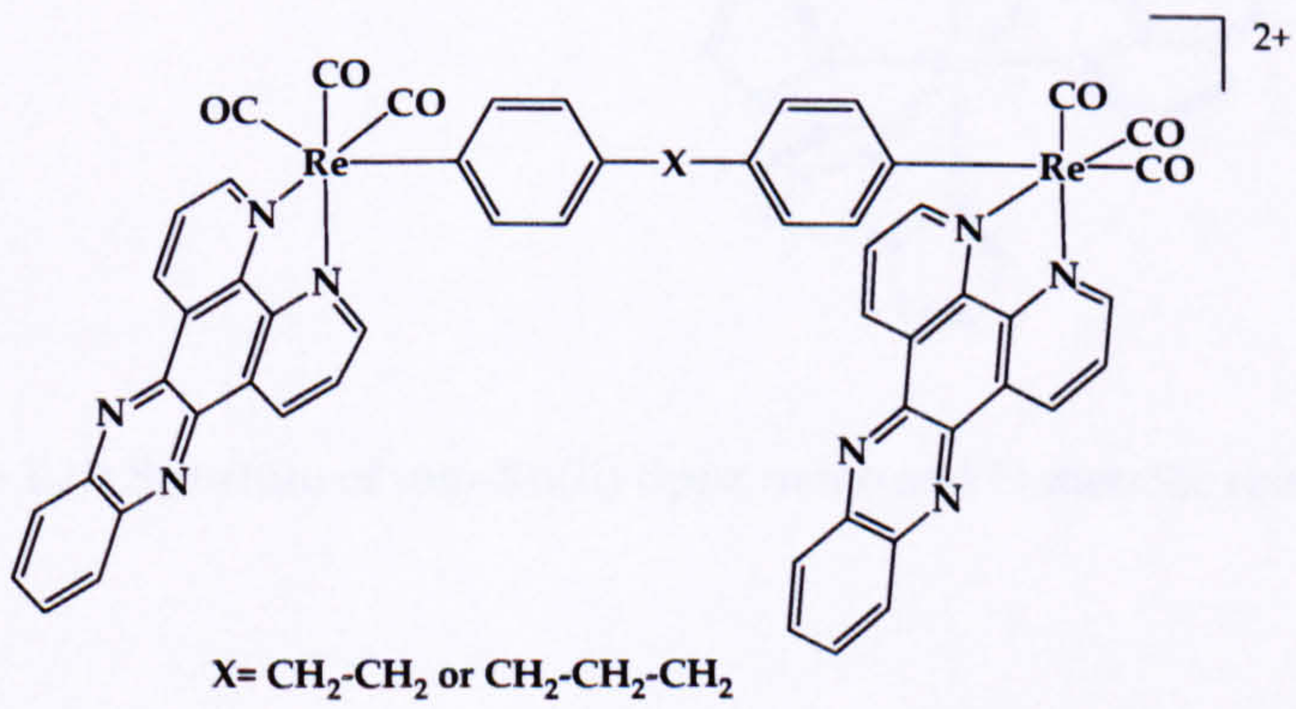

X= CH_2-CH_2 or CH_2-CH_2-CH_2

Figure 1.37: Structure of Re(I) dppz complexes

Binding studies on tpm-Ru(II)-dppz systems linked together by 4,4'-dipyridyl-1,5-pentane (figure 1.38) with DNA were reported[90]. Luminescence and ITC titrations showed similar affinities for both complexes with DNA ($K_b \approx 10^5$ M^{-1}), but significant differences in the nature of these interactions compared with other simpler monometallic systems. The bulky ancillary ligand in the monomer complex produced a loss in the selectivity for GC sequences seen for other mononuclear tpm-Ru(II)-dppz systems[91]. In the other hand the bis-intercalator was expected to greatly enhance the binding constant of the monomeric analogues, although such behaviour was not seen. This result was interpreted by consideration of the length and rigidity of the linker employed in the complex.

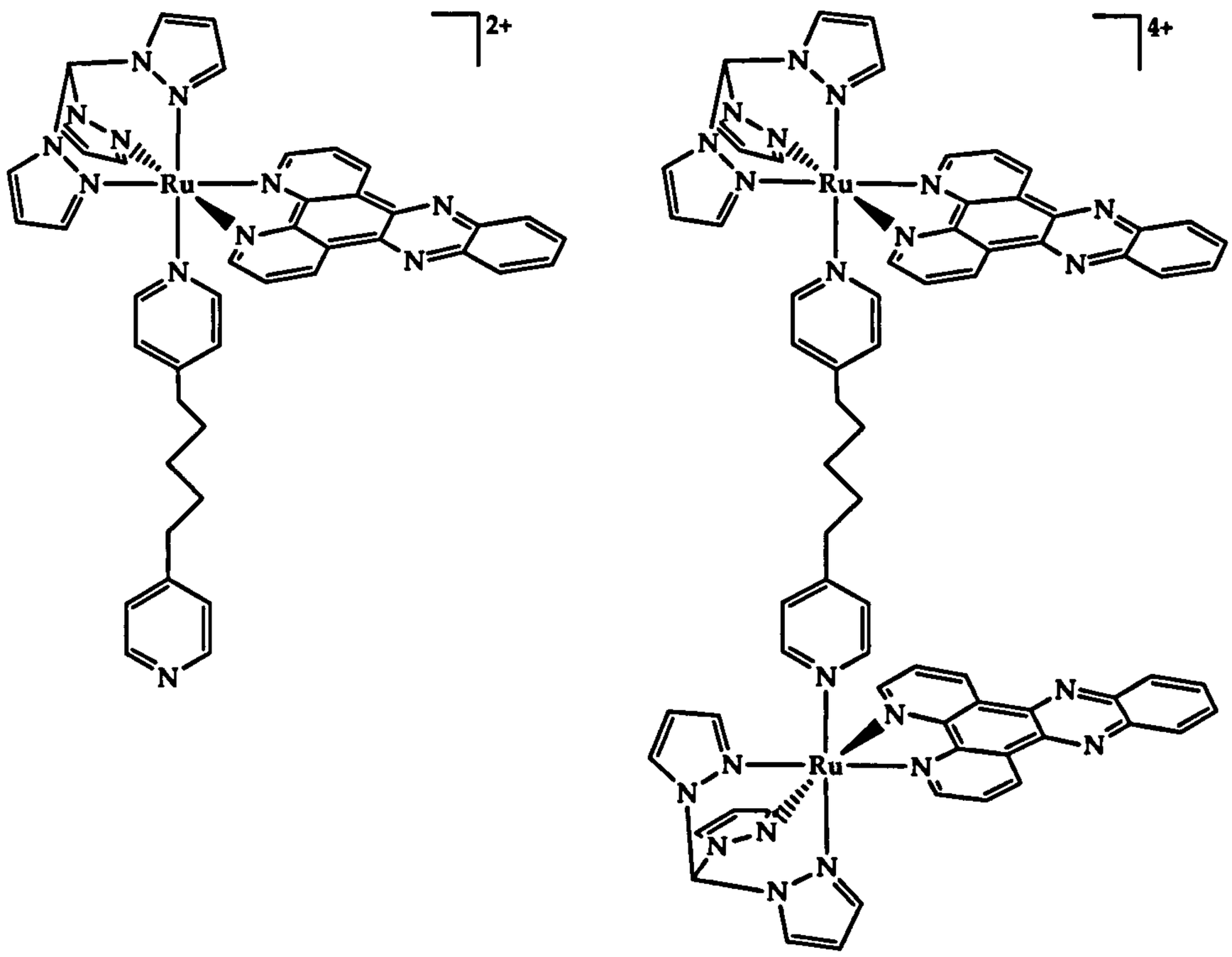

Figure 1.38: Structure of tpm-Ru(II)-dppz mono and bi metallic complexes

4 Summary

The sequence of nucleotides in DNA specifies a complementary sequence in RNA which specifies the amino acids of a protein. The transcription of duplex DNA results in the formation of messenger RNA, therefore inhibition of transcription can result in incomplete coding of mRNA and lead to cell death. Consequently synthetic molecules that interact with nucleic acids can be used for a variety of biophysical and therapeutic studies. Metal complexes can function as a scaffold to arrange ligands in optimal positions to interact specifically with DNA. These metal complexes can also introduce redox/photochemical functionality to a DNA binding system. Therefore transition metal complexes are being investigated as a new group of compounds that bind with moderate selectivity to DNA.

5 Aim of studies

The aim of this thesis was to study new mixed recognition motif Ru(II)-tpm complexes containing ligands capable of intercalation between the base pairs of DNA and ancillary ligands with hydrogen accepting and/or donating substitutes. The introduction of hydrogen accepting and/or donating groups may produce specific contacts in the grooves of DNA, producing binding to a particular sequence.

6 References

(1) Stryer, L. *Biochemistry*; 4th ed.; W. H. Freeman and Company: New York, 1995.

(2) Belmont, P.; Constant, J. F.; Demeunynck, M. *Chem. Soc. Rev.* **2001**, *30*, 70-81.

(3) Roat-Malone, R. M. *Bioinorganic chemistry*; John Wiley & Sons, Inc.: New Jersey, 2002.

(4) Takahara, P. M.; Rosenzweig, A. C.; Frederick, C. A.; Lippard, S. J. *Nature* **1995**, *377*, 649-652.

(5) Lebwohl, D.; Canetta, R. *Eur. J. Cancer* **1998**, *34*, 1522-1534.

(6) Clarke, M. J.; Zhu, F.; Frasca, D. R. *Chem. Rev. (Washington)* **1999**, *99*, 2511-2533.

(7) Morris, R. E.; Aird, R. E.; Murdoch, P. d. S.; Chen, H.; Cummings, J.; Hughes, N. D.; Parsons, S.; Parkin, A.; Boyd, G.; Jodrell, D. I.; Sadler, P. J. *J. Med. Chem.* **2001**, *44*, 3616-3621.

(8) Aird, R. E.; Cummings, J.; Ritchie, A. A.; Muir, M.; Morris, R. E.; Chen, H.; Sadler, P. J.; Jodrell, D. I. *Br. J. Cancer* **2002**, *86*, 1652-1657.

(9) Record, M. T.; Lohman, T. M.; Haseth, P. d. **1976**, 145-158.

(10) Shui, X.; McFail-Isom, L.; Hu, G. G.; Williams, L. D. *Biochemistry* **1998**, *37*, 8341-8355.

(11) McFail-Isom, L.; Shui, X.; Williams, L. D. *Biochemistry* **1998**, *37*, 17105-17111.

(12) Tabor, C. W.; Tabor, H. *Annu. Rev. Biochem.* **1984**, *53*, 749-790.

(13) Basu, H. S.; Marton, L. J. *Biochem. J.* **1987**, *244*, 243-246.

(14) Basu, H. S.; Schwietert, H. C. A.; Feuerstein, B. G.; Marton, L. J. *Biochem. J.* **1990**, *269*, 329-334.

(15) Zimmer, C.; Wahnert, U. *Prog. Biophys. Mol. Biol.* **1986**, *47*, 31-112.

(16) Patel, D. J. *Proc. Natl. Acad. Sci. U.S.A.* **1982**, *79*, 6424-6428.

(17) Kopka, M. L.; Yoon, C.; Goodsell, D.; Pjura, P.; Dickerson, R. E. *Proc. Natl. Acad. Sci. U.S.A.* **1985**, *82*, 1376-1380.

(18) Coll, M.; Frederick, C. A.; Wang, A. H. J.; Rich, A. *Proc. Natl. Acad. Sci. U.S.A.* **1987**, *84*, 8385-8389.

(19) Marky, L. A.; Breslauer, K. J. *Proc. Natl. Acad. Sci. U.S.A.* **1987**, *84*, 4359-4363.

(20) Harshman, K. D.; Dervan, P. B. *Nucleic Acids Res.* **1985**, *13*, 4825-4835.

(21) Abu-Daya, A.; Brown, P. M.; Fox, K. R. *Nucleic Acids Res.* **1995**, *23*, 3385-3392.

(22) Mrksich, M.; Dervan, P. B. *J. Am. Chem. Soc.* **1993**, *115*, 2572-2576.

(23) Mrksich, M.; Wade, W. S.; Dwyer, T. J.; Geierstanger, B. H.; Wemmer, D. E.; Dervan, P. B. *Proc. Natl. Acad. Sci. U.S.A.* **1992**, *89*, 7586-7590.

(24) Mrksich, M.; Parks, M. E.; Dervan, P. B. *J. Am. Chem. Soc.* **1994**, *116*, 7983-7988.

(25) White, S.; Baird, E. E.; Dervan, P. B. *Biochemistry* **1996**, *35*, 12532-12537.

(26) White, S.; Szewczyk, J. W.; Turner, J. M.; Baird, E. E.; Dervan, P. B. *Nature* **1998**, *391*, 468-471.

(27) Lerman, L. S. *J. Mol. Biol.* **1961**, *3*, 18-30.

(28) Chaires, J. B.; Dattagupta, N.; Crothers, D. M. *Biochemistry* **1982**, *21*, 3933-3940.

(29) Chaires, J. B. *Biochemistry* **1983**, *22*, 4204-4211.

(30) Wang, A. H. J.; Ughetto, G.; Quigley, G. J.; Rich, A. *Biochemistry* **1987**, *26*, 1152-1163.

(31) Brown, S. C.; Mullis, K.; Levenson, C.; Shafer, R. H. *Biochemistry* **1984**, *23*, 403-408.

(32) Kamitori, S.; Takusagawa, F. *J. Mol. Biol.* **1992**, *225*, 445-456.

(33) Scott, E. V.; Jones, R. L.; Banville, D. L.; Zon, G.; Marzilli, L. G.; Wilson, W. D. *Biochemistry* **1988**, *27*, 915-923.

(34) Searle, M. S. *Prog. Nucl. Magn. Reson. Spectrosc.* **1993**, *25*, 403-480.

(35) Phillips, T.; Haq, I.; Meijer, A. J. H. M.; Adams, H.; Soutar, I.; Swanson, L.; Sykes, M. J.; Thomas, J. A. *Biochemistry* **2004**, *43*, 13657-13665.

(36) Bresloff, J. L.; Crothers, D. M. *J. Mol. Biol.* **1975**, *95*, 103-123.

(37) Garbett, N. C.; Hammond, N. B.; Graves, D. E. *Biophysical Journal* **2004**, *87*, 3974-3981.

(38) Jennette, K. W.; Lippard, S. J.; Vassiliades, G. A.; Bauer, W. R. *Proc. Natl. Acad. Sci. U.S.A.* **1974**, *71*, 3839-3843.

(39) Barton, J. K.; Dannenberg, J. J.; Raphael, A. L. *J. Am. Chem. Soc.* **1982**, *104*, 4967-4969.

(40) Barton, J. K.; Danishefsky, A.; Goldberg, J. *J. Am. Chem. Soc.* **1984**, *106*, 2172-2176.

(41) Barton, J. K.; Raphael, A. L. *J. Am. Chem. Soc.* **1984**, *106*, 2466-2468.

(42) Barton, J. K.; Goldberg, J. M.; Kumar, C. V.; Turro, N. J. *J. Am. Chem. Soc.* **1986**, *108*, 2081-2088.

(43) Rehmann, J. P.; Barton, J. K. *Biochemistry* **1990**, *29*, 1710-1717.

(44) Satyanarayana, S.; Dabrowiak, J. C.; Chaires, J. B. *Biochemistry* **1992**, *31*, 9319-9324.

(45) Friedman, A. E.; Chambron, J. C.; Sauvage, J. P.; Turro, N. J.; Barton, J. K. *J. Am. Chem. Soc.* **1990**, *112*, 4960-4962.

(46) Hartshorn, R. M.; Barton, J. K. *J. Am. Chem. Soc.* **1992**, *114*, 5919-5925.

(47) Westerlund, F.; Pierard, F.; Eng, M. P.; Norden, B.; Lincoln, P. *J. Phys. Chem. B* **2005**, *109*, 17327-17332.

(48) Olson, E. J. C.; Hu, D.; Hoermann, A.; Jonkman, A. M.; Arkin, M. R.; Stemp, E. D. A.; Barton, J. K.; Barbara, P. F. *J. Am. Chem. Soc.* **1997**, *119*, 11458-11467.

(49) Nair, R. B.; Cullum, B. M.; Murphy, C. J. *Inorg. Chem.* **1997**, *36*, 962-965.

(50) Turro, C.; Bossmann, S. H.; Jenkins, Y.; Barton, J. K.; Turro, N. J. *J. Am. Chem. Soc.* **1995**, *117*, 9026-9032.

(51) Oenfelt, B.; Olofsson, J.; Lincoln, P.; Norden, B. *J. Phys. Chem. A* **2003**, *107*, 1000-1009.

(52) Duveneck, G. L.; Kumar, C. V.; Turro, N. J.; Barton, J. K. *J. Phys. Chem.* **1988**, *92*, 2028-2032.

(53) Kumar, C. V.; Barton, J. K.; Gould, I. R.; Turro, N. J.; Van Houten, J. *Inorg. Chem.* **1988**, *27*, 648-651.

(54) Amouyal, E.; Homsi, A.; Chambron, J. C.; Sauvage, J. P. *J. Chem. Soc., Dalton Trans.* **1990**, 1841-1845.

(55) Kumar, C. V.; Barton, J. K.; Turro, N. J. *J. Am. Chem. Soc.* **1985**, *107*, 5518-5523.

(56) Hiort, C.; Lincoln, P.; Norden, B. *J. Am. Chem. Soc.* **1993**, *115*, 3448-3454.

(57) Tuite, E.; Lincoln, P.; Norden, B. *J. Am. Chem. Soc.* **1997**, *119*, 239-240.

(58) Holmlin, R. E.; Stemp, E. D. A.; Barton, J. K. *Inorg. Chem.* **1998**, *37*, 29-34.

(59) Greguric, A.; Greguric, I. D.; Hambley, T. W.; Aldrich-Wright, J. R.; Collins, J. G. *J. Chem. Soc., Dalton Trans.* **2002**, 849-855.

(60) Metcalfe, C.; Thomas, J. A. *Chem. Soc. Rev.* **2003**, *32*, 215-224.

(61) Maheswari, P. U.; Rajendiran, V.; Palaniandavar, M.; Parthasarathi, R.; Subramanian, V. *J. Inorg. Biochem.* **2006**, *100*, 3-17.

(62) Liu, J.-G.; Zhang, Q.-L.; Shi, X.-F.; Ji, L.-N. *Inorg. Chem.* **2001**, *40*, 5045-5050.

(63) Jing, B.; Zhang, M.; Shen, T. *Spectrochim. Acta, Part A* **2004**, *60*, 2635-2641.

(64) Moucheron, C.; Kirsch-De Mesmaeker, A.; Choua, S. *Inorg. Chem.* **1997**, *36*, 584-592.

(65) Erkkila, K. E.; Odom, D. T.; Barton, J. K. *Chem. Rev.* **1999**, *99*, 2777-2795.

(66) Pyle, A. M.; Long, E. C.; Barton, J. K. *J. Am. Chem. Soc.* **1989**, *111*, 4520-4522.

(67) Sitlani, A.; Long, E. C.; Pyle, A. M.; Barton, J. K. *J. Am. Chem. Soc.* **1992**, *114*, 2303-2312.

(68) Campisi, D.; Morii, T.; Barton, J. K. *Biochemistry* **1994**, *33*, 4130-4139.

(69) Hudson, B. P.; Dupureur, C. M.; Barton, J. K. *J. Am. Chem. Soc.* **1995**, *117*, 9379-9380.

(70) Kielkopf, C. L.; Erkkila, K. E.; Hudson, B. P.; Barton, J. K.; Rees, D. C. *Nat. Struct. Biol.* **2000**, *7*, 117-121.

(71) Terbrueggen, R. H.; Johann, T. W.; Barton, J. K. *Inorg. Chem.* **1998**, *37*, 6874-6883.

(72) Franklin, S. J.; Barton, J. K. *Biochemistry* **1998**, *37*, 16093-16105.

(73) Fu, P. K. L.; Turro, C. *Chem. Commun.* **2001**, 279-280.

(74) Fu, P. K. L.; Bradley, P. M.; Turro, C. *Inorg. Chem.* **2003**, *42*, 878-884.

(75) Jackson, B. A.; Barton, J. K. *J. Am. Chem. Soc.* **1997**, *119*, 12986-12987.

(76) Jackson, B. A.; Barton, J. K. *Biochemistry* **2000**, *39*, 6176-6182.

(77) Junicke, H.; Hart, J. R.; Kisko, J.; Glebov, O.; Kirsch, I. R.; Barton, J. K. *Proc. Natl. Acad. Sci. U.S.A.* **2003**, *100*, 3737-3742.

(78) Ruba, E.; Hart, R. J.; Barton, K. J. *Inorg. Chem.* **2004**, *43*, 4570-4578.

(79) Wakelin, L. P. G.; Romanos, R.; Chen, T. K.; Glaubiger, D.; Canellakis, E. S.; Waring, M. J. *J. Am. Chem. Soc.* **1978**, *17*, 5057-5063.

(80) Fechter, E. J.; Olenyuk, B.; Dervan, P. B. *Angew. Chem., Int. Ed.* **2004**, *43*, 3591-3594.

(81) Carlson, D. L.; Huchital, D. H.; Mantilla, E. J.; Sheardy, R. D.; Murphy, W. R., Jr. *J. Am. Chem. Soc.* **1993**, *115*, 6424-6425.

(82) Zou, X.-H.; Ye, B.-H.; Li, H.; Liu, J.-G.; Xiong, Y.; Ji, L.-N. *J. Chem. Soc., Dalton Trans.* **1999**, 1423-1428.

(83) O'Reilly, F.; Kelly, J.; Kirsch-De Mesmaeker, A. *Chem. Commun.* **1996**, 1013-1014.

(84) O'Reilly, F. M.; Kelly, J. M. *New J. Chem.* **1998**, 22, 215-217.

(85) Lincoln, P.; Norden, B. *Chem. Commun.* **1996**, 2145-2146.

(86) Wilhelmsson, L. M.; Westerlund, F.; Lincoln, P.; Norden, B. *J. Am. Chem. Soc.* **2002**, *124*, 12092-12093.

(87) Oenfelt, B.; Lincoln, P.; Norden, B. *J. Am. Chem. Soc.* **1999**, *121*, 10846-10847.

(88) Onfelt, B.; Lincoln, P.; Norden, B. *J. Am. Chem. Soc.* **2001**, *123*, 3630-3637.

(89) Metcalfe, C.; Webb, M.; Thomas, J. A. *Chem. Commun.* **2002**, 2026-2027.

(90) Metcalfe, C.; Haq, I.; Thomas, J. A. *Inorg. Chem.* **2004**, *43*, 317-323.

(91) Metcalfe, C.; Adams, H.; Haq, I.; Thomas, J. A. *Chem. Commun.* **2003**, 1152-1153.

Chapter Two

Synthesis of Rh(III) complexes

2.1 Introduction

Kinetically inert complexes based on d^6- octahedral metals are commonly employed for the construction of metal-based DNA binding agents[1,2].

In previous work from the Thomas group, tripodal ligands were use to synthesise achiral octahedral Ru(II) complexes and their binding to DNA was studied[3]. These tripodal ligands are also convenient building blocks for construction of dinuclear complexes, as they are achiral and coordinatively saturated they offer facile routes of synthesis.

In an attempt to develop a new tripodal system containing rhodium suitable for the possible interaction with aqueous DNA solutions, we have synthesised [Rh(tpm*)Cl_3] and studied its reaction with pyridyl-based ligands.

Trofimenko first reported the synthesis of the tripodal anionic ligand hydridotris(pyrazolyl)borate anion, Tp (figure 2.1), and introduced it as a ligand for transition metals[4]. Since then many different complexes containing the Tp ligand have been synthesised[5-8]. Tp is a bulky ligand and thus disfavours high coordination numbers. The Tp ligand is often compared to the cyclopentadiene ligand (Cp). Both of them donate six electrons and can occupy three coordination sites, but the Tp ligand produces more often stable monomeric species[9].

The polypyrazolyl borates have been employed in the synthesis of complexes with catalytic activity or as models for biological activities[5]. Tp ligand is unstable toward hydrolysis and therefore unsuitable for aqueous DNA binding studies.

The coordination chemistry of tris(pyrazolyl)methane, tpm, another tripodal ligand, which is a neutral analogue of Tp, where the central boron anion has been replaced with a carbon atom (figure 2.1) has been less studied. This is partly due to the difficulties in the synthesis of this ligand. Reger *et al.*, in 2000[10] , improved the synthesis of tpm, and a new variety of derivatives were also obtained. Trofimenko also studied the geminal poly(1-pyrazolyl) alkanes and their coordination chemistry[11], showing that the $R_nC(pz)_{4-n}$ ligand resembles $[R_nB(pz)_{4-n}]^-$ in its

coordination behaviour and the geometry is identical but differing by one charge unit per ligand.

Nucleic acids are negative charged, using tpm as a capping tripodal ligand, allows us to synthesise complexes with higher cationic charge compared to Tp. This will enhance electrostatic binding to DNA.

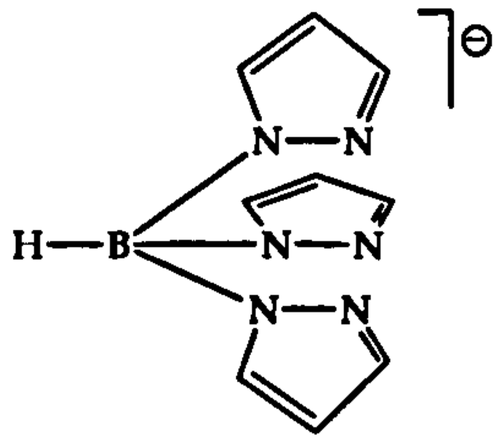

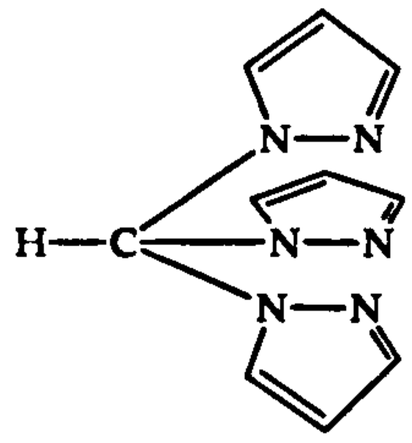

Figure 2.1: Structure of Tp (left) and Tpm (right) ligands

2.2 Synthetic studies

Our first attempt to synthesise suitable Rh(III) starting materials was to investigate the reaction of tpm with $RhCl_3 3H_2O$. We began our studies using a variety of conditions but in all the cases we obtained pale yellow intractable solids that showed little solubility. It was postulated that these solids were ligand-bridged oligo- or polymeric products. Due to steric demand, coordination of bulkier tripodal ligands such us tp* often yields monomeric metal complexes therefore the reaction of tpm* (tris (3,5-dimethyl-1-pyrazol) methane) with $RhCl_3 3H_2O$ was investigated.

It was observed that if such reactions are carried out in air or under nitrogen complex mixtures which presumably contain dinitrogen coordinated products were obtained. However reactions under argon atmosphere were more successful.

2.2.1 Synthesis of tris (3,5-dimethyl-1-pyrazol) methane, tpm* [2.1]

Tris (3,5-dimethyl-1-pyrazol) methane, tpm*, was synthesised following the method reported by Reger et al[10]. Direct reaction of the 3,5-dimethyl pyrazole and chloroform in phase transfer conditions (tetra-n-butylammonium bromide), using sodium carbonate as a base, produces the tpm* ligand in high yield (scheme 2.1).

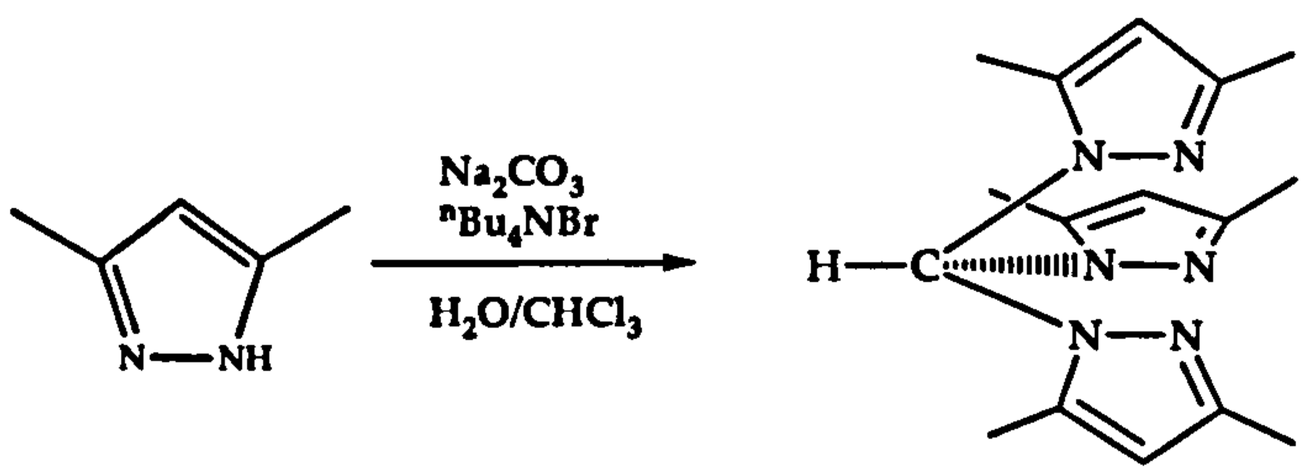

Scheme 2.1: Synthesis of tpm* ligand

2.2.2 Synthesis of [Rh(tpm*)Cl3] [2.2]

[Rh(tpm*)Cl3] was synthesised by the reaction of $RhCl_3 \cdot 3H_2O$ and tpm* ligand in methanol/water conditions, under an argon atmosphere, scheme 2.2. The fine orange solid obtained was collected by centrifugation and dried under vacuum. Complex **[2.2]** was characterised by ^1H NMR, mass spectral and elemental analyses.

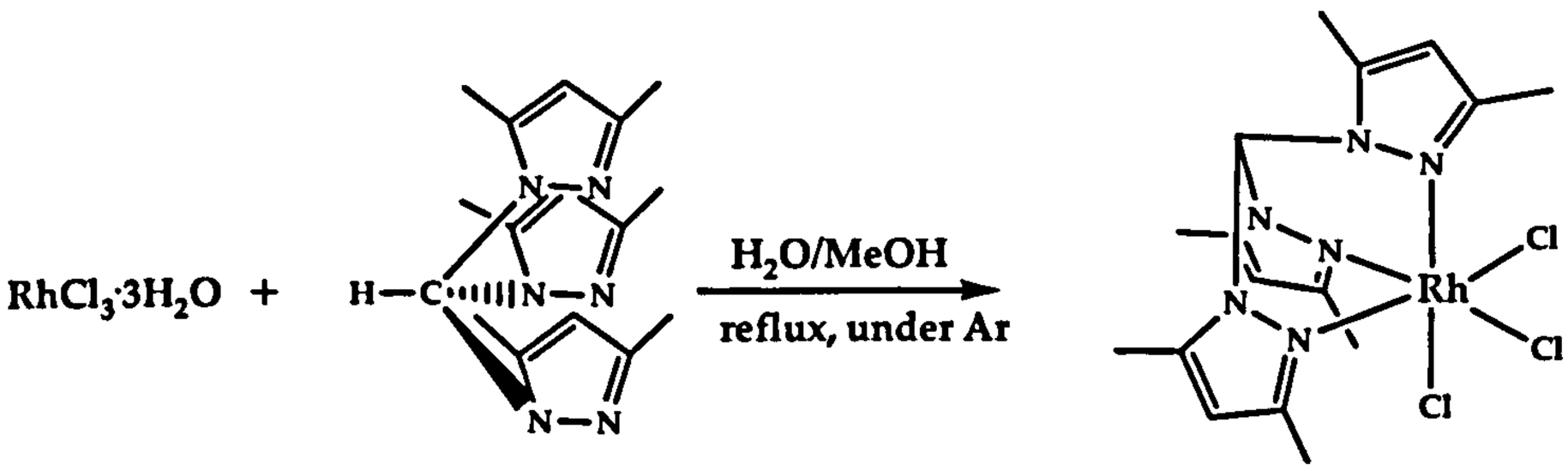

Scheme 2.2: Synthesis of **[2.2]** complex

2.2.3 Synthesis of $[Rh(tpm^*)(bpy)(Cl)](PF_6)_2$ and $[Rh(tpm^*)(phen)Cl](PF_6)_2$ [2.3] and [2.4]

The starting material $[Rh(tpm^*)Cl_3]$ and the corresponding bidentate ligand (2,2'-bipyridyl or 1,10-phenanthroline) were refluxed under argon in methanol/water (1:1) for one hour. Precipitation of the complexes was obtained by addition of NH_4PF_6 and the solids were collected by centrifugation, washed carefully with ethanol and dried under vacuum (scheme 2.3). Complex **[2.3]** and **[2.4]** were characterised by ^1H NMR, mass spectrum and elemental analysis. X-ray quality crystals were obtained from slow vapour diffusion of acetonitrile/diethyl ether mixtures.

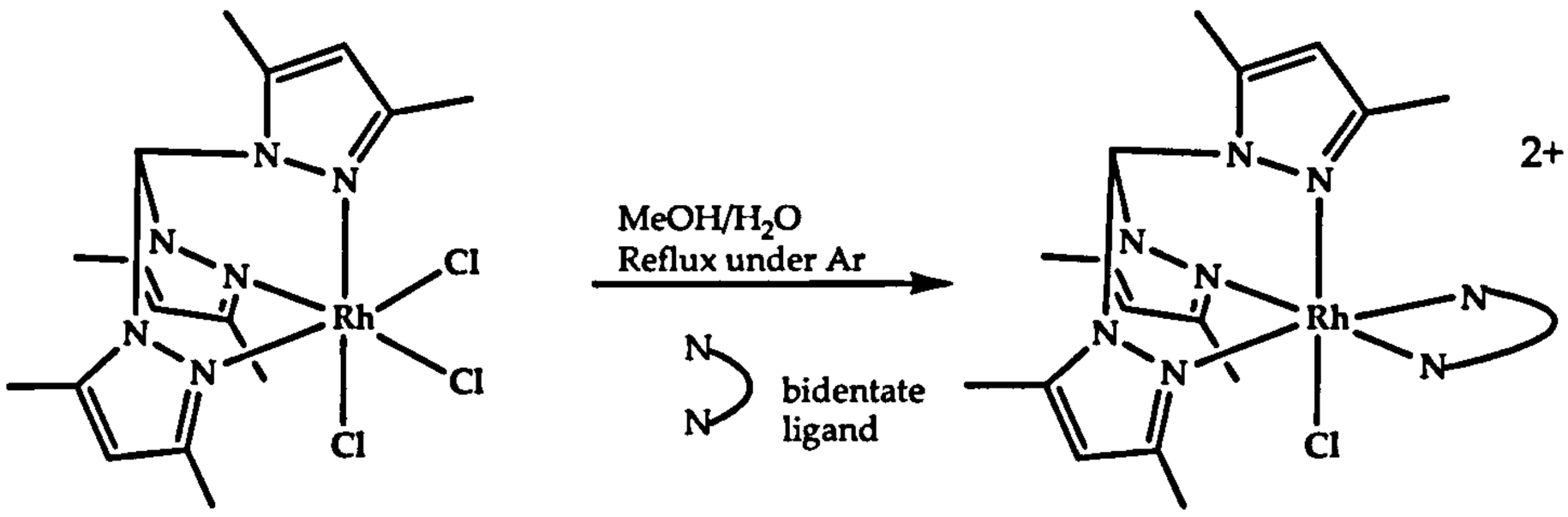

Scheme 2.3: Synthesis of $[(tpm^*)RhL]^{2+}$ when L is bidentate ligand

2.2.4 Synthesis of $[Rh(tpm^*)(py)Cl_2](PF_6)$ [2.5]

The starting material $[Rh(tpm^*)Cl_3]$ and pyridine (1:1 eq) were refluxed under argon in methanol/water (1:1) for one hour. The solid obtained by addition of NH_4PF_6 was dissolved in the minimum amount of acetone and the solution was concentrated by rotary evaporation. Diethyl ether was added and the precipitate was collected by centrifugation and dried under vacuum. Complex **[2.5]** was characterised by ^1H NMR, mass spectrum and elemental analysis. X-ray quality crystals were grown through vapour diffusion of acetonitrile/diethyl ether mixtures.

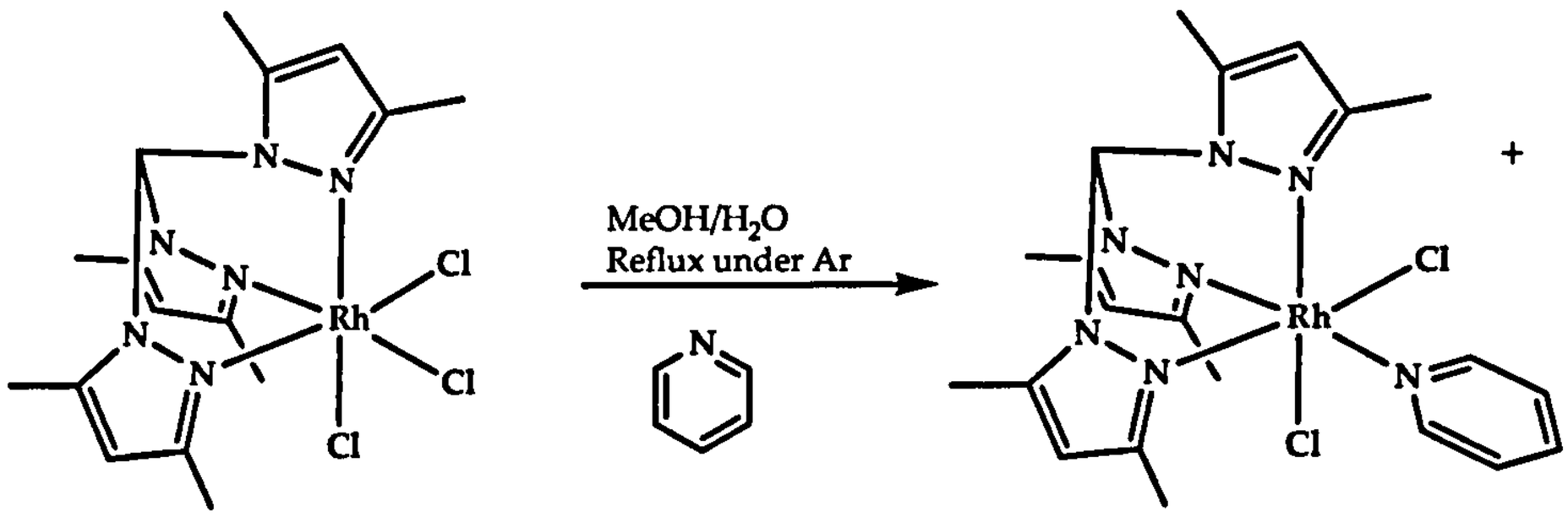

Scheme 2.4: Synthesis of **[2.5]**

2.2.5 Synthesis of $[Rh(tpm^*)(py)_2Cl](PF_6)_2$ [2.6]

The starting material $[Rh(tpm^*)Cl_3]$, pyridine and silver nitrate (1:2:2 eq) were refluxed under an argon atmosphere in methanol/water (1:1) for one hour. After filtration, NH_4PF_6 was added and the solid obtained was collected by filtration and washed with water, ethyl ether and dried under vacuum. Complex **[2.6]** was characterised by ^1H NMR, mass spectrum and elemental analysis. X-ray quality crystals were obtained from slow vapour diffusion of acetonitrile/diethyl ether mixtures.

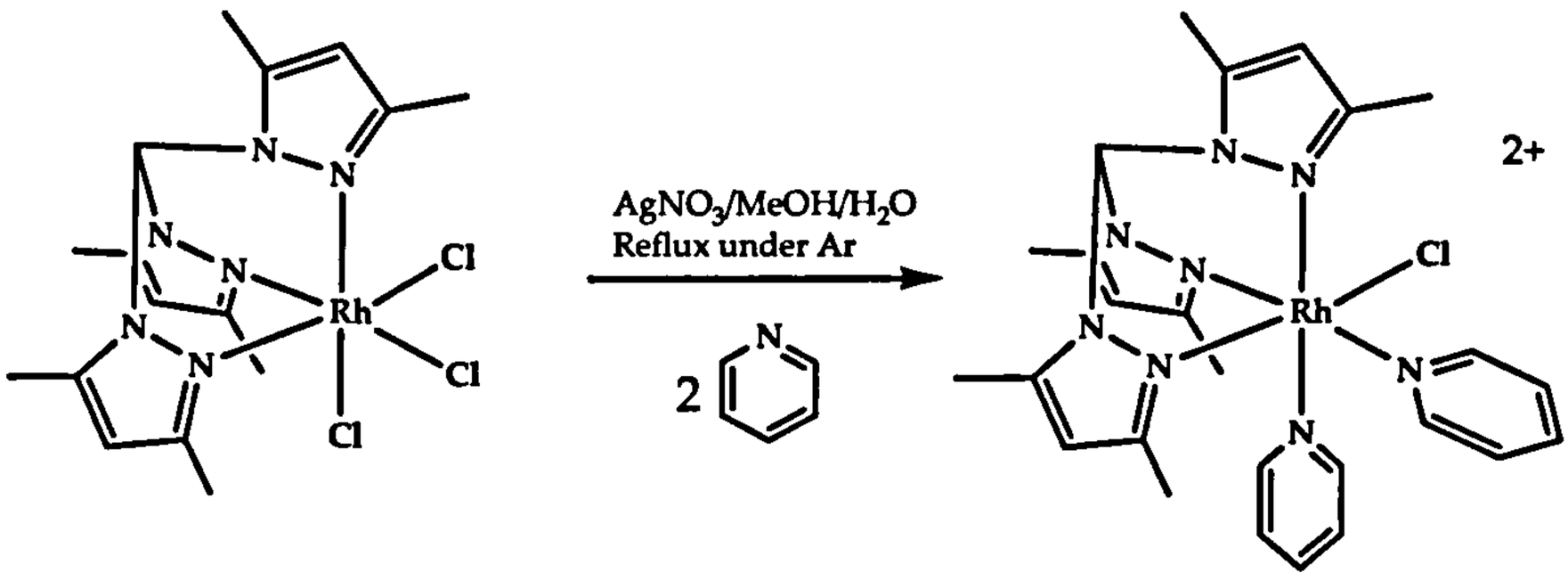

Scheme 2.5: Synthesis of **[2.6]**

Attempts to produce tricationic complexes such us $[Rh(tpm^*)(py)_3]^{3+}$ and $[Rh(tpm^*)(bpy)(py)]^{3+}$ were less successful. Reaction between **[2.2]** or **[2.6]** and excess pyridine in the presence of silver chloride yielded only to the starting materials. ^1H NMR and mass spectra data revealed that the reaction of pyridine with **[2.2]** yielded to a mixture containing **[2.6]** and unreacted **[2.2]** as the major component.

2.3 ^{1}H NMR spectroscopy studies

2.3.1 [Rh(tpm*)Cl$_3$] [2.2]

The ^{1}H NMR spectrum of **[2.2]** shows that the signals of the protons of the tpm* ligand are shifted relative to the free ligand, figure 2.2: at 6.30 ppm, a singlet that integrates for three protons, is assigned to the proton in the middle of the pyrazole rings (position three), at 7.85 ppm the shielded proton for the methine (position one) and at 2.65 ppm a singlet that integrates for eighteen protons, corresponding to the methyl protons (position five and six), figure 2.3.

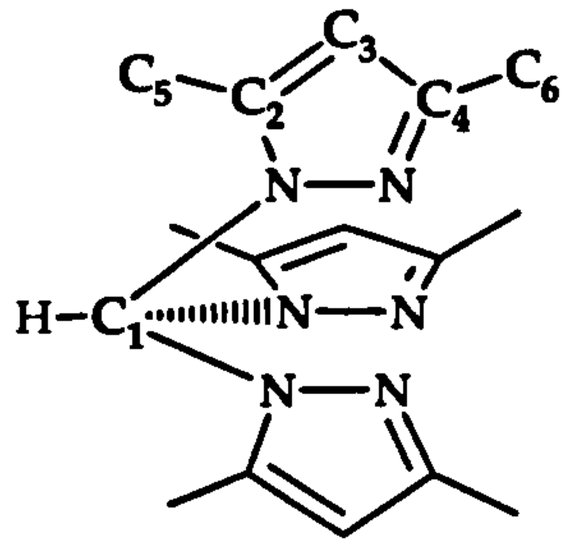

Figure 2.3: Carbons labelling numbers for one ring of the tpm* ligand

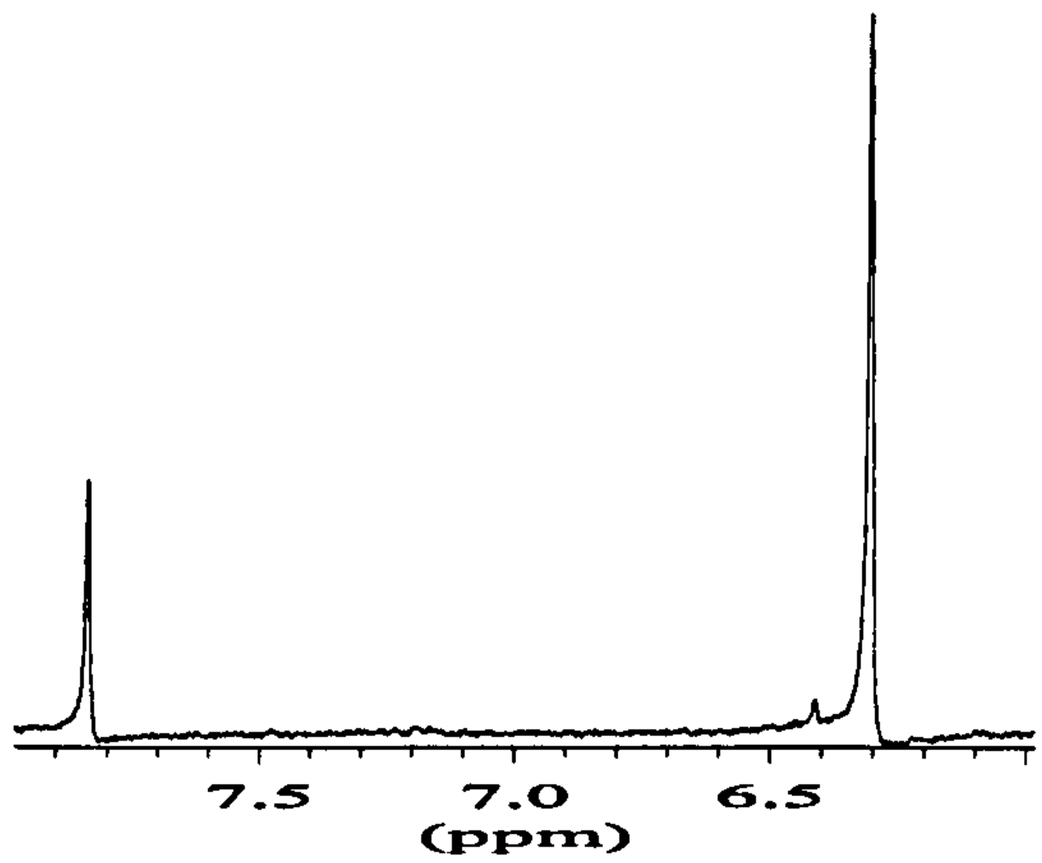

Figure 2.2: Aromatic ^{1}H NMR region of Rh(tpm*)Cl$_3$ in d$_6$-acetone

2.3.2 [Rh(tpm*)(bpy)Cl](PF$_6$)$_2$ and [Rh(tpm*)(phen)Cl](PF$_6$)$_2$ [2.3] and [2.4]

^{1}H NMR spectrum of **[2.3]** shows the signals of the protons of the pyrazolyl rings as two singlets that integrate for two and one protons (6.60 ppm and 6.30 ppm respectively) (figure 2.3). This confirms that when the 2,2'- bipyridyl is coordinated to the metal centre, the three pyrazolyl rings are no longer equivalent (the bidentate ligand is breaking the symmetry of the tpm* ligand), and the complexes possess σ_v symmetry. At 8.55 ppm the signal of the shielded proton of the methine of the tpm*, is shifted compared to the starting material. The other signals are assigned to the protons of the bpy ligand.

The ^{1}H NMR spectrum of **[2.4]** is quite similar to that one of **[2.3]**, with the singlet seen in the starting material for the equivalents pyrazolyl rings also observed as a doublet at 6.60 and 6.30 ppm. A singlet at 8.55 ppm corresponds to the shielded proton of the methylene of the tpm* (figure 2.4).

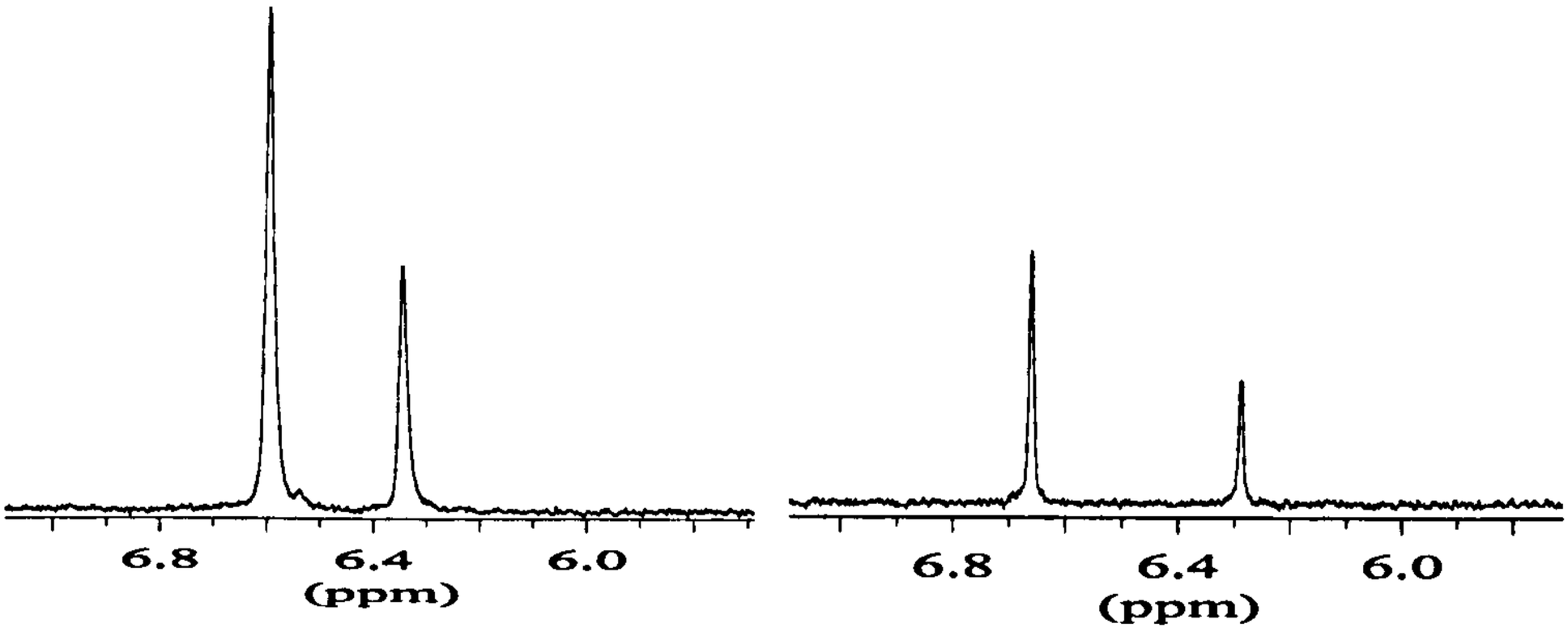

Figure 2.4: Aromatic ^{1}H NMR of **[2.3]** (left) and **[2.4]** (right) in acetone-d$_6$

2.3.3 [Rh(tpm*)(py)Cl$_2$](PF$_6$) [2.5]

^{1}H NMR spectrum of **[2.5]** shows a singlet at 6.40 ppm that integrates for three protons, in this case the pyridine ligand is also changing the symmetry of the tpm* ligand but just one signal for the three protons of the pyrazole rings is observed (figure 2.5). It seems that the symmetry change is balanced by shift changes due different environments, producing accidental anisochronous resonances.

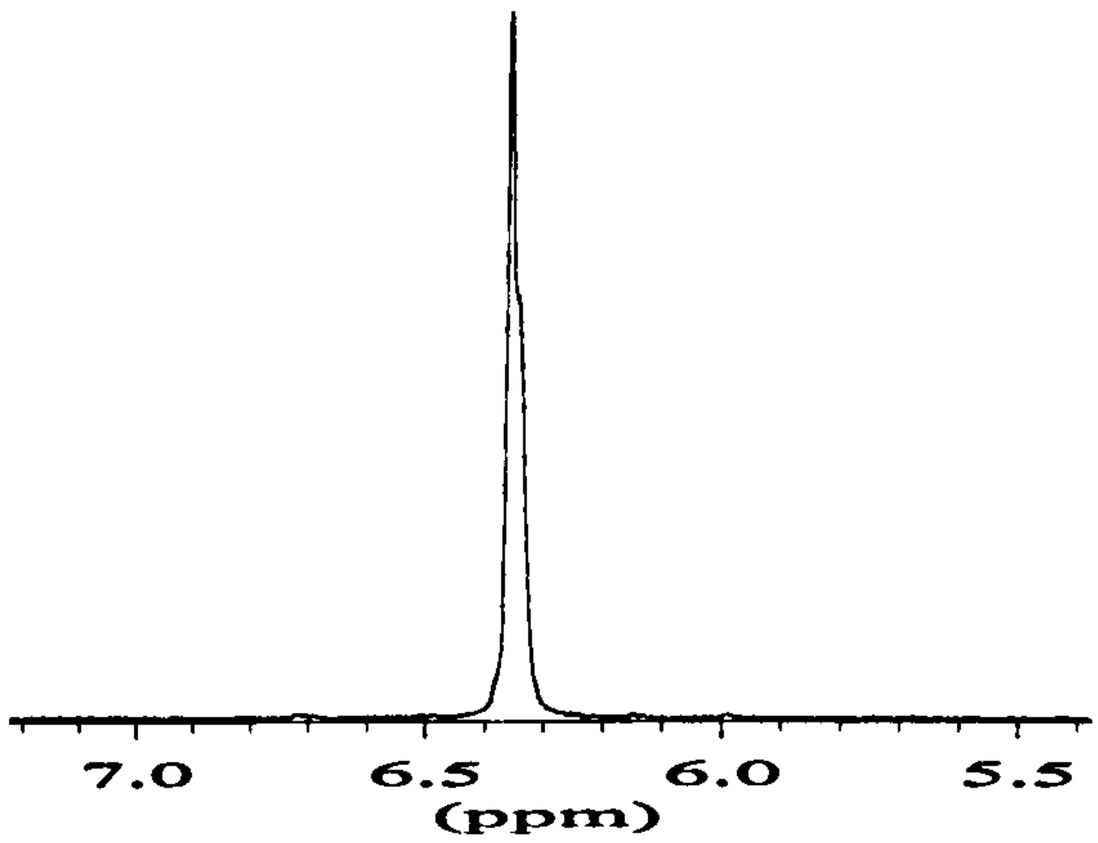

Figure 2.5: Aromatic ^{1}H NMR region of **[2.5]** in acetone-d_6

2.3.4 $[Rh(tpm^*)(py)_2Cl](PF_6)_2$ [2.6]

In contrast to **[2.5]** the ^{1}H NMR spectrum of **[2.6]** shows two different signals for the protons of the pyrazole rings, in this case the signal at 6.60 ppm integrates for one proton and the signal at 6.45 ppm integrates for two protons (figure 2.6).

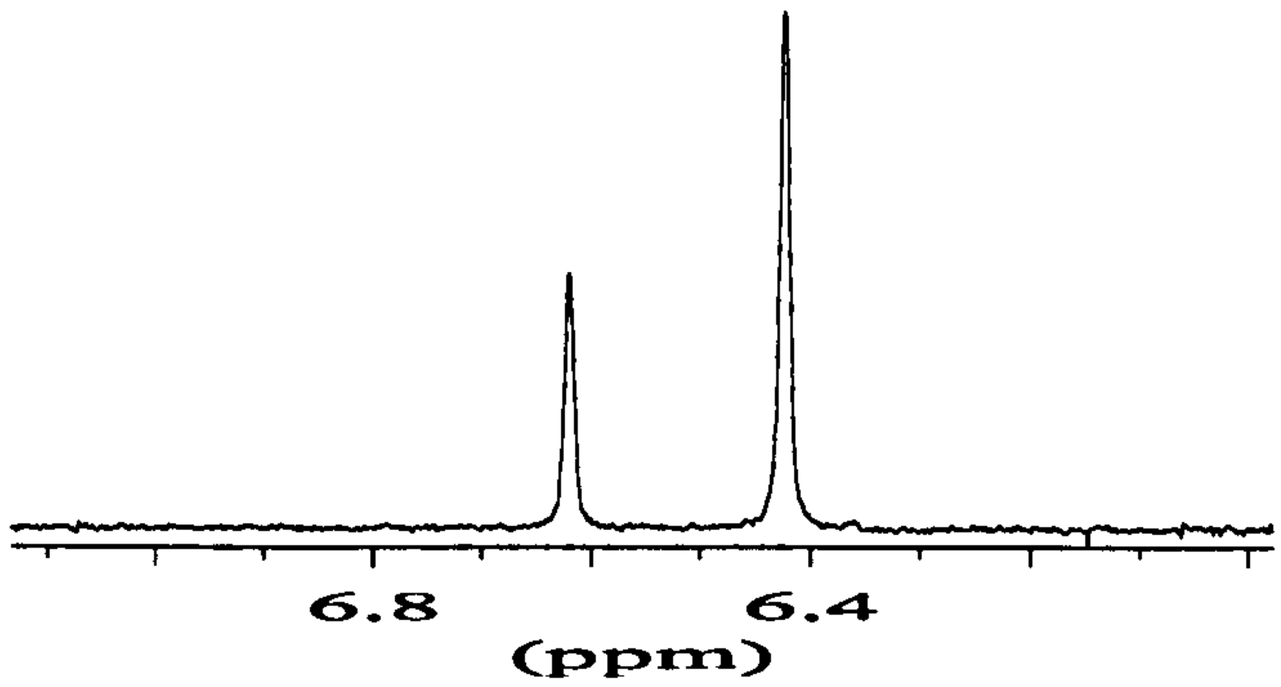

Figure 2.6: Aromatic ^{1}H NMR region of the complex **[2.6]**

2.4 X-ray Crystallography studies

X-ray quality crystals of **[2.3]**, **[2.4]**, **[2.5]** and **[2.6]** were obtained from slow vapour diffusion of acetonitrile/diethyl ether mixtures.

The crystal structure of **[2.3]** is shown in figure 2.7, and table 2.2 shows selected bond lengths and angles of the complex. The rhodium centre has a distorted octahedral coordination. The trans angles at the Rh(III) centre are 176.94(18), 178.77(17) and 179.55(12)°, close to octahedral. The Rh-N bond length involving the tpm* ligand are longer that the ones involving the bpy: Rh-(tpm*) bond lengths are around 2.60 Å, while the bond lengths for the Rh-bpy are smaller, around 2.017 Å. The bite angle of the bpy is 80.00(17)°, and the bite angles for the tpm* are 88.00 (16), 88.91(15) and 84.16(17)°, similar to ones previously observed for this kind of ligand. The methyl groups of the tpm* distort the bpy ring away from planarity, leading to an angle of 19.7° between the two rings. The Rh-Cl distance is 2.31(13) Å similar to the distance observed in other complexes[12].

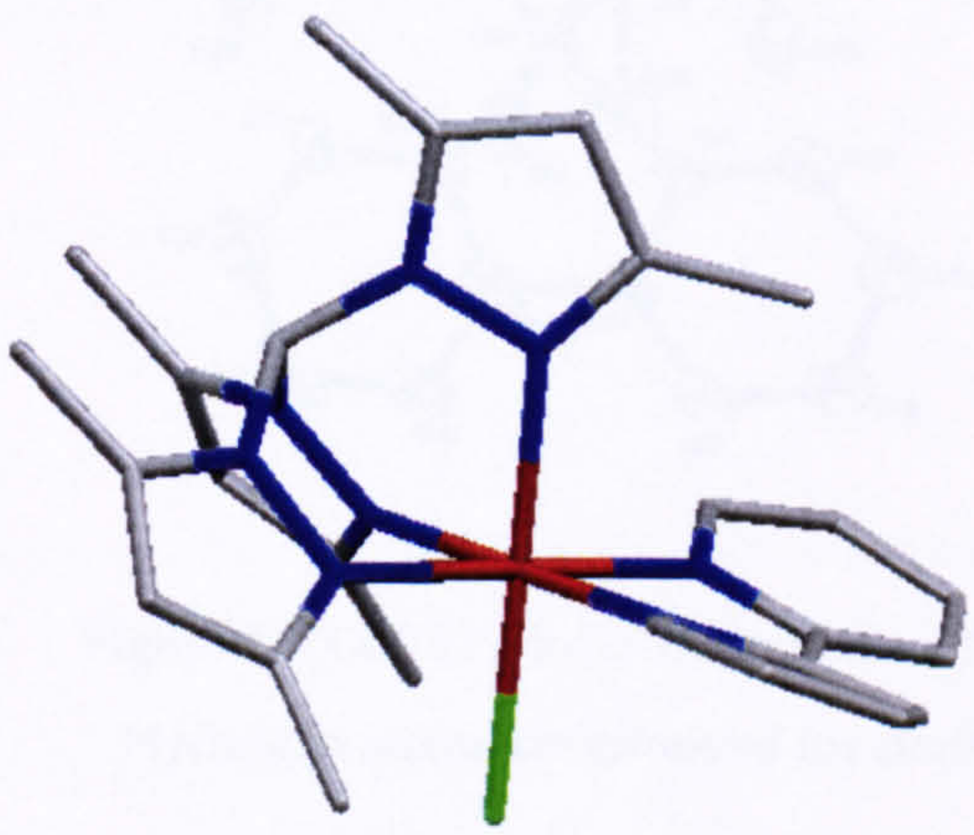

Figure 2.7: Structural representation of the cations found in the crystal structure of **[2.3]**. Hydrogen atoms are removed for clarity

Table 2.2: Selected bond lengths [Å] and angles [°] of the complex **[2.3]**

Bond lengths (Å)					
	Rh-N(1)	2.062(4)	Rh-N(7)	2.019(4)	
	Rh-N(3)	2.055(4)	Rh-N(8)	2.015(4)	
	Rh-N(5)	2.073(4)	Rh-Cl(1)	2.3157(13)	
Bond angles (⁰)					
N(1)-Rh-N(3)	88.00(16)	N(3)-Rh-N(7)	176.94(18)	N(7)-Rh-Cl(1)	87.53(12)
N(1)-Rh-N(5)	88.91(15)	N(3)-Rh-N(8)	97.07(17)	N(8)-Rh-Cl(1)	88.93(12)
N(1)-Rh-N(7)	92.90(16)	N(5)-Rh-N(7)	98.78(17)	N(1)-Rh-Cl(1)	179.55(12)
N(1)-Rh-N(8)	91.29(16)	N(5)-Rh-N(8)	178.77(17)	N(3)-Rh-Cl(1)	91.58(12)
N(3)-Rh-N(5)	84.16(17)	N(7)-Rh-N(8)	80.00(17)	N(5)-Rh-Cl(1)	90.88(11)

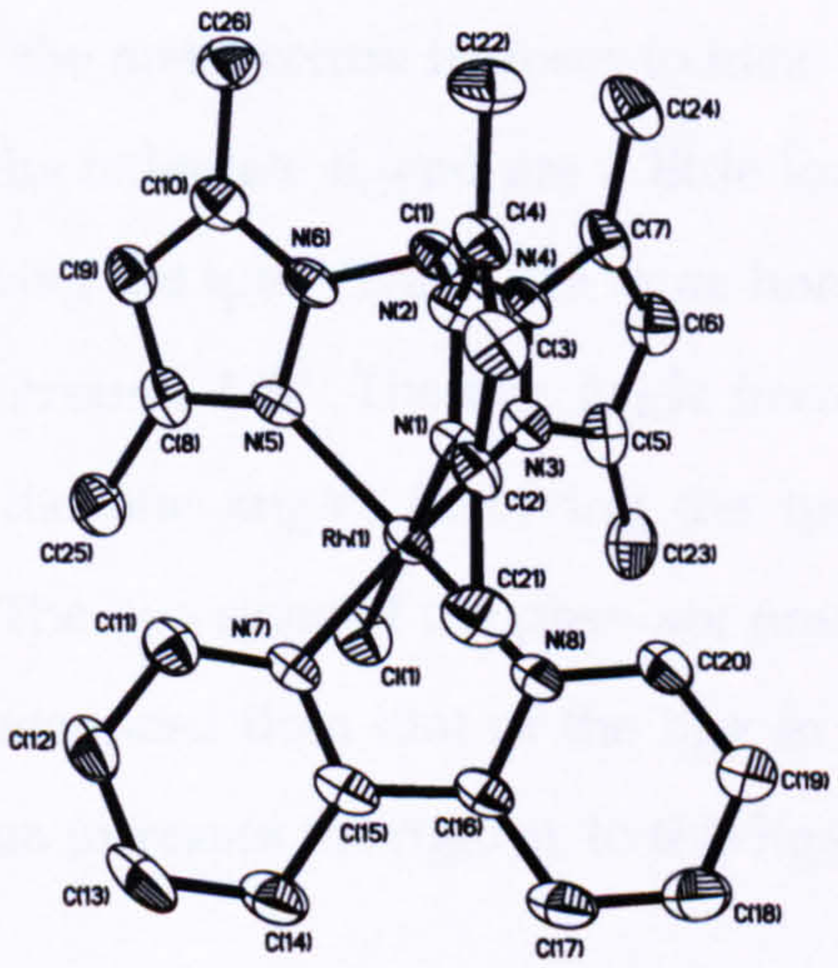

Figure 2.8: ORTEP plot of the cation in **[2.3]**.

Hydrogen atoms are removed for clarity

The structure of **[2.4]** is similar to that of **[2.3]**. Figure 2.9 and table 2.3 shows the structure and the selected bond lengths and angles of the complex

Figure 2.9: Structural representation of the cations found in the crystal structure of **[2.4]**. Hydrogen atoms are removed for clarity

The coordination around the metal centre is closer to ideal octahedral. All the Rh-N bond lengths involving the bidentate ligand are a little longer than those for **[2.3]**. The Rh-N distance involving the tpm* ligand are more homogenous, around 2.55 Å and the trans angles are around 178°. The bite angle involving the phen ligand is wider 81.38(19)°, while the bite angles involving the tpm* ligand are 85.26(19), 87.99(19) and 88.18(19)°. The two rings of the phen are now distorted with an angle of 17.3°, slightly less pronounced than that of the bpy in **[2.3]**, indicating that the third aromatic ring of phen increases the rigidity to this ligand compared to bpy.

Table 2.3: Selected bond lengths [Å] and angles [°] of the complex **[2.4]**

Bond lengths (Å)					
Rh-N(1)	2.054(5)2		Rh-N(7)	2.025(5)	
Rh-N(3)	2.056(5)		Rh-N(8)	2.026(5)	
Rh-N(5)	2.058(5)		Rh-Cl(1)	2.3202(15)	
Bond angles (°)					
N(1)-Rh-N(3)	85.26(19)	N(3)-Rh-N(7)	97.33(19)	N(7)-Rh-Cl(1)	87.61(15)
N(1)-Rh-N(5)	87.99(19)	N(3)-Rh-N(8)	178.7(2)	N(8)-Rh-Cl(1)	88.63(14)
N(1)-Rh-N(7)	177.3(2)	N(5)-Rh-N(7)	91.5(2)	N(1)-Rh-Cl(1)	92.97(14)
N(1)-Rh-N(8)	96.02(19)	N(5)-Rh-N(8)	91.76(19)	N(3)-Rh-Cl(1)	91.41(14)
N(3)-Rh-N(5)	88.18(19)	N(7)-Rh-N(8)	81.38(19)	N(5)-Rh-Cl(1)	178.92(13)

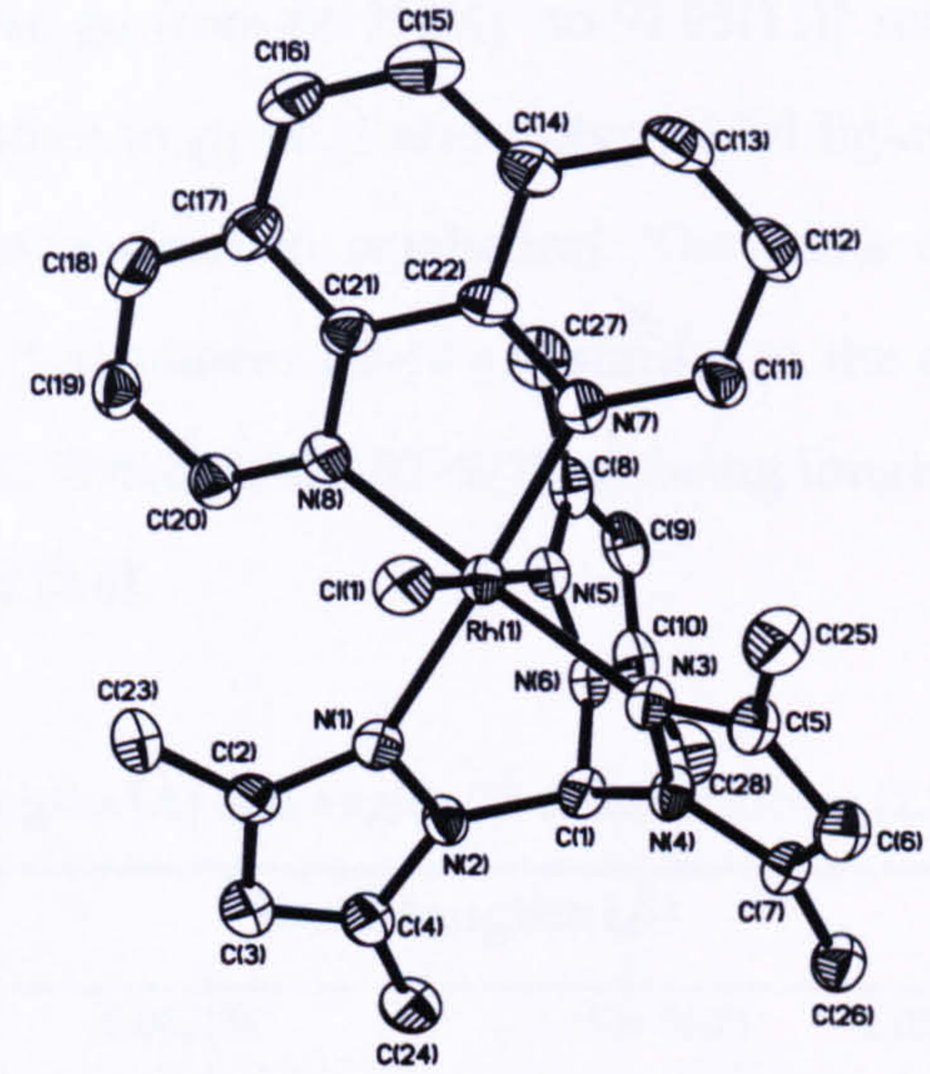

Figure 2.10: ORTEP plot of the cation in **[2.4]**.

Hydrogen atoms are removed for clarity

Complexes **[2.5]** and **[2.6]** have monodentate ligands and these are easier to accommodate sterically. Figure 2.11 and 2.13 show the crystal structure of these two complexes and the selected bond length and angles are summarised in table 2.4 and 2.5.

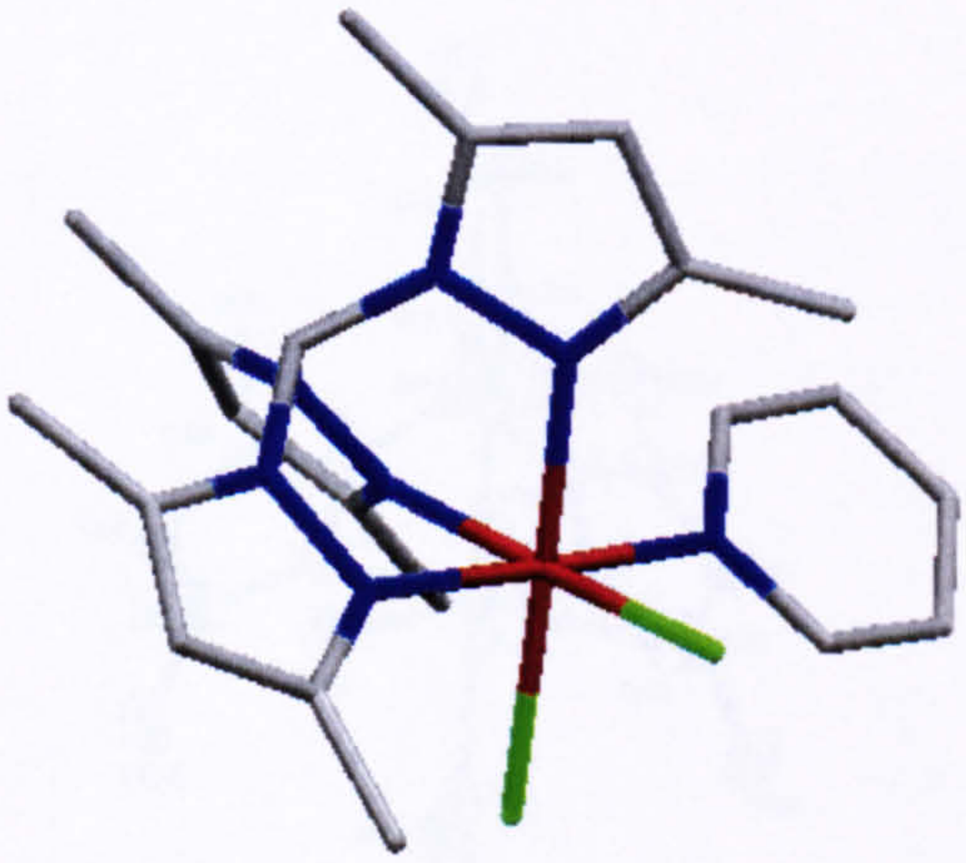

Figure 2.11: Structural representation of the cations found in the crystal structure of **[2.5]**.

Hydrogen atoms are removed for clarity

In this case, the cis angles go from 86.95(14)° to 91.95(11)° reflecting the low steric demand of chloride relative to pyridyl and polypyridyl ligands. The coordination around the metal centre is close to octahedral. The trans angles are 177.28(15), 178.55(15) and 176.20(11)°, distances Rh-N are similar to the ones in **[2.3]** and **[2.4]** and distances Rh-Cl are 2.3398(8) and 2.3229(10) Å being longer distance compare to complexes **[2.3]**, **[2.4]** and **[2.6]**.

Table 2.4: Selected bond lengths [Å] and angles [°] of the complex **[2.5]**

Bond lengths (Å)					
	Rh-N(1)	2.067(3)	Rh-N(7)	2.034(4)	
	Rh-N(3)	2.042(2)	Rh-Cl(1)	2.3398(8)	
	Rh-N(5)	2.059(4)	Rh-Cl(2)	2.3229(10)	
Bond angles (⁰)					
N(1)-Rh-N(3)	87.67(15)	N(7)-Rh-N(5)	90.81(13)	N(7)-Rh-Cl(2)	91.65(11)
N(1)-Rh-N(5)	86.80(15)	N(7)-Rh-Cl(1)	90.05(11)	N(3)-Rh-Cl(2)	90.12(10)
N(1)-Rh-N(7)	177.28(15)	N(1)-Rh-Cl(1)	91.32(9)	N(5)-Rh-Cl(2)	176.20(11)
N(3)-Rh-N(5)	86.95(14)	N(3)-Rh-Cl(1)	178.55(15)	N(1)-Rh-Cl(2)	90.68(10)
N(3)-Rh-N(7)	90.92(15)	N(5)-Rh-Cl(1)	91.95(11)	Cl(2)-Rh-Cl(1)	90.94(4)

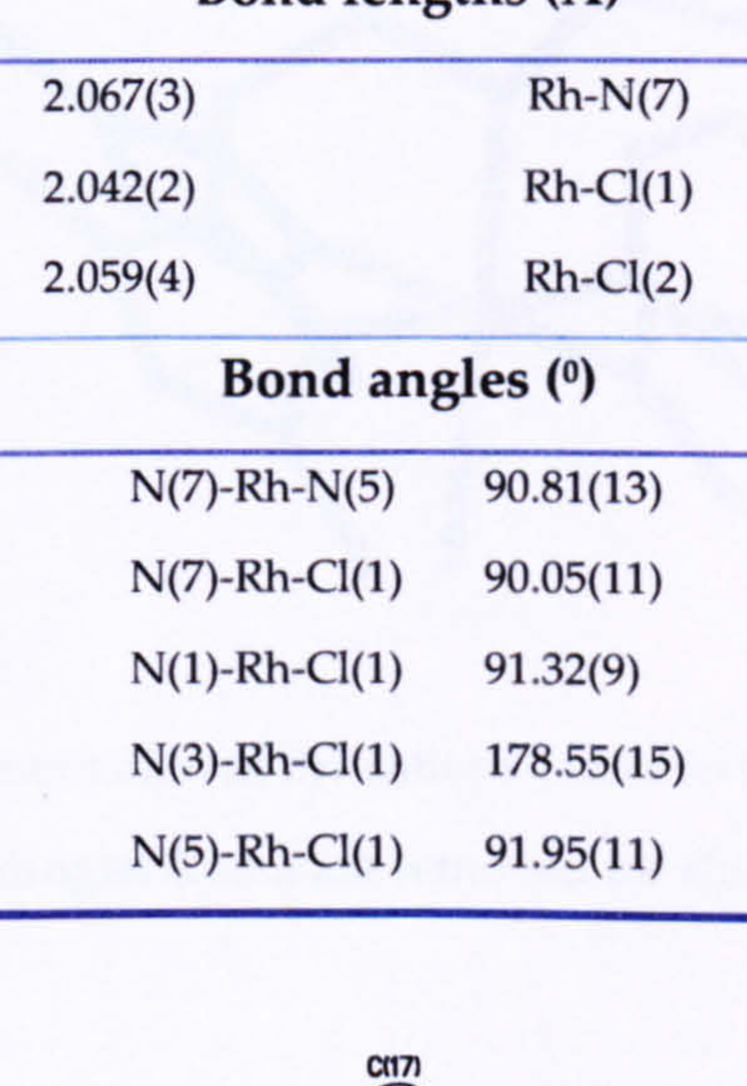

Figure 2.12: ORTEP plot of the cation in **[2.5]**.

Hydrogen atoms are removed for clarity

In contrast to the bidentate ligands in **[2.3]** and **[2.4]**, the py rings of **[2.6]** are able to rotate to a mutual 60° thus decreasing the unfavoured steric interactions caused by the tpm* methyl groups (figure 2.13). The bond length involving the Rh and the two py are 2.037 and 2.026 Å, and these distances are little longer that those for **[2.3]** and **[2.4]** complexes with the bpy and phen ligands respectively.

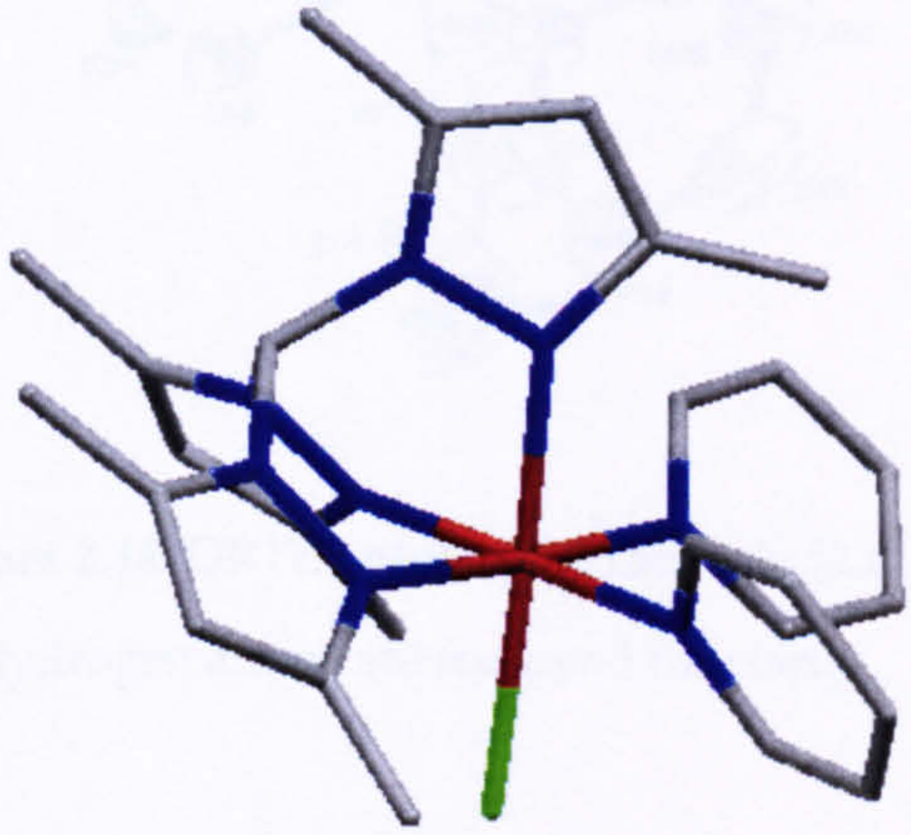

Figure 2.13: Structural representation of the cations found in the crystal structure of **[2.6]**. Hydrogen atoms are removed for clarity

Table 2.5: Selected bond lengths [Å] and angles [°] of the complex **[2.6]**

Bond lengths (Å)					
	Rh-N(1)	2.025(9)	Rh-N(7)	2.037(9)	
	Rh-N(3)	2.035(9)	Rh-N(8)	2.042(9)	
	Rh-N(5)	2.027(8)	Rh-Cl(1)	2.317(3)	
Bond angles (⁰)					
N(1)-Rh-N(3)	86.5(3)	N(3)-Rh-N(7)	175.3(4)	N(7)-Rh-Cl(1)	92.3(3)
N(1)-Rh-N(5)	87.2(3)	N(3)-Rh-N(8)	88.5(3)	N(8)-Rh-Cl(1)	89.9(3)
N(1)-Rh-N(7)	89.7(3)	N(7)-Rh-N(5)	89.2(3)	N(1)-Rh-Cl(1)	90.9(2)
N(1)-Rh-N(8)	175.0(3)	N(8)-Rh-N(5)	91.9(3)	N(3)-Rh-Cl(1)	90.5(3)
N(3)-Rh-N(5)	87.9(3)	N(7)-Rh-N(8)	95.2(3)	N(5)-Rh-Cl(1)	177.6(2)

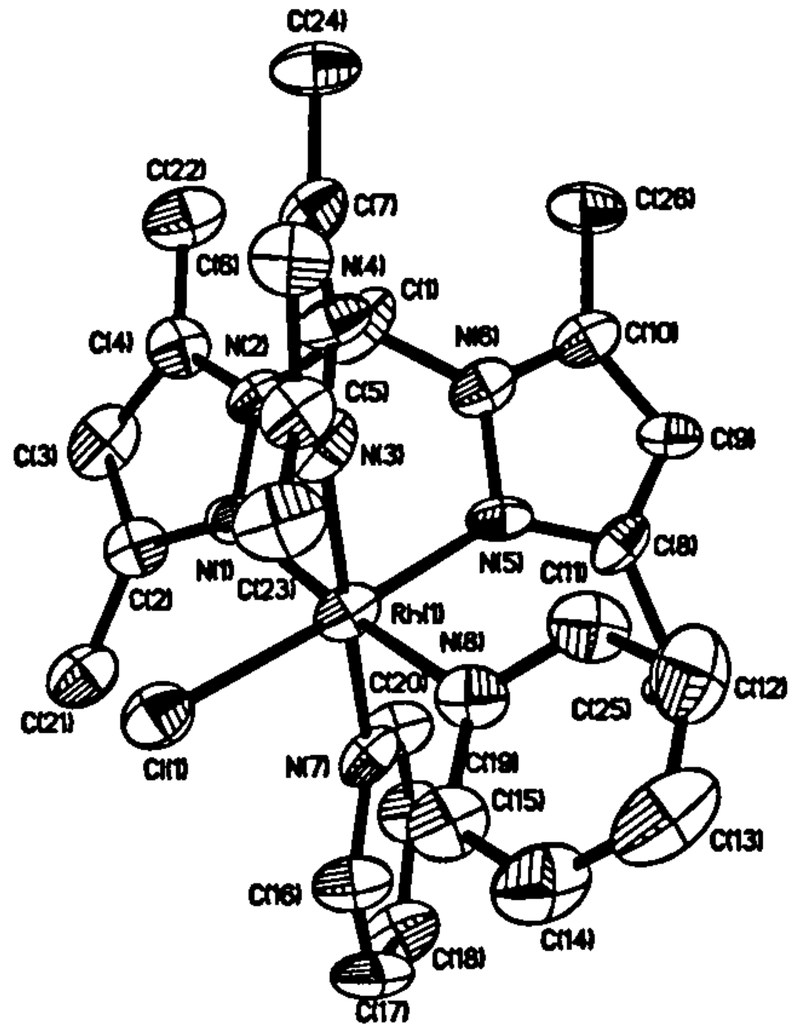

Figure 2.14: ORTEP plot of the cation in **[2.6]**.

Hydrogen atoms are removed for clarity

2.5 Electrochemistry studies

Cyclic voltammograms of **[2.3]**, **[2.4]**, **[2.5]** and **[2.6]** were carried out at a scan rate 200 mV s^{-1} in acetonitrile containing 0.1 M TBAP, as supporting electrode, under nitrogen atmosphere. Potentials were measured vs. Ag/AgCl. Data are summarised in table 2.6.

All the reductions couples for the complexes show poor reversibility, the first reduction at -0.4 - -0.6 V is assigned to a metal-based reduction. A series of ligand based reduction from -0.75 to -1.70 are also observed. Complex **[2.5]** is most readily reduced as it contains two π-donor chloride ligands and only a single π-accepting pyridyl ligand, thus the Rh(III) oxidation state is relatively destabilised. The reduction of Rh(III) becomes more cathodic when the Cl^- are replaced with higher π–accepting ability ligands.

Table 2.6: Cyclic voltammetry data of **[2.3]**, **[2.4]**, **[2.5]** and **[2.6]**

Complex	Reduction(V)[a]
[2.3]	-0.60, -0.90, -1.55
[2.4]	-0.56, -0.75, -1.50, -1.70
[2.5]	-0.46, -0.78, -1.5
[2.6]	-0.43, -0.78, -1.5

(a) All couple are chemically irreversible, therefore only E_p value quoted

2.6 UV-Vis spectroscopy studies

UV-Vis absorption spectra of **[2.3]**, **[2.4]**, **[2.5]** and **[2.6]** were recorded in acetonitrile solutions at room temperature (figure 2.15). Data are summarised in table 2.7.

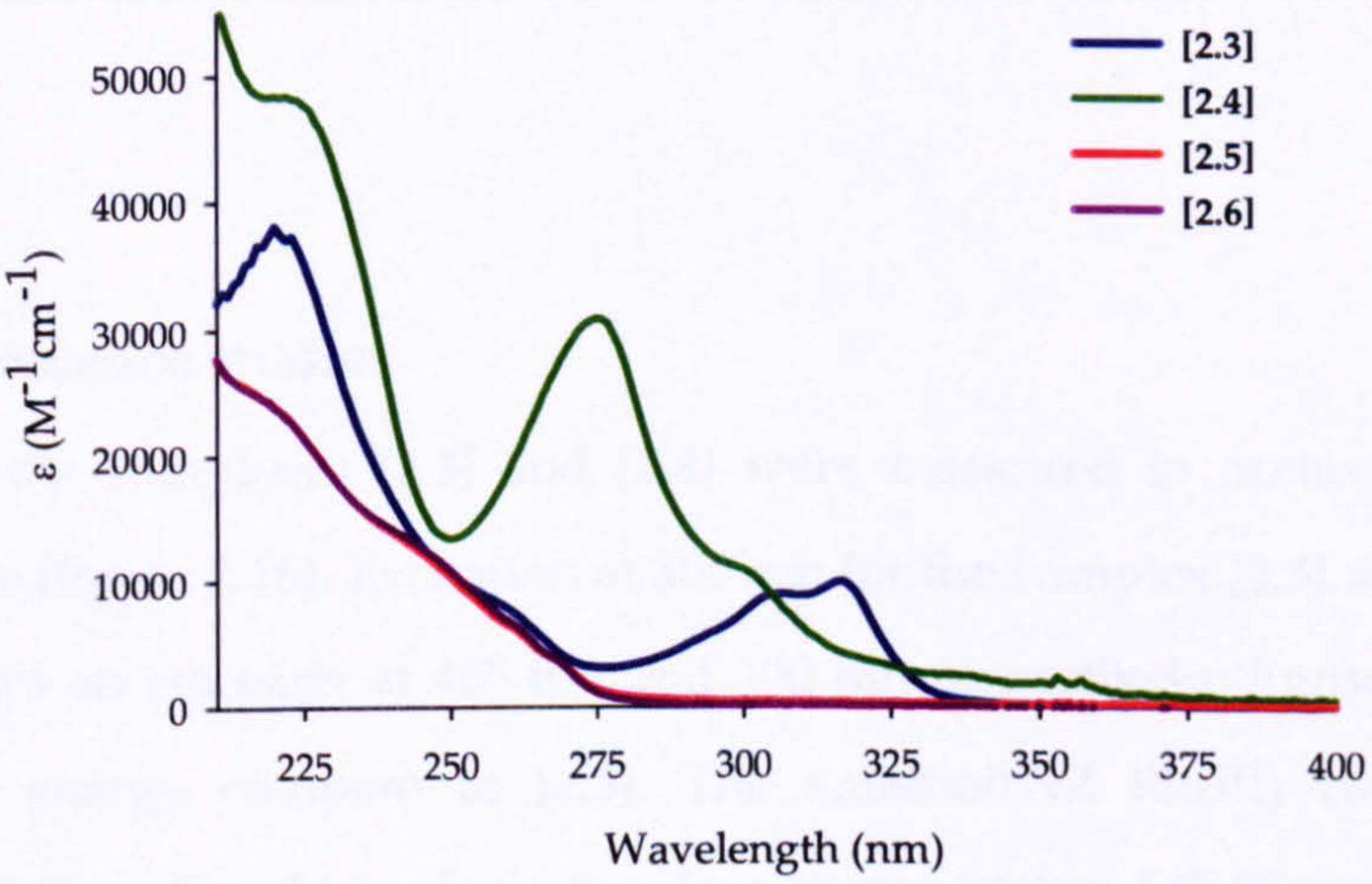

Figure 2.15: UV-Vis spectra of **[2.3]**, **[2.4]**, **[2.5]** and **[2.6]** in acetonitrile

The complexes show absorption bands around 200-250 nm that are assigned to $\pi \rightarrow \pi^*$ intraligand transitions characteristic in aromatic nitrogen donor ligands. The absorption band at 330 nm in **[2.3]** and at 353 nm for **[2.4]** can be assigned to MC (metal centred) d-d transition[13].

Table 2.7: UV-Vis data for complexes **[2.3]** to **[2.6]** recorded in acetonitrile

Compound	λ_{max} (nm)	ε ($M^{-1}cm^{-1}$)	Assignation
[2.3]	220	38195	$\pi \rightarrow \pi^*$
	258	sh	$\pi \rightarrow \pi^*$
	306	8973	d-d
	317	9959	d-d
[2.4]	204	59866	$\pi \rightarrow \pi^*$
	220	48453	$\pi \rightarrow \pi^*$
	275	30870	d-d
	300	10964	d-d
	353	2373	d-d
[2.5]	205	sh	$\pi \rightarrow \pi^*$
	221	23663	$\pi \rightarrow \pi^*$
	248	sh	d-d
[2.6]	205	sh	$\pi \rightarrow \pi^*$
	219	24353	$\pi \rightarrow \pi^*$
	240	sh	d-d

2.7 Luminescence studies

Spectra of the complexes **[2.3]** and **[2.4]** were measured in acetonitrile at room temperature (figure 2.16). Excitation at 300 nm for the complex **[2.3]** and 225 nm for **[2.4]** displays an emission at 405 nm and 300 nm respectively. Emission of **[2.4]** is quite high energy compare to **[2.3]**. The emission of Rh(III) complexes with polypyridyl ligand could be from two low energy states: LC (ligand centered) or MC (metal centered) states[14]. Studies on the emission properties of Rh(III)-phen complexes showed that is possible to tune the gap between the MC and LC states by using different ligands[15]. In both cases emissions are non-gaussian and show evidence of structure, for these reasons emissions are assigned to LC luminescence. After repeated purifications of the complex **[2.4]** the high energy luminescence was still present, indicating that is a property of the system and not due to impurities. Complexes **[2.5]** and **[2.6]** are non-emissive.

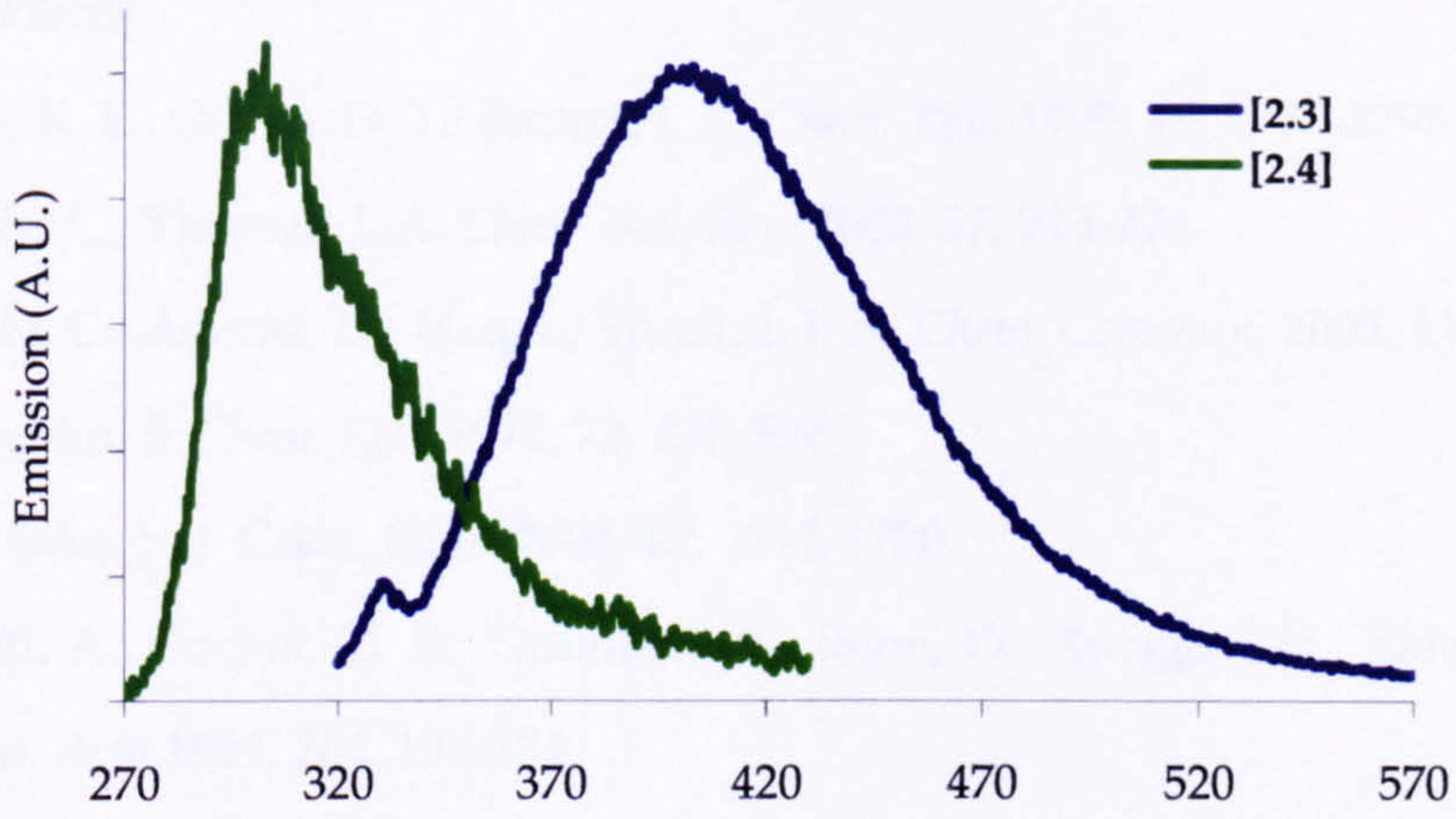

Figure 2.16: Emission spectra of **[2.3]** and **[2.4]** in acetonitrile

2.8 Conclusions and future work

New tripodal systems containing rhodium centre have been synthesised and their physical properties have been studied. In order to use these systems as metallo-intercalators it will be necessary to increase the surface area of the polypyridyl ligand coordinated to the metal centre. Initial studies on the reaction between Rh(tpm*)Cl_3 and dppz ligand in similar condition to the ones described in this chapter did not produce the expected complex. Different condition, using a variety of different solvents and temperatures were investigated with no success. The increase in rigidity of the dppz ligand compared to the phen or bpy ligands may be the reason for this lack of interaction between Rh(III)-tpm* and dppz ligand.

However, Barton and co-workers have established that Rh(III)-phi complexes interact with high affinity with DNA[1] (see chapter one). Therefore future work may be centre on the synthesis of new Rh(III)-tpm* complexes based on the phi ligand. When the phi ligand is coordinated to a metal centre, the imines groups project the phi ligand away from the centre, and therefore the tpm* ligand might produce less steric clashes.

2.9 References

(1) Erkkila, K. E.; Odom, D. T.; Barton, J. K. *Chem. Rev.* **1999**, *99*, 2777-2795.

(2) Metcalfe, C.; Thomas, J. A. *Chem. Soc. Rev.* **2003**, *32*, 215-224.

(3) Metcalfe, C.; Adams, H.; Haq, I.; Thomas, J. A. *Chem. Commun.* **2003**, 1152-1153.

(4) Trofimenko, S. *Chem. Rev.* **1972**, *72*, 497-509.

(5) Trofimenko, S. *J. Chem. Educ.* **2005**, *82*, 1715-1720.

(6) Albinati, A.; Bucher, U. E.; Gramlich, V.; Renn, O.; Ruegger, H.; Venanzi, L. M. *Inorg. Chim. Acta* **1999**, *284*, 191-204.

(7) Bhambri, S.; Tocher, D. A. *J. Chem. Soc., Dalton Trans.* **1997**, 3367-3372.

(8) Carmona, E.; Cingolani, A.; Marchetti, F.; Pettinari, C.; Pettinari, R.; Skelton, B. W.; White, A. H. *Organometallics* **2003**, *22*, 2820-2826.

(9) Trofimenko, S. *Scorpionates, the coordination chemistry of polypyrazolylborate ligands*; Imperial college press: London, 1999.

(10) Reger, D. L.; Grattan, T. C.; Brown, K. J.; Little, C. A.; Lamba, J. J. S.; Rheingold, A. L.; Sommer, R. D. *J. Organomet. Chem.* **2000**, *607*, 120-128.

(11) Trofimenko, S. *J. Am. Chem. Soc.* **1970**, *92*, 5118-5126.

(12) Renn, O.; Rueegger, H.; Venanzi, L. M.; Gallus, J.; Gramlich, V.; Martelletti, A. *Inorg. Chim. Acta* **1995**, *240*, 575-580.

(13) Nishizawa, M.; Suzuki, T. M.; Sprouse, S.; Watts, R. J.; Ford, P. C. *Inorg. Chem.* **1984**, *23*, 1837-1841.

(14) Forster, L. S. *Coord. Chem. Rev.* **2002**, *227*, 59-92.

(15) Indelli, M. T.; Scandola, F. *Inorg. Chem.* **1990**, *29*, 3056-3058.

Chapter Three

Synthesis of ruthenium (II) complexes

3.1 Introduction

In previous work in the group, achiral Ru(II)-dppz complexes using a tripodal ligand (tpm) have been synthesised, this ligand caps one face of the octahedral complex, and still leaves three positions to introduce other groups onto the octahedral centre. Two of those positions can be used for an intercalative ligand such as dppz, dppn or phi and there is still one free position for further substitutions (scheme 3.1).

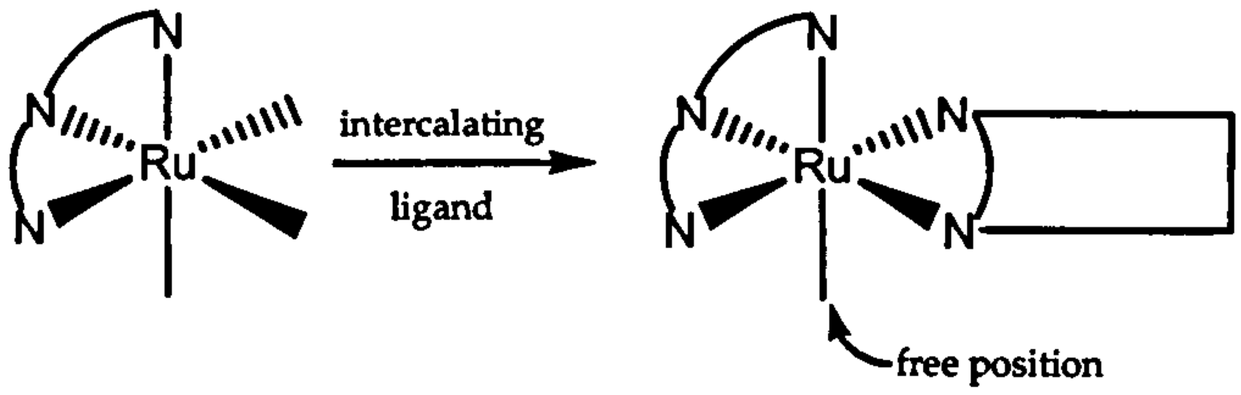

Scheme 3.1: Schematic path of synthesis

Using $[Ru(tpm)(dppz)Cl]^{+}$ as a starting material, $[Ru(tpm)(dppz)(Py)]^{2+}$ was synthesised (scheme 3.2) and the interaction of this complexes with DNA was studied[1]. The affinity of $[Ru(tpm)(dppz)(Py)]^{2+}$ with CT-DNA is in the micromolar range. Using calorimetric techniques, the interaction of $[Ru(tpm)(dppz)(Py)]^{2+}$ with poly(dA)·poly(dT) and poly(dG)·poly(dC) was also reported. This complex shows preference for binding to poly(dG)·poly(dC) over poly(dA)·poly(dT) (almost an order of magnitude bigger), suggesting modulation of binding by the ancillary ligands. Such behaviour has been reported before in Rh(III)-phi systems.

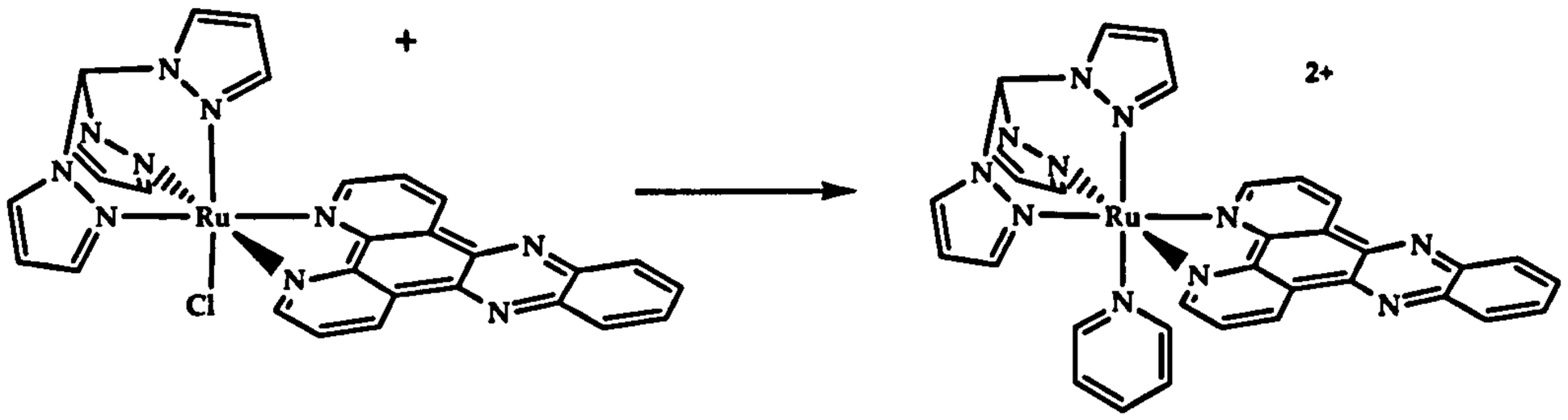

Scheme 3.2: $[Ru(tpm)(dppz)Cl]^{+}$ and $[Ru(tpm)(dppz)(Py)]^{2}$ complexes

Barton and co-workers have studied the interaction of several Rh-phi complexes with different DNA recognition characteristics such as shape selection or hydrogen bonds and van der Waals contacts (see chapter one)[2-6]. Additionally, DNA binding of $[Rh(bpy)_2(phi)]^{3+}$ and $[Rh(phen)_2(phi)]^{3+}$ with guanidium, amine or amido functionalities derivatives (figure 3.2) was reported. For example they observed that the presence of guanidinium groups allows hydrogen bonding between the complex and DNA, resulting in a preference for 5'-GC-3' sites[7].

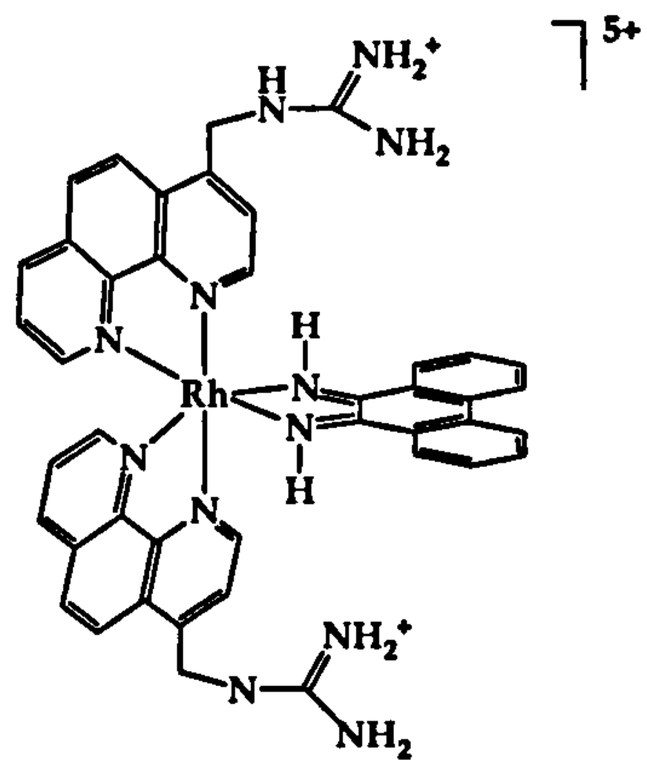

Figure 3.1: Structure of $[Rh(MGP)_2(phi)]^{5+}$

One possibility to modulate the binding properties of metallo-intercalators based on the Ru-dppz unit is to introduce hydrogen bonding motifs. Therefore we have synthesised $[Ru(tpm)(dppz)(Py)]^{2+}$ derivatives with hydrogen accepting and/or donating substitutes in the pyridine ring, to study the effect of these ancillary ligands on DNA-binding behaviour.

3.2 Synthesis studies of achiral-[Ru(tpm)(dppz)] complexes

3.2.1 Synthesis of the ligands

Tris(1-pyrazol)methane (tpm) **[3.1]** and dipyrido[3,2-a:2',3'-c]phenazine (dppz) **[3.2]** were synthesised following published procedures.

The tpm ligand was synthesised in a similar way to the tpm* ligand[8] (scheme 3.3).

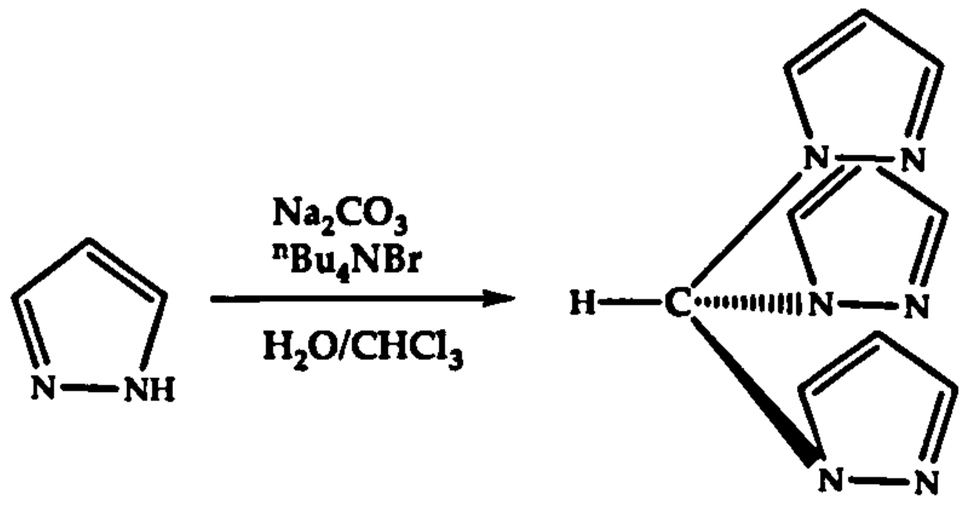

Scheme 3.3: Synthesis of tpm ligand

The ligand dppz was prepared by condensation of 1,10-phenanthroline-5,6-dione (dpq) with o-phenyline-diamine in ethanol[9]. The dpq ligand is obtained by oxidation of the 1, 10-phenanthroline (phen) in Br_2, nitric and sulphuric acid[9] (scheme 3.4).

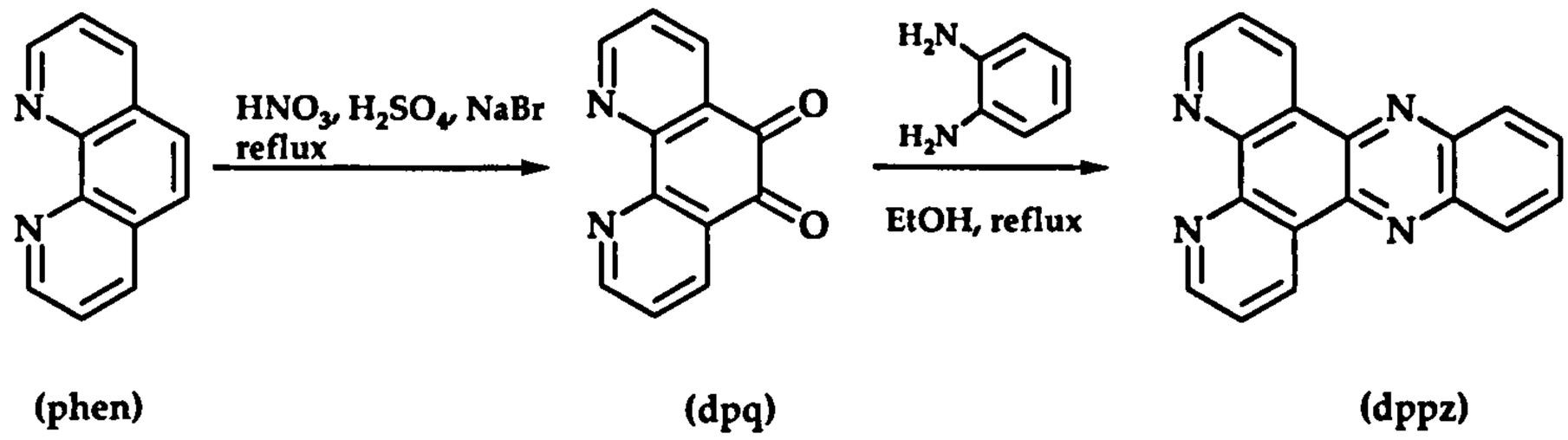

Scheme 3.4: Synthesis of dpq and dppz ligands

3.2.2 Synthesis of $Ru(tpm)Cl_3$ and $[Ru(tpm)(dppz)Cl]PF_6$ [3.3] and [3.4]

$Ru(tpm)Cl_3$ **[3.3]** and $[Ru(tpm)(dppz)Cl]PF_6$ **[3.4]** were synthesised following the method reported by Meyer et al [10].

$Ru(tpm)Cl_3$ is obtained by reaction of tpm with $RuCl_3 \cdot xH_2O$ in ethanol. $[Ru(tpm)(dppz)Cl]PF_6$ is then obtained by refluxing $tpmRuCl_3$ with dppz in presence of LiCl and NEt_3 in a mixture ethanol/water (3:1). $[Ru(tpm)(dppz)Cl]^+$ is precipitated by addition of NH_4PF_6 aq. to the solution and the product is purified by column chromatography on alumina grade I, using toluene: acetonitrile as an eluent.

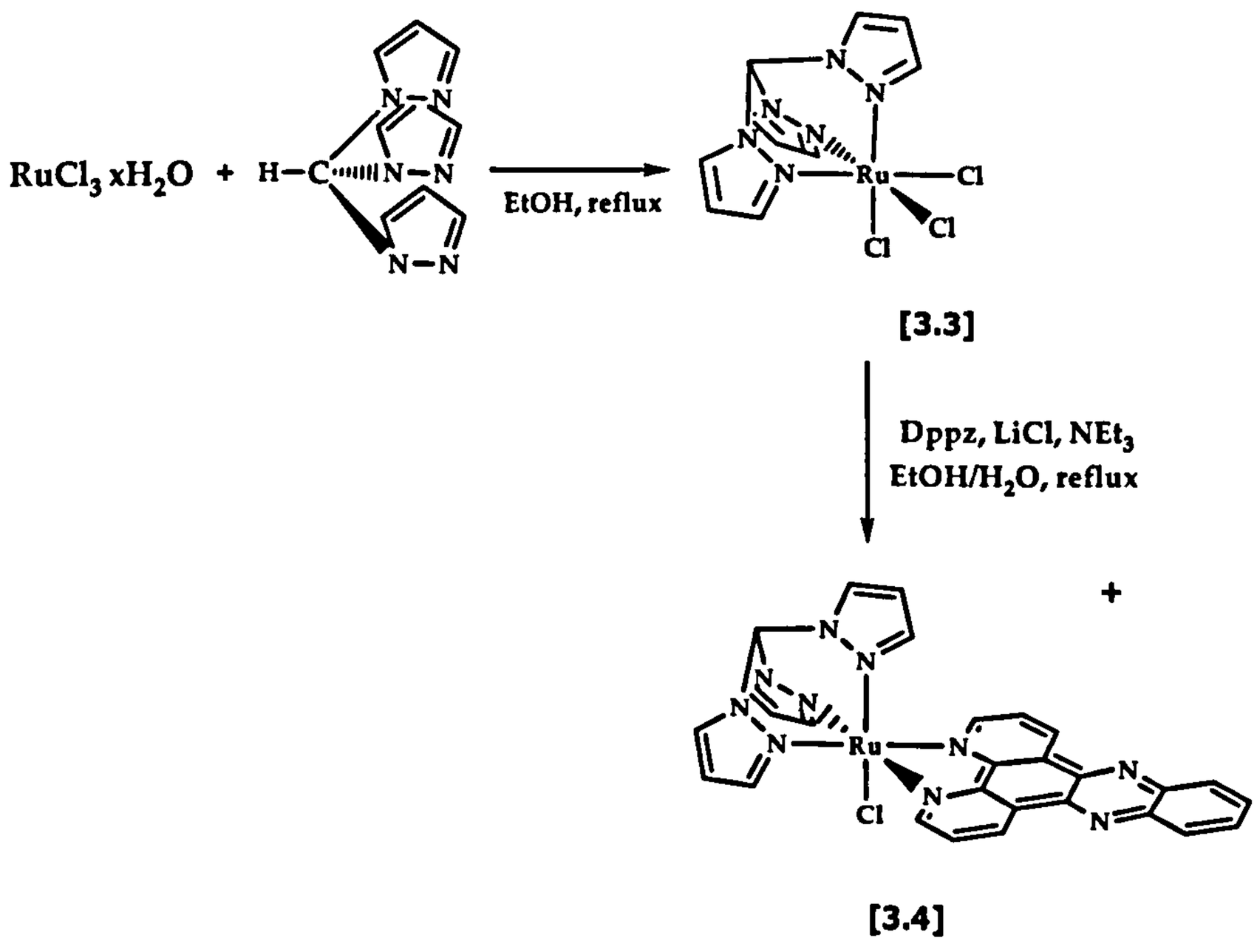

Scheme 3.5: Synthesis of **[3.3]** and **[3.4]**

3.2.3 Synthesis of $[Ru(tpm)(dppz)(L)](PF_6)_2$

Using $[Ru(tpm)(dppz)Cl]PF_6$ as a starting material, several derivatives of this complex were synthesised. The new complexes generated are designed to have two recognition motifs for the interaction with DNA (*e.g.* intercalation and hydrogen-bond recognition), for this reason the ligands selected, L, have hydrogen accepting and/or donating groups in addition to the intercalating motif (dppz ligand). The

ligands, L, used are: nicotinamide (Nic) (amide group in position three of the pyridine ring), 3-aminopyridine (3-NH_2py), pyridine-3-carboxaldehyde (3-CHOpy), and analogous with the H-bond unit in the position four of the pyridine ring, i.e. isonicotimide (Ison), 4-aminopyridine (4-NH_2py) and pyridine-4-carboxaldehyde (4-CHOpy). To complete the study, complexes containing an alkyl electron donating group without H-bond units, 3-picoline (3-pic) (methyl group in position three of the pyridine) and 4-picoline (4-pic) were also synthesised, table 3.1

Table 3.1: Structure of the ligands, L

Structure	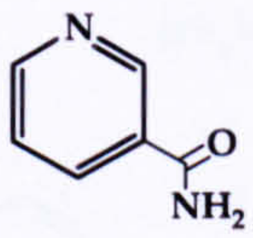	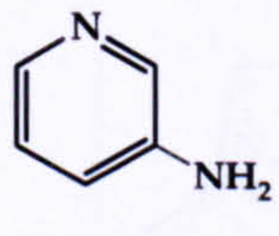	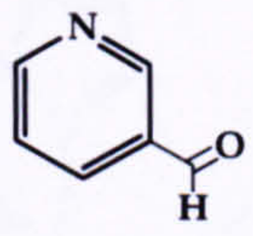	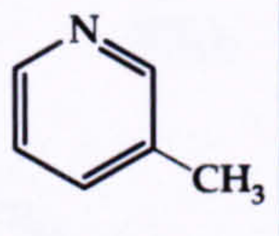
Name	**Nic**	**3- NH_2py**	**3-CHOpy**	**3-pic**
Structure	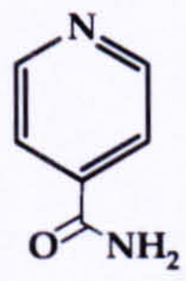	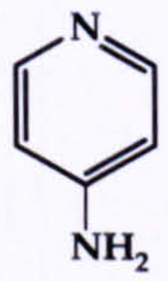	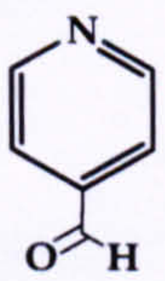	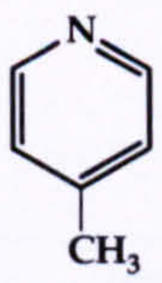
Name	**Ison**	**4-NH_2py**	**4-CHOpy**	**4-pic**

The general reaction for the synthesis of these complexes is shown in the scheme 3.6. Refluxing [Ru(tpm)(dppz)Cl]PF_6 with silver nitrate for five hours in ethanol:water allowed the removal of the axial chloride ligand. The silver chloride generated was removed by filtration through celite and the target complexes were synthesised by addition of the relevant ligands, L. Precipitation of the cationic complexes was accomplished by addition of NH_4PF_6, the solids were collected by filtration, washed with water and diethyl ether and then dried under vacuum. Products were shown to be pure without further work up and were characterised by ^{1}H NMR, mass spectrum and elemental analysis.

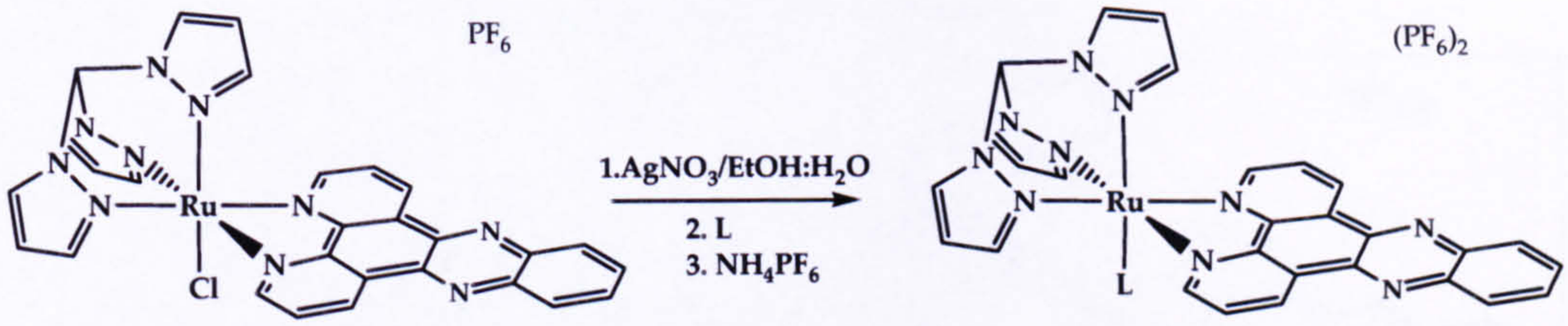

Scheme 3.6: Synthesis of [Ru(tpm)(dppz)(L)](PF6)2

Table 3.2: Structure of [Ru(tpm)(dppz)(3L)](PF6)2 complexes

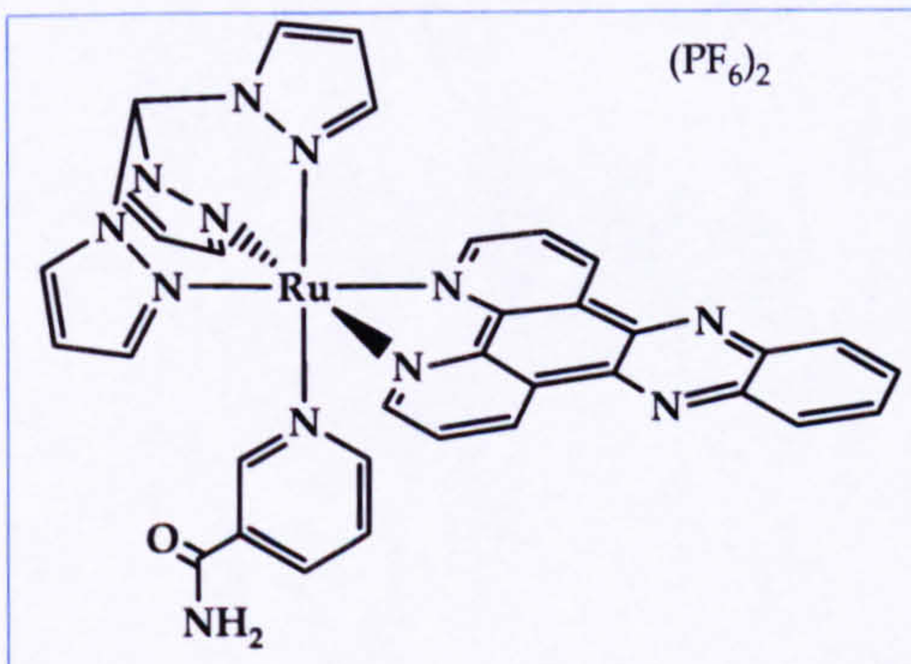 [3.5]	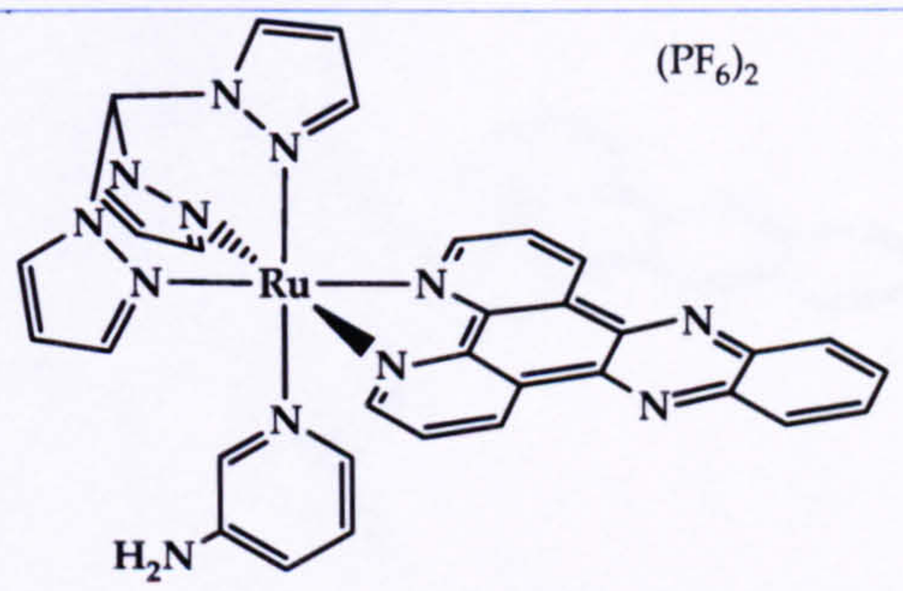 [3.6]
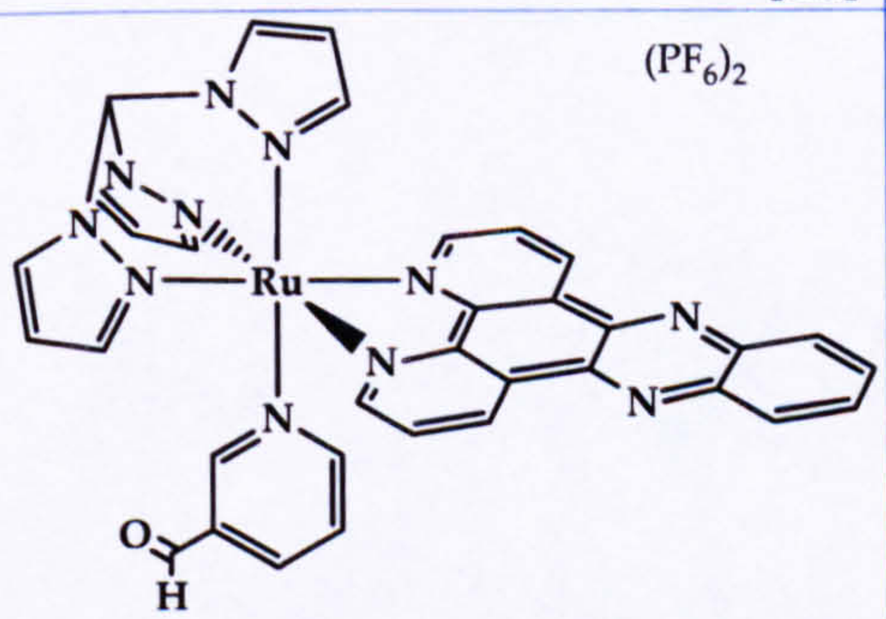 [3.7]	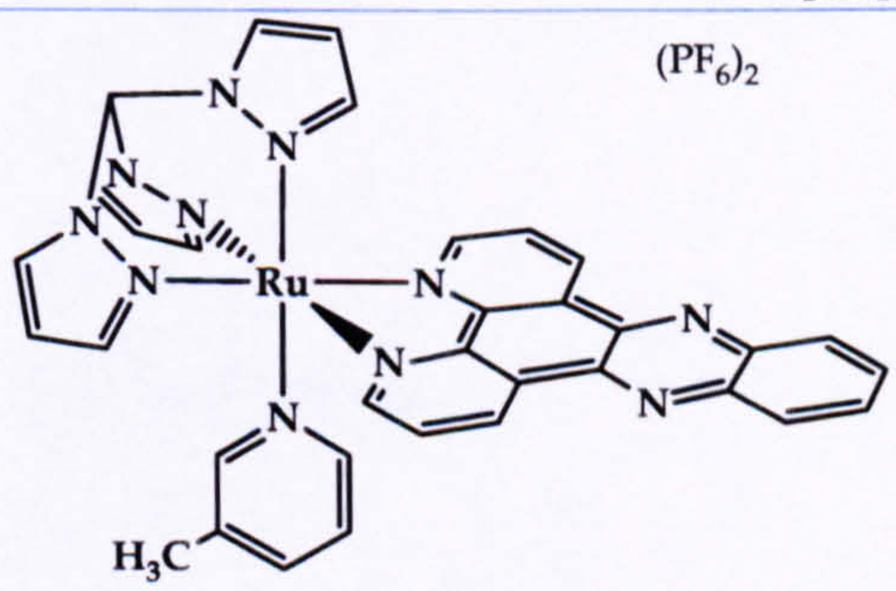 [3.8]

Table 3.3: Structure of $[Ru(tpm)(dppz)(4L)](PF_6)_2$ complexes

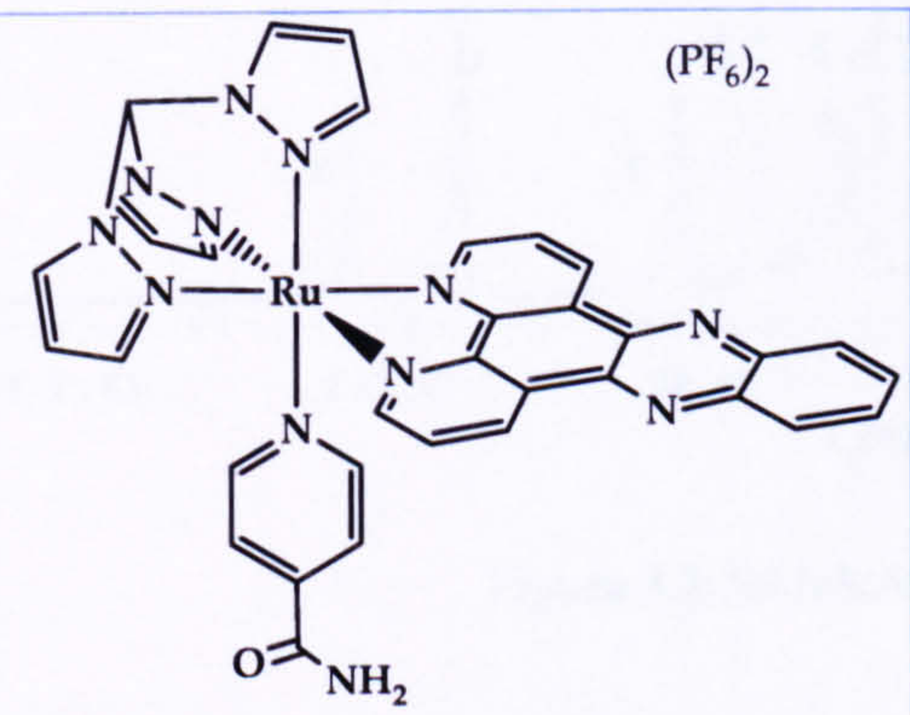 **[3.9]**	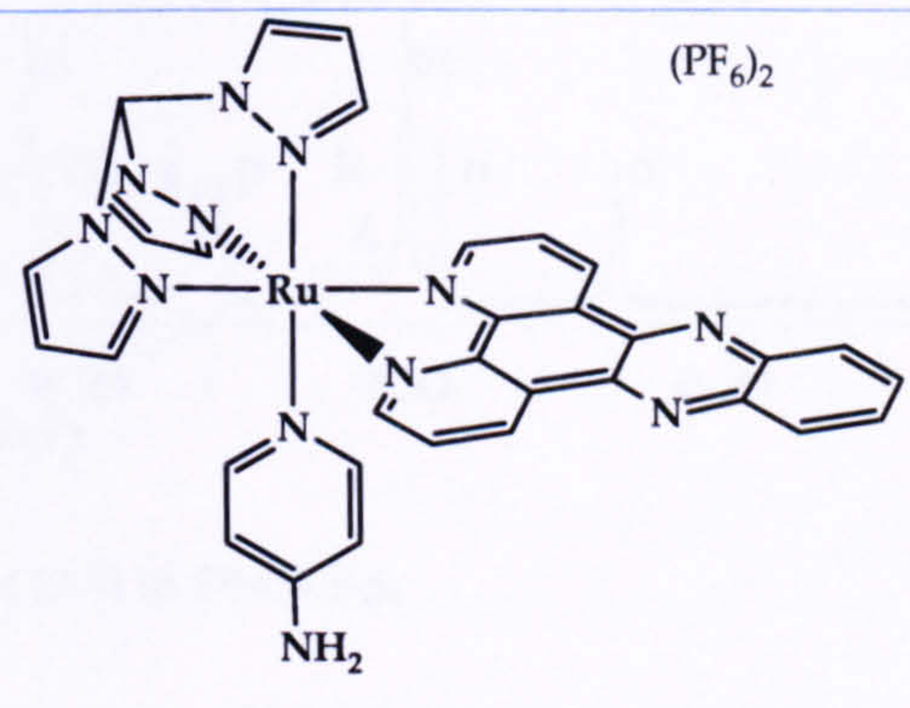 **[3.10]**
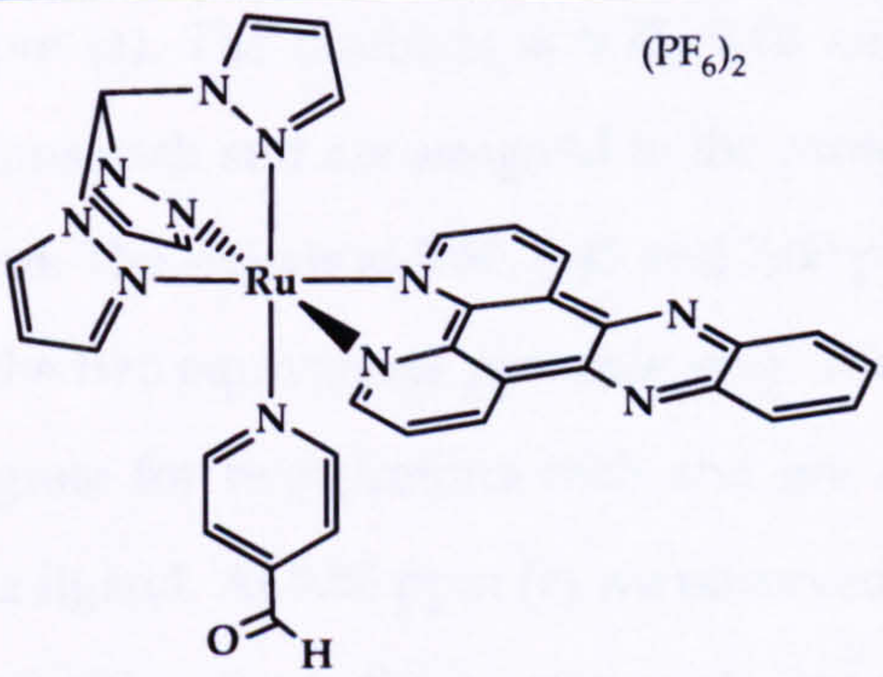 **[3.11]**	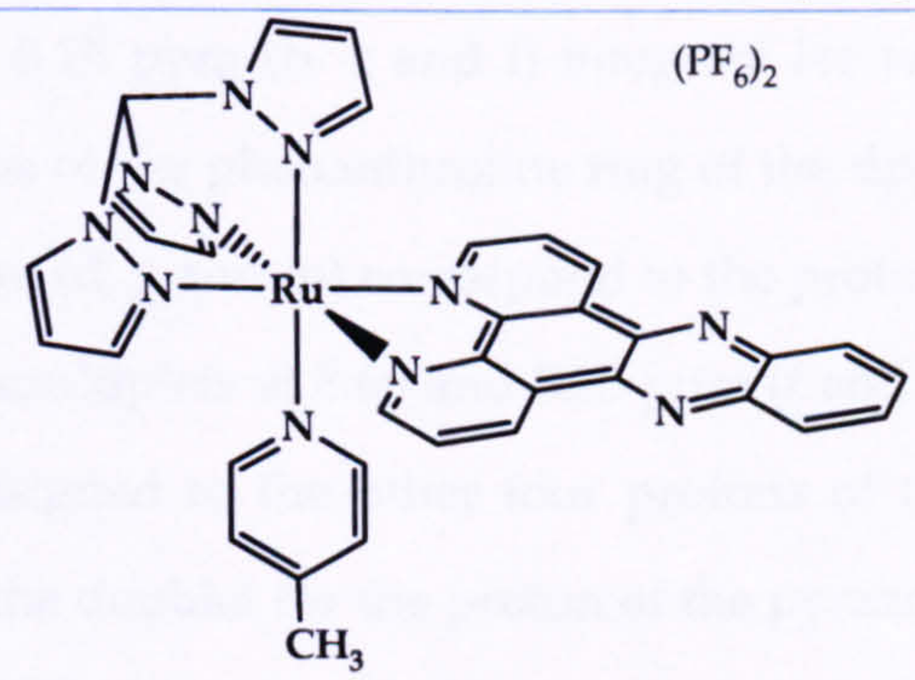 **[3.12]**

3.3 Characterisation of $[Ru(tpm)(dppz)(L)]^{2+}$ complexes

3.3.1 ^{1}H NMR spectroscopy studies

All the complexes show well resolved ^{1}H NMR spectra.

The shifts and couplings of the protons of the tpm and dppz ligands are quite similar in all the compounds. Figure 3.2 shows the ^{1}H NMR spectrum of **[3.5]** dissolved in DMSO-d_6.

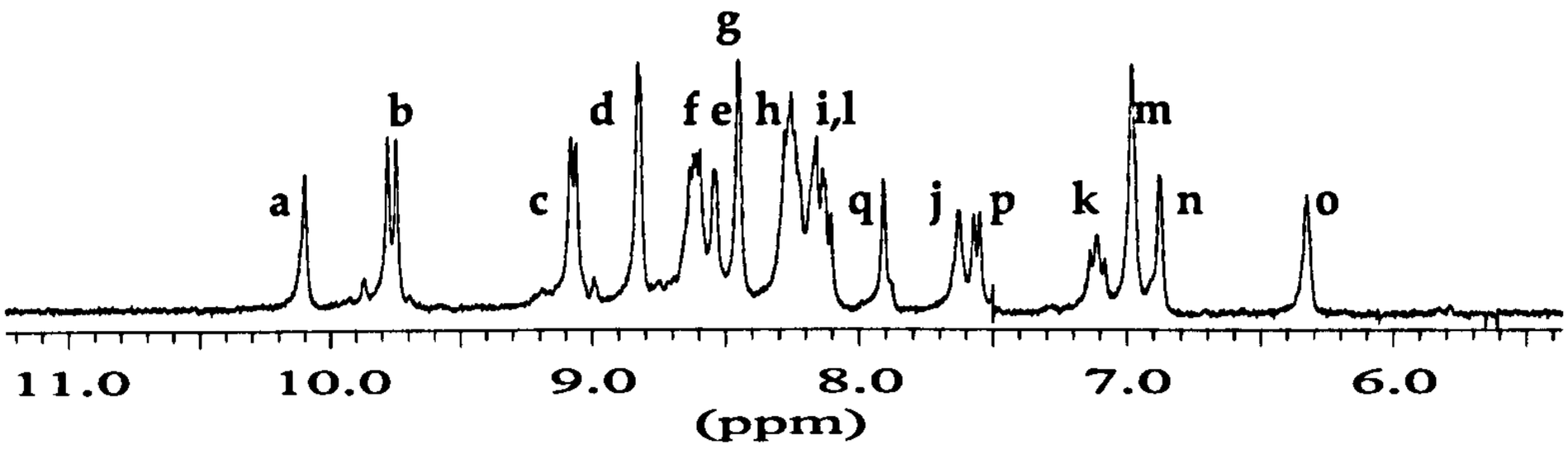

Figure 3.2: ^{1}H NMR of **[3.5]** in DMSO-d_6

The singlet at 10.10 ppm can be assigned to the shielded proton of the methyl group of tpm (a). The doublets at 9.75, 9.10 and 8.15 ppm (b, c and i) integrate for two protons each and are assigned to the protons of the phenanthroline ring of the dppz ligand. The signals at 8.80, 8.45 and 7.00 ppm (d, g and m) correspond to the protons for the two equivalents pyrazole ring. The multiplets at 8.60 and 8.25 ppm (f and h) integrate for two protons each and are assigned to the other four protons of the dppz ligand. At 8.55 ppm (e) we observed the doublet for the proton of the pyrazole ring that is trans to the nicotinamide ligand. The singlet at 8.12 ppm (q) corresponds to the NH_2 group of the nicotinamide. The singlet at 7.90 ppm (p) integrates for one proton and corresponds to the proton in the position two of the pyridine ring. The signals at 7.62, 7.57 and 7.13 ppm (l, j and k) can be assigned to the protons in the positions six, four and five of the pyridine ring respectively. The last two signals at 6.87 ppm (n) and 6.32 ppm (o) integrate for one proton each and are assigned to the protons of the pyrazole ring which has the nicotinamide ligand in trans (figure 3.3).

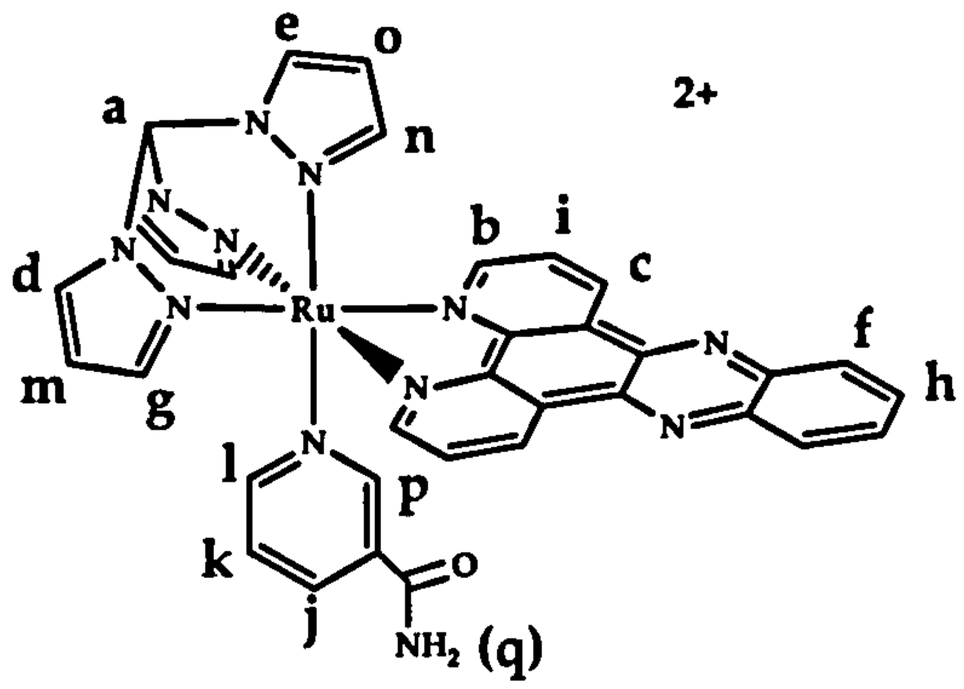

Figure 3.3: Proton labelling of **[3.5]**

The ^{1}H NMR spectra of **[3.6]**, **[3.7]** and **[3.8]** are very similar to the one described above, with the major difference being the position of the protons for the ligands, L. ^{1}H NMR spectrum of **[3.6]** shows the tpm and dppz protons at similar chemical shifts to **[3.5]**. The protons for the 3-aminopyridine are in different positions, the amino group increases the electron density of the ring so the protons are downfield shifted (figure 3.4). Shifts for the protons of the 3-aminopyridine ligand are: multiplet at 6.80-6.77 ppm for the ones in the position five and six (k and l), singlet at 6.67 ppm for the one in the position two (p) and doublet at 6.54 ppm for the one in position four (j). The singlet at 5.36 ppm that integrates for two protons is assigned to the protons of the amino group (q).

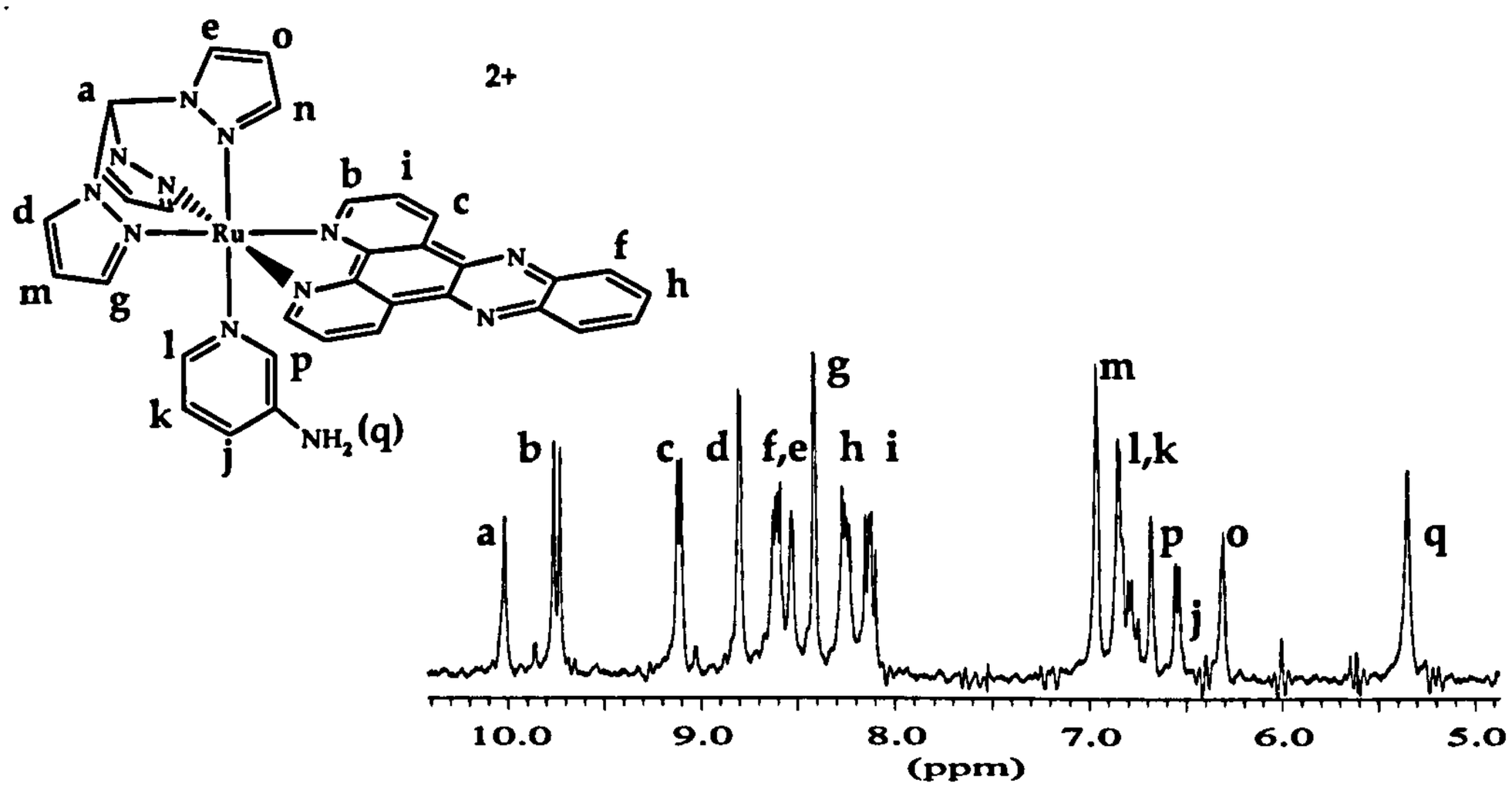

Figure 3.4: Proton labelling (top) and ^{1}H NMR spectrum (down) of **[3.6]**

Figure 3.5 shows the ^{1}H NMR-COSY of **[3.7]** dissolved in DMSO-d_6. In this case at 9.8 ppm the proton that corresponds to the aldehyde group of the pyridine-3-carboxaldehyde ligand (q) is observed. Around 8.11 ppm there is a singlet for the proton in position two of the pyridine-3-carboxaldehyde ligand (p) that is shifted downfield (orto to this carbon there are two groups withdrawing electron density). The others chemical shifts for the protons of the pyridine-3-carboxaldehyde ligand are: singlet at 7.87 ppm (j), doublet at 7.71 ppm (l) and multiplet at 7.27 ppm (k) (figure 3.5).

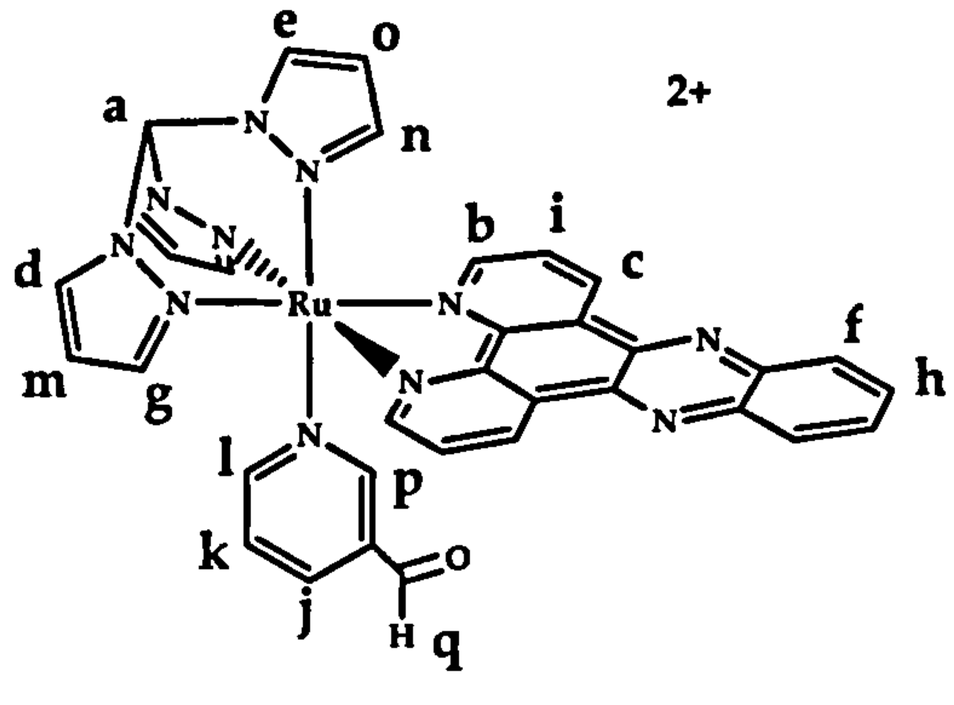

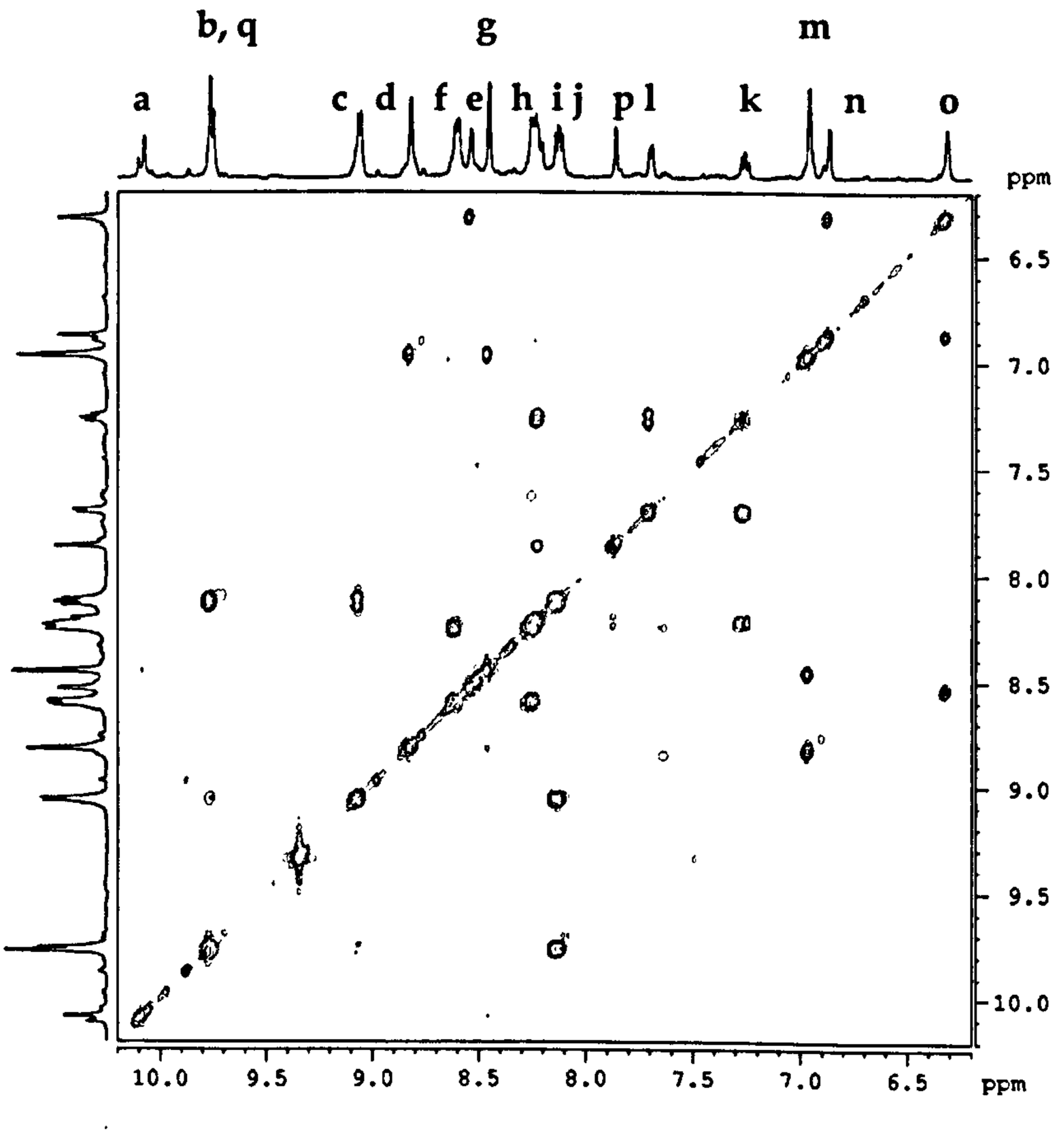

Figure 3.5: Proton labelling (up) and ^{1}H COSY-NMR of **[3.7]** in DMSO-d_6 (down)

The ^1H NMR shifts of the protons of the tpm and dppz ligands in $[Ru(tpm)(dppz)(4L)]^{2+}$ complexes display similar positions and couplings to the ^1H NMR spectra of $[Ru(tpm)(dppz)(3L)]^{2+}$ compounds. The ^1H NMR spectrum of **[3.9]** dissolved in DMSO-d_6 shows the same shifts for the tpm and dppz ligand as **[3.5]**. Chemical shifts for the isonicotinamide ligand are: a singlet at 7.80 ppm that corresponds to the NH_2 group of the isonicotinamide (l) and two doublets at 7.60 and 7.45 ppm that integrate for two protons each that are assigned to the four protons of the pyridine ring (j and k) (figure 3.6)

^1H NMR spectra of **[3.10]**, **[3.11]** and **[3.12]** are very similar to the ones described above. The differences are in the chemical shift of the protons for the derivatives of the pyridine ligand. The ^1H NMR spectrum of **[3.10]** shows the tpm and dppz protons at similar δ to the others complexes. Chemical shifts for the protons of the 4-aminopyridine ligand are at 6.75 and 6.15 ppm (j and k) and 6.65 ppm for the amino group (l) (figure 3.6).

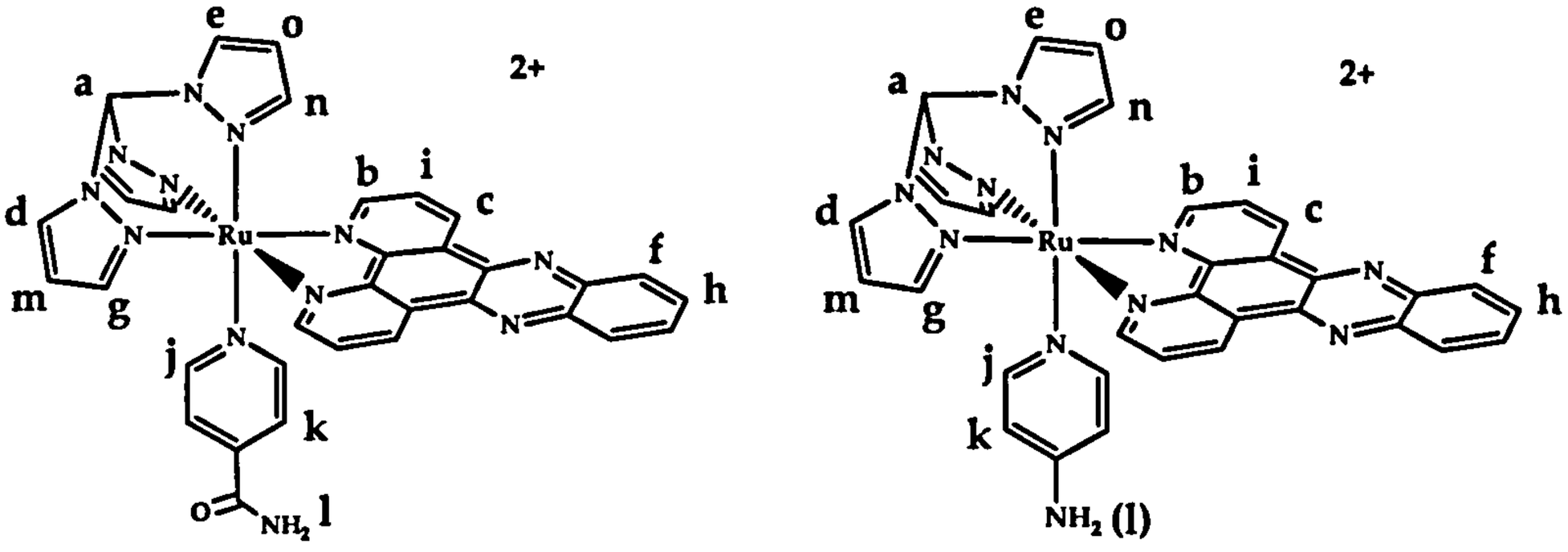

Figure 3.6: Proton labelling of **[3.9]** (left) and **[3.10]** (right)

The ^1H NMR spectrum of **[3.12]** in acetone-d_6 is shown in figure 3.7. In this case the chemical shifts are at different position because deuterated acetone was used as a solvent. At 2.25 ppm (l) a singlet that integrates for three protons is observed, this corresponds to the methyl group of the picoline. Signals at 7.60 and 7.05 ppm (j and k) are the protons for the 4-picoline ligand.

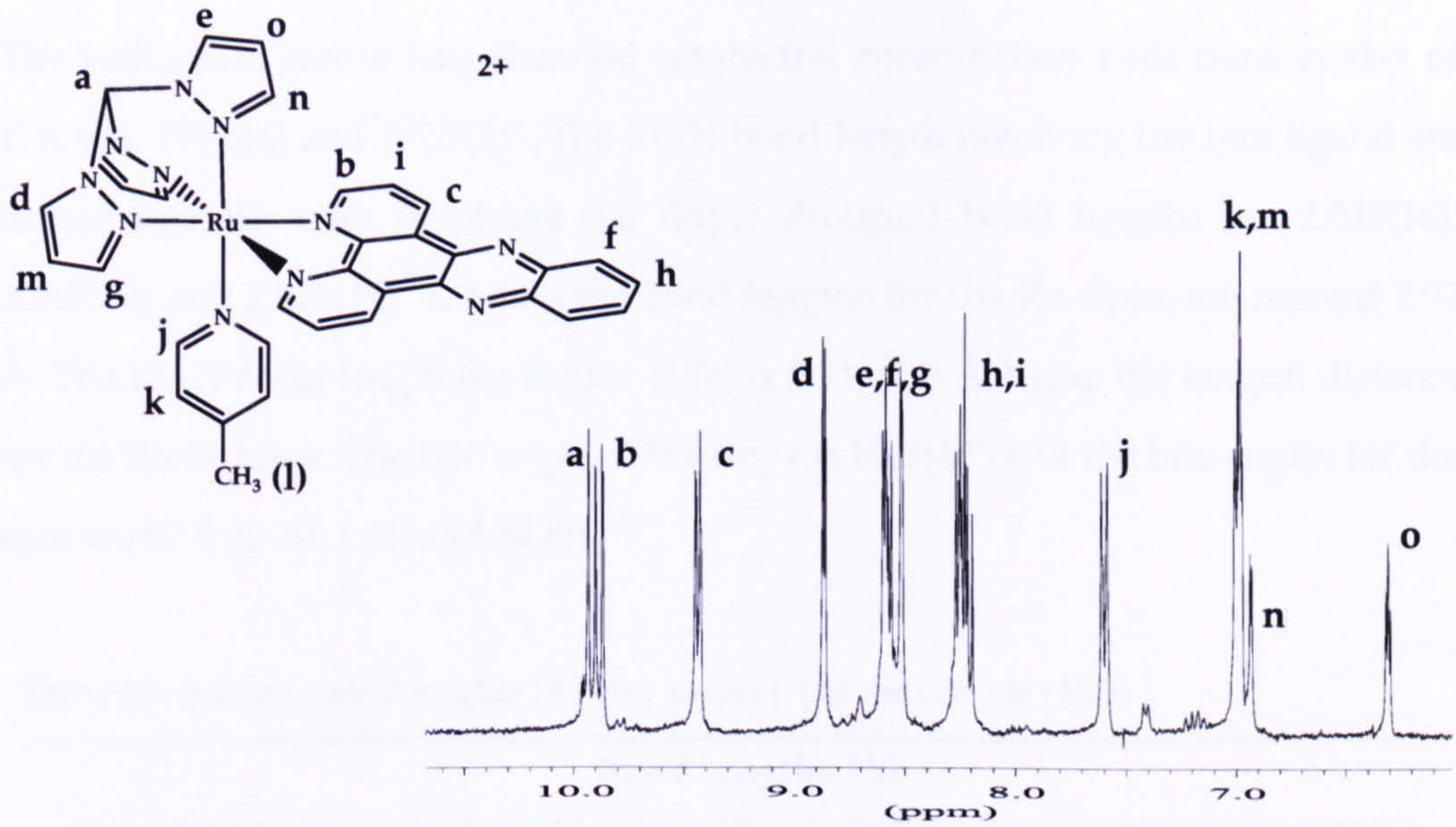

Figure 3.7: Proton labelling (left) and ^{1}H NMR aromatic region (right) of **[3.12]**

3.3.2 X-ray crystallography studies

The crystal structure of **[3.5]** is shown in figure 3.8, and table 3.2 shows selected bond lengths and angles of the complex. Two PF_6^- anions and three acetonitrile solvent molecules all are removed for clarity. The final refinement of the data for this crystal was 15% and while it is not of sufficient quality for publication, it allows us to confirm the structure of **[3.5]**.

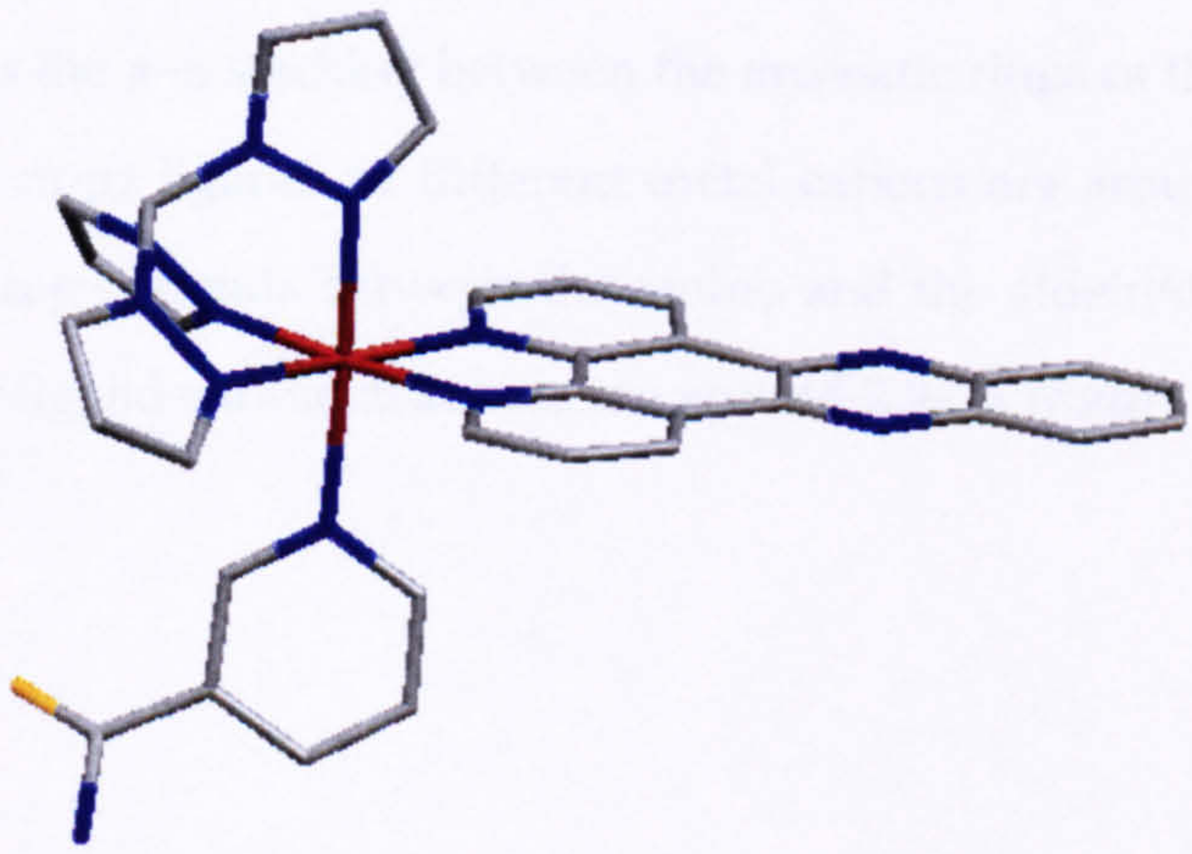

Figure 3.8 Structural representation of the cation found in the crystal structure of **[3.5]**. Hydrogen atoms, PF_6^- anions and solvent molecules are removed for clarity

The ruthenium centre has distorted octahedral coordination with trans angles of 176.1(4), 176.6(4) and 177.7(4)°. The Ru-N bond length involving the tpm ligand are longer that the ones involving the dppz: Ru-(tpm) bond lengths are 2.045(10), 2.045(12) and 2.073(10) Å, while the bond lengths for the Ru-dppz are around 2.07 Å. The Ru-N bond length for the Ru-(Nic) is 2.111(10) Å, being the longest distance for the Ru-N bond. The bite angle of the dppz is 80.2(4)°, and the bite angles for the tpm are 87.8 (4), 86.1 (4) and 82.8(4)°.

Table 3.2: Selected bond lengths [Å] and angles [°] of the complex **[3.5]**

Bond lengths (Å)					
	Ru-N(1)	2.045(10)	Ru-N(7)	2.049(10)	
	Ru-N(3)	2.045(12)	Ru-N(8)	2.074(11)	
	Ru-N(5)	2.073(10)	Ru-N(11)	2.111(10)	
Bond angles (⁰)					
N(1)-Ru-N(3)	87.8(4)	N(3)-Ru-N(7)	98.1(4)	N(1)-Ru-N(11)	177.7(4)
N(1)-Ru-N(5)	86.1(4)	N(3)-Ru-N(8)	176.1(4)	N(3)-Ru- N(11)	90.5(4)
N(1)-Ru-N(7)	90.7(4)	N(5)-Ru-N(7)	176.6(4)	N(5)-Ru-N(11)	92.3(4)
N(1)-Ru-N(8)	88.8(4)	N(5)-Ru-N(8)	98.6(4)	N(7)-Ru-N(11)	91.0(4)
N(3)-Ru-N(5)	82.8(4)	N(7)-Ru-N(8)	80.2(4)	N(8)-Ru-N(11)	93.0(4)

Packing of **[3.5]** reveals the π–π stacking between the aromatic rings of the dppz, the distance between two dppz ligands of different metal cations are around 3.26-3.46 Å. There are also hydrogen bonds between the amino and the aldehyde groups of different nicotinamide ligands, these distances are around 2.92 Å (figure 3.9).

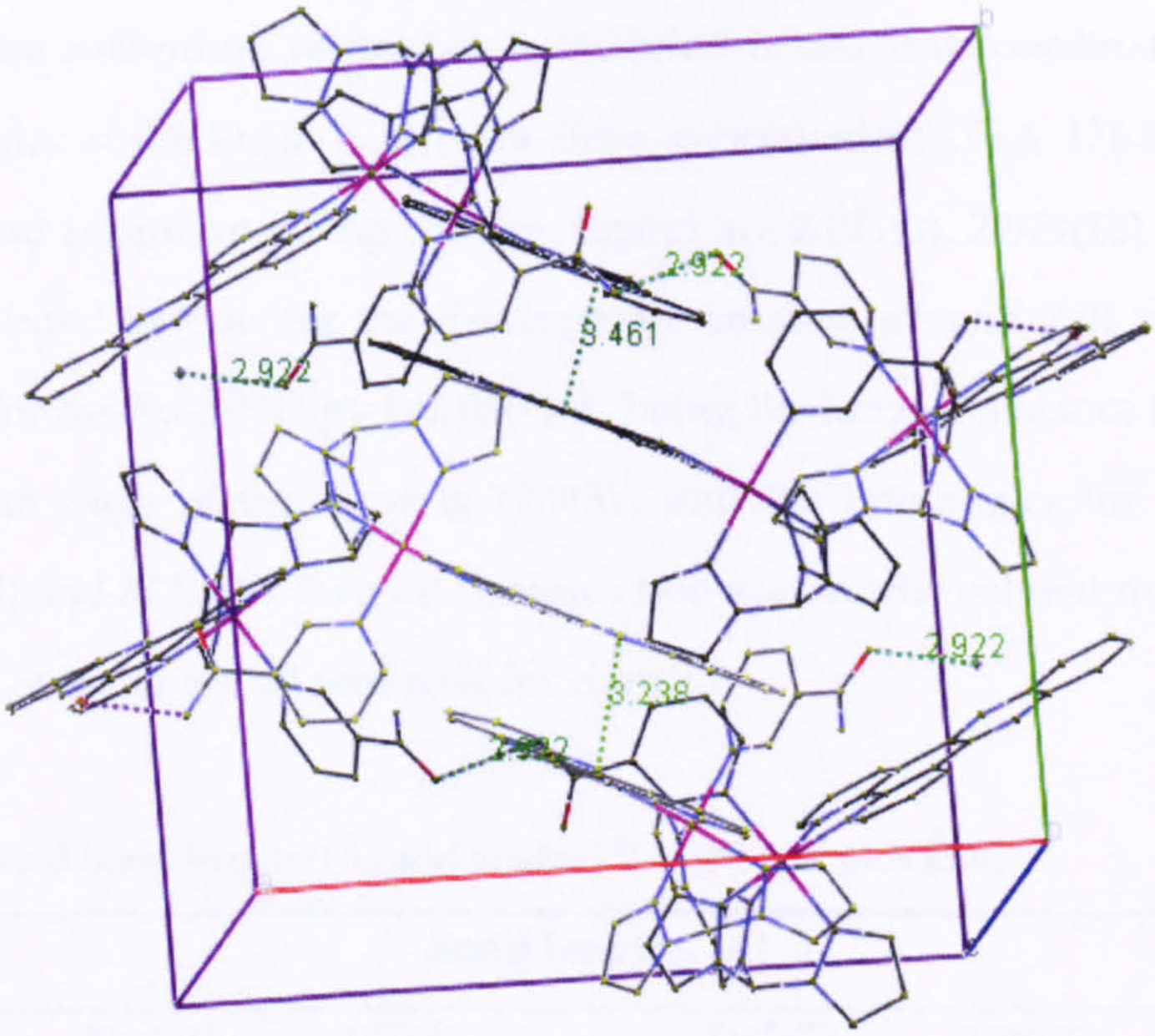

Figure 3.9: Structure of **[3.5]** with H-bond contacts between the cations shown. PF_6^- anions, hydrogen atoms and solvent molecules omitted for clarity

The crystal structure of **[3.6]** is shown in figure 3.10, and table 3.3 shows selected bond lengths and angles of the complex.

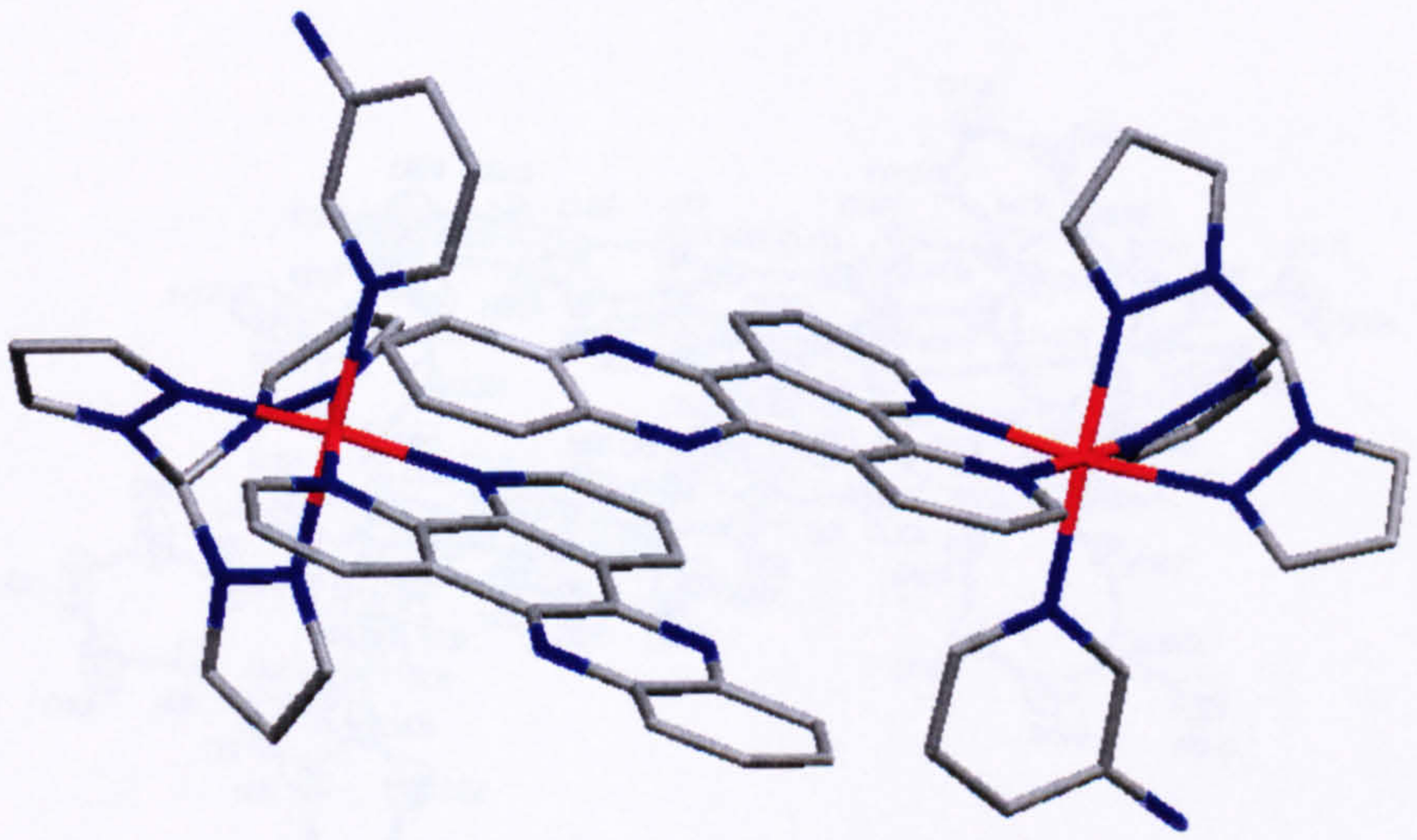

Figure 3.10: Structural representation of two cations found in the crystal structure of **[3.6].** Hydrogen atoms, PF_6^- anions and solvent molecules are removed for clarity

In this case the ruthenium centre has a distorted octahedral coordination as well. The trans angles at the Ru(II) centre are close to octahedral 176.4, 176.8 and 174.9°. The Ru-N bond length involving the tpm ligand are 2.071(9), 2.079(10) and 2.064(9) Å, while the bond lengths for the Ru-dppz are smaller, around 2.04 Å. The Ru-N bond length for the Ru-3-NH_2py is 2.08(9) Å, being the longest distance for the Ru-N bond. The bite angle of the dppz is 79.9(3)°, and the bite angles for the tpm are 84.7(4), 84.3(4) and 87.8(4)°. Two PF_6^- anions, two acetonitrile solvent molecules and one molecule of water are all removed for clarity.

Table 3.3: Selected bond lengths [Å] and angles [°] of the complex **[3.6]**

Bond lengths (Å)					
	Ru-N(1)	2.071(9)	Ru-N(7)	2.038(9)	
	Ru-N(3)	2.079(10)	Ru-N(10)	2.042(9)	
	Ru-N(5)	2.064(9)	Ru-N(11)	2.080(9)	
Bond angles (⁰)					
N(1)-Ru-N(3)	84.7(4)	N(3)-Ru-N(7)	91.7(4)	N(1)-Ru-N(11)	92.1(4)
N(1)-Ru-N(5)	84.3(4)	N(3)-Ru-N(10)	88.9(4)	N(3)-Ru- N(11)	176.8(4)
N(1)-Ru-N(7)	176.4(4)	N(5)-Ru-N(7)	96.3(4)	N(5)-Ru-N(11)	92.1(4)
N(1)-Ru-N(10)	99.3(3)	N(5)-Ru-N(10)	174.9(4)	N(7)-Ru-N(11)	91.4(3)
N(3)-Ru-N(5)	87.8(4)	N(7)-Ru-N(10)	79.9(3)	N(10)-Ru-N(11)	91.4(3)

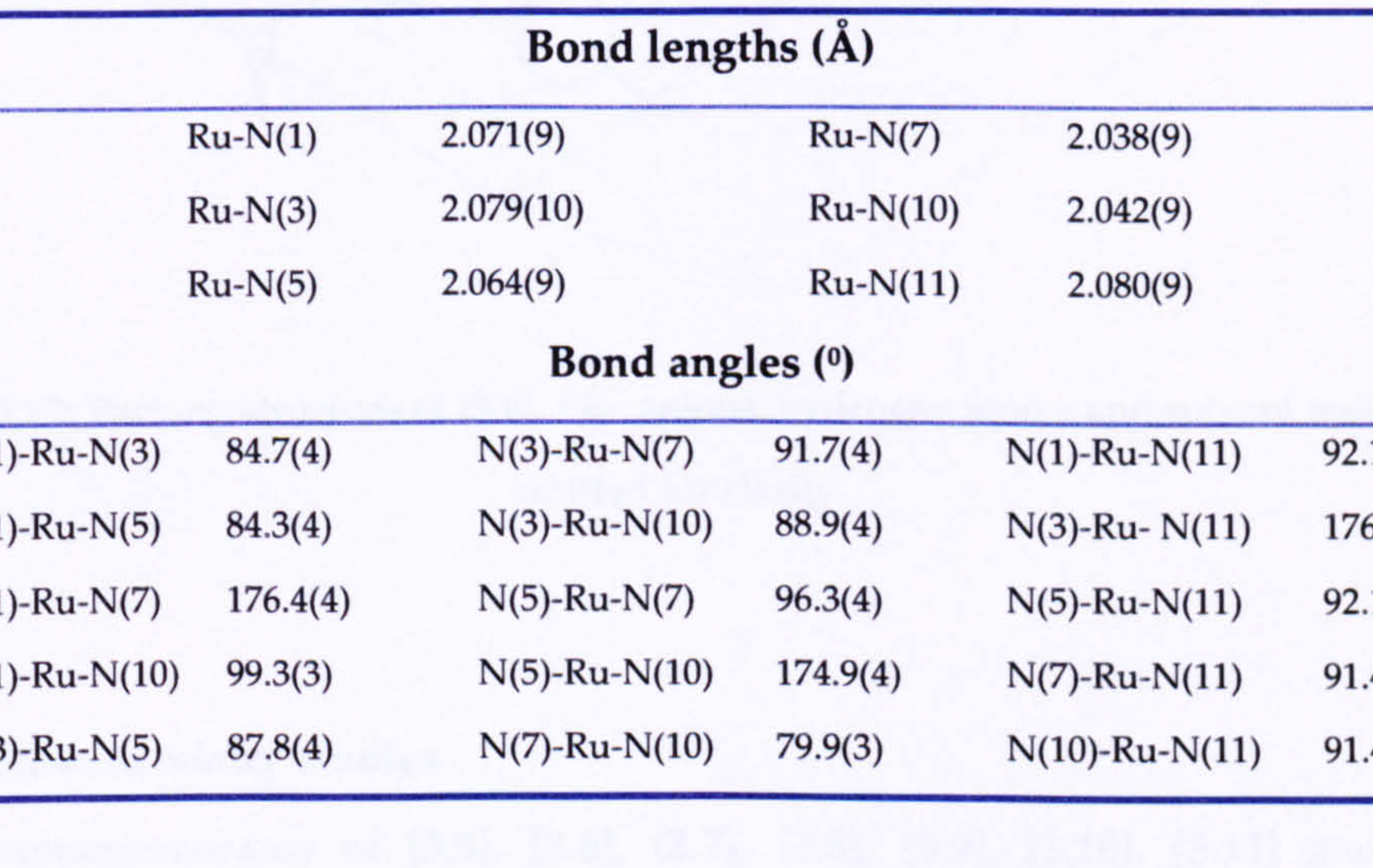

Figure 3.11: ORTEP plot of the cation in **[3.6][$(PF_6)_2$]**. Hydrogen atoms, PF_6^- anions and solvent molecules are removed for clarity

Again, packing of **[3.6]** reveals π–π stacking between the aromatic rings of the dppz, in this case the distance is around 3.33 Å (figure 3.12).

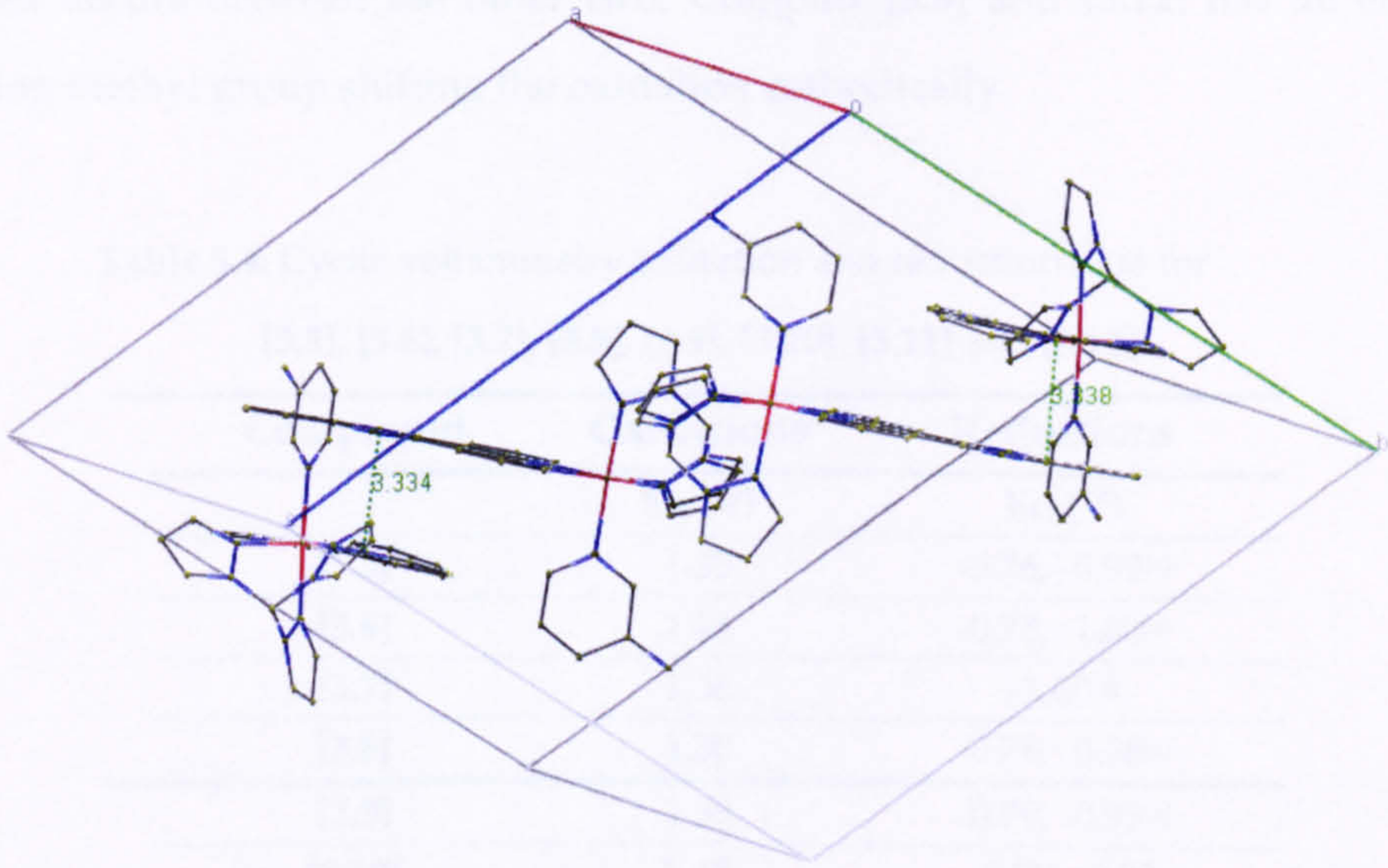

Figure 3.12: Packing structure of **[3.6]**. PF_6^- anions, hydrogen atoms and solvent molecules omitted for clarity

3.3.3 Electrochemistry studies

Cyclic voltammograms of **[3.5]**, **[3.6]**, **[3.7]**, **[3.8]**, **[3.9]**, **[3.10]**, **[3.11]** and **[3.12]** complexes were carried out at a scan rate 200 mV s^{-1} in acetonitrile containing 0.1 M TBAP, as supporting electrode, under nitrogen atmosphere. Potentials were measured vs. Ag/AgCl. Data are summarised in table 3.4.

The chemically reversible one electron oxidation of the Ru(II)/Ru(III) occurs around 1.2-1.4 V which is in agreement with similar complexes such us $[Ru(tpm)(bpy)(4\text{-}Etpy)]^{2+}$, $[Ru(tpm)(4,4\text{-}(CH_3)\text{-}bpy)(py)]^{2+}$ and $[Ru(tpm)(py)_3]^{2+}$ that have been described in literature[10-14]. The position of the Ru(II)/Ru(III) oxidation couple is highly dependent on the nature of the axial ligand. Oxidation of **[3.6]** and **[3.10]** occurs at lower potentials than in other reported complexes, as the amino group of to the pyridine ring increases donation of electron density onto the metal centre, making them easier to oxidise. In contrast, oxidation of **[3.7]** and **[3.11]** takes

place at higher potentials, the aldehyde group is removing electron density from the pyridine ring so the metal centre is consequently more difficult to oxidise. Complex **[3.5]** and **[3.9]** have an amine and an aldehyde group so the oxidation in this complex occurs between the other two. Complex **[3.8]** and **[3.12]** has an electron donating methyl group shifting the oxidation cathodically.

Table 3.4: Cyclic voltammetry oxidation and reduction data for **[3.5]**, **[3.6]**, **[3.7]**, **[3.8]**, **[3.9]**, **[3.10]**, **[3.11]** and **[3.12]**

Compound	Oxidations	Reductions
	$E_{1/2}$ (V)	$E_{1/2}$ (V)
[3.5]	1.33	-0.76, -0.99[a]
[3.6]	1.23	-0.78, -1.00[a]
[3.7]	1.36	-1.00[a]
[3.8]	1.30	-0.78, -0.98[a]
[3.9]	1.35	-0.79, -0.93[a]
[3.10]	1.15	-0.70, -0.93
[3.11]	1.38	-0.90, -1.08[a]
[3.12]	1.27	-0.79, -1.02[a]

[a] Reduction not fully chemically reversible, only E_p values are quoted

Reductions of the complexes were also studied. These reductions are not completely reversible. The dppz ligand is easier to reduce than the other N-donor ligands, so probably the first wave is caused by the reduction of the dppz ligand and the second one to the reduction of the other ligands.

The oxidation of the complexes with the same H-bonding substituent in the pyridine ring is at similar potentials, indicating that the changes in the oxidation potential are not affected by the position of the substituent on the pyridine ring.

As an example, figure 3.13 shows the CV voltammogram of complex **[3.6]** recorded in acetonitrile.

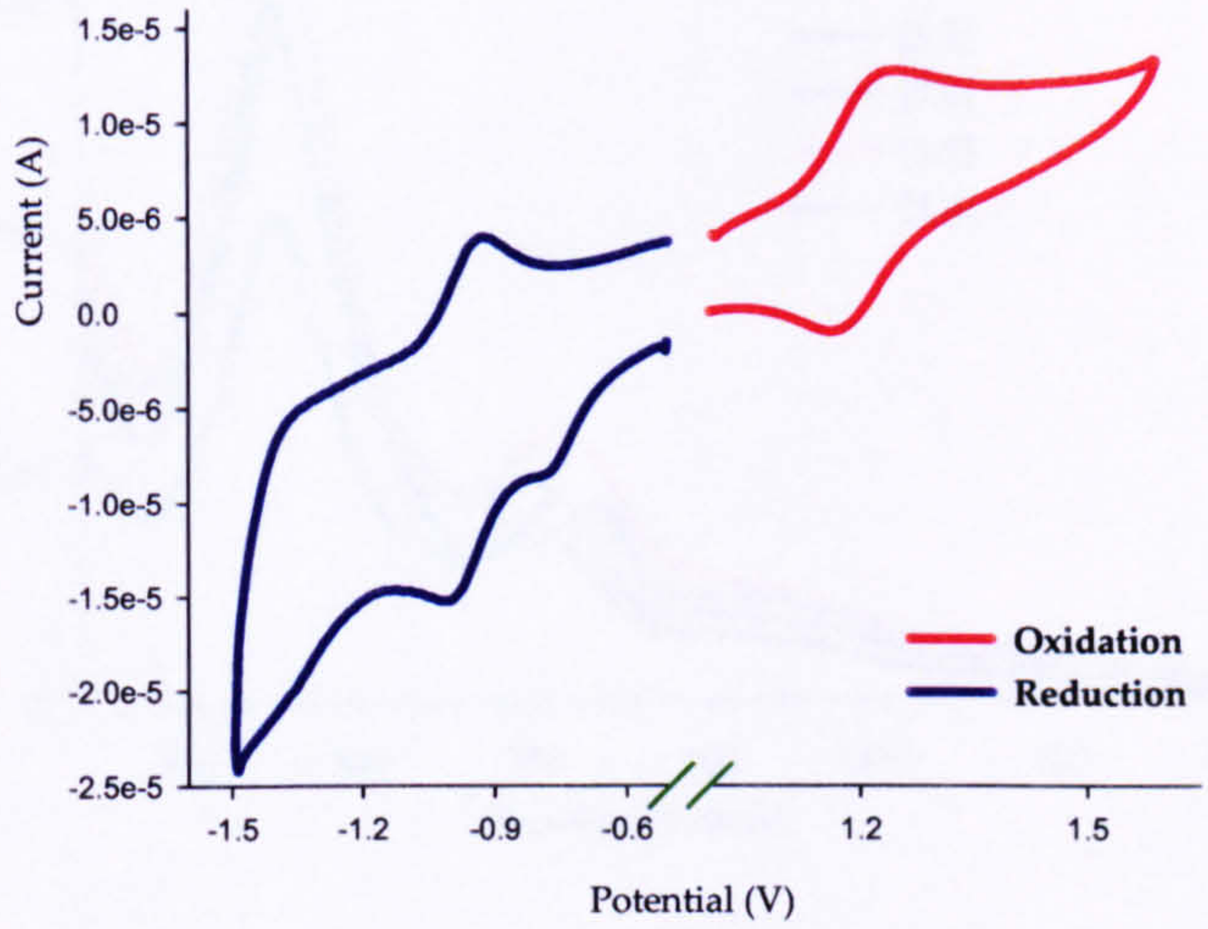

Figure 3.13: CV voltragramm of **[3.6]** recorded in acetonitrile

3.3.4 UV-Vis spectroscopy studies

UV-Vis absorption spectra of **[3.5]**, **[3.6]**, **[3.7]**, **[3.8]**, **[3.9]**, **[3.10]**, **[3.11]** and **[3.12]** complexes were recorded in acetonitrile solutions at room temperature (figure 3.14 shows UV-Vis spectra of $[Ru(tpm)(dppz)(3L)](PF_6)_2$ complexes).

All the complexes show a band between 250-300 nm that can be assigned to high energy $\pi \rightarrow \pi^*$ transition in aromatic nitrogen donor ligands. The UV-Vis spectrum of the dppz ligand in DMF shows structured transitions between 340-380 nm, which can be assigned to HOMO-LUMO ($\pi \rightarrow \pi^*$) transitions[15]. All complexes show such band around 350 nm, in **[3.5]** complex that band is at 356 nm, for the **[3.7]** complex at 354 nm and for **[3.6]** and **[3.8]** it is seen at 347 and 348 nm respectively. Metal-ligand charge transfer transitions (MLCT) are observed for all the complexes at around 400-500 nm; this is typical for Ru(II)→ L MLCT bands. Data are summarised in table 3.5.

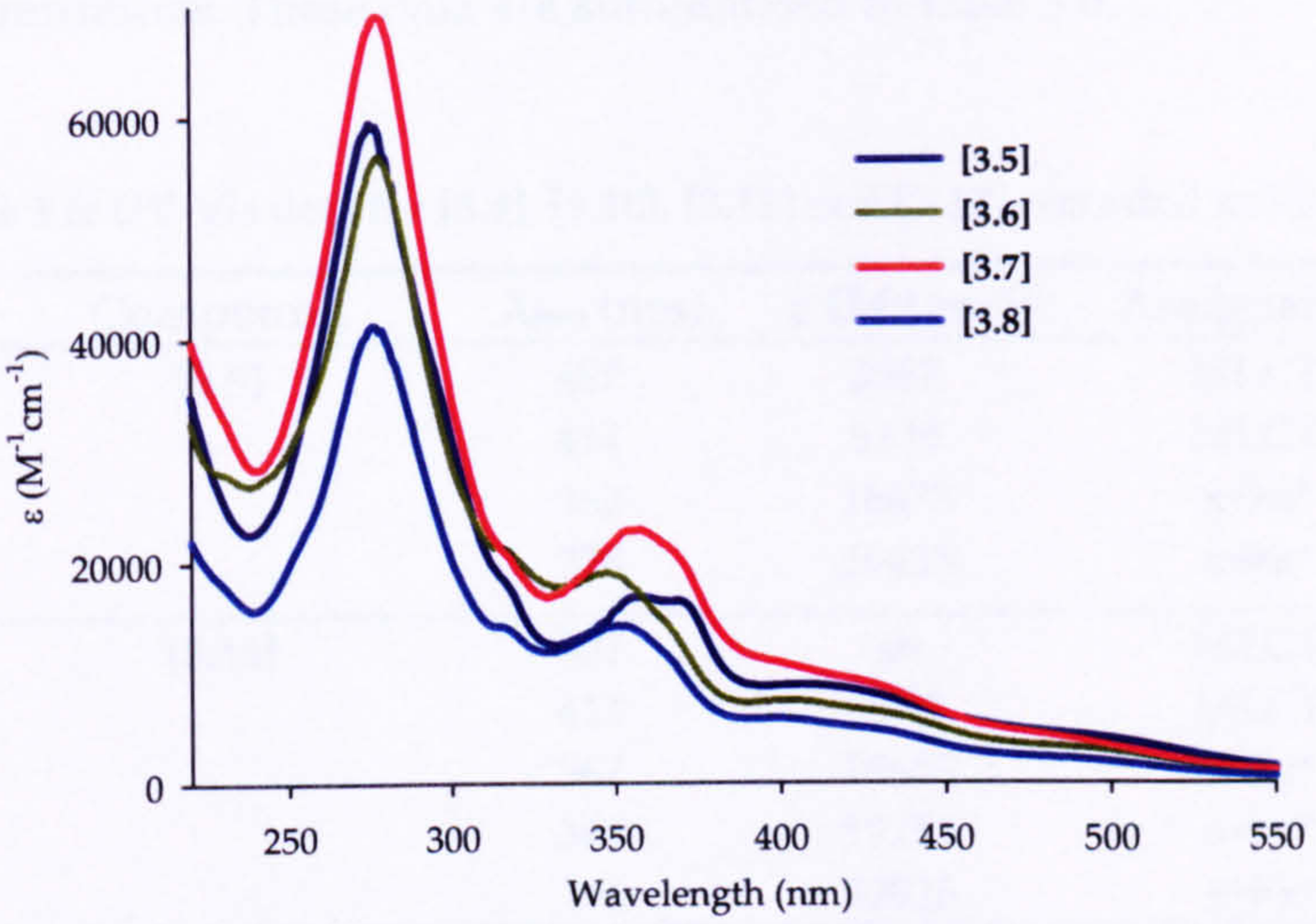

Figure 3.14: UV-Vis of **[3.5]**, **[3.6]**, **[3.7]** and **[3.8]** recorded in acetonitrile

Table 3.5: UV-Vis data of **[3.5]**, **[3.6]**, **[3.7]** and **[3.8]** recorded in MeCN

Compound	λ_{max} (nm)	ε ($M^{-1}cm^{-1}$)	Assignation
[3.5]	489	sh	MLCT
	415	8781	MLCT
	369	16606	$\pi \rightarrow \pi^*$
	356	16922	$\pi \rightarrow \pi^*$
	276	59111	$\pi \rightarrow \pi^*$
[3.6]	501	sh	MLCT
	415	7045	MLCT
	348	19118	$\pi \rightarrow \pi^*$
	278	56617	$\pi \rightarrow \pi^*$
[3.7]	473	sh	MLCT
	413	9851	MLCT
	354	22888	$\pi \rightarrow \pi^*$
	277	69125	$\pi \rightarrow \pi^*$
[3.8]	492	2132	MLCT
	420	5173	MLCT
	348	14326	$\pi \rightarrow \pi^*$
	276	41298	$\pi \rightarrow \pi^*$

For the [Ru(tpm)(dppz)(4L)]$(PF_6)_2$ complexes, similar bands can be assigned to analogous transitions. These data are summarised in table 3.6.

Table 3.6: UV-Vis data for **[3.9]**, **[3.10]**, **[3.11]** and **[3.12]** recorded in MeCN

Compound	λ_{max} (nm)	ε ($M^{-1}cm^{-1}$)	Assignation
[3.9]	487	3387	MLCT
	414	9139	MLCT
	362	16673	$\pi \rightarrow \pi^*$
	278	59425	$\pi \rightarrow \pi^*$
[3.10]	501	sh	MLCT
	411	9612	MLCT
	367	16655	$\pi \rightarrow \pi^*$
	349	19751	$\pi \rightarrow \pi^*$
	276	72926	$\pi \rightarrow \pi^*$
[3.11]	438	9235	MLCT
	357	13693	$\pi \rightarrow \pi^*$
	278	50108	$\pi \rightarrow \pi^*$
[3.12]	490	sh	MLCT
	411	8648	MLCT
	348	22561	$\pi \rightarrow \pi^*$
	276	59946	$\pi \rightarrow \pi^*$

3.3.5 Luminescence studies

Emission spectra of **[3.5]**, **[3.6]**, **[3.7]**, **[3.8]**, **[3.9]**, **[3.10]**, **[3.11]** and **[3.12]** were recorded in acetonitrile at room temperature.

Spectra of [Ru(tpm)(dppz)(3L)]$(PF_6)_2$ are shown in figure 3.15 (Data are normalised for clarity). All the complexes were excited at the wavelength characteristic of the transition MLCT. In the case of **[3.5]** the excitation wavelength is at 425nm, for **[3.6]**, λex= 455 nm and λex= 425 and 490 nm for **[3.7]** and **[3.8]** respectively.

The emission of **[3.6]** and **[3.7]** are around 600 nm, while the emission of **[3.5]** is at 645 nm and the emission of **[3.8]** is at 664 nm. Data are summarised in table 3.7

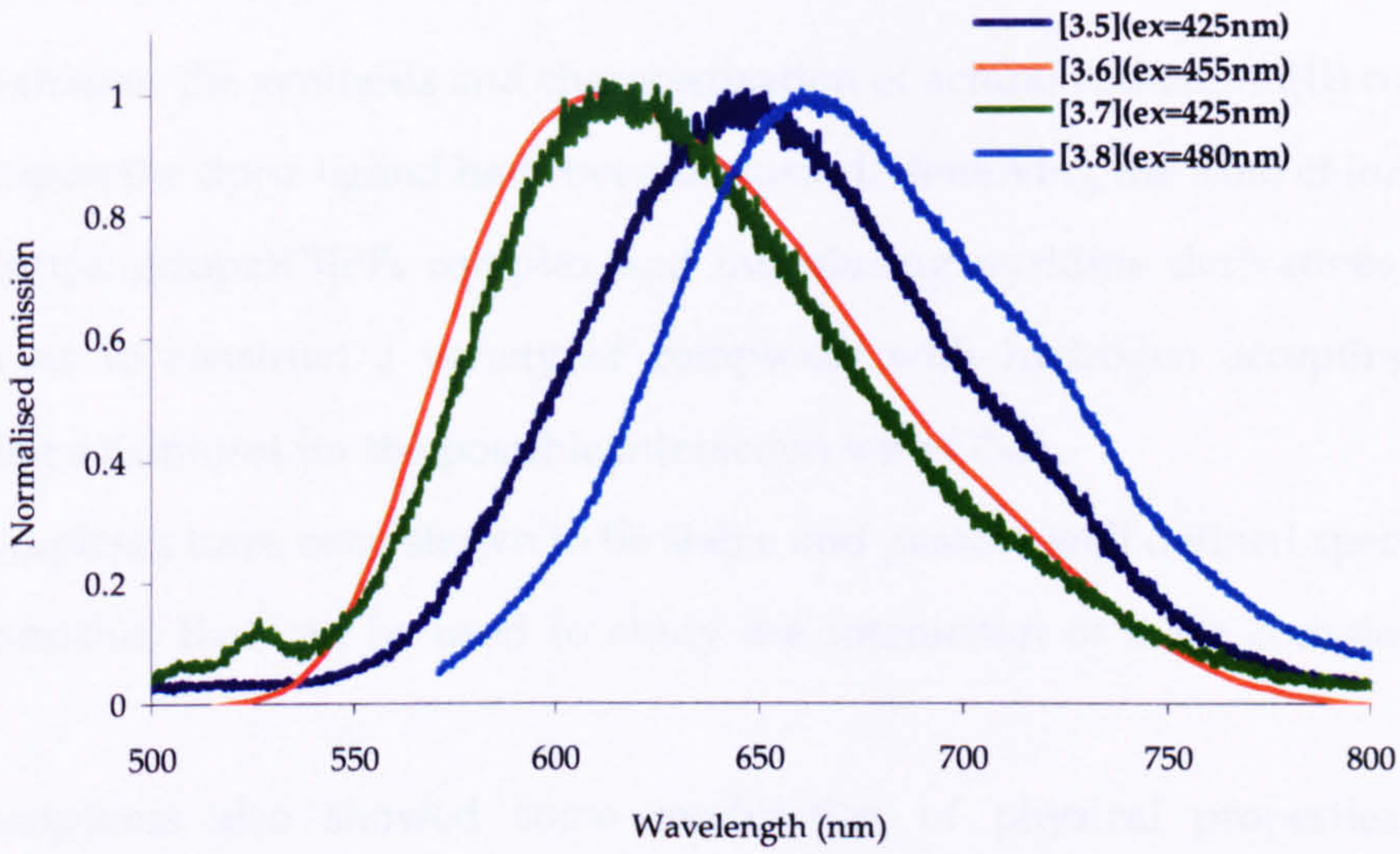

Figure 3.15: Luminescence spectra of **[3.5], [3.6], [3.7]** and **[3.8]** recorded in acetonitrile

Complexes $[Ru(tpm)(dppz)(4L)]^{2+}$ also show emissions around 600 nm when excited at the wavelength characteristic of the transition MLCT. In the case of **[3.9]** the excitation wavelength is at 482nm, for **[3.10]**, λex= 420 nm and λex= 450 and 480 nm for **[3.11]** and **[3.12]** respectively. Emissions of **[3.10]** and **[3.11]** are around 600 nm and the emission for **[3.9]** and **[3.12]** are a longer wavelength compared to the other two compounds. Data summarised in table 3.7.

Table 3.7: Luminescence data for complexes **[3.5], [3.6], [3.7], [3.8], [3.9], [3.10], [3.11]** and **[3.12]** recorded in MeCN

Compound	λexc (nm)	λem (nm)
[3.5]	425	650
[3.6]	455	615
[3.7]	425	612
[3.8]	480	660
[3.9]	482	638
[3.10]	420	603
[3.11]	450	605
[3.12]	480	662

3.4 Conclusions and future work

In this chapter the synthesis and characterisation of achiral ruthenium(II) complexes based upon the dppz ligand have been discussed. Removing the axial chloride from the [Ru(tpm)(dppz)Cl]PF_6 complex and introducing pyridine derivatives ligands, allows us to construct a variety of complexes with hydrogen accepting and/or donating substitutes for the possible interaction with DNA.

The complexes have been shown to be stable and possess well defined spectroscopy characteristics that can be used to study the interaction of these complexes with DNA.

All complexes also showed some modulation of physical properties that is dependent on the ancillary ligand used. For example, oxidations of the ruthenium metal centre can be modified using an amine or a carboxyl group as a substituent in the pyridine ring. Emission wavelength also showed distinctive change due to the variation in pyridyl based ligand.

3.5 References

(1) Metcalfe, C.; Adams, H.; Haq, I.; Thomas, J. A. *Chem. Commun.* **2003**, 1152-1153.

(2) Sitlani, A.; Dupureur, C. M.; Barton, J. K. *J. Am. Chem. Soc.* **1993**, *115*, 12589-12590.

(3) Pyle, A. M.; Rehmann, J. P.; Meshoyrer, R.; Kumar, C. V.; Turro, N. J.; Barton, J. K. *J. Am. Chem. Soc.* **1989**, *111*, 3051-3058.

(4) Sitlani, A.; Long, E. C.; Pyle, A. M.; Barton, J. K. *J. Am. Chem. Soc.* **1992**, *114*, 2303-2312.

(5) Campisi, D.; Morii, T.; Barton, J. K. *Biochemistry* **1994**, *33*, 4130-4139.

(6) Hudson, B. P.; Barton, J. K. *J. Am. Chem. Soc.* **1998**, *120*, 6877-6888.

(7) Terbrueggen, R. H.; Johann, T. W.; Barton, J. K. *Inorg. Chem.* **1998**, *37*, 6874-6883.

(8) Reger, D. L.; Grattan, T. C.; Brown, K. J.; Little, C. A.; Lamba, J. J. S.; Rheingold, A. L.; Sommer, R. D. *J. Organomet. Chem.* **2000**, *607*, 120-128.

(9) Paw, W.; Eisenberg, R. *Inorg. Chem.* **1997**, *36*, 2287-2293.

(10) Llobet, A.; Doppelt, P.; Meyer, T. J. *Inorg. Chem.* **1988**, *27*, 514-520.

(11) Jones, W. E., Jr.; Bignozzi, C. A.; Chen, P.; Meyer, T. J. *Inorg. Chem.* **1993**, *32*, 1167-1178.

(12) Amouyal, E.; Homsi, A.; Chambron, J. C.; Sauvage, J. P. *J. Chem. Soc., Dalton Trans.* **1990**, 1841-1845.

(13) Laurent, F.; Plantalech, E.; Donnadieu, B.; Jimenez, A.; Hernandez, F.; Martinez-Ripoll, M.; Biner, M.; Llobet, A. *Polyhedron* **1999**, *18*, 3321-3331.

(14) Bargawi, K. R.; Llobet, A.; Meyer, T. J. *J. Am. Chem. Soc.* **1988**, *110*, 7751-7759.

(15) Fees, J.; Kaim, W.; Moscherosch, M.; Matheis, W.; Klima, J.; Krejcik, M.; Zalis, S. *Inorg. Chem.* **1993**, *32*, 166-174.

Chapter Four

DNA binding studies on mixed recognition motif Ru(II) complexes

4.1 Introduction

In the previous chapter the syntheses and characterisation of some Ru(II) complexes containing ligands capable of intercalation between the base pairs of DNA and ancillary ligands with hydrogen accepting and/or donating substitutes were described. In this chapter the interaction of these complexes with different DNA sequences such as CT-DNA, poly(dA)·poly(dT), poly(dG)·poly(dC), etc, is reported.

4.2 Techniques used

Several different techniques were used to study binding and thermodynamics of binding of these complexes to DNA. What follows is a brief introduction into these methods.

4.2.1 Melting points

When the temperature of a DNA solution is increased, there is a point where the double stranded DNA separates and melting occurs. The midpoint of this melting process is called the melting temperature (T_m).

The temperature at which dissociation of the double helix occurs depends on base composition, sequence, chain length of the DNA, salt concentration and pH of the solvent. In particular, the melting temperatures of double stranded DNA are strongly dependent on base pair composition, with A-T region melting before C-G regions (figure 4.1), following the equation:

$$T_m = \mathrm{X} + 0.41 \cdot [\%(C+G)] \qquad (4.1)$$

where the constant X is dependent on salt concentration and pH[1].

The percent hyperchromicity (%H) for a melting point can be calculated as:

$$\%H = \frac{A_{ss} - A_h}{A_{ss}} \times 100 \qquad (4.2)$$

where A_h is the absorbance of the helical nucleic acid and A_{ss} is the absorbance of the single stranded nucleic acid.

Drug- nucleic acid binding interactions usually stabilise the structure of the DNA. Classical intercalators, such as ethidium bromide, acridines and metallo-intercalators stabilise the DNA helix and this leads to increase the T_m[2,3].

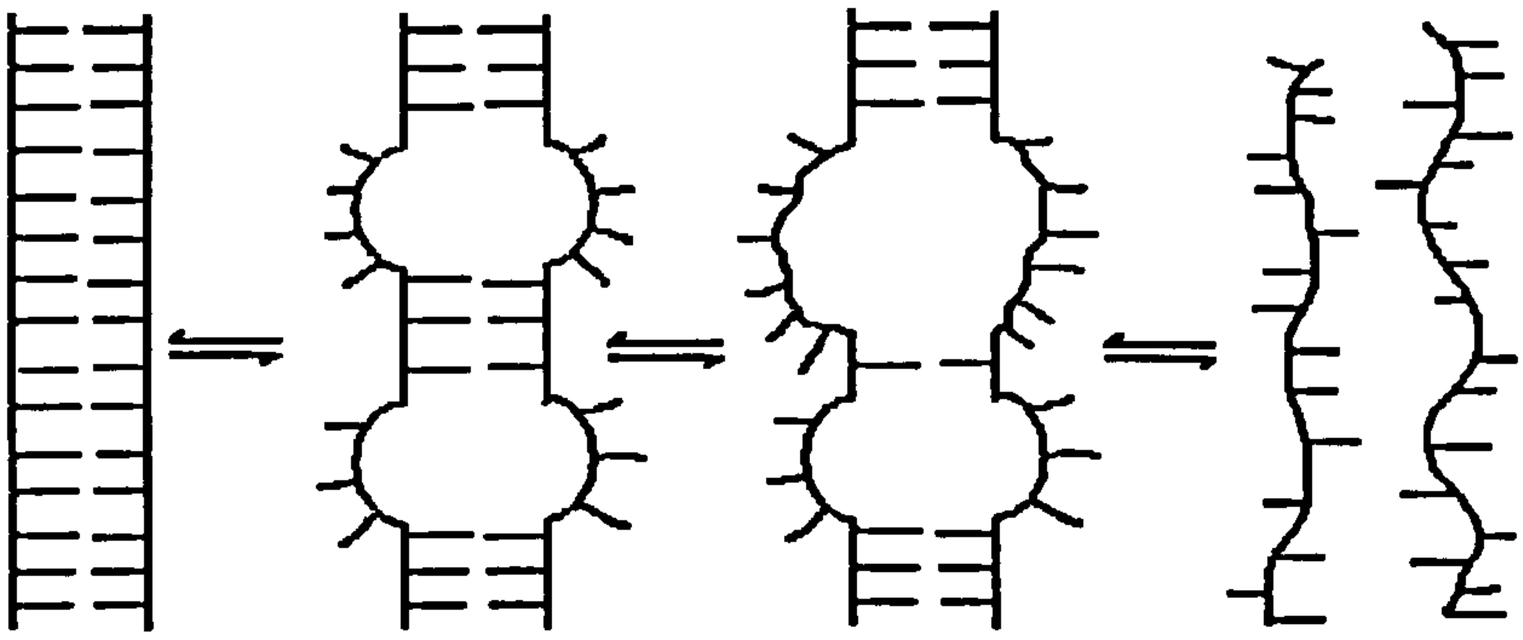

Figure 4.1: Schematic showing melting point of DNA, increasing temperature from left to right. The purple colour indicates A-T base pairs

4.2.2 Viscosity

Viscosity (η) is related to the bulk movement of a solution; an increase in viscosity implies more resistance to flow. The relative viscosity of a solution is defined as the relation between the viscosity of the solution and the viscosity of the pure solvent. In 1961, Lerman studied the interaction of DNA with intercalating acridines, seeing that, as a result of the intercalation into the base pairs, the acridines enhanced the DNA viscosity[4].

The relative viscosities for DNA in the presence or absence of ligand can be calculated from:

$$\eta = \frac{t - t_0}{t_0} \qquad (4.3)$$

where t is the flow time of the DNA and t_0 the flow time of buffer alone.

The changes in viscosity of the free and complexed DNA are given by[5]:

$$\frac{L}{L_0} = \left[\frac{\eta}{\eta_0}\frac{f(p)_0}{f(p)}\right]^{1/3} \approx 1 + r \qquad (4.4)$$

where L is the contour length of rodlike macromolecules, p is the axial ratio of the rods and r is ratio of bound complex to DNA.

If the relative viscosity, $(\eta/\eta_0)^{1/3}$, is plotted versus r an intercalator should give an increase in the relative viscosity of the DNA, but a groove binder, that does not lengthen the DNA helix, should not increase the viscosity[6-8]

4.2.3 Continuous variation analysis (Job plots)

In the continuous variation method, the total concentration of DNA and complex is kept constant, but their molar fractions are varied. Luminescence emission is plotted against the molar fraction of one of the components and inflection points yield the stoichiometry of the interaction[9].

Generally for an interaction with n equivalents and non-interacting sites:

$$A + B \leftrightarrow AB$$

$$K_d = \frac{\left(n[A]_0 - \sum_{i=1}^{n} i[AB]_i\right)\left([B]_0 - \sum_{i=1}^{n} i[AB]_i\right)}{\sum_{i=1}^{n} i[AB]_i} \qquad (4.5)$$

where $[A]_0$ and $[B]_0$ are the total concentrations of component A and B, respectively, and $\sum_{i=1}^{n} i[AB]_i$ is the summation of all the forms of AB complex, which is equal to $[AB] + 2[AB]_2 + \ldots + n[AB]_n$.

If the total concentration of A and B is kept constant at $[C]_0$ concentration, we have:

$$[A]_0 + [B]_0 = [C]_0 \qquad (4.6)$$

Rearranging equation (4.6):

$$\frac{[A]_0}{[C]_0} + \frac{[B]_0}{[C]_0} = 1 \qquad (4.7)$$

By defining the molar fraction of A equal to χ and the molar fraction of B equal to γ, it is possible to rewrite equation (4.7):

$$\chi + \gamma = 1 \qquad (4.8)$$

and

$$[A]_0 = C_0 \cdot \chi$$
$$[B]_0 = C_0 \cdot \gamma = (1-\chi)\cdot C_0 \qquad (4.9)$$

Let $\Sigma = \sum_{i=1}^{n} i[AB]_i$ and substitute equation (4.9) in equation (4.5) yielding:

$$K_d \cdot \Sigma = (n \cdot [C]_0 \cdot \chi)\cdot[[C]_0 \cdot (1-\chi) - \Sigma] \qquad (4.10)$$

Differentiating equation (4.10) with respect to χ:

$$K_d \cdot \left(\frac{d\Sigma}{d\chi}\right) = (n \cdot [C]_0 \cdot \chi)\cdot\left(-[C]_0 - \frac{d\Sigma}{d\chi}\right) + [[C]_0 \cdot (1-\chi) - \Sigma]\cdot\left(n \cdot [C]_0 - \frac{d\Sigma}{d\chi}\right) \qquad (4.11)$$

When the mole fraction of A approaches zero ($\chi \rightarrow 0$), the concentration of AB complexes also approaches zero and equation (4.11) becomes:

$$K_d \cdot \left(\frac{d\Sigma}{d\chi}\right)_{\chi\to 0} = [C]_0\left[n \cdot [C]_0 - \left(\frac{d\Sigma}{d\chi}\right)_{\chi\to 0}\right] \qquad (4.12)$$

The limiting slope of the curve as $\chi \rightarrow 0$ is:

$$\left(\frac{d\Sigma}{d\chi}\right)_{\chi\to 0} = \frac{n \cdot [C]_0^2}{K_d + [C]_0} \qquad (4.13)$$

And the line with this limiting slope has the expression:

$$\Sigma = \chi \cdot \left(\frac{d\Sigma}{d\chi}\right)_{\chi\to 0} = \frac{\chi \cdot n \cdot [C]_0^2}{K_d + [C]_0} \qquad (4.14)$$

Similarly, when mole fraction of B approaches zero ($\gamma \rightarrow 0$ or $\chi \rightarrow 1$):

$$K_d \cdot \left(\frac{d\Sigma}{d\chi}\right)_{\chi\to 1} = n \cdot [C]_0\left[-[C]_0 - \left(\frac{d\Sigma}{d\chi}\right)_{\chi\to 1}\right] \qquad (4.15)$$

$$\left(\frac{d\Sigma}{d\chi}\right)_{\chi\to 1} = \frac{-n\cdot[C]_0^2}{K_d+[C]_0} \qquad (4.16)$$

And the line with limiting slope given in equation (4.16) is:

$$\Sigma = \gamma\cdot\left(\frac{d\Sigma}{d\gamma}\right)_{\gamma\to 0} = \frac{\gamma\cdot n\cdot[C]_0^2}{K_d+n\cdot[C]_0} \qquad (4.17)$$

At the intersection point the two lines described by equations (4.14) and (4.17):

$$\frac{\chi_i\cdot n\cdot[C]_0^2}{K_d+[C]_0} = \frac{\gamma_i\cdot n\cdot[C]_0}{K_d+n\cdot[C]_0} \qquad (4.18)$$

or

$$\frac{\chi_i}{\gamma_i} = \frac{K_d+n\cdot[C]_0}{K_d+[C]_0} \qquad (4.19)$$

If $[C]_0 >> K_d$, then,

$$\frac{\chi_i}{\gamma_i} = \frac{n\cdot[C]_0}{[C]_0} = n \qquad (4.20)$$

Thus, the binding stoichiometry can be determined from the molar ratio of fraction bound of ligand and complex at the intersection point only if the sum of concentration $[C]_0$ is high relative to K_d.

4.2.4 UV-Vis and luminescence titrations

When there is an interaction between a metallo-intercalator and DNA, the well defined spectroscopic characteristics of the complex changes. This is because the environment of the complex changes from full solvation in aqueous solution, to the hydrophobic environment of the DNA. Usually the UV-Vis spectrum of the complex is slightly shifted to longer wavelength (bathochromic shift) and the absorption decreases (hypochromic effect). Additionally, on going from aqueous solution to being bound to DNA, the excited state of a metal complex can radically change producing large changes in emission[10,11].

These changes in the absorption or emission properties can be used as a tool to study the interaction of these metal complexes with DNA.

The fraction of complex bound (χ) to DNA is estimated from the equation:

$$\chi = \frac{A_f - A_{obs}}{A_f - A_b} \qquad (4.21)$$

where A_f is the absorption of free complexes, A_b is the absorption of the fully bound complex and A_{obs} is the absorption at a given point.

Similarly for luminescence titrations when the emission of the complex is enhanced by addition of DNA:

$$\chi = \frac{I_{obs} - If}{I_b - If} \qquad (4.22)$$

where I_f, I_b and I_{obs} are the emission of the free complex, fully bound and the emission at any specific concentration respectively.

Knowing the initial concentration of complex (C_i) and the fraction bound (χ), the concentration of bound complex (C_b) can be calculated at any given time by:

$$C_b = \chi \times C_i \qquad (4.23)$$

C_f is the concentration of free complex, then

$$C_i = C_f + C_b \qquad (4.24)$$

Rearranging equation (4.24):

$$C_f = C_i - C_b \qquad (4.25)$$

Thus the binding ratio *r*, where *r* is the ratio of bound complex to total concentration of DNA in base pairs, can be determined:

$$r = \frac{C_b}{[DNA]} \qquad (4.26)$$

Traditionally binding data can be fitted to a simple binding model, first proposed by Scatchard in 1949[12], plotting r/C_f *vs.* r:

$$\frac{r}{C_f} = K_i(n-r) \qquad (4.27)$$

where K_i is the intrinsic equilibrium binding constant and n the number of DNA binding sites occupied by the bound complex.

This model works well with simple 1:1 binding systems, but when the systems are more complicated data is not linear and the Scatchard model is inadequate. This is the case for CT-DNA, where there are many overlapping possible binding site. So for binding to DNA, this linear relationship is not commonly used and the data are fitted using the McGhee-von Hippel model[13]:

$$\frac{r}{C_f} = K \cdot (1-nr)\left[\frac{(1-nr)}{1-(n-1)r}\right]^{n-1} \qquad (4.28)$$

This model considers the binding sites of a homogeneous lattice with N identical repeating units. A ligand molecule is assumed to bind to the lattice and cover n consecutives lattice residues. Ligand-ligand interactions are only allowed between nearest neighbours (neighbour exclusion model).

4.2.5 Circular dichroism (CD) spectra

Circular dichroism (CD) measures differences in the absorption of left-handed polarised light and right-handed polarised light that occurs due to structural asymmetries in a molecule (figure 4.2).

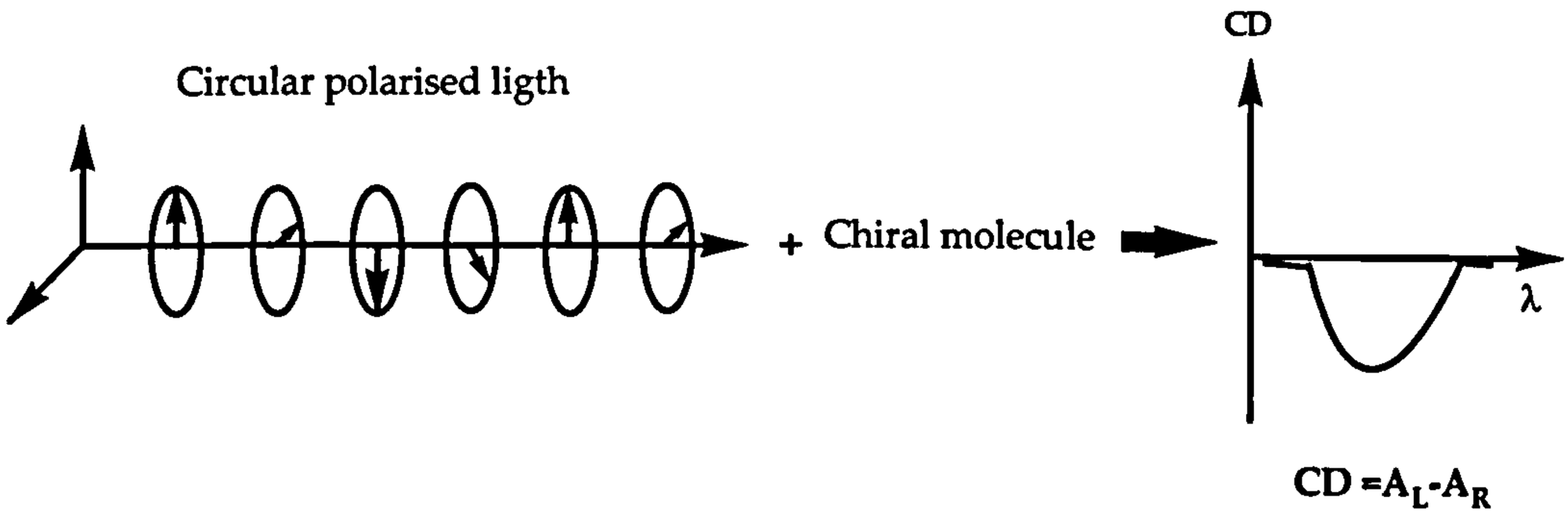

Figure 4.2: Principle of CD measurements

Nonchiral compounds have no CD signal, although when bound to DNA, as a consequence of the chiral surrounding of the molecule, they can show a signal: an

induced CD (ICD). The insertion of planar aromatic molecules between base pairs of the DNA results in changes in the DNA structure with separation of the base pairs and unwinding of the helix. These conformational alterations often produce CD signals that are difficult to interpret due to difficulties in distinguishing changes due complex-complex stacking, complex-base pair interaction and changes in the DNA. The CD signal arises from interactions between the chromophore transition moment and the transition of the chirally arranged surrounding DNA bases; the sign and magnitude of induced CD bands depend mainly on factors such as the orientation of the intercalator in its binding site. If an intercalator is located at the centre of the DNA helix, theoretical calculations predict the induced CD to be weak and negative for an intercalator whose transitions are along the axis of the intercalation pocket (perpendicular to the pseudo-dyad axis) and positive for transitions in the intercalation plane that are perpendicular to the intercalator pocket long axis (parallel to the pseudo-dyad axis) (figure 4.3). The induced CD signal of groove binders is generally an order of magnitude stronger than those of intercalators and is usually positive[14,15].

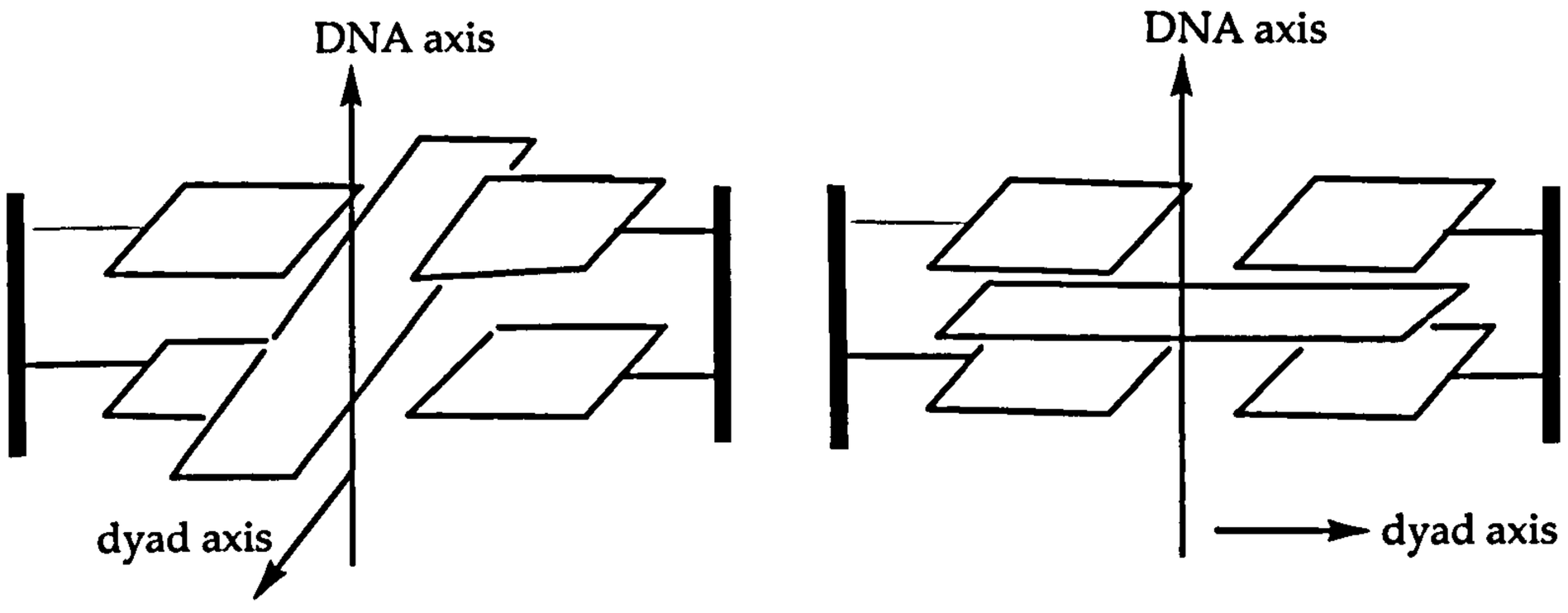

Figure 4.3: In each case the intercalator is perpendicular to the DNA axis with its long direction, perpendicular (right) and parallel (left) to long axis.

4.2.6 Isothermal Titration Calorimetry (ITC)

Isothermal titration calorimetry (ITC) is a technique that measures heat changes during a binding reaction. ITC can be used to measure the association constant, enthalpy and therefore free energy and entropy of binding.

a) ITC experiment

The ITC instrument consists of a reference cell, a sample cell and a syringe. The reference cell is filled with the same solvent used in the sample cell (for aqueous solution the reference cell is filled with distilled water). The sample cell contains the host for the interaction and the syringe is filled with the guest, dissolved in the same solvent. Both cells are maintained at constant temperature (figure 4.4).

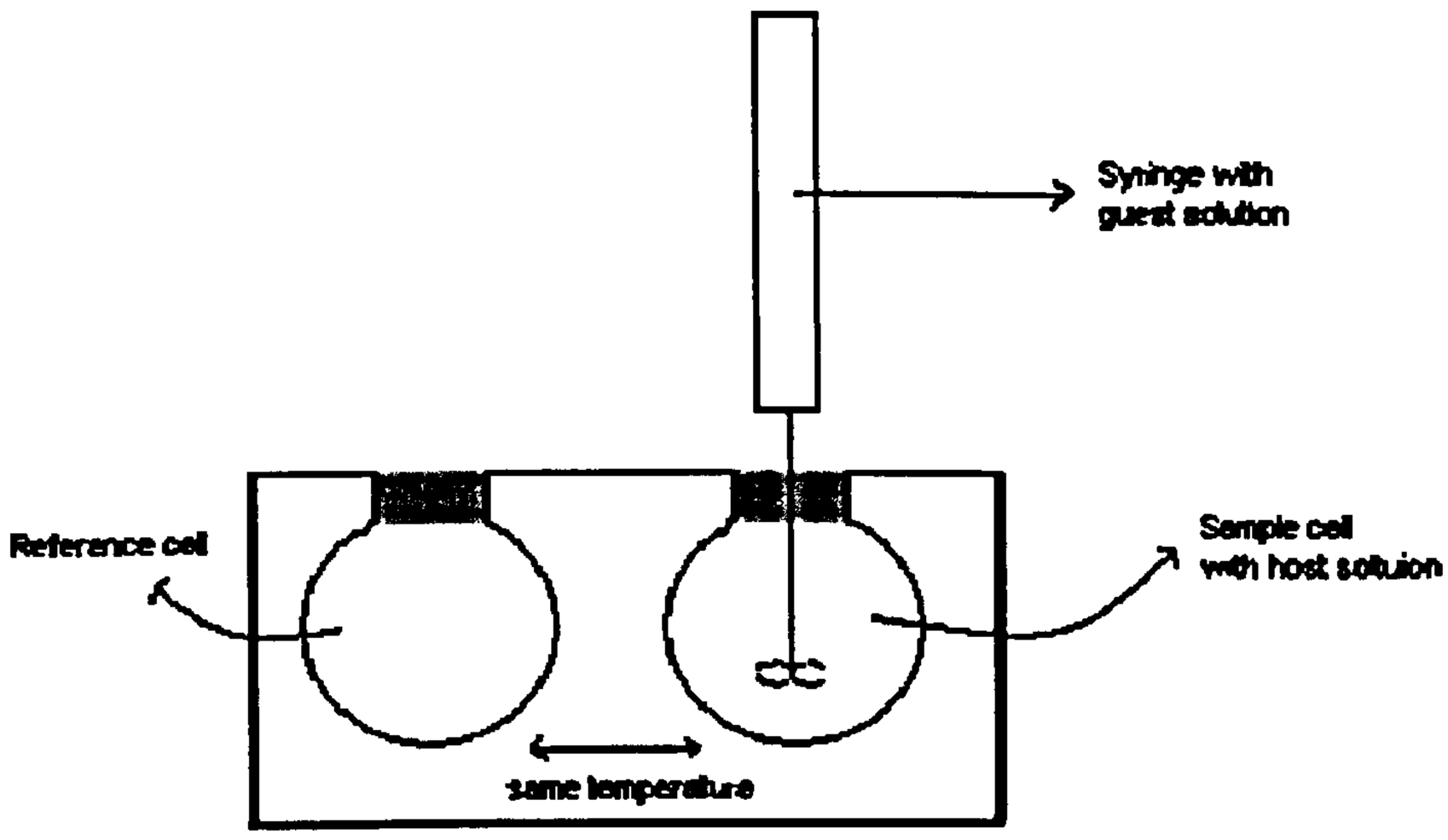

Figure 4.4: Schematic showing ITC instrument

After equilibration the syringe injects a certain volume of guest solution into the host solution at prefixed time intervals. The host-guest interaction absorbs/releases heat, producing a difference in temperature between the cells, and the calorimeter modulates heating to return the system to equilibrium. This energy is then measured and integrated and the process is repeated until the saturation point for binding is reached.

b) ITC experiment-analysis

For a general bimolecular reaction, the association constant for the reaction is (where A is sample and B is the injectant)[16]:

$$A + B \leftrightarrow AB \qquad K_a = \frac{[AB]}{[A][B]} \qquad (4.29)$$

$$[A]_{tot} = [A] + [AB] \qquad (4.30)$$

$$[B]_{tot} = [B] + [AB] \qquad (4.31)$$

Using equations (4.30) and (4.31) into (4.29):

$$K = \frac{[AB]}{[A]_{tot}[B]_{tot} - [AB]([B]_{tot} + [A]_{tot}) + [AB]^2} \qquad (4.32)$$

$$[AB] = \frac{[B]_{tot} + [A]_{tot} + \frac{1}{K} - \sqrt{\left([B]_{tot} + [A]_{tot} + \frac{1}{K}\right)^2 - 4[A]_{tot}[B]_{tot}}}{2} \qquad (4.33)$$

Differentiation and rearrangement of equation (4.33) leads to:

$$\frac{d[AB]}{d[B]_{tot}} = \frac{1}{2} + \frac{[A]_{tot} - \left(\frac{[B]_{tot} + [A]_{tot} + \frac{1}{K}}{2}\right)}{\sqrt{([B]_{tot} + [A]_{tot} + \frac{1}{K})^2 - 4[B]_{tot}[A]_{tot}}} \qquad (4.34)$$

Since for each injection the heat absorbed or released is proportional to the change in [AB]:

$$dq = V \cdot \Delta H^0 \cdot d[AB] \qquad (4.35)$$

where V is the volume in sample cell and ΔH^0 is the enthalpy of binding.

Therefore substituting into equation (4.34):

$$\frac{1}{V_0}(dq/d[B]_{tot}) = \Delta H^0{}_{bind} \cdot \left\{ \frac{1}{2} + \frac{[A]_{tot} - \left(\frac{[B]_{tot} + [A]_{tot} + \frac{1}{K}}{2} \right)}{\sqrt{([B]_{tot} + [A]_{tot} + \frac{1}{K})^2 - 4[B]_{tot}[A]_{tot}}} \right\} \quad (4.36)$$

Binding curves can be generated from equation 4.37, and therefore the binding constant and enthalpies for the interaction can be calculated.

The free energy change for a reaction can be calculated from the equilibrium constant:

$$\Delta G^0 = -RT \ln K \quad (4.37)$$

where ΔG^0 is the Gibb's free energy, R is the gas constant (R = 1.98 $\times 10^{-3}$ kcal/mol·deg) and T the temperature in Kelvin (T(K)=273 + T(°C)).

Knowing ΔG^0 and ΔH^0 we can calculate ΔS^0:

$$\Delta G^0 = \Delta H^0 - T\Delta S^0 \quad (4.38)$$

4.2.7 Surface Plamon Resonance (SPR)

The surface plasmon resonance technique can be used to detect changes in the refractive index near a sensor surface. To describe SPR it is necessary to know about total internal reflection (TIR): total internal reflection is a phenomenon which involves the reflection of incident light off the interface occurring when the angle of incidence is greater than the critical angle for the particular combination of materials (figure 4.5).

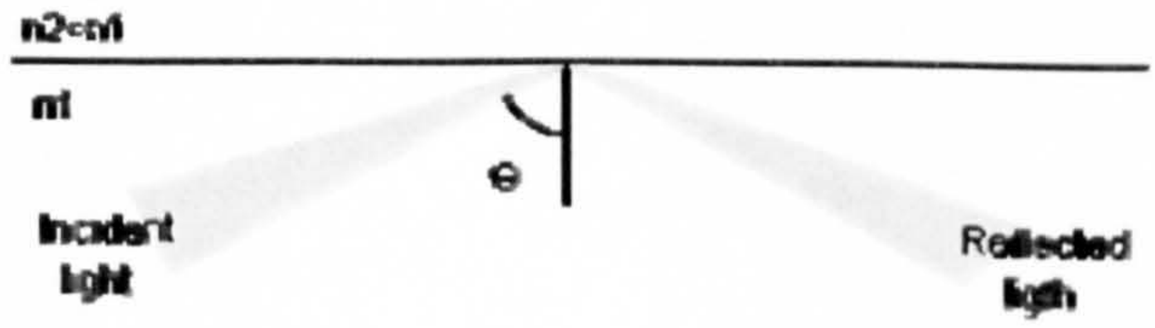

Figure 4.5: Total internal reflection phenomenon

If the TIR surface is coated with a metal like gold, the polarised light penetrates the metal layer and photons can interact with free electrons in the gold surface. Under certain conditions, these photons can be converted to plasmons and the incident light is no longer completely reflected (minimum reflection). The electronmagnetic plasmons generated, are affected by changes in the medium surrounding the film. When biomolecular interactions occur at the sensor surface, the refractive index changes and the incident light required for the SPR to have the minimum reflection is altered. SPR measures the changes in the particular angle required to create the extinction of light.

In the SPR instrument a continuous flow of an aqueous solution (the running buffer) passes through the sensor chip. The substrate (in this case DNA) is immobilised onto the sensor surface. When molecules bind to the DNA on the surface of the chip, the concentration (and therefore the refractive index) at the surface changes which leads to a change in the reflected light angle and an SPR response is detected (figure 4.6):

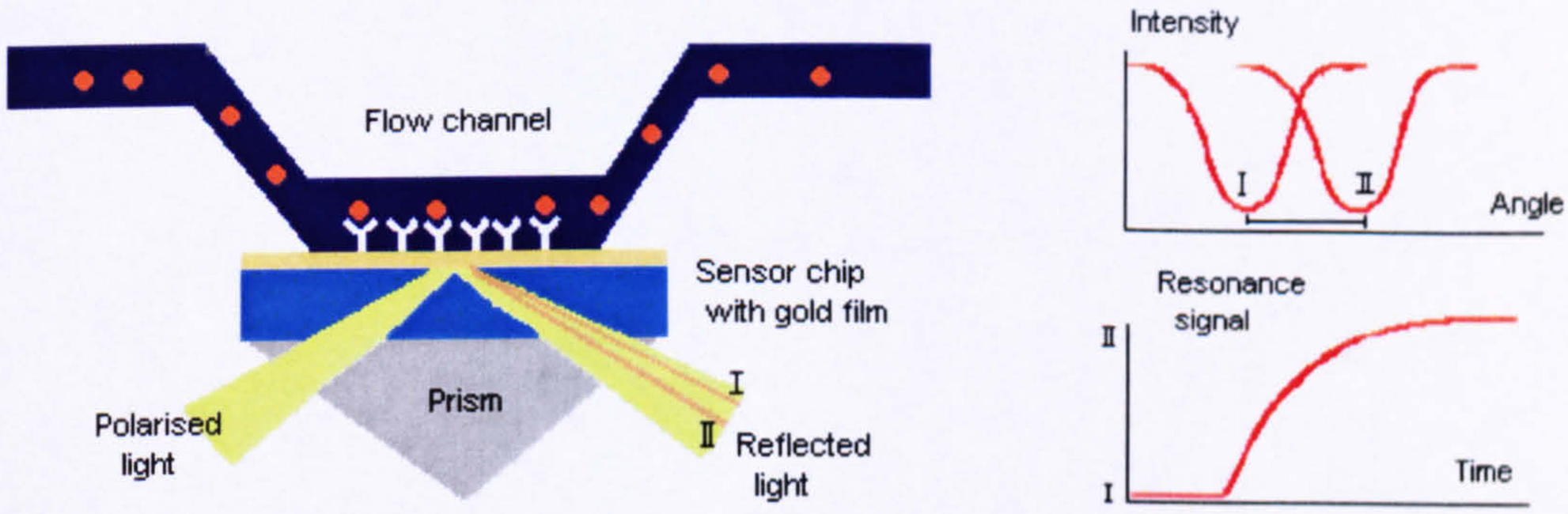

Figure 4.6: Schematic SPR

A typical SPR sensorgram is shown in figure 4.7:

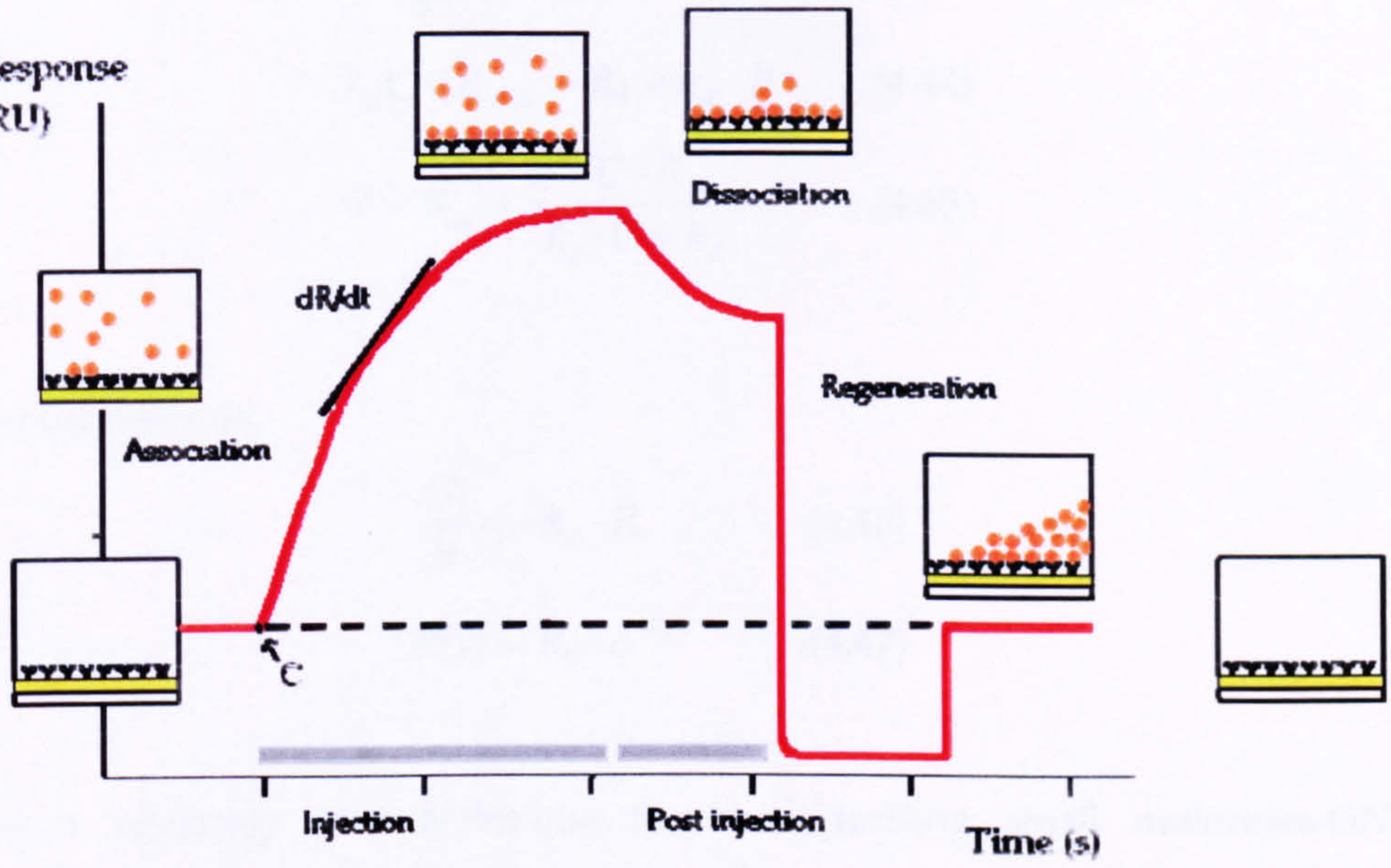

Figure 4.7: Example of an ideal SPR sensorgram

In a general bimolecular reaction:

$$A + B \leftrightarrow AB$$

$$\frac{d[AB]}{dt} = k_a \cdot [A][B] - k_d[AB] \qquad (4.39)$$

$$\frac{dR}{dt} = k_a \cdot C \cdot (R_{\max} - R) - k_d \cdot R \qquad (4.40)$$

where k_a and k_d are the association and dissociation rate constants (respectively), C the analyte concentration, R_{max} the maximum response of the analyte and R the response of the complex already formed.

At the moment of the injection:

$$\frac{dR}{dt} = k_a \cdot C \cdot (R_{\max} - R) - k_d \cdot R \qquad (4.41)$$

$$R(t) = R_{eq} - R_{eq} \cdot e^{-Kobs \cdot t} \qquad (4.42)$$

In the equilibrium:

$$\frac{dR}{dT} = 0 \qquad (4.43)$$

$$k_a C \cdot (R_{max} - R) = k_d \cdot R \qquad (4.44)$$

$$R = R_{eq} = \frac{k_a \cdot C \cdot R_{max}}{k_a \cdot C + k_d} \qquad (4.45)$$

At the post injection:

$$\frac{dR}{dt} = -k_d \cdot R \qquad (4.46)$$

$$R(t) = R_0 \cdot e^{-k_d \cdot t} \qquad (4.47)$$

SPR is a relatively new technique for characterising small molecules-DNA interactions. SPR is rapid, shows data in real time and the concentration required is small compared to other techniques. It also provides kinetics and equilibrium characterisation for the interaction being studied[17].

4.3 Sample preparation for binding studies

All complexes were converted to chloride salts by treating the PF_6^- salt with $^nBu_4NCl$ in acetone. The chloride salt was collected by centrifugation and copiously washed with acetone.

The concentration of the DNA was determined by UV spectroscopy using the following: ε_{260} = 12000 M^{-1} cm^{-1} for poly(dA)poly(dT), ε_{260} = 13100 M^{-1} cm^{-1} for poly(dA-dT)poly(dA-dT), ε_{254} = 14000 M^{-1} cm^{-1} for poly(dG)poly(dC) and ε_{254} = 16800 M^{-1} cm^{-1} for poly(dG-dC)poly(dG-dC)[18].

All the experiments were carried out in a 25 mM NaCl, 5 mM Tris, pH 7.0 buffer.

As a reminder, the complexes used for binding studies are summarised in table 4.1

Table 4.1: Structure of $[Ru(tpm)(dppz)(3L)]^{2+}$ and $[Ru(tpm)(dppz)(4L)]^{2+}$ complexes

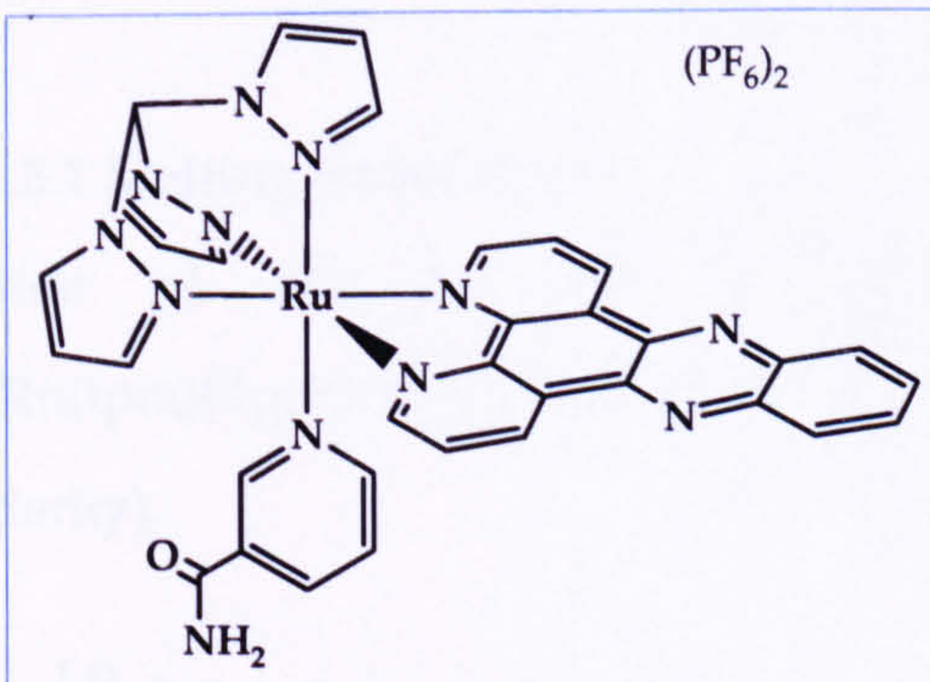

[3.5]

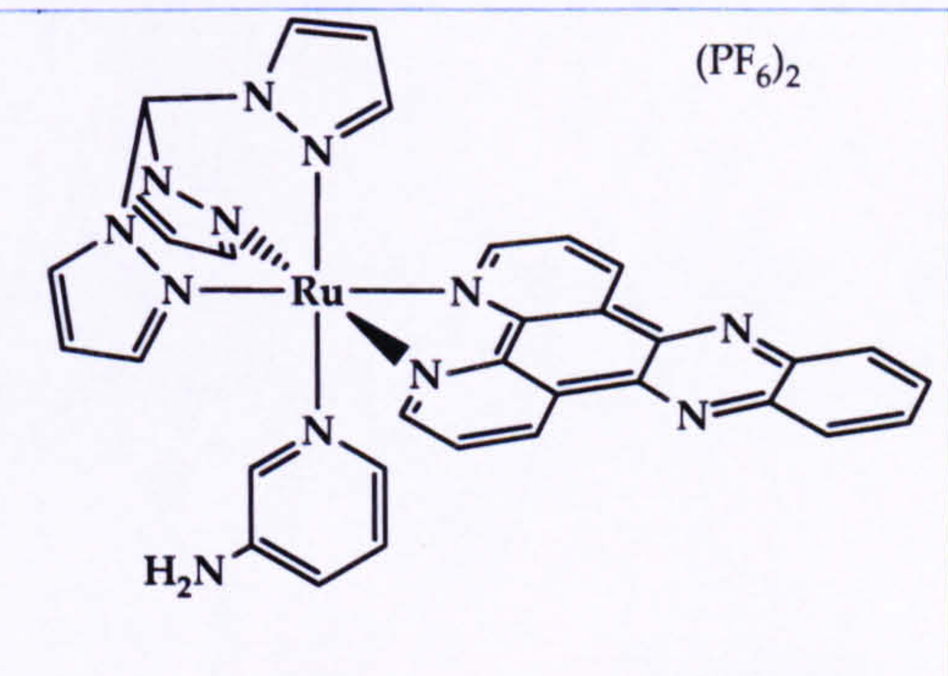

[3.6]

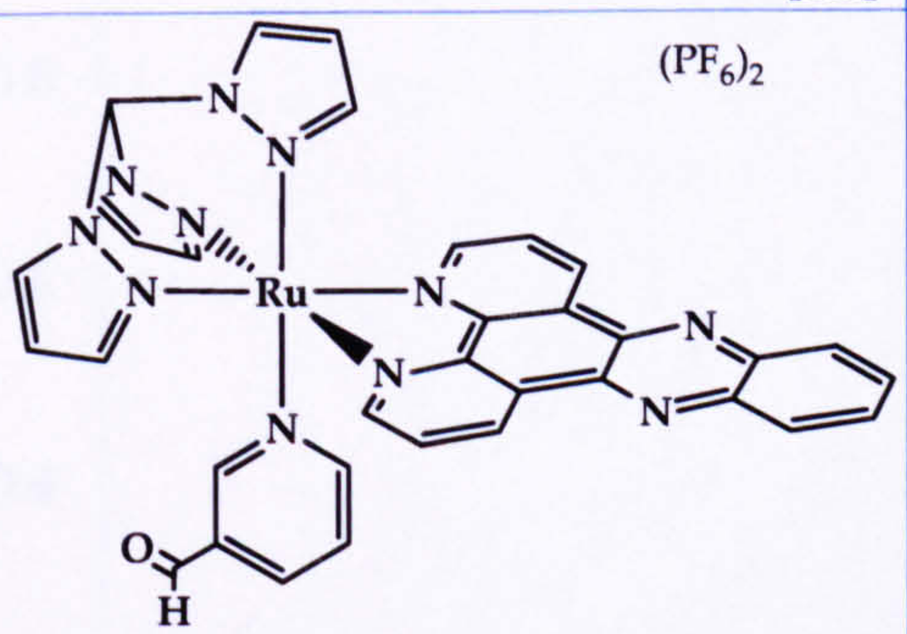

[3.7]

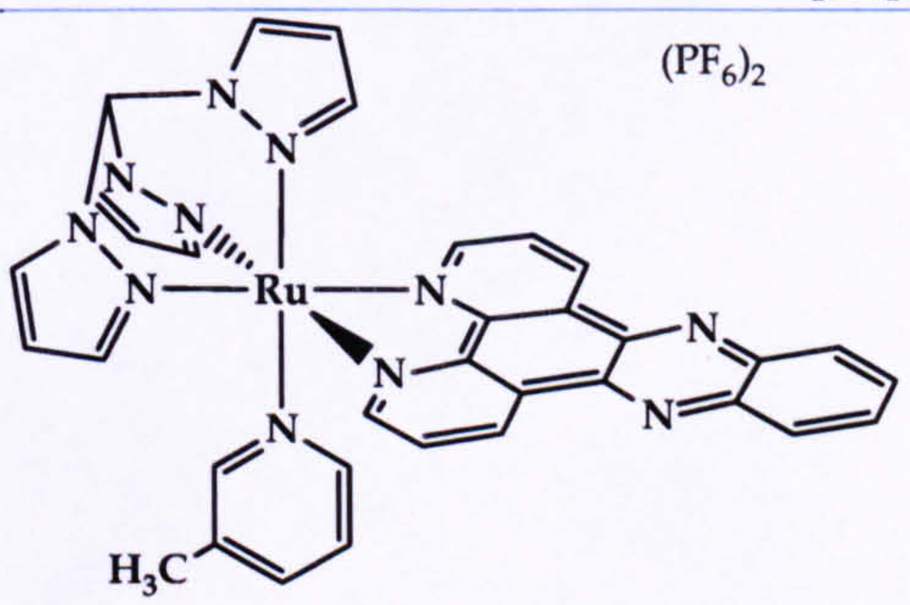

[3.8]

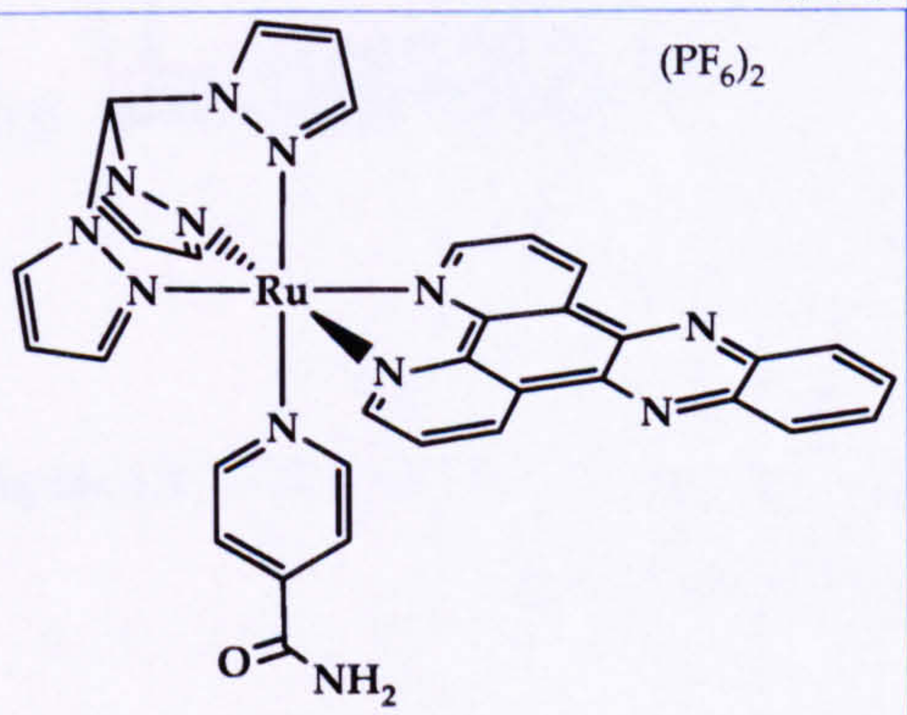

[3.9]

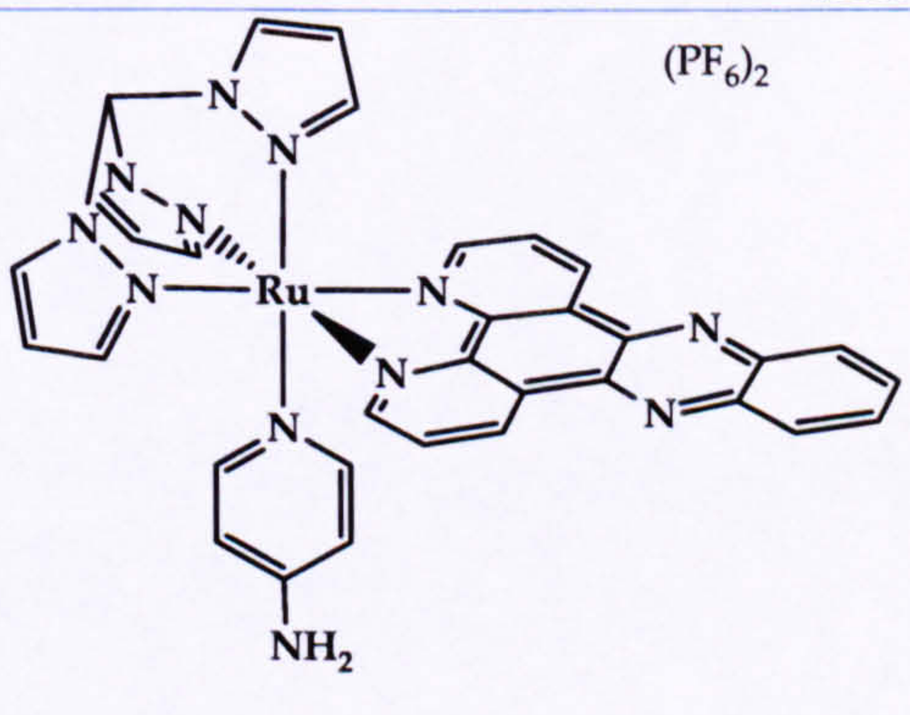

[3.10]

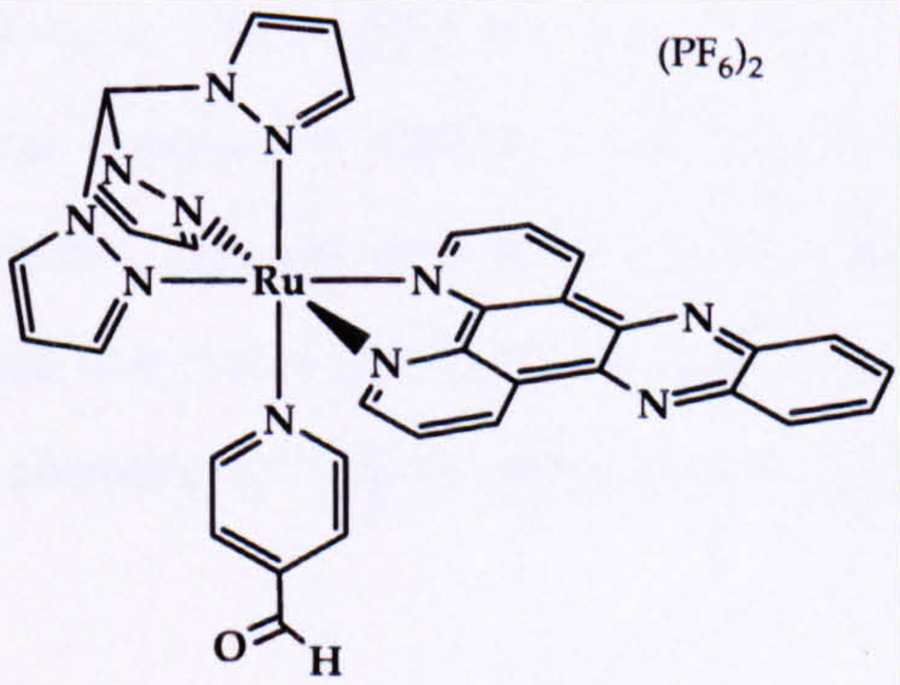

[3.11]

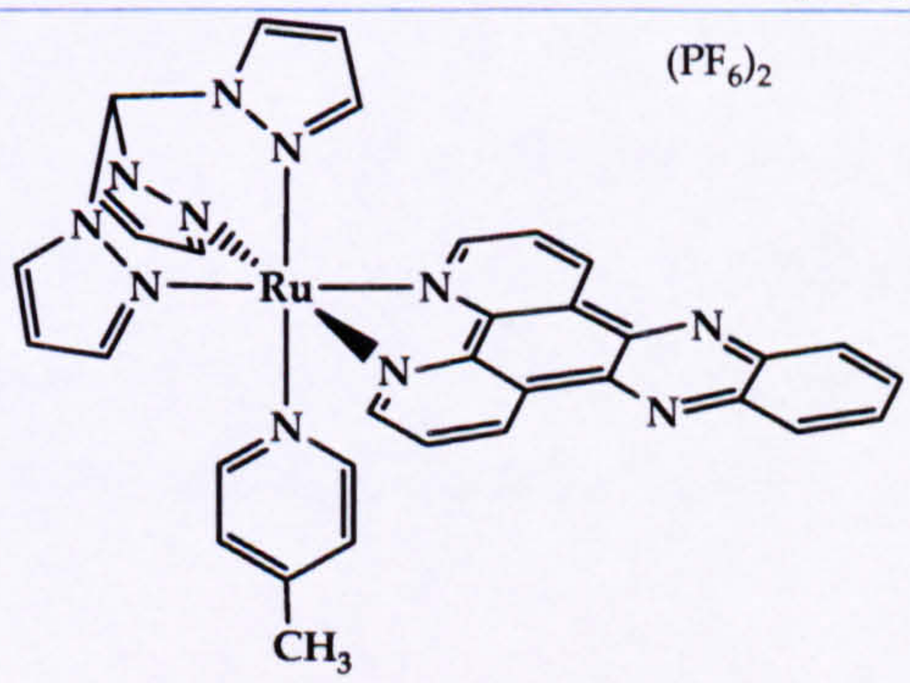

[3.12]

4.5 Binding studies of [tpmRudppz(L)]$^{2+}$ complexes

4.5.1 Melting points (T_m)

First of all, the ΔT_m of CT-DNA with [Ru(tpm)(dppz)(3L)]$^{2+}$ and [Ru(tpm)(dppz)(4L)]$^{2+}$ complexes was studied (figure 4.8, data is normalised for clarity).

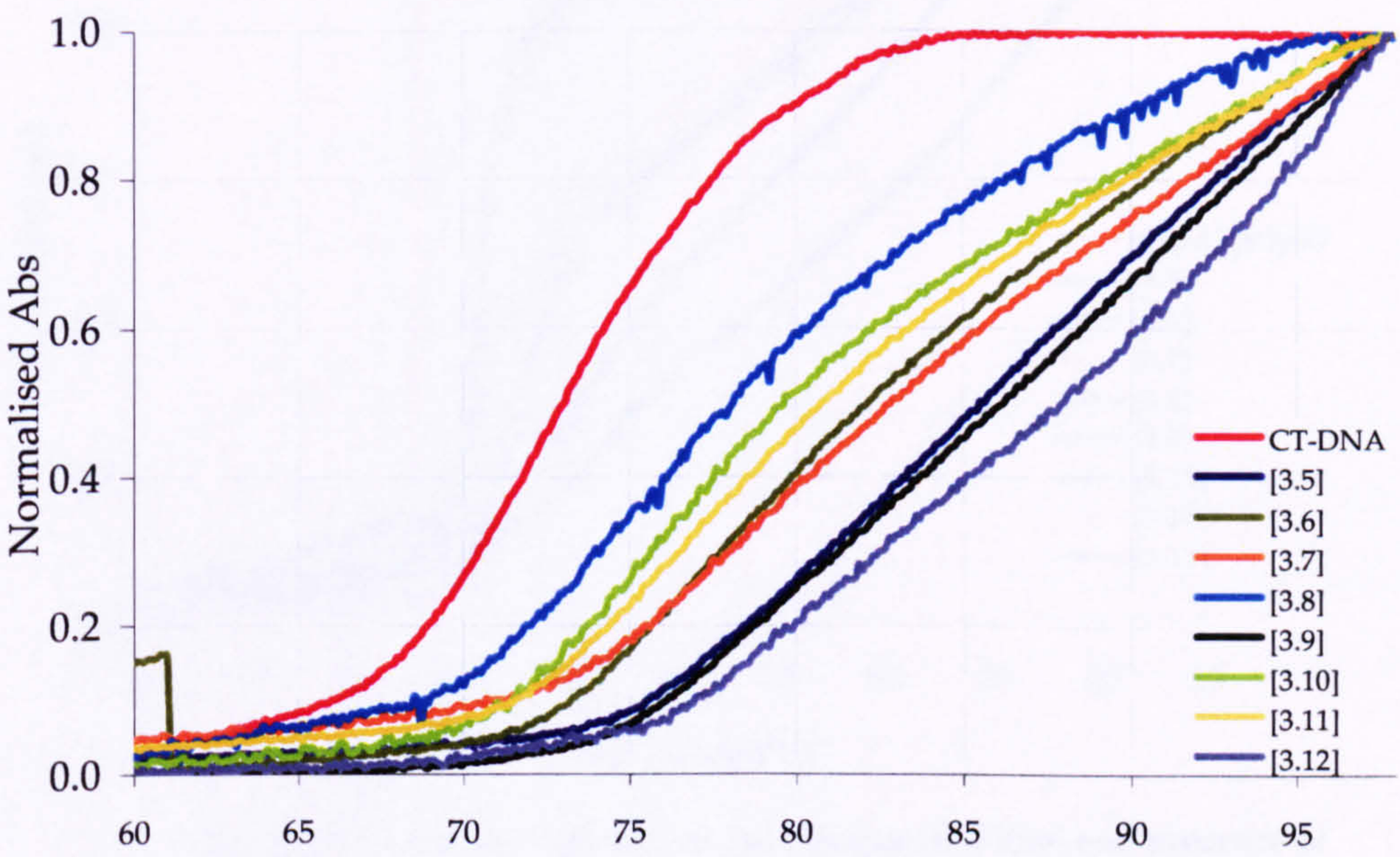

Figure 4.8: T_m of CT-DNA in the absence (red line) and presence of [Ru(tpm)(dppz)(3L)]$^{2+}$ and [Ru(tpm)(dppz)(4L)]$^{2+}$ complexes.

The T_m of CT-DNA in the experimental condition is 72.7 °C. In all of the cases the metal complexes stabilised CT-DNA. In fact the T_m of the complexes bound to CT-DNA can not be accurately determined because the end of the melting point curve was not reached, but is possible to conclude that the stabilisation is at least 15 °C, showing that all the complexes interact with DNA stabilising the duplex.

The melting point of poly(dA)·poly(dT) with the complexes was also studied. In the experimental conditions used the T_m of poly(dA)·poly(dT) is 57.5 °C. Once again the addition of the complexes to the DNA solution stabilised this duplex DNA, figure 4.9.

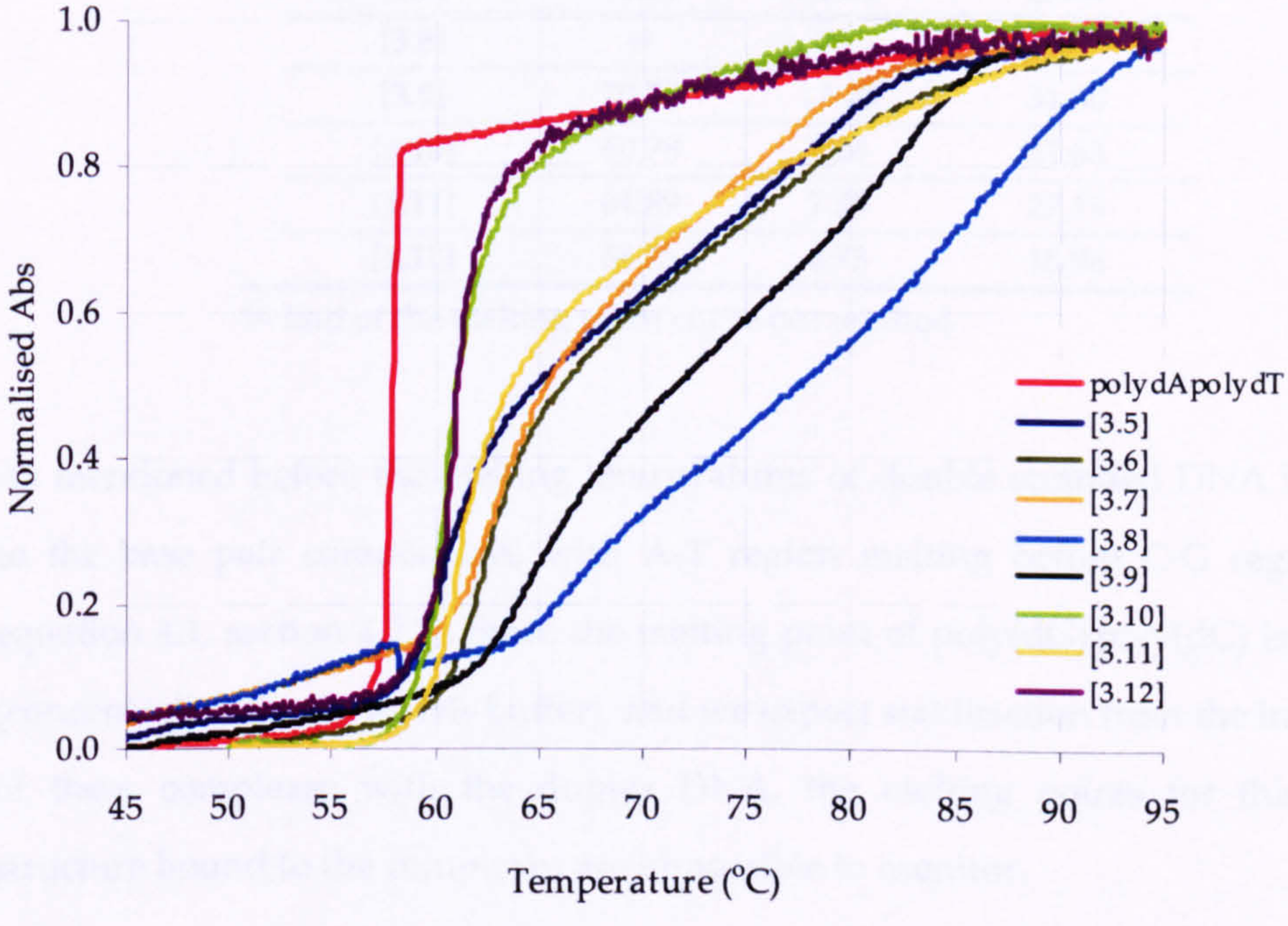

Figure 4.9: T_m of polydApolydT in the absence (red line) and presence of $[Ru(tpm)(dppz)(3L)]^{2+}$ and $[Ru(tpm)(dppz)(4L)]^{2+}$ complexes.

As can be see in figure 4.9, complexes **[3.10]** and **[3.12]** stabilise the double stranded DNA by ~4 °C, while **[3.5]**, **[3.6]**, **[3.7]** and **[3.11]** stabilise poly(dA)·poly(dT) by around 10 °C. Complexes **[3.8]** and **[3.9]** show the greatest stabilisation of poly(dA)·poly(dT). This data is summarised in tale 4.2.

Table 4.2: Melting points of the complexes **[3.5]**, **[3.6]**, **[3.7]**, **[3.8]**, **[3.9]**, **[3.10]**, **[3.11]** and **[3.12]** with poly(dA)·poly(dT)

Compound	T_m (°C)	ΔT_m	%H
[3.5]	68.20	10.70	30.54
[3.6]	64.32	6.82	31.13
[3.7]	69.00	11.50	29.63
[3.8]	(a)	(a)	(a)
[3.9]	70.78	13.28	31.60
[3.10]	60.78	3.28	21.63
[3.11]	64.89	7.39	27.19
[3.12]	64.23	6.73	16.96

(a) End of the melting point curve not reached

As mentioned before the melting temperatures of double stranded DNA is related to the base pair composition, with A-T region melting before C-G regions (see equation 4.1, section 4.2.2). Since the melting point of poly(dG)·poly(dC) is 91.75 °C (concentration 50 μM in Tris buffer), and we expect stabilisation from the interaction of these complexes with the duplex DNA, the melting points for this duplex structure bound to the complexes are impossible to monitor.

Clearly all of the compounds stabilise DNA, but given the difference in ΔTm, not all of them show the same strength of interaction with the double helix. In order obtain information on the nature of these interactions further studies were carried out.

4.5.2 Viscosity

When a molecule intercalates into the base pairs of the DNA, the DNA unwinds and increases its length in order to accommodate the compound between the base pairs. Viscosity measurements provide a direct and sensitive method to determinate if a compound is an intercalator.

Figure 4.10 shows the increase of the viscosity of CT-DNA upon addition of **[3.5]**, **[3.6]**, **[3.7]** and **[3.8]** complexes, indicating that all these complexes interact with CT-DNA via intercalation[6,8].

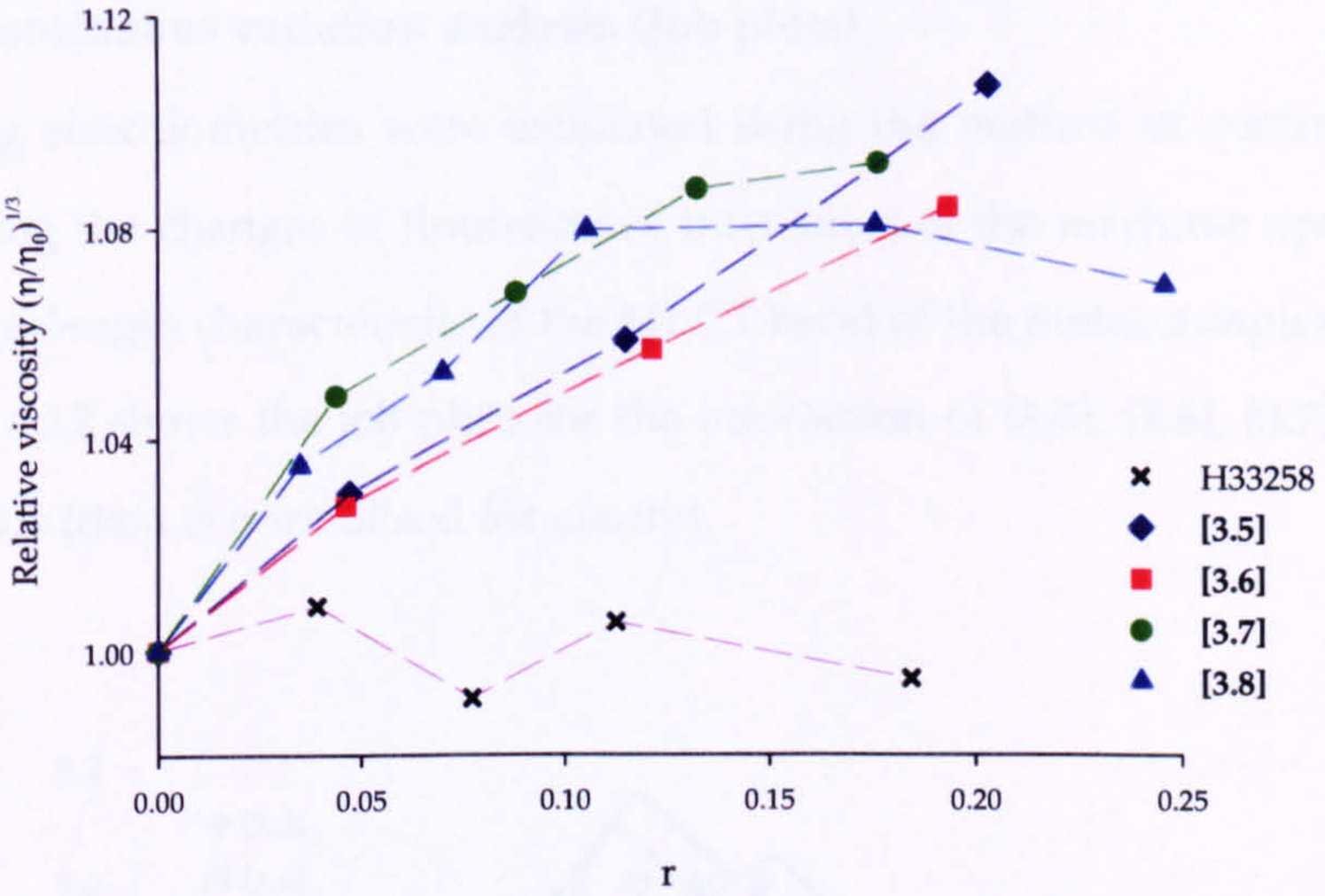

Figure 4.10: Relative viscosity of CT-DNA upon addition of $[Ru(tpm)(dppz)(3L)]^{2+}$ complexes and H33258 (purple), a known minor groove binder

The viscosity of CT-DNA in the presence of **[3.9]**, **[3.10]**, **[3.11]** and **[3.12]** is shown in figure 4.11. Complexes **[3.9]** and **[3.11]** produce large increases in the relative viscosity of CT-DNA, showing that they bind to DNA via intercalation. Complex **[3.10]** showed little or no effect on viscosity when bound to CT-DNA, indicating that it does not intercalate between the base pairs. When bound to complex **[3.12]**, CT-DNA showed a smaller increase in viscosity compared to the other complexes, this may imply that this complex intercalates less deeply into the CT-DNA[19,20].

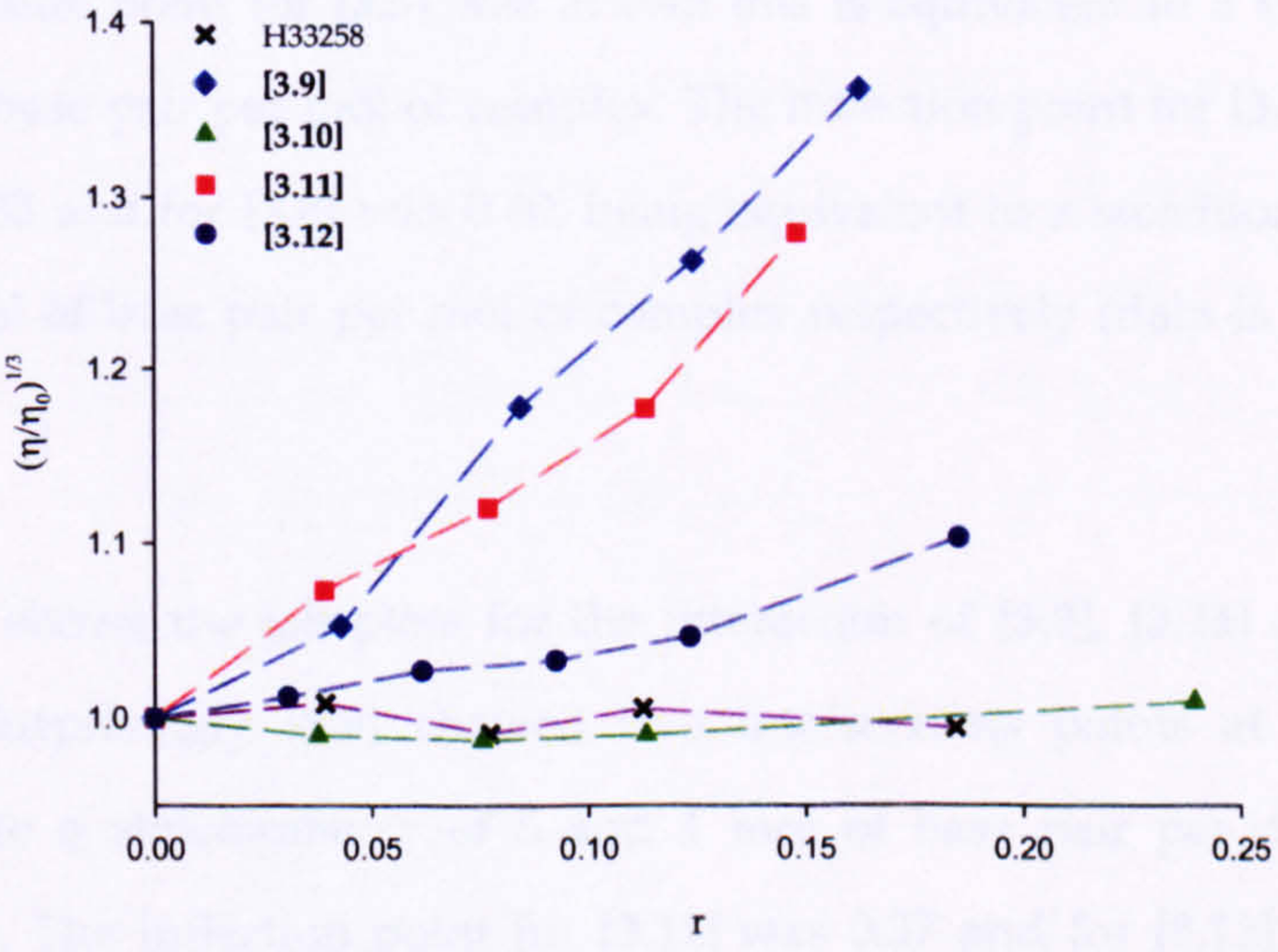

Figure 4.11: Relative viscosity of CT-DNA upon addition of $[Ru(tpm)(dppz)(4L)]^{2+}$ complexes and H33258 (purple), a known minor groove binder

4.5.3 Continuous variation analysis (Job plots)

Binding stoichiometries were estimated using the method of continuous variation following the changes in fluorescence intensities of the mixtures upon excitation at the wavelength characteristic of the MLCT band of the metal complex.

Figure 4.12 shows the job plots for the interaction of **[3.5]**, **[3.6]**, **[3.7]** and **[3.8]** with CT-DNA (data is normalised for clarity).

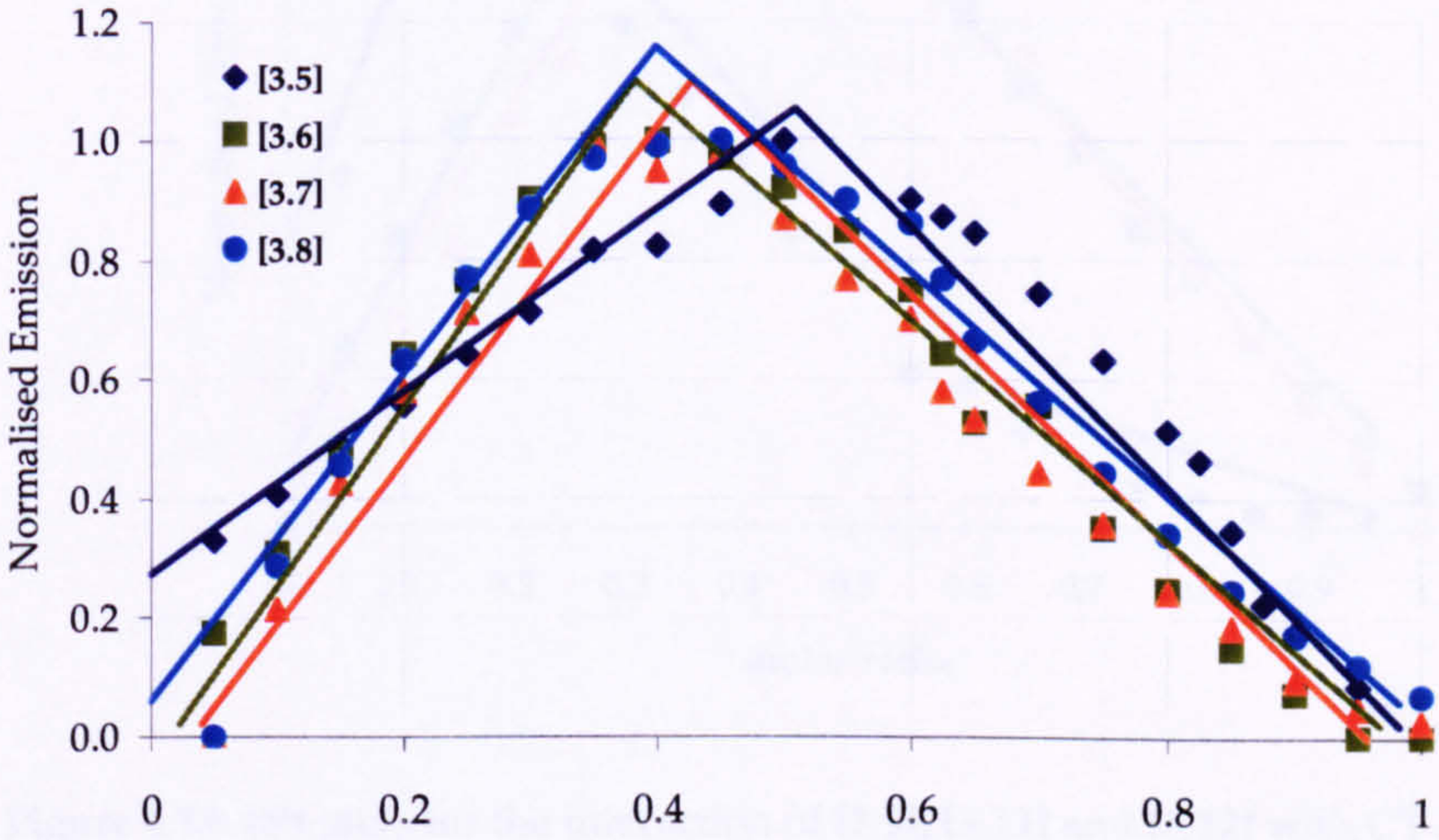

Figure 4.12: Job plots for the interaction of **[3.5]**, **[3.6]**, **[3.7]** and **[3.8]** with CT-DNA.

The intersection point for **[3.5]** was at 0.45 this is equivalent to a stoichiometry of 1.22 mol of base pair per mol of complex. The inflection point for **[3.6]** was 0.39, for **[3.7]** was 0.35 and for **[3.8]** was 0.40, being equivalent to a stoichiometry of 1.70, 2 and 1.50 mol of base pair per mol of complex respectively (data is summarised in table 4.3).

Figure 4.13 shows the job plots for the interaction of **[3.9]**, **[3.11]** and **[3.12]** with CT-DNA. Surprisingly **[3.9]** showed two intersections points at 0.17 and 0.60, equivalent to a stoichiometry of 5 and 1 mol of base pair per mol of complex respectively. The inflection point for **[3.11]** was 0.37 and for **[3.12]** was 0.4, being equivalent to a stoichiometry of 1.70 and 1.30 mol of base pair per mol of complex

respectively. Since the complex **[3.10]** did not show any emission upon addition of CT-DNA, a job plot could not be constructed by this method (data is summarised in table 4.3).

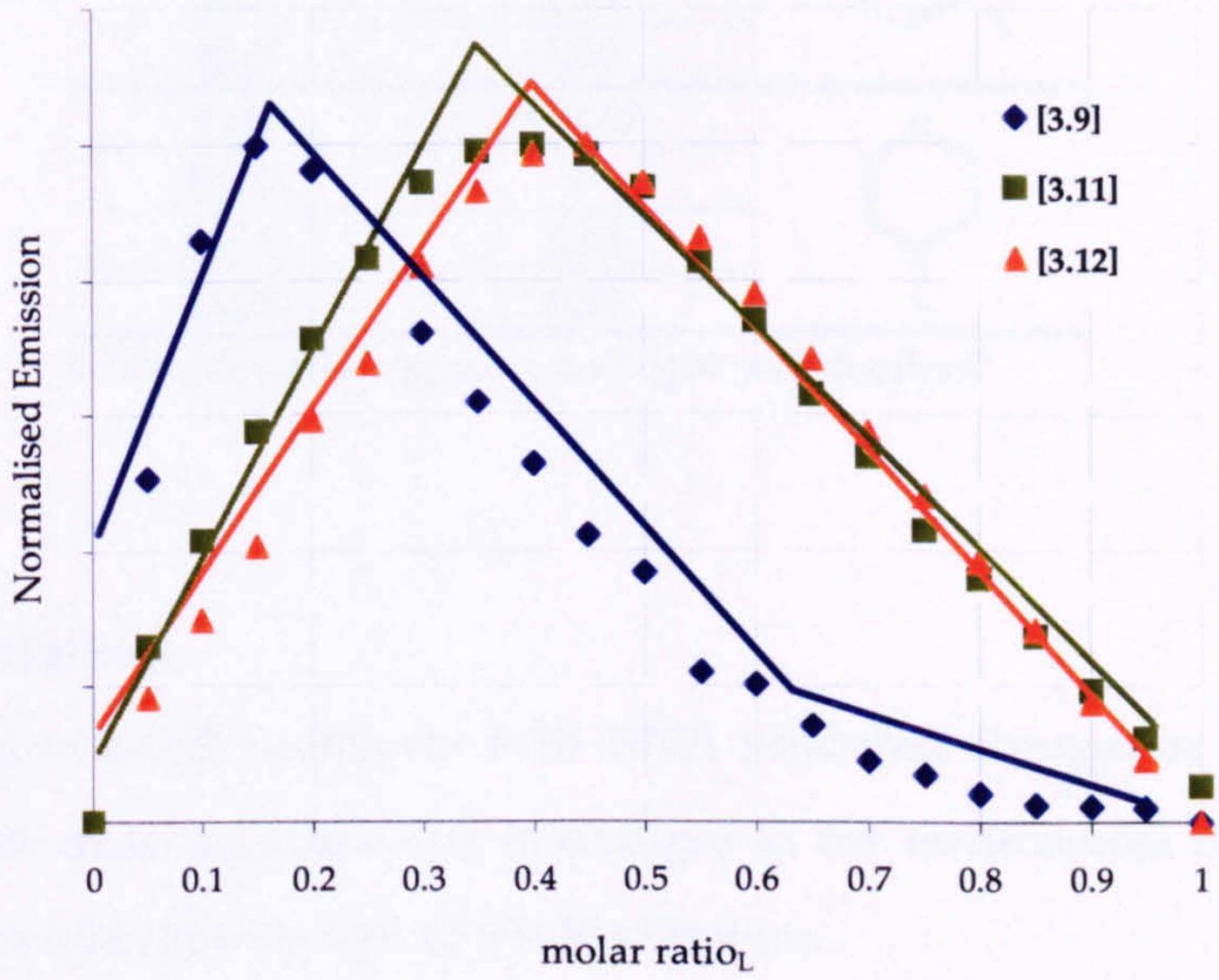

Figure 4.13: Job plots for the interaction of **[3.9], [3.11]** and **[3.12]** with CT-DNA.

Typical stoichiometries for metallo-intercaltors binding to DNA are two to three base pair per mol of ligand[21]. For the interaction of most of these complexes with CT-DNA we obtained stoichiometres from 1 to 2 mol of base pair per mol of complex. Such behaviour has been observed before for example, Murphy *et al.* found that the stoichiometry for the interaction of $[Ru(NH_3)_4(dppz)]^{2+}$ with CT-DNA was smaller than one, suggesting that the intercalator might also stack with itself on the DNA surface[3,22].

Table 4.3: Binding stoichiometries for the interaction of [tpmRudppz(L)]$^{2+}$ with CT-DNA obtained by continuous variation analysis

Compound	N (bp)	
[3.5]	1.22	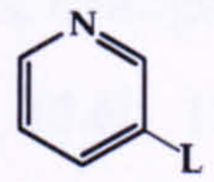
[3.6]	2.00	
[3.7]	1.70	
[3.8]	1.50	
[3.9]	5, 0.67	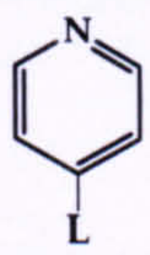
[3.10]	(a)	
[3.11]	1.70	
[3.12]	1.50	

(a) No change in viscosity, no "light switch effect"

4.5.4 UV-Vis titrations

The interaction of metal complexes with DNA produced changes in the UV-Vis spectrum of the metal complex due to changes in the environment of the metal complex. Figure 4.14 shows a typical UV-Vis titration.

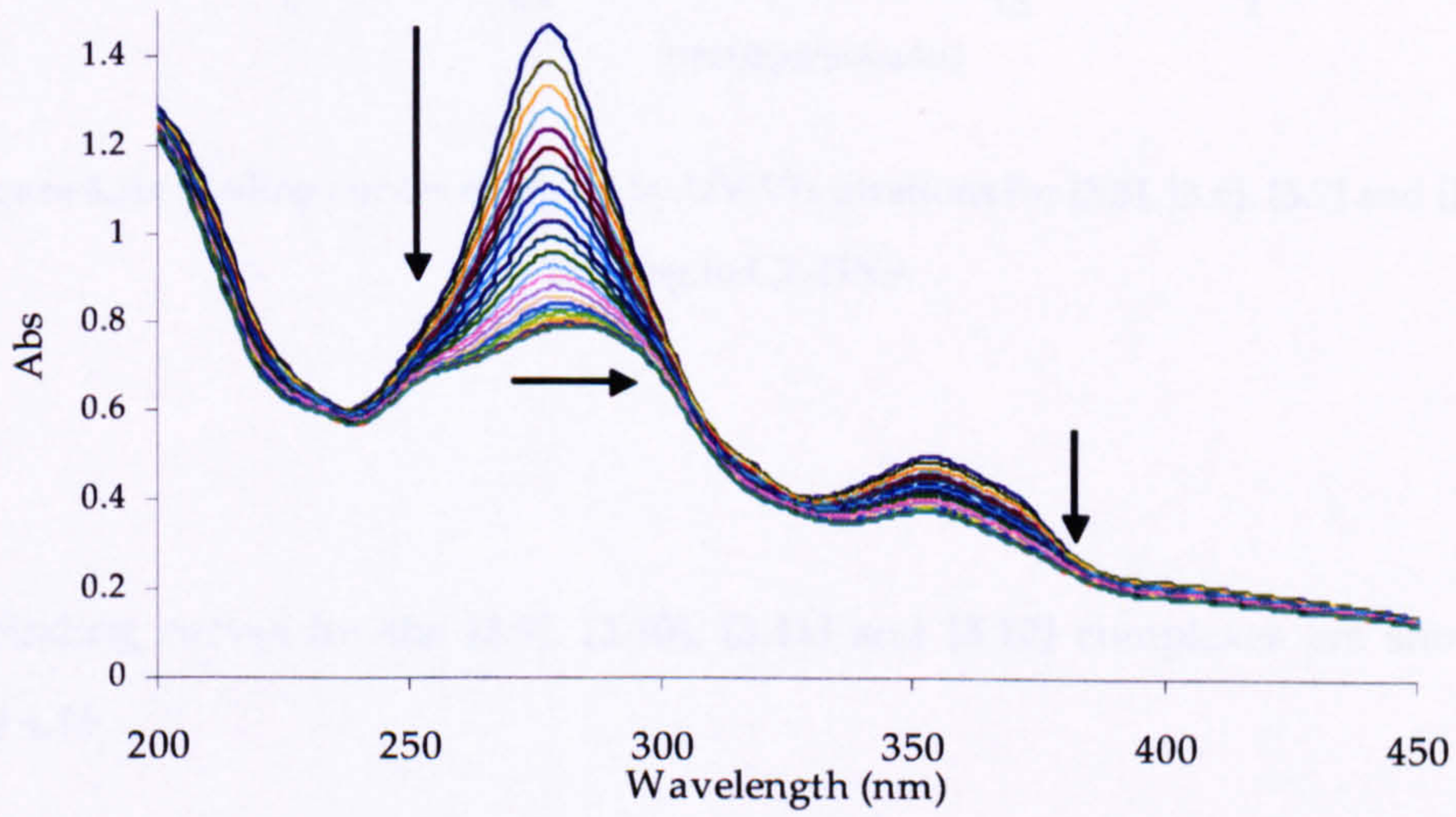

Figure 4.14: UV-Vis titration of **[3.8]** with CT-DNA

Both bands at 277 nm and 350 nm showed hypochromicity and when saturation is close, the band at 277 nm also showed also a bathochromic shift. Hypochromicity and bathchromic effects are typically observed for the stacking of aromatic ligands

between the base pairs, and are indicative of the interaction of the π-orbital of the ligand and the DNA base pairs[23,24].

For the study of interaction of these complexes to DNA, changes in the 277 nm band were followed and the binding curves for **[3.5]**, **[3.6]**, **[3.7]** and **[3.8]** were constructed, figure 4.15. They all showed that saturation binding had taken place.

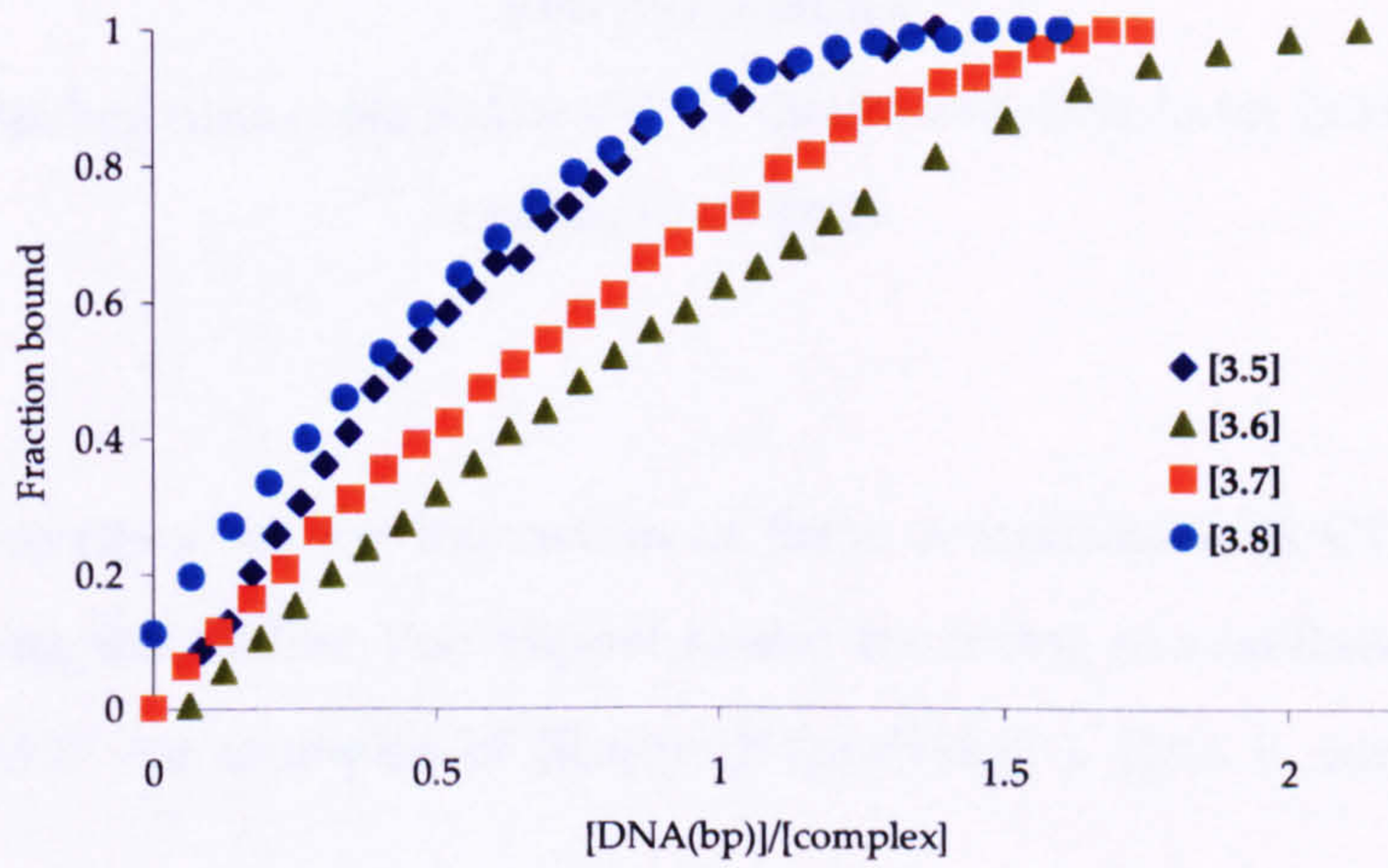

Figure 4.15: Binding curves obtained by UV-Vis titrations for **[3.5]**, **[3.6]**, **[3.7]** and **[3.8]** binding to CT-DNA

The binding curves for the **[3.9]**, **[3.10]**, **[3.11]** and **[3.12]** complexes are shown in figure 4.16.

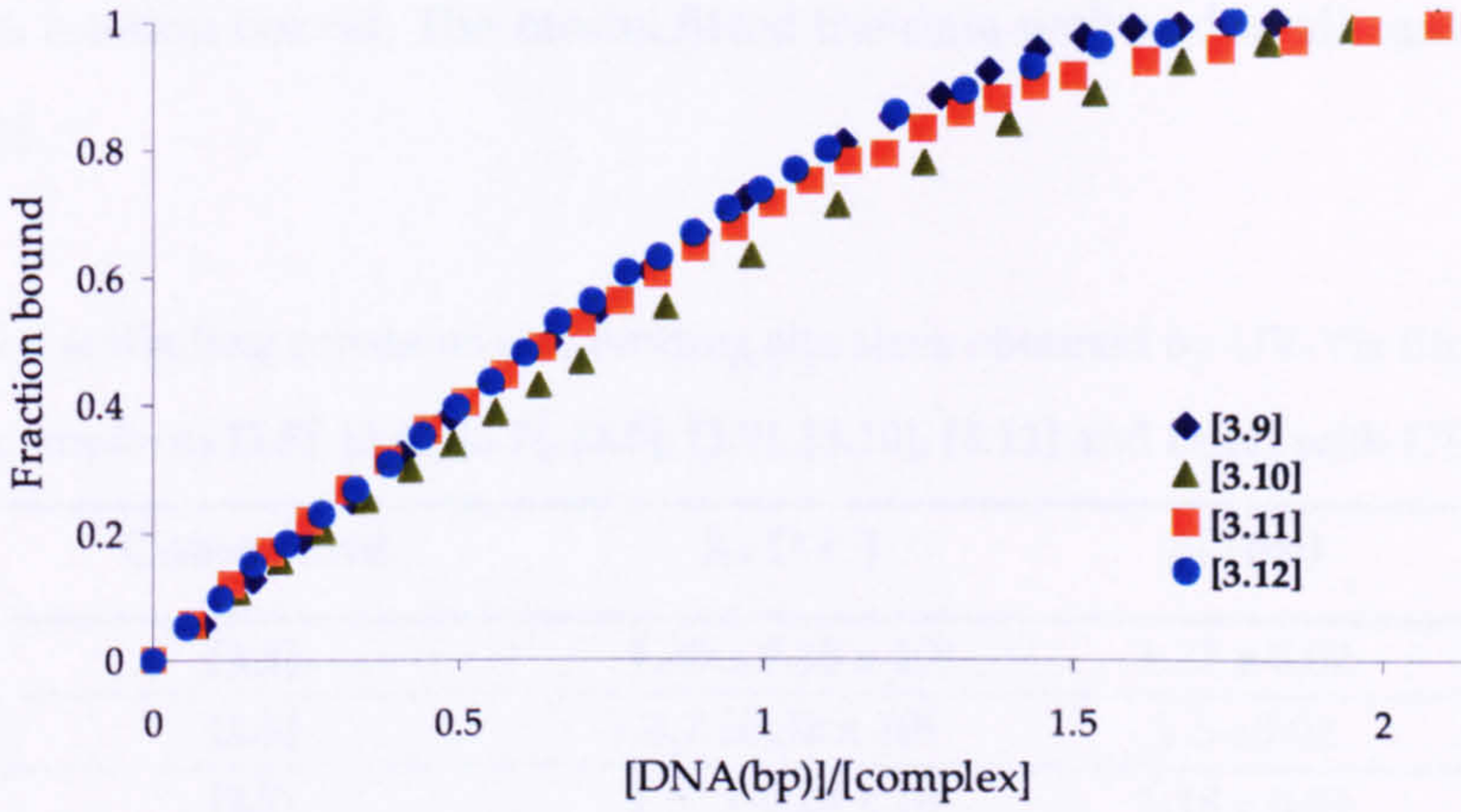

Figure 4.16: Binding curves obtained by UV-Vis titrations for **[3.9]**, **[3.10]**, **[3.11]** and **[3.12]** binding to CT-DNA

The binding constant for the interaction of these complexes with CT-DNA were calculated using the McGee Von Hippel model for fitting of non-linear Scatchard plots (figure 4.17 for examples of $[Ru(tpm)(dppz)(3L)]^{2+}$). Data is summarised in table 4.4.

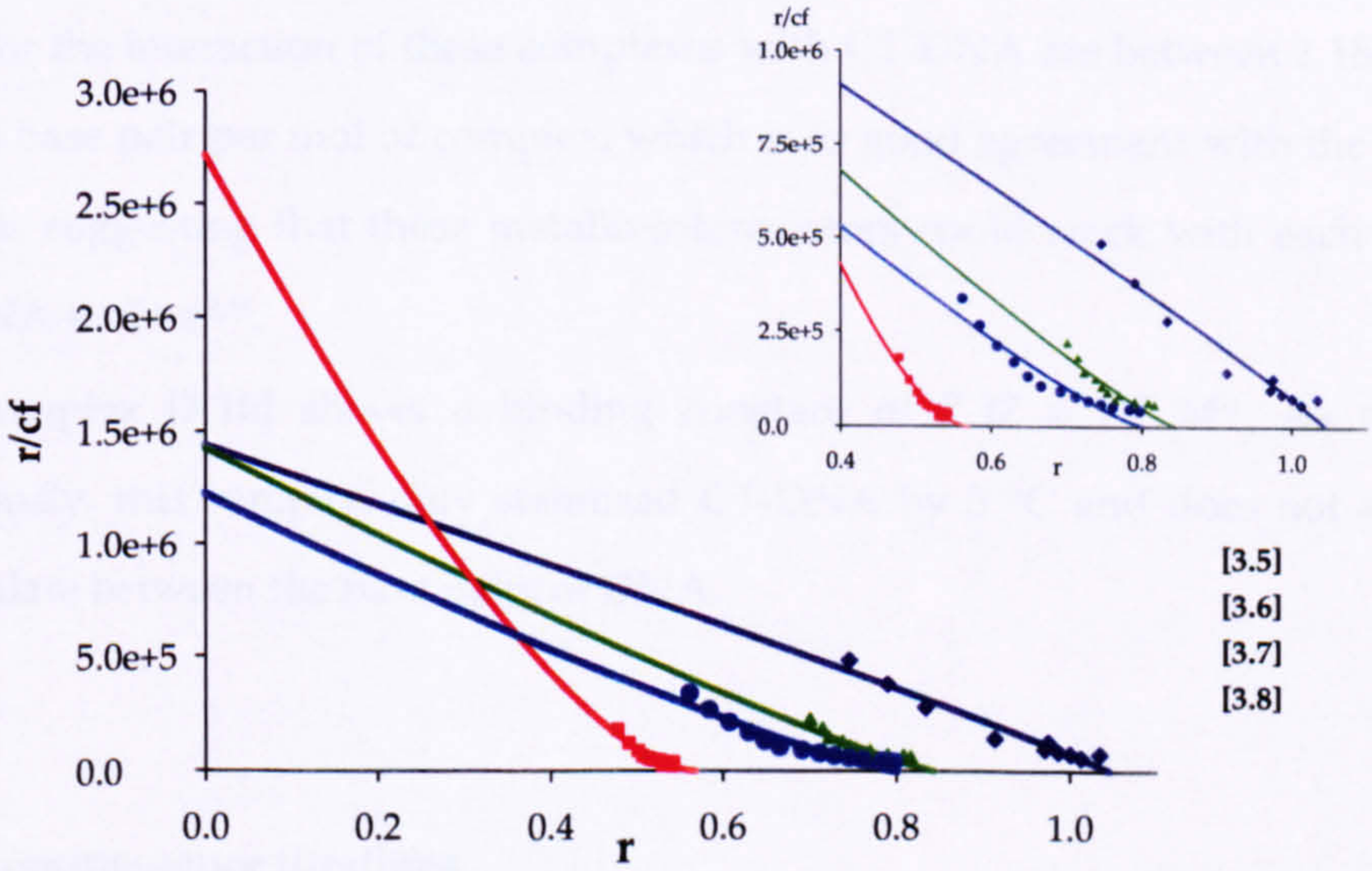

Figure 4.17: Examples of Scatchard plots with Mc Ghee von Hippel best fit obtained by UV-Vis titrations for **[3.5]**, **[3.6]**, **[3.7]** and **[3.8]** binding to CT-DNA

The Scatchard plots were obtained from binding data of each complex between 30 and 95 % fraction bound. The model fitted the data well and in all cases the R^2 value was >0.95.

Table 4.4: Binding constants and binding site sizes obtained by UV-Vis titration of the complexes **[3.5]**, **[3.6]**, **[3.7]**, **[3.8]**, **[3.9]**, **[3.10]**, **[3.11]** and **[3.12]** with CT-DNA

Compound	K_a (M^{-1})	N (bp)	% H
[3.5]	$1.20 \pm 0.15 \times 10^6$	1.21 ± 0.02	43.38
[3.6]	$4.7 \pm 0.32 \times 10^6$	1.5 ± 0.02	46.17
[3.7]	$1.42 \pm 0.24 \times 10^6$	1.18 ± 0.01	38.39
[3.8]	$1.22 \pm 0.14 \times 10^6$	1.24 ± 0.02	46.62
[3.9]	$3.50 \pm 0.47 \times 10^6$	1.59 ± 0.01	34.16
[3.10]	$7.37 \pm 1.1 \times 10^5$	1.3 ± 0.02	47.89
[3.11]	$1.30 \pm 0.11 \times 10^6$	1.3 ± 0.01	50.35
[3.12]	$1.07 \pm 0.07 \times 10^6$	1.19 ± 0.006	56.04

(where %H is the percent in hypochroism, $\%H=(A_o-A_b)/(A_b)$)

Binding constants for the interaction of these complexes with CT-DNA are in the micromolar range similar to other Ru(II)-dppz complexes[21,24,25]. The binding sites sizes for the interaction of these complexes with CT-DNA are between 1.18 and 1.59 mol of base pair per mol of complex, which is in good agreement with the job plots studies, suggesting that these metallo-intercalators could stack with each other on the DNA surface[3,21].

The complex **[3.10]** shows a binding constant of 7.37×10^5 M^{-1}. As discussed previously, this complex only stabilised CT-DNA by 5 °C and does not appear to intercalate between the base pairs of DNA.

4.5.5 Luminescence titrations

Luminescence titrations were carried out using a procedure similar to the UV-Vis titrations. The changes in fluorescence intensities for the interaction of $[Ru(tpm)(dppz)(L)]^{2+}$ upon addition of CT-DNA were measured using the excitation wavelength characteristic of each metal complex at 25°C. Most of the complexes

showed a light switch effect: no emission in aqueous solution unless bound to DNA. Figure 4.18 shows a typical luminescence titration.

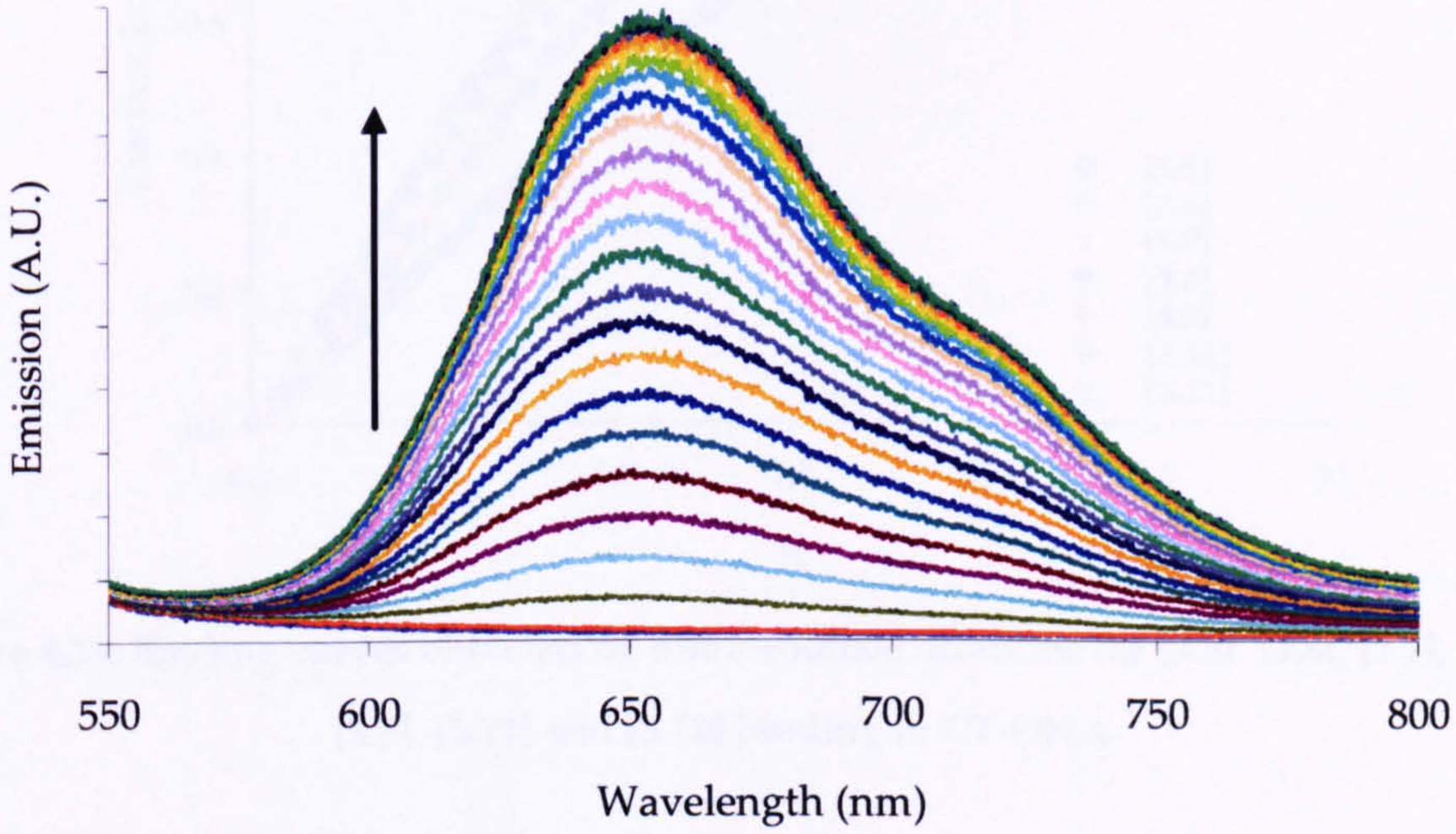

Figure 4.18: Luminescence titration of **[3.12]** with CT-DNA

In all the cases, the emission of the complexes when bound to CT-DNA is shifted to longer wavelength compared to the emission of the complexes dissolved in acetonitrile. For example the emission of **[3.6]** is at 615 nm when excited at the wavelength characteristic of the MLCT transition, but when bound to CT-DNA the emission is shifted to 658 nm and **[3.11]** when bound to DNA shows emission at 645 nm, 33 nm red shifted compared to the free complex.

Complex **[3.10]** showed completely different behaviour, upon addition of CT-DNA the emission was not switched on. Viscosity measurements established that this complex does not intercalate between the base pair of DNA and UV-Vis titrations indicate an affinity in the 10^5 M^{-1} range. Again this data is consistent with a non-intercalative interaction between **[3.10]** and DNA.

The binding curves for the interaction of **[3.5]**, **[3.6]**, **[3.7]**, **[3.8]**, **[3.9]**, **[3.11]** and **[3.12]** with CT-DNA are shown in figure 4.19. Once again they all show that saturation binding had taken place. Binding parameters obtained from fits to the McGhee-von Hippel model[13] are summarised in table 4.5.

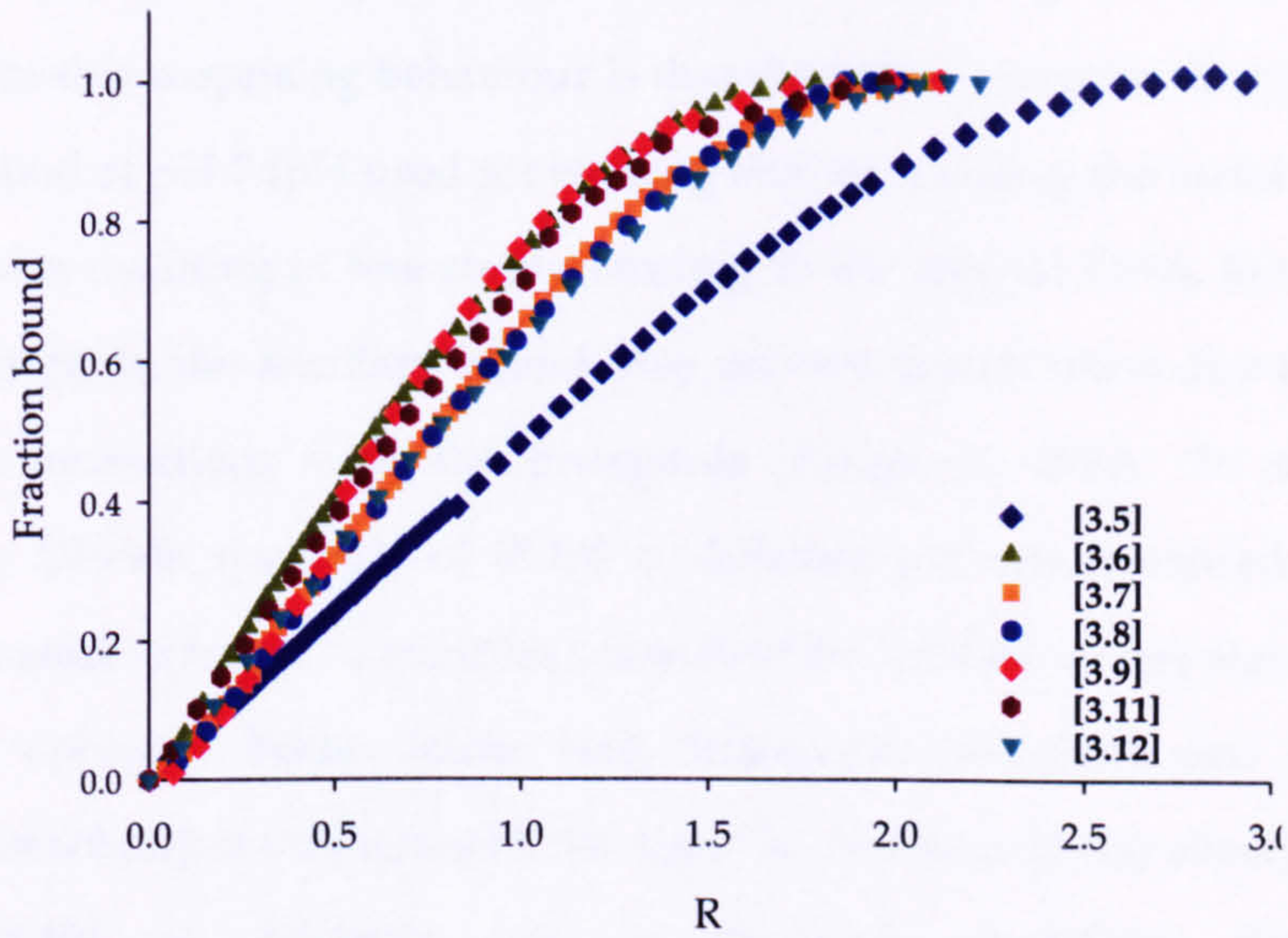

Figure 4.19: Binding curves obtained by luminescence titrations for **[3.5]**, **[3.6]**, **[3.7]**, **[3.8]** **[3.9]**, **[3.11]** and **[3.12]** binding to CT-DNA

Table 4.5: Binding constants and binding site sizes obtained by luminescence titration of the complexes **[3.5]**, **[3.6]**, **[3.7]**, **[3.8]**, **[3.9]**, **[3.10]**, **[3.11]** and **[3.12]** with CT-DNA

Compound	K_a (M^{-1})	N (bp)	I/I_0
[3.5]	2.59 ±0.09 x 10^6	1.90 ± 0.004	55.55
[3.6]	1.73 ± 0.1 x 10^6	1.16 ± 0.004	28.71
[3.7]	2.53 ± 0.17x 10^6	1.46 ± 0.007	29.29
[3.8]	3.36 ± 0.31 x 10^6	1.50 ± 0.01	36.25
[3.9]	1.88 ± 0.18 x 10^6	1.23 ± 0.01	34.12
[3.10]	(a)	(a)	(a)
[3.11]	1.47 ± 0.08 x 10^6	1.28 ± 0.006	50.95
[3.12]	1.7 ± 0.13 x 10^6	1.48 ± 0.13	63.68

(a) No light switch effect

Binding affinities of these complexes to CT-DNA are in the micromolar range and are in good agreement with the binding affinities obtained by UV-Vis titrations. The binding site sites are between 1.16 and 1.90 bp per ligand (depending on the complex), these values are a bit smaller than those expected for classical intercalators. Once more this data is consistent with some stacking of these complexes on the DNA surface[3,21].

As mentioned before, complex **[3.10]** does not show a light switch effect. One possibility for this surprising behaviour is that the amino group in the pyridine ring is deprotonated at pH 7 (pH used for binding studies) causing the metal complex to be less cationic resulting in less strong binding to the anionic DNA. Furthermore a negative charge on the ancillary ligand may prevent intercalation due to repulsive electrostatic interactions with the phosphate groups of DNA. To study these possibilities, UV-Vis spectrum of **[3.10]** at different pH was recorded. The same volume of a stock solution of complex (dissolved in distilled water) was added to 2 mL of the universal buffer (citric acid, trisodium phosphate and boric acid, described elsewhere) at different pH. No significant change in the absorption of the complex **[3.10]** at different pH is observed, therefore, the possible protonation/deprotonation of the amine group attached to the pyridine ring does not appear to be a factor in the lowered binding affinity of the complex.

The acid/base properties of $[Ru(tpm)(phen)(py)]^{2+}$ and $[Ru(tpm)(phen)(4\text{-}NH_2py)]^{2+}$ were also studied. Ru(II)-phen complexes are known to have good emission properties that can be useful for following changes. For that reason we decided to synthesise the analogues of $[Ru(tpm)(dppz)(py)]^{2+}$ and $[Ru(tpm)(dppz)(4\text{-}NH_2py)]^{2+}$ using the phen ligand instead of the dppz. The excitation wavelength used for $[Ru(tpm)(phen)(py)]^{2+}$ and $[Ru(tpm)(phen)(4\text{-}NH_2py)]^{2+}$ was 450 nm and the emission band followed was between 500-800 nm. No significant changes in the emission of both complexes at different pHs were observed.

Emission of **[3.10]** when bound to poly(dA)·poly(dT) and poly(dG)·poly(dC) was also explored. Little changes if any were observed upon addition of these homopolymers to an aqueous solution of the complex.

We also investigated the emission of this complex at different temperatures when bound to CT-DNA. No light switch effect was observed at 10 °C and 35 °C. The reason for this effect is still not clear.

4.5.6 Circular dichroism (CD) spectra

The interaction of these new metal complexes with DNA was studied by circular dichroism. To aid comparisons with the metal complexes, the circular dichroism spectrum of the dicationic dibromide salt of dppz ligand derivative (synthesised by Tim Phillips, a member of the Thomas' group) is first reported over a range of DNA/ligand ratios (figure 4.20).

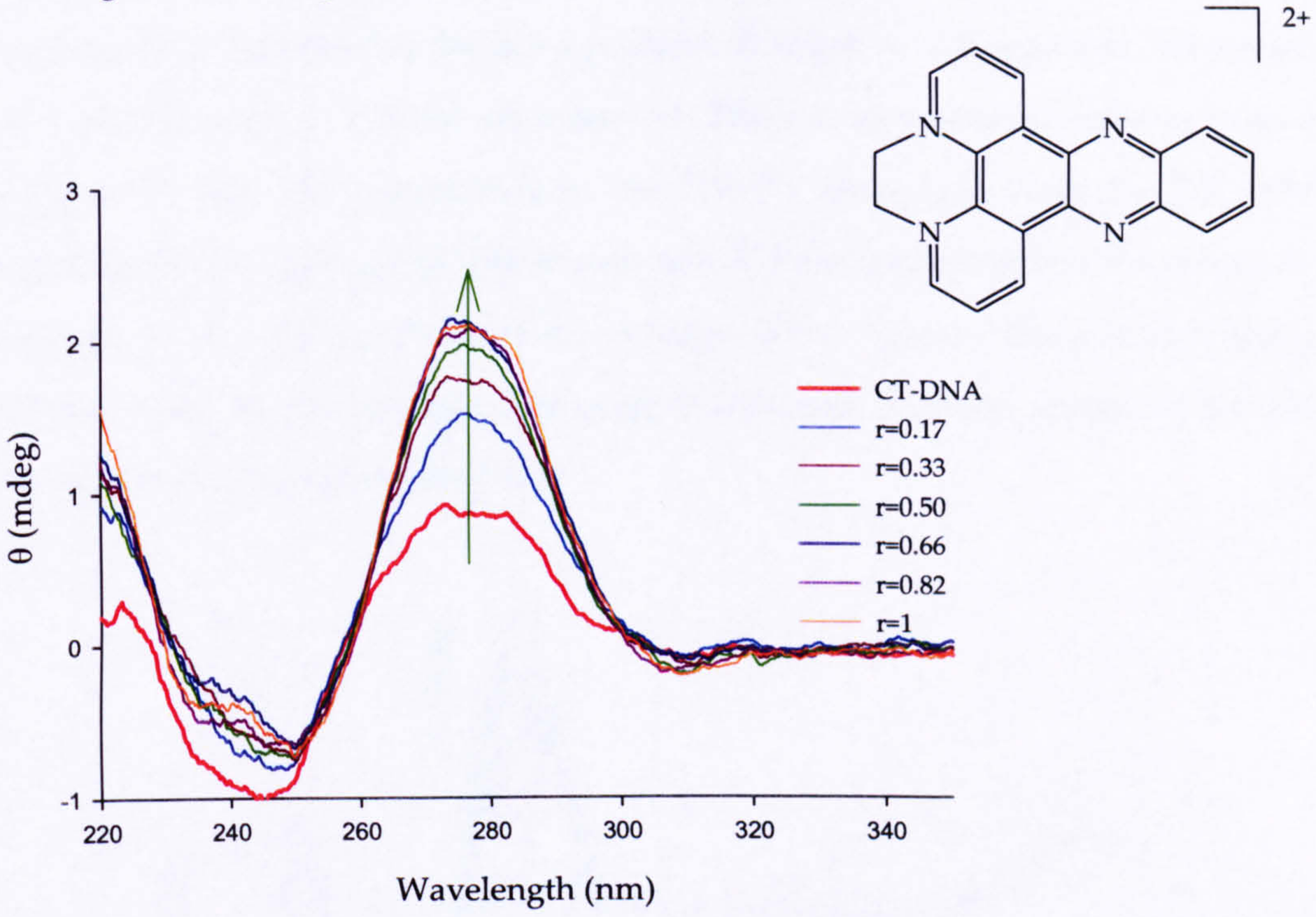

Figure 4.20: Structure of the dppz ligand derivative (top right) and CD spectrum of CT-DNA upon addition this ligand at different molar ratios (down)

CT-DNA exhibits a positive CD band at 278 nm due to base stacking and a negative band at 245 nm due to the helicity of B-DNA. Upon addition of this ligand there is a growth in a positive signal at 280 nm that could be induced by the interaction of this known intercalative compound[26] between the base pair of the DNA. It is know that changes in the 275 nm CD band of DNA are linear functions of changes in the helix winding angle and the base pairs twist: when the winding angle increases, the twist angle increases and the magnitude of the band increases[27]. This is in agreement with the insertion of the ligand between the π–π stacking of the DNA.

Circular dichroism of complexes **[3.5]**, **[3.6]**, **[3.7]**, **[3.8]**, **[3.9]**, **[3.10]**, **[3.11]** and **[3.12]** with CT-DNA have been measured over a range of complex/DNA ratios.

All complexes are achiral, CD spectra of these complexes in solution showed no signals. Figure 4.21 shows a typical CD spectrum of the interaction of these complexes with CT-DNA (buffer absorption is removed). Upon addition of the complexes, the positive band of the DNA shifts to lower wavelength and the negative band remained at the same position. A negative ICD signal at 290 nm and an isosbestic point at 278 nm are observed. There is also a weak negative band at around 350 nm that corresponds to the UV-Vis absorption band for the $\pi \rightarrow \pi^*$ transition of the dppz ligand. The wavelength 278 nm corresponds to the absorption maxima of the $\pi \rightarrow \pi^*$ transition of the nitrogen donor ligands. The positive band at 273 nm could be due changes due complex-complex stacking, complex-base pair interaction and changes in the DNA.

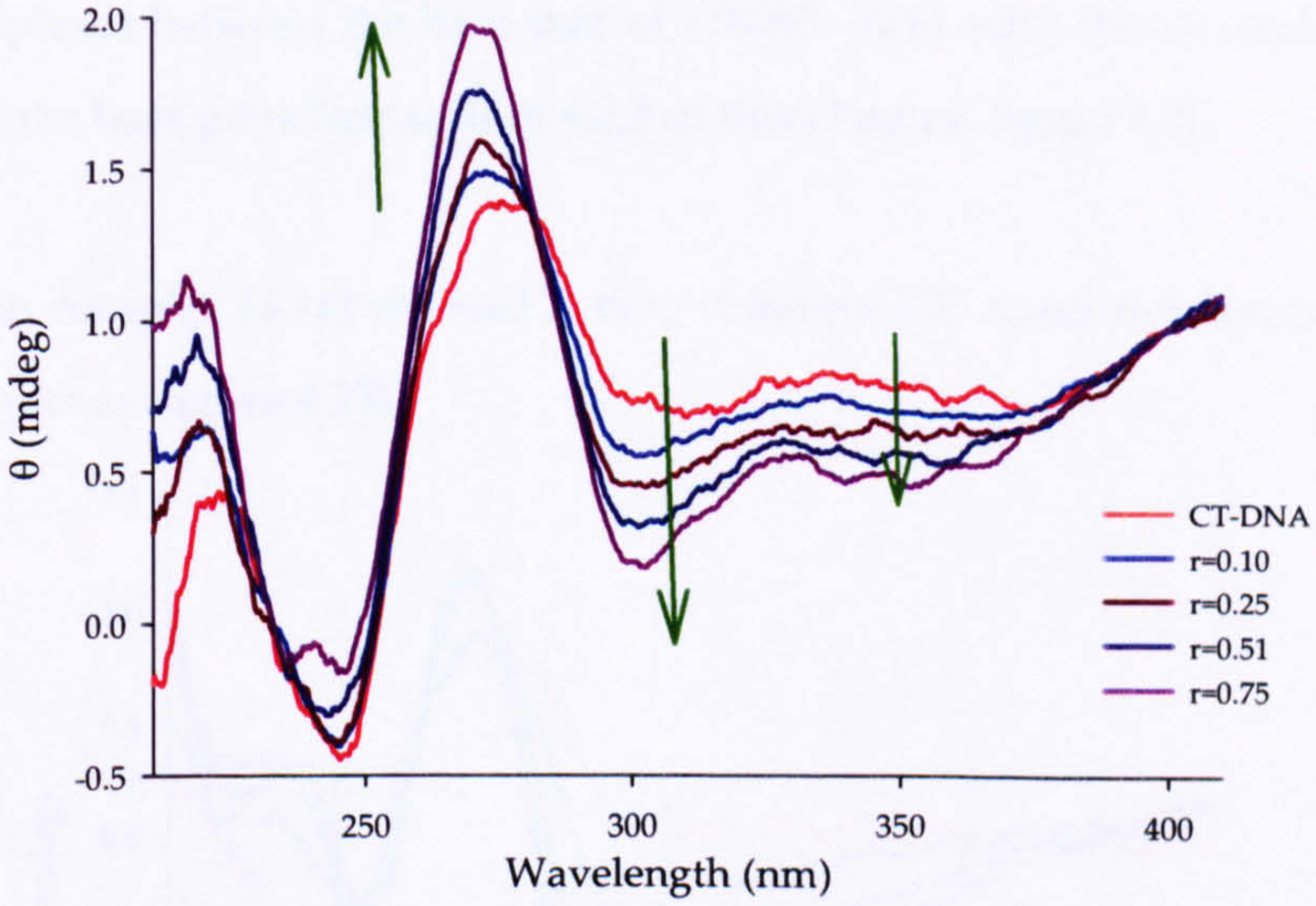

Figure 4.21: CD spectrum of CT-DNA upon addition of **[3.6]** at different molar ratios

Clearly, in contrast to the ICD signals of the dppz derivative interacting with CT-DNA, the ICD of the metal complexes showed more complicated signals. The new bands may be induced by the non-intercalating ligands moving to the chiral environment of the CT-DNA. If the signals for the CT-DNA alone are removed, is possible to see the ICD changes more clearly (figure 4.22).

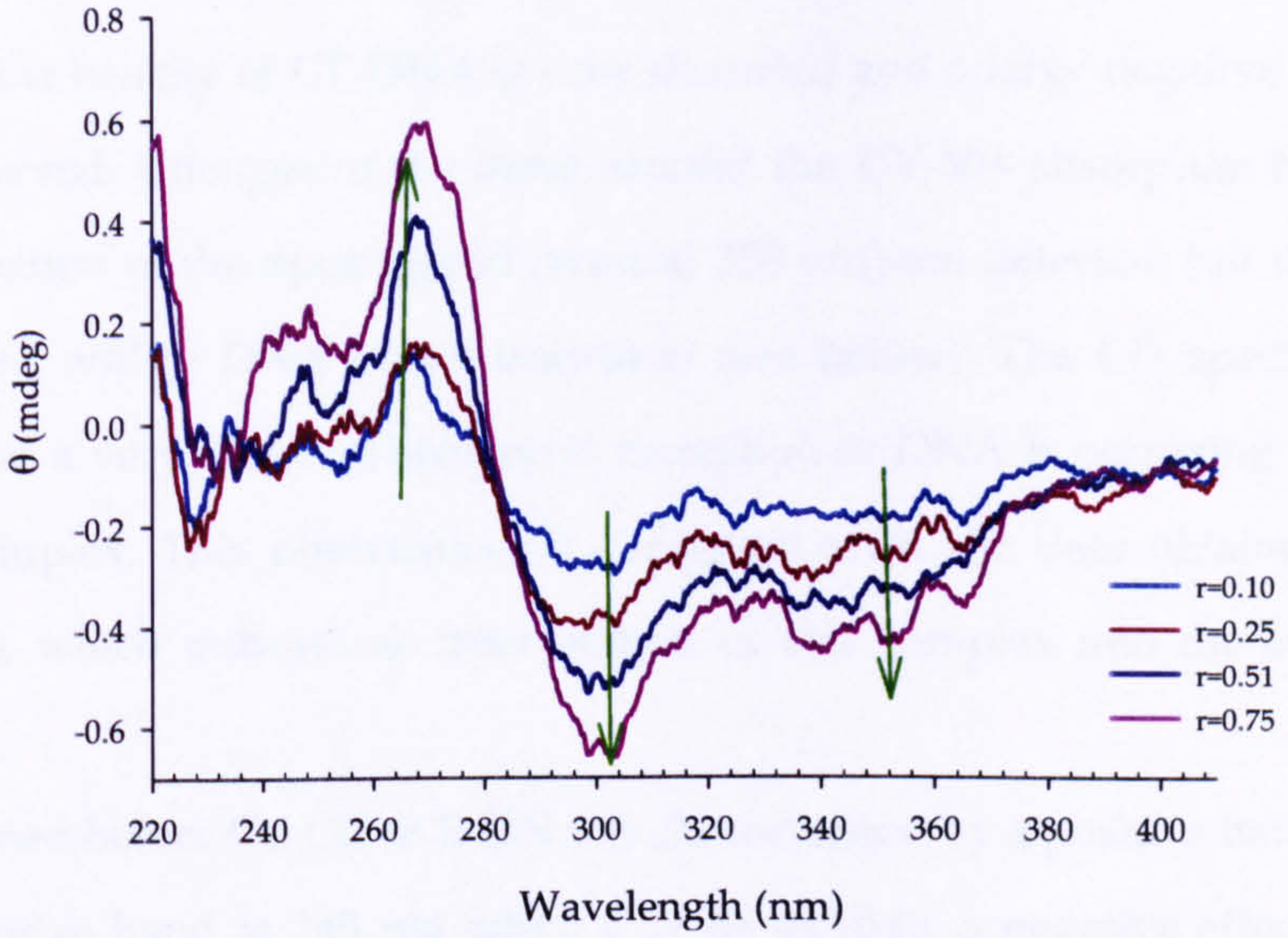

Figure 4.22: ICD spectra of complex **[3.6]** bound to CT-DNA

The magnitude and sign of ICD bands are in agreement with the intercalations of these complexes between the base pair of DNA[17]. And with the intercalation along the axis of the base pairs (see section 4.2.5 of this chapter, figure 4.3).

Once again complex **[3.10]** showed a very different CD spectrum compared to the other complexes (figure 4.23).

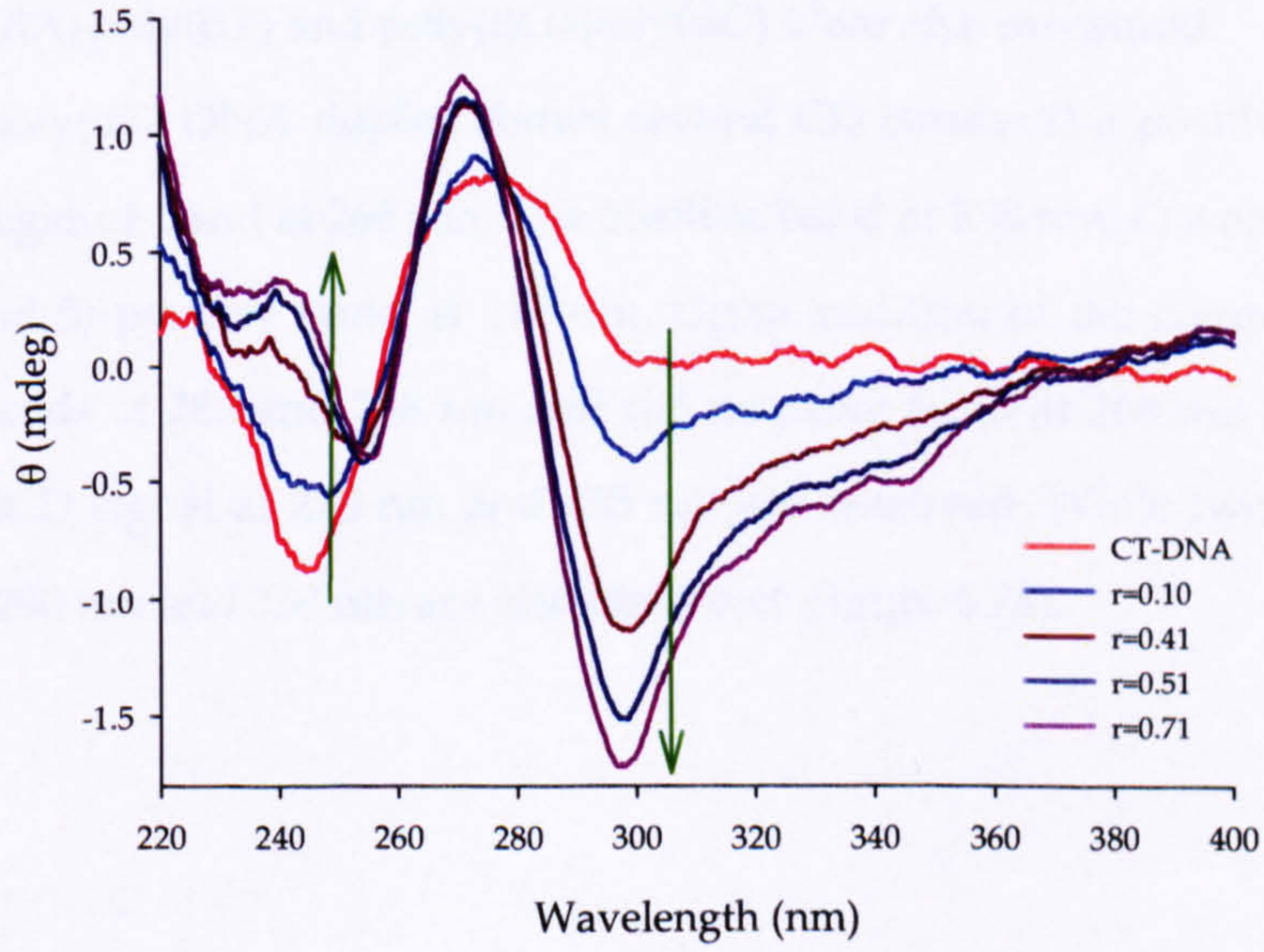

Figure 4.23: CD spectrum of CT-DNA upon addition of **[3.10]** at different molar ratios

In the interactions of **[3.10]** with CT-DNA more dramatic changes are observed. The band due the helicity of CT-DNA is now distorted and a large negative band at 300 nm is observed. Changes in the band around the UV-Vis absorption band for the $\pi \rightarrow \pi^*$ transition of the dppz ligand (around 350 nm) are detected, but these appear to be mixed with a DNA based transition (see below). The CD spectral changes suggest that a very different structural distortion of DNA is occurring when **[3.10]** binds to duplex. This observation is consistent with the data obtained by other techniques, which indicate no intercalation of this complex into the base pairs of DNA.

As mentioned before the CD of B-DNA is characterised by a positive band at 278 nm and a negative band at 245 nm while Z-DNA exhibits a negative effect at 293 nm and a positive band at 263 nm. The changes in the CD spectrum of CT-DNA upon addition of **[3.10]** show a negative band around 298 nm and a positive band at 272 nm; while the band changes observed are not exactly the same as those previously observed for this transition, they are close, suggesting that a complex induced B->Z conversion is a possibility. Such metal complex induced changes are well know and studied[28].

CD spectra for the binding of **[3.5]**, **[3.6]**, **[3.7]**, **[3.8]**, **[3.9]**, **[3.10]**, **[3.11]** and **[3.12]** with poly(dA)·poly(dT) and poly(dG)·poly(dC) were also measured.

Poly(dA)·poly(dT) DNA duplex shows several CD bands: 1) a positive band at 283 nm, 2) a negative band at 268 nm, 3) a positive band at 258 nm, 4) a negative band at 247 nm and 5) positive band at 217 nm. Upon addition of the complexes, the two positive bands at 283 and 258 nm and the negative band at 268 nm disappear and two new ICD signal at 270 nm and 435 nm are observed. While two negative ICD signals at 290 nm and 350 nm are also observed (figure 4.24).

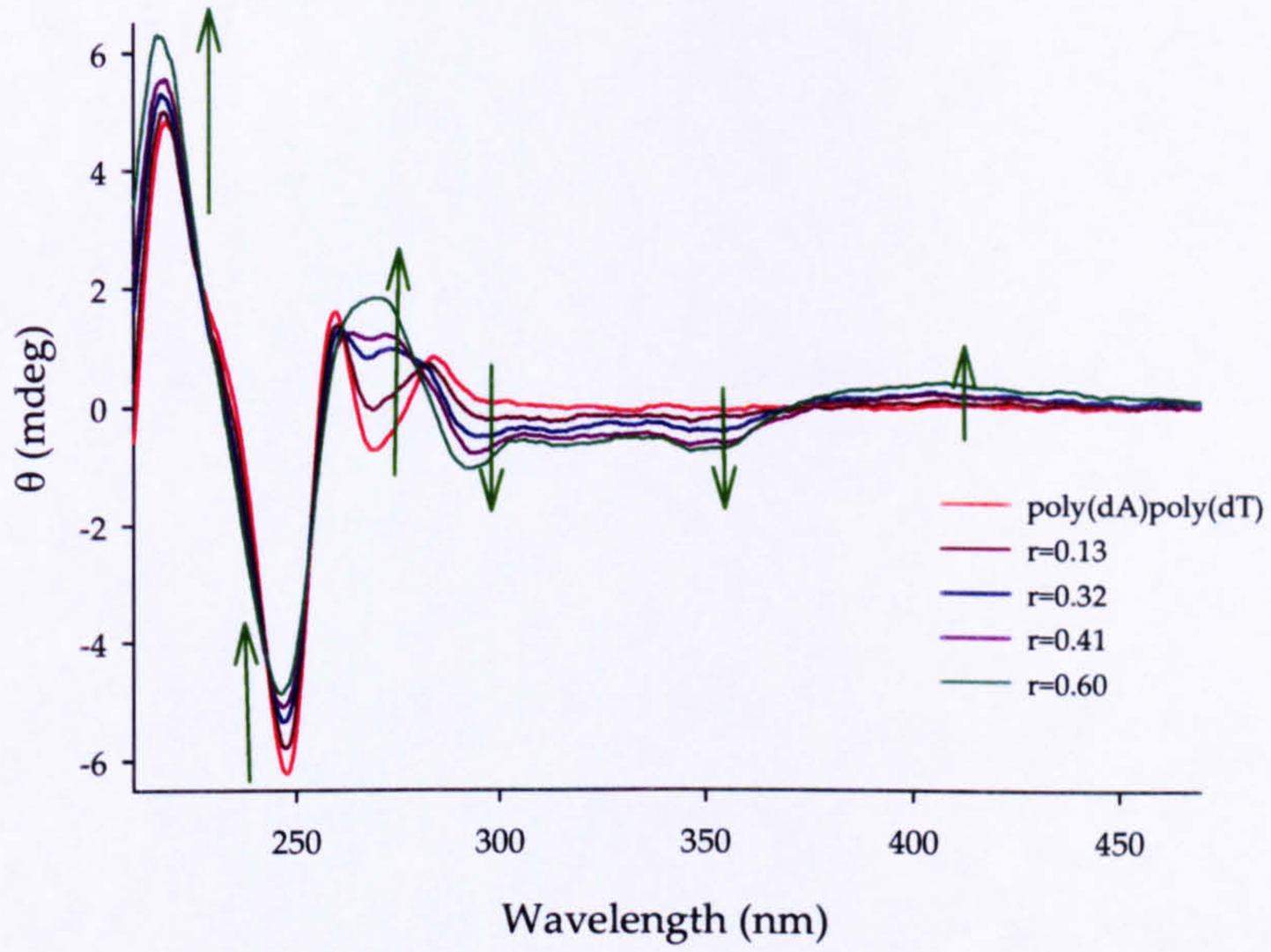

Figure 4.24: CD spectra of poly(dA)·poly(dT) upon addition of **[3.12]** at different molar ratios

It should be noted that the new ICD signals present in the interaction of these complexes with poly(dA)·poly(dT) are in the same position and sign that for the interactions with CT-DNA, indicating that the interaction of these complexes with CT-DNA and poly(dA)·poly(dT) probably takes place in a similar manner.

Complex **[3.10]** showed different CD behaviour compared to the other complexes when bound to poly(dA)·poly(dT) (figure 4.25).

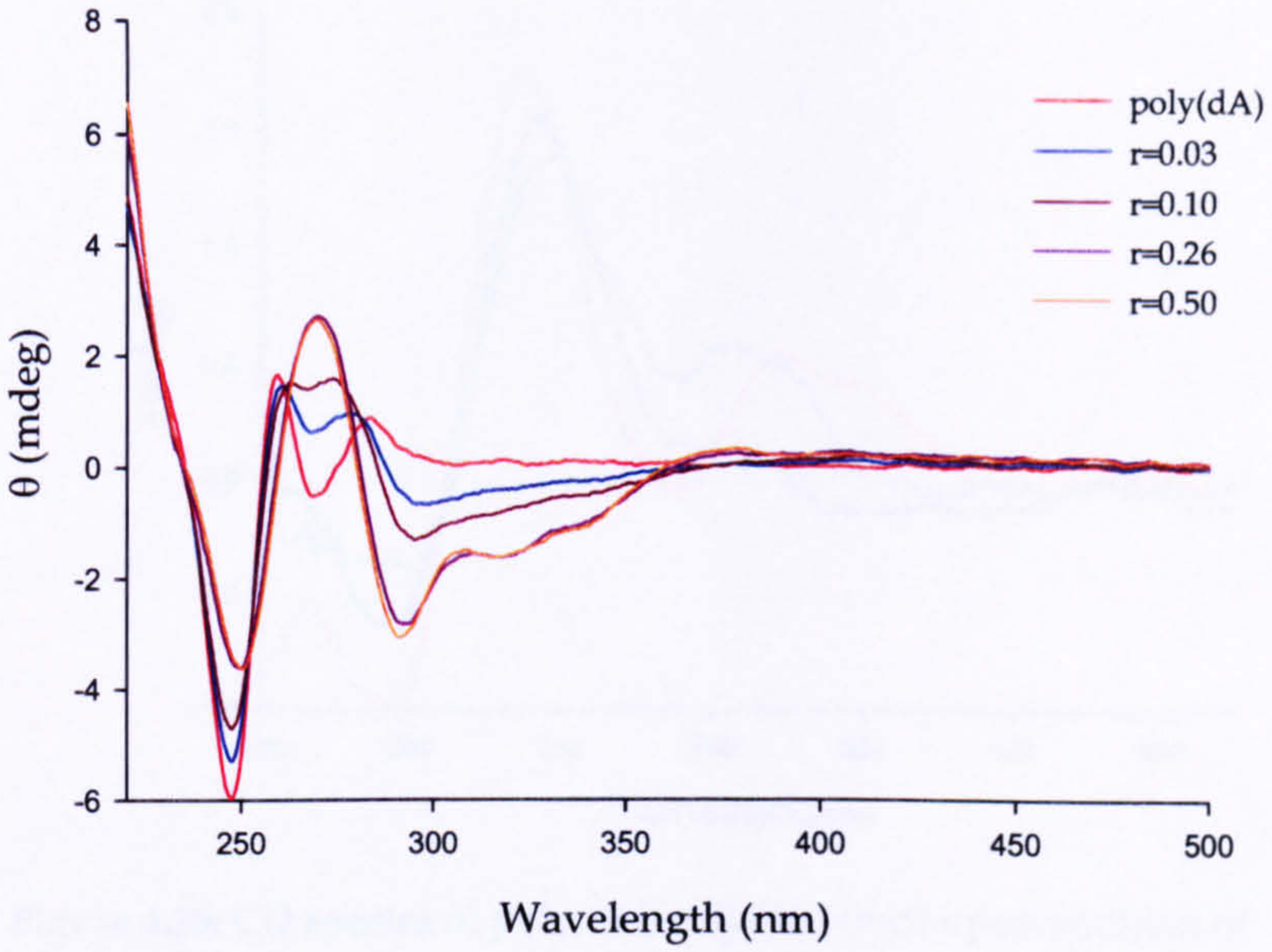

Figure 4.25: CD spectra of **[3.10]** at different DNA/complex molar ratios

As we can see in figure 4.25 the CD spectra for the interaction of **[3.10]** with poly(dA)·poly(dT) shows several ICD bands. The new bands observed for the interaction of $[Ru(tpm)(dppz)(L)]^{2+}$ complexes with this duplex DNA at 270 and 290 nm are quite similar to the ones observed for **[3.10]**, but at higher molar ratios the CD spectra of **[3.10]** binding to poly(dA)·poly(dT) showed several humped bands. The negative ICD signal at 350 nm only appears at high molar ratios accompanied by a weak positive band at 360 nm. This suggests more than one mode of binding to this homopolymer.

In the interaction of **[3.5]**, **[3.6]**, **[3.7]**, **[3.8]**, **[3.9]**, **[3.10]**, **[3.11]** and **[3.12]** with poly(dG)·poly(dC) different behaviours are observed. Poly(dG)·poly(dC) exhibits three CD signals: two positive bands at 288 nm and 254 nm and a negative band at 236 nm. Upon addition of the complexes **[3.5]**, **[3.6]**, **[3.7]**, **[3.8]** and **[3.9]** the positive band at 288 nm of the DNA disappeared and the bands at 254 nm and 236 decreased (figure 4.26). In contrast, complexes **[3.11]** and **[3.12]** produced an increase in the intensity of the 288 nm band accompanied of blue shift (figure 4.26).

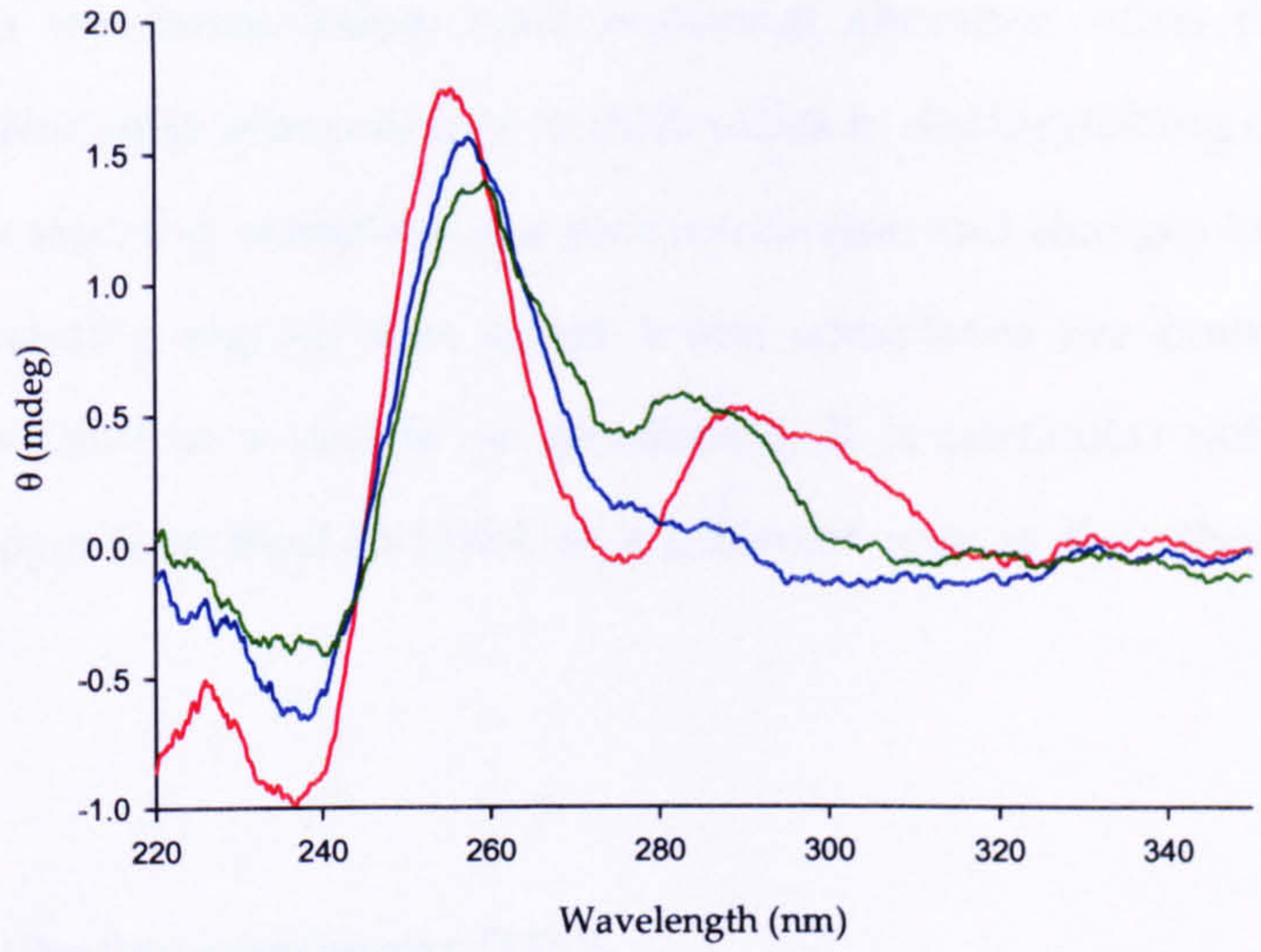

Figure 4.26: CD spectra of poly(dG)·poly(dC) (red) upon addition of **[3.7]** (blue) and **[3.12]** (green)

In the case of the interaction of **[3.10]** with poly(dG)·poly(dC), the CD spectral changes showed more complex behaviour, first the band at 288 nm decreases, but at higher molar ratios this band increases in intensity, suggesting interaction of this complex with this homopolymer in two different modes. In both cases the band is shifted to shorter wavelengths (figure 4.27).

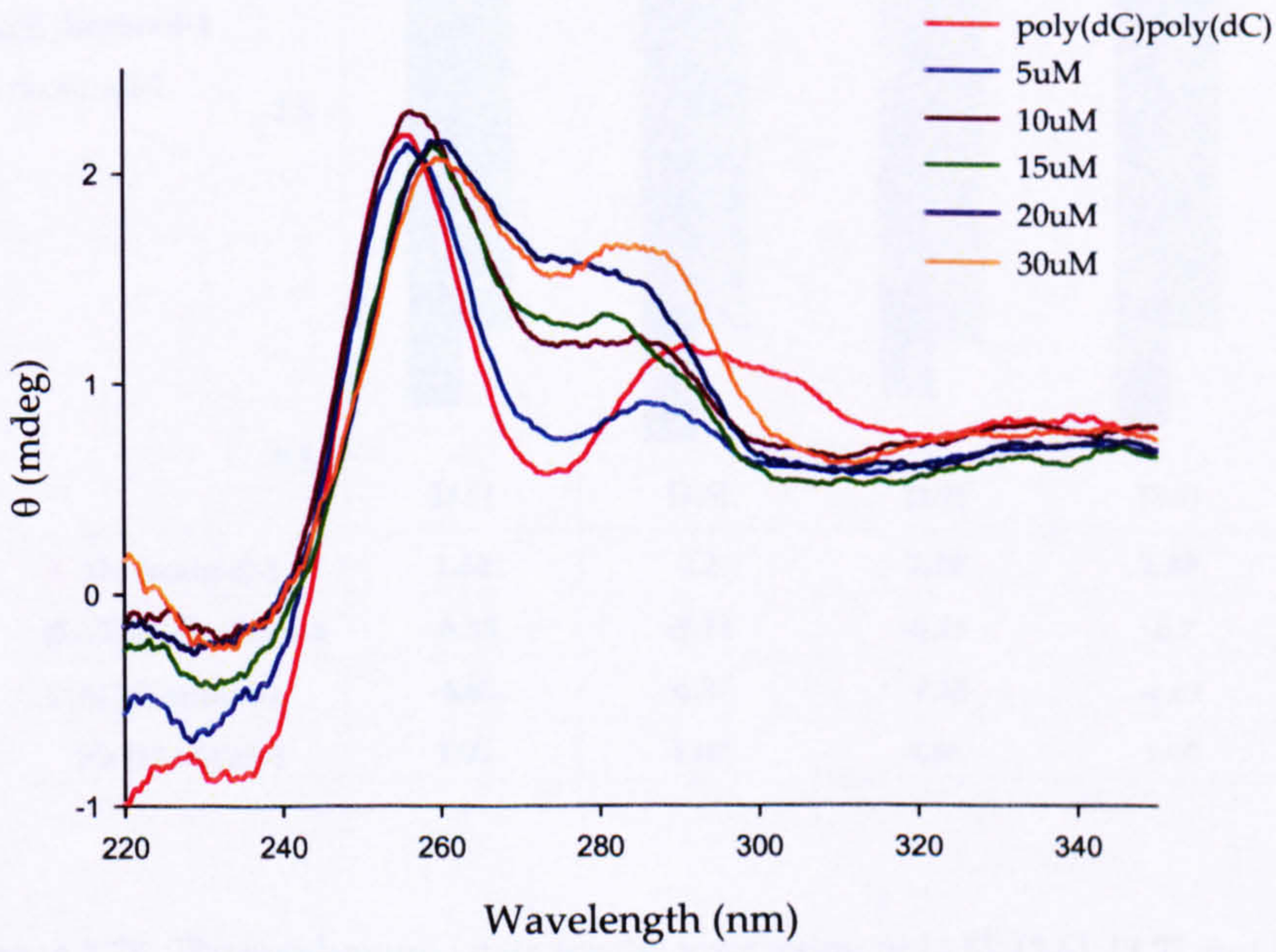

Figure 4.27: CD spectra of poly(dG)·poly(dC) upon addition of **[3.10]** at different molar ratios

As mentioned in the introduction, conformational alteration often produce CD signals that are difficult to interpret due to difficulties in distinguishing changes due complex-complex stacking, complex-base pair interaction and changes in the DNA. Clearly the contrasting signals that occur when complexes are bound to DNA suggest that they bind in a variety of geometries. It is particular noticeable that complex **[3.10]** appears to bind to DNA in a different way to the other complexes under study.

4.5.7 Isothermal titration calorimetry (ITC)

To further characterise the interaction of the complexes with nucleic acids, the thermodynamics of the binding of **[3.5]**, **[3.6]**, **[3.7]**, **[3.8]**, **[3.9]**, **[3.10]**, **[3.11]** and **[3.12]** with different types of DNA were determined by ITC. First of all, the interaction of these complexes with CT-DNA at 25 °C was studied. A comparison of the enthalpic and entropic contributions to the binding of $[Ru(tpm)(dppz)(3L)]^{2+}$ with CT-DNA is summarised in figure 4.28.

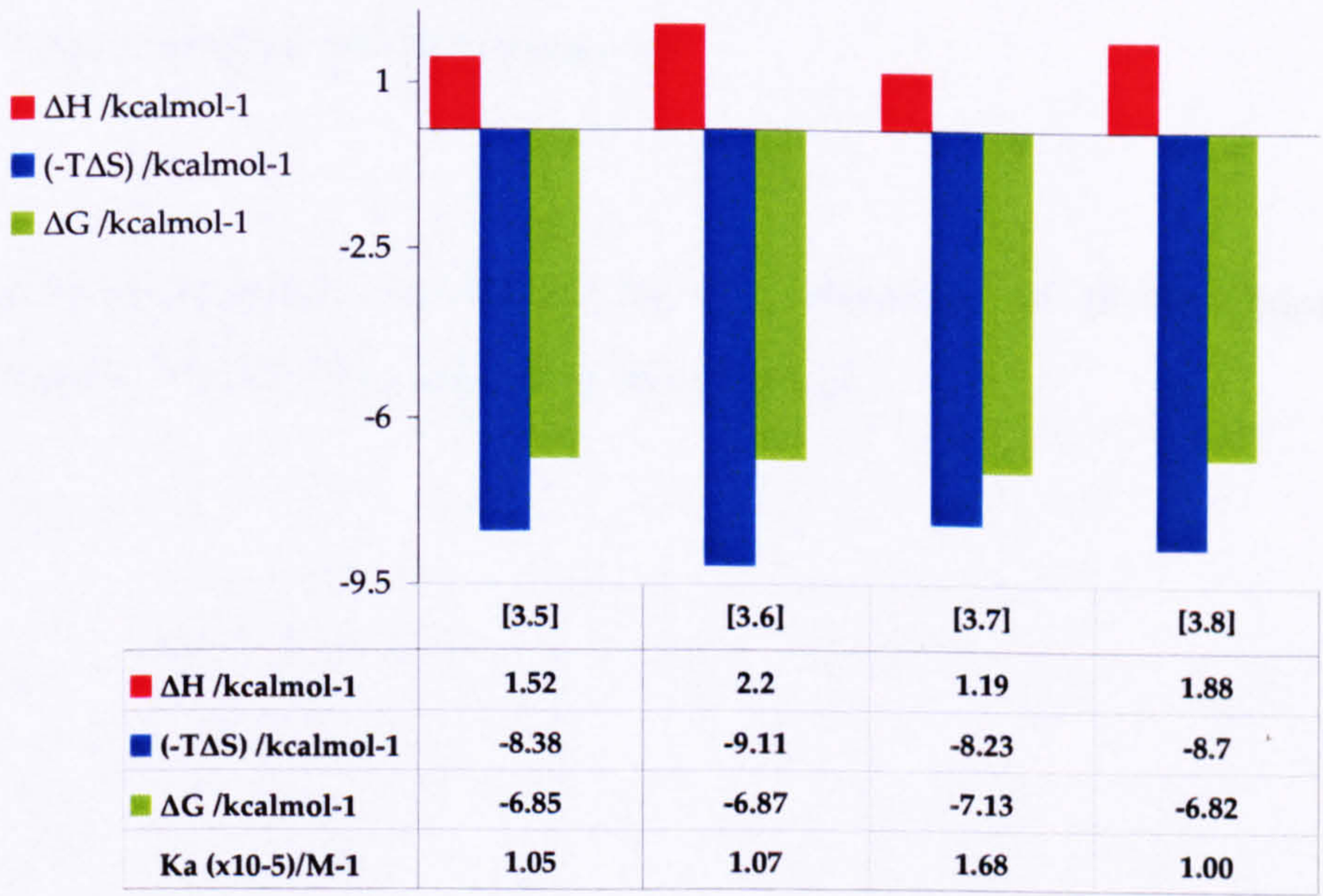

	[3.5]	[3.6]	[3.7]	[3.8]
ΔH /kcalmol-1	1.52	2.2	1.19	1.88
(-TΔS) /kcalmol-1	-8.38	-9.11	-8.23	-8.7
ΔG /kcalmol-1	-6.85	-6.87	-7.13	-6.82
Ka (x10-5)/M-1	1.05	1.07	1.68	1.00

Figure 4.28: Thermodynamic data for the interaction of **[3.5]**, **[3.6]**, **[3.7]** and **[3.8]** with CT-DNA

The interaction of these complexes with CT-DNA showed small positive changes in enthalpy (from 1.18 Kcal/mol to 2.2 kcal/mol) and positive entropies indicating that the interactions are entropically driven. The binding constants obtained by ITC were in the order of 10^5 M^{-1}, and the site sizes varied from 3.12 bp ([3.6]) to 1.76 bp ([3.8]). Hydrophobic interactions are usually characterised by small enthalpy changes and large entropy changes[29]. Electrostatic interaction are more difficult to determine, but the interaction of cations with DNA is usually entropically driven with small unfavourable changes in enthalpy[30].

It should be noted that binding constants for the interaction of the complexes with CT-DNA are smaller than the ones obtained by spectroscopic techniques. ITC data was analysed using a different model compared to the spectroscopic data. The ITC model uses a single set of identical binding sites, whereas the McGhee-von Hippel model, used for the spectroscopic data, assumes DNA as a lattice of identical and non-interacting potential binding sites where ligand binding to any site excludes neighbour sites. These differences mean that usually ITC estimates of K_a are lower than the more accurate figures obtain by spectroscopic titrations. However, we primarily use ITC to obtain information on enthalpy and entropy of interaction and to compare affinities between sequences.

The thermodynamics parameters for the interaction of $[Ru(tpm)(dppz)(4L)]^{2+}$ complexes with CT-DNA are shown in figure 4.29

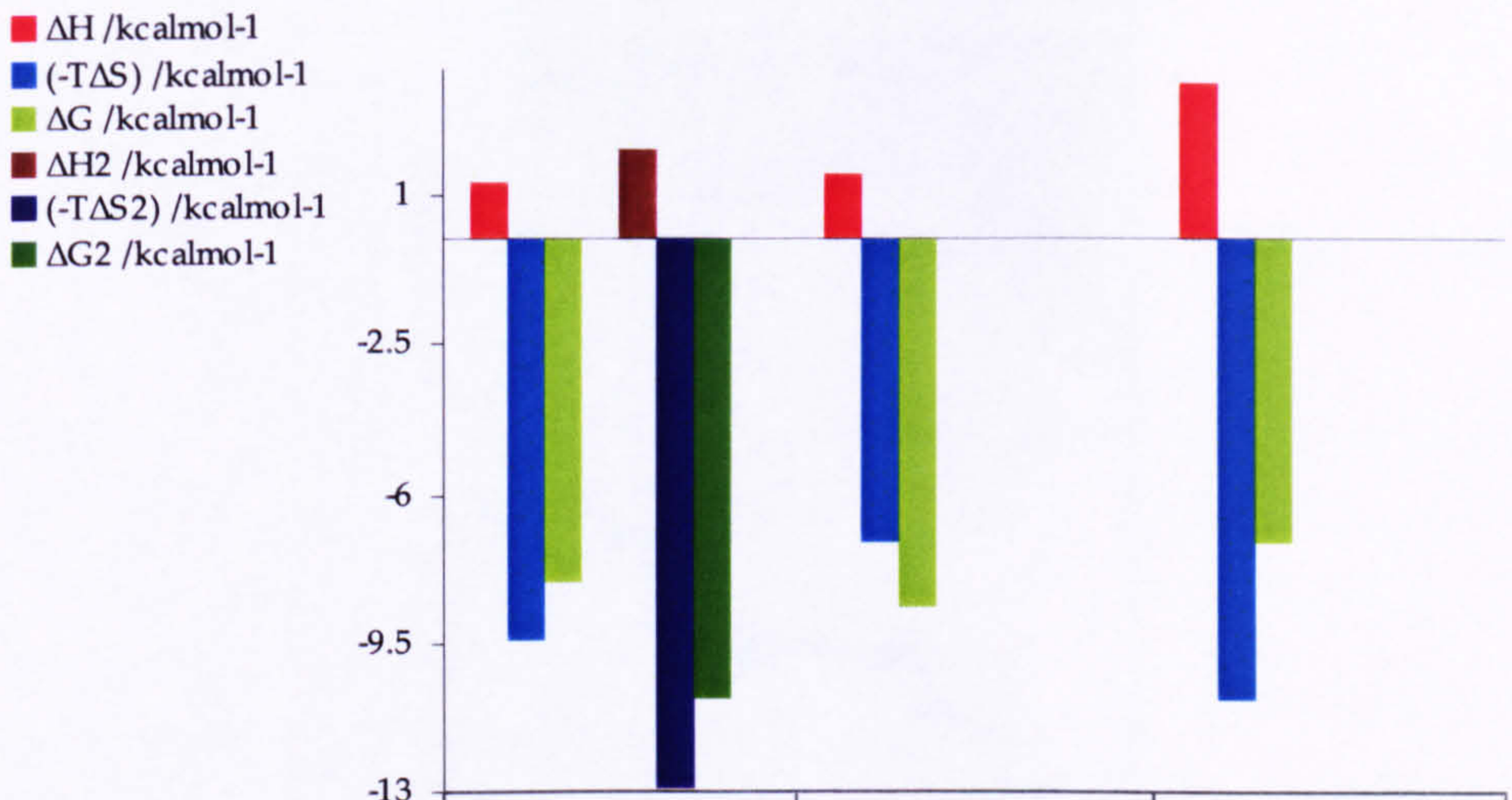

	[3.9]	[3.11]	[3.12]
ΔH /kcalmol-1	1.33	1.5	3.64
(-TΔS) /kcalmol-1	-9.42	-7.14	-10.8
ΔG /kcalmol-1	-8.08	-8.65	-7.15
Ka (x10-5)/M-1	8.33	1.71	1.77
ΔH2 /kcalmol-1	2.12		
(-TΔS2) /kcalmol-1	-12.9		
ΔG2 /kcalmol-1	-10.8		
Ka2 (x10-5)/M-1	803.00		

Figure 4.29: ITC thermodynamic data for the interaction of **[3.9]**, **[3.10]**, **[3.11]** and **[3.12]** with CT-DNA

In the case of the interaction of $[Ru(tpm)(dppz)(4L)]^{2+}$ complexes with CT-DNA a wider range of binding behaviours were observed. In the interaction of **[3.9]** with CT-DNA, two modes of binding were distinguished (figure 4.30), both showed small positive enthalpies and positive changes in entropy, indicating that the reaction is also entropic favoured.

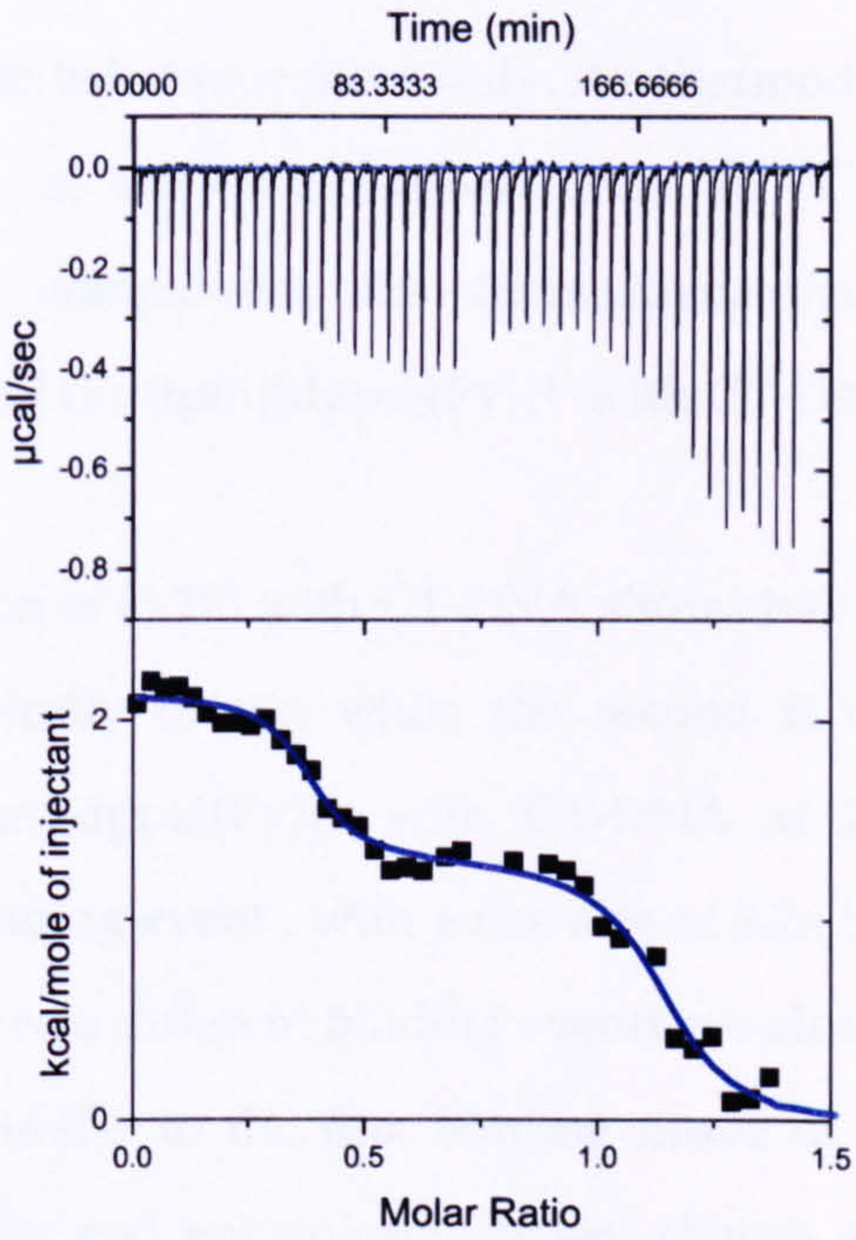

Figure 4.30: ITC raw data for the interaction of **[3.9]** to CT-DNA

The observation of two binding modes is in agreement with the data obtained from job plots which showed two different bindings stoichiometries for the interaction of **[3.9]** with CT-DNA. The affinity of this complex with DNA for the first event is in the order of 10^7 M^{-1} and the second event shows a binding affinity in 10^5 M^{-1} range. Again, the thermodynamic parameters obtained for **[3.5]**, **[3.6]**, **[3.7]**, **[3.8]**, **[3.11]** and **[3.12]** are in good agreement with the data obtained by Chaires *et al.*[22] for the interaction of Δ- and Λ- $[Ru(phen)_2(dppz)]^{2+}$ with CT-DNA at 25 °C, where interactions are entropically driven with small positive changes in enthalpy, which is typical for hydrophobic interactions (as a consequence of transferring the dppz ligand from the aqueous solution to inside the DNA), release of counterions and changes in hydration.

Surprisingly, the titration of **[3.10]** with CT-DNA only showed heat changes due to dilution of the complex at 25 °C. The titration was repeated at different concentration of complex or/and CT-DNA. In all the cases the same behaviour (no detectable enthalpy changes for the interaction of **[3.10]** with CT-DNA at 25 °C) was observed.

To explore this unusual behaviour more fully, the thermodynamics of interaction of **[3.10]** with CT-DNA at different temperatures, 10 °C and 35 °C were also investigated. To aid comparison, the thermodynamics of the interaction of $[Ru(phen)_2(dppz)]^{2+}$ and $[Ru(tpm)(dppz)(Py)]^{2+}$ with CT-DNA at these temperatures were studied as well.

At 10 °C, the interaction of **[3.10]** with CT-DNA shows two binding modes. The first interaction is enthalpically driven while the second is entropically driven. The interaction of $[Ru(tpm)(dppz)(Py)]^{2+}$ with CT-DNA at 10 °C displays a single entropically driven binding event , with a site size of 2.26 bp per ligand. In the case of $[Ru(phen)_2(dppz)]^{2+}$ two different binding events are also observed, the first one is entropically driven (similar to the first binding mode of **[3.10]**) while the second binding is enthalpically and entropically driven (figure 4.31). A racemic mixture was used for these experiments, the changes in enthalpy and entropy may be mixture of the interaction of two different enantiomers.

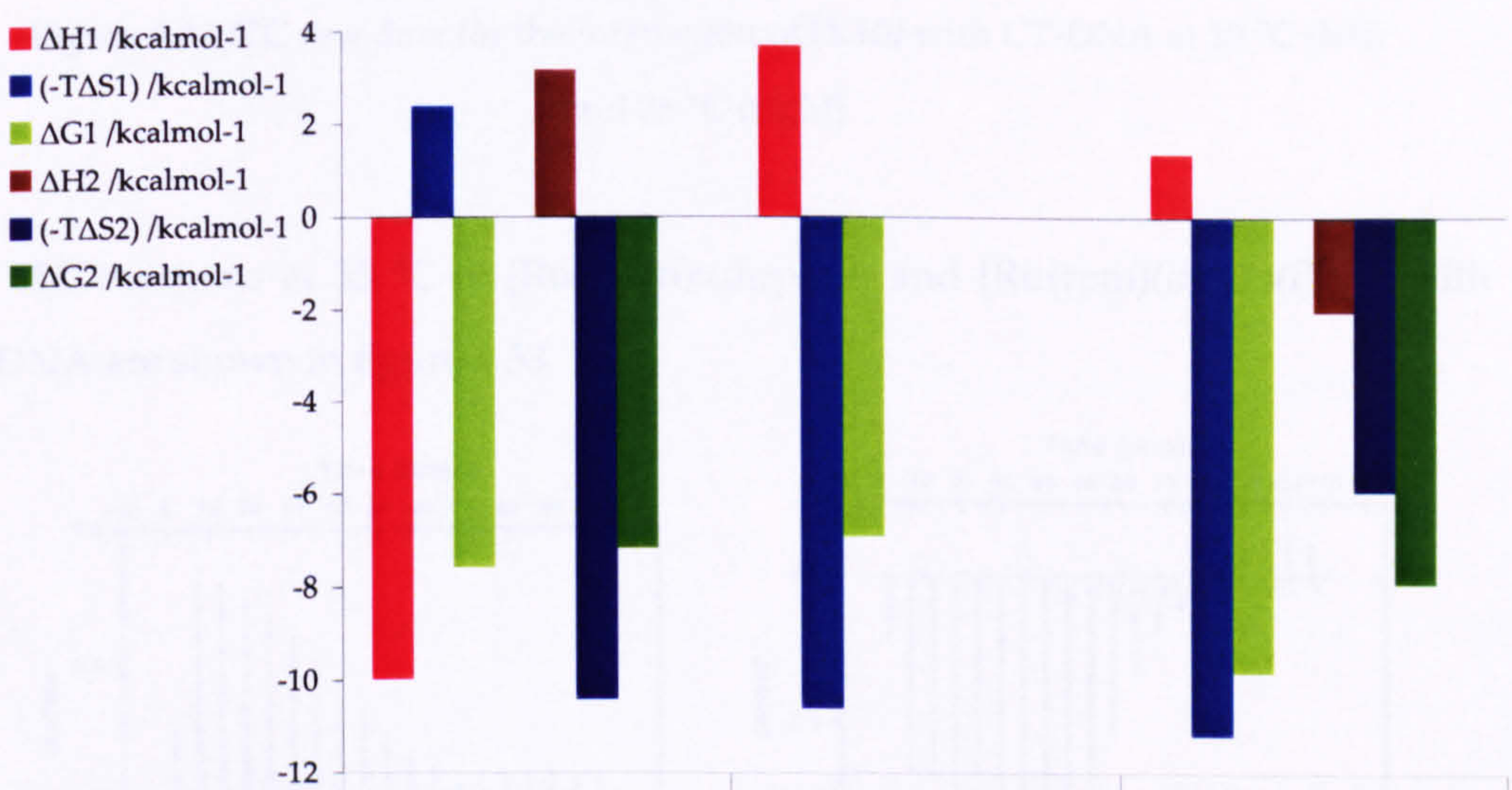

	[3.10]	[Ru(tpm)(dppz)(Py)]2+	[Ru(phen)2(dppz)]2+
ΔH1 /kcalmol-1	-9.96	3.67	1.35
(-TΔS1) /kcalmol-1	2.38	-10.6	-11.17
ΔG1 /kcalmol-1	-7.59	-6.93	-9.82
Ka1/M-1	3.63E+05	1.19E+05	1.54E+07
ΔH2 /kcalmol-1	3.17		-2.02
(-TΔS2) /kcalmol-1	-10.4		-5.91
ΔG2 /kcalmol-1	-7.18		-7.93
Ka2/M-1	1.82E+05		6.46E+05

Figure 4.31 ITC thermodynamic data for the interaction of **[3.10]**, $[Ru(tpm)(dppz)(Py)]^{2+}$ and $[Ru(phen)_2(dppz)]^{2+}$ with CT-DNA at 10 °C

At 35 °C, the binding of **[3.10]** to CT-DNA showed three modes of binding (figure 4.32), it is impossible to fit data for such a situation using commercially available software, because it only allows us two sets of binding.

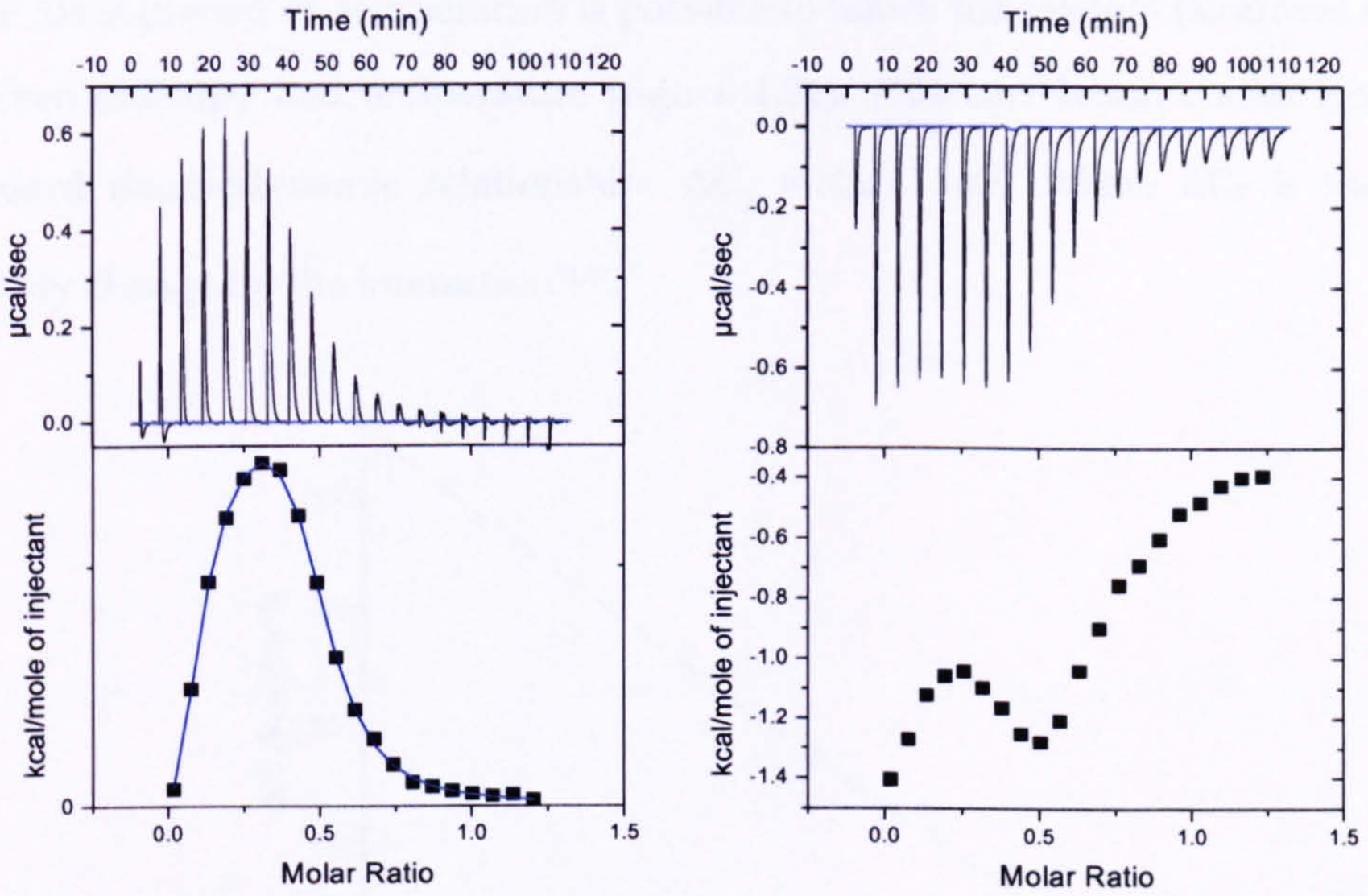

Figure 4.32 ITC raw data for the interaction of **[3.10]** with CT-DNA at 10 °C (left) and 35 °C (right)

The ITC titrations at 35 °C of $[Ru(phen)_2(dppz)]^{2+}$ and $[Ru(tpm)(dppz)(Py)]^{2+}$ with CT-DNA are shown in figure 4.33.

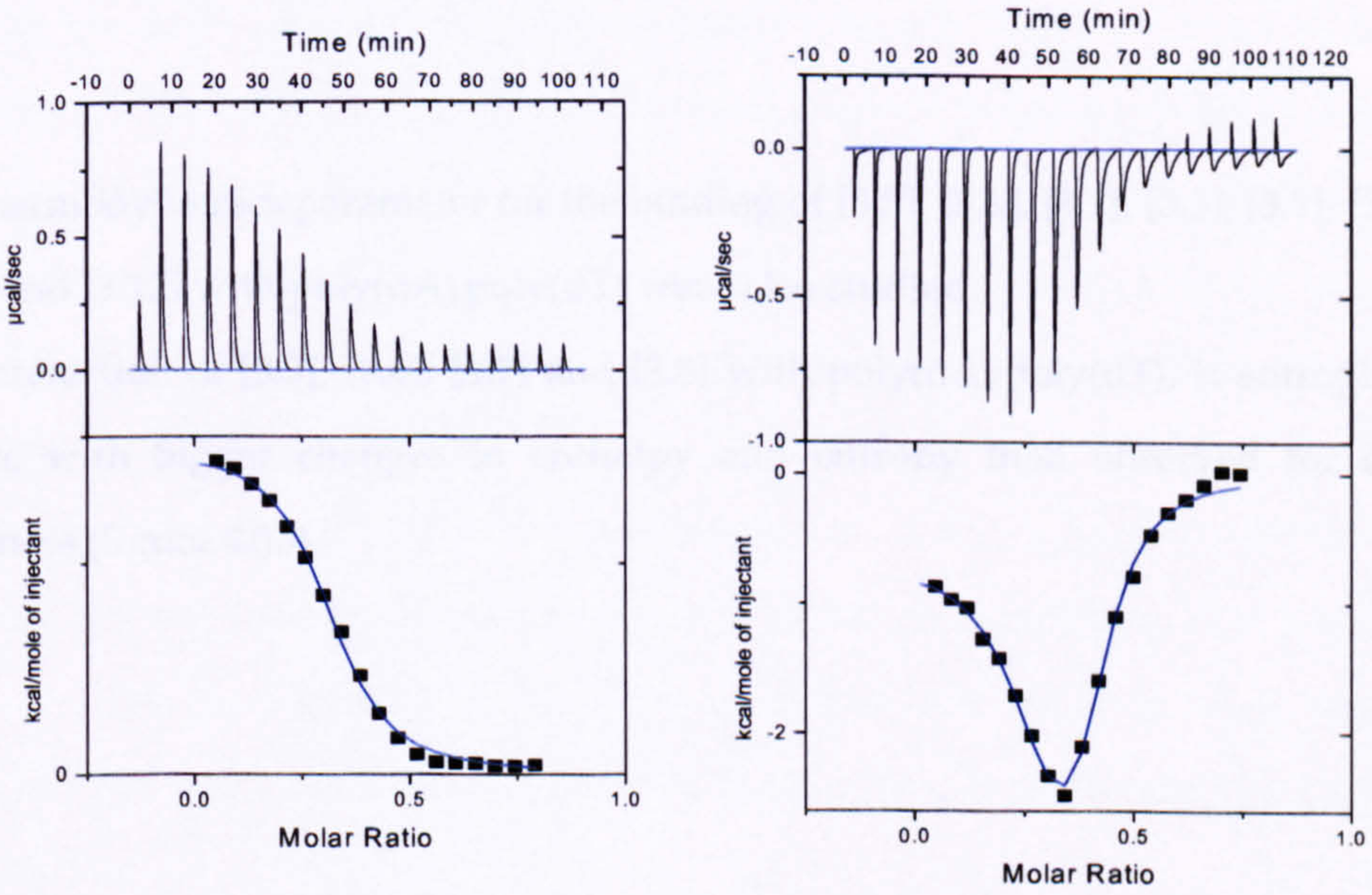

Figure 4.33: ITC raw data for the interaction of $[Ru(tpm)(dppz)(Py)]^{2+}$ (left) and $[Ru(phen)_2(dppz)]^{2+}$ (right) with CT-DNA at 35 °C.

The interaction of $[Ru(tpm)(dppz)(Py)]^{2+}$ with CT-DNA at 35 °C showed one entropically driven binding mode, while the interaction of $[Ru(phen)_2(dppz)]^{2+}$ again showed two binding modes, both of which are enthalpically driven.

If the ΔH is plotted *vs.* temperature is possible to notice the relation (assumed linear) between enthalpy and temperature (figure 4.34). This correlation comes from the standard thermodynamic relationship: $\Delta C_p = d\Delta H^0 / dT$ where ΔC_P is the heat capacity change for the interaction[31,32].

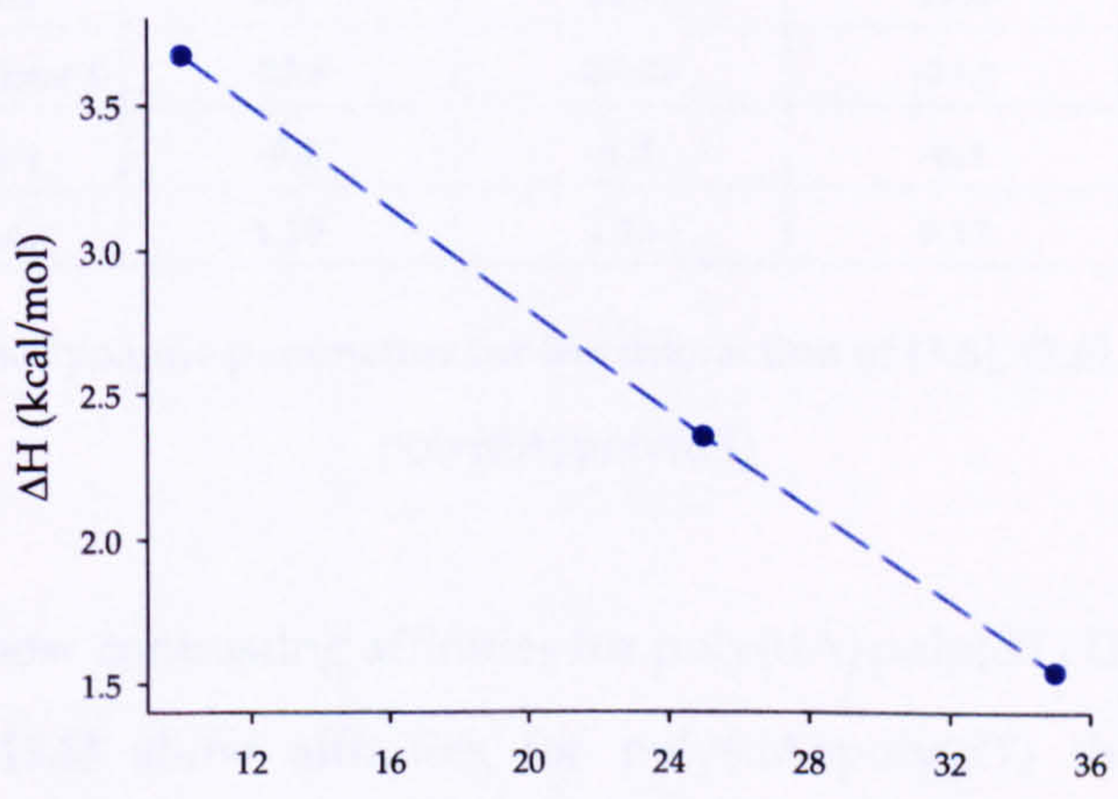

Figure 4.34: Enthalpy changes of $[Ru(tpm)(dppz)(Py)]^{2+}$ related to different temperatures

The thermodynamics parameter for the binding of **[3.5]**, **[3.6]**, **[3.7]**, **[3.8]**, **[3.9]**, **[3.10]**, **[3.11]** and **[3.12]** with poly(dA)·poly(dT) were also studied.

The interaction of **[3.5]**, **[3.6]**, **[3.7]** and **[3.8]** with poly(dA)·poly(dT), is entropically driven, with bigger changes in enthalpy and entropy than observed for other sequences (figure 4.35).

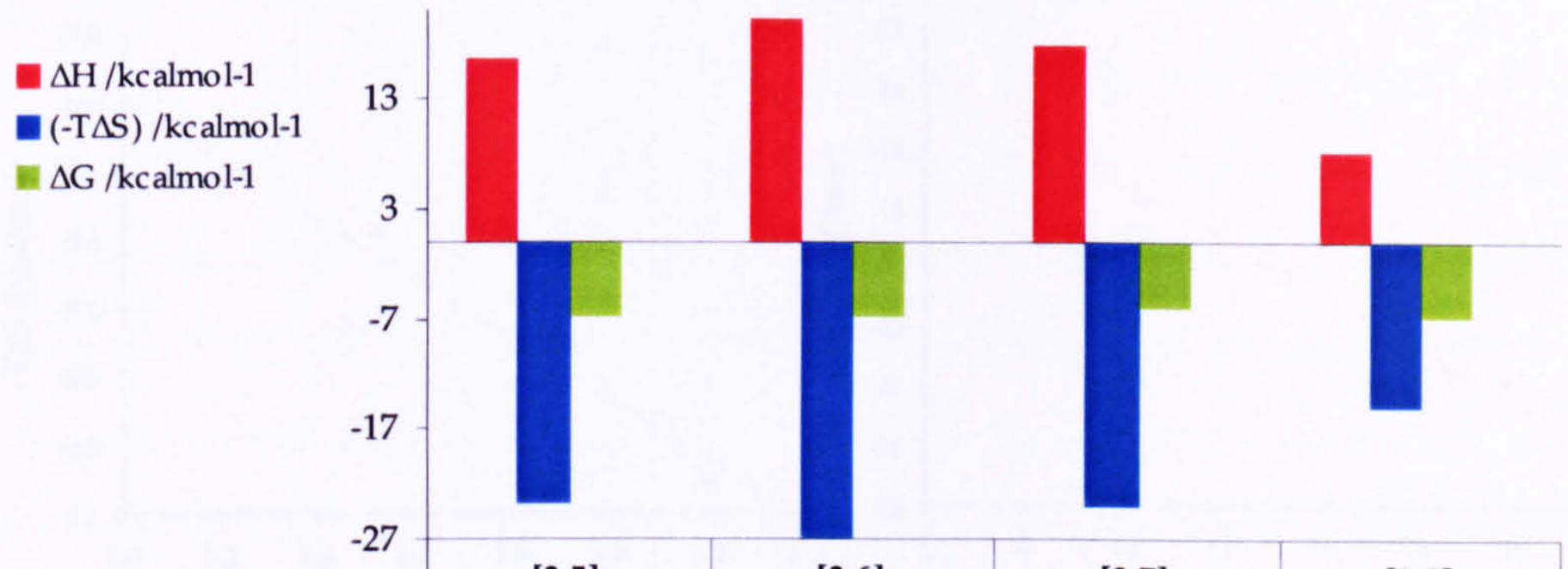

	[3.5]	[3.6]	[3.7]	[3.8]
ΔH /kcalmol-1	16.7	20.2	17.8	8.2
(-TΔS) /kcalmol-1	-23.6	-27.09	-23.9	-15.1
ΔG /kcalmol-1	-6.8	-6.8	-6.1	-6.82
Ka (x10-5)/M-1	1.10	1.13	0.17	0.99

Figure 4.35: Thermodynamic parameters for the interaction of **[3.5]**, **[3.6]**, **[3.7]** and **[3.8]** with poly(dA)·poly(dT)

The complexes show contrasting affinities for poly(dA)·poly(dT) DNA duplex: while **[3.5]**, **[3.6]** and **[3.8]** show affinities for poly(dA)·poly(dT) that are similar to CT-DNA, **[3.7]** shows a lower binding constant of $1.74 \times 10^4\ M^{-1}$, indicating a lower preference for this sequence.

Marky *et al.* studied the different hydration states of poly(dA)·poly(dT) and other DNA sequences[33]. Their studies showed that poly(dA)·poly(dT) is more hydrated than other DNA sequences. Binding of intercalators to poly(dA)·poly(dT) displace these water molecules, producing conformational changes in the polymer that cause dehydration. The release of the water molecules from the DNA polymer produce bigger changes in entropy and this is also reflected in the enthalpy changes (due to enthalpy/entropy compensation)[34].

Enthalpy/entropy compensation is characterised by a linear relation between the enthalpy changes and the entropy changes in a binding interaction. This relation is expected since increasing bonding in an interaction will result in more negative enthalpies but this requires an increase in order, leading to more negative entropies (figure 4.36).

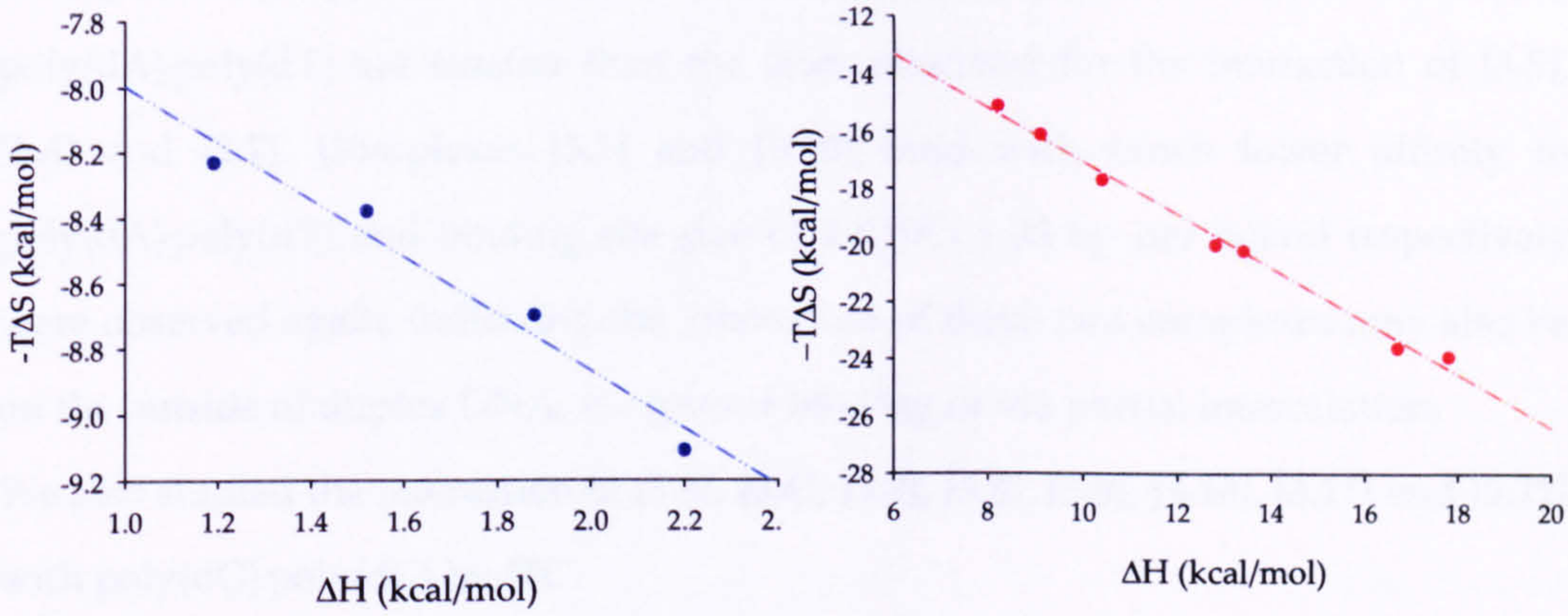

Figure 4.36: Examples of enthalpy/entropy compensation for the interaction of $[Ru(tpm)(dppz)(L)]^{2+}$ with CT-DNA (left) and poly(dA)·poly(dT) (right)

As the comparison of the enthalpic and entropic contributions for the interaction of **[3.9]**, **[3.10]**, **[3.11]** and **[3.12]** with poly(dA)·poly(dT) shown in figure 4.37 displays the binding of these complexes to DNA shows the expected relationship. Again the interaction between these complexes and this type of DNA duplex is entropically driven with large changes in entropy and enthalpy. The affinity of these complexes for poly(dA)·poly(dT) is in the 10^5 M^{-1} range except in the case of **[3.10]** where the binding constant is 5.11 x10^4 M^{-1}.

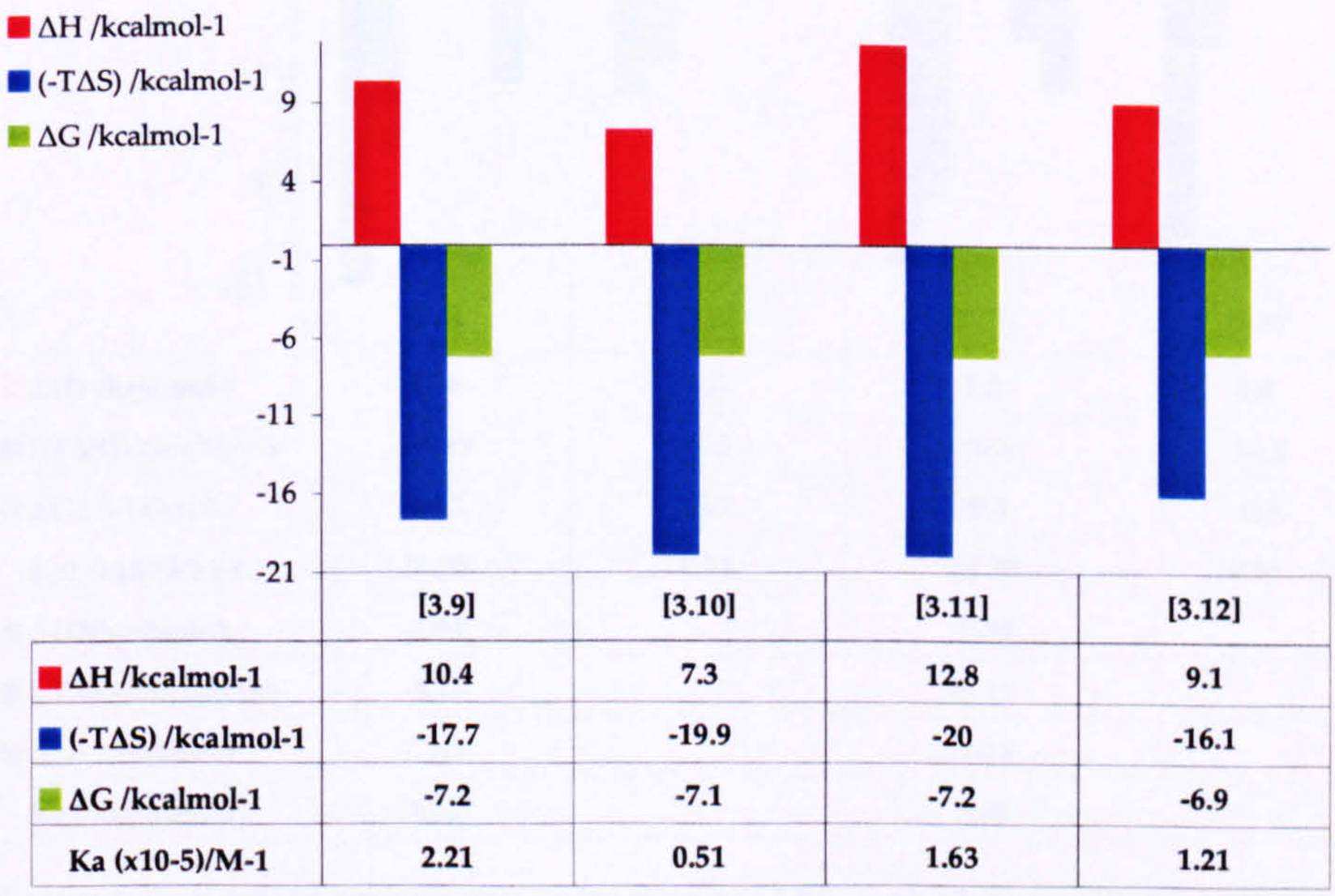

	[3.9]	[3.10]	[3.11]	[3.12]
ΔH /kcalmol-1	10.4	7.3	12.8	9.1
(-TΔS) /kcalmol-1	-17.7	-19.9	-20	-16.1
ΔG /kcalmol-1	-7.2	-7.1	-7.2	-6.9
Ka (x10-5)/M-1	2.21	0.51	1.63	1.21

Figure 4.37: Thermodynamic parameters for the interaction of **[3.9]**, **[3.10]**, **[3.11]** and **[3.12]** with poly(dA)·poly(dT)

Changes in entropy for the interaction of **[3.8]**, **[3.9]**, **[3.10]**, **[3.11]** and **[3.12]** with poly(dA)·poly(dT) are smaller than the ones observed for the interaction of **[3.5]**, **[3.6]** and **[3.7]**. Complexes **[3.7]** and **[3.10]** bind with much lower affinity to poly(dA)·poly(dT) and binding site size of 1.8 and 1.03 bp per ligand respectively were observed again, indicating the interaction of these two complexes may also be on the outside of duplex DNA, via groove binding or via partial intercalation.

We also studied the interaction of **[3.5]**, **[3.6]**, **[3.7]**, **[3.8]**, **[3.9]**, **[3.10]**, **[3.11]** and **[3.12]** with poly(dG)·poly(dC) by ITC.

The binding thermodynamics of the interaction of **[3.5]**, **[3.6]**, **[3.7]** and **[3.8]** complexes with poly(dG)·poly(dC) are shown in figure 4.38. Complexes **[3.6]** and **[3.8]** bind to poly(dG)·poly(dC) with low affinity (10^4 M^{-1}) and the interactions are entropically driven, with small changes in enthalpy in both cases.

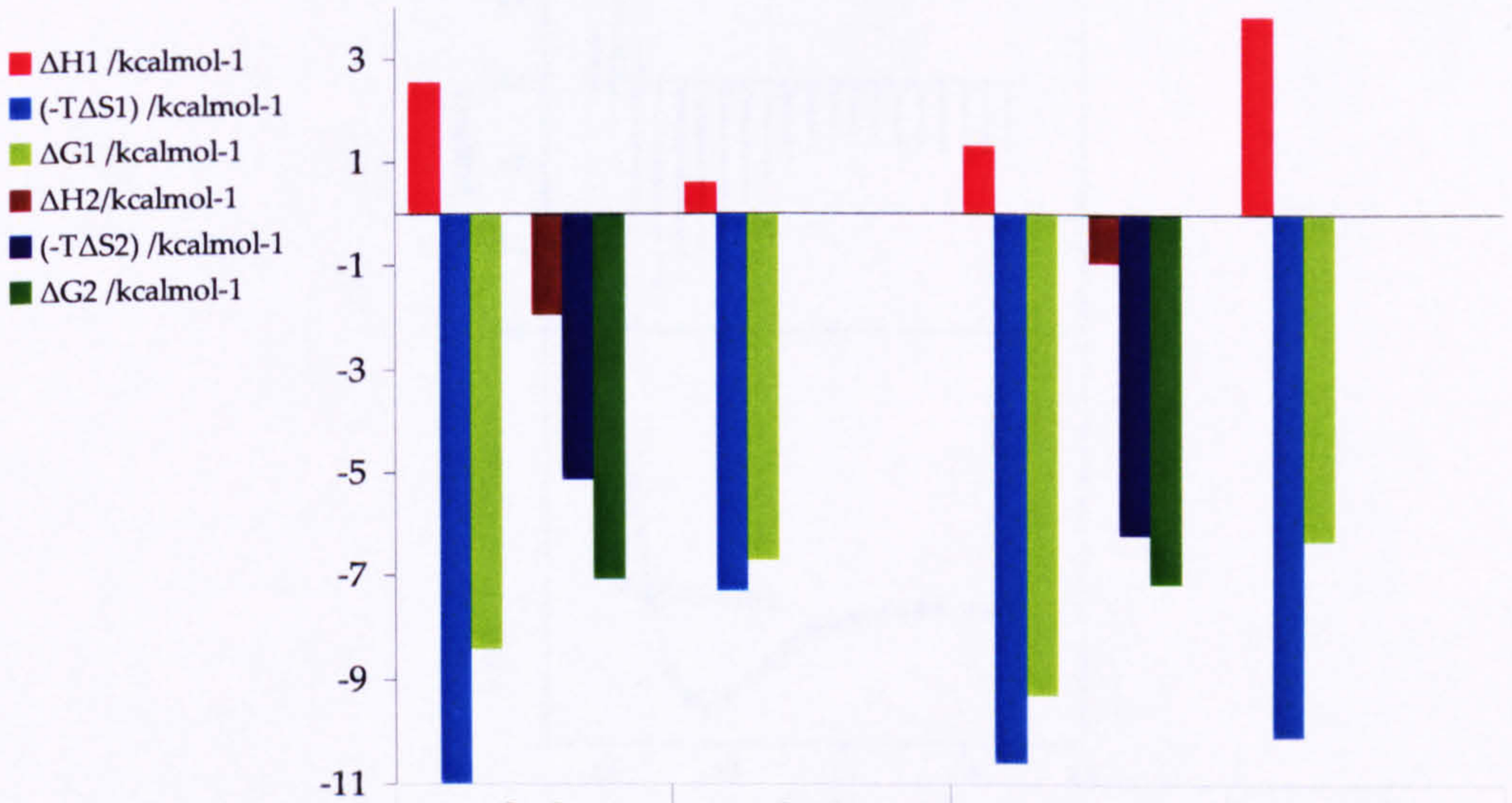

	[3.5]	[3.6]	[3.7]	[3.8]
ΔH1 /kcalmol-1	2.56	0.6	1.3	3.8
(-TΔS1) /kcalmol-1	-10.99	-7.3	-10.6	-10.1
ΔG1 /kcalmol-1	-8.43	-6.7	-9.3	-6.3
Ka1 (x10-5)/M-1	15.00	0.78	64.70	0.39
ΔH2/kcalmol-1	-1.94		-0.94	
(-TΔS2) /kcalmol-1	-5.13		-6.19	
ΔG2 /kcalmol-1	-7.07		-7.13	
Ka2(x10-5)/M-1	1.50		1.65	

Figure 4.38: Binding thermodynamics data of **[3.5]**, **[3.6]**, **[3.7]** and **[3.8]** binding to poly(dG)·poly(dC) at 25 °C

The interaction of **[3.5]** and **[3.7]** with poly(dG)·poly(dC) showed different behaviour compared to the other two complexes. Both these complexes which contain carbonyl groups, display two different interactions, the first event shows small positive changes in enthalpy and for both complexes the interaction is entropically driven. The second event shows small negative changes in enthalpy with the interaction being entropically and enthalpy driven. Favoured enthalpies are indicative of the formation of hydrogen bonds and/or van der Waals contacts[35]. It may be possible that these two complexes recognise G-C binding sites by hydrogen bonding and / or specific van der Waals contacts. The binding constant for the first event was ~10^6 M^{-1} and for the second K_a ~1.5 x 10^5 M^{-1}.

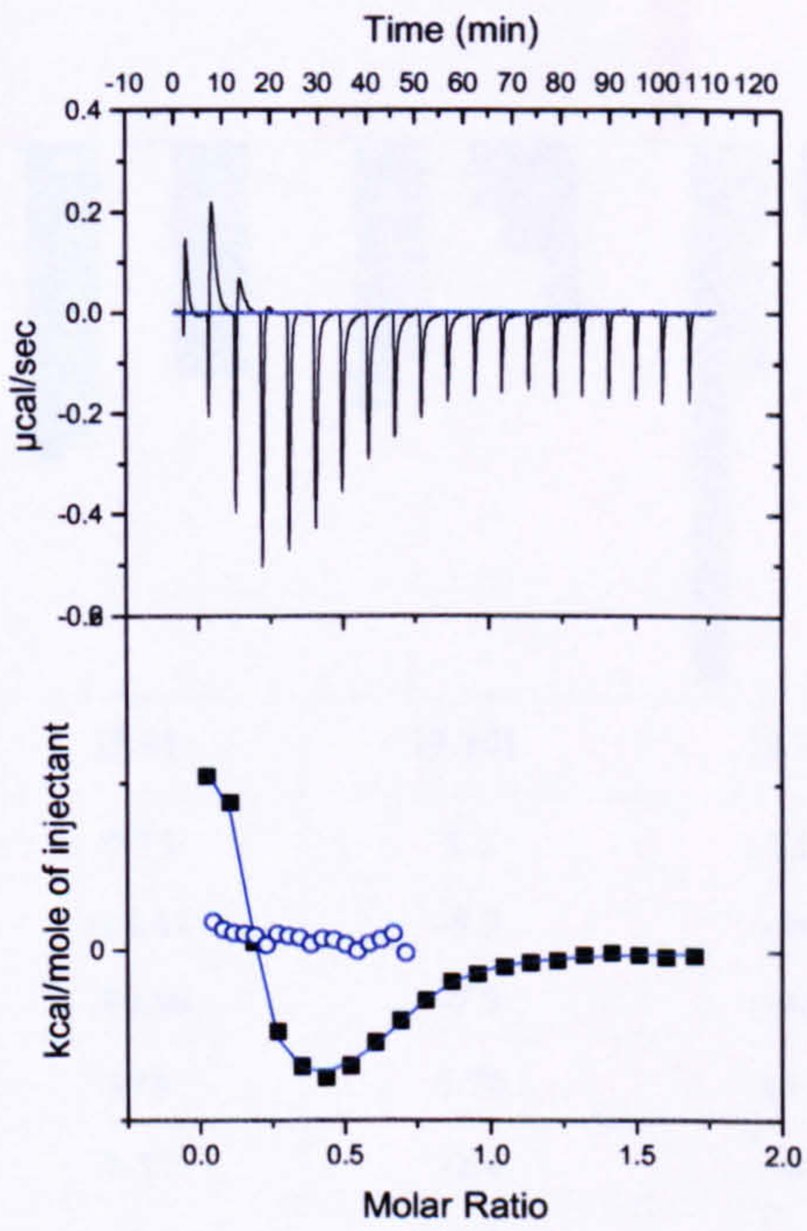

Figure 4.39: ITC raw data for the interaction of **[3.7]** with poly(dG)·poly(dC) (black square) and dilution experiment (open blue) at 25 °C

Figure 4.40 shows the thermodynamic parameters for the interaction of **[3.9]**, **[3.10]**, **[3.11]** and **[3.12]** complexes with poly(dG)·poly(dC). Binding of these complexes to poly(dG)·poly(dC) shows completely different behaviours. Complex **[3.9]** showed

two binding events, both with small changes in enthalpy and entropically. The affinity of **[3.9]** for poly(dG)·poly(dC) is in the 10^7 and 10^6 M^{-1} range with binding site size of 3.6 and 1.62 bp per ligand respectively.

Complexes **[3.10]**, **[3.11]** and **[3.12]** also show two different bindings to poly(dG)·poly(dC) and in these cases, the first event is entropically driven while the second one is enthalpy and entropy favoured, possibly suggesting the specific recognition of the DNA duplex by the ancillary groups in the complex.

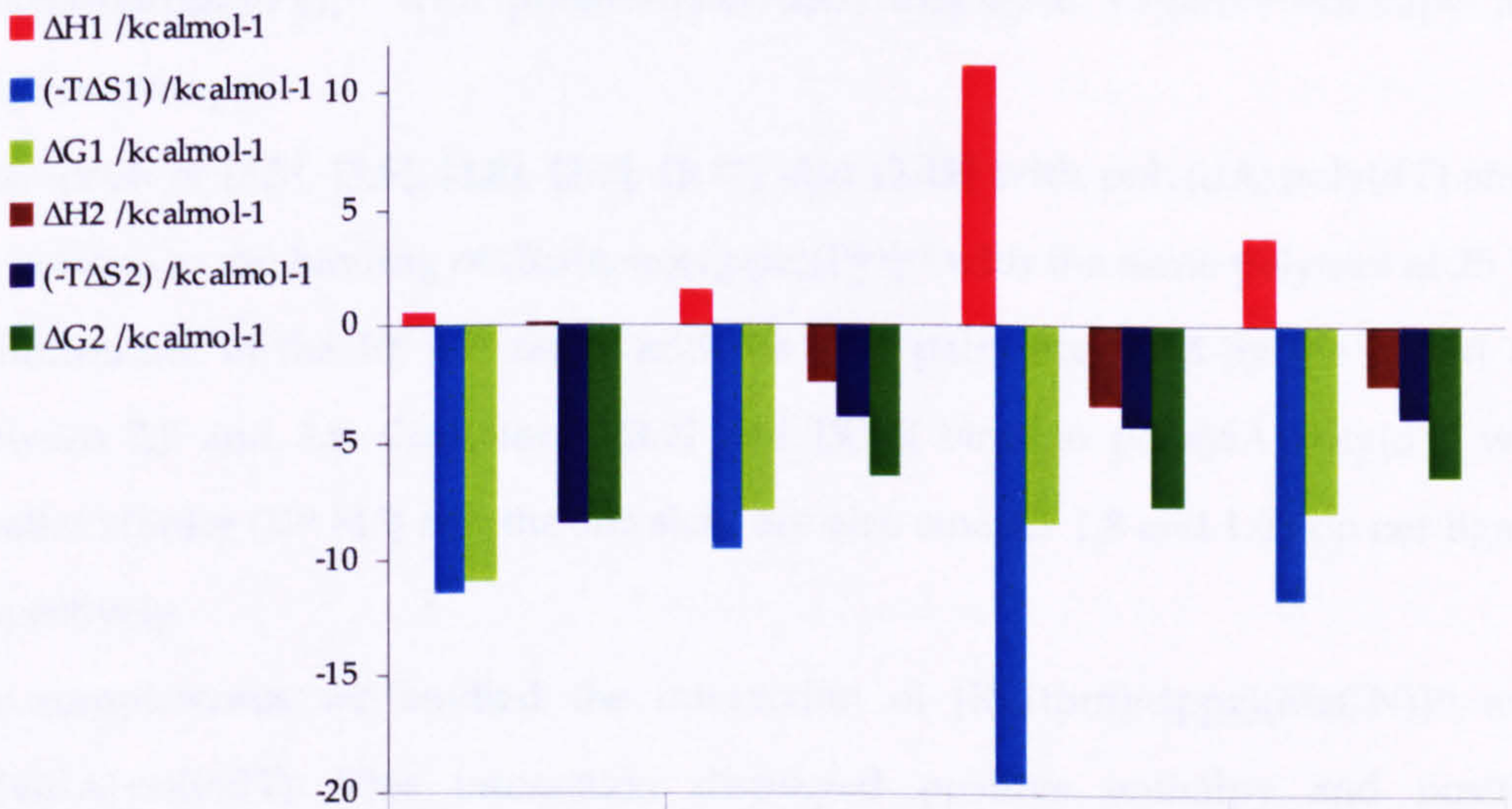

	[3.9]	[3.10]	[3.11]	[3.12]
ΔH1 /kcalmol-1	0.53	1.6	11.1	3.8
(-TΔS1) /kcalmol-1	-11.41	-9.5	-19.5	-11.7
ΔG1 /kcalmol-1	-10.88	-7.9	-8.37	-7.9
Ka1 (x10-5)/M-1	933	6.70	13.50	5.06
ΔH2 /kcalmol-1	0.17	-2.4	-3.4	-2.5
(-TΔS2) /kcalmol-1	-8.4	-3.9	-4.2	-3.9
ΔG2 /kcalmol-1	-8.23	-6.4	-7.7	-6.4
Ka2 (x10-5)/M-1	10.58	0.50	4.43	0.51

Figure 4.40: Binding thermodynamics data for the interaction of **[3.9]**, **[3.10]**, **[3.11]** and **[3.12]** with poly(dG)·poly(dC).

The above results reveal a variety of binding behaviours for the complex with natural and synthetic oligonucleotides.

Previously, Metcalfe *et al.* studied the interaction of $[Ru(tpm)(dppz)(Py)]^{2+}$ with poly(dA)·poly(dT) and poly(dG)·poly(dC) by ITC[24]. This complex showed preference for binding to poly(dG)·poly(dC) over poly(dA)·poly(dT) (almost an order of magnitude bigger) and the thermodynamic parameters for the binding with the homopolymers were quite different. The interaction of $[Ru(tpm)(dppz)(Py)]^{2+}$ with poly(dA)·poly(dT) is endothermic and hence entropically driven. Interaction of $[Ru(tpm)(dppz)(Py)]^{2+}$ with poly(dG)·poly(dC) displayed negative enthalpy and positive entropy.

Interaction of **[3.5]**, **[3.6]**, **[3.8]**, **[3.9]**, **[3.11]** and **[3.12]** with poly(dA)·poly(dT) show similarities to the binding of $[Ru(tpm)(dppz)(Py)]^{2+}$ with the same polymer at 25 °C. Affinities are in the 10^5 M^{-1} range and the base pairs occupied by the ligand are between 2.5 and 3.5. Complexes **[3.7]** and **[3.10]** bind to poly(dA)·poly(dT) with smaller affinity (10^4 M^{-1}) and the site sizes are also smaller 1.8 and 1.03 bp per ligand respectively.

For completeness we studied the interaction of $[Ru(tpm)(dppz)(MeCN)]^{2+}$ with poly(dA)·poly(dT). This interaction displayed positive enthalpy and positive entropy. The affinity of the complex for poly(dA)·poly(dT) is ~10^4 M^{-1}, having a site size of 1.38 bp per ligand. Complexes **[3.7]** and **[3.10]** interact with poly(dA)·poly(dT) in a similar way to $[Ru(tpm)(dppz)(MeCN)]^{2+}$ showing low affinity for this polymer.

Binding of $[Ru(tpm)(dppz)(Py)]^{2+}$ to poly(dG)·poly(dC) displays two binding events, the first one is endothermic and hence entropically driven while the second event displays a favoured enthalpy and entropic contribution with an affinity in the micromolar regime. Binding of **[3.5]**, **[3.7]**, **[3.10]**, **[3.11]** and **[3.12]** show similar profile with two different binding events. The first being entropically driven with enthalpies around 2.5-1.6 kcal mol^{-1}, with large binding site sizes (between four and seven) and the second being enthalpy and entropic driven, showing enthalpies between -1.9 / -2.5 kcal mol^{-1}. Binding site sizes for this second event are around 2-2.8 bp per ligand.

Interaction of $[Ru(tpm)(dppz)(MeCN)]^{2+}$ with poly(dG)·poly(dC) displayed positive enthalpy and positive entropy. The affinity of the complex for poly(dG)·poly(dC) is in the 10^4 M^{-1} range with site sizes bigger than three base pair per ligand.

Binding of **[3.6]** and **[3.8]** to poly(dG)·poly(dC) is characterised as well by low affinity and binding site sizes bigger than three base pair per ligand, similar to $[Ru(tpm)(dppz)(MeCN)]^{2+}$.

Complex **[3.9]** shows two different events, but in this case both of them enthalpic unfavoured.

Complexes **[3.5]**, **[3.10]** and **[3.11]** bind to poly(dA)·poly(dT) and poly(dG)·poly(dC) with similar affinities. Complex **[3.6]** shows a preference for binding to poly(dA)·poly(dT) over poly(dG)·poly(dC) (an order of magnitude bigger) as do **[3.8]** and **[3.12]**. In contrast complexes **[3.7]** and **[3.9]** show preference for binding to poly(dG)·poly(dC).

Since all the complexes show quite different bindings, affinities and site sizes on binding to these synthetic oligonucleotides sequences, binding thermodynamics with alternating DNA co-polymers were also examined.

Thermodynamics for the binding of **[3.5]**, **[3.6]**, **[3.7]**, **[3.8]**, **[3.9]**, **[3.10]**, **[3.11]** and **[3.12]** to poly(dA-dT)·poly(dA-dT) were studied.

The binding thermodynamics of the interaction of **[3.5]**, **[3.6]**, **[3.7]** and **[3.8]** complexes with poly(dA-dT)·poly(dA-dT) are shown in figure 4.41.

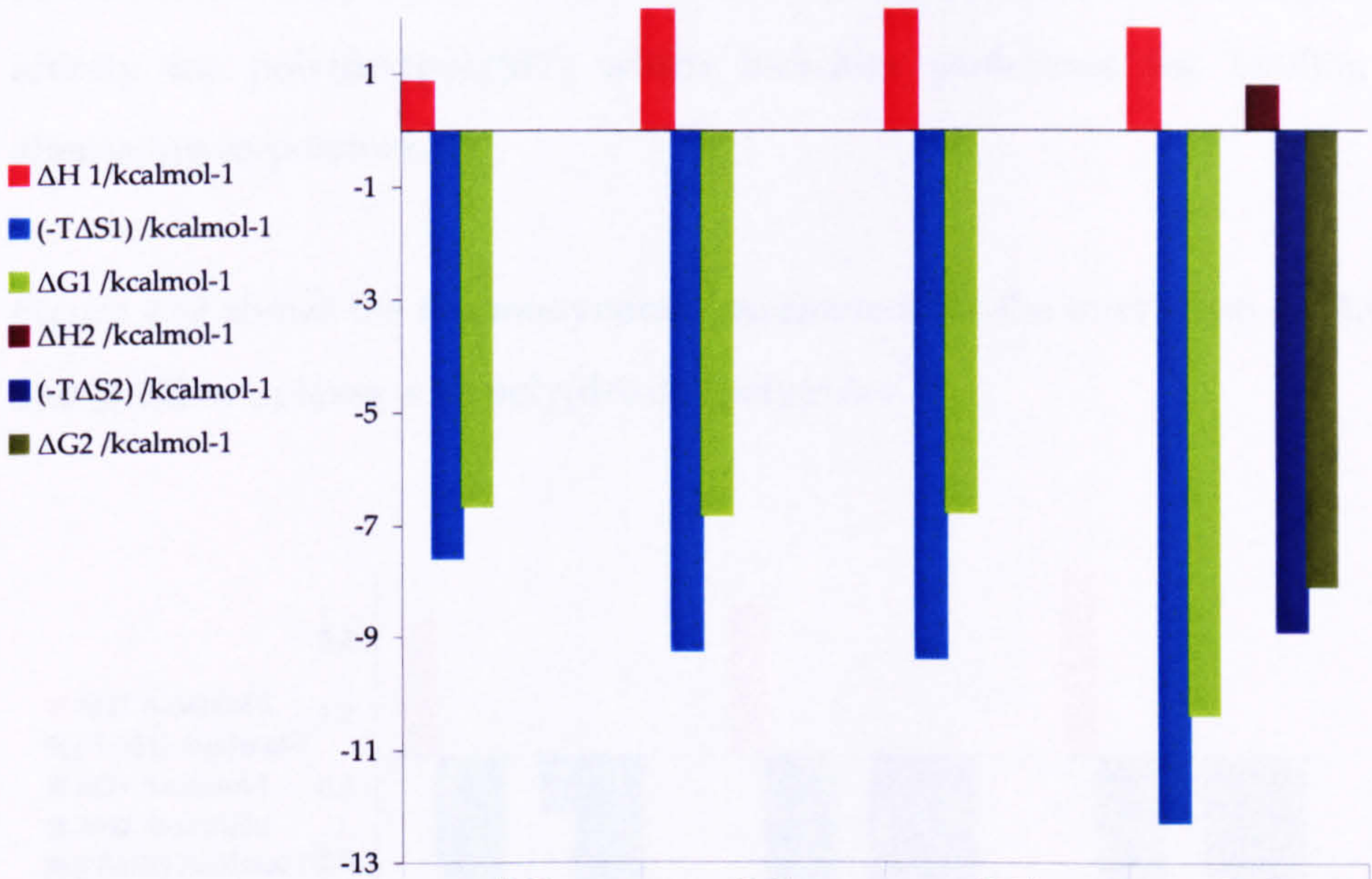

	[3.5]	[3.6]	[3.7]	[3.8]
ΔH 1/kcalmol-1	0.9	2.43	2.6	1.8
(-TΔS1) /kcalmol-1	-7.6	-9.27	-9.4	-12.3
ΔG1 /kcalmol-1	-6.68	-6.84	-6.8	-10.4
Ka1 (x10-5)/M-1	0.78	1.03	1.00	440.00
ΔH2 /kcalmol-1				0.8
(-TΔS2) /kcalmol-1				-8.9
ΔG2 /kcalmol-1				-8.1
Ka2 (x10-5)/M-1				8.60

Figure 4.41: Binding thermodynamics data of **[3.5]**, **[3.6]**, **[3.7]** and **[3.8]** binding to poly(dA-dT)·poly(dA-dT).

Complex **[3.5]** shows an entropically driven interaction with poly(dA-dT)·poly(dA-dT) with low affinity, smaller that the affinity of this complex for the poly(dA)·poly(dT) duplex, suggesting a preference for AAA or TTT tracks. Interaction of **[3.6]** and **[3.7]** with poly(dA-dT)·poly(dA-dT) are in 10^5 M^{-1} range with a site size of 3.8 and 3.59 bp per ligand respectively. Complex **[3.6]** binds to poly(dA)·poly(dT) and poly(dA-dT)·poly(dA-dT) with similar binding constants and similar site size which indicates that the two types of DNA are not discriminated by this complex. Complex **[3.7]** shows preference for binding to the co-polymer over binding to poly(dA)·poly(dT). Interaction of **[3.8]** with poly(dA-dT)·poly(dA-dT) displays two different events, both of them endothermic and therefore entropically

driven. The affinity of this complex for poly(dA-dT)·poly(dA-dT) is larger than the affinity for poly(dA)·poly(dT) which indicates preference for binding to the alternating co-polymer.

Figure 4.42 shows the thermodynamic parameters for the interaction of **[3.9]**, **[3.10]** and **[3.12]** complexes with poly(dA-dT)·poly(dA-dT).

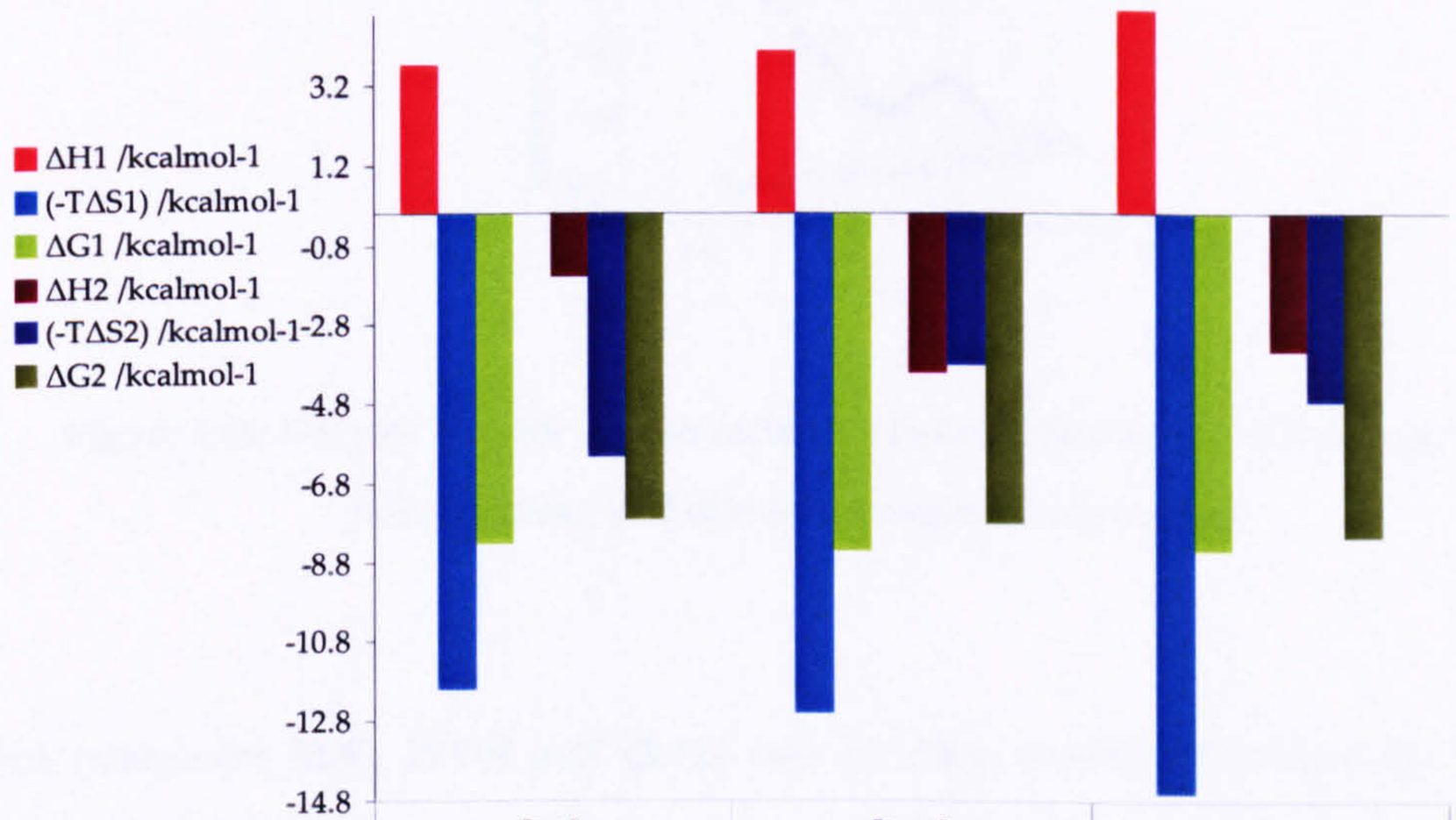

	[3.9]	[3.10]	[3.12]
ΔH1 /kcalmol-1	3.73	4.1	6.14
(-TΔS1) /kcalmol-1	-12.02	-12.6	-14.59
ΔG1 /kcalmol-1	-8.29	-8.5	-8.45
Ka1 (x10-5)/M-1	11.80	16.00	15.30
ΔH2 /kcalmol-1	-1.56	-4	-3.42
(-TΔS2) /kcalmol-1	-6.13	-3.8	-4.72
ΔG2 /kcalmol-1	-7.69	-7.8	-8.14
Ka2 (x10-5)/M-1	4.28	4.73	9.13

Figure 4.42: Binding thermodynamics of **[3.9]**, **[3.10]** and **[3.12]** binding to poly(dA-dT)·poly(dA-dT)

Complex **[3.11]** showed three different binding events (figure 4.43) again this could not be fitted with the program Origin 5.0.

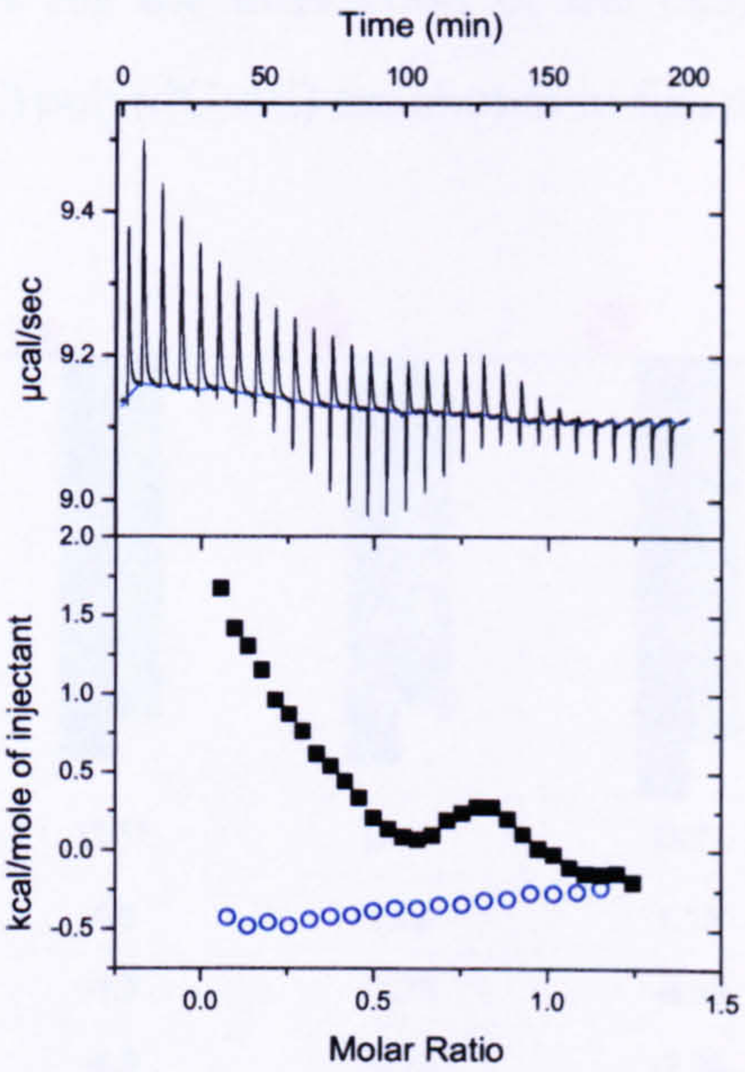

Figure 4.43: ITC raw data for the interaction of **[3.11]** with poly(dA-dT)·poly(dA-dT) (black square) and dilution experiment (open blue)

For complexes **[3.9]**, **[3.10]** and **[3.12]** two binding modes are observed. The first event is entropically driven with binding affinities in the micromolar range and large binding site sizes of 3.9-6.6 bp per ligand. The second event is enthalpy and entropy favoured with enthalpies between -1.56 and -4 kcal/mol. This negative enthalpy can be interpreted as H-bonding and/or van der Waals specific recognitions. Affinities for this second interaction are in 10^5 M^{-1} range with binding site sizes of 2-3.3 bp per ligand.

In order to complete the study, thermodynamics of the binding of **[3.5]**, **[3.6]**, **[3.7]**, **[3.8]**, **[3.9]**, **[3.10]**, **[3.11]** and **[3.12]** with poly(dG-dC)·poly(dG-dC) alternating co-polymer were also studied.

Thermodynamic parameters for the interaction of the **[3.5]**, **[3.6]**, **[3.7]** and **[3.8]** complexes with poly(dG-dC)·poly(dG-dC) are shown in figure 4.44.

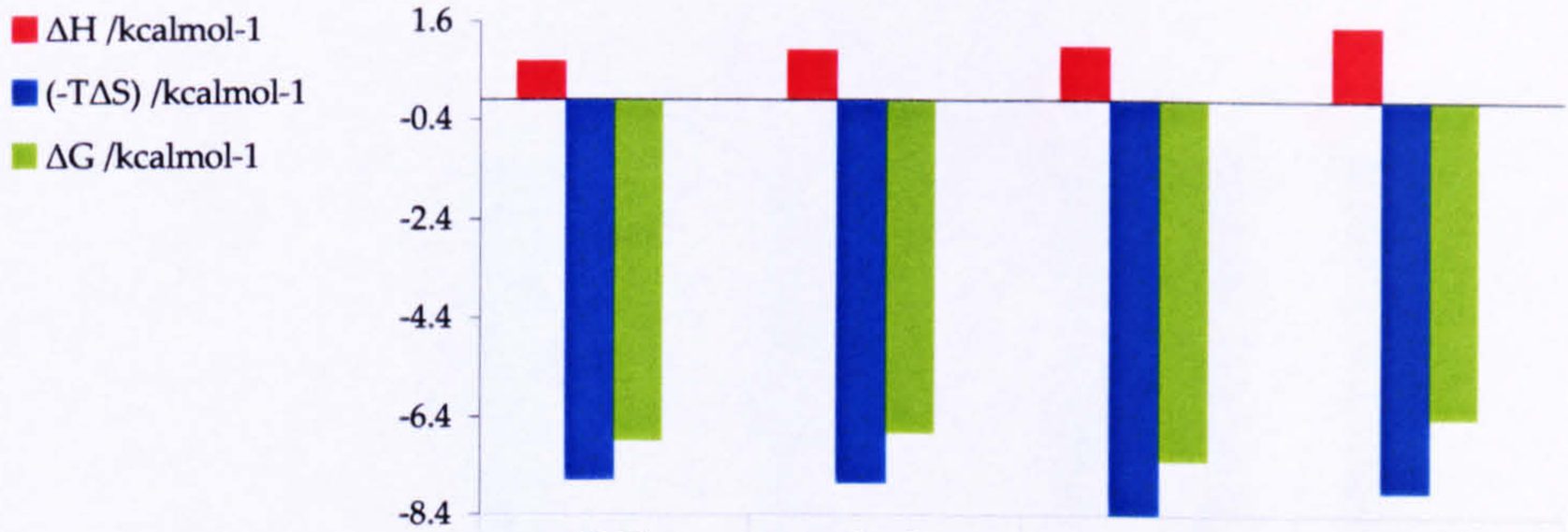

	[3.5]	[3.6]	[3.7]	[3.8]
ΔH /kcalmol-1	0.8	1.02	1.11	1.5
(-TΔS) /kcalmol-1	-7.7	-7.75	-8.39	-7.9
ΔG /kcalmol-1	-6.9	-6.73	-7.28	-6.4
Ka (x10-5)/M-1	1.00	0.85	2.15	0.46

Figure 4.44: Binding thermodynamics of **[3.5]**, **[3.6]**, **[3.7]** and **[3.8]** binding to poly(dG-dC)·poly(dG-dC)

All complexes bind to poly(dG-dC)·poly(dG-dC) in a entropic favourable way with small positive changes in enthalpy. Affinities of **[3.5]** and **[3.7]** for this polymer are in 10^5 M^{-1} range, while complexes **[3.6]** and **[3.8]** bind to poly(dG-dC)·poly(dG-dC) with smaller affinity.

Complex **[3.6]** binds to poly(dG)·poly(dC) and poly(dG-dC)·poly(dG-dC) with similar affinity and similar binding site size (3.2 and 2.9 bp per ligand respectively), which indicates that **[3.6]** does not distinguishes between CC or GG and CG sites. Similar behaviour for the complex **[3.8]** binding to both, homopolymer and co-polymer, was observed.

Thermodynamic parameters for the interaction of the **[3.9]**, **[3.10]**, **[3.11]** and **[3.12]** complexes with poly(dG-dC)·poly(dG-dC) are shown in figure 4.45.

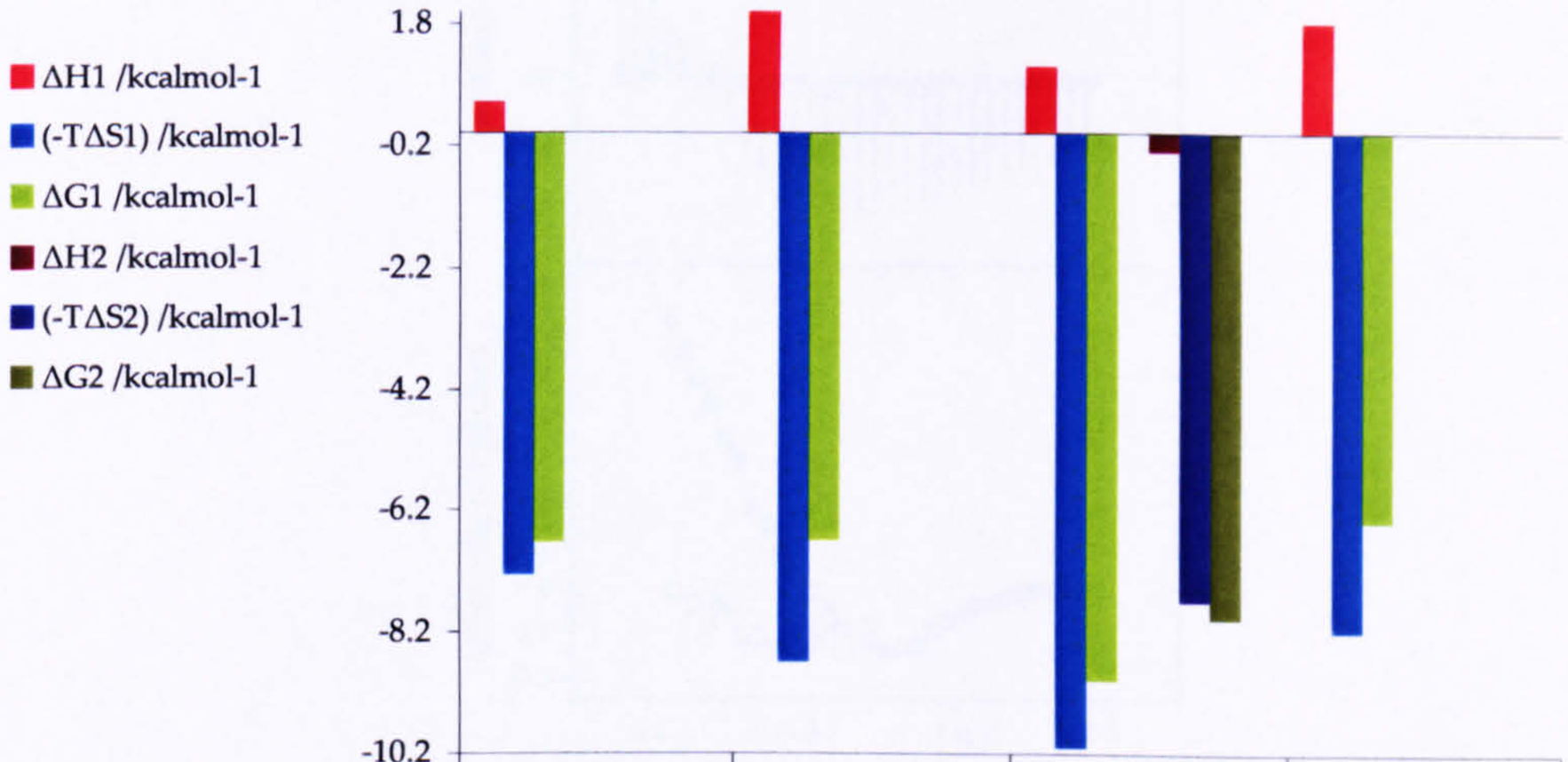

	[3.9]	[3.10]	[3.11]	[3.12]
ΔH1 /kcalmol-1	0.52	2	1.1	1.8
(-TΔS1) /kcalmol-1	-7.26	-8.7	-10.1	-8.2
ΔG1 /kcalmol-1	-6.73	-6.7	-9	-6.4
Ka1 (x10-5)/M-1	0.85	0.88	39.90	0.49
ΔH2 /kcalmol-1			-0.3	
(-TΔS2) /kcalmol-1			-7.7	
ΔG2 /kcalmol-1			-8	
Ka2 (x10-5)/M-1			7.51	

Figure 4.45: Binding thermodynamics parameters of **[3.9]**, **[3.10]**, **[3.11]** and **[3.12]** binding to poly(dG-dC)·poly(dG-dC)

Interaction of **[3.9]**, **[3.10]** and **[3.12]** with poly(dG-dC)·poly(dG-dC) is endothermic hence entropically driven, with small affinity (~10^4 M^{-1}). Interaction of **[3.11]** with poly(dG-dC)·poly(dG-dC) displays two events, one of them presents an unfavourable entropic contribution and is therefore entropically driven, while the second event shows small negative enthalpy and is also entropically favoured (figure 4.46). Binding affinities of **[3.11]** for poly(dG-dC)·poly(dG-dC) are in micromolar and 10^5 M^{-1} range, respectively, showing similar affinities for poly(dG)·poly(dC) and the alternating polymer.

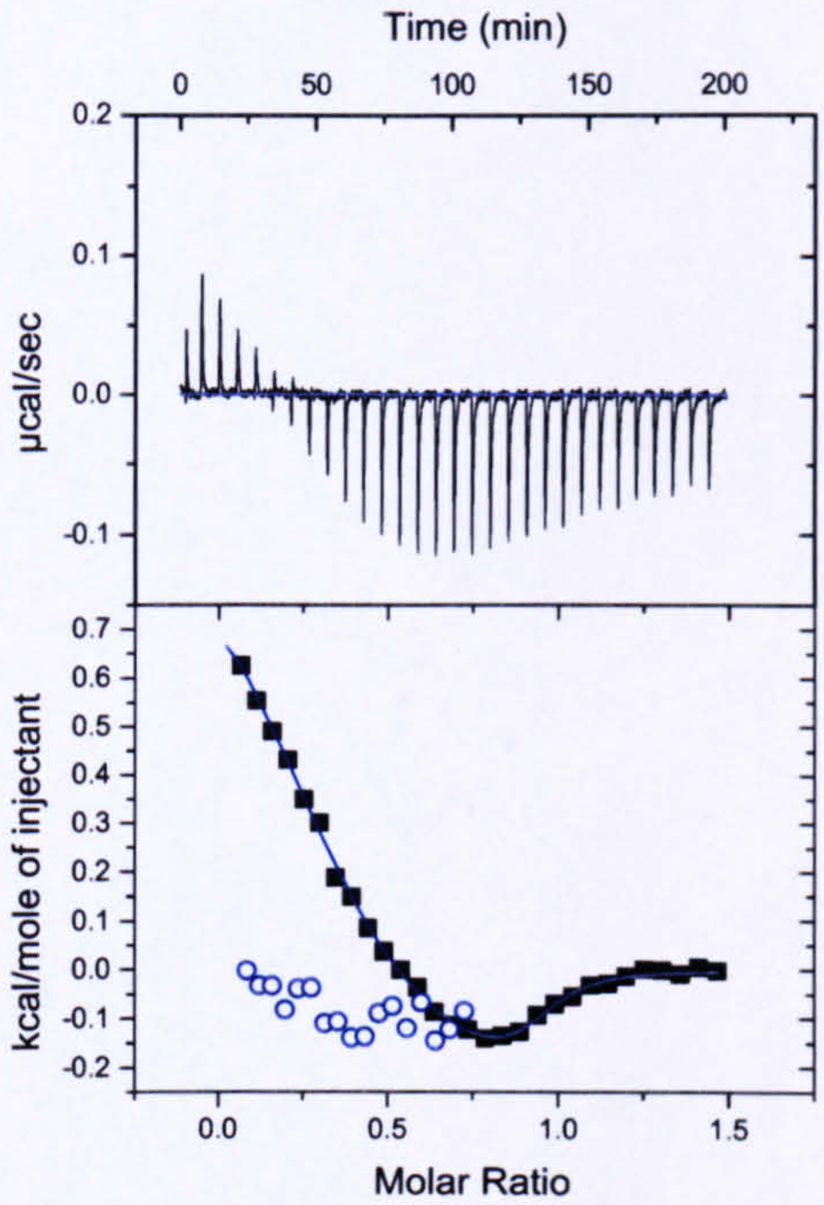

Figure 4.46: ITC raw data for the interaction of **[3.11]** with poly(dG-dC)·poly(dG-dC) (black squares) and dilution experiment (open blue)

These latter studies indicate that the complexes show different behaviour binding to poly(dA-dT)·poly(dA-dT) or poly(dG-dC)·poly(dG-dC) compared to the homopolymer. Complex **[3.5]** shows an order of magnitude bigger affinity for poly(dG-dC)·poly(dG-dC) over poly(dA-dT)·poly(dA-dT). In contrast complexes **[3.6]**, **[3.8]**, **[3.9]**, **[3.10]** and **[3.12]** all show an order of magnitude bigger affinity for poly(dA-dT)·poly(dA-dT) over poly(dG-dC)·poly(dG-dC). Complex **[3.7]** shows little preference for any of the alternating co-polymers.

Overall complex **[3.5]** binds with similar affinity to poly(dA)·poly(dT), poly(dG)·poly(dC) and poly(dG-dC)·poly(dG-dC) and with low affinity for poly(dA-dT)·poly(dA-dT). Complex **[3.10]**, also with an amide group in the pyridine ring, binds preferentially to poly(dG)·poly(dC) ($K_a \sim 10^6$ M^{-1}), showing little affinity for the alternating co-polymer. Binding of **[3.10]** to A-T tracks are in similar range, 10^5 M^{-1}.

Binding of **[3.6]** to poly(dA)·poly(dT) shows the biggest affinity compared to any other sequences. Complex **[3.11]** also show binding preference for A-T tracks but in this case affinity to poly(dA-dT)·poly(dA-dT) is in the 10^5 M^{-1} range.

Complex **[3.7]** binds with similar affinity to poly(dG)poly(dC), poly(dA-dT)·poly(dA-dT)and poly(dG-dC)·poly(dG-dC) and shows less preference for binding to poly(dA)·poly(dT). Complex **[3.11]** binds to all the different sequences studied with similar affinity.

Complex **[3.8]** and **[3.12]** binds with higher affinity to poly(dA-dT)·poly(dA-dT) than to the other sequences used.

These studies show that the complexes display different sequence selectivity and thermodynamics behaviour on binding to DNA. Further studies with shorter mixed sequences should be done in order to explore the possible binding of these complexes to highly specific DNA sequences. Also modelling studies to ascertain the nature and contacts on intercalation into DNA should be carried out.

4.6 Surface plasmon resonance (SPR)

SPR is a relatively new technique for characterising small molecules-DNA interactions. As discussed in the introduction, SPR is rapid, shows data in real time and the concentration required is small compared to other techniques. As a preliminary study into the kinetics of DNA binding we decided to investigate the interaction of $[Ru(phen)_2(dppz)]^{2+}$, $[Ru(tpm)(dppz)(Py)]^{2+}$ and $[Ru(tpm)(dppz)(MeCN)]^{2+}$ with double and single stranded DNA using the SPR. Figure 4.47 shows a typical sensorgram for the interaction of $[Ru(tpm)(dppz)(MeCN)]^{2+}$ with duplex DNA (blank reference subtracted).

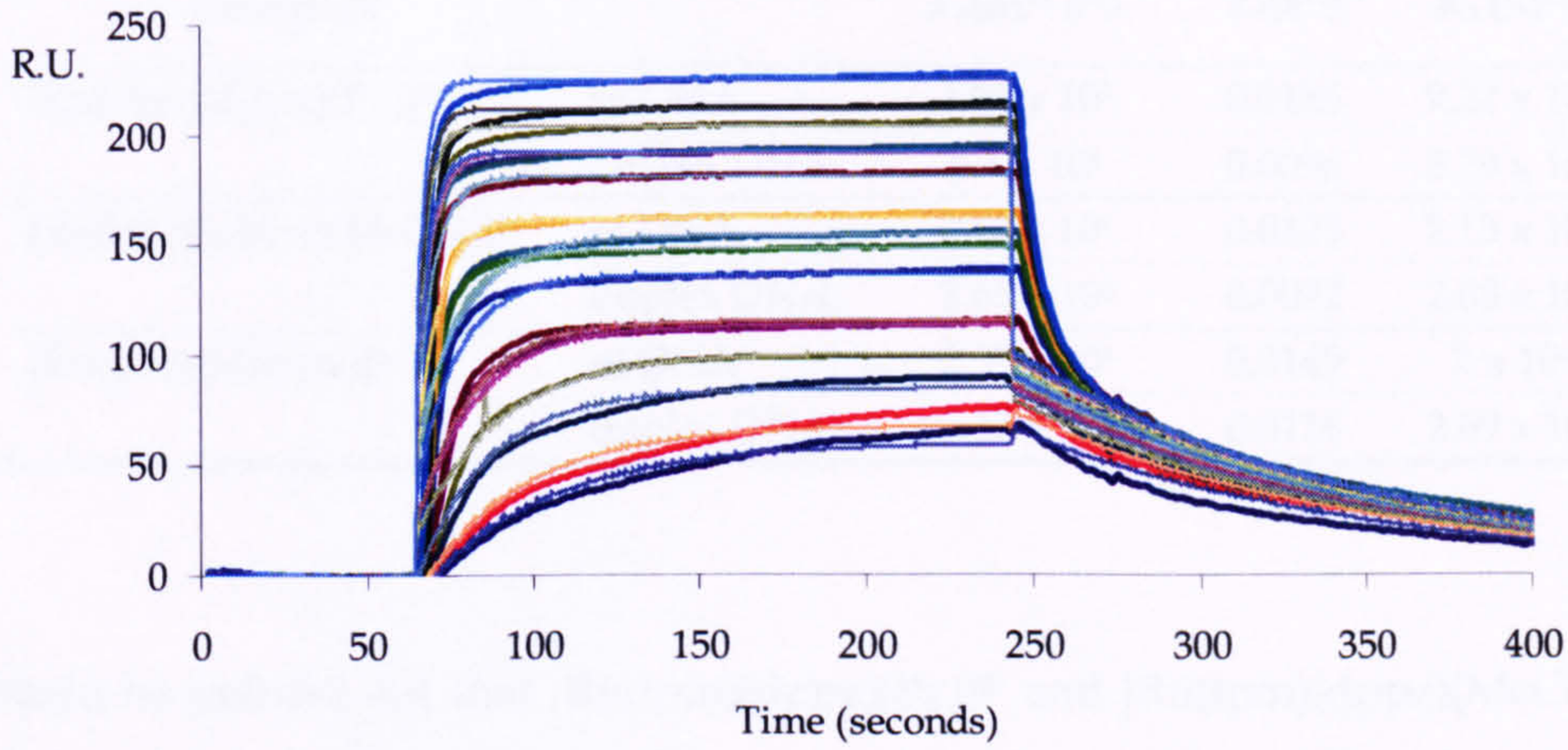

Figure 4.47: SPR sensorgram for the interaction of $[Ru(tpm)(dppz)(MeCN)]^{2+}$ with double stranded DNA

Piehler *et al.* studied the kinetics of the interaction of some organic intercalator such as actinomycin D and doxorubicin with DNA using a label-free detection technique[36]. Association rate constants between 6 x 10^3 M^{-1} s^{-1} and 10^5 M^{-1} s^{-1} were obtained for such intercalators with dissociation rate constants between 0.02 - 0.2 s^{-1}. There are very little studies on the kinetics of [Ru(dppz)] complex binding to DNA. Nordén and colleagues used stopped flow experiments to investigate dinuclear systems that, due threading onto duplex DNA, having very slow dissociations rates[37].

In this case, equilibrium constants for binding to duplex DNA obtained with SPR are in the micromolar range (non specific bindings were excluded by using a blank channel containing only buffer as a control) and are consistent with binding constants obtained with other techniques[22,24]. Surprisingly, SPR also reveals that these metal complexes bind with the same strength to single stranded DNA (ss-DNA) as to duplex DNA. Association rate constants for the interaction of these complexes with double stranded DNA are between 2.65 x 10^4 M^{-1} s^{-1} and 8.4 x 10^4 M^{-1} s^{-1} and between 2.63 x 10^4 M^{-1} s^{-1} and 1.71 x 10^5 M^{-1} s^{-1} for the interaction with ss-DNA. Disassociation rate constants between 0.0092 s^{-1} and 0.0185 s^{-1} were obtained (table 4.6).

Table 4.6: SPR data

Complex		k_a(M^{-1} s^{-1})	k_d(s^{-1})	K_a (M^{-1})
$[Ru(tpm)(dppz)(Py)]^{2+}$	ss-DNA	1.71 x 10^5	0.0185	9.22 x 10^6
	duplex DNA	8.4 x 10^4	0.0096	8.79 x 10^6
$[Ru(tpm)(dppz)(MeCN)]^{2+}$	ss-DNA	2.63 x 10^4	0.0123	2.13 x 10^6
	duplex DNA	2.65 x 10^4	0.0092	2.88 x 10^6
$[Ru(phen)_2(dppz)]^{2+}$	ss-DNA	2.99 x 10^4	0.0149	2 x 10^6
	duplex DNA	3.12 x 10^4	0.0116	2.69 x 10^6

It should be pointed out that $[Ru(tpm)(dppz)(Py)]^{2+}$ and $[Ru(tpm)(dppz)(MeCN)]^{2+}$ are achiral but $[Ru(phen)_2(dppz)]^{2+}$ was used as a racemic mixture. However, it has been proved that Δ- and Λ- $[Ru(phen)_2(dppz)]^{2+}$ have very similar binding affinities with no distinctive enantioselectivity[21]. Complexes $[Ru(tpm)(dppz)(MeCN)]^{2+}$ and $[Ru(phen)_2(dppz)]^{2+}$ show similar kinetic and thermodynamics properties while $[Ru(tpm)(dppz)(Py)]^{2+}$ shows slightly higher binding affinity. All three complexes dissociate from ss-DNA faster than duplex. In particular complex $[Ru(tpm)(dppz)(Py)]^{2+}$ shows a dissociation rate ss-DNA that is twice that of the duplex.

As mentioned before binding affinities for the interaction of these three metallo-interacalators with single stranded DNA showed little difference with the affinities for duplex DNA.

To confirm the high affinity for ss-DNA, luminescence titrations of rac-$[Ru(phen)_2(dppz)]^{2+}$ with a available ss-DNA were carried out. Emission of the complex is switched on when ss-DNA (5′-ACGTTCGAACCGTGA-3′) was added to a complex solution (figure 4.48). This is in agreement with the data presented by Coates and co-workers which showed that $[Ru(phen)_2(dppz)]^{2+}$ does show a light switch effect with ss-DNA but is required a minimum of 6 base pairs to produce this effect.

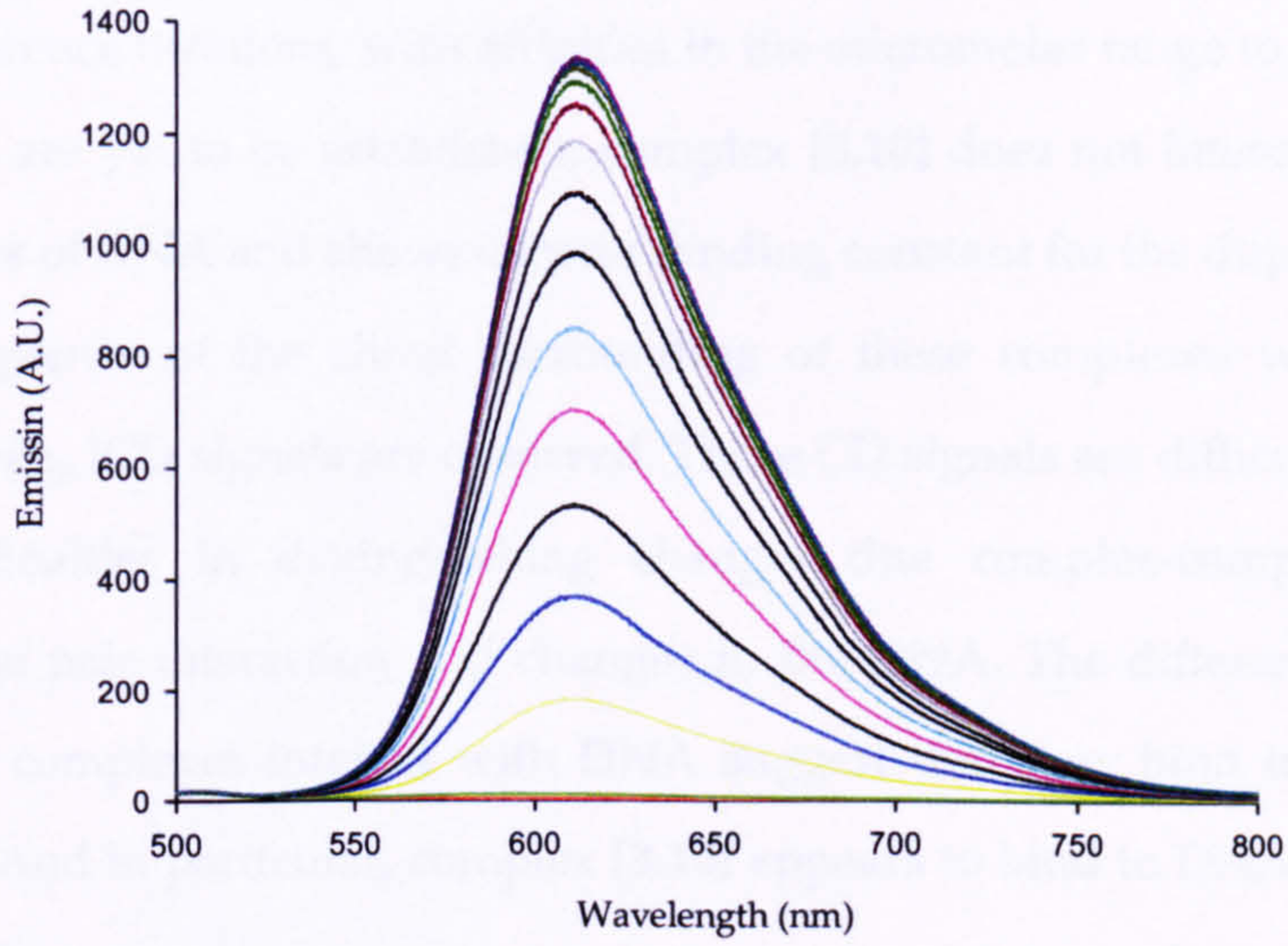

Figure 4.48: Luminescence titration of *rac*-$[Ru(phen)_2(dppz)]^{2+}$ with ss-DNA

The binding curves for this interaction and binding parameters obtained from fits to the McGhee-von Hippel model did not give reasonable data, and therefore the binding parameters were not measured due the poor quality of the data.

Further luminescence studies with the same single strand sequence used with the SPR should be done in order to compare the affinities obtained with both methods.

4.7 Conclusions and future work

In this chapter the interaction of several Ru(II)-tpm complexes with different types of DNA is reported. The complexes contain both ligands capable of intercalation between the base pairs of DNA and ancillary ligands with hydrogen accepting and/or donating moieties.

While studying the interaction of these complexes with DNA, different techniques were used. First of all, melting points were used to determine whether these metal complexes produce stabilisation of CT-DNA. To assess the DNA-binding mode of the metal complexes viscosity measurements were performed and it was found that in most of the cases these complexes bind via intercalation.

Binding affinities of these complexes to CT-DNA were then determined by UV-Vis and luminescence titrations, with affinities in the micromolar range to CT-DNA. For reasons that are yet to be established, complex **[3.10]** does not intercalate between the base pairs of DNA and shows a lower binding constant for the duplex.

As a consequence of the chiral surrounding of these complexes when they are bound to DNA, ICD signals are observed. These CD signals are difficult to interpret due to difficulties in distinguishing changes due complex-complex stacking, complex-base pair interaction and changes in the DNA. The different signals that occur when complexes interact with DNA suggest that they bind in a variety of geometries. And in particular, complex **[3.10]** appears to bind to DNA in a different way to the other complexes.

From the thermodynamics profiles for the interactions of these complexes with different types of DNA, we can observe that complexes containing a carbonyl group show binding preference for the interaction with GC sequences. In contrast the complexes without CO unit show binding preferentially to AT sequences.

In contrast with analogous complexes containing other pyridine derivatives, complex **[3.9]**, which contains the isonicotinamide group, showed two different modes of interaction when binding to CT-DNA. It is striking that **[3.9]** shows different binding behaviour compared to **[3.5]** (which contains a nicotinamide ligand). This observation suggests that modulation of binding can be dependant on the position of the H-boding substituent.

Different sequence selectivity and thermodynamics behaviour are observed depending on the ancillary ligand used. Whether this is due to specific H-bonds contacts has been not established.

Further studies should be done in order to understand the interaction of these complexes with DNA, for example study of the interaction with shorter mixed sequences to explore any selectivity or computational modelling studies. Additionally, in vivo studies may reveal whether these complexes can interact with biomolecules in cells.

Other techniques, such as, emission life times, photoexcitation of these complexes in the presence and absence of oxygen, time resolved anisotropy measurements

(TRAMS), SPR, AFM, etc could also be carried out to fully characterise the interaction of these complexes with DNA.

4.8 References

(1) *Nucleic Acids in Chemistry and Biology*; 2nd ed.; Blackburn, G. M.; Gait, M. J., Eds.; Oxford University Press, 1996.

(2) Satyanarayana, S.; Dabrowiak, J. C.; Chaires, J. B. *Biochemistry* **1993**, *32*, 2573-2584.

(3) Nair, R. B.; Teng, E. S.; Kirkland, S. L.; Murphy, C. J. *Inorg. Chem.* **1998**, *37*, 139-141.

(4) Lerman, L. S. *J. Mol. Biol.* **1961**, *3*, 18-30.

(5) Cohen, G.; Eisenberg, H. K. *Biopolymers* **1969**, *8*, 45-55.

(6) Long, E. C.; Barton, J. K. *Acc. Chem. Res.* **1990**, *23*, 271-273.

(7) Satyanarayana, S.; Dabrowiak, J. C.; Chaires, J. B. *Biochemistry* **1992**, *31*, 9319-9324.

(8) Suh, D.; Chaires, J. B. *Bioorg. Med. Chem.* **1995**, *3*, 723-728.

(9) Huang, C. Y. *Methods Enzymol.* **1982**, *87*, 509-525.

(10) Duveneck, G. L.; Kumar, C. V.; Turro, N. J.; Barton, J. K. *J. Phys. Chem.* **1988**, *92*, 2028-2032.

(11) Kumar, C. V.; Barton, J. K.; Turro, N. J. *J. Am. Chem. Soc.* **1985**, *107*, 5518-5523.

(12) Scatchard, G. *Ann. N. Y. Acad. Sci.* **1949**, *51*, 660-672.

(13) McGhee, J. D.; von-Hippel, P. H. *J. Mol. Biol.* **1974**, *86*, 469-489.

(14) Norden, B.; Kurucsev, T. *J. Mol. Rec.* **1994**, *7*, 141-155.

(15) Norden, B.; Tjerneld, F. *Biopolymers* **1982**, *21*, 1713-1734.

(16) Wiseman, T.; Williston, S.; Brandts, J. F.; Lin, L. N. *Anal. Biochem.* **1989**, *179*, 131-137.

(17) *Methods in enzymology*; Chaires, J. B.; Waring, M. J., Eds.; Academic press, 2001; Vol. 340.

(18) Ren, J.; Chaires, J. B. *Biochemistry* **1999**, *38*, 16067-16075.

(19) Liu, J.-G.; Zhang, Q.-L.; Ji, L.-N.; Cao, Y.-Y.; Shi, X.-F. *Transition Met. Chem.* **2001**, *26*, 733-738.

(20) Liu, J.-G.; Zhang, Q.-L.; Shi, X.-F.; Ji, L.-N. *Inorg. Chem.* **2001**, *40*, 5045-5050.

(21) Hiort, C.; Lincoln, P.; Norden, B. *J. Am. Chem. Soc.* **1993**, *115*, 3448-3454.

(22) Haq, I.; Lincoln, P.; Suh, D.; Norden, B.; Chowdhry, B. Z.; Chaires, J. B. *J. Am. Chem. Soc.* **1995**, *117*, 4788-4796.

(23) Dougherty, G.; Pilbrow, J. R. *Int. J. Biochem.* **1984**, *16*, 1179-1192.

(24) Metcalfe, C.; Adams, H.; Haq, I.; Thomas, J. A. *Chem. Commun.* **2003**, 1152-1153.

(25) Nair, R. B.; Murphy, C. J. *J. Inorg. Biochem.* **1998**, 129-133.

(26) Phillips, T.; Haq, I.; Meijer, A. J. H. M.; Adams, H.; Soutar, I.; Swanson, L.; Sykes, M. J.; Thomas, J. A. *Biochemistry* **2004**, *43*, 13657-13665.

(27) Johnson, B. B.; Dahl, K. S.; Tinoco, I., Jr.; Ivanov, V. I.; Zhurkin, V. B. *Biochemistry* **1981**, *20*, 73-78.

(28) Spingler, B.; Da Pieve, C. *Dalton Trans.* **2005**, 1637-1643.

(29) Srinivas, V. R.; Bhanuprakash Reddy, G.; Surolia, A. *FEBS Lett.* **1999**, *450*, 181-185.

(30) Matulis, D.; Rouzina, I.; Bloomfield, V. A. *J. Mol. Biol.* **2000**, *296*, 1053-1063.

(31) Jung, H.-I.; Bowden, S. J.; Cooper, A.; Perham, R. N. *Protein Sci.* **2002**, *11*, 1091-1100.

(32) Jung, H.-I.; Cooper, A.; Perham, R. N. *Biochemistry* **2002**, *41*, 10446-10453.

(33) Marky, L. A.; Kupke, D. W. *Biochemistry* **1989**, *28*, 9982-9988.

(34) Qu, X.; Ren, J.; Riccelli, P. V.; Benight, A. S.; Chaires, J. B. *Biochemistry* **2003**, *42*, 11960-11967.

(35) Haq, I.; Ladbury, J. *J. Mol. Rec.* **2000**, *13*, 188-197.

(36) Piehler, J.; Brecht, A.; Gauglitz, G.; Zerlin, M.; Maul, C.; Thiericke, R.; Grabley, S. *Anal. Biochem.* **1997**, *249*, 94-102.

(37) Onfelt, B.; Lincoln, P.; Norden, B. *J. Am. Chem. Soc.* **2001**, *123*, 3630-3637.

Chapter Five

Chiral Ru(II) complexes and Ru(II) complexes with an extended intercalative ligand

5.1 Introduction

In previous chapters the synthesis and interaction of Ru(II)-dppz complexes, containing hydrogen accepting and/or donating groups, with DNA were studied. In an attempt to investigate new system with different properties, derivatives of Ru(II)-tpm complexes containing chiral ancillary ligands or a longer intercalative motif were synthesised and the effect on DNA-binding behaviour was examined.

5.1.1 Chiral-Ru(tpm)(dppz) complexes

Octahedral metal complexes containing three bidentate ligands are chiral. Therefore substitution with one functional group on one bidentate ligand generates two isomers each of which is a pair of enantiomers (figure 5.1). The tpm ligand allows us to synthesise achiral metal complexes and hence it is possible to create enantiomerically pure metal complex relatively easy by attaching chiral ancillary ligands to the centre. Therefore Ru(II)-(tpm)-dppz complexes based on chiral amino acids were synthesised and their interaction with DNA was studied.

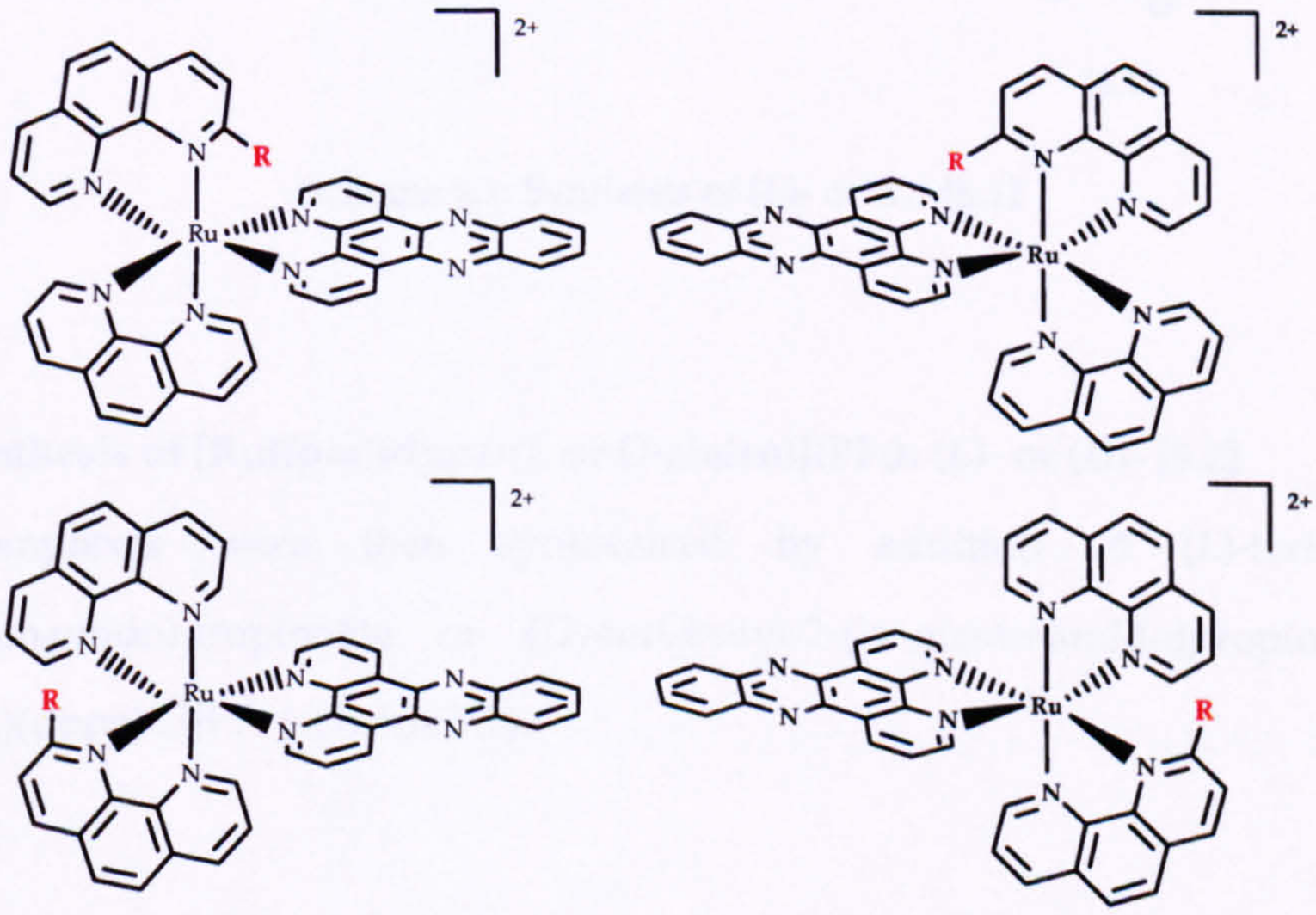

Figure 5.1: Λ and Δ- $[Ru(phen)_2(dppz)]^{2+}$derivatives. Substitutions in one of the phen ring (R) results in two isomers for each enantiomer

5.1.2 Ru(tpm)-complexes with an extended intercalative ligand

Complexes containing the extended intercalator ligand, dppn, have also been synthesised with hydrogen accepting and/or donating substitutes on the pyridine ring. The aim of this research was to investigate the effect of an increase in intercalative surface areas has on sequence selectivity in DNA binding.

5.2 Synthesis studies of chiral-Ru(tpm)(dppz) complexes

5.2.1 Synthesis of (*L*)- and (*D*)- tert-butyl 2-(isonicotinamido)propanoate (*L*)- or (*D*)- [5.1]

(*L*) or (*D*) -tert-butyl 2-(isonicotinamido)propanoate were prepared according to the method of Vagg *et al.*[1], through reaction of isonicotinic chloride with (*L*)- or (*D*)-alanine tert-butyl ester hydrochloride (scheme 5.1).

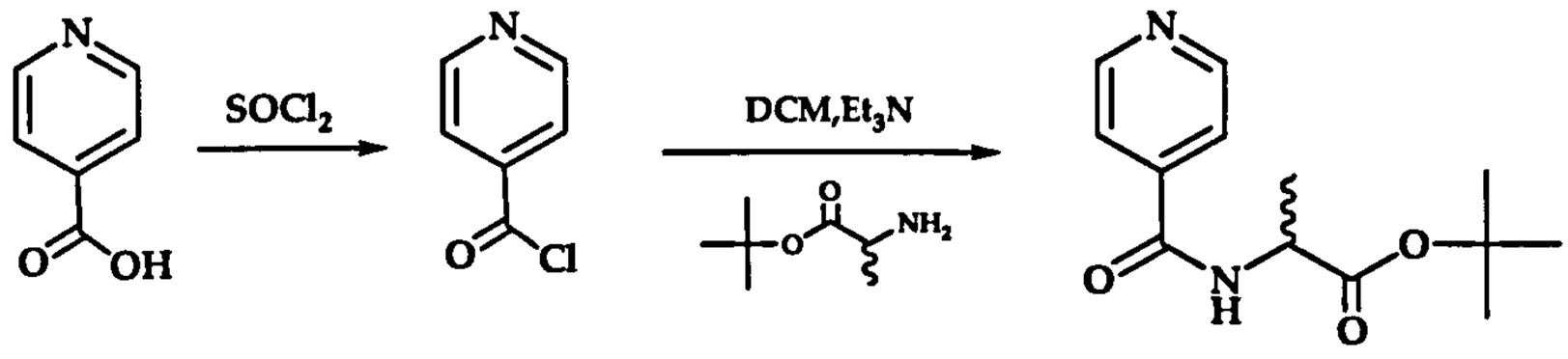

Scheme 5.1: Synthesis of (*L*)- or (*D*)-[5.1]

5.2.2 Synthesis of [Ru(tpm)(dppz)(*L* or *D*-alaiso)]$(PF_6)_2$ (*L*)- or (*D*)- [5.2]

The complexes were then synthesised by addition of (*L*)-tert-butyl-2-(isonicotinamido)propionate or (*D*)-tert-butyl-2-(isonicotinamido)propionate to [Ru(tpm)(dppz)Cl]PF_6 (scheme 5.2).

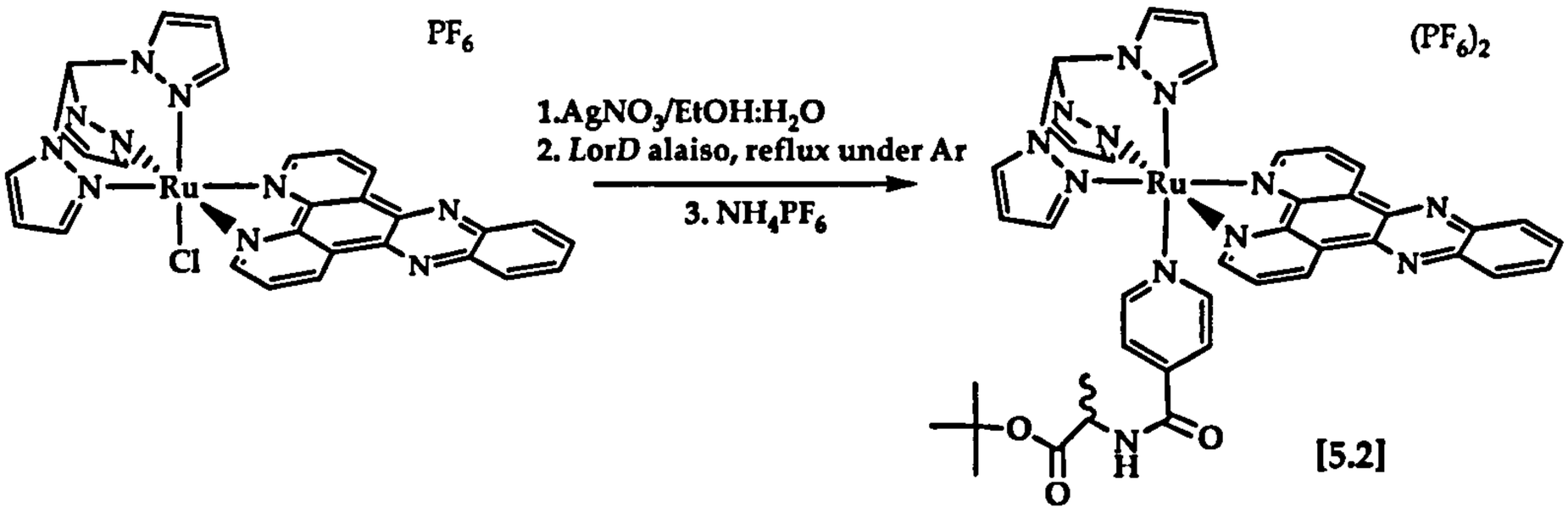

Scheme 5.2: Synthesis of **(*L*)- [5.2]** and **(*D*)- [5.2]** complexes

5.2.3 Synthesis of [Ru(tpm)(dppz)(*L* or *D*-hist)]$(PF_6)_2$ (*L*)- or (*D*)- [5.3]

Using a similar method, *L*- or *D*- histidine derivatives were also synthesised (scheme 5.3).

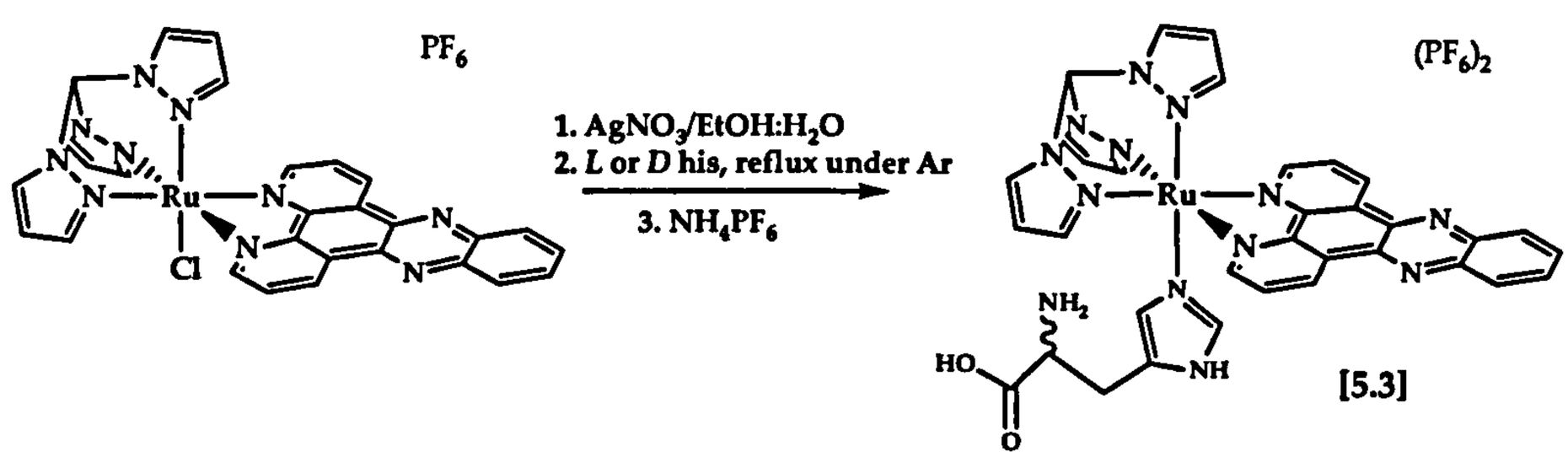

Scheme 5.3: Synthesis of **(*L*)- [5.3]** and **(*D*)- [5.3]** complexes

5.3 Characterisation of chiral-[Ru(tpm)(dppz)] complexes

All the amino acid based complexes were characterised by ^1H NMR spectroscopy and FAB-MS.

5.3.1 Electrochemistry studies

Cyclic voltammgrams for **(*L*)-, (*D*)- [5.2]** and **(*L*)-, (*D*)- [5.3]** were carried out at a scan rate 200 mV s^{-1} in acetonitrile containing 0.1 M TBAP, as supporting electrode, under nitrogen atmosphere. Potentials were measured *vs.* Ag/AgCl.

Complexes **(*L*)-** and **(*D*)- [5.2]** showed a chemically reversible one electron oxidation for the Ru(III)/Ru(II) couple at + 1.15 V. The oxidation of the Ru(II) centre in the $[Ru(tpm)(dppz)(Ison)]^{2+}$ complex (**[3.9]**, see chapter three) is at + 1.35 V. The (*L*)- or (*D*)-tert-butyl-2-(isonicotinamido)propionate ligand appears to increase the electron density at the metal centre, shifting the oxidation cathodically.

Complexes **(*L*)-** and **(*D*)- [5.3]** showed a chemically and electrochemically reversible oxidation of the Ru(III)/Ru(II) at + 1.24 V. The imidazole group is considered an aromatic ring with much less electron rich density than pyrrole, and therefore oxidation of the Ru(III)/Ru(II) couple in complexes **[5.3]** occurs at higher potential. Data are summarised in table 5.1.

The reductions of these complexes were also studied and once more reductions were not completely reversible. The dppz ligand is easier to reduce than the other N-donor ligands, so probably the first wave is caused by the reduction of the dppz ligand (the same effect has been seen in complexes studied in chapter four with similar structures, having the first reduction between -0.70 and -0.90 V). The second wave is due the reduction of aromatic residues on the ancillary ligands present in the complexes.

Table 5.1: Cyclic voltammetry data for **(*L*)-, (*D*)- [5.2]** and **(*L*)-, (*D*)- [5.3]**

Complex	Oxidations	Reductions
	$E_{1/2}$ (V)	$E_{1/2}$ (V)[a]
(*L*)- and **(*D*)- [5.2]**	1.15	-0.82, -1.06
(*L*)- and **(*D*)- [5.3]**	1.24, 1.47	-0.718, -0.99

[a] Reductions are not fully chemically reversible, only E_p values are quoted.

5.3.2 UV-Vis spectroscopy studies

UV-Vis absorption spectra of **(*L*)-, (*D*)- [5.2]** and **(*L*)-, (*D*)- [5.3]** complexes were recorded in acetonitrile solutions at room temperature (figure 5.2). Data are summarised in table 5.2.

All complexes show a band between 250-300 nm that can be assigned to the high energy $\pi \rightarrow \pi^*$ transition in aromatic nitrogen donor ligands. All of them also show a band around 350 nm which can be assigned to HOMO-LUMO transitions of the dppz ligand[2]. The low energy metal-ligand charge transfer transitions (MLCT) are between 413-460 nm, typical for Ru(II)→ L, MLCT bands.

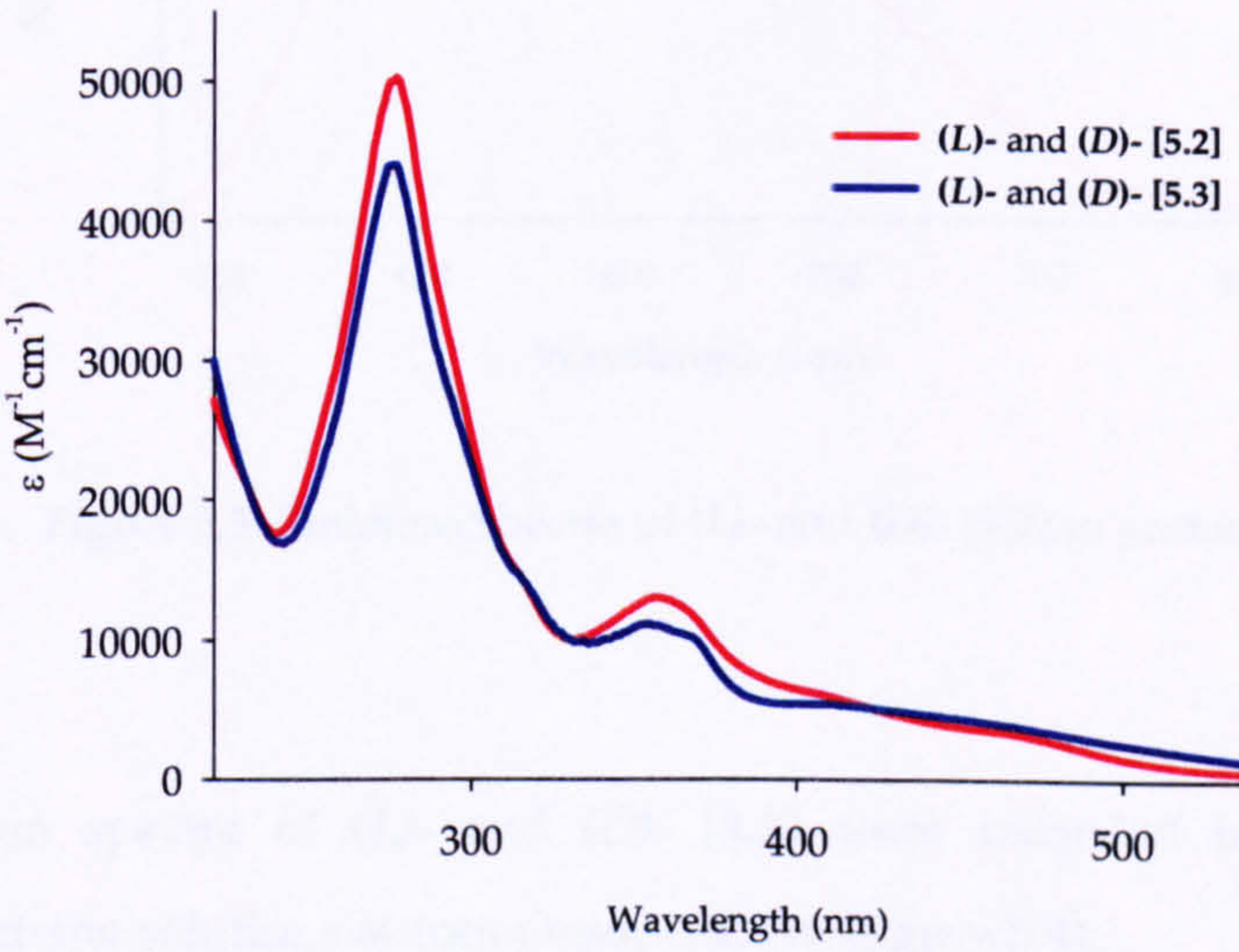

Figure 5.2: UV-Vis spectra **(*L*)-, (*D*)- [5.2]** and **(*L*)-, (*D*)- [5.3]** complexes recorded in acetonitrile

Table 5.2: UV-Vis data of **(*L*)-, (*D*)- [5.2]** and **(*L*)-, (*D*)- [5.3]**

Complex	λ_{max} (nm)	ε ($M^{-1}cm^{-1}$)	Assignment
(*L*)- and (*D*)- [5.2]	460	sh	MLCT
	357	12964	$\pi \rightarrow \pi^*$
	276	49968	$\pi \rightarrow \pi^*$
(*L*)- and (*D*)- [5.3]	413	5368	MLCT
	367	10206	$\pi \rightarrow \pi^*$
	352	10968	$\pi \rightarrow \pi^*$
	276	43868	$\pi \rightarrow \pi^*$

5.3.3. Luminescence studies

Emission spectra of **(*L*)-** and **(*D*)- [5.2]** were recorded in acetonitrile (figure 5.3). Both complexes show an emission around 630 nm when the excitation is in the MLCT, at around 460 nm. Data are normalised for clarity.

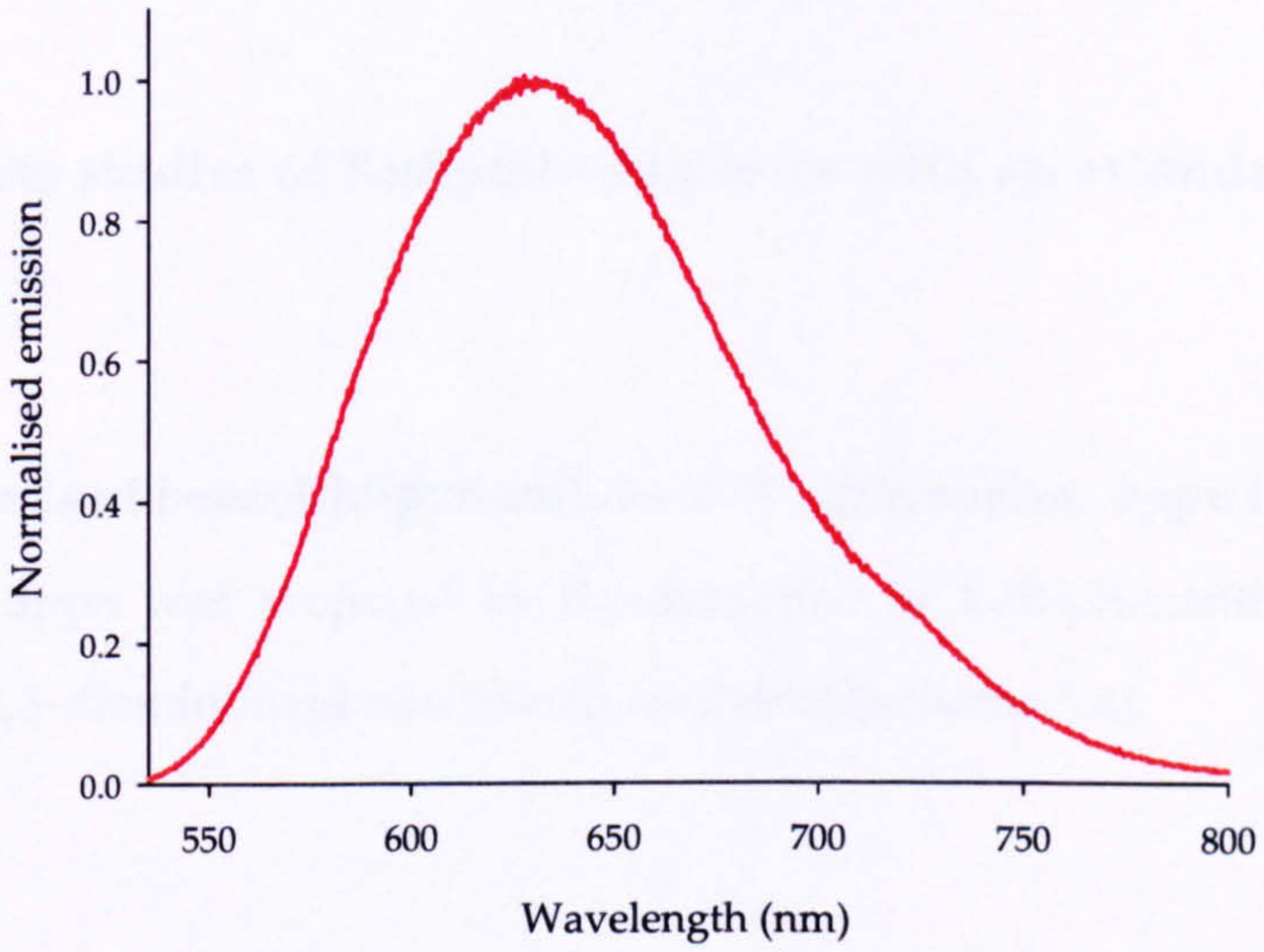

Figure 5.3: Emission spectra of **(*L*)-** and **(*D*)- [5.2]** in acetonitrile

The emission spectra of **(*L*)-** and **(*D*)- [5.3]** were recorded in acetonitrile and dichloromethane solutions at room temperature (figure 5.4).

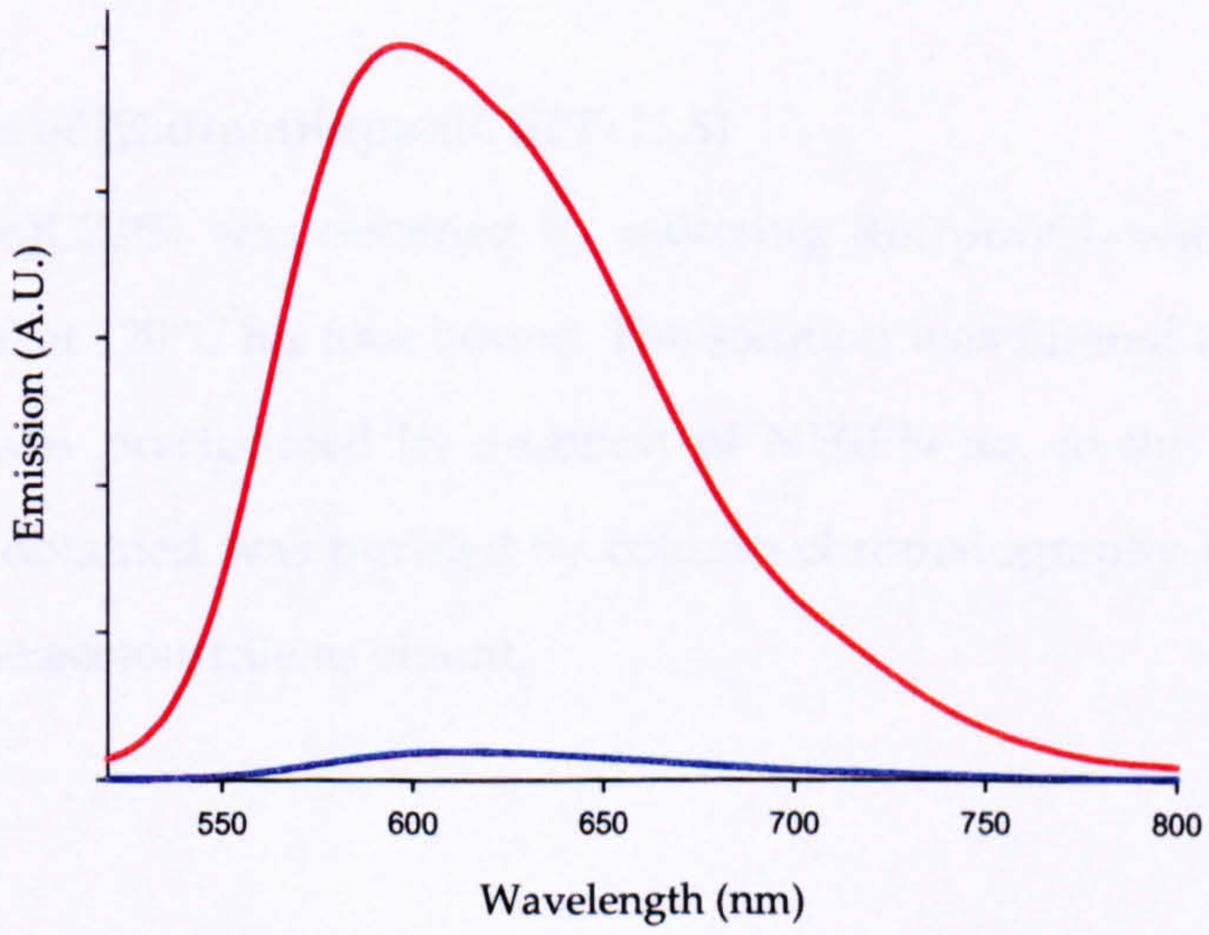

Figure 5.4: Emission spectra of **(*L*)-** and **(*D*)- [5.3]** dissolved in DCM (red) and MeCN (blue)

Unusually, in this case the emission of the complexes is complete quenched when the spectra is recorded in acetonitrile, but when the complexes are dissolved in dichloromethane, acetone or nitromethane both show an emission around 625 nm. The reason for this effect is unclear.

5.5 Synthesis studies of Ru(tpm)-complexes with an extended intercalative ligand

5.5.1. Synthesis of benzo[*i*]dipyrido[3,2-a:2′,3′-c]phenazine, dppn [5.4]

The ligand dppn was prepared by condensation of 1,10-phenanthroline-5,6-dione (dpq) with 2,3-diaminonaphathalene in methanol[3](scheme 5.4).

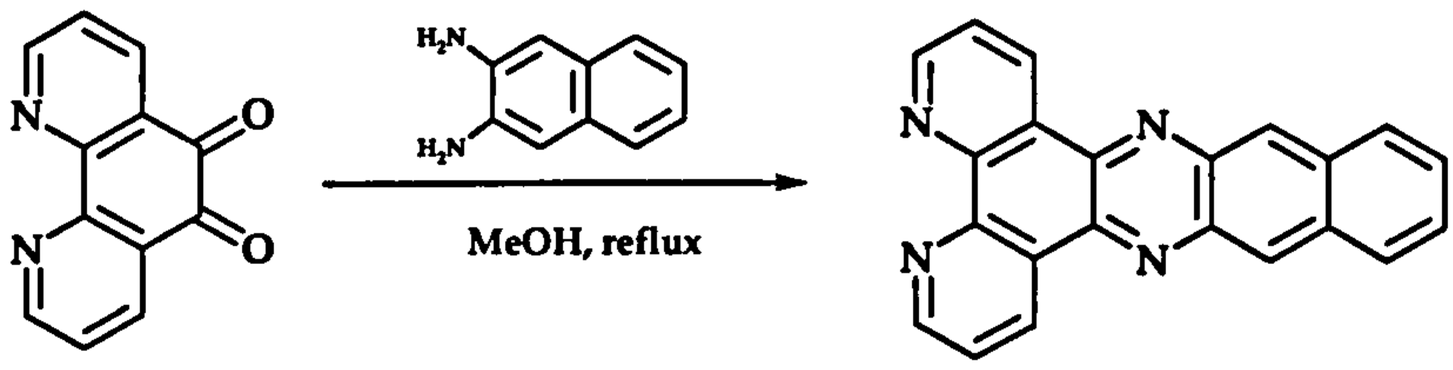

Scheme 5.4: Synthesis of dppn ligand

5.5.2 Synthesis of [Ru(tpm)(dppn)Cl]PF_6 [5.5]

[Ru(tpm)(dppn)Cl]PF_6 was obtained by refluxing Ru(tpm)Cl_3 with dppn ligand in ethylene glycol at 120°C for four hours[4]. The solution was filtered through celite and the complex was precipitated by addition of NH_4PF_6 aq. to the solution (scheme 5.5).The solid obtained was purified by column chromatography on alumina grade I, using toluene:acetonitrile as eluent.

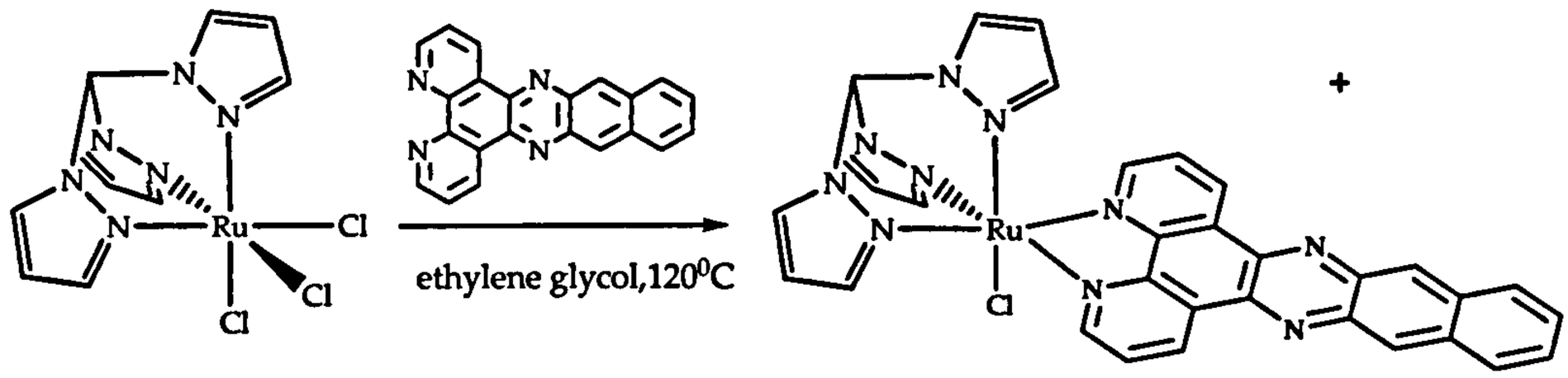

Scheme 5.5: Synthesis of **[5.5]**

5.5.3 Synthesis of $[Ru(tpm)(dppn)(Nic)](PF_6)_2$ and $[Ru(tpm)(dppn)(4\text{-}NH_2py)](PF_6)_2$ [5.6] and [5.7]

Refluxing $[Ru(tpm)(dppn)Cl]PF_6$ with silver nitrate for five hours in ethanol/water (3:1) allowed the removal of the chloride ligand. The target complexes were then synthesised by addition of the relevant ligand and refluxed overnight. Precipitation of the complexes was obtained by addition of NH_4PF_6 (scheme 5.6).

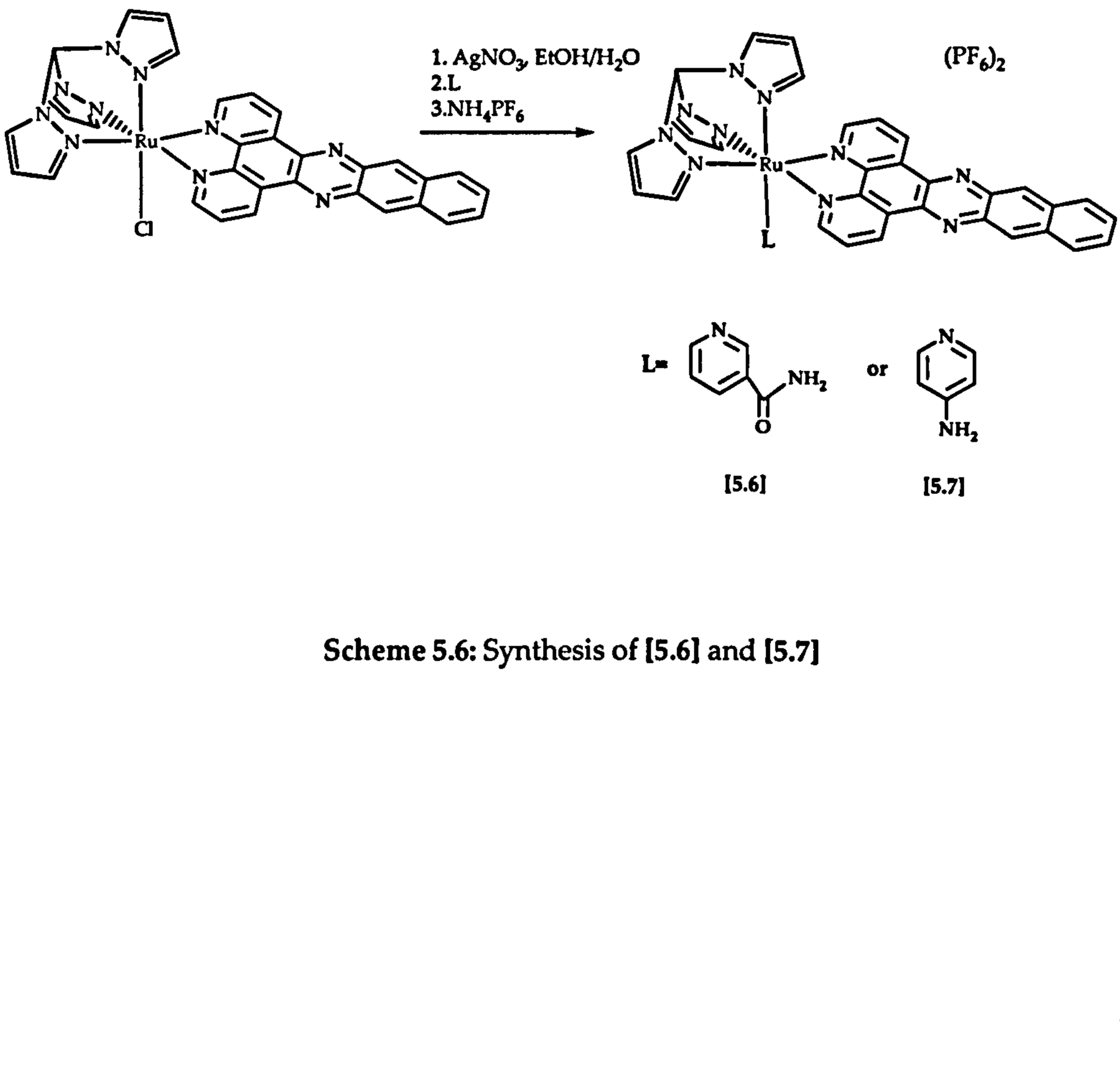

Scheme 5.6: Synthesis of **[5.6]** and **[5.7]**

5.6 Characterisation of [Ru(tpm)(dppn)(L)](PF$_6$)$_2$

5.6.1 ^{1}H NMR spectroscopy studies

The complexes were fully characterised by NMR spectroscopy. As an example, the ^{1}H NMR spectrum of **[5.7]** in DMSO-d$_6$ is shown in figure 5.5. The singlet at 10.00 ppm can be assigned to the shielded proton of the methyl group of tpm (a). The doublets at 9.75, 9.10 and 8.10 ppm (b, c and i) integrate for two protons each and can be assigned to the protons of the phenanthroline ring of the dppz ligand. The doublets at 8.80, 8.40 and 6.90 ppm (d, g and m) correspond to the protons for the two equivalents pyrazole ring. The signals at 9.35, 8.55 and 7.75 ppm (f, h and ñ) integrate for two protons each and are assigned to four protons of the dppz. At 8.55 ppm (e) we observed the doublet for the proton of the pyrazole ring that is trans to the aminopyridine ligand. The signal at 6.90 and 6.30 ppm (n and o) integrates for one proton each and correspond to the protons of the pyrazole ring of the tpm ligand. The signals at 6.75 and 6.20 ppm (j and k) can be assigned to the protons in the positions two and three of the pyridine ring respectively. The singlet at 6.55 ppm (l) corresponds to the NH$_2$ group of the 4-aminopyridine.

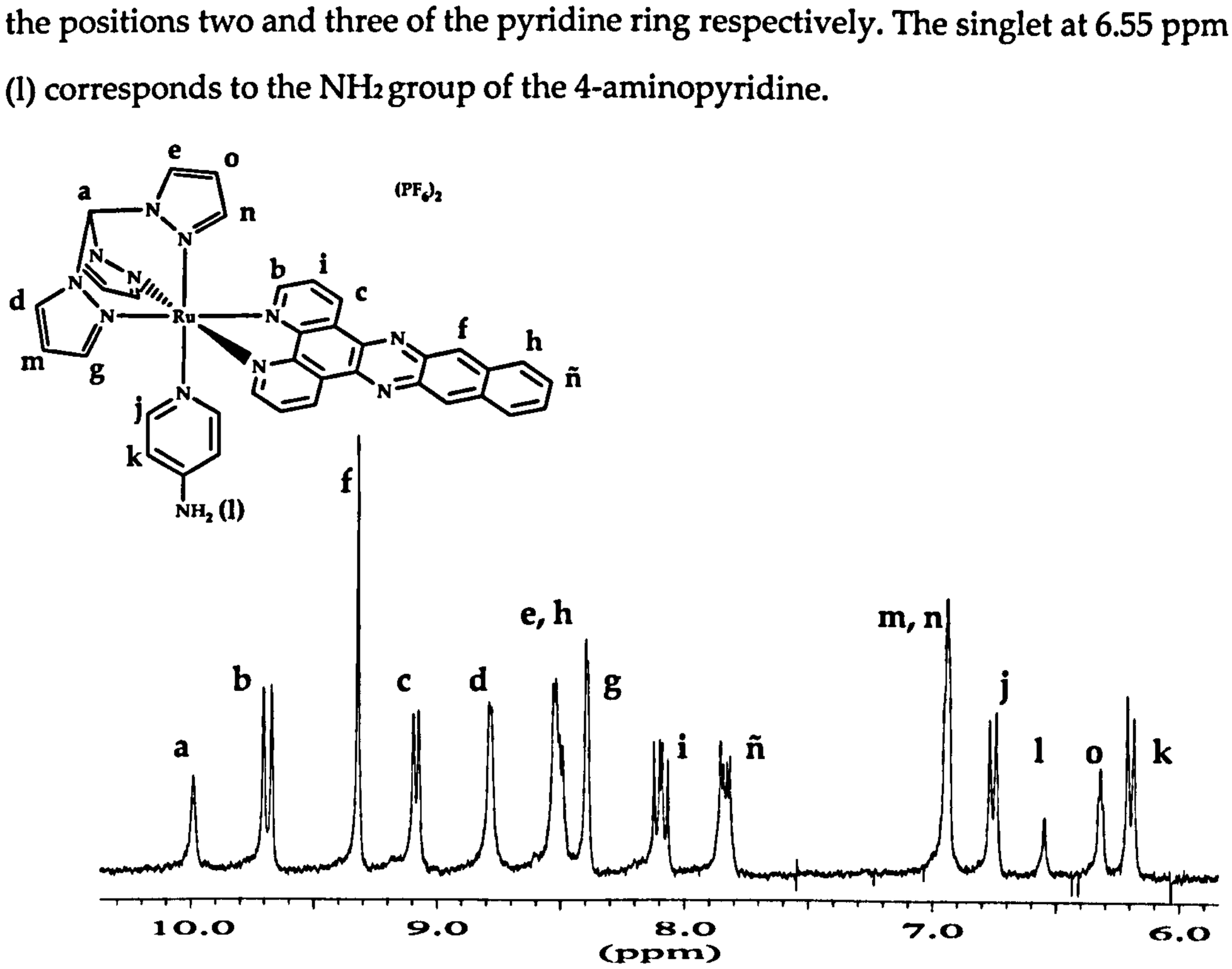

Figure 5.5: ^{1}H NMR spectrum of **[5.7]** in DMSO-d$_6$

^{1}H NMR spectrum of **[5.6]** is similar to the one described above, the difference is in the position of the protons of the pyridine ring.

5.6.2 Electrochemistry studies

Cyclic voltammograms for **[5.6]** and **[5.7]** were carried out in acetonitrile (figure 5.6) under nitrogen atmosphere. As observed previously, the oxidation potential of Ru(II)/Ru(III) couple depends on the nature of the axial ligand. Oxidation of $[Ru(tpm)(dppn)(Py)](PF_6)_2$ occurs at 1.28 V[4]. In the case of **[5.6]** oxidation of the metal centre occurs at 1.33 V, the pyridine group is a good σ-donor and π-acceptor, but the influence of the two different groups in the nicotinamide ligand (amino and carbonyl groups) are acting in different ways: the carbonyl group is withdrawing electron density from the pyridine ring and therefore the metal centre, but the amino group donates electron density. In contrast, oxidation of **[5.7]** occurs at lower potential, 1.03 V, as the amino group donates electron density to the metal ring increasing electron density on the metal and thus making the complex easier to oxidise. Data are summarised in table 5.3.

The oxidation of the complexes with dppz or dppn ligand varies little, indicating oxidation potential is not affected by this change in intercalating ligand.

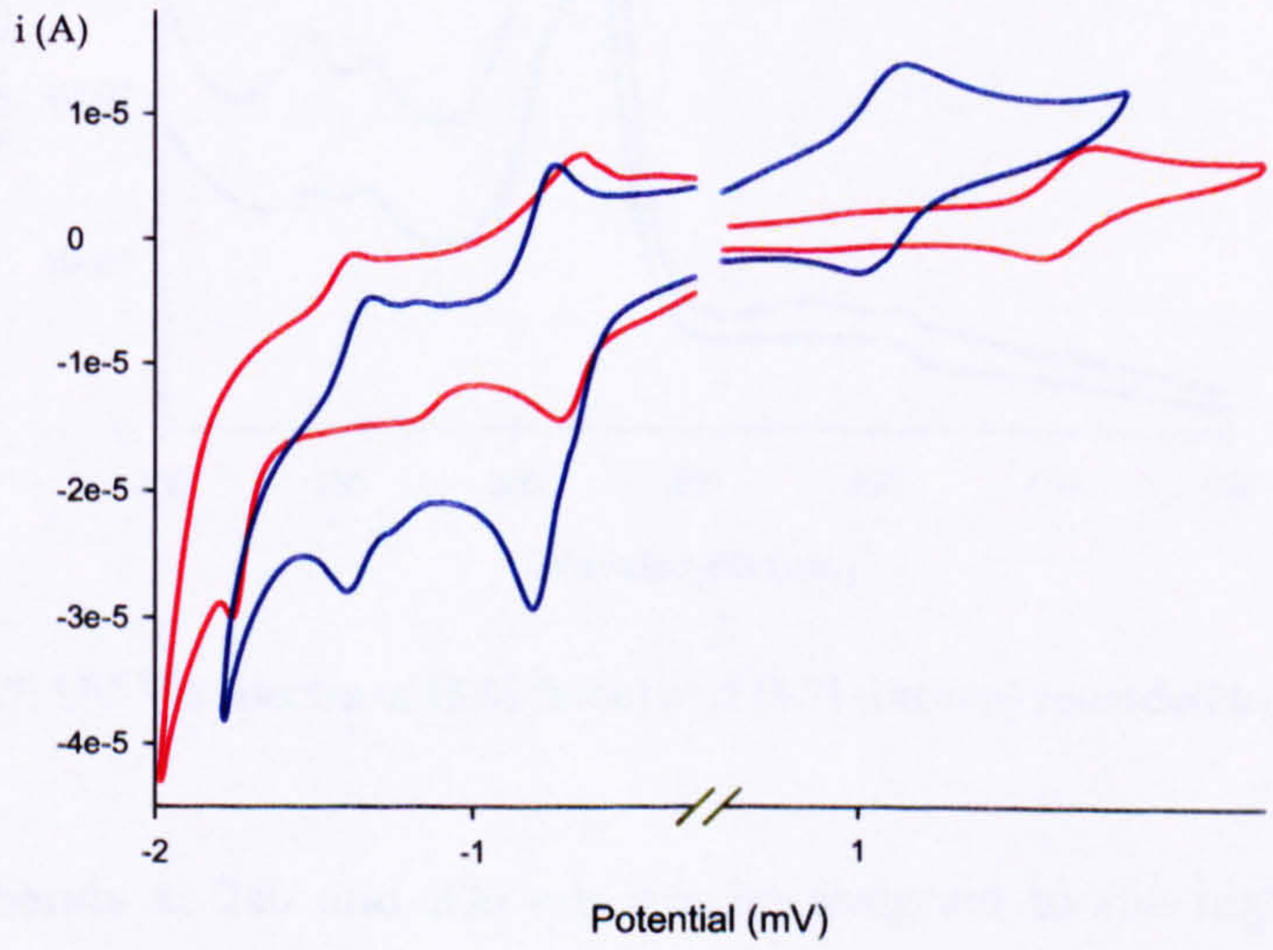

Figure 5.6: Voltagramms of **[5.6]** (red) and **[5.7]** (blue) in acetonitrile

Reductions of the complexes were also studied. The first of these waves is reversible in each compound; however subsequent waves are not reversible. The dppn ligand is easier to reduce than the other N-donor ligands, so probably the first wave is caused by the reduction of the dppn ligand and the second by the reduction of ancillary ligands.

Table 5.3: Cyclic voltammetry data of **[5.6]** and **[5.7]**

Compound	Oxidations	Reductions
	$E_{1/2}$ (V)	$E_{1/2}$ (V)
[5.6]	1.33	-0.69, -1.56[(a)]
[5.7]	1.08	-0.77, -1.36 [(a)]

[(a)] Reductions are not fully chemically reversible, only E_p values are quoted.

5.6.3 UV-Vis spectroscopy studies

UV-Vis absorption spectra of **[5.6]** and **[5.7]** were recorded in acetonitrile solutions at room temperature (figure 5.7). Data are summarised in table 5.4.

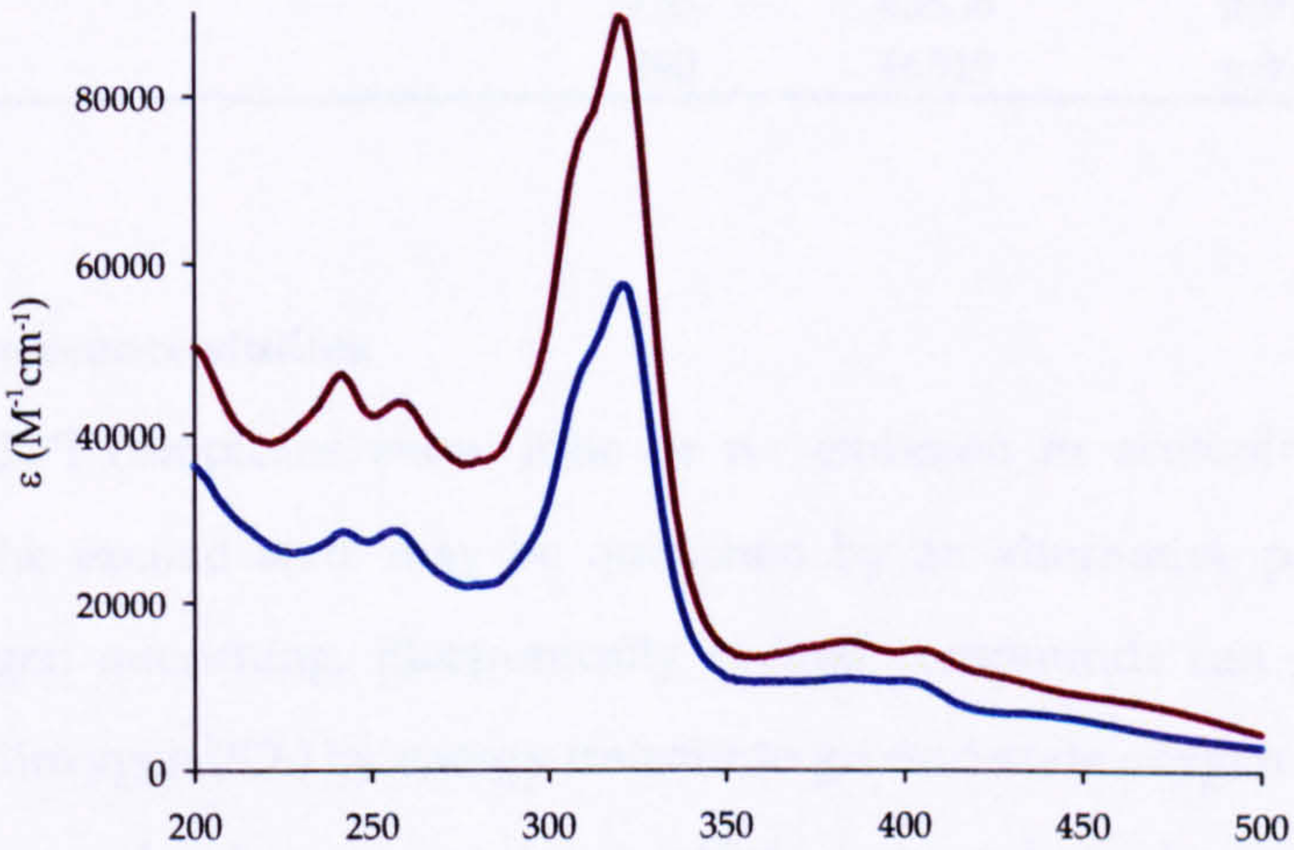

Figure 5.7: UV-Vis spectra of **[5.6]** (blue) and **[5.7]** (brown) recorded in acetonitrile

Absorption bands at 240 and 300 nm can be assigned to the high energy $\pi \rightarrow \pi^*$ transition in aromatic of nitrogens donors (intraligand, IL). The absorption spectrum of the free dppn ligand in acetonitrile shows a "double-humped" absorption in the

near UV region with maxima at 390 and 411 nm, and therefore in these cases the bands at 385 and 400 nm can be assigned to transition in the dppn ligand[4]. Between 400 and 500 nm the low energy band that is assigned to MLCT transition is observed. The MLCT absorptions of the dppn complexes occur at lower energies than those of the analogous complexes with the dppz ligand, this is in agreement with the more extended π conjugation in the dppn ligand resulting in a stabilization of (dppn)-based LUMO.

Table 5.4: UV-Vis data for **[5.6]** and **[5.7]**

Complex	λmax (nm)	ε ($M^{-1}cm^{-1}$)	Assignment
[5.6]	474	sh	MLCT
	400	10739	MLCT
	385	11007	$\pi \rightarrow \pi^*$
	321	57410	$\pi \rightarrow \pi^*$
	256	27898	$\pi \rightarrow \pi^*$
	243	28418	$\pi \rightarrow \pi^*$
[5.7]	474	sh	MLCT
	404	14540	MLCT
	384	15474	$\pi \rightarrow \pi^*$
	320	89348	$\pi \rightarrow \pi^*$
	258	43638	$\pi \rightarrow \pi^*$
	240	46519	$\pi \rightarrow \pi^*$

5.6.4 Luminescence studies

[5.6] and **[5.7]** complexes show little or no emission in acetonitrile or aqueous solution. The excited state may be quenched by an alternative pathway such as triplet oxygen quenching. Electronically excited compounds can generate singlet molecular dioxygen ($^1O_2$) by energy transfer to ground-state oxygen ($^3O_2$)[5-7]. It is well known, that molecular oxygen is an efficient quencher of photoexcited Ru(II) polypyridyl complexes[8-11]. Preliminaries studies on emission life times and quenching of $[Ru(tpm)(dppn)(Py)]^{2+}$ by O_2, reveal that compared to [Ru(dppz)] complexes, it is highly efficient at sensitising triplet to singlet oxygen conversion[12]. Detailed studies on photoexcitation of these complexes in presence and absence of oxygen are underway.

Binding studies

5.7 Binding studies of chiral-Ru(tpm)(dppz) complexes

5.7.1 Melting points (T_m)

The ΔT_m of CT-DNA with ***(L)-***, ***(D)-*** **[5.2]** and ***(L)-***, ***(D)-*** **[5.3]** complexes were investigated (figure 5.8, Data are normalised for clarity).

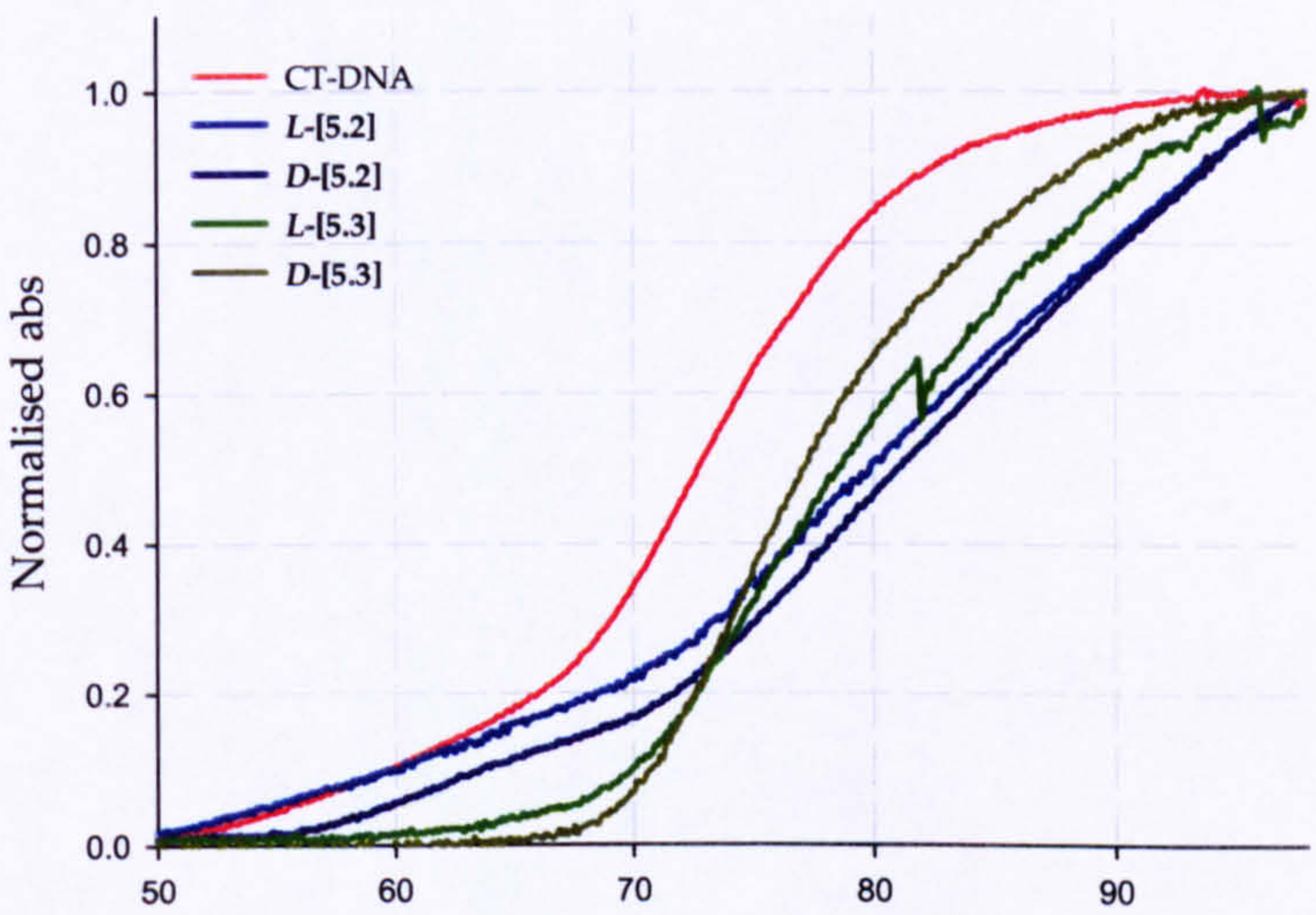

Figure 5.8: T_m of CT-DNA in the absence (purple line) and presence of ***(L)-***, ***(D)-*** **[5.2]** and ***(L)-***, ***(D)-*** **[5.3]** complexes.

The T_m of CT-DNA in the experimental condition is 73.3 °C. In all of the cases the metal complex stabilised CT-DNA. Complexes ***(L)-*** and ***(D)-*** **[5.3]** showed smaller stabilisation effect compared to ***(L)-*** and ***(D)-*** **[5.2]** (5 and 7 °C respectively). In the case of ***(L)-*** and ***(D)-*** **[5.2]** the end of the melting point is not reached and stabilisation is estimated to be at least 15 °C.

5.8.2 Viscosity

The effects of **(*L*)-, (*D*)- [5.2]** and **(*L*)-, (*D*)- [5.3]** on the relative viscosity of CT-DNA are shown in figure 5.9.

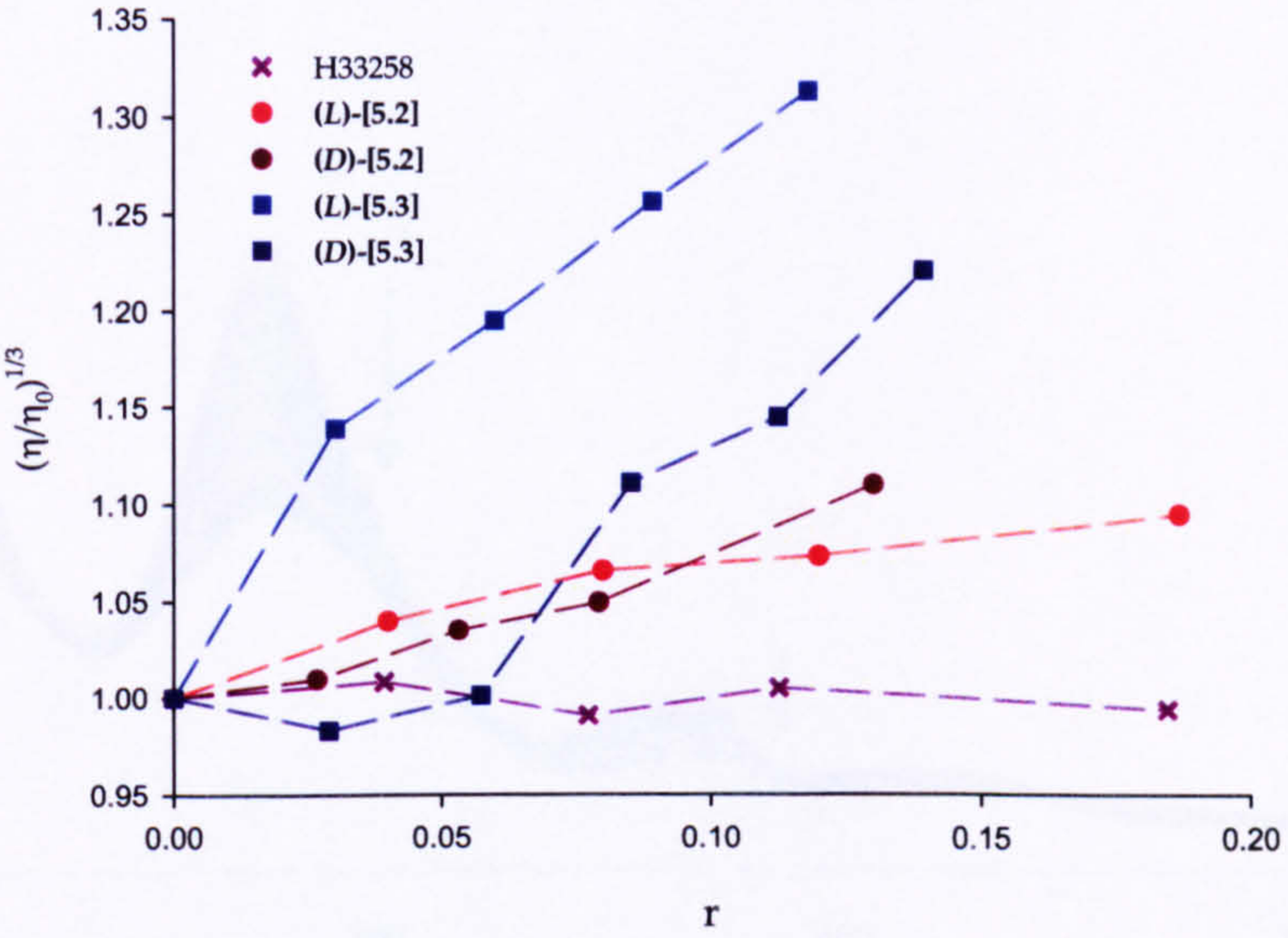

Figure 5.9: Relative viscosity of CT-DNA upon addition **(*L*)-, (*D*)- [5.2]** and **(*L*)-, (*D*)- [5.3]** and H33258 (purple).

Increase in relative viscosity is observed in all the cases. However the viscosity of CT-DNA when bound to the complexes **(*L*)-** and **(*D*)- [5.2]** showed lower increases compared to the other two complexes, this may implied that these complexes intercalate less deeply into the CT-DNA[13,14]. In the case of **(*L*)-** and **(*D*)- [5.3]** both complexes intercalates between the base pairs of DNA. The changes in viscosity for complex **(*L*)-[5.3]** and **(*D*)-[5.3]** are different, suggesting a difference in their interaction with CT-DNA.

5.8.3 UV-Vis titrations

The interaction of metal complexes with DNA produced changes in the UV-Vis spectrum of the metal complex due changes in the environment of the metal complex. Figure 5.10 shows the UV-Vis titration of complex ***(D)*- [5.2]** binding to CT-DNA.

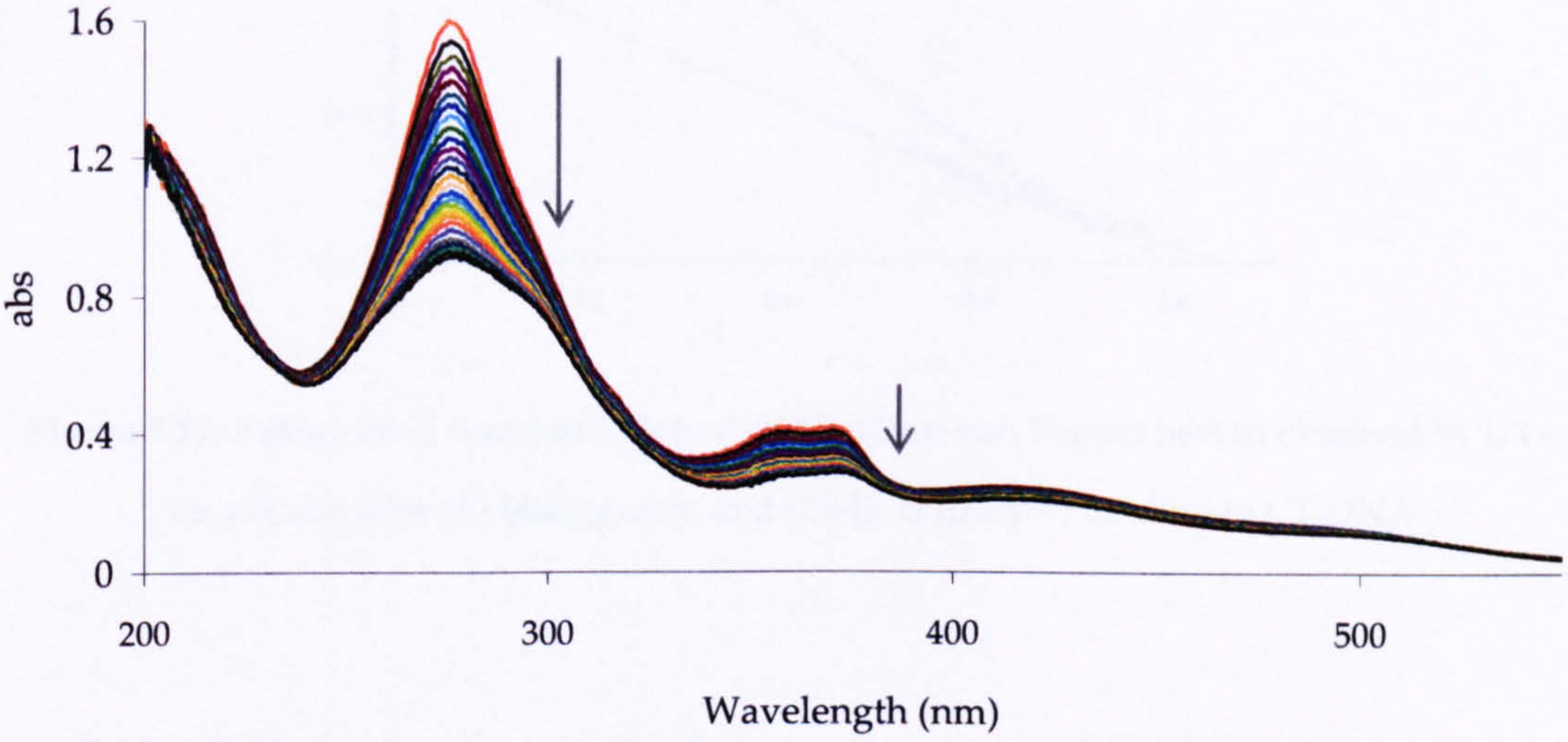

Figure 5.10: UV-Vis titration of ***(D)*- [5.2]** with CT-DNA

Both bands at 277 nm and 350 nm showed hypochromicity and when saturation is close, the band at 277 nm also showed also a bathochromic shift. For the study of interaction of these complexes to DNA, changes in the 277 nm band were followed and the binding curves for ***(L)*-, *(D)*- [5.2]** and ***(L)*-, *(D)*- [5.3]** were constructed. The binding constant for the interaction of these complexes with CT-DNA were calculated using the McGhee Von Hippel model for fitting of non-linear Scatchard plots (figure 5.11). Data are summarised in table 5.5.

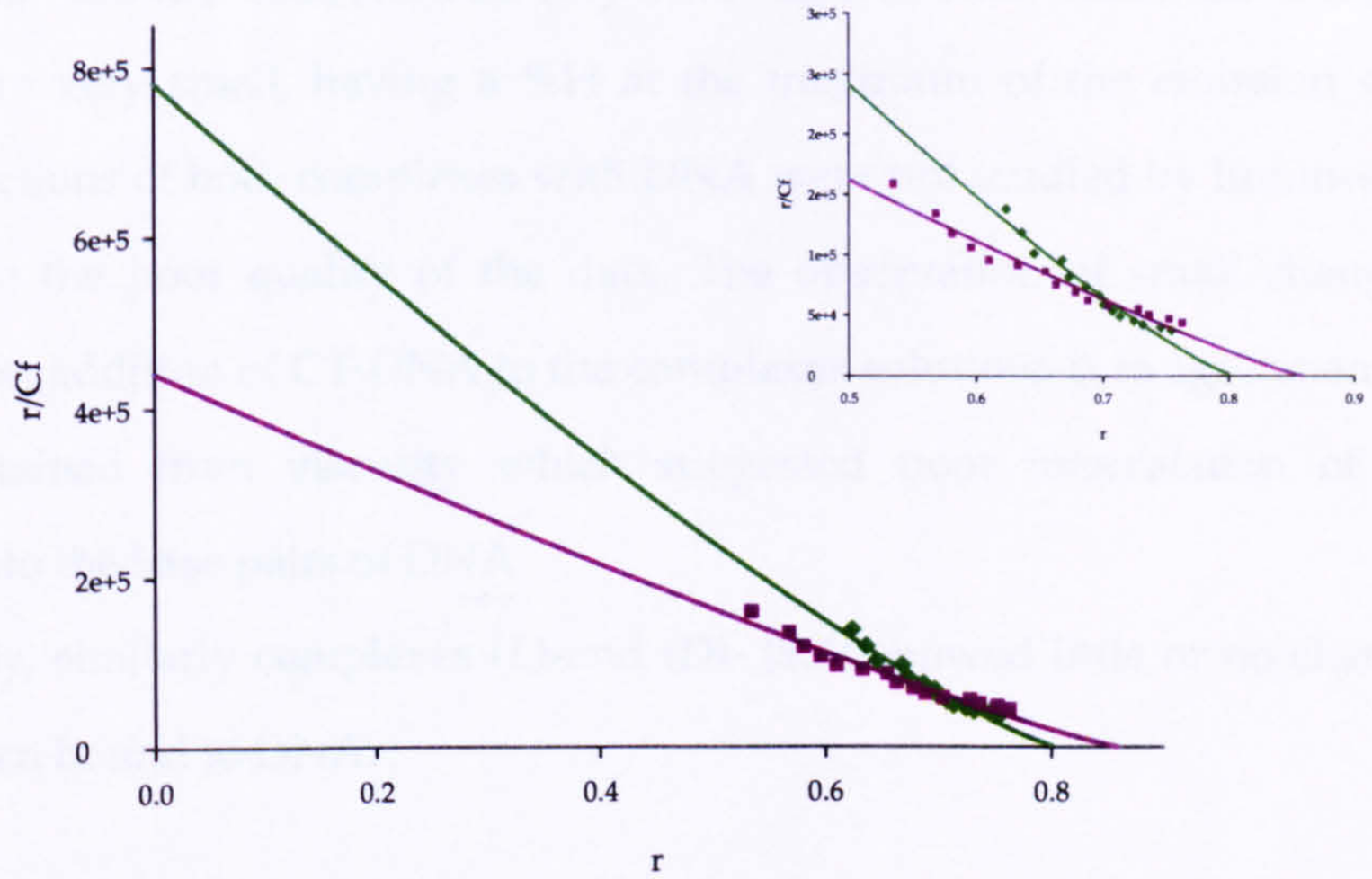

Figure 5.11: Examples of Scatchard plots with Mc Ghee von Hippel best fit obtained by UV-Vis titrations for (*L*)-**[5.2]** (green) and **(*D*)-[5.2]** (purple) binding to CT-DNA

Table 5.5: Binding constants and binding site sizes obtained by UV-Vis titration of the complexes (*L*)-, (*D*)- **[5.2]** and (*L*)-, (*D*)- **[5.3]** with CT-DNA

Compound	K_a (M^{-1})	N (bp)	% H
(*L*)-[5.2]	$7.73 \pm 0.43 \times 10^5$	1.27 ± 0.05	66.48
(*D*)-[5.2]	$3.44 \pm 0.29 \times 10^5$	1.17 ± 0.02	74.27
(*L*)-[5.3]	$4.24 \pm 0.21 \times 10^5$	0.77 ± 0.01	39.74
(*D*)-[5.3]	$2.23 \pm 0.14 \times 10^5$	0.59 ± 0.01	44.67

(where %H is the percent in hypochroism, $\%H=(A_o-A_b)/(A_b)$)

Binding affinities of these complexes for CT-DNA are in the 10^5 M^{-1} range, one order of magnitude smaller compared to other Ru(II)-dppz complexes studied. The chiral amino acids produce some unfavourable steric interactions.

One interesting aspect is the different in affinities between enantiomers. Complexes with *L*- chiral amino acids showed double affinity for CT-DNA than the *D*-isomer, and therefore some enantioselectivity.

5.8.4 Luminescence titrations

Complexes (*L*)- and (*D*)- **[5.2]** showed very little "light switch" effect: the changes in emission were very small, having a %H at the maximum of the emission < 3 %. Hence interactions of both complexes with DNA were not studied by luminescence titrations due the poor quality of the data. The observation of small changes in emission upon addition of CT-DNA to the complexes solutions is in agreement with the data obtained from viscosity which suggested poor intercalation of these complexes into the base pairs of DNA.

Unfortunately, similarly complexes (*L*)-and (*D*)- **[5.3]** showed little or no change in emission when bound to DNA.

5.8.5 Circular dichroism (CD) spectra

Circular dichroism spectra of complexes (*L*)-, (*D*)- **[5.2]** and (*L*)-, (*D*)- **[5.3]** with CT-DNA have been measured over a range of complex/DNA ratios.

As mentioned before, CT-DNA exhibits a positive band at 278 nm due to base stacking and a negative band at 245 nm due to the helicity of B-DNA. Upon addition of (*L*)-, (*D*)- **[5.2]** and (*L*)-, (*D*)- **[5.3]** a positive band at 266 nm and a negative band at 298 nm with an isosbestic point at 276 nm are observed. There is also a weak negative band at around 373 nm that corresponds to the UV-Vis absorption band for the $\pi \rightarrow \pi^*$ transition of the dppz ligand and a weak positive band around 450 nm that correspond to the absorption band for the MLCT transition. The 276 nm cross corresponds to the absorption maxima of the $\pi \rightarrow \pi^*$ transition of the nitrogen donor ligands (figure 5.12). Once again, the positive band at 266 nm could be due changes due complex-complex stacking, complex-base pair interaction and changes in the DNA being difficult to distinguish the possible origin of these signals.

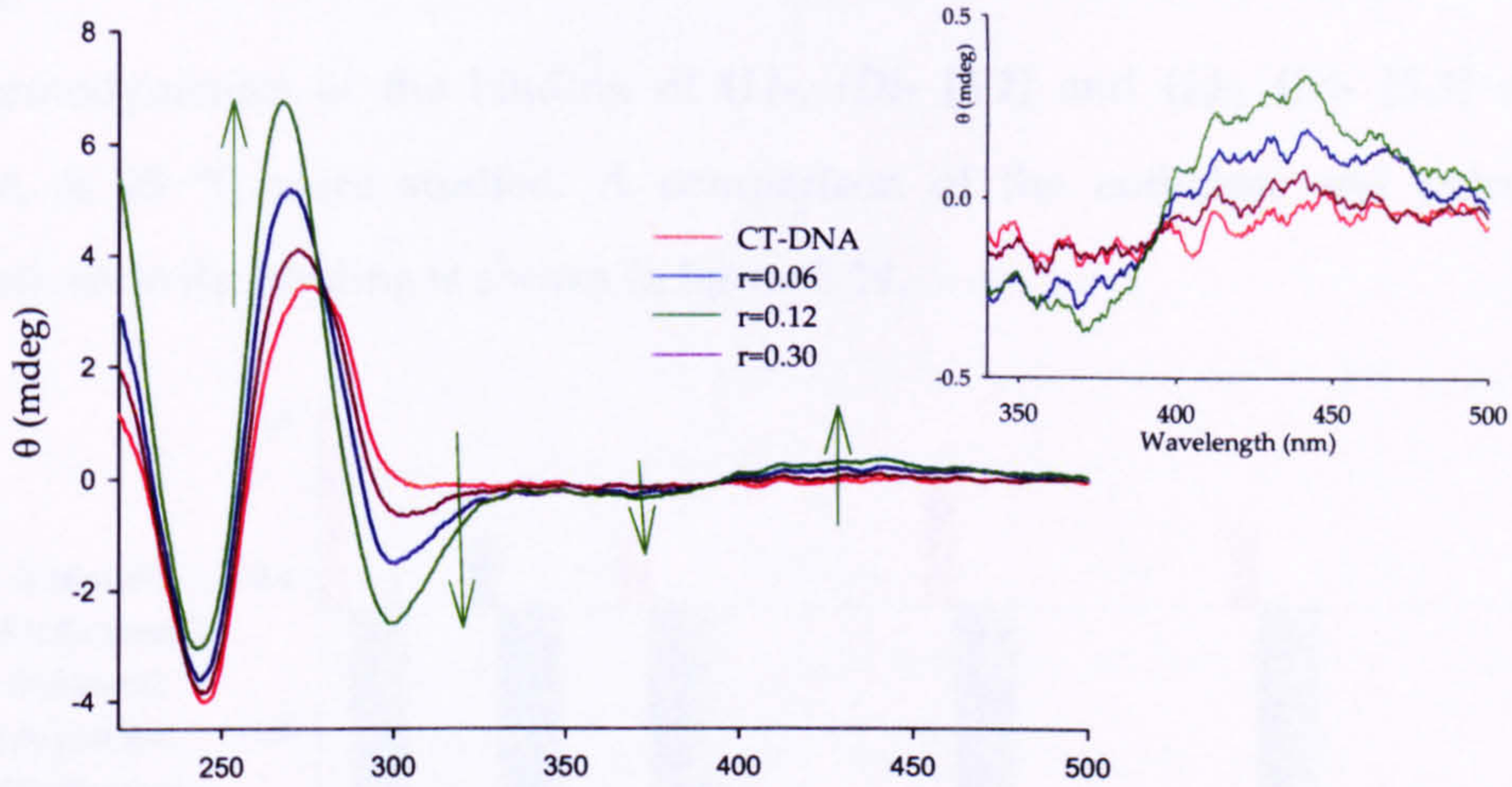

Figure 5.12: CD spectra of CT-DNA upon addition of **(*D*)-[5.2]** at several molar ratios. Inset: details of 300-500 nm region.

If the signals for the CT-DNA are removed, is possible to see clearly the induced CD changes of the complex on moving to a chiral environment (figure 5.13).

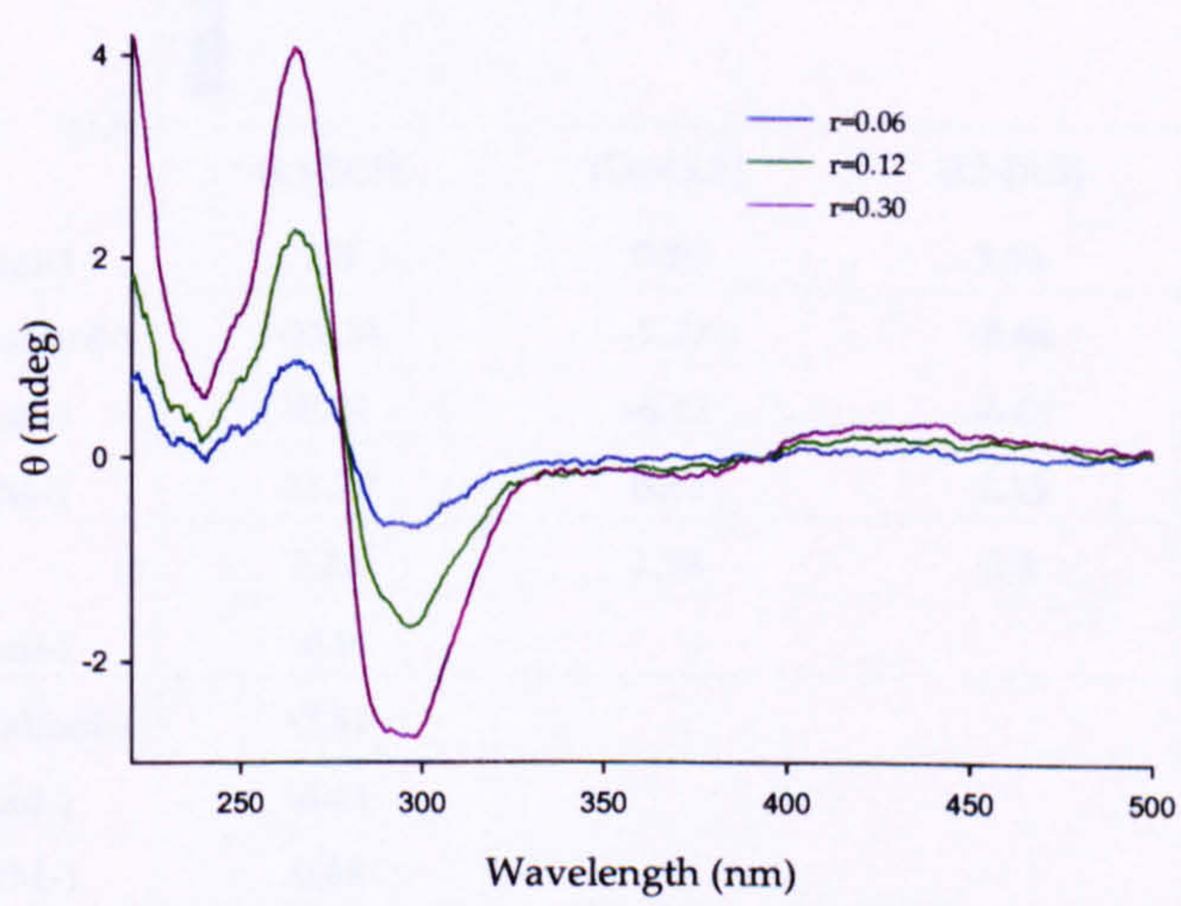

Figure 5.13: ICD spectra of **(*D*)-[5.2]** when bound to CT-DNA

Similar effects for the complex **(*D*)-[5.3]** when it is added to CT-DNA are observed only at molar ratios larger than 0.15 complex/DNA; at small molar ratios the CD spectrum of CT-DNA is not altered. This is in agreement with the viscosity data, where the complex produced an increased in the relative viscosity of CT-DNA at molar ratios bigger than 0.1 complex/DNA.

5.8.6 ITC

The thermodynamics of the binding of ***(L)-, (D)-* [5.2]** and ***(L)-, (D)-* [5.3]** with CT-DNA at 25 °C were studied. A comparison of the enthalpic and entropic contributions to the binding is shown in figure 5.14.

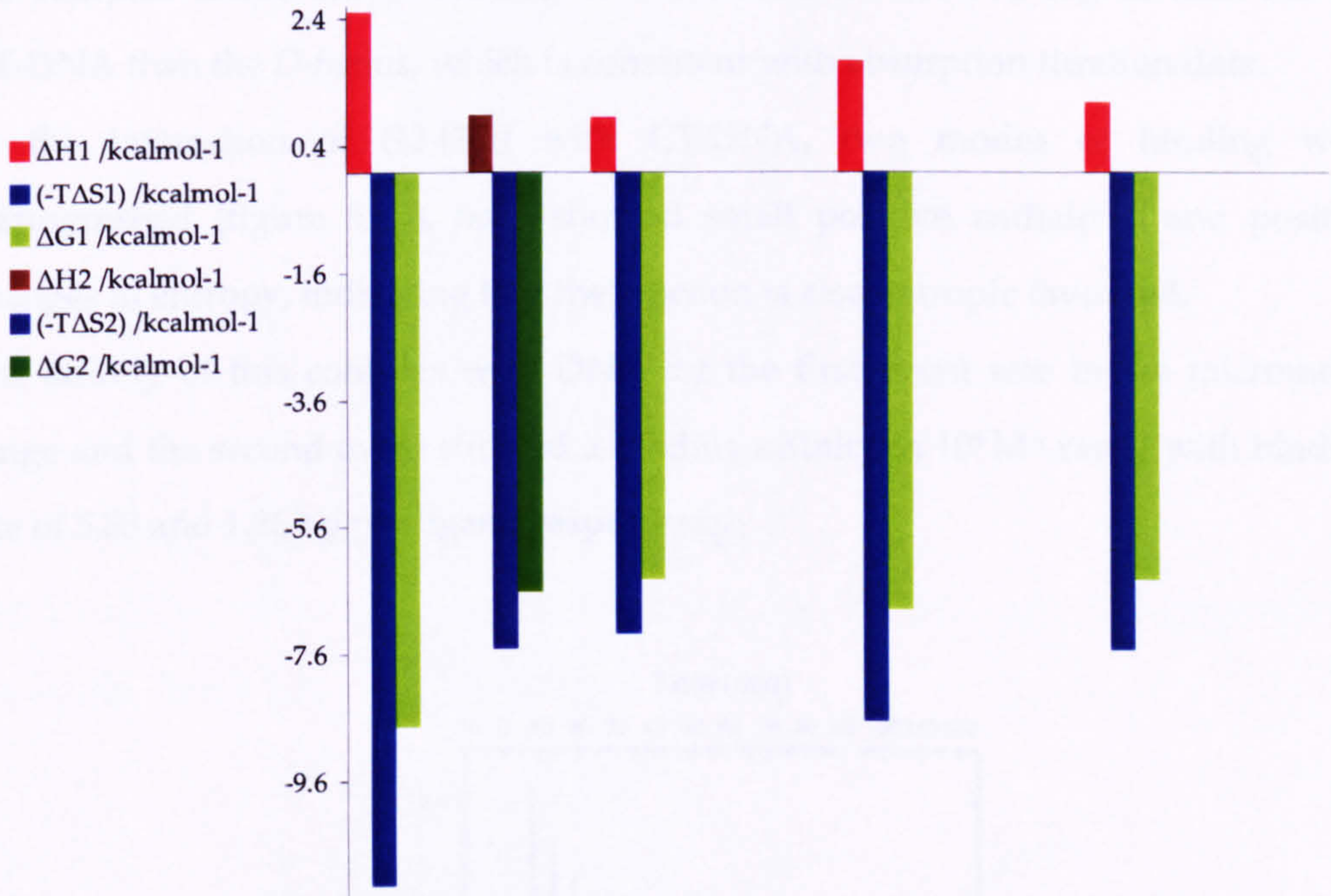

	(L)-[5.2]	(D)-[5.2]	(L)-[5.3]	(L)-[5.3]
ΔH1 /kcalmol-1	2.5	0.85	1.74	1.09
(-TΔS1) /kcalmol-1	-11.24	-7.27	-8.64	-7.51
ΔG1 /kcalmol-1	-8.74	-6.42	-6.89	-6.41
Ka1(x10-5)/M-1	25.20	0.50	1.13	0.49
N1(bp/L)	5.88	1.95	3.3	1.5
ΔH2 /kcalmol-1	0.9			
(-TΔS2) /kcalmol-1	-7.51			
ΔG2 /kcalmol-1	-6.61			
Ka2 (x10-5)/M-1	0.69			
N2(bp/L)	1.86			

Figure 5.14: Thermodynamic data for the interaction of ***(L)-, (D)-* [5.2]** and ***(L)-, (D)-* [5.3]** with CT-DNA

The interaction of these complexes with CT-DNA showed small positive changes in enthalpy (from 2.5 kcal/mol to 1.09 kcal/mol) and positive entropies indicating that the interactions are entropically driven. As mentioned before, hydrophobic

interactions are usually characterised by small enthalpy changes and large entropy changes[15] and electrostatic interaction are usually entropically driven with small unfavourable changes in enthalpy[16].

The binding constants obtained by ITC showed different behaviour depending on the complex under study. Binding of *L*-enantiomers showed higher affinities for CT-DNA than the *D*-forms, which is consistent with absorption titration data.

In the interaction of **(*L*)-[5.2]** with CT-DNA, two modes of binding were distinguished (figure 5.15), both showed small positive enthalpies and positive changes in entropy, indicating that the reaction is also entropic favoured.

The affinity of this complex with DNA for the first event was in the micromolar range and the second event showed a binding affinity in 10^5 M^{-1} range with binding site of 5.88 and 1.86 bp per ligand respectively.

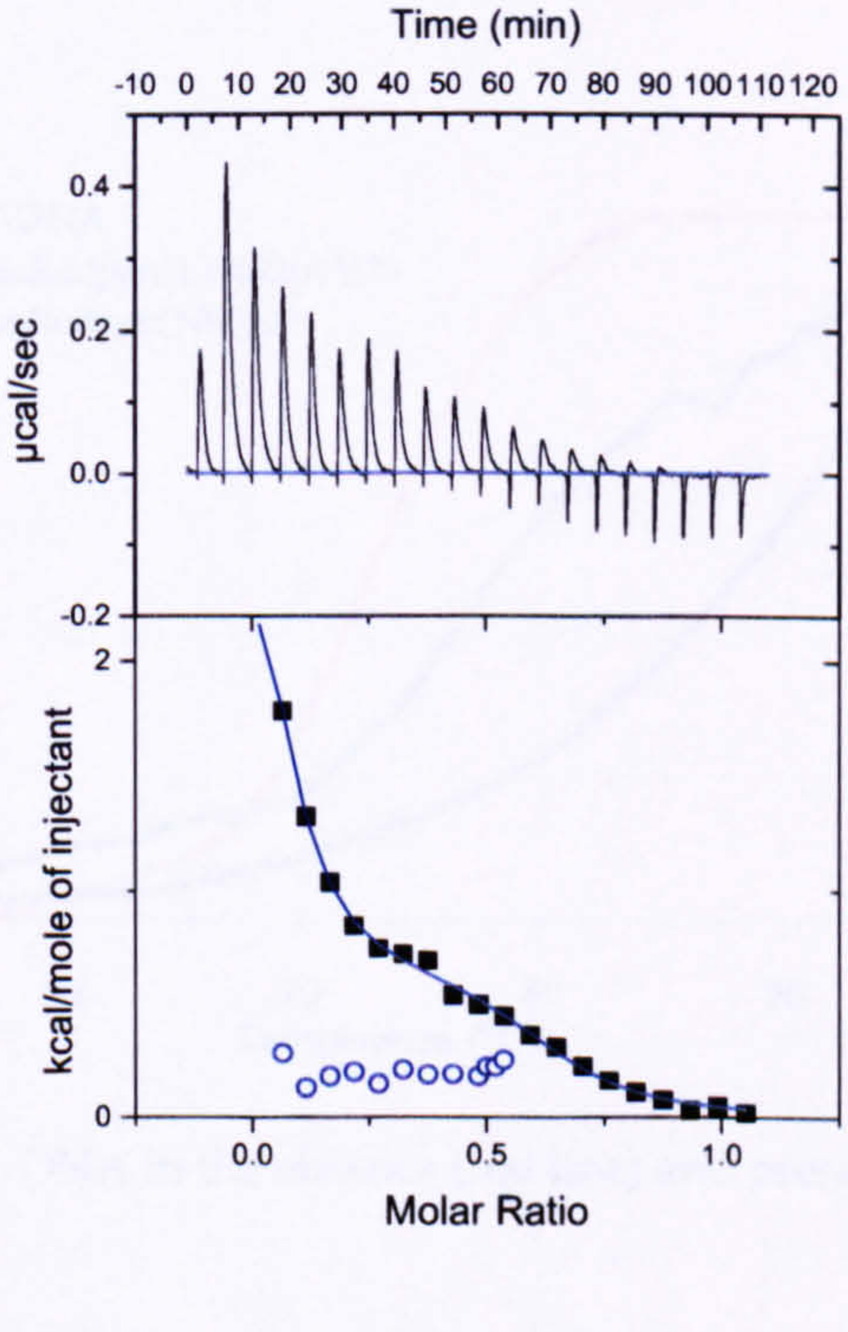

Figure 5.15: ITC raw data for the interaction of **(*L*)-[5.2]** with CT-DNA (black square) and dilution experiment (open blue) at 25 °C

In the case of **(*D*)-[5.2],** the interaction with CT-DNA showed one event with small changes in enthalpy, entropically driven. Affinity of this complex for CT-DNA is in 10^5 M^{-1} range with stoichiometry of 1.95 base pair per ligand.

The interaction between **(*L*)-[5.3]** and **(*D*)-[5.3]** and CT-DNA was entropic driven with small changes in enthalpy. The affinity of these complexes for CT-DNA is in the micromolar range for the *L*-enantiomer and in the 10^5 M^{-1} range for the *D*-enantiomer.

5.9 Binding studies of $[Ru(tpm)(dppn)(L)]^{2+}$ complexes

5.9.1 Melting points (T_m)

The T_m of CT-DNA in absence and presence of Ru(II)(tpm)(dppn)-L complexes were measured, figure 5.16.

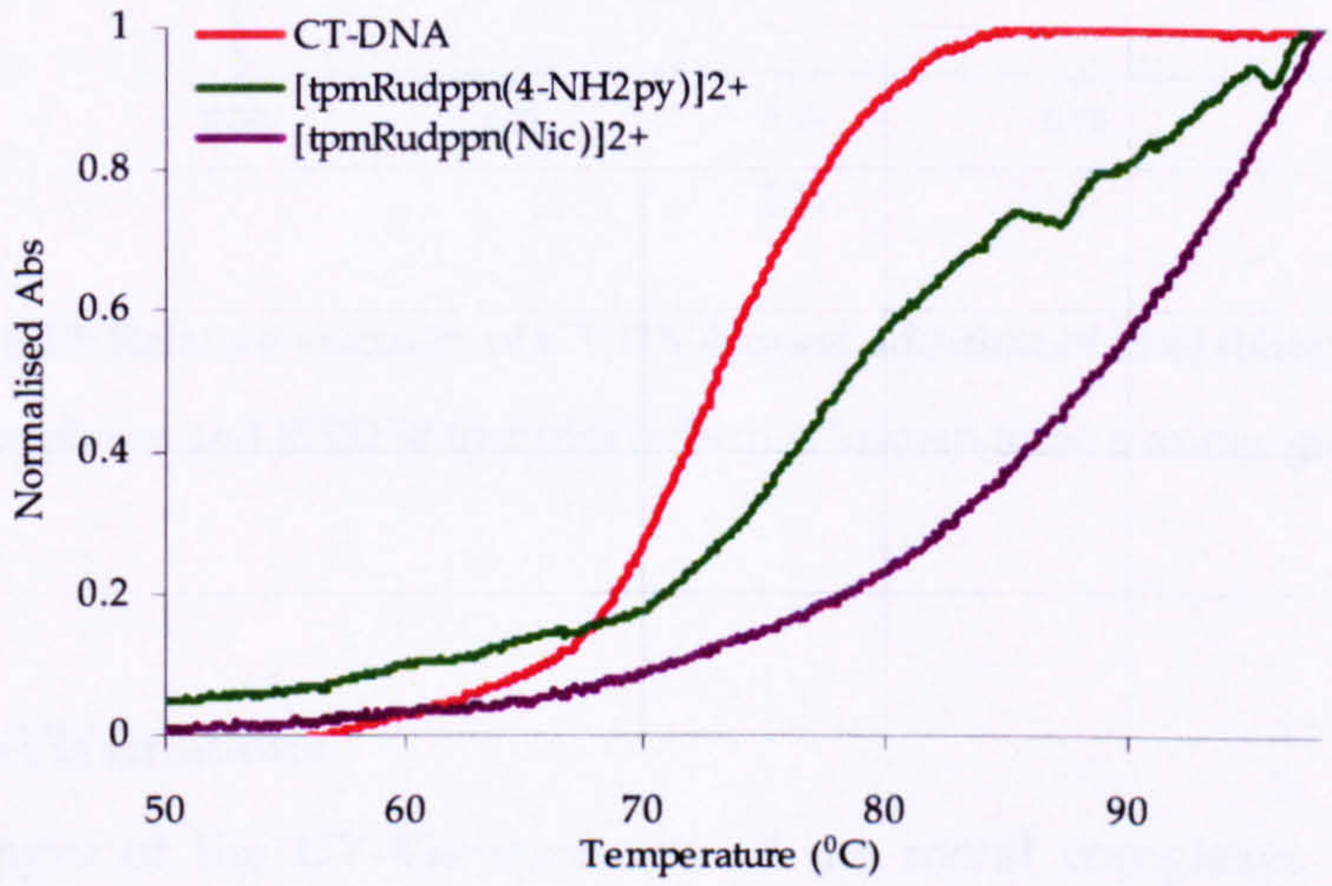

Figure 5.16: T_m of CT-DNA in the absence (red line) and presence of **[5.6]** and **[5.7]**

In both cases the metal complex stabilised CT-DNA, but it is not possible to calculate the T_m of the complexes bound to CT-DNA because the end of the melting point is not reached, however complex **[5.6]** appeared to produce a longer stabilisation than **[5.7]**.

5.9.2 Viscosity

The effects of **[5.6]** and **[5.7]** on the relative viscosity of CT-DNA are shown in figure 5.17. The relative viscosity of CT-DNA bound to the complexes increases, indicating that both complexes intercalates between the base pairs of DNA[17-20]. Similar complexes with extended intercalating ligand showed the same effect[21]. Interestingly the complex $[Ru(tpm)(dppn)(4\text{-}NH_2py)]^{2+}$ is clearly an intercalator, this behaviour is in direct contrast to the analogous dppz complex (chapter four).

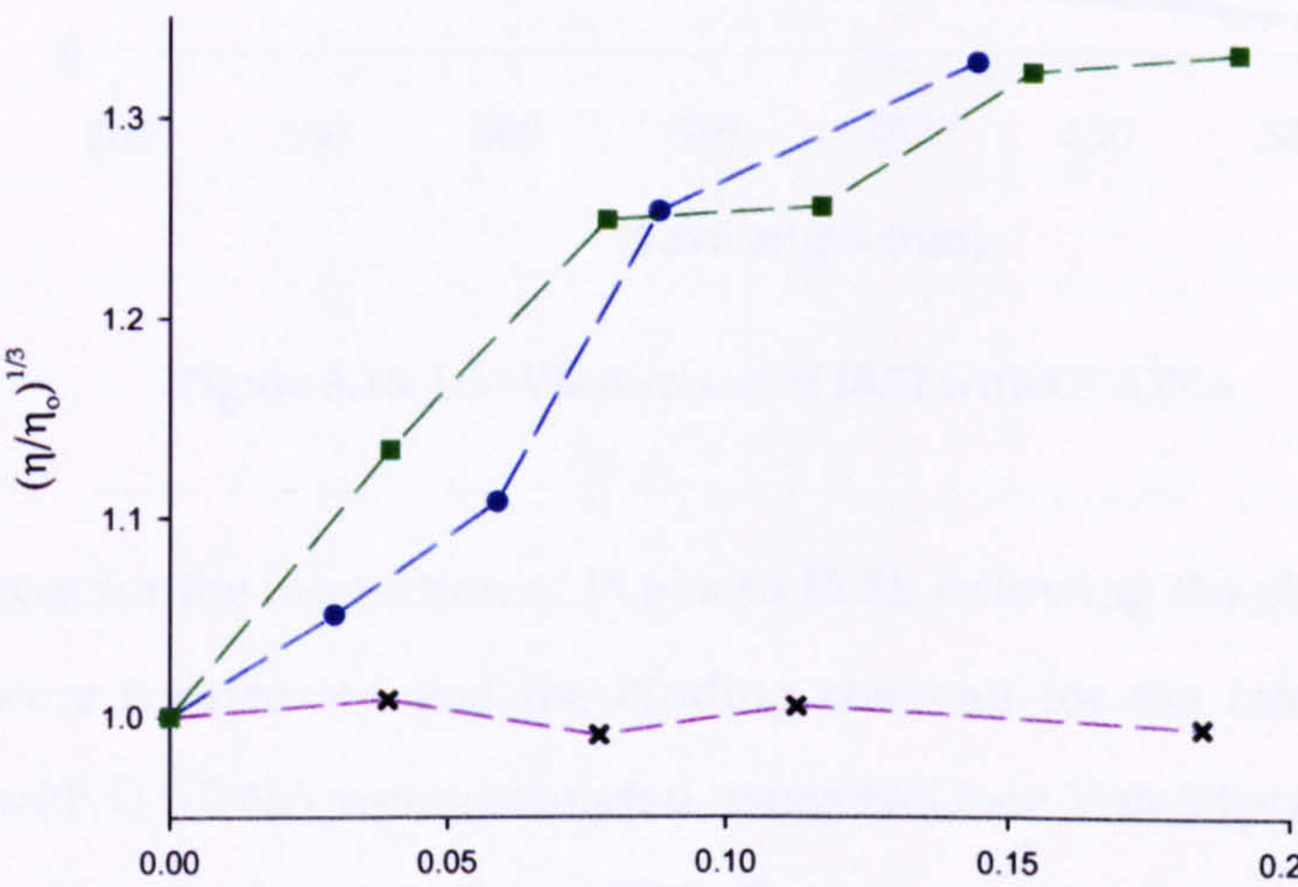

Figure 5.17: Relative viscosity of CT-DNA upon addition of **[5.6]** (blue) and **[5.7]** (green) complexes and H33258 (purple) (which is known to be a minor groove binder)

5.9.3 UV-Vis titrations

The changes of the UV-Vis spectrum of the metal complexes upon addition of CT-DNA can be used to measure their interaction with the double helix. Changes in the UV-Vis spectrum of **[5.7]** upon addition of CT-DNA are shown in figure 5.18. In both cases the bands at 320 nm and 404 nm are shifted to longer wavelengths and the intensity of the absorption is decreased upon addition of DNA until saturation is reached. There is an isosbestic point at 360 nm. The hypochromicity and bathchromic effect are typical for the stacking of aromatic ligands in between the base pairs of DNA[19,22-24] .

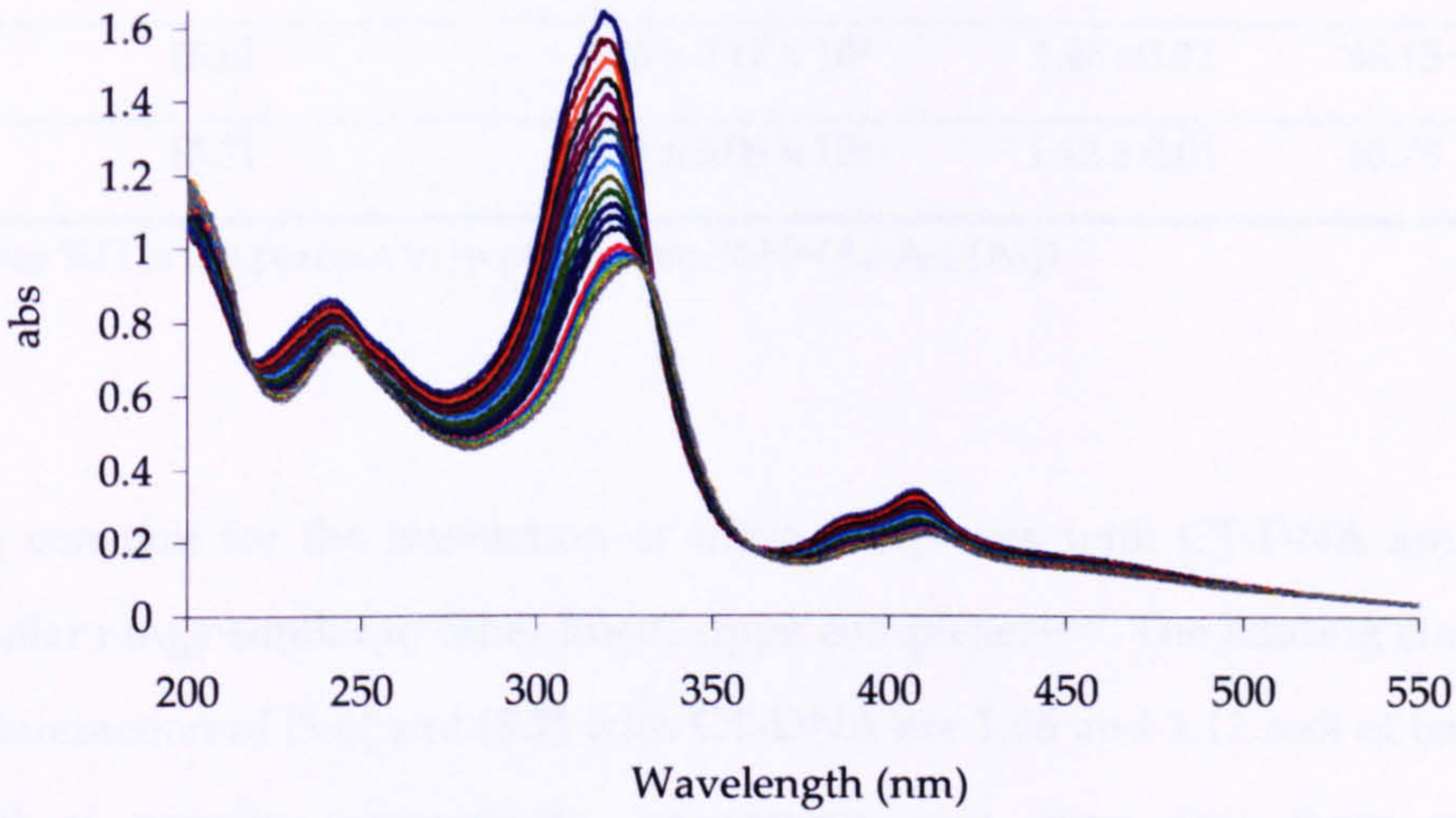

Figure 5.18: UV-Vis titration of **[5.7]** with CT-DNA

Binding curves for the interaction of **[5.6]** and **[5.7]**, following the changes in the 320 nm band, were constructed and the binding constant for the interaction of these complexes with CT-DNA were calculated using McGhee Von Hippel model[25] fitting of non-linear Scatchard plots[26] (figure 5.19). Data are summarised in table 5.5.

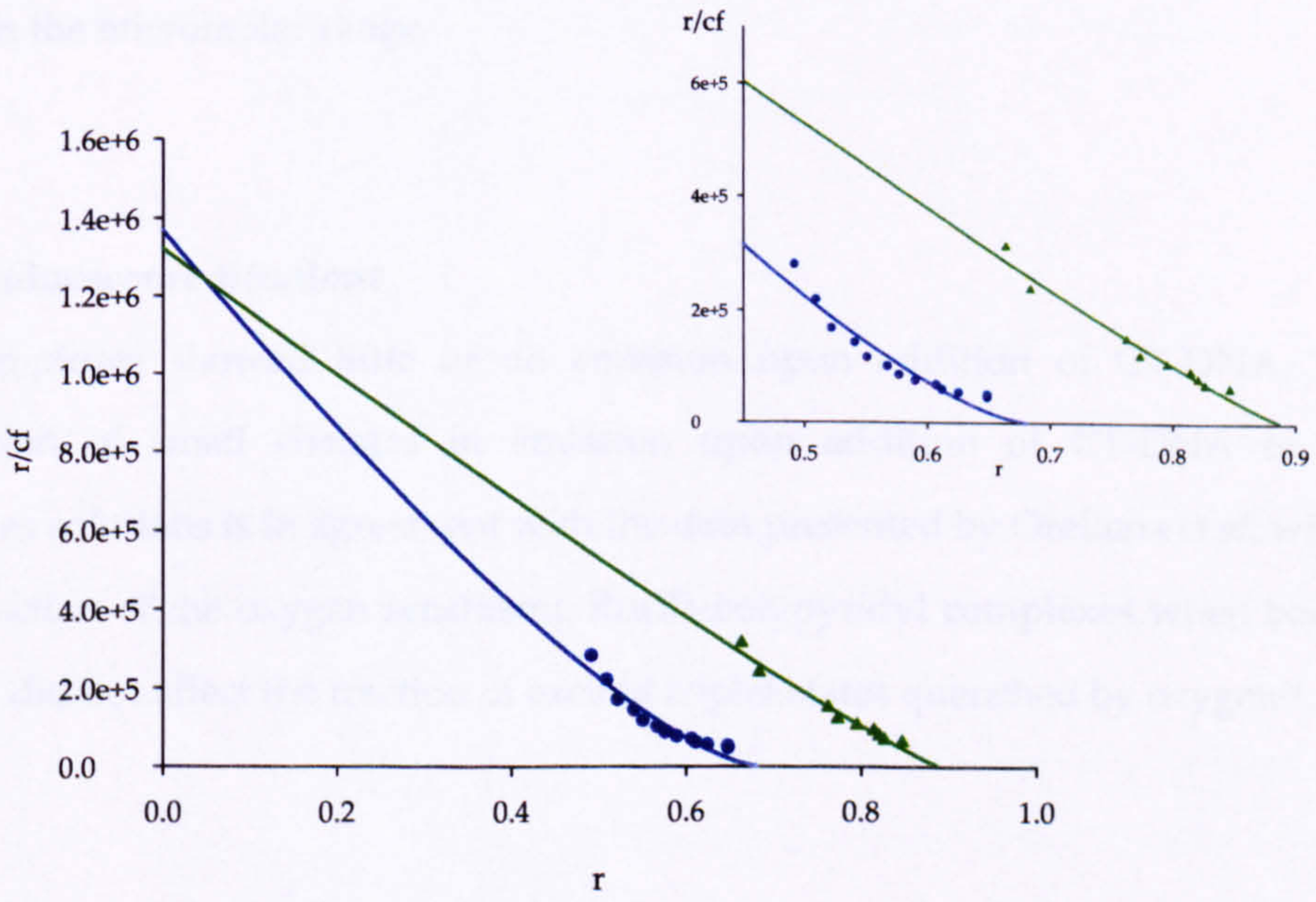

Figure 5.19: Example of Scatchard plots with Mc Ghee von Hippel best fit obtained by UV-Vis titrations for **[5.6]** (blue) and **[5.7]** (green) binding to CT-DNA

Table 5.6: UV-Vis binding data for the interaction of **[5.8]** and **[5.9]** with CT-DNA

Compound	K_a (M^{-1})	N (bp)	% H
[5.6]	$1.36 \pm 0.17 \times 10^6$	1.46 ±0.02	46.13
[5.7]	$1.32 \pm 0.09 \times 10^6$	1.12 ± 0.01	45.78

(where %H is the percent in hypochroism, $\%H=(A_o-A_b)/(A_b)$)

Binding constant for the interaction of these complexes with CT-DNA are in the micromolar range similar to other Ru(II)-dppz complexes[27-29]. The binding sites sizes for the interaction of **[5.6]** and **[5.7]** with CT-DNA are 1.46 and 1.12 mol of base pair per mol of complex respectively, suggesting once more that these metallo-intercalators could stack with each other on the DNA surface[28,30].

Increasing the surface area of the intercalator was expected to improve the affinity of complexes for DNA. Unfortunately complex **[5.6]** shows an affinity for CT-DNA that is very similar to the analogous complex with dppz ($K_a = 1.20 \times 10^6\ M^{-1}$, N= 1.21 bp/L for the interaction of $[Ru(tpm)(dppz)(Nic)]^{2+}$ with CT-DNA, see chapter four). Complex **[5.7]**, not only showed a different mode of binding to DNA with respect to the analogous dppz complex, it has also shows an affinity one order of magnitude bigger, in the micromolar range.

5.9.4 Luminescence titrations

Both complexes showed little or no emission upon addition of CT-DNA. The observation of small changes in emission upon addition of CT-DNA to the complexes solutions is in agreement with the data presented by Orellana *et al.* where the protection of the oxygen sensitising Ru(II)-polypyridyl complexes when bound to DNA, did not affect the fraction of excited triplet states quenched by oxygen[31].

5.9.5 Circular dichroism (CD) spectra

The interaction of these new metal complexes with DNA was studied by circular dichroism. To aid comparisons, the circular dichroism spectra of a dppn ligand derivative (synthesised by Tim Phillips, a member of the Thomas' group) was first reported over a range of DNA/ligand ratios (figure 5.20).

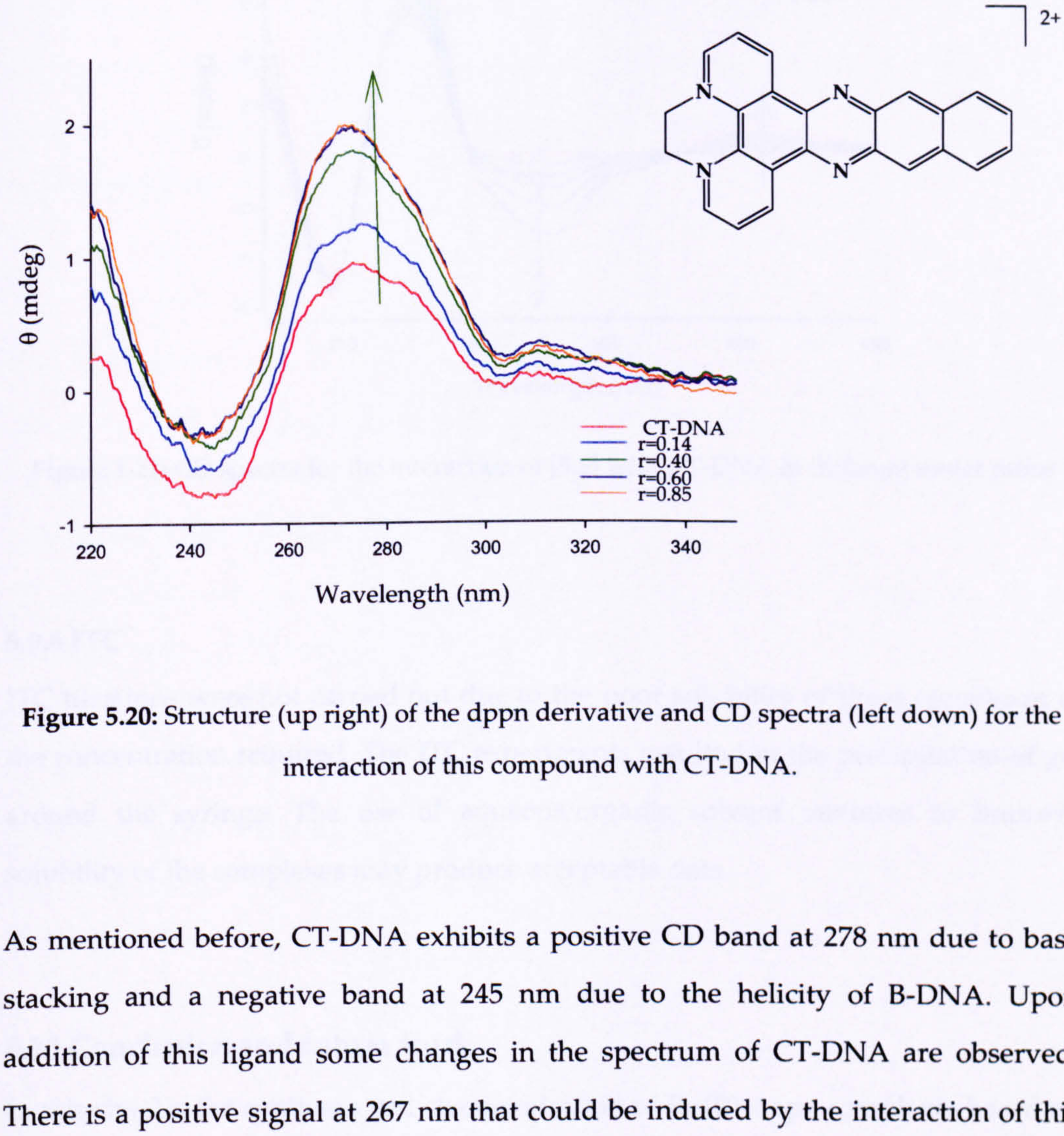

Figure 5.20: Structure (up right) of the dppn derivative and CD spectra (left down) for the interaction of this compound with CT-DNA.

As mentioned before, CT-DNA exhibits a positive CD band at 278 nm due to base stacking and a negative band at 245 nm due to the helicity of B-DNA. Upon addition of this ligand some changes in the spectrum of CT-DNA are observed. There is a positive signal at 267 nm that could be induced by the interaction of this known intercalative compound[32] between the base pair of the DNA.

In contrast, interaction of complexes **[5.6]** and **[5.7]** with CT-DNA produce large changes in the CD spectrum of CT-DNA. The positive band of the DNA at 275 nm increased in intensity while the negative band at 245 nm remained at the same position. New ICD signals at 325 nm (negative) and 405 nm (positive) and two

isosbestic points at 296 nm and 405 nm are observed. UV-Vis absorption band for the $\pi \rightarrow \pi^*$ transition of the dppn ligand occurs at 321 nm and 400 nm (figure 5.21).

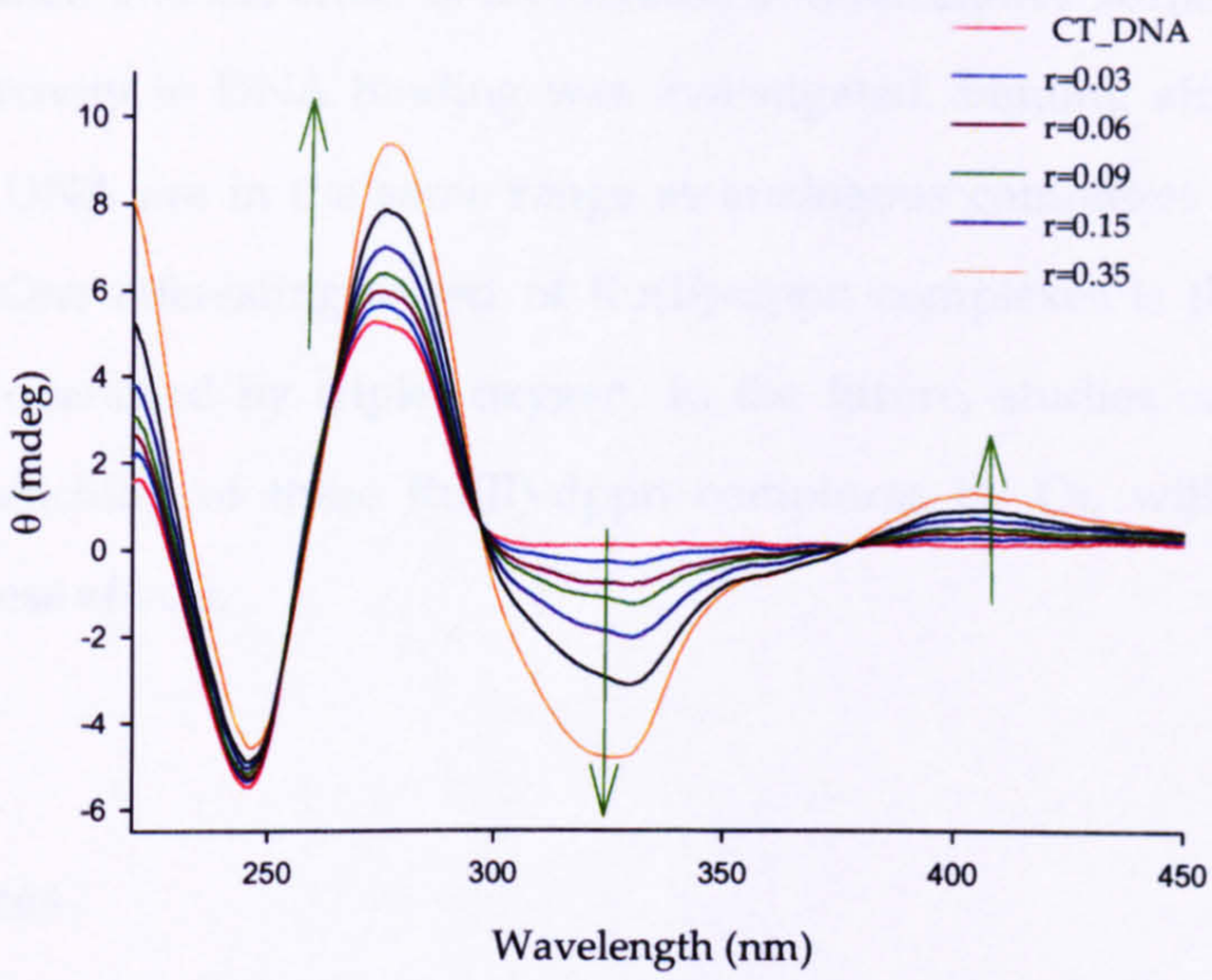

Figure 5.21: CD spectra for the interaction of **[5.6]** with CT-DNA at different molar ratios

5.9.6 ITC

ITC titrations were not carried out due to the poor solubility of these complexes at the concentration required. The ITC experiments resulted in the precipitation of gel around the syringe. The use of aqueous/organic solvent mixtures to improve solubility of the complexes may produce acceptable data.

5.10 Conclusion and future work

In this chapter the synthesis and characterisation of Ru(II)-dppz complexes based on chiral amino acids have been discussed and the interaction with DNA was studied. These complexes were shown to bind to CT-DNA via intercalation, but with smaller affinities compared to other Ru(II)-dppz metallo-intercalators. Interestingly complexes with *L*- amino acid ligand showed bigger affinity for CT-DNA than the

D-isomer suggesting some modulation of the binding due the chirality of the ancillary ligand.

In this chapter as well, complexes containing the extended intercalator ligand, dppn, have been studied and the effect of an increase in intercalative surface areas has on sequence selectivity in DNA binding was investigated. Binding affinities of these complexes to DNA are in the same range as analogous complexes containing the dppz ligand. One interesting aspect of Ru(II)-dppn complexes is that the excited state may be quenched by triplet oxygen. In the future, studies on emission life times and quenching of these Ru(II)-dppn complexes by O_2, will be carried to understand these effects.

5.11 References

(1) Garas, A. M. S.; Vagg, R. S. *J. Heretocyclic Chem.* **2000**, *37*, 151-158.

(2) Fees, J.; Kaim, W.; Moscherosch, M.; Matheis, W.; Klima, J.; Krejcik, M.; Zalis, S. *Inorg. Chem.* **1993**, *32*, 166-174.

(3) Yam, V. W.-W.; Lo, K. K.-W.; Cheung, K.-K.; Kong, R. Y.-C. *J. Chem. Soc., Chem. Commun.* **1995**, 1191-1193.

(4) Foxon, S.; Metcalfe, C.; Adams, H.; Webb, M.; Thomas, J. A. *in preparation*.

(5) Xu, W.; Kneas, K. A.; Demas, J. N.; DeGraff, B. A. *Anal. Chem.* **1996**, *68*, 2605-2609.

(6) Demas, J. N.; DeGraff, B. A. *J. Chem. Educ.* **1997**, *74*, 690-695.

(7) Gouterman, M. *J. Chem. Educ.* **1997**, *74*, 697-702.

(8) Kalyanasundaram, K. *Coord. Chem. Rev.* **1982**, *46*, 159-244.

(9) Sasso, M. G.; Quina, F. H.; Bechara, E. J. *Anal. Biochem.* **1986**, *156*, 239-43.

(10) Tan-Sien-Hee, L.; Jacquet, L.; Kirsch-De Mesmaeker, A. *J. Photochem. Photobiol., A* **1994**, *81*, 169-76.

(11) Kneas, K. A.; Xu, W.; Demas, J. N.; Degraff, B. A. *J. Chem. Educ.* **1997**, *74*, 696.

(12) Foxon, S.; Weinstein, J.; Thomas, J. A. In *Unpublished results* 2006.

(13) Liu, J.-G.; Zhang, Q.-L.; Ji, L.-N.; Cao, Y.-Y.; Shi, X.-F. *Transition Met. Chem.* **2001**, *26*, 733-738.

(14) Liu, J.-G.; Zhang, Q.-L.; Shi, X.-F.; Ji, L.-N. *Inorg. Chem.* **2001**, *40*, 5045-5050.

(15) Srinivas, V. R.; Bhanuprakash Reddy, G.; Surolia, A. *FEBS Lett.* **1999**, *450*, 181-185.

(16) Matulis, D.; Rouzina, I.; Bloomfield, V. A. *J. Mol. Biol.* **2000**, *296*, 1053-1063.

(17) Long, E. C.; Barton, J. K. *Acc. Chem. Res.* **1990**, *23*, 271-273.

(18) Suh, D.; Chaires, J. B. *Bioorg. Med. Chem.* **1995**, *3*, 723-728.

(19) Dougherty, G.; Pilbrow, J. R. *Int. J. Biochem.* **1984**, *16*, 1179-1192.

(20) Gabbay, E. J.; Scofield, R. E.; Baxter, C. S. *J. Am. Chem. Soc.* **1973**, *95*, 7850-7857.

(21) Zhen, Q.-X.; Zhang, Q.-L.; Liu, J.-G.; Ye, B.-H.; Ji, L.-N.; Wang, L. *J. Inorg. Biochem.* **2000**, *78*, 293-298.

(22) Friedman, A. E.; Chambron, J. C.; Sauvage, J. P.; Turro, N. J.; Barton, J. K. *J. Am. Chem. Soc.* **1990**, *112*, 4960-4962.

(23) Maheswari, P. U.; Rajendiran, V.; Palaniandavar, M.; Parthasarathi, R.; Subramanian, V. *J. Inorg. Biochem.* **2006**, *100*, 3-17.

(24) Phillips, T.; Haq, I.; Meijer, A. J. H. M.; Adams, H.; Soutar, I.; Swanson, L.; Sykes, M. J.; Thomas, J. A. *Biochemistry* **2004**, *43*, 13657-13665.

(25) McGhee, J. D.; von-Hippel, P. H. *J. Mol. Biol.* **1974**, *86*, 469-489.

(26) Scatchard, G. *Ann. N. Y. Acad. Sci.* **1949**, *51*, 660-672.

(27) Metcalfe, C.; Adams, H.; Haq, I.; Thomas, J. A. *Chem. Commun.* **2003**, 1152-1153.

(28) Hiort, C.; Lincoln, P.; Norden, B. *J. Am. Chem. Soc.* **1993**, *115*, 3448-3454.

(29) Nair, R. B.; Murphy, C. J. *J. Inorg. Biochem.* **1998**, 129-133.

(30) Nair, R. B.; Teng, E. S.; Kirkland, S. L.; Murphy, C. J. *Inorg. Chem.* **1998**, *37*, 139-141.

(31) Hergueta-Bravo, A.; Jimenez-Hernandez, M. E.; Montero, F.; Oliveros, E.; Orellana, G. *J. Phys. Chem. B* **2002**, *106*, 4010-4017.

(32) Phillips, T.; Rajput, C.; Twyman, L.; Haq, I.; Thomas, J. A. *Chem. Commun.* **2005**, 4327-4329.

Chapter Six

Ru(II)-azo(bpy)s

6.1 Introduction

Polynuclear transition metal polypyridine complexes are under much study because they possess favourable optical and electronic properties for use in light energy conversion and molecular devices[1,2]. Different ligands have been designed to give desired properties to metal centres, in particular the azo group has been used to confer photochromic, proton response and redox active properties to such metal complex[3,4].

In previous chapters, a range of monomeric Ru(II) complexes have been shown to bind to DNA. Recent studies have showed that bimetallic systems can also be used as DNA probes (see chapter one). In this chapter the DNA binding properties of some monomeric and bimetallic Ru(II)-azo(bpy)s complexes synthesised in the Otsuki's group are explored[5]. Figure 6.1 and figure 6.2 show the azo ligands and the Ru(II)-azo(bpy)s complexes used in the study. These complexes have not been chirally resolved.

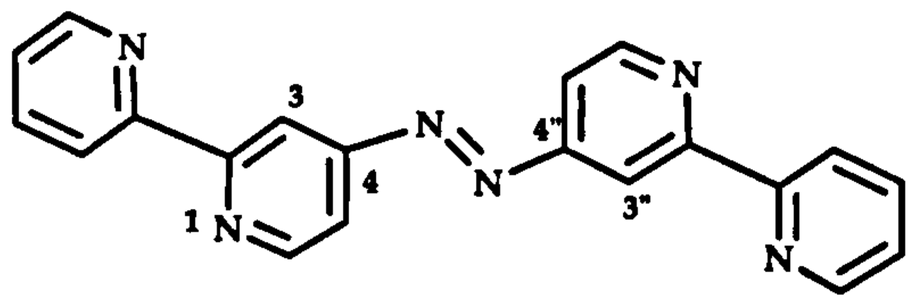

4,4"-azo ligand

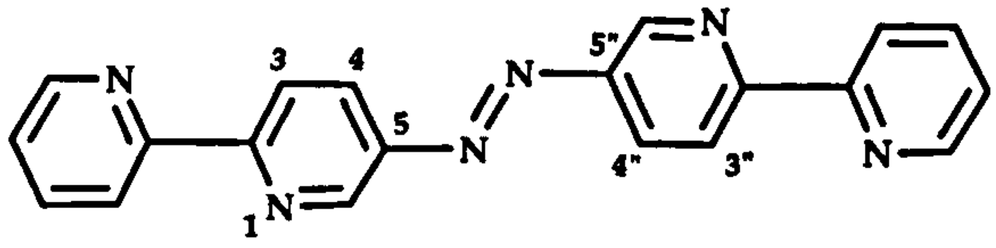

5,5"-azo ligand

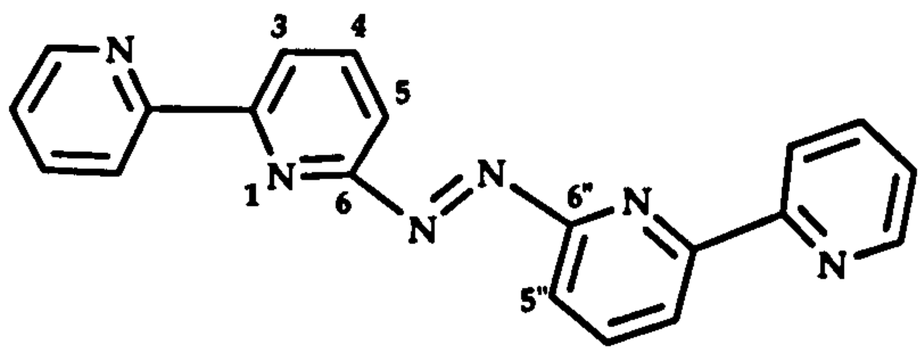

6,6"-azo ligand

Figure 6.1: Structure of azo ligands synthesised by Otsuki's group

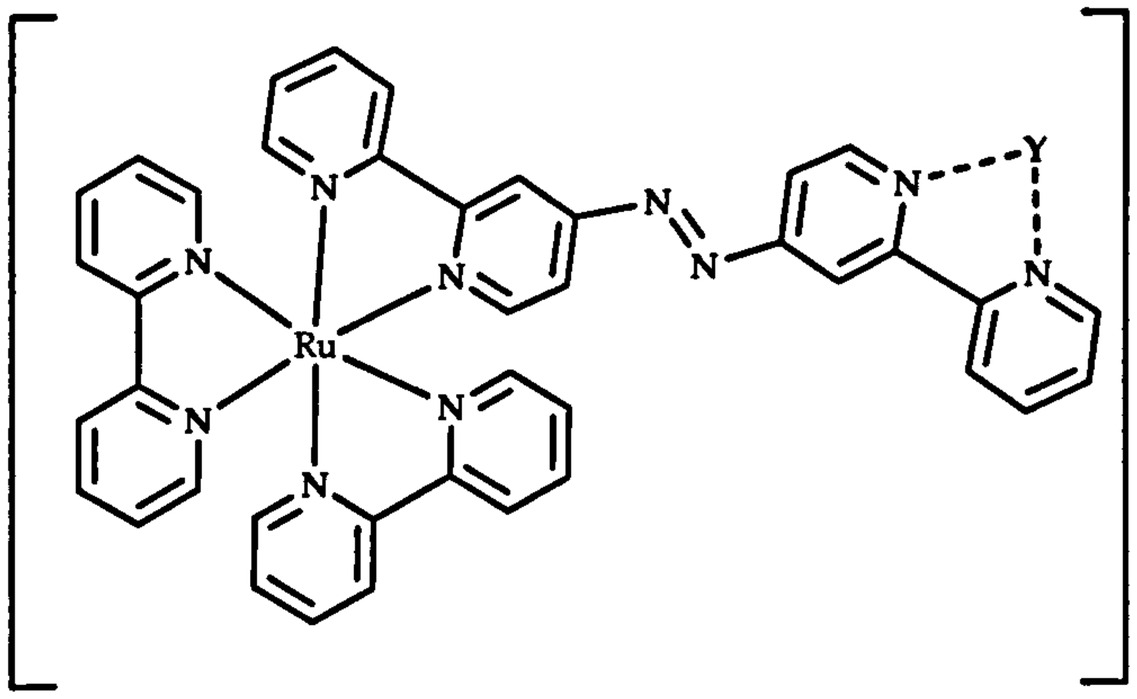

Y = 0, n =2 $[Ru(bpy)_2(4,4"\text{-azo})]^{2+}$ **Ru-(4,4"-azo)**
Y = $Ru(bpy)_2$, n = 4 $[Ru_2(bpy)_4(4,4"\text{-azo})]^{4+}$ **Ru-(4,4"-azo)-Ru**

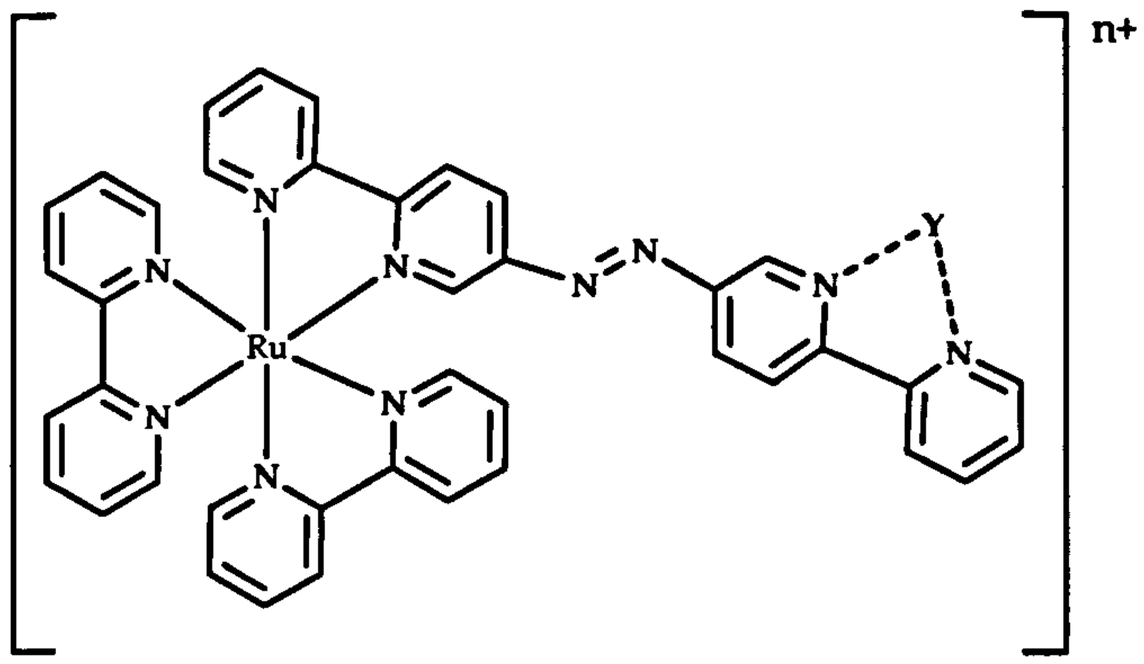

Y = 0, n = 2 $[Ru(bpy)_2(5,5"\text{-azo})]^{2+}$ **Ru-(5,5"-azo)**
Y = $Ru(bpy)_2$, n = 4 $[Ru_2(bpy)_4(5,5"\text{-azo})]^{4+}$ **Ru-(5,5"-azo)-Ru**

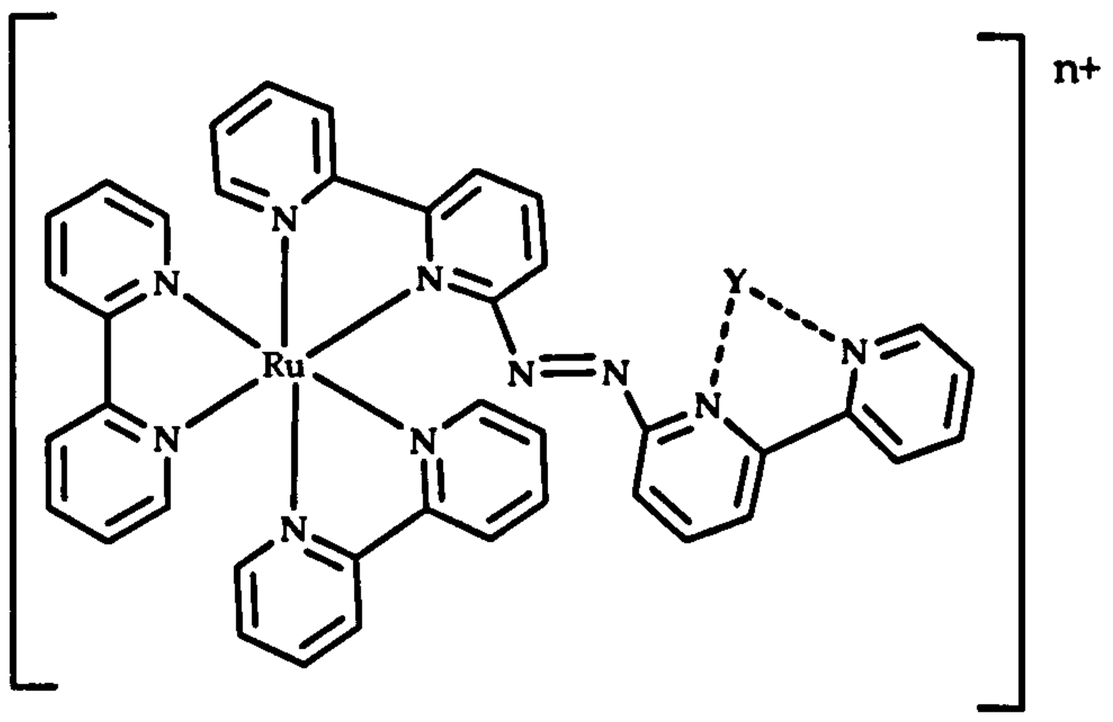

Y = $Ru(bpy)_2$, n = 4 $[Ru_2(bpy)_4(6,6"\text{-azo})]^{4+}$ **Ru-(6,6"-azo)-Ru**

Figure 6.2: Structure of Ru(II)-azo(bpy)s complexes synthesised by Otsuki's group

6.2 Binding studies

6.2.1 Melting points

T_m of CT-DNA in absence and presence of Ru(II)-azobis(bpy)s complexes were measured. In most of the cases the addition of the complexes to nucleic acid solution results in an increase in the melting point of the DNA, indicating a stabilising interaction (figure 6.3)

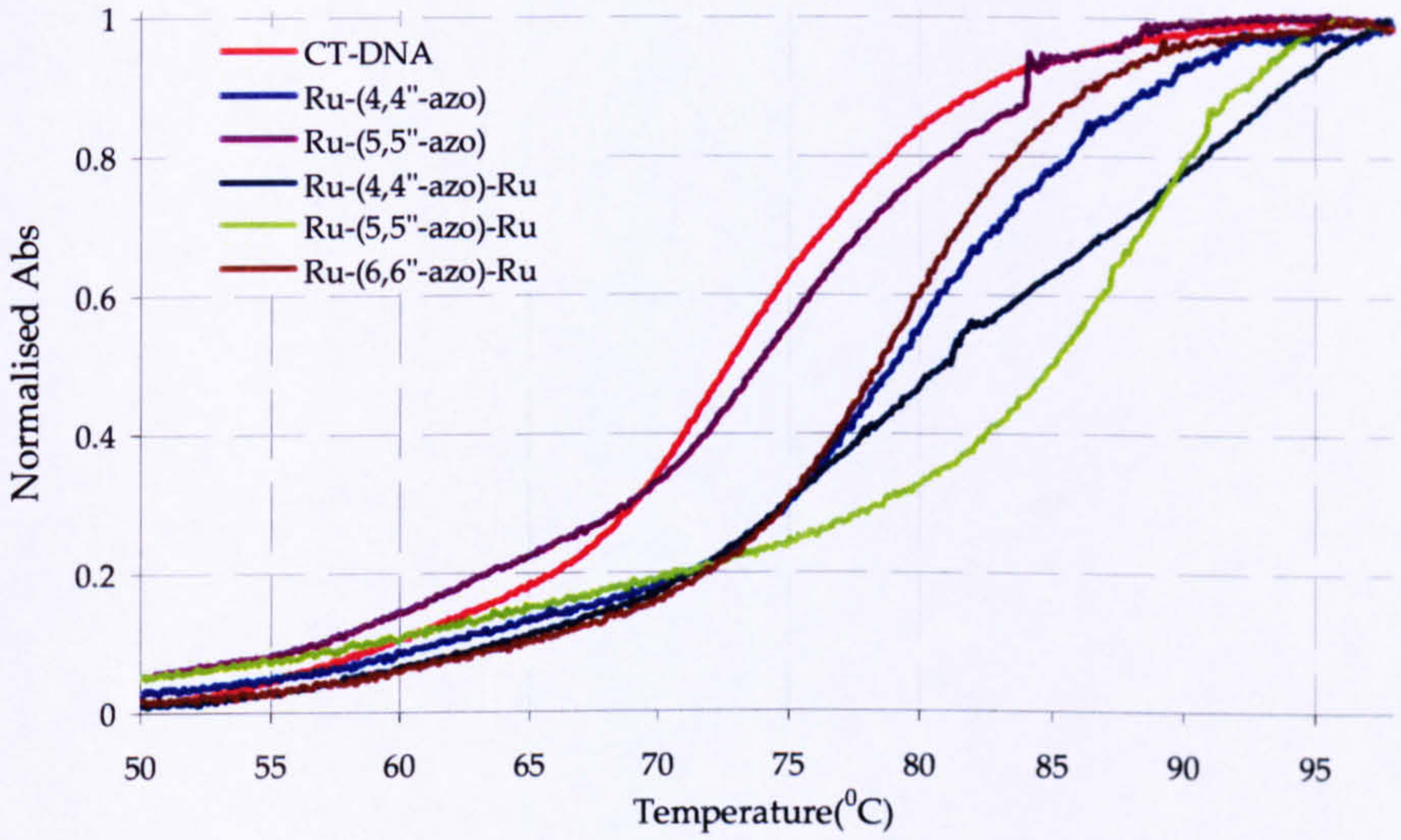

Figure 6.3: T_m of CT-DNA in the absence (red line) and presence of Ru(II)-azobis(bpy)s complexes

The T_m of CT-DNA in the experimental conditions is 72.7 °C. As can be see in figure 6.2, complex Ru-(5,5"-azo) produces very little stabilisation of CT-DNA, in contrast the dimer containing the same bridge ligand, stabilises DNA by almost 15 °C, showing that the bimetallic complex exhibits higher affinity than the monomer for CT-DNA. The same effect is observed for the (4,4"-azo) complexes, where Ru-(4,4"-azo) stabilises CT-DNA by around 10 °C and the T_m of the bimetallic Ru-(4,4"-azo)-Ru bound to CT-DNA can not be determined because the end of the melting point curve is not reached, but is possible to estimate that the stabilisation is at least 20 °C. Complex Ru-(6,6"-azo)-Ru stabilises this duplex by 7 °C. This data is summarised in table 6.1.

Table 6.1: Melting points of Ru(II)-azobis(bpy)s complexes with CT-DNA

Compound	T_m (°C)	ΔT_m	%H
Ru-(4,4"-azo)	80.41	7.71	20.45
Ru-(5,5"-azo)	77.08	4.38	30.20
Ru-(4,4"-azo)-Ru	[a]	[a]	[a]
Ru-(5,5"-azo)-Ru	87.29	14.59	18.18
Ru-(6,6"-azo)-Ru	79.62	6.92	17.48

[a] End of the melting point curve not reached

6.2.2 UV-Vis titrations

The interaction of the metal complexes with DNA results in changes in the UV-Vis spectrum of the metal complex due to changes in the environment of the metal complex.

The UV-Vis spectra of complexes Ru-(5,5"-azo) and Ru-(5,5"-azo)-Ru consists of several well defined bands at 245, 286, 377, 444 and 520 nm[5]. When bound to DNA both complexes showed hypochromicity effects at 286 and 377 nm and bathochromic shifts having two isosbestic points at 380 nm and 450 nm (figure 6.4).

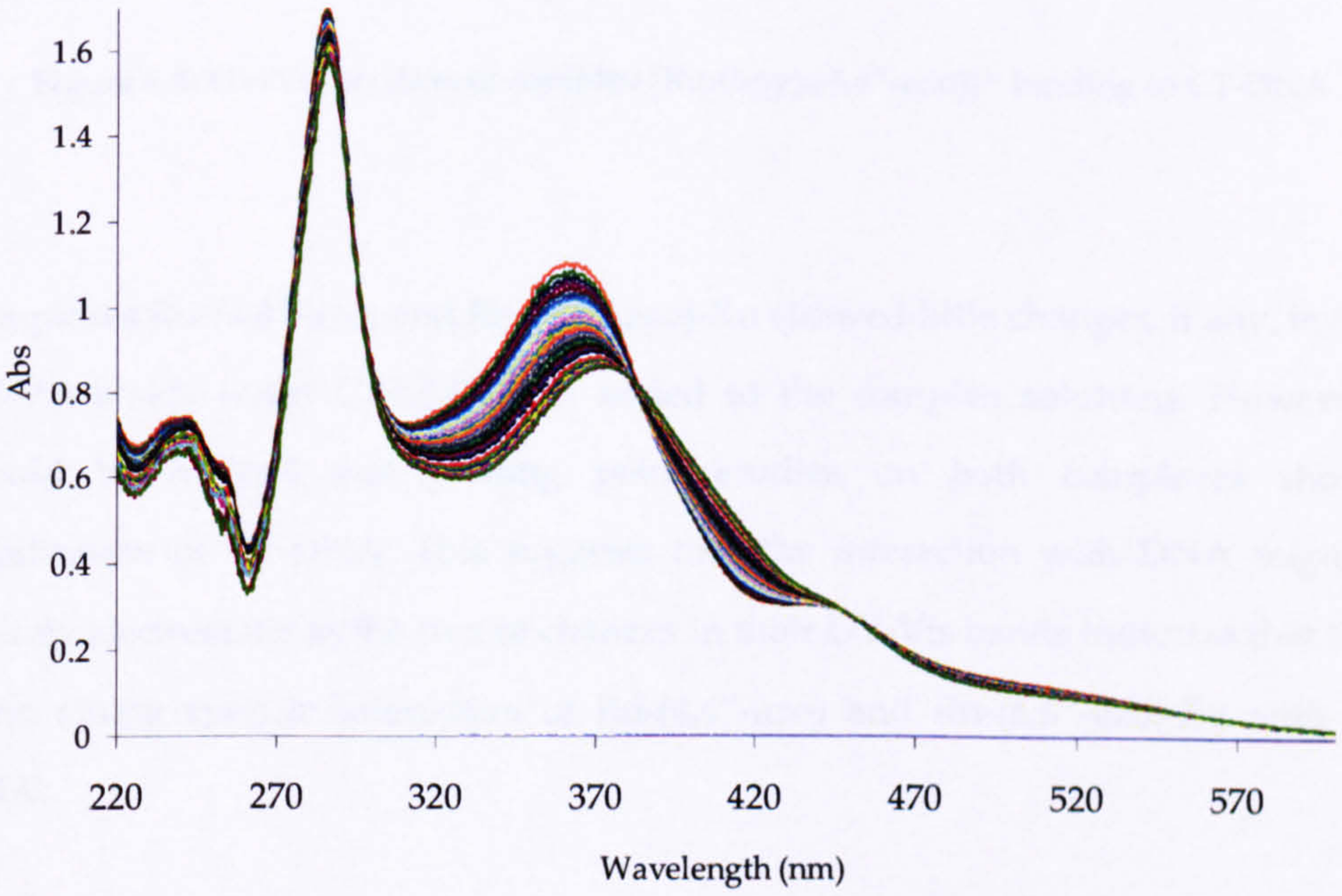

Figure 6.4: UV-Vis titration of $[Ru(bpy)_2(5,5"\text{-azo})]^{2+}$ binding to CT-DNA

UV-Vis spectrum of complexes Ru-(4,4″-azo) and Ru-(4,4″-azo)-Ru shows bands at 245, 286 and 440 nm. Both complexes also show a MLCT band at 496 nm (for the monomer) and 558 nm (for the dimer)[5]. In the titration of the complex Ru-(4,4″-azo)-Ru with CT-DNA, the bands at 245, 286 nm and 558 nm showed hypochromicity and the band at 558 nm also showed also a large bathochromic shift with an isosbestic point at 600 nm (figure 6.5).

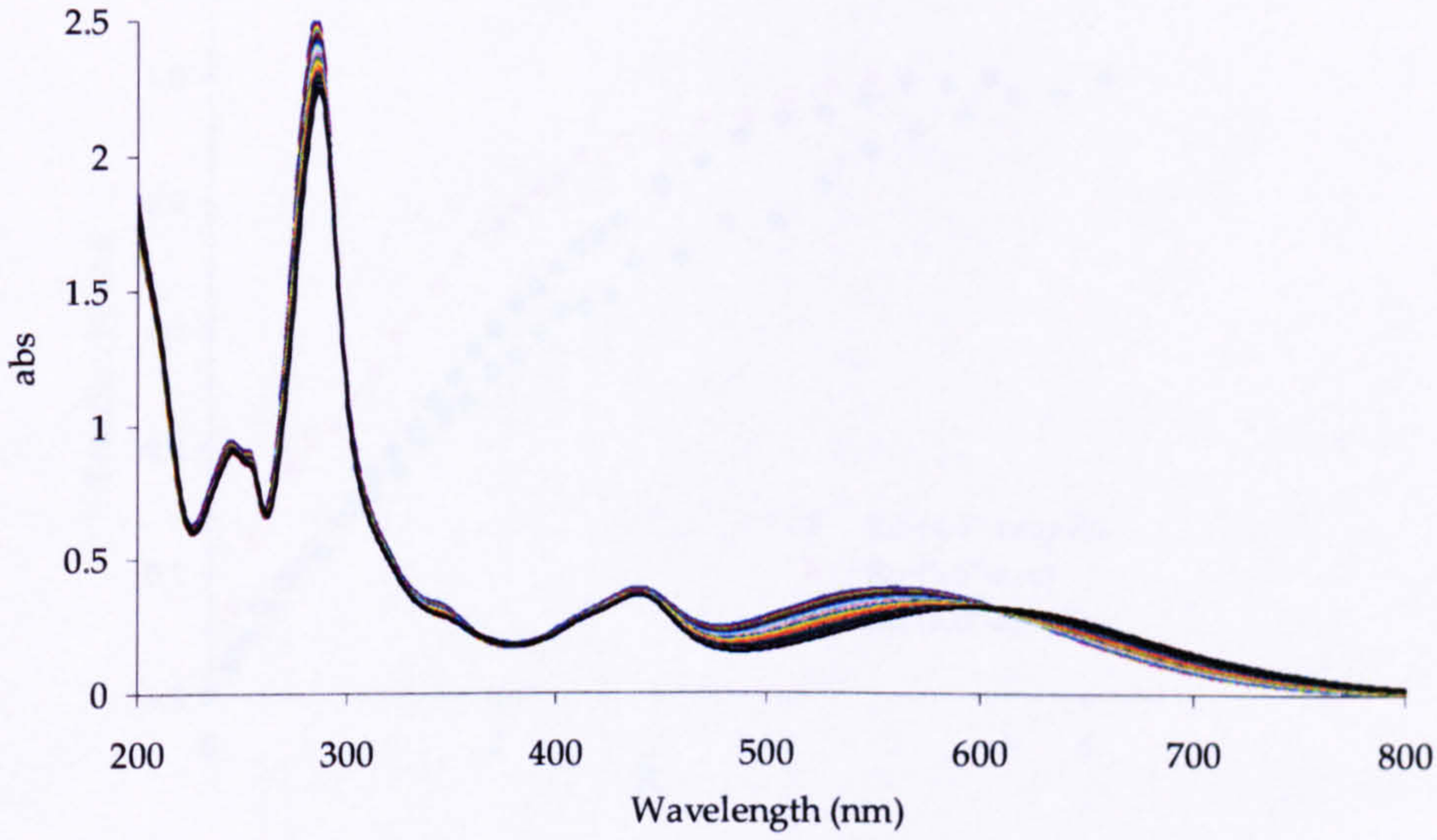

Figure 6.5: UV-Vis titration of complex $[Ru_2(bpy)_2(4,4''\text{-azo})]^{4+}$ binding to CT-DNA

Complexes Ru-(4,4″-azo) and Ru-(6,6″-azo)-Ru showed little changes, if any, in their UV-Vis bands when CT-DNA was added to the complex solutions. However it should be noticed that melting point studies on both complexes showed stabilisation of CT-DNA. This suggests that the interaction with DNA might be entirely electrostatic as the lack of changes in their UV-Vis bands indicates that there is no strong specific interaction of Ru-(4,4″-azo) and Ru-(6,6″-azo)-Ru with CT-DNA.

For the study of the interaction of Ru-(5,5"-azo), Ru-(4,4"-azo)-Ru and Ru-(5,5"-azo)-Ru with CT-DNA, changes in the 358 nm band for Ru-(5,5"-azo), and in the bands 558 nm and 369 nm for Ru-(4,4"-azo)-Ru and Ru-(5,5"-azo)-Ru respectively, were used to binding curves, figure 6.5. These all showed that saturation binding had taken place.

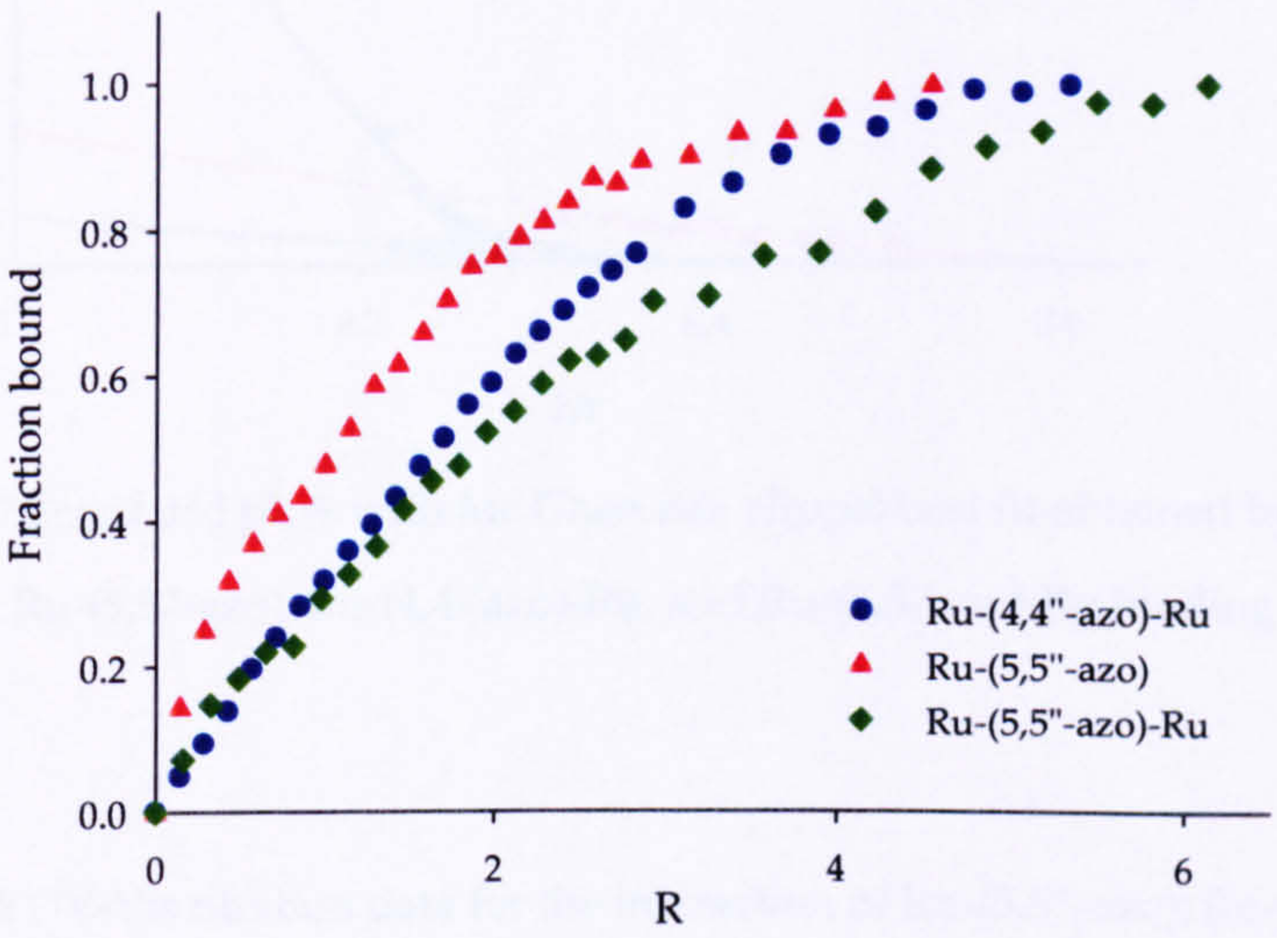

Figure 6.6: Binding curves obtained by UV-Vis titrations Ru-(5,5"-azo), Ru-(4,4"-azo)-Ru and Ru-(5,5"-azo)-Ru binding to CT-DNA

The binding constant for the interaction of these complexes with CT-DNA were calculated using the McGhee Von Hippel model for fitting of non-linear Scatchard plots (figure 6.7). Data is summarised in table 6.2.

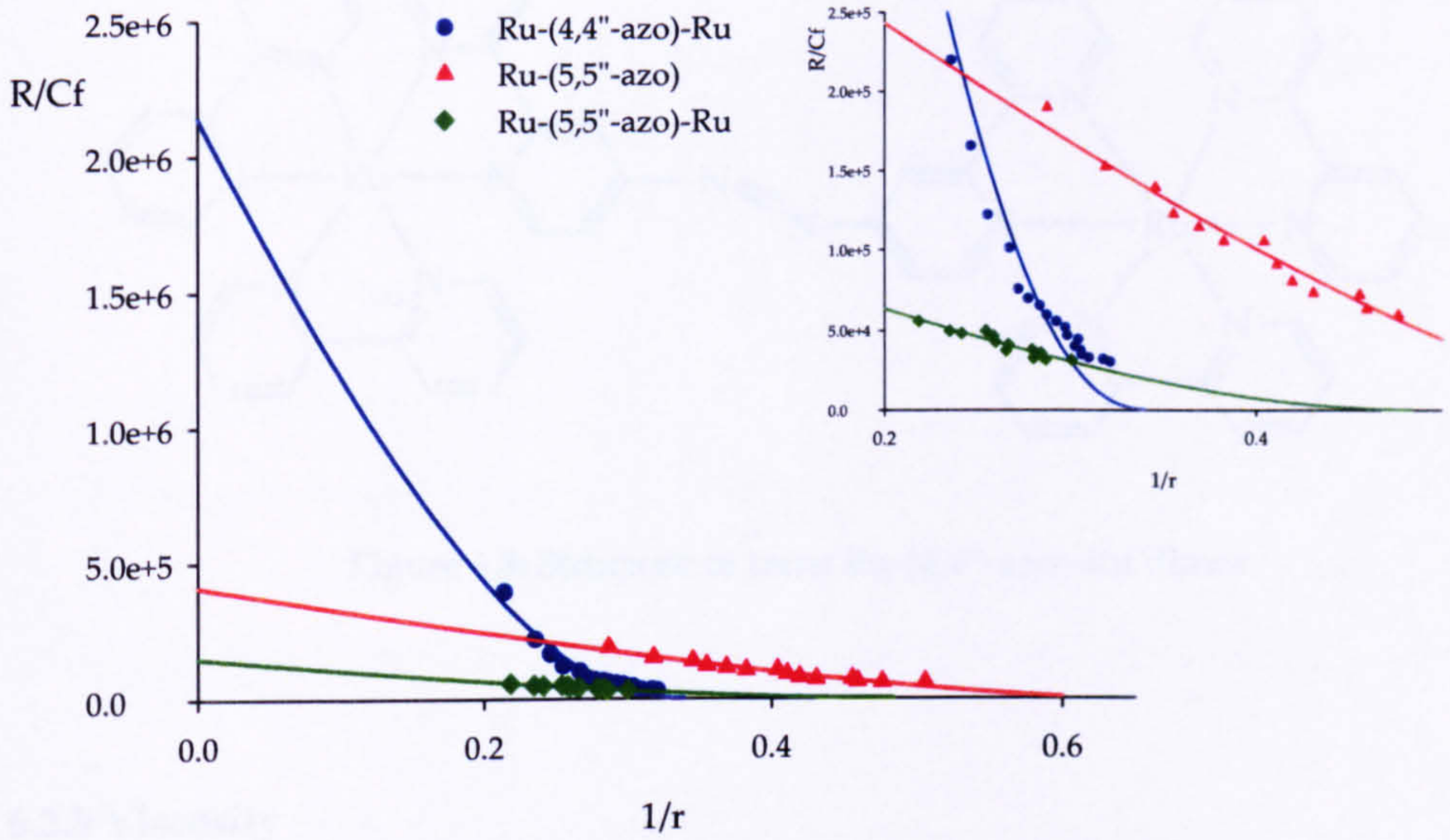

Figure 6.7 Scatchard plots with Mc Ghee von Hippel best fit obtained by UV-Vis titrations for Ru-(5,5″-azo), Ru-(4,4-'azo)-Ru, and Ru-(5,5-'azo)-Ru binding to CT-DNA

Table 6.2: UV-Vis titration data for the interaction of Ru-(5,5″-azo), Ru-(4,4″-azo)-Ru, and Ru-(5,5″-azo)-Ru with CT-DNA

Compound	K_a (M^{-1})	N (bp)	% Hyp
Ru-(5,5"-azo)	$1.46 \pm 0.16 \times 10^5$	2.01 ± 0.09	26.03
Ru-(4,4"-azo)-Ru	$1.61 \pm 0.17 \times 10^6$	3.00 ± 0.04	47.04
Ru-(5,5"-azo)-Ru	$1.48 \pm 0.13 \times 10^5$	2.06 ± 0.07	23.18

Complex Ru-(4,4″-azo)-Ru binds to CT-DNA with an affinity in the micromolar range, and a stoichiometry of 3 base pairs per ligand. This complex binds with higher affinity than the other complexes studied in this chapter and is similar to Ru(II) complexes that intercalate into DNA. As we have seen in the introduction, groove binding compounds fit well in between the walls of the DNA helix[6]. The structure of Ru-(4,4″-azo)-Ru can be drawn as in figure 6.8, suggesting that this complex has the right shape to interact with the DNA as a groove binder.

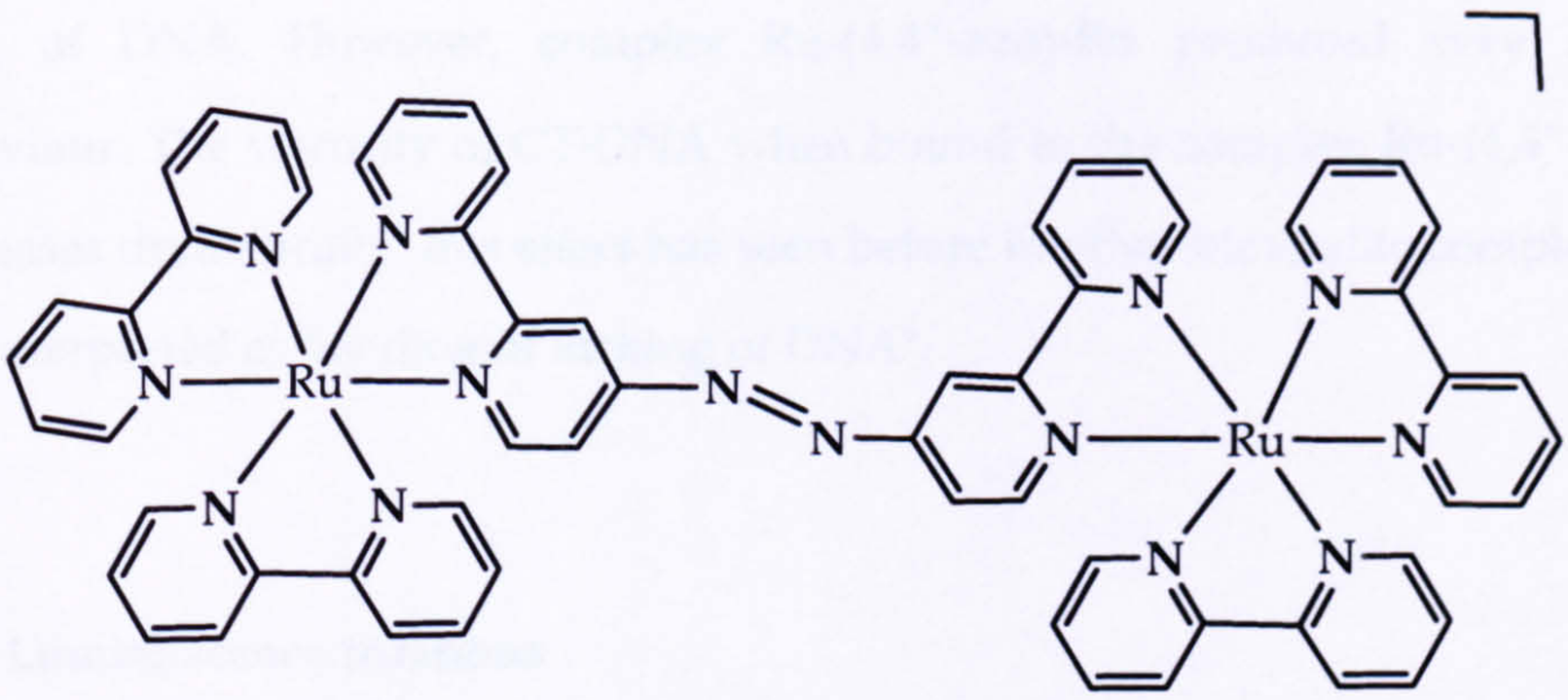

Figure 6.8: Structure of trans Ru-(4,4″-azo)-Ru dimer

6.2.3 Viscosity

To assess the DNA-binding mode of complexes Ru-(5,5″-azo), Ru-(4,4″-azo)-Ru and Ru-(5,5″-azo)-Ru viscosity measurements were performed. The changes in the relative viscosity of CT-DNA upon addition of these complexes are represented in figure 6.9.

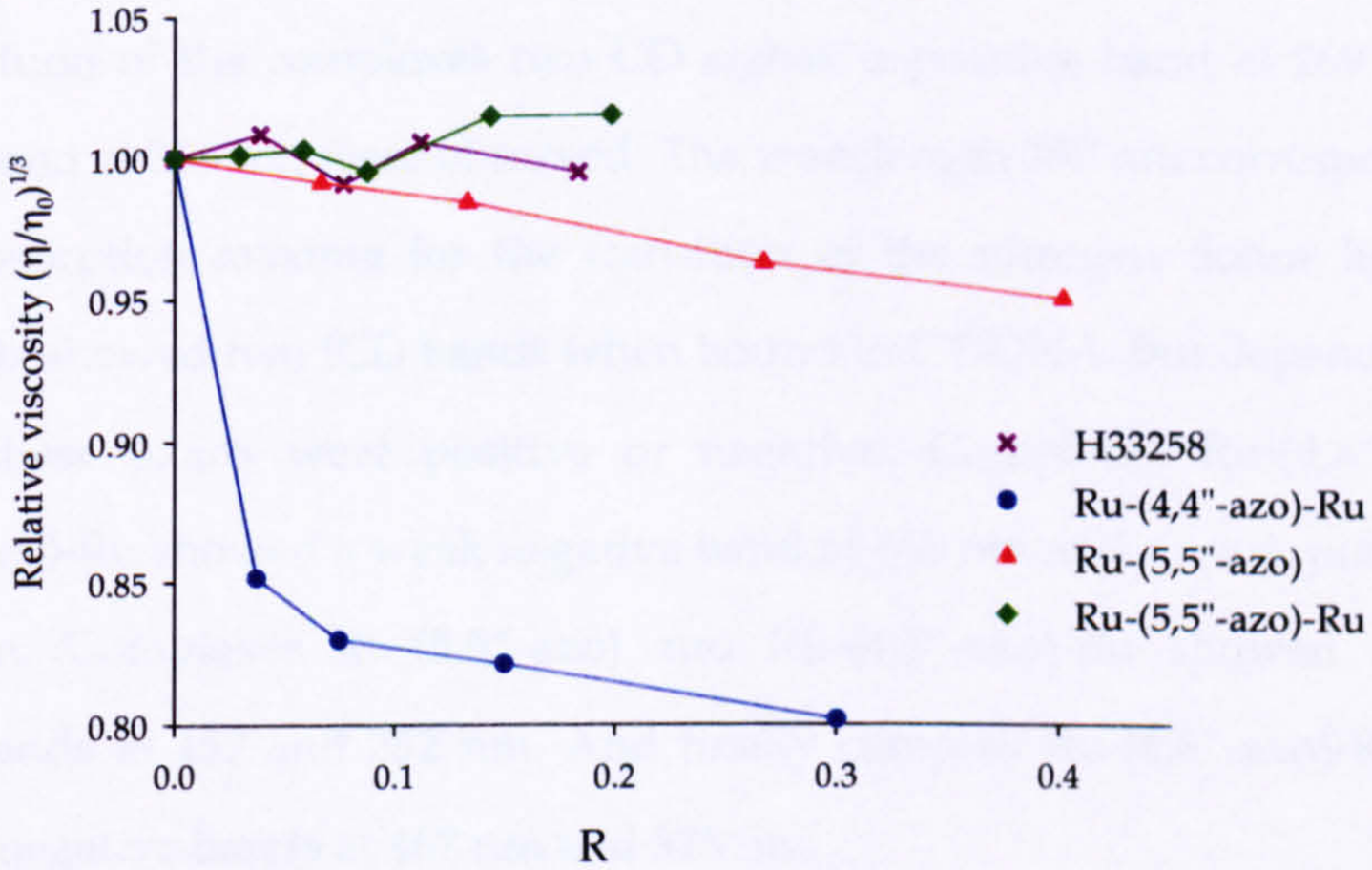

R

Figure 6.9: Relative viscosity of CT-DNA upon addition Ru-(5,5″-azo), Ru-(4,4″-azo)-Ru, and Ru-(5,5″-azo)-Ru $^{+}$ complexes and H33258 (purple)

The viscosity of CT-DNA showed very little change on the addition of complexes Ru-(5,5″-azo) and Ru-(5,5″-azo)-Ru, indicating no intercalation between the base

pairs of DNA. However, complex Ru-(4,4"-azo)-Ru produced very different behaviour. The viscosity of CT-DNA when bound to the complex Ru-(4,4"-azo)-Ru decreases dramatically, this effect has seen before in other bimetallic complexes and it is interpreted as bending or kicking of DNA[7].

6.2.4 Luminescence titrations

All complexes showed little or no emission in organic solvents and addition of CT-DNA in aqueos solution did not enhance emission. Therefore interactions of these complexes with DNA were not studied by luminescence titrations.

6.2.5 Circular dichroism (CD) spectra

Since these complexes are racemic mixtures they display no CD signals. Circular dichroism of Ru(II)-azo(bpy)s complexes with CT-DNA have been measured over a range of complex/DNA ratios. Figure 6.10 shows a typical CD spectrum of the interaction of these complexes with CT-DNA.

Upon addition of the complexes two CD signal, a positive band at 269 nm and a negative band at 288 nm were observed. The wavelength 280 nm corresponds to the UV-Vis absorption maxima for the transition of the nitrogen donor ligands. All compounds showed two ICD bands when bound to CT-DNA, but depending on the complex these bands were positive or negative. Complexes Ru-(4,4"-azo) and Ru-(5,5"-azo)-Ru showed a weak negative band at 465 nm and a weak positive band at 376 nm. Complexes Ru-(5,5"-azo) and Ru-(4,4"-azo)-Ru showed two weak positive bands at 457 and 352 nm. And finally complex Ru-(6,6"-azo)-Ru showed two weak negative bands at 467 nm and 375 nm.

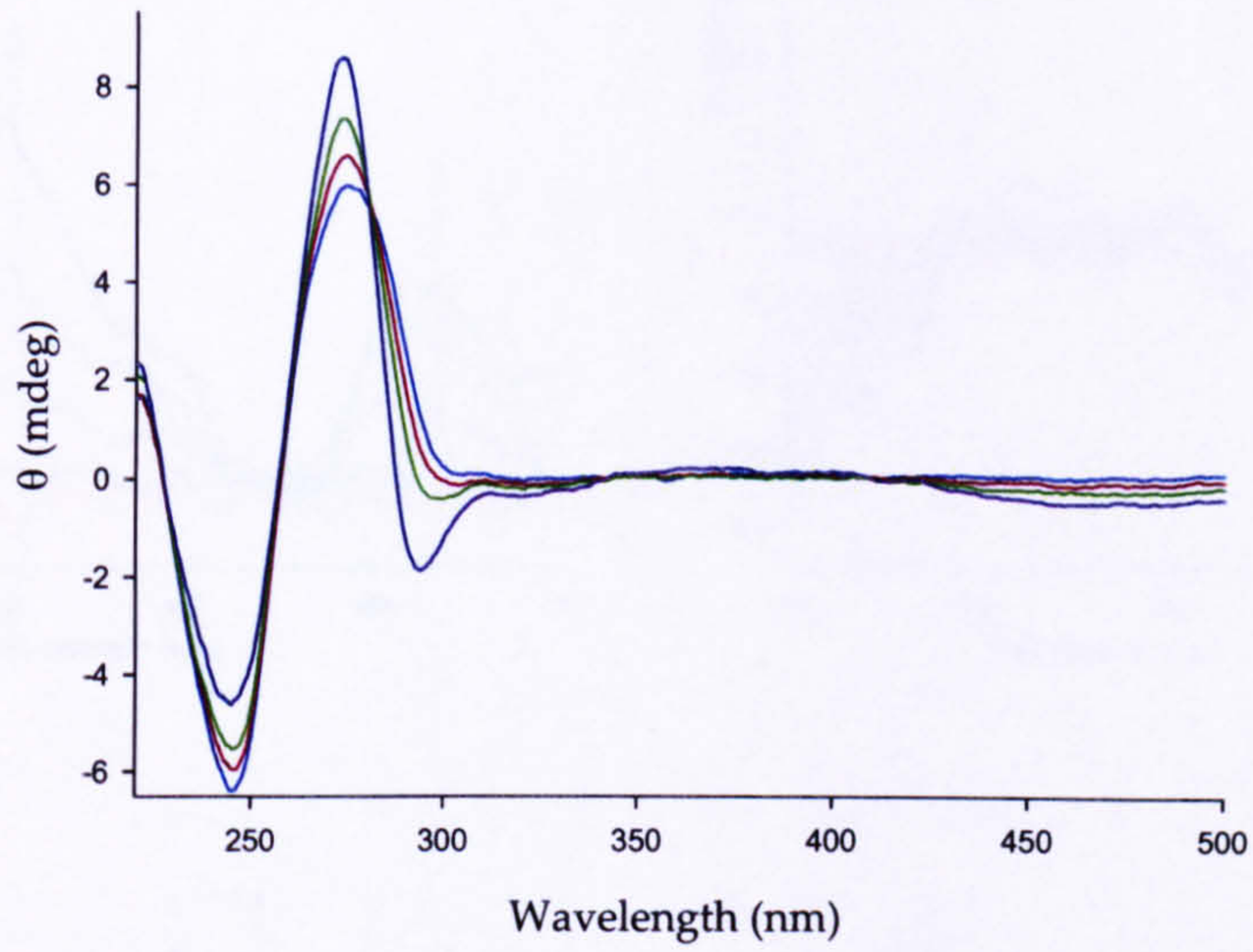

Figure 6.10: CD spectrum of CT-DNA upon addition of Ru-(4,4″-azo) at different molar ratios

Figure 6.11 and figure 6.12 shows the changes in the ICD spectrum, from 300 to 500 nm upon addition of Ru(II)-azo(bpy)s monomers and dimmers (respectively) to CT-DNA.

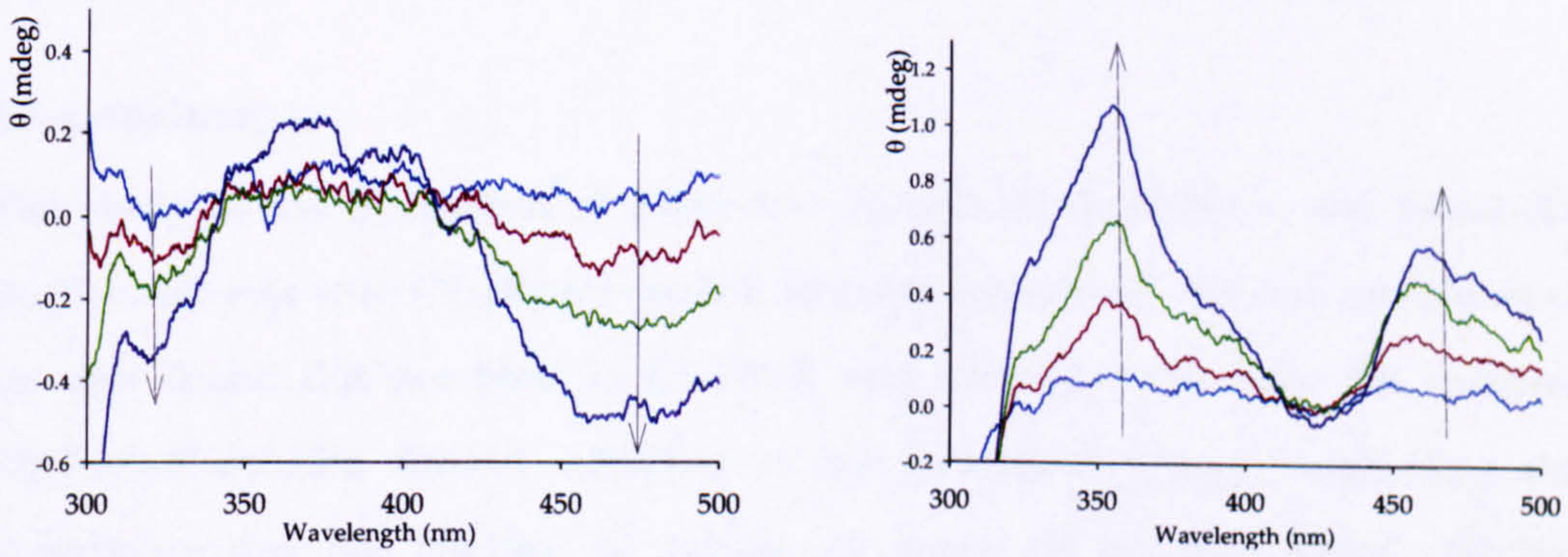

Figure 6.11: ICD spectrum of Ru-(4,4″-azo) (left) and Ru-(5,5″-azo) (right) complexes when bound to CT-DNA

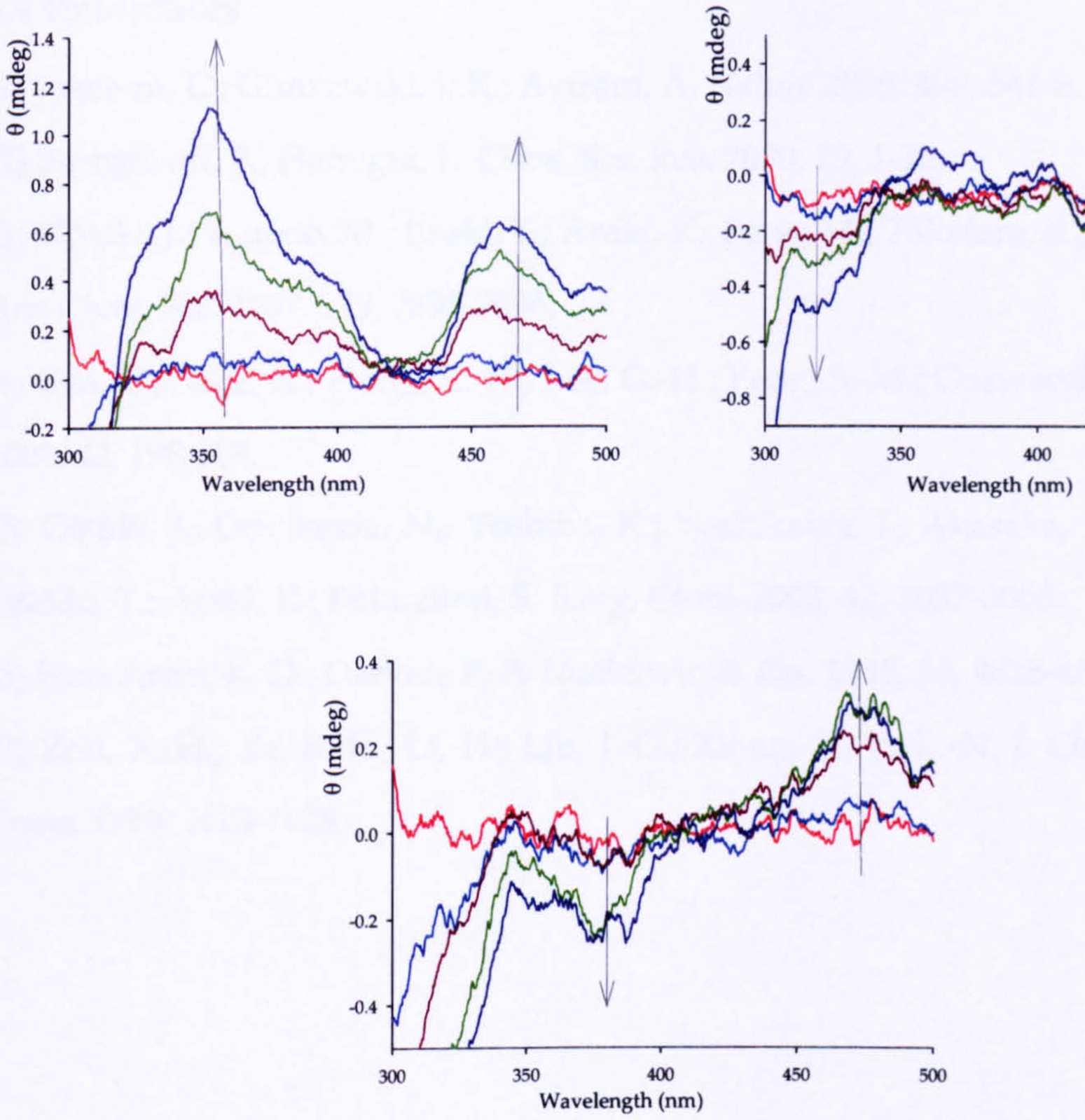

Figure 6.12: ICD spectrum of Ru-(4,4″-azo)-Ru (up left), Ru-(5,5″-azo)-Ru (up right) and Ru-(6,6″-azo)-Ru (down) complexes when bound to CT-DNA

6.3 Conclusions

The study of the interaction of geometric isomers of monomeric and bimetallic Ru(II)-azo(bpy)s with CT-DNA revealed different behaviours. Several complexes of the azo ligand did not bind to CT-DNA very strongly. However the complex Ru(II)-(4,4″-azo)-Ru showed affinities in the micromolar range, suggesting the importance, for the binding to duplex, of shape of the azo ligand. Further thermodynamic studies of this complex binding to different types of DNA could illustrate the energy profile of binding and also reveal any preference for binding (many groove binder show strong preference for binding A-T base pairs).

6.4 References

(1) Joachim, C.; Gimzewski, J. K.; Aviram, A. *Nature* **2000**, *408*, 541-8.

(2) Barigelletti, F.; Flamigni, L. *Chem. Soc. Rev.* **2000**, *29*, 1-12.

(3) Otsuki, J.; Tsujino, M.; Iizaki, T.; Araki, K.; Seno, M.; Takatera, K.; Watanabe, T. *J. Am. Chem. Soc.* **1997**, *119*, 7895-7896.

(4) Das, C.; Saha, A.; Hung, C.-H.; Lee, G.-H.; Peng, S.-M.; Goswami, S. *Inorg. Chem.* **2003**, *42*, 198-204.

(5) Otsuki, J.; Omokawa, N.; Yoshiba, K.; Yoshikawa, I.; Akasaka, T.; Suenobu, T.; Takido, T.; Araki, K.; Fukuzumi, S. *Inorg. Chem.* **2003**, *42*, 3057-3066.

(6) Harshman, K. D.; Dervan, P. B. *Nucleic Acids Res.* **1985**, *13*, 4825-4835.

(7) Zou, X.-H.; Ye, B.-H.; Li, H.; Liu, J.-G.; Xiong, Y.; Ji, L.-N. *J. Chem. Soc., Dalton Trans.* **1999**, 1423-1428.

Chapter Seven

Experimental procedures

7.1 Chemicals

All chemicals were purchased from commercial sources and were used as supplied unless otherwise stated.

7.2 Nuclear magnetic resonance spectra

Standard ^1H NMR spectra were recorded on a Brucker AM250 machine, working in Fourier transform mode. The following abbreviations are used in the annotation of ^1H NMR spectra: br-broad, s-singlet, d –doublet, dd-double doublet, dt-double triplet, t-triplet, q-quartet and m-multiplet.

7.3 Mass spectrum

FAB spectra were obtained on a Kratos MS80 machine working positive ion mode, with m-nitrobensyl alcohol matrix.

7.4 Electrochemistry studies

Cyclic voltammograms were recorded using an EG&G model 3362 potentiostat and either the Condecon 310 hardware/software package or the EG & G electrochemistry power suite package. Measures were made using approx. 2 mmol solutions of material made up in freshly distilled acetonitrile that contained 0.1 M Bu_4NPF_6 as the support electrolyte. Potentials were measured against Ag/AgCl reference electrode and ferrocene was used as an internal reference.

7.5 UV-VIS absorption spectra.

UV-VIS spectra were recorded in a Cary 3 Bio UV-Vis spectrophotometer in twin beam mode. Spectra were recorded in matched quartz cells and were baseline corrected.

7.6 Emission spectra

Luminescence titrations were carried out in a Hitachi Fluorescence Spectrophotometer F-4500.

7.7 X-ray crystallography

Data collected were measured on Bruker Smart CCD area detector with Oxford Crysosystems low temperature system and complex scattering factors taken from the program package SHELXTL.

Data for the crystals are included in the accompanying CD.

7.8 Sample preparation for binding studies

All complexes were converted to chloride salts by treating the PF_6^- salt with $^nBu_4Cl$ in acetone. The chloride salt was collected by centrifugation and copiously washed with acetone.

Calf thymus DNA (CT-DNA) was purchased from the Sigma-Aldrich company as a lyophilised solid sodium salt and dissolved in 25 mM NaCl, 5 mM Tris, pH 7.0 buffer. The purity of the sample was determined by UV-visible spectroscopy, with $A_{260}/A_{280} > 1.9$ indicating a protein free sample. The CT-DNA was broken into an average of 150-200 base pair (bp) by sonication, after that it was dialysed (dialysis tubing with a MWCO of 3,500 Daltons) in 2 L of the Tris buffer for 24 h. The concentration of the resulting solution was determined by UV spectroscopy using: $\varepsilon_{260} = 13200\ M^{-1}\ cm^{-1}$.

poly(dA)·poly(dT), poly(dG)·poly(dC) (DNA duplexes) and poly(dA-dT)·poly(dA-dT), poly(dG-dC)·poly(dG-dC) (DNA alternating co-polymers) were purchased from Amersham Pharmacia Biotech. Each sample was dissolved in 2 mL of the Tris buffer and dialysed for at least 24 hours. The concentration of the DNA was determined by UV spectroscopy using the following: $\varepsilon_{260} = 12000\ M^{-1}\ cm^{-1}$ for poly(dA)·poly(dT), $\varepsilon_{260} = 13100\ M^{-1}\ cm^{-1}$ for poly(dA-dT)·poly(dA-dT), $\varepsilon_{254} = 14000\ M^{-1}\ cm^{-1}$ for poly(dG)·poly(dC) and $\varepsilon_{254} = 16800\ M^{-1}\ cm^{-1}$ for poly(dG-dC)·poly(dG-dC)[1].

7.9 Binding studies protocols

7.9.1 Melting points

Melting points (T_m) of the complexes with double stranded DNA were carried out in a Cary 3 Bio UV-Vis spectrophotometer, using a 1 cm path length cuvette. Samples were prepared in buffer, using typical concentrations of 50 μM of DNA and 8.3 μM of metal complex. T_m measurements were initiated near 35 °C and temperature was increased at rate of 0.25 °C per min until 98 °C. The wavelength used to follow the changes in absorbance (melting point) was 260 nm.

7.9.2 Viscosity

Viscosity measurements were carried out in a Cannon-Manning semi-micro viscometer (size 50) immersed in a thermostatted bath maintained at 27 °C. The viscometer requires 1 mL of sample. The concentration of CT-DNA was kept constant at 0.5 mM (bp), and the different samples were prepared by adding ligand to the DNA solution to give an increase in the ligand/bp ratios. The flow times were measured after thermal equilibration of 20 minutes. Each sample was measured three times and the average time was calculated.

7.9.3 Continuous variation analysis (Job plots)

Continuous variation analyses were carried out in a Fluorescence Spectrophotometer F-4500. The sum of the concentrations of CT-DNA and metal complex was kept constant at 50μM, and the concentration of DNA and metal complex was varied. The fluorescence intensities of these mixtures were measured using the excitation wavelength characteristic of each metal complex at 25 °C.

7.9.4 UV-Vis titrations

UV-Vis titrations were carried out in a Cary 3 Bio UV-Vis spectrophotometer. 3 mL of buffer were loaded in a 1 cm path length cuvette; a volume of buffer was removed with a pipette and replaced with the same volume of a stock solution of complex, to give a final concentration of around 50 μM. This cuvette was loaded

into the spectrometer and kept at 25 °C. 3 mL of buffer were loaded into an identical cuvette and placed in the reference cell in the spectrometer. After equilibration the spectrum was recorded between 200-600 nm. 2 μL of a concentrated stock CT-DNA solution were added to both cuvettes and mixed. The spectrum was recorded after leaving them to equilibrate and checking that no bubbles were present. This procedure was continued until the absorbance became constant or the increase of DNA concentration caused small increases in the absorption.

UV-Vis titrations not shown in the chapters are included in the accompanying CD.

7.9.5 Luminescence titrations

Luminescence titrations were carried out in a Hitachi Fluorescence Spectrophotometer F-4500 in a procedure similar to the UV-Vis titrations. Both buffer and complex solutions show insignificant emission, so no reference cell was used. 3 mL of buffer were loaded in a 1 cm path length luminescence cuvette; a volume of buffer was removed and replaced with the same volume of a stock solution of complex, to give a final concentration of 50 μM. The cuvette was loaded into the spectrophotometer and kept at 25 °C. After equilibration, the emission spectrum of the solution was recorded using the excitation wavelength characteristic of the complex. 2 μL of a concentrated stock CT-DNA solution were added to the cuvette and mixed, and then the emission spectrum was recorded, showing an enhancement in emission. This procedure was continued until the emission became constant.

Luminescence titrations not shown in the chapters are included in the accompanying CD.

7.9.6 Circular Dichroism (CD)

CD spectra were recorded on a Jasco J-810 Spectropolarimeter at 25 °C. The concentration of the nucleic acid was kept constant at 50 μM and the different samples were prepared by adding complex to the DNA solution to increase the ligand/bp ratios. The CD spectra were recorded at rate of 100 nm/min from 200 nm to 500 nm with an instrument response of 4 seconds.

CD spectra not shown in the chapters are included in the accompanying CD.

7.9.7 Isothermal Titration Calorimetry (ITC)

Calorimetric data were obtained using a MicroCalorimeter. The reference cell was filled with distilled water. The sample cell was filled with a large excess of DNA (typical concentration of around 0.3 mM) and aliquots of the complexes solutions (concentrations between 1-1.5 mM) were titrated into the DNA solution. The DNA solution was stirred continuously at 300 rpm over all the experiment which were carried at 25 °C (unless is specified). Heats of dilution for each compound were determinated by titrating the complex into the buffer solution. These dilution heats were subtracted from the ΔH° value for DNA-complex titration to give a corrected heat effect. Each titration was repeated at least two times and calculated the average of ΔH°.

ITC titrations not shown in the chapters are included in the accompanying CD.

7.9.8 Surface Plasmon Resonance (SPR)

Surface plasmon resonance bindings were carried out using a BioCore 3000 instrument. A streptavadin (SA5) sensor chip was equilibrated in 10 mM Hepes, 150 mM NaCl, 3 mM EDTA. The DNA 5′ biotin labelled duplex and single-stranded DNA were diluted into the equilibrium buffer and immobilised onto the four channels of a sensor chip giving a response between 100 and 200 RU. To correct for non-specific binding and bulk refractive index changes a blank channel containing only buffer was used as a control. All binding experiment were carried out at 25 °C, the complexes were diluted into Tris buffer (binding buffer) to give a range of concentrations of 10^{-7}-10^{-5} M. The samples were injected at 50 μL min^{-1} flow rate, for 100 s and allowed to dissociate for three minutes. The surface was regenerated with 1 M NaCl and 50 mM NaOH. Analysis of the data was done using the BioEvaluation software supplied with the BioCore after subtraction of the control sensogram, using one to one binding model.

Duplex DNA was prepared by incubating the following oligonucleotides at 90 °C for ten minutes and cooling slowly to 4 °C.

D1 5'-GTCGACTTATGCCAAGTGGTACGTCTCCGT-3'

D2 5'bio-ACGGAGACGTACCACTTGGCATAAGTCGAC-3'

SPR titrations not shown in the chapters are included in the accompanying CD.

7.10 Synthesis

7.10.1 Synthesis of tris(1-pyrazoyl)methane $(tpm)^2$ [3.1]

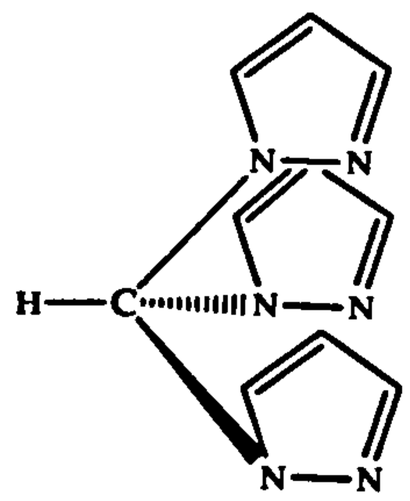

Distilled water (294 mL) was added to a flask containing a mixture of pyrazole (20 g, 294 mmol) and tetra-n-butylammonium bromide (4.7 g, 14.7 mmol). With vigorous stirring (mechanical agitation) sodium carbonate (187 g, 1.8 mol) was added. After cooling to room temperature, chloroform (147 mL) was added. The mixture was heated at gentle reflux, under nitrogen atmosphere for three days. After cooling to room temperature the solution was filtered (to removed excess of sodium carbonate) and the solid was washed with water. An extraction with diethyl ether and water was carried out. The combined organic layer were washed with saturated brine solution (200 mL) and dried over sodium sulphate. The solvent was removed by rotary evaporation and the solid was dried under vacuum. Mass = 10.53 g (53 %) yellow solid. ^{1}H NMR (acetone-d_6): δ 6.40 (dd, 3H), 7.62 (d, 3H), 7.86 (d, 3H) 8.73 (s, 1H).

7.10.2 Synthesis of tris (3,5-dimethyl-1-pyrazol) methane (tpm*)[2] [2.1]

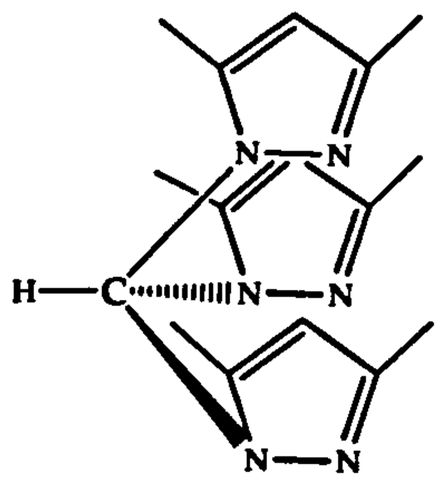

Distilled water was added to a flask containing a mixture of 3,5-dimethyl pyrazole (68.1 g, 707 mmol) and tetra-n-butylammonium bromide (11.4 g, 35 mmol). With vigorous stirring (mechanical agitation), sodium carbonate (586 g, 4.2 mmol) was added. After cooling to room temperature, chloroform was added and the flask was equipped with a reflux condenser. This mixture was heated at gentle reflux, under nitrogen atmosphere, for three days. After cooling to room temperature the mixture was filtered through a Büchner funnel. An extraction with diethyl ether and water was carried out. After drying the combined organic layers, the solvent was removed by rotary evaporation. Unreacted 3,5-dimethyl pyrazole was removed by sublimation (80°C in oil bath under vacuum). The remaining solid was then dissolved in dichloromethane and flushed through a plug of silica with dichloromethane. The solvent was removed by rotary evaporation and the solid was dried under vacuum. Mass = 20.5 g (67.3 %) yellow-white solid. ^{1}H NMR (acetone-d_6): δ 2.03 (s, 9H), 2.09 (s, 9H), 5.92 (s, 3H), 8.20 (s, 1H).

7.10.3 Synthesis of 1,10 phenanthroline-5, 6-dione (dpq)[3]

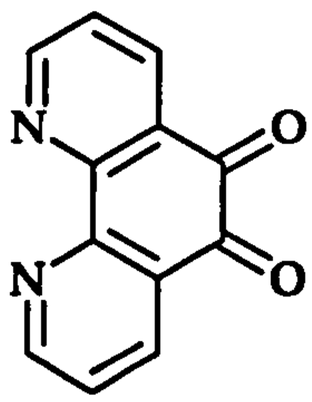

1,10-phenanthroline (5 g, 27.78 mmol) was dissolved in small portions into concentrate sulphuric acid (30 mL). Sodium bromide (2.5 g) and nitric acid (15 mL) were then carefully added and the mixture was refluxed for 40 minutes. The solution was cooled and poured over ice (400 g) and neutralised to pH 7.0 by addition of sodium hydroxide aq. An extraction with dichloromethane was carried out. The organic layers were dried with magnesium sulphate and the solvent was removed by rotary evaporation. The yellow product was recrystallised from water/methanol. Mass = 2.4 g (41.1 %) yellow solid. ^{1}H NMR ($CDCl_3$): δ 7.56 (dd, 2H), 8.47 (dd, 2H), 9.07 (dd, 2H). MS (%) = 211 [M^+].

7.10.4 Synthesis of dipyrido [3, 2-a, 3′-c] phenazine (dppz)[3] [3.2]

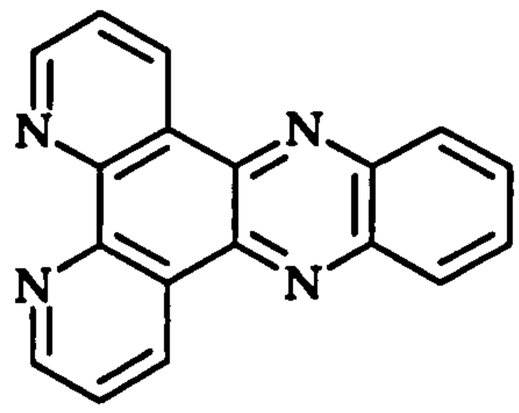

1,10-phenanthroline-5,6-quinone (0.5 g, 2.7 mmol) and o-phenylendiamine (0.3 g, 2.73 mmol) were refluxed in ethanol (50 mL) for twenty minutes. The brown solid was recrystallised from ethanol/water (1:1). The solid was collected by filtration and then dried under vacuum. Mass = 0.57 g (71.95 %) pale needles. ^{1}H NMR (acetone-d_6): δ 7.90 (dd, 2H), 8.10 (dd, 2H), 8.40 (dd, 2H), 9.20 (dd, 2H), 9.65 (dd, 2H).

7.10.5 Synthesis of benzo[*i*]dipyrido[3,2-a:2′,3′-c]phenazine (dppn)[4] [3.18]

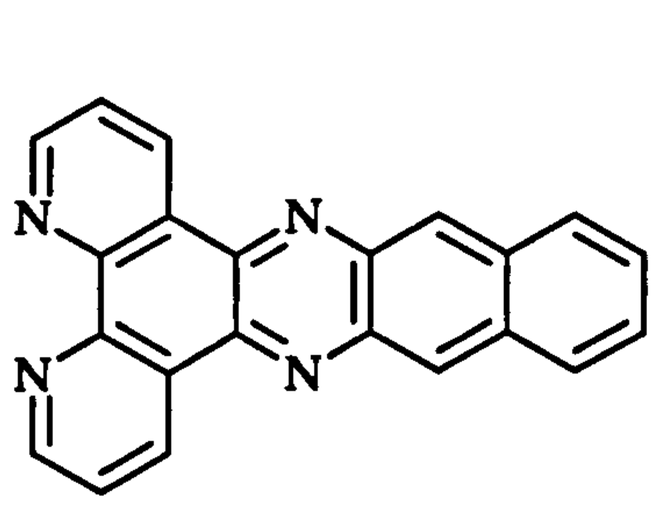

1,10-phenanthroline-5,6-quinone (1.00 g, 4.76 mmol) and 2,3-diaminonaphathalene (0.84 g, 5.31 mmol) were refluxed in methanol (100 mL) for one hour. The orange solid formed was collected, washed with water, methanol and ethyl ether and dried under vacuum. Mass = 1.50 g (94 %) orange solid. ^{1}H NMR ($CDCl_3$): δ 7.60 (dd, 2H), 7.76 (dd, 2H), 9.16 (dd, 2H), 8.87 (s, 2H), 9.22 (dd, 2H), 9.56 (dd, 2H). MS m/z (%): 333 (100) [MH^+]

7.10.6 Synthesis of (*L*)-tert-butyl 2-(isonicotinamido)propanoate[5] (*L*)-[5.1]

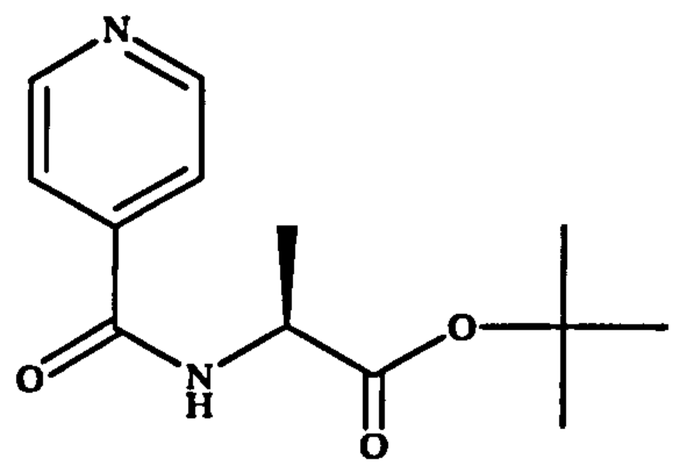

Isonicotinic acid (0.23 g, 1.82 mmol) and thionyl chloride (5 mL) were refluxed for six hours. The solution was concentrated to 1 mL, and toluene (5 mL) was added, which then was removed by rotary evaporation. To the residue, *L*-alanine tert-butyl ester hydrochloride (0.30 g, 1.65 mmol), dichloromethane (20 mL) and triethylamine (2 mL) were added. The solution was stirred for three days at room temperature and then was poured into a solution of sodium bicarbonate (50 mL), and the organic layer separated and washed with water. The extracts were dried and concentrated by rotary evaporation to leave a thick oil. Mass = 0.20 g yellow oil. ^{1}H NMR (DMSO-d_6): δ 1.40 (s, 9H), 2.10 (s, 3H), 4.35 (q, 1H), 7.80 (dd, 2H), 8.25 (dd, 2H), 9.00 (d, 1H). MS m/z (%): 251 (30) [MH^+]

7.10.7 Synthesis of (*D*)-tert-butyl 2-(isonicotinamido)propanoate[5] (*D*)-[5.1]

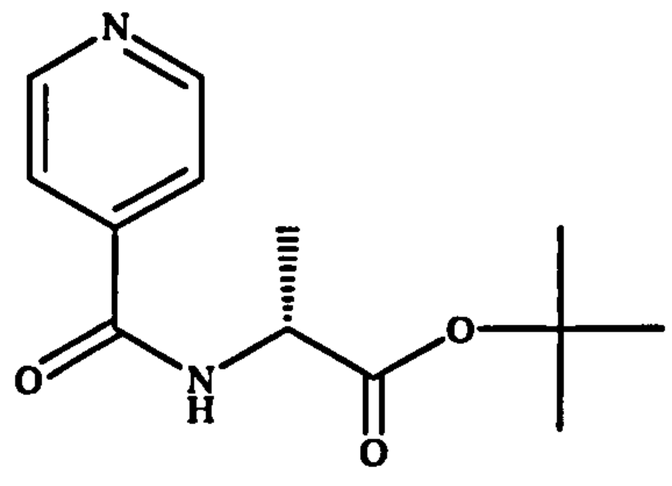

Isonicotinic acid (0.22 g, 1.62 mmol) and thionyl chloride (5 mL) were refluxed for six hours. The solution was concentrated to 1 mL, and toluene (5 mL) was added, which was removed by rotary evaporation. To the residue, D-alanine tert-butyl ester hydrochloride (0.30 g, 1.65 mmol), dichloromethane (20 mL) and triethylamine (2 mL) were added. The solution was stirred for three days at room temperature, then was pored into a solution of sodium bicarbonate (50 mL), and the organic layer separated and washed with water. The extracts were dried and concentrated by rotary evaporation to leave a thick oil. Mass = 0.25 g yellow oil. ^{1}H NMR (DMSO-d_6): δ 1.40 (s, 9H), 2.10 (s, 3H), 4.35 (q, 1H), 7.80 (dd, 2H), 8.25 (dd, 2H), 9.00 (d, 1H). MS m/z (%): 251 (82) [MH^+].

7.10.8 Synthesis of $[RhCl_3(tpm^*)]$[6] [2.2]

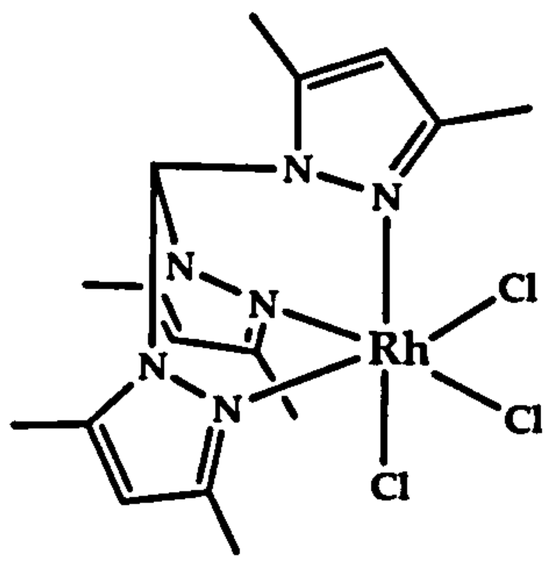

Tpm* (0.57 g, 1.91 mmol) dissolved in the minimum amount of methanol was added to an aqueous solution of $RhCl_3 3H_2O$ (0.5 g, 1.91 mmol). This mixture was refluxed for three hours under argon atmosphere. After cooling to room temperature the solid formed was collected by centrifugation and then dried under vacuum. Mass = 0.6 g (61%) orange solid. ^{1}H NMR (acetone-d_6): δ 6.15 (s, 3H), 8.05 (s, 1H). MS m/z (%): 471 (100) [M^+-Cl]. Elemental analysis calculated for $C_{16}H_{22}C_{13}N_6Rh \cdot 1/2H_2O$: C, 37.20; H, 4.49; N, 16.27. Found: C, 36.88; H, 4.53; N, 16.58.

7.10.9 Synthesis of [Rh(Cl)(bpy)(tpm*)] $(PF_6)_2$[6] [2.3]

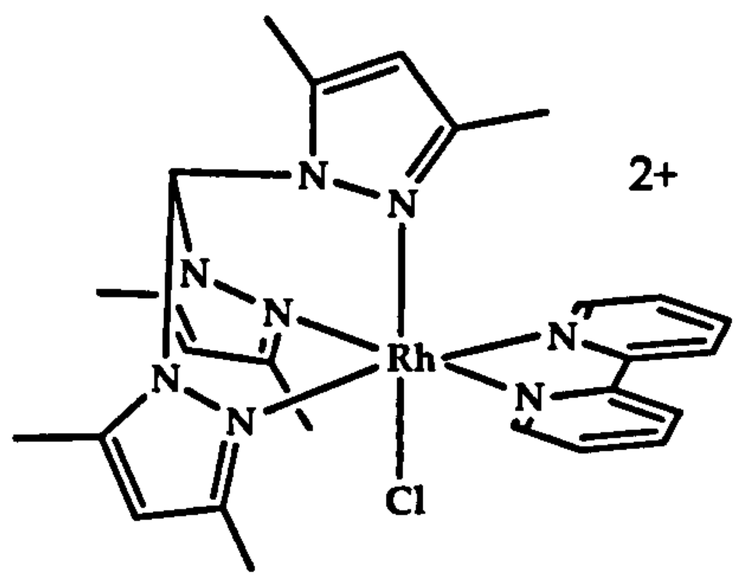

$RhCl_3$(tpm*) (0.16 g, 0.3 mmol) and 2,2'- bipyridyl (0.068 g, 0.43 mmol) were refluxed in ethanol/water (1:1) for one hour under argon atmosphere. After cooling to room temperature, excess NH_4PF_6 was added to the solution. The precipitated formed was collected by centrifugation, washed with ethanol and then dried under vacuum. Mass = 0.227 g (85%) pale pink solid. ^{1}H NMR (acetone-d_6): δ 6.30 (s, 1H), 6.60 (s, 2H), 8.20 (t, 2H), 8.5 (s, 1H), 8.65 (t, 2H), 8.95 (d, 2H), 9.05 (d, 2H). MS m/z (%): 737 [M^+], 296 [M^{2+}/2]. Elemental analysis calculated for $C_{26}H_{30}ClF_{12}N_8P_2Rh\,H_2O$: C, 34.66;H, 3.58; N, 12.44. Found: C, 34.76; H, 3.36; N, 12.8.

7.10.10 Synthesis of [RhCl(phen)(tpm*)] $(PF_6)_2$[6] [2.4]

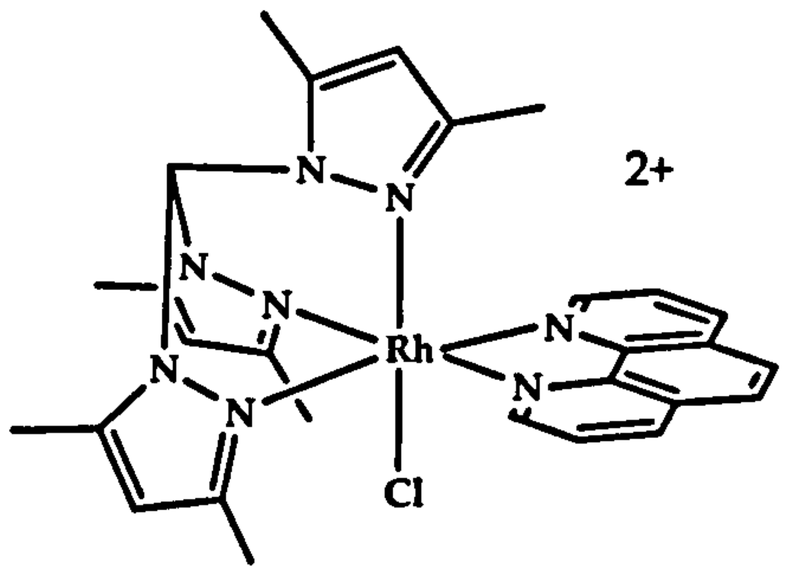

$RhCl_3$(tpm*) (0.16 g, 0.3 mmol) and 1,10-phenanthroline (0.062 g, 0.34 mmol) were refluxed in ethanol/water (1:1) one hour under argon atmosphere. Excess NH_4PF_6 was added to the bright orange solution and the resultant precipitated was collected

by centrifugation, washed with ethanol and then dried under vacuum. Mass = 0.114 g (53%) orange solid.^{1}H NMR (acetone-d_6): δ 6.20 (s, 1H), 6.65 (s, 2H), 8.45 (dd, 2H), 8.55 (s, 1H), 8.65 (s, 2H), 9.30 (td, 4H). MS m/z (%): 761 (100) [M^+], 616 (35) [M^{2+}], 581 (20) [M^+-(Cl)], 308 (50) [M^{2+}/2]. Elemental analysis calculated for $C_{28}H_{30}ClF_{12}N_8OP_2Rh$·EtOH: C, 37.10; H, 3.65; N, 11.76. Found: C, 37.33; H, 3.10; N, 11.25.

7.10.11 Synthesis of [$RhCl_2$(py)(tpm*)] (PF_6)^6 [2.5]

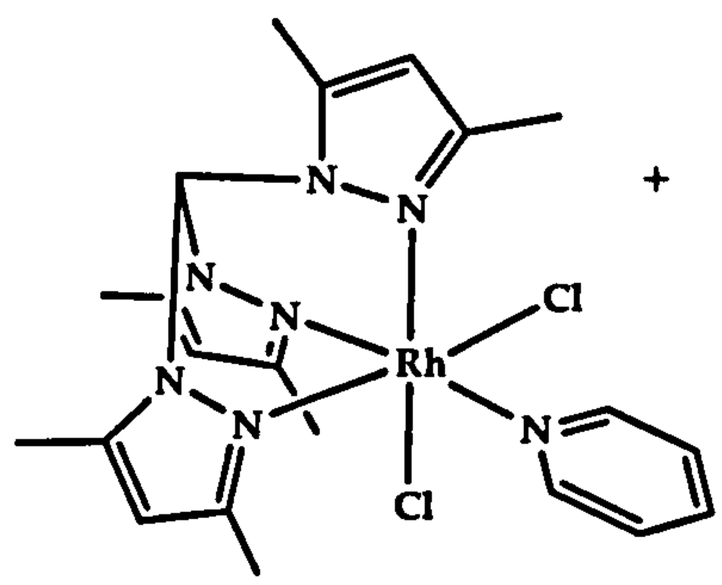

$RhCl_3$(tpm*) (0.146 g, 0.26 mmol) and pyridine (400μL) were refluxed in ethanol/water (1:1) one hour under argon atmosphere. After cooling to room temperature, excess NH_4PF_6 was added to the solution. The precipitate formed was collected by centrifugation. The solid was dissolved in minimum amount of acetone and the solution was concentrated by rotary evaporation. Diethyl ether was added and the solid formed was collected by centrifugation and then dried under vacuum. Mass = 0.082 g (45%) white solid. ^{1}H NMR (acetone-d_6): δ 6.40 (d, 3H), 7.50 (m, 1H), 7.85 (m, 1H), 8.05 (d, 1H), 8.25 (m, 1H), 8.40 (s, 1H), 9.50 (d, 1H). MS m/z (%): 550 (100) [M^+], 515 (15) [M^+-Cl], 471 (15) [M^+-(py)], 436 (15) [M^+-(Cl, py)]. Elemental analysis calculated for $C_{21}H_{27}Cl_2F_6N_7PRh$·1/2$H_2O$: C, 35.76; H, 4.00; N, 13.90. Found: C, 35.53; H, 3.92; N, 13.91.

7.10.12 Synthesis of [RhCl(py)$_2$(tpm*)] (PF$_6$)$_2$[6] [2.6]

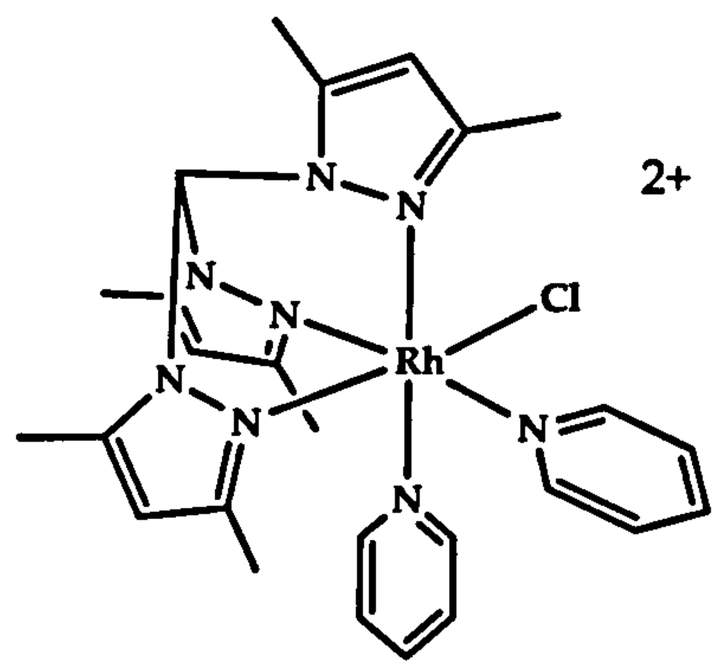

$RhCl_3$(tpm*) (0.146 g, 0.26 mmol), pyridine (600μL) and $AgNO_3$ (0.15 g) were refluxed in ethanol/water (1:1) one hour under argon atmosphere. After cooling to room temperature, NH_4PF_6 was added to the solution. The precipitate formed was washed with water, diethyl ether, collected by centrifugation and then dried under vacuum. Mass= 0.23 g (65%) green solid. ^{1}H NMR (acetone-d$_6$): δ 6.45 (s, 2H), 6.60 (s, 1H), 7.40 (m, 2H), 8.00 (m, 4H), 8.20 (m, 4H), 8.45 (m, 2H), 8.60 (s, 1H), 9.90 (d, 2H). MS m/z (%): 739.2 (100) [M$^+$]. Elemental analysis calculated for $C_{26}H_{32}ClF_{12}N_8P_2Rh{\cdot}H_2O$: C, 34.59; H, 3.79; N, 12.41. Found: C, 34.43; H, 3.55; N, 11.85.

7.10.13 Synthesis of (tpm)RuCl$_3$[7] [3.3]

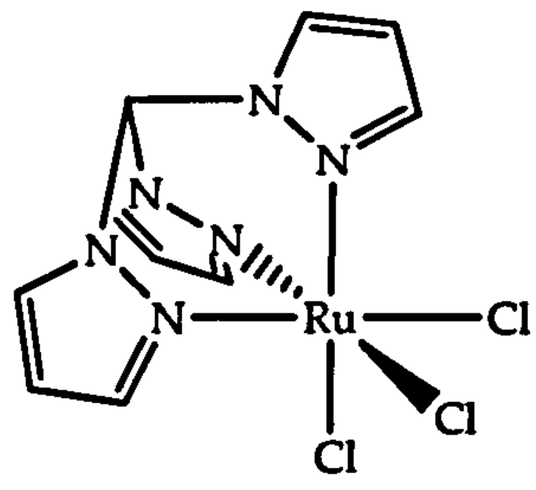

Tris (1-pyrazoyl) methane (1 g, 4.67 mmol) and $RuCl_3{\cdot}3H_2O$ (1.22 g, 4.67 mmol) were refluxed in ethanol (50 mL) for three hours. After cooling the dark precipitate was filtered and washed with cold ethanol and ethyl ether and dried under vacuum. Mass = 1.45 g (73.8 %) brown solid. MS m/z (%): 386 (20) [M$^+$-Cl].

7.10.14 Synthesis of [Ru(tpm)(Cl)(dppz)](PF$_6$)$_2$[7] [3.4]

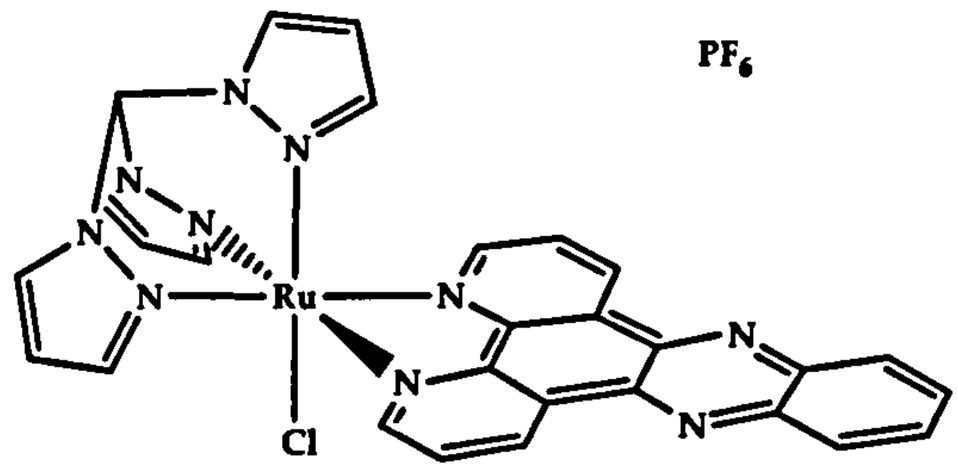

(tpm)RuCl$_3$ (1.11 g, 2.61 mmol), dppz (0.75 g, 2.66 mmol) and LiCl (0.40 g) were refluxed in ethanol: water (3:1) (100 mL) for ten minutes. Twelve drops of triethylamine were added and refluxed for half hour under nitrogen atmosphere. After cooling, the solvent was removed and the residue was dissolved in methanol (20 mL) and the fine dark solid was filtered out. The product was precipitated by addition of aqueous NH_4PF_6 and collected by filtration. The crude product was chromatographed on grade I alumina with acetonitrile: toluene (1:1). The purple band was collected and concentrated by rotary evaporation. Addition of diethyl ether precipitated the product as a dark solid. Mass= 1.32 g (65.00 %). ^{1}H NMR (acetone-d$_6$): δ 6.30 (td, 1H), 6.87 (m, 3H), 8.06 (dd, 2H), 8.17 (dd, 2H), 8.42 (dd, 2H), 8.52 (dd, 2H), 8.57 (m, 3H), 9.17 (dd, 2H), 9.57 (dd, 2H), 9.63 (s, 1H). MS m/z (%): 633 (100) [M$^+$], 597 (30) [M$^+$-(Cl)].

7.10.15 Synthesis of [Ru(tpm)(dppz)(MeCN)](PF$_6$)$_2$[8]

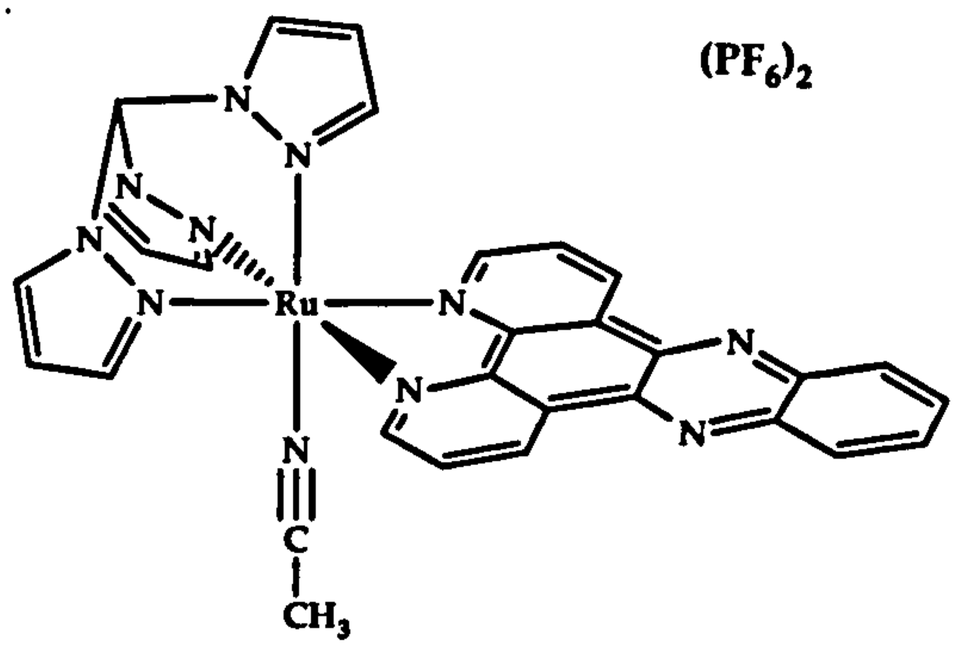

[RuCl(tpm)(dppz)][PF_6] (0.1 g, 0.13 mmol) and $AgCF_3SO_3$ (0.36 g, 0.14 mmol, 1.1 eq.) were refluxed in freshly distilled acetonitrile (50 mL) for ten hours. After cooling to room temperature the solvent was removed and the residue was taken up into methanol (20 mL) and filtered through celite to remove AgCl. The mother liquor was treated with aqueous NH_4PF_6 to precipitate the product, which was collected by filtration and dried under vacuum. Mass = 0.12 g (98 %) red solid. ^1H NMR (d^6-acetone): δ_H = 2.29 (s, 3H), 6.37 (dd, 1H), 6.95 (dd, 2H), 7.07 (dd, 1H), 8.22 (dd, 2H), 8.27 (dd, 2H), 8.56 (t, 2H), 8.62 (dd, 1H), 8.80 (dd, 2H), 9.42 (dd, 2H), 9.86 (dd, 2H), 9.87 (dd, 2H), 10.01 (s, 1H). MS m/z (%): 784 (100) [M^+], 638 (70) [M^+], 597 (80) [M^+-(MeCN)].

7.10.16 Synthesis of [Ru(tpm)(dppz)(Py)]$(PF_6)_2$[8]

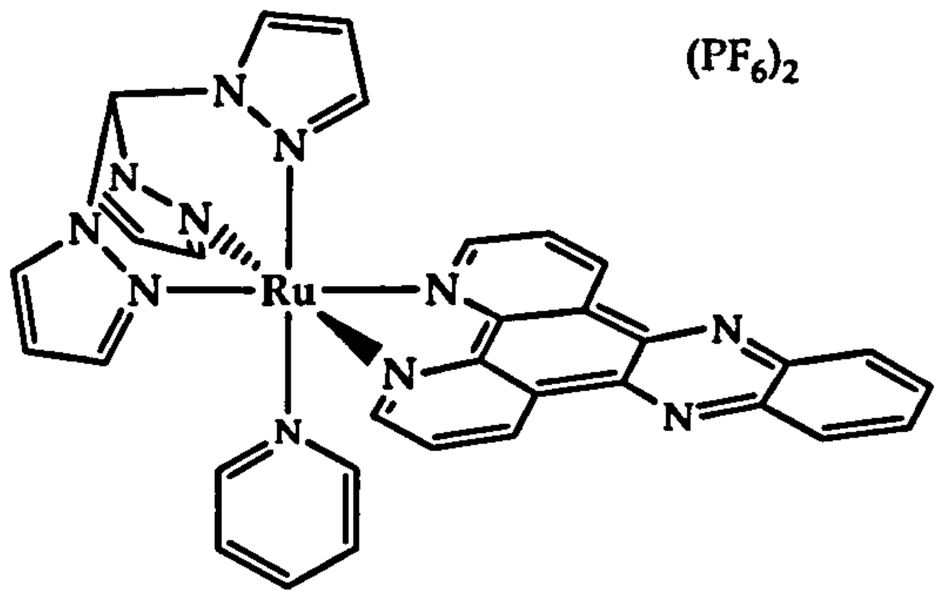

$(PF_6)_2$

[RuCl(tpm)(dppz)]PF_6 (0.07g, 0.09 mmol) and $AgNO_3$ (0.035 g, 0.22 mmol, 2.4 eq) were refluxed in ethanol/water (3:1) (40 mL) for five hours. After cooling to room temperature the solution was filtered through celite (to remove solid AgCl). To the solution, excess of pyridine (1 mL) was added and refluxed overnight. After cooling to room temperature the solution was filtered again through celite and aqueous NH_4PF_6 was added. The precipitate was collected by filtration and washed with water, diethyl ether and then dried under vacuum. Mass = 0.055 g (60.8 %) orange solid. ^1H NMR (acetone-d_6): δ 6.30 (dd, 1H), 6.93 (dd, 1H), 6.98 (m, 2H), 7.15 (dd, 2H), 7.76 (dd, 2H), 7.80 (t, 1H), 8.21 (dd, 2H), 8.24 (dd, 2H), 8.52 (dd, 2H), 8.56 (m, 2H), 8.58 (dd, 1H), 8.85 (dd, 2H), 9.42 (dd, 2H), 9.87 (dd, 2H), 9.93 (s, 1H). MS m/z (%): 865 (45) [M^+], 719 (35) [M^{2+}], 597 (55) [M^{2+}-(Py)].

7.10.17 Synthesis of [Ru(tpm)(dppz)(Nic)](PF$_6$)$_2$ [3.5]

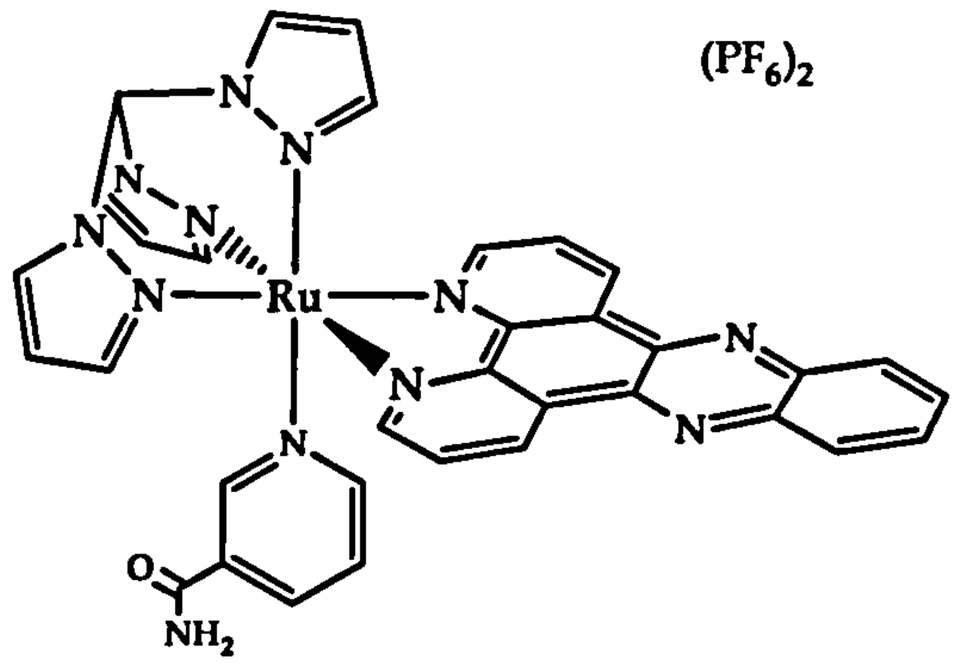

[Ru(tpm)(Cl)(dppz)]PF$_6$ (0.08 g, 0.10 mmol) and $AgNO_3$ (0.04 g, 0.24 mmol, 2.4 eq.) were refluxed in ethanol/water (3:1) (40 mL) for five hours. After cooling to room temperature the solution was filtered through celite (to remove solid AgCl). To the solution, excess nicotinamide (Nic) (0.15 g, 1.23 mmol, 12.3 eq.) was added and refluxed overnight. After cooling to room temperature the solution was filtered again through celite and aqueous NH_4PF_6 was added. The precipitate was collected by filtration and washed with water, diethyl ether and then dried under vacuum. Mass = 0.072g (67.2 %) orange solid. ^{1}H NMR (DMSO-d$_6$): δ 6.30 (s, 1H). 6.90 (s, 1H), 7.00 (s, 2H), 7.10 (t, 1H), 7.55 (d, 1H), 7.62 (s, 1H), 7.90 (s, 1H), 8.15 (m, 2H), 8.25 (m, 3H), 8.45 (s, 2H), 8.55 (s, 1H), 8.65 (m, 2H), 8.80 (s, 2H), 9.10 (d, 2H), 9.75 (d, 2H), 10.10 (s, 1H). MS m/z (%): 865 (100) [M$^+$], 719 (45) [M^{2+}], 597 (20) [M^{2+}- (Nic)]. Elemental analysis calculated for $C_{34}H_{26}F_{12}N_{12}OP_2Ru$ $3H_2O$: C, 38.29; H, 3.03; N, 15.80. Found: C, 38.06; H, 2.57; N, 14.78.

7.10.18 Synthesis of [Ru(tpm)(dppz)(3-NH$_2$py)](PF$_6$)$_2$ [3.6]

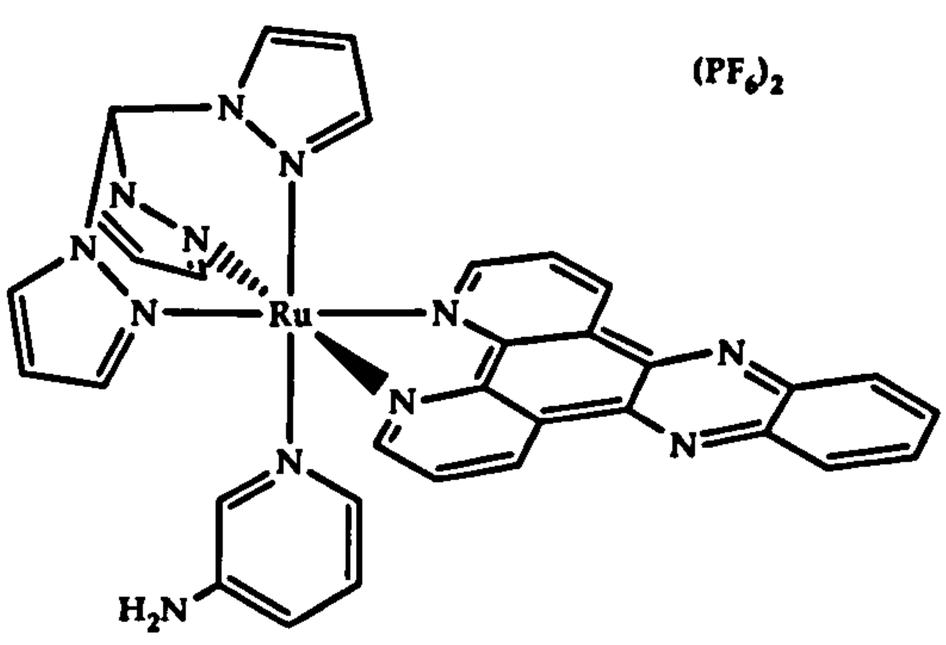

[Ru(tpm)(Cl)(dppz)]PF_6 (0.09 g, 0.12 mmol) and $AgNO_3$ (0.04 g, 0.24 mmol, 2 eq) were refluxed in ethanol/water (3:1) (40 mL) for five hours. After cooling to room temperature the solution was filtered through celite (to remove solid AgCl). To the solution, excess 3-aminopyridine (3-NH_2py) (0.14 g, 1.49 mmol, 12.4 eq.) was added and refluxed overnight. After cooling to room temperature the solution was filtered again through celite and aqueous NH_4PF_6 was added. The precipitate was collected by filtration and washed with water, diethyl ether and then dried under vacuum. Mass = 0.072g (62 %) orange solid. ^{1}H NMR (DMSO-d_6): δ 5.36 (s, 2H), 6.31 (s, 1H), 6.54 (d, 1H), 6.67 (s, 1H), 6.77 (s, 1H), 6.80 (s, 2H), 8.10 (m, 2H), 8.25 (m, 2H), 8.41 (s, 2H), 8.58 (m, 3H), 8.84 (s, 2H), 9.11 (d, 2H), 9.73 (d, 2H), 10.17 (d, 1H). MS m/z (%): 837 (95) [M^+], 691 (100) [M^{2+}], 597 (75) [M^{2+}-(3-NH_2py)]. Elemental analysis calculated for $C_{33}H_{26}F_{12}N_{12}P_2Ru$ $3H_2O$: C, 38.27; H, 3.11; N, 16.23. Found: C, 38.69; H, 2.53; N, 16.23.

7.10.19 Synthesis of [Ru(tpm)(dppz) (3-CHOpy)]$(PF_6)_2$ [3.7]

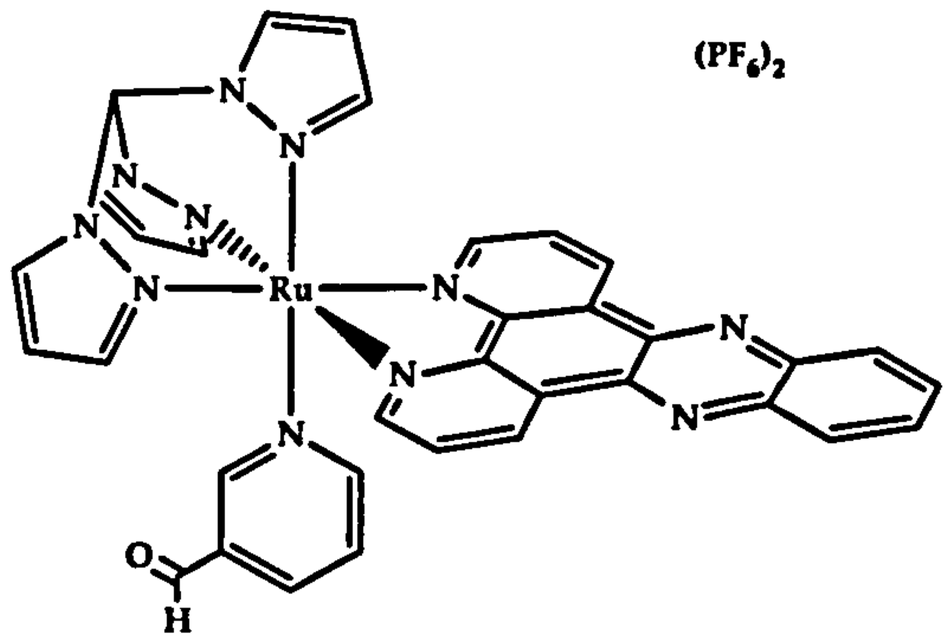

[Ru(tpm)(Cl)(dppz)]PF_6 (0.12 g, 0.15 mmol) and $AgNO_3$ (0.06 g, 0.35 mmol, 2.3 eq.) were refluxed in ethanol/water (3:1) (40 mL) for five hours. After cooling to room temperature the solution was filtered through celite. To the solution, excess pyridine-3-carboxaldehyde (3-CHOpy) (1 mL) was added and refluxed overnight. After cooling to room temperature the solution was filtered again through celite and aqueous NH_4PF_6 was added. The precipitate was collected by filtration and washed with water, diethyl ether and then dried under vacuum. Mass = 0.078 g (55.6 %) brown solid. ^{1}H NMR (DMSO-d_6): δ 6.3 (s, 1H), 6.9 (s, 2H), 7 (s, 1H), 7.3 (t, 1H), 7.5

(d, 1H), 7.9 (s, 1H), 8.25 (m, 2H), 8.3 (m, 3H), 8.5 (s, 2H), 8.55 (s, 1H), 8.7 (m, 2H), 8.9 (s, 2H), 9.1 (d, 2H), 9.8 (d, 3H), 10.1 (d, 1H). MS m/z (%): 850 (65) [M^+], 704 (45) [M^{2+}], 597 (100) [M^{2+}-(3-CHOpy)]. Elemental analysis calculated for $C_{34}H_{25}F_{12}N_{11}OP_2Ru$ $3H_2O$: C, 38.94; H, 2.98; N, 14.69. Found: C, 39.34; H, 2.37; N, 14.18.

7.10.20 Synthesis of [Ru(tpm)(dppz)(3-pic)]$(PF_6)_2$ [3.8]

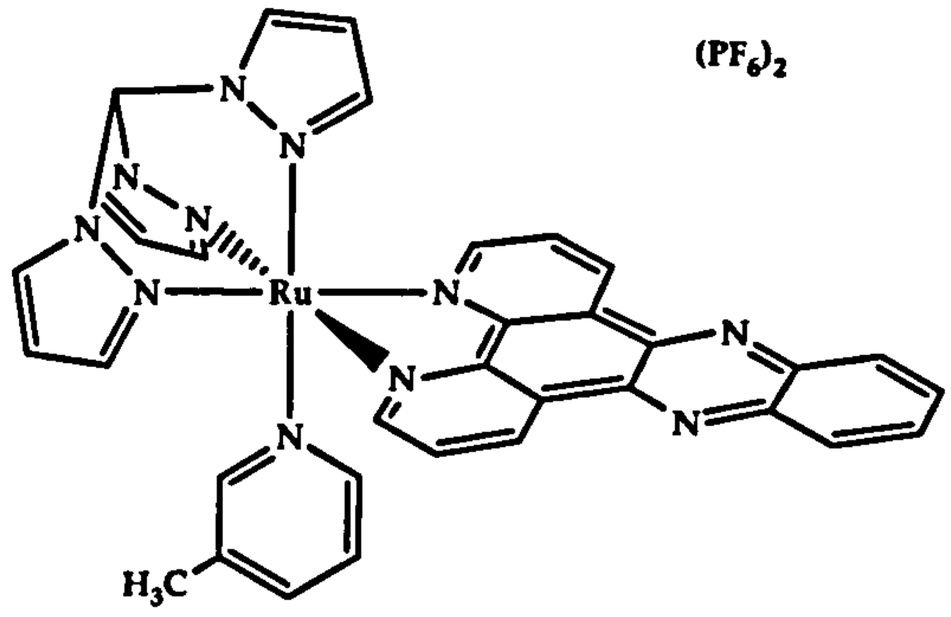

[Ru(tpm)(Cl)(dppz)]PF_6 (0.06 g, 0.08 mmol) and $AgNO_3$ (0.027 g 0.16 mmol, 2 eq) were refluxed in ethanol/water (3:1) (40 mL) for five hours. After cooling to room temperature the solution was filtered through celite (to remove solid AgCl). To the solution, excess 3-picoline (3-pic) (1 mL) was added and refluxed overnight. After cooling to room temperature the solution was filtered again through celite and aqueous NH_4PF_6 was added. The precipitate was collected by filtration and washed with water, diethyl ether and then dried under vacuum. Mass = 0.05 g (63.73 %) orange solid. ^{1}H NMR (acetone-d_6): δ 1.90 (s,3H), 6.30 (s, 1H), 6.84 (d, 1H), 6.97 (m, 1H), 7.03 (m, 2H), 7.22 (s, 1H), 7.25 (m, 1H), 7.63 (m, 1H), 8.41 (m, 2H), 8.53 (d, 1H), 8.62 (d, 2H), 8.80 (d, 2H), 9.09 (d, 2H), 9.75 (dd, 2H), 10.05 (d, 1H). MS m/z (%): 836 (98) [M^+], 690 (80) [M^{2+}], 597 (100) [M^{2+}-(3-pic)]. Elemental analysis calculated for $C_{34}H_{27}F_{12}N_{11}P_2Ru$ $3H_2O$: C 39.47; H, 3.21; N, 14.89. Found: C 38.45; H, 2.46; N, 13.89.

7.10.21 Synthesis of [Ru(tpm)(Isonic)(dppz)]$(PF_6)_2$ [3.9]

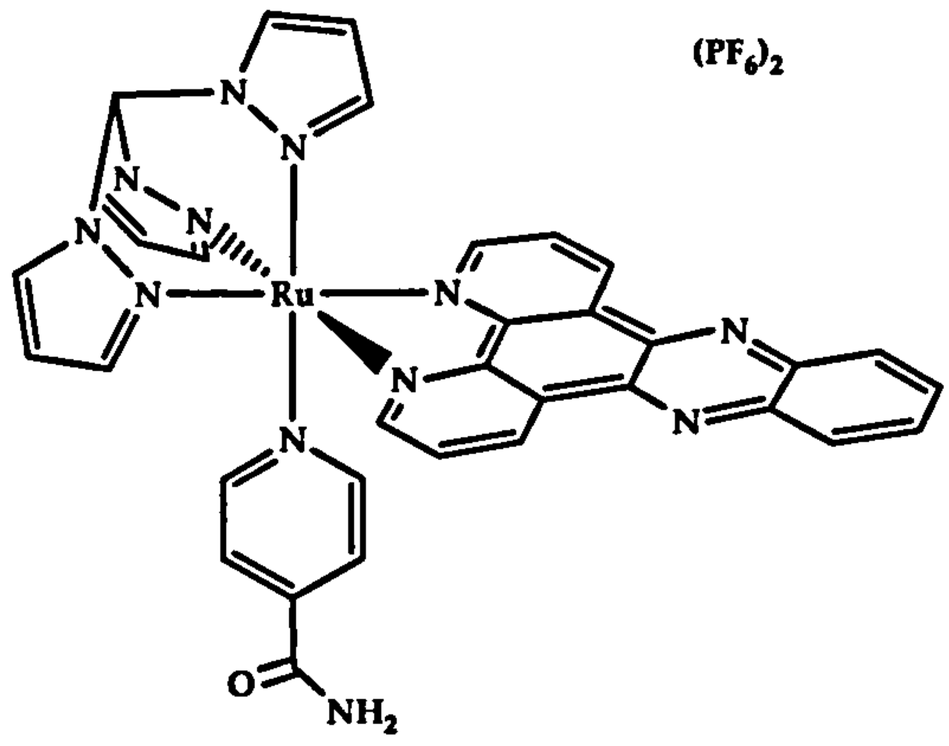

$[Ru(tpm)(Cl)(dppz)]PF_6$ (0.07 g, 0.09 mmol) and $AgNO_3$ (0.035 g, 0.21 mmol, 2.3 eq) were refluxed in ethanol/water (3:1) (40 mL) for five hours. After cooling to room temperature the solution was filtered through celite. To the solution, excess isonicotinamide (Isonic) (0.10 g, 0.82 mmol, 9.1 eq.) was added and refluxed overnight. After cooling to room temperature the solution was filtered again through celite and aqueous NH_4PF_6 was added. The precipitate was collected by filtration and washed with water, diethyl ether and then dried under vacuum. Mass = 0.055 g (60.53 %) orange solid. ^1H NMR (DMSO-d_6): δ 6.30 (m, 1H), 6.90 (m, 1H), 7.01 (m, 2H), 7.45 (dd, 2H), 7.60 (dd, 2H), 7.80 (dd, 2H), 8.15 (dd, 2H), 8.25 (s, 2H), 8.45 (d, 2H), 8.60 (m, 3H), 8.80 (dd, 2H), 9.10 (dd, 2H), 9.75 (dd, 2H), 10.05 (s, 1H). MS m/z (%): 865 (32) $[M^+]$, 719 (20) $[M^{2+}]$, 597 (42) $[M^{2+}$-(Isonic)]. Elemental analysis calculated for $C_{34}H_{26}F_{12}N_{12}OP_2Ru$ $3H_2O$: C, 37.13; H, 3.30; N, 15.28. Found: C, 36.41; H, 2.37; N, 14.81.

7.10.22 Synthesis of [Ru(tpm)(dppz)(4-NH_2py)]$(PF_6)_2$ [3.10]

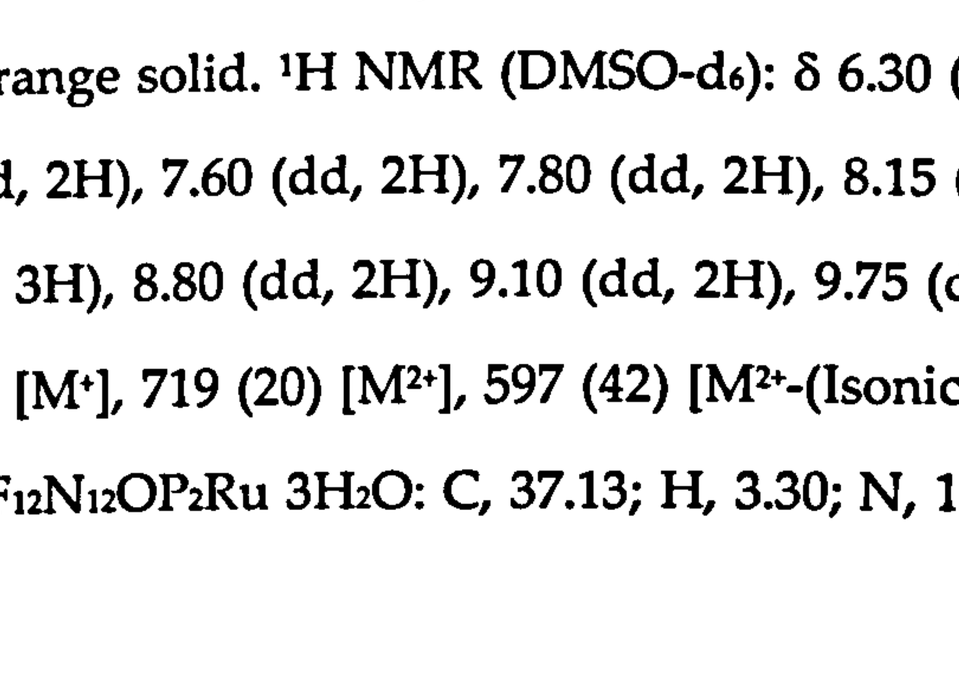

[Ru(tpm)(Cl)(dppz)]PF_6 (0.06 g, 0.08 mmol) and $AgNO_3$ (0.029 g, 0.17 mmol, 2.1 eq) were refluxed in ethanol/water (3:1) (40 mL) for five hours. After cooling to room temperature the solution was filtered through celite (to remove AgCl). To the solution, excess 4-aminopyridine (4-NH_2py) (0.088 g, 0.93 mmol, 12 eq.) was added and refluxed overnight. After cooling to room temperature the solution was filtered again through celite and aqueous NH_4PF_6 was added. The precipitate was collected by filtration and washed with water, diethyl ether and then dried under vacuum. Mass = 0.058 g (76.5 %) orange solid. ^{1}H NMR (DMSO-d_6): δ 6.15 (d, 2H), 6.25 (m, 1H), 6.55 (s, 2H), 6.75 (d, 2H), 6.80 (d, 1H), 6.90 (m, 2H), 8.10 (dd, 2H), 8.40 (d, 2H), 8.50 (d, 1H), 8.60 (m, 2H), 8.80 (d, 2H), 9.10 (dd, 2H), 9.70 (dd,2H), 10.05 (s, 1H). MS m/z (%): 837 (87) [M^+], 691 (100) [M^{2+}], 597 (56) [M^{2+}-(4-NH_2py)]. Elemental analysis calculated for $C_{33}H_{26}F_{12}N_{12}P_2Ru$ $3H_2O$: C, 38.27; H, 3.11; N, 16.23. Found: C, 38.19; H, 2.55; N, 15.85.

7.10.23 Synthesis of [Ru(tpm)(dppz)(4-CHOpy)]$(PF_6)_2$ [3.11]

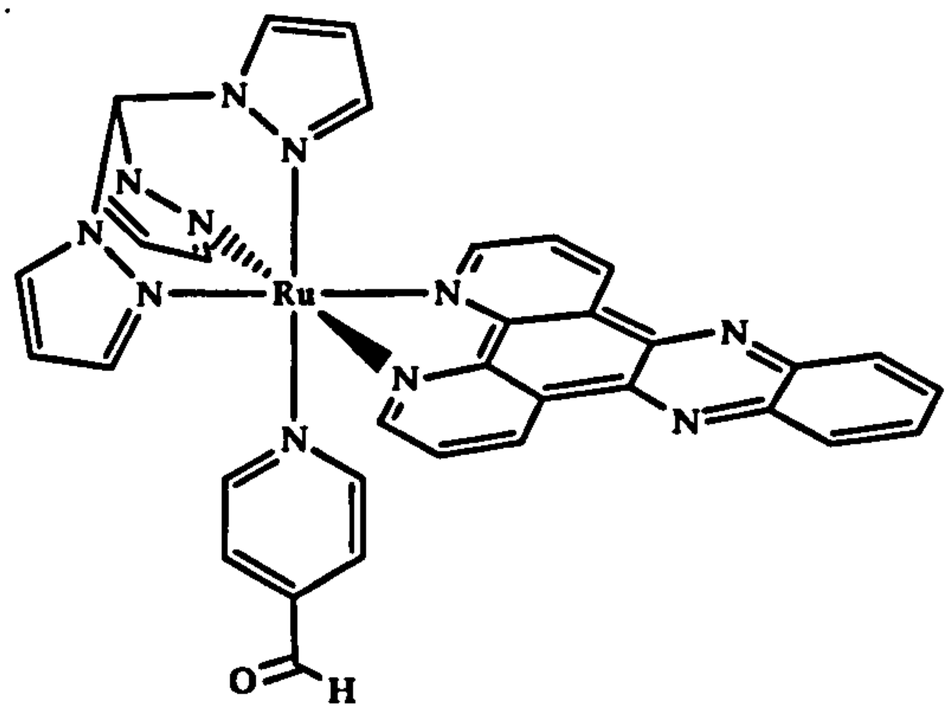

[Ru(tpm)(Cl)(dppz)]PF_6 (0.072 g, 0.09 mmol) and $AgNO_3$ (0.033 g, 0.19 mmol, 2.1 eq) were refluxed in ethanol/water (3:1) (40 mL) for five hours. After cooling to room temperature the solution was filtered through celite (to remove AgCl). To the solution, excess pyridine-4-carboxaldehide (4-CHOpy) (1 mL) was added and refluxed overnight. After cooling to room temperature the solution was filtered again through celite and aqueous NH_4PF_6 was added. The precipitate was collected by filtration and washed with water, diethyl ether and then dried under vacuum. Mass = 0.08 g (89.6 %) orange solid. ^{1}H NMR (acetone-d_6): δ 6.30 (m, 1H), 7.00 (m,

3H), 7.50 (m, 2H), 8.12 (m, 4H), 8.60 (m, 5H), 8.90 (d, 2H), 9.45 (dd, 2H), 9.90 (dd, 2H), 10.05 (s, 1H), 10.30 (s, 1H). MS m/z (%): 850 (30) [M^+], 704 (20) [M^{2+}], 597 (55) [M^{2+}-(4-CHOpy)]. Elemental analysis calculated for $C_{34}H_{25}F_{12}N_{11}OP_2Ru$ 2MeOH: C, 40.84; H, 3.14; N, 14.55. Found: C, 40.31; H, 2.67; N, 14.55.

7.10.24 Synthesis of [Ru(tpm)(dppz)(4-pic)]$(PF_6)_2$ [3.12]

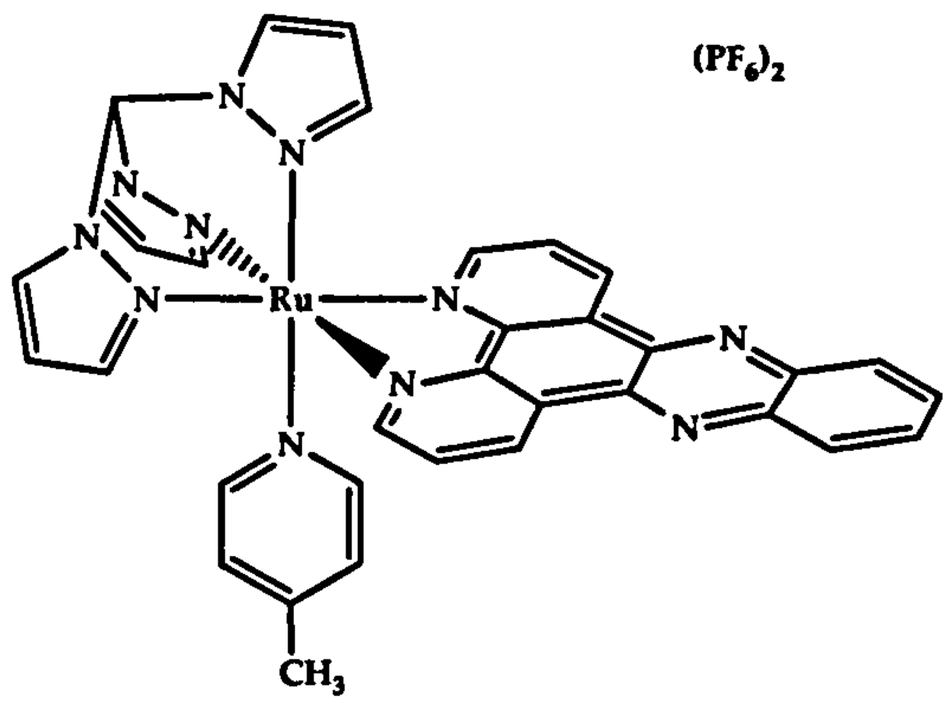

[Ru(tpm)(Cl)(dppz)]PF_6 (0.068 g, 0.087 mmol) and $AgNO_3$ (0.031 g, 0.18 mmol, 2.1 eq.) were refluxed in ethanol/water (3:1) (40 mL) for five hours. After cooling to room temperature the solution was filtered through celite (to remove solid AgCl). To the solution, excess 4-picoline (4- pic) (1mL) was added and refluxed overnight. After cooling to room temperature the solution was filtered again through celite and aqueous NH_4PF_6 was added. The precipitate was collected by filtration and washed with water, diethyl ether and then dried under vacuum. Mass = 0.08 g (93.6 %) orange solid. ^{1}H NMR (acetone-d_6): δ 2.25 (s, 3H), 6.30 (m, 1H), 6.90 (d, 1H), 7.05 (m, 4H), 7.60 (dd, 2H),8.25 (m, 4H), 8.45 (m, 5H), 8.85 (d, 2H), 9.45 (dd, 2H), 9.90 (dd, 2H), 9.95 (s, 1H). MS m/z (%): 836 (100) [M^+], 690 (70) [M^{2+}], 597 (60) [M^{2+}-(4-pic)]. Elemental analysis calculated for $C_{34}H_{27}F_{12}N_{11}P_2Ru$ $3H_2O$: C 39.47; H, 3.21; N, 14.89. Found: C 38.62; H, 2.39; N, 13.45.

7.10.25 Synthesis of [Ru(tpm)(dppz)(*L*-alaiso)]$(PF_6)_2$ (*L*)-[5.2]

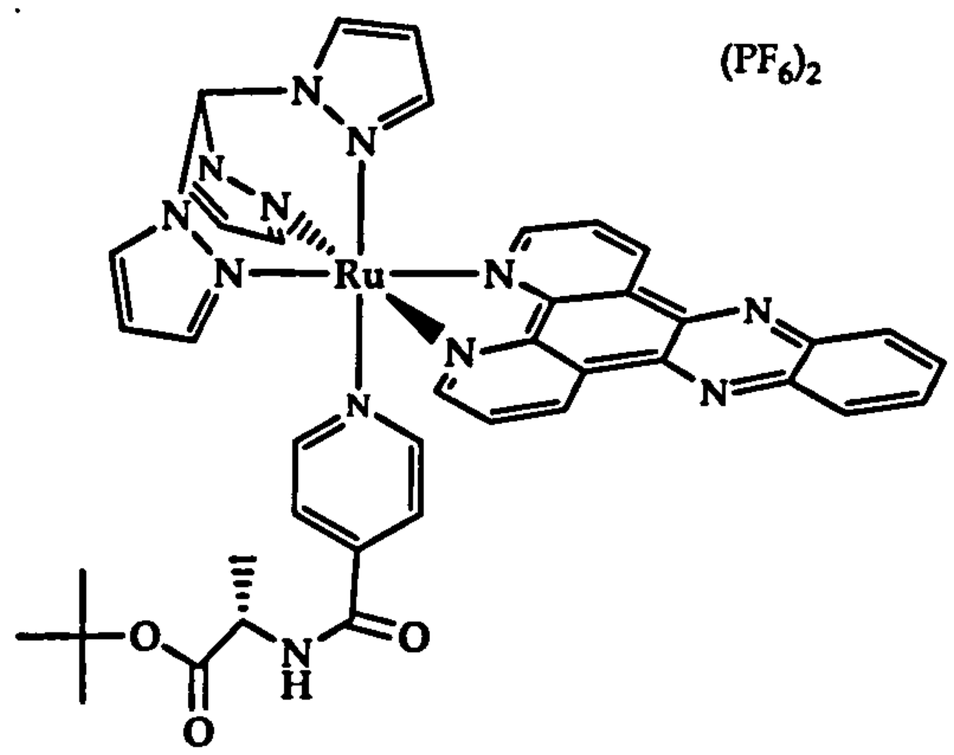

$[Ru(tpm)(Cl)(dppz)]PF_6$ (0.096 g, 0.12 mmol) and $AgNO_3$ (0.042 g, 0.25 mmol, 2.1 eq) were refluxed in ethanol/water (3:1) (40 mL) for five hours. After cooling to room temperature the solution was filtered through celite (to remove solid AgCl). To the solution, excess (*L*)-tert-butyl 2-(isonicotinamido)propanoate (L-alaiso) (0.06 g, 0.23 mmol) was added and refluxed overnight. After cooling to room temperature the solution was filtered again through celite and aqueous NH_4PF_6 was added. The precipitate was collected by filtration and washed with water, diethyl ether and then dried under vacuum. Mass = 0.081 g (58.33 %) orange solid. ^1H NMR (acetone-d_6): δ 5.75 (s, 1H), 6.30 (m, 1H), 6.90 (m, 1H), 7.01 (m, 2H), 7.80 (m, 2H), 8.25 (m, 4H), 8.60 (m, 5H), 8.80 (dd, 2H), 8.90 (dd, 2H), 9.45 (dd, 2H), 9.90 (m, 3H). MS m/z (%): 993 (87) $[M^+]$, 847 (70) $[M^{2+}]$, 597(100) $[M^{2+}$-(L-alaiso)].

7.10.26 Synthesis of [Ru(tpm)(dppz)(*D*-alaiso)]$(PF_6)_2$ (*D*)-[5.2]

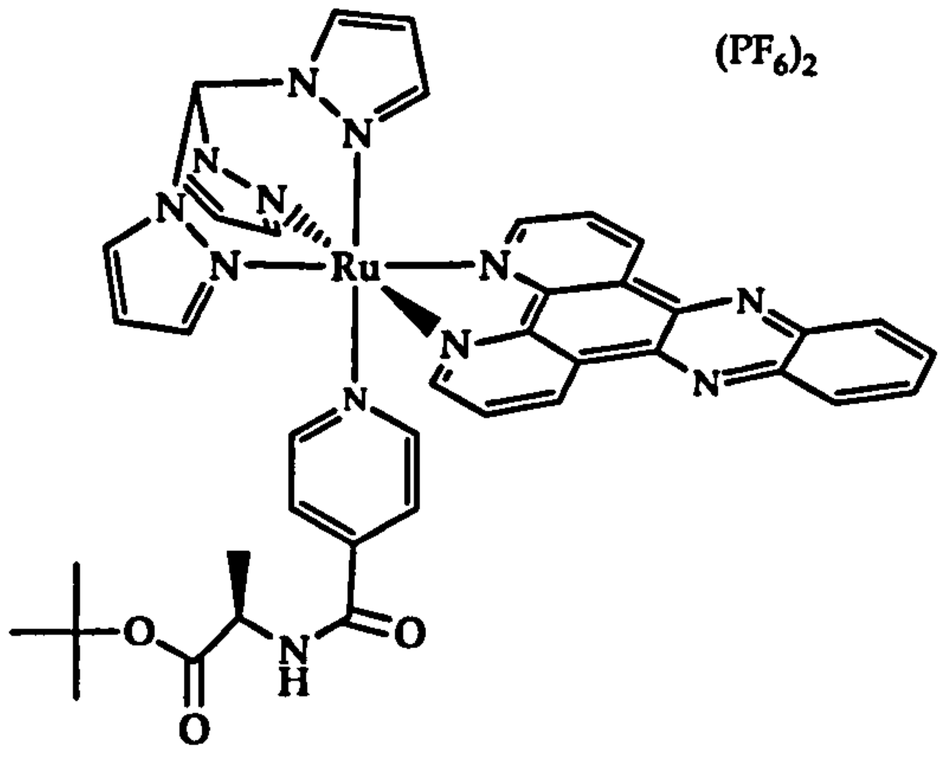

[Ru(tpm)(Cl)(dppz)]PF_6 (0.06 g, 0.08 mmol) and $AgNO_3$ (0.03 g, 0.18 mmol, 2.2 eq) were refluxed in ethanol/water (3:1) (40 mL) for five hours. After cooling to room temperature the solution was filtered through celite (to remove solid AgCl). To the solution, excess (*D*)-tert-butyl 2-(isonicotinamido)propanoate (D-alaiso) (0.05 g, 0.20 mmol) was added and refluxed overnight. After cooling to room temperature the solution was filtered again through celite and aqueous NH_4PF_6 was added. The precipitate was collected by filtration and washed with water, diethyl ether and then dried under vacuum. Mass = 0.056 g (62.5 %) orange solid. ^1H NMR (acetone-d_6): δ 5.75 (s, 1H), 6.30 (m, 1H), 6.90 (m, 1H), 7.01 (m, 2H), 7.80 (m, 2H), 8.25 (m, 4H), 8.60 (m, 5H), 8.80 (dd, 2H), 8.90 (dd, 2H), 9.45 (dd, 2H), 9.90 (m, 3H). MS m/z (%): 993 (50) [M^+], 847 (30) [M^{2+}], 597(100) [M^{2+}-(D-alaiso)].

7.10.27 Synthesis of [Ru(tpm)(dppz)(*L*-his)]$(PF_6)_2$ (*L*)-[5.3]

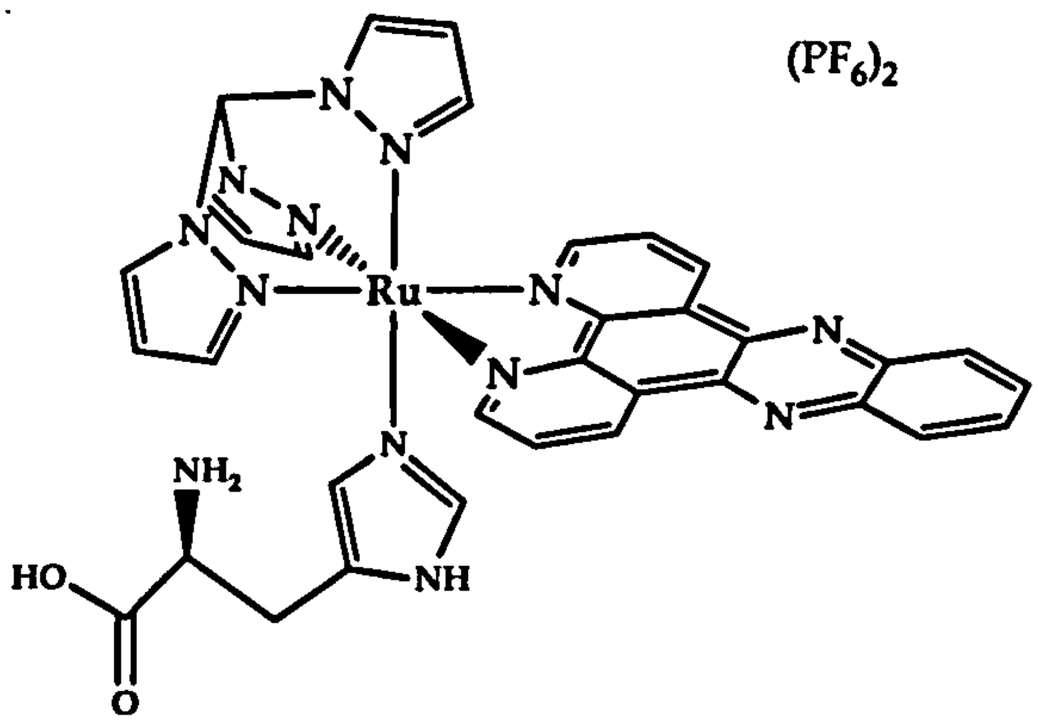

[Ru(tpm)(Cl)(dppz)]PF_6 (0.15 g, 0.20 mmol) and $AgNO_3$ (0.07 g, 0.41 mmol, 2 eq) were refluxed in ethanol/water (3:1) (40 mL) for five hours. After cooling to room temperature the solution was filtered through celite (to remove solid AgCl). To the solution, excess *L*-histidine (L-his) (0.25 g, 1.6 mmol, 8 eq.) was added and heated at gentle reflux for two days under argon atmosphere. After cooling to room temperature the solution was filtered again through celite and aqueous NH_4PF_6 was added. The precipitate was collected by filtration and washed with water, diethyl ether and then dried under vacuum. Mass = 0.065 g (31.2 %) orange solid. ^1H NMR (DMSO-d_6): δ 5.80 (s, 2H), 6.30 (m, 1H), 6.90 (m, 1H), 7.01 (m, 2H), 7.45 (s, 2H), 8.10

(m, 2H), 8.25 (m, 2H), 8.30 (s, 1H), 8.45 (d, 2H), 8.60 (m, 3H), 8.75 (dd, 2H), 9.10 (dd, 2H), 9.75 (dd, 2H), 10.05 (s, 1H). MS m/z (%): 898 (50) [M^+], 752 (100) [M^{2+}], 597 (80) [M^{2+}-(L-his)].

7.10.28 Synthesis of [Ru(tpm)(dppz)(*D*-his)]$(PF_6)_2$ (*D*)-[5.3]

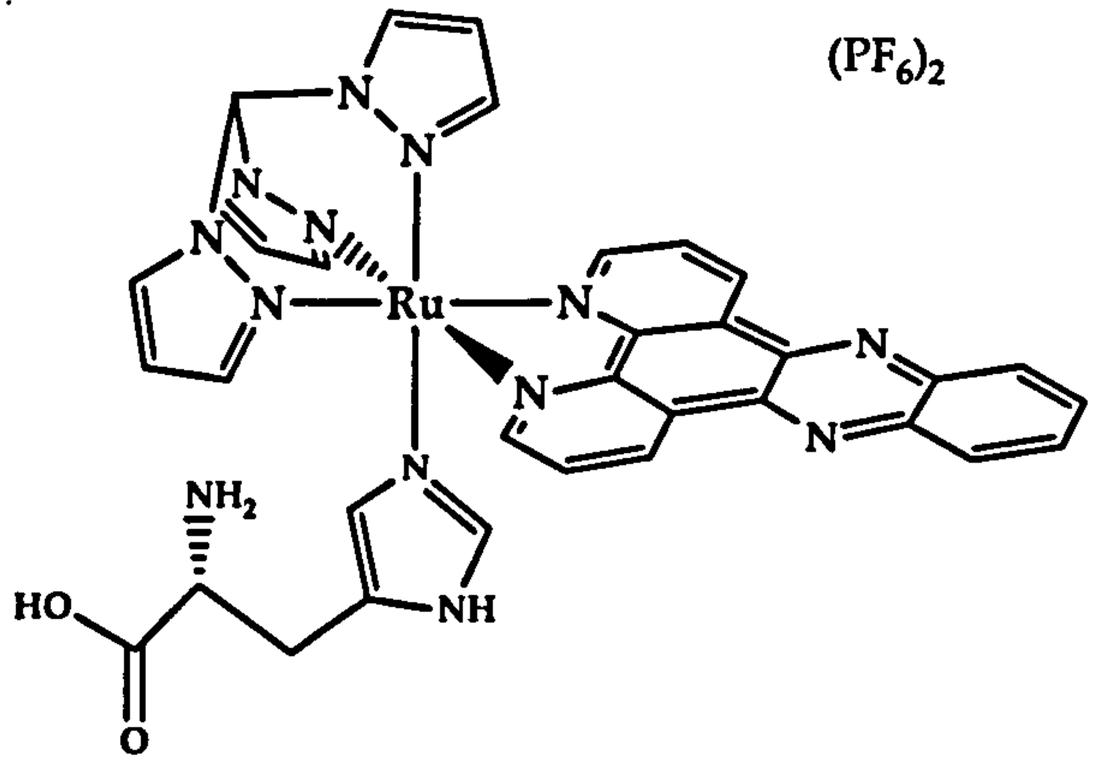

[Ru(tpm)(Cl)(dppz)]PF_6 (0.08 g, 0.10 mmol) and $AgNO_3$ (0.035 g, 0.20 mmol, 2.1 eq) were refluxed in ethanol/water (3:1) (40 mL) for five hours. After cooling to room temperature the solution was filtered through celite (to remove solid AgCl). To the solution, excess *D*-histidine (D-hist) (0.10 g, 0.64 mmol, 6.4 eq.) was added and heated at gentle reflux for two days under argon atmosphere. After cooling to room temperature the solution was filtered again through celite and aqueous NH_4PF_6 was added. The precipitate was collected by filtration and washed with water, diethyl ether and then dried under vacuum. Mass= 0.05 g (47.95 %) orange solid. ^{1}H NMR (DMSO-d_6 δ 5.80 (s, 2H), 6.30 (m, 1H), 6.90 (m, 1H), 7.01 (m, 2H), 7.45 (s, 2H), 8.10 (m, 2H), 8.25 (m, 2H), 8.30 (s, 1H), 8.45 (d, 2H), 8.60 (m, 3H), 8.75 (dd, 2H), 9.10 (dd, 2H), 9.75 (dd, 2H), 10.05 (s, 1H). MS m/z (%): 898 (20) [M^+], 752 (85) [M^{2+}], 597(100) [M^{2+}-(D-his)].

7.10.29 Synthesis of [Ru(tpm)(Cl)(dppn)]PF_6 [5.5]

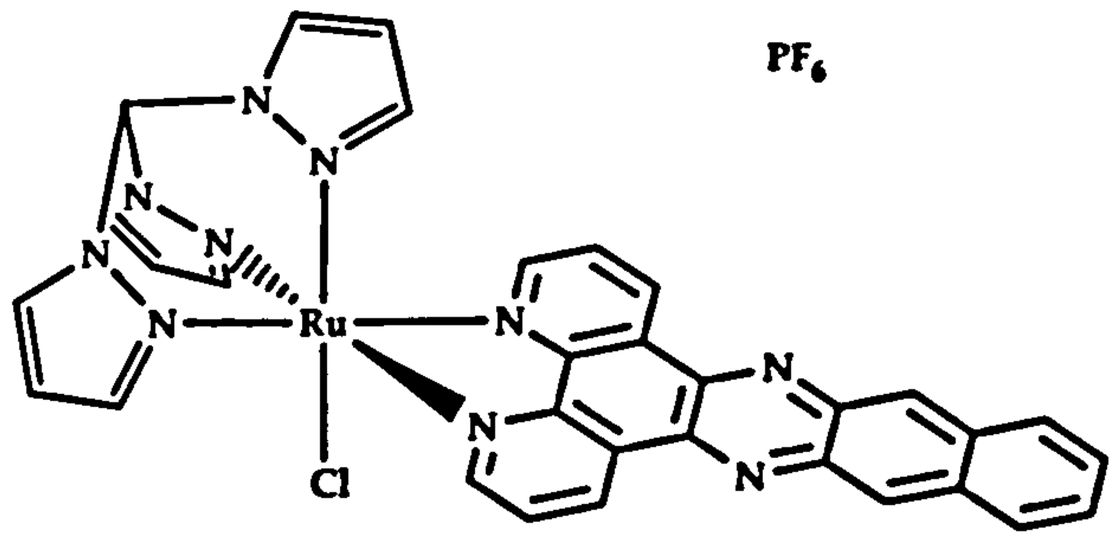

$RuCl_3(tpm)\cdot 3H_2O$ (0.218 g, 0.46 mmol) and dppn (0.21 g, 0.63 mmol, 1.3 eq) were refluxed in ethylene glycol (60mL) at 120°C for four hours. After cooling at room temperature, the solution was poured into methanol and filtered through celite. Aqueous NH_4PF_6 was added to the solution and the precipitate formed was collected by filtration, washed with water and dried under vacuum. The dark brown solid was chromatographed on grade I alumina with acetonitrile: toluene (1:1) as an eluent. The brown band was collected and concentrated by rotary evaporation. Addition of diethyl ether precipitated the product. Mass = 0.18 g (47.25 %) dark brown solid. ^1H NMR (CD_3CN-d_6): δ 6.27 (t, 1H), 6.69 (d, 1H), 6.82 (t, 2H), 7.69 (dd, 2H), 8.04 (dd, 2H), 8.32 (dd, 2H), 8.37 (d, 1H), 8.51 (m, 4H), 9.00 (s, 1H), 9.04 (s, 2H), 9.10 (dd, 2H), 9.64 (dd, 2H). MS m/z (%): 683 (100) [M^+], 647 (15) [M^+-(Cl)].

7.10.30 Synthesis of [Ru(tpm)(dppn)(Nic)]$(PF_6)_2$ [5.6]

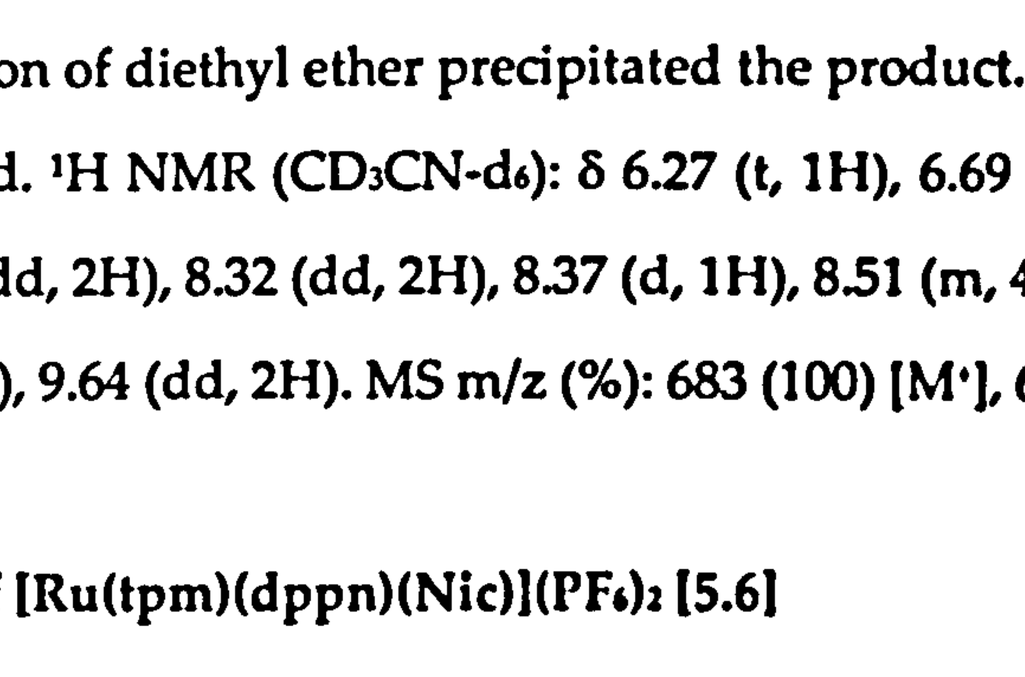

[Ru(tpm)(Cl)(dppn)]PF_6 (0.03 g, 0.04 mmol) and $AgNO_3$ (0.015 g, 0.09 mmol, 2.2 eq.) were refluxed in ethanol/water (3:1) (40 mL) for five hours. After cooling to room temperature the solution was filtered through celite (to remove solid AgCl). To the solution, excess nicotinamide (Nic) (0.05 g, 0.41 mmol, 10.2 eq.) was added and refluxed overnight. After cooling to room temperature the solution was filtered again through celite and aqueous NH_4PF_6 was added. The precipitate was collected by filtration and washed with water, diethyl ether and then dried under vacuum. Mass = 0.072g (67.2 %) orange solid. ^1H NMR (acetone-d_6): δ 6.34 (m, 1H), 6.98 (m, 2H), 7.06 (d, 1H), 7.20 (dd, 1H), 7.81 (m, 2H), 7.98 (d, 1H), 8.25 (m, 4H), 8.48 (m, 2H), 8.55 (m, 2H), 8.89 (d, 2H), 9.27 (s, 2H), 9.41 (s, 2H), 9.90 (d, 2H), 10.05 (s, 1H). MS m/z (%): 915 (80) [M^+], 769 (57) [M^{2+}], 647 (100) [M^{2+}-(nic)].

7.10.31 Synthesis of [Ru(tpm)(dppn)(4-NH_2py)]$(PF_6)_2$ [5.7]

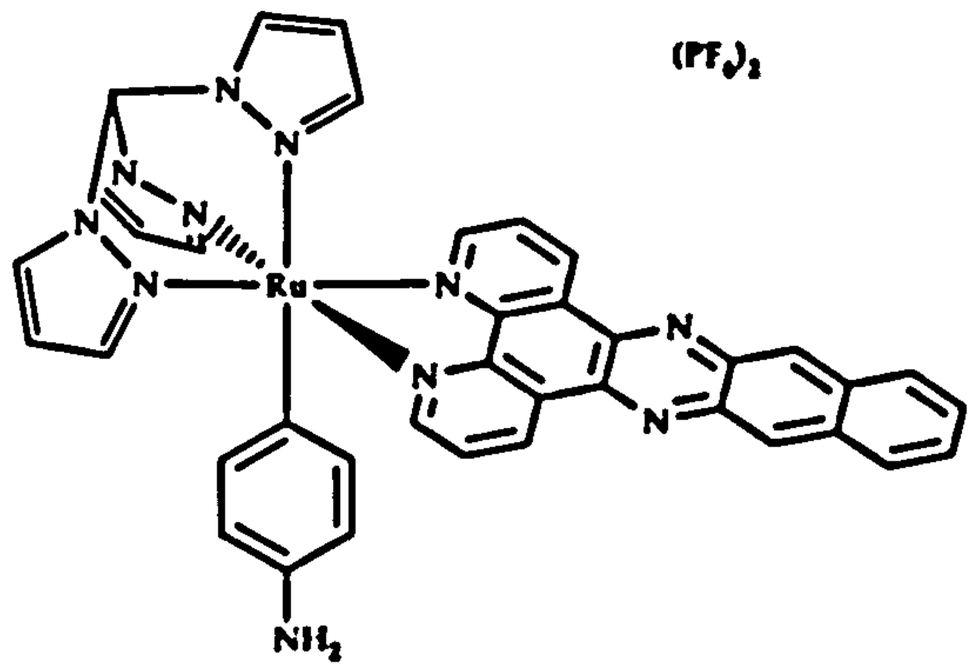

[Ru(tpm)(Cl)(dppn)]PF_6 (0.043 g, 0.05 mmol) and $AgNO_3$ (0.02 g, 0.12 mmol, 2.4 eq) were refluxed in ethanol/water (3:1) (40 mL) for five hours. After cooling to room temperature the solution was filtered through celite (to remove solid AgCl). To the solution, excess 4-aminopyridine (4-NH_2py) (0.05 g, 0.53 mmol, 10.6 eq.) was added and refluxed overnight. After cooling to room temperature the solution was filtered again through celite and aqueous NH_4PF_6 was added. The precipitate was collected by filtration and washed with water, diethyl ether and then dried under vacuum. Mass = 0.03 g (60 %) orange solid. ^1H NMR (DMSO-d_6): δ 6.20 (dd, 2H), 6.30 (m, 1H), 6.55 (s, 2H), 6.75 (d, 2H), 6.90 (m, 3H), 7.75 (m, 2H), 8.10 (m, 2H), 8.40 (d, 2H), 8.55 (m, 3H), 8.80 (d, 2H), 9.10 (dd, 2H), 9.35 (s, 2H), 9.75 (dd, 2H), 10.00 (s, 1H). MS m/z (%): 887 (100) [M^+], 741 (75) [M^{2+}], 647 (60) [M^{2+}-(4-NH_2py)].

7.10.32 Synthesis of [Ru(tpm)(Cl)(phen)]PF_6

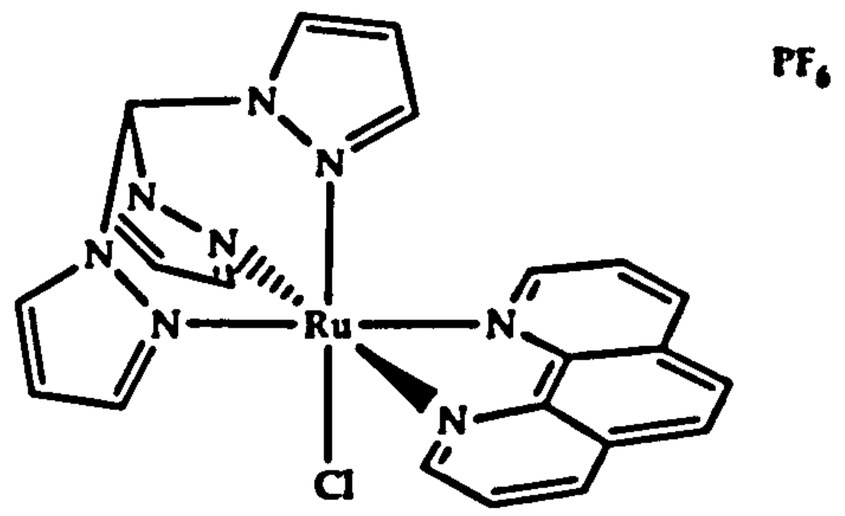

(tpm)$RuCl_3$ (0.19 g, 2.61 mmol), 1,10-phenanthroline (0.09 g, 2.66 mmol) and LiCl (0.11 g) were refluxed in ethanol: water (3:1) (30 mL) for ten minutes. Six drops of triethylamine were added and refluxing for half hour under nitrogen atmosphere. After cooling, the solvent was removed and the residue was dissolved in methanol (20 mL) and the fine dark solid was filtered out. The product was precipitated by addition of aqueous NH_4PF_6 and collected by filtration and washed with water, ethyl ether and dried under vacuum. Mass = 0.92 (52.14 %) dark solid. ^1H NMR (acetone-d_6): δ 6.30 (td, 1H), 6.87 (m, 3H), 8.06 (dd, 2H), 8.17 (dd, 2H), 8.42 (dd, 2H), 8.52 (dd, 2H), 8.57 (m, 3H), 9.17 (dd, 2H), 9.57 (dd, 2H), 9.63 (s, 1H). MS m/z (%): 531 (40) [M^+].

7.10.33 Synthesis of [Ru(tpm)(Py)(phen)]$(PF_6)_2$

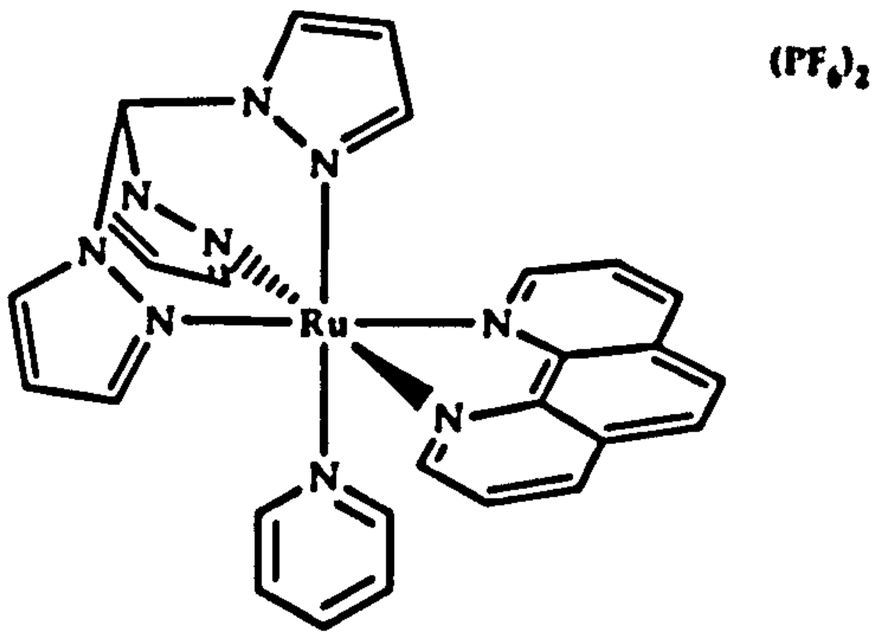

[RuCl(tpm)(phen)]PF_6 (0.04 g, 0.06 mmol) and $AgNO_3$ (0.02 g, 0.12 mmol, 2 eq) were refluxed in ethanol/water (3:1) (30 mL) for five hours. After cooling to room temperature the solution was filtered through celite (to remove solid AgCl). To the

solution, excess of pyridine (1mL, 10 eq.) was added and refluxed overnight. After cooling to room temperature the solution was filtered again through celite and aqueous NH_4PF_6 was added. The precipitate was collected by filtration and washed with water, diethyl ether and then dried under vacuum. Mass = 0.05 g (96.3 %) dark solid. ^1H NMR (acetone-d_6): δ 6.30 (m, 1H), 6.55 (dd, 1H), 6.98 (m, 2H), 7.75 (m, 2H), 8.05 (dd, 2H), 8.20 (m, 2H), 8.52 (dd, 3H), 8.70 (m, 2H), 8.90 (dd, 2H), 9.42 (dd, 2H), 9.87 (dd, 2H), 9.93 (s, 1H). MS m/z (%): 720 (20) [M^+], 589 (10) [M^{2+}], 495 (20) [M^{2+}-(Py)].

7.10.34 Synthesis of [Ru(tpm)(4-NH_2py)(phen)](PF_6)$_2$

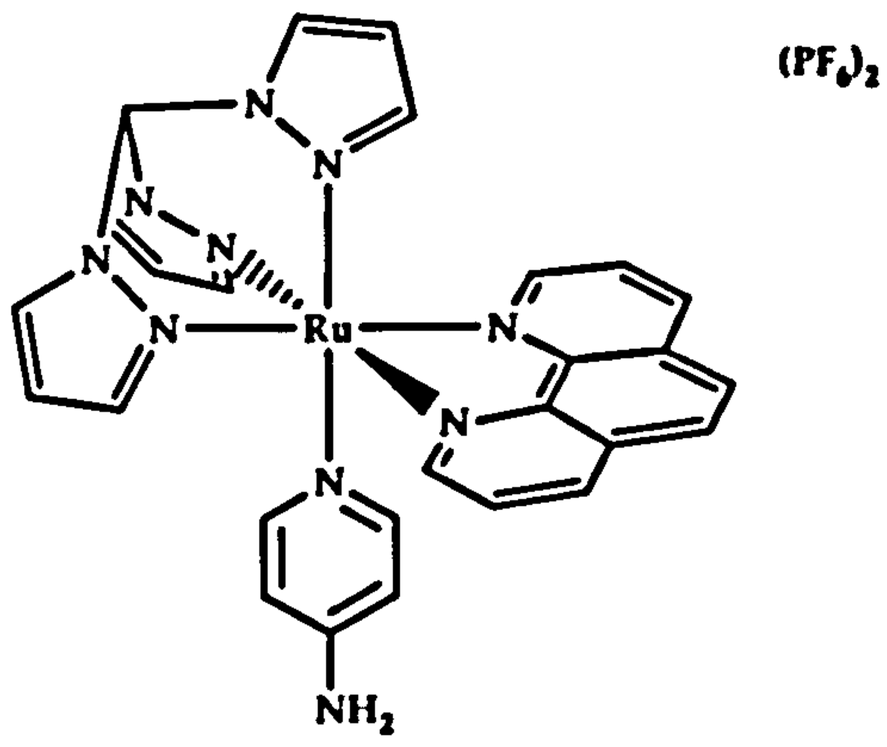

[Ru(tpm)(Cl)(phen)]PF_6 (0.04 g, 0.06 mmol) and $AgNO_3$ (0.03 g, 0.18 mmol, 3 eq) were refluxed in ethanol/water (3:1) (30 mL) for five hours. After cooling to room temperature the solution was filtered through celite. To the solution, excess 4-aminopyridine (4-NH_2py) (0.06g, 0.49 mmol, 8.2eq.) was added and refluxed overnight. After cooling to room temperature the solution was filtered again through celite and aqueous NH_4PF_6 was added. The precipitate was collected by filtration and washed with water, diethyl ether and then dried under vacuum. Mass = 0.03 g (56.85 %) dark solid. ^1H NMR (acetone-d_6): δ 6.10 (d, 2H), 6.30 (m, 1H), 6.55 (dd, 1H), 6.80 (m, 2H), 6.98 (m, 2H), 8.05 (dd, 2H), 8.20 (m, 2H), 8.52 (dd, 3H), 8.70 (m, 2H), 8.90 (dd, 2H), 9.42 (dd, 2H), 9.87 (dd, 2H), 9.93 (s, 1H). MS m/z (%): 735 (40) [M^+], 589 (10) [M^{2+}].

7.11 References

(1) Ren, J.; Chaires, J. B. *Biochemistry* 1999, *38*, 16067-16075.

(2) Reger, D. L.; Grattan, T. C.; Brown, K. J.; Little, C. A.; Lamba, J. J. S.; Rheingold, A. L.; Sommer, R. D. *J. Organomet. Chem.* 2000, *607*, 120-128.

(3) Paw, W.; Eisenberg, R. *Inorg. Chem.* 1997, *36*, 2287-2293.

(4) Yam, V. W.-W.; Lo, K. K.-W.; Cheung, K.-K.; Kong, R. Y.-C. *J. Chem. Soc., Chem. Commun.* 1995, 1191-1193.

(5) Garas, A. M. S.; Vagg, R. S. *J. Heretocyclic Chem.* 2000, *37*, 151-158.

(6) Gonzalez, V.; Adams, H.; Thomas, J. A. *Dalton Trans.* 2005, 110-115.

(7) Llobet, A.; Doppelt, P.; Meyer, T. J. *Inorg. Chem.* 1988, *27*, 514-520.

(8) Metcalfe, C., University of Sheffield, 2002.

(9) Foxon, S.; Metcalfe, C.; Adams, H.; Webb, M.; Thomas, J. A. *in preparation.*